TTI: 0-6937

Fracture Critical Steel Twin Tub Girder Bridges: Technical Report

Technical Report 0-6937-R1

Cooperative Research Program

TEXAS A&M TRANSPORTATION INSTITUTE
COLLEGE STATION, TEXAS

in cooperation with the
Federal Highway Administration and the
Texas Department of Transportation
http://tti.tamu.edu/documents/0-6937-R1.pdf

1. Report No. FHWA/TX-18/0-6937-R1	2. Government Accession No.	3. Recipient's Catalog No.

4. Title and Subtitle FRACTURE CRITICAL STEEL TWIN TUB GIRDER BRIDGES: TECHNICAL REPORT	5. Report Date Published: November 2018 6. Performing Organization Code
7. Author(s) Stefan Hurlebaus, John B. Mander, Tevfik Terzioglu, Natasha C. Boger, and Amreen Fatima	8. Performing Organization Report No. Report 0-6937-R1
9. Performing Organization Name and Address Texas A&M Transportation Institute The Texas A&M University System College Station, Texas 77843-3135	10. Work Unit No. (TRAIS) 11. Contract or Grant No. Project 0-6937
12. Sponsoring Agency Name and Address Texas Department of Transportation Research and Technology Implementation Office 125 E. 11th Street Austin, Texas 78701-2483	13. Type of Report and Period Covered Technical Report: September 2016–August 2018 14. Sponsoring Agency Code

15. Supplementary Notes

Project performed in cooperation with the Texas Department of Transportation and the Federal Highway Administration.
Project Title: Fracture Critical Steel Twin Tub Girder Bridges
URL: http://tti.tamu.edu/documents/0-6937-R1.pdf

16. Abstract

Steel twin tub girder bridges are an aesthetically pleasing structural option offering long-span solutions in tight radii-direct connectors. However, these bridges require a routine two-year inspection frequency, as well as a thorough hands-on inspection, because of their fracture critical designation. The heightened inspection requirements for fracture critical bridges come at a significant cost to the Texas Department of Transportation (TxDOT). Recent research has shown that tangent, or nearly tangent, twin steel tub girder sections can redistribute load to the intact girder after fracture of one of the girder bottom flanges. Additional research is required to develop recommendations for practical analysis of typical twin steel tub span configurations with the degree of curvature common to twin steel tub direct connectors. The finite element method (FEM) Abaqus and SAP2000 software for both rigorous FEM and grillage solutions, along with push-down plastic analyses, are typically available to TxDOT and its consultant bridge designers. These analysis and modeling methods take into account the capacity of the fractured girder, especially at the support locations, and realistically model the load distribution between the intact girder and the fractured girder. The modeling and analysis methods are incorporated in a straightforward manner on a large scale to the inventory of the steel tub bridges. The requirements outlined in the Federal Highway Administration memorandum, dated June 12, 2012, and titled “Clarification of Requirements for Fracture Critical Members,” were met in the employed analysis methods.

17. Key Words Twin Tub Girder, Fracture Critical, Parametric Study, Finite Element Analysis	18. Distribution Statement No restrictions. This document is available to the public through NTIS: National Technical Information Service Alexandria, Virginia http://www.ntis.gov

19. Security Classif.(of this report) Unclassified	20. Security Classif.(of this page) Unclassified	21. No. of Pages 470	22. Price

FRACTURE CRITICAL STEEL TWIN TUB GIRDER BRIDGES: TECHNICAL REPORT

by

Stefan Hurlebaus
Professor of Civil Engineering
Texas A&M University

John B. Mander
Zachry Professor of Civil Engineering
Texas A&M University

Tevfik Terzioglu
Post Doctorate Researcher
Texas A&M Transportation Institute

Natasha C. Boger
Graduate Research Assistant
Texas A&M Transportation Institute

and

Amreen Fatima
Graduate Research Assistant
Texas A&M Transportation Institute

Report 0-6937-R1
Project 0-6937
Project Title: Fracture Critical Steel Twin Tub Girder Bridges

Performed in cooperation with the
Texas Department of Transportation
and the
Federal Highway Administration

Published: November 2018

TEXAS A&M TRANSPORTATION INSTITUTE
College Station, Texas 77843-3135

DISCLAIMER

ACKNOWLEDGMENTS

This project was conducted in cooperation with TxDOT and FHWA. The authors thank Chris Glancy, Charlie Reed, Greg Turco, Jamie Farris, Jason Tucker, Steven Austin, Teresa Michalk, Yi Qiu, and Yongqian Lin.

TABLE OF CONTENTS

Page

List of Figures ..... **x**
List of Tables ..... **xv**
1 Introduction **1**
2 Literature Review **5**
2.1 Introduction 5
2.2 Approaches to Analyzing the Behavior of Bridge Structures 6
2.2.1 Elastic Structural Analysis 6
2.2.2 Plastic Methods of Analysis (Limit Analysis) 9
2.2.3 Computational Nonlinear Finite Element Solutions 13
2.3 Fatigue and Fracture in Bridges 13
2.3.1 Fatigue and Fracture Failures in Bridge Structures 14
2.3.2 Addressing Fatigue Problems by Design 17
2.4 Redundancy 19
2.5 Fracture Critical Investigations on Slab-on-Steel Girder Bridges 24
2.6 Fracture Critical Steel Twin Tub Girder Bridges 25
2.7 Research Questions Arising from Literature review 29
2.8 Recent Related Research 30
3 Computational Modeling of Fracture Critical Steel Twin Tub Girder Bridges **33**
3.1 Introduction 33
3.2 Description of the Test Bridge Used for Model Verification 34
3.2.1 Geometric and Material Properties 35
3.2.2 Experimental Methodology and Test Results 45
3.3 Nonlinear Finite Element Model of the Test Bridge 51
3.3.1 Inelastic Steel Model 53
3.3.2 Nonlinear Concrete Model 54
3.3.3 Modeling Shear Stud and Haunch Behavior 57
3.4 Verification of Finite Element Modeling Approach 60
3.4.1 Simulating the Vehicle Loading 60
3.4.2 Simulating the First Test (Bottom Flange Removal) 62
3.4.3 Simulating the Second Test (Removal of the Webs of the Fractured Girder) 63
3.5 Concluding Remarks 66
4 Parametric Study for Steel Twin Tub Girder Bridges Using Nonlinear Finite Element Analysis **67**
4.1 Introduction 67
4.2 Evaluation of TxDOT Steel Twin Tub Bridge Inventory 68
4.2.1 General 68
4.2.2 Distribution of Texas STTG Bridges 68
4.2.3 Selection of Fifteen Representative Steel Twin Tub Girder Bridges 71
4.3 Nonlinear Finite Element Model of Steel Twin Tub Girder Bridges 73
4.3.1 General 73
4.3.2 Element Type and Mesh Size 74
4.3.3 Constitutive Material Models 75

4.3.4 Simulating the Design Loading 79
4.4 Finite Element Analysis of Selected STTG Bridges 81
4.4.1 Bridge 0—FSEL Bridge 82
4.4.2 Bridge 1—NBI #12-102-3256-01-403 84
4.4.3 Bridge 2—NBI #12-102-0271-17-530 86
4.4.4 Bridge 3—NBI #12-102-0508-01-294 89
4.4.5 Bridge 4—NBI #12-102-0271-07-637 91
4.4.6 Bridge 5—NBI #14-227-0-0015-13-452 95
4.4.7 Bridge 6—NBI #12-102-0271-07-575 98
4.4.8 Bridge 7—NBI #12-102-0177-07-394 101
4.4.9 Bridge 8—NBI #12-102-0271-06-661 105
4.4.10 Bridge 9—NBI #12-102-0177-07-394 109
4.4.11 Bridge 10—NBI #14-227-0-0015-13-450 114
4.4.12 Bridge 11—NBI #12-102-0271-07-593 120
4.4.13 Bridge 12—NBI # 12-102-0271-07-639 125
4.4.14 Bridge 13—NBI #14-227-0-0015-13-452 130
4.4.15 Bridge 14—NBI #18-057-0-0009-11-460 134
4.4.16 Bridge 15—NBI #12-102-0271-06-689 138
4.5 Conclusions 142
5 Yield Line Analysis of Steel Twin Tub Girder Bridges 147
5.1 Introduction 147
5.2 Yield Line Theory 148
5.2.1 Internal Work Done 148
5.2.2 External Work Done 148
5.3 Validation of Yield Line Analysis with Experimental Results 150
5.3.1 General Overview of Collapse Mechanism 150
5.3.2 Potential Collapse Mechanisms for the Experimental Bridge 150
5.3.3 Bridge Specifications and Details 156
5.3.4 Ultimate Collapse Load 159
5.4 General Theory for Fracture Critical Sections 163
5.4.1 Virtual Work Equations 163
5.4.2 Overstrength Capacity for Factored Applied Loads for Single-Span Bridge 173
5.4.3 Analysis for Spans with Plastic End Moments 176
5.4.4 Location of Maximum Positive Moment for Collapse Analysis of Fractured Girder 179
5.5 Yield Line Analysis of Selected STTG Bridges 184
5.5.1 Bridge 1—NBI #12-102-3256-01-403 184
5.5.2 Bridge 2—NBI #12-102-0271-17-530 185
5.5.3 Bridge 3—NBI #12-102-0508-01-294 185
5.5.4 Bridge 4—NBI #12-102-0271-07-637 185
5.5.5 Bridge 5—NBI #14-227-0-0015-13-452 186
5.5.6 Bridge 6—NBI #12-102-0271-07-575 186
5.5.7 Bridge 7—NBI #12-102-0177-07-394 186
5.5.8 Bridge 8—NBI #12-102-0271-06-661 187
5.5.9 Bridge 9—NBI #12-102-0177-07-394 187
5.5.10 Bridge 10—NBI # 14-227-0-0015-13-450 187

5.5.11 Bridge 11—NBI #12-102-0271-07-593 ... 188
5.5.12 Bridge 12—NBI # 12-102-0271-07-639 ... 188
5.5.13 Bridge 13—NBI #14-227-0-0015-13-452 ... 188
5.5.14 Bridge 14—NBI #18-057-0-0009-11-460 ... 188
5.5.15 Bridge 15—NBI #12-102-0271-06-689 ... 189
5.6 Closure ... 190
6 Parametric Study for Steel Twin Tub Girder Bridges Using Grillage Method Push-Down Analysis ... 195
6.1 Introduction ... 195
6.2 Grillage Method Push-Down Analysis ... 196
6.2.1 Introduction ... 196
6.2.2 Material Models ... 197
6.2.3 Grillage Beam Elements ... 199
6.2.4 Grillage Plastic Hinges ... 201
6.2.5 Simulating HL-93 Loading ... 203
6.3 Grillage Analysis of Selected STTG Bridges ... 206
6.3.1 Grillage Analysis of Bridge 0—FSEL: TxDOT Project # 0-6937 ... 206
6.3.2 Grillage Analysis of Bridge 1—NBI #12-102-3256-01-403 ... 209
6.3.3 Grillage Analysis of Bridge 2—NBI #12-102-0271-17-530 ... 211
6.3.4 Grillage Analysis of Bridge 3—NBI #12-102-0508-01-294 ... 213
6.3.5 Grillage Analysis of Bridge 4—NBI #12-102-0271-07-637 ... 215
6.3.6 Grillage Analysis of Bridge 5—NBI #14-227-0-0015-13-452 ... 218
6.3.7 Grillage Analysis of Bridge 6—NBI #12-102-0271-07-575 ... 221
6.3.8 Grillage Analysis of Bridge 7—NBI #12-102-0177-07-394 ... 224
6.3.9 Grillage Analysis of Bridge 8—NBI #12-102-0271-06-661 ... 227
6.3.10 Grillage Analysis of Bridge 9—NBI #12-102-0177-07-394 ... 230
6.3.11 Grillage Analysis of Bridge 10—NBI #14-227-0-0015-13-450 ... 234
6.3.12 Grillage Analysis of Bridge 11—NBI #12-102-0271-07-593 ... 238
6.3.13 Grillage Analysis of Bridge 12—NBI #12-102-0271-07-639 ... 242
6.3.14 Grillage Analysis of Bridge 13—NBI #14-227-0-0015-13-452 ... 246
6.3.15 Grillage Analysis of Bridge 14—NBI #18-057-0-0009-11-460 ... 250
6.3.16 Grillage Analysis of Bridge 15—NBI #12-102-0271-06-689 ... 253
6.4 Conclusion ... 256
7 Discussion and Implications ... 259
7.1 Introduction and Scope ... 259
7.2 Single Spans (Zero Fixity at Supports) ... 259
7.3 Interior Spans with Two Degrees of Longitudinal Fixity ... 263
7.4 Exterior Spans (One Support Fixed, One Support Free) ... 268
8 Findings ... 283
References ... 285
Appendix A. Structural Drawings ... 1
Appendix B. Grillage ... 1

LIST OF FIGURES

Page

Figure 2.1. Silver Bridge After the Collapse in 1967 (NTSB 1971). 15
Figure 2.2. Collapse of the Mianus River Bridge (Fisher 1997). 16
Figure 2.3. Cracked Girder of the I-79 Glenfield Bridge in 1977 (Fisher 1984)......................... 17
Figure 2.4. STTG Bridge, I-35/US 290 Interchange, Austin, Texas (Coletti et al. 2005)........... 26
Figure 2.5. External Bracing Types: (a) K-type Cross-Frames; (b) Solid Diaphragms (Hunley and Harik 2012). 27
Figure 2.6. FSEL Bridge Test: (a) Surveyed Deflections and Assumed Yield Line; (b) Damaged Deck After Test (Samaras et al. 2012)... 29
Figure 2.7. Yield Line Model Adapted from Jackson and Middleton (2013) Showing Observed Cracks as Tested by Hazell (1999). 31
Figure 2.8. Beam Deflections Due to Scaled Ultimate Design Loads (Jiang 2015).................... 31
Figure 3.1. The FSEL Test Bridge (Barnard et al. 2010). 35
Figure 3.2. Typical Cross-Section of FSEL Test Bridge (TxDOT 1996)................................... 37
Figure 3.3. Plan View of FSEL Test Bridge with Cross-Bracing Stations (Neuman 2009)......... 38
Figure 3.4. Haunch Detail: (a) Cross-Section of Haunch; (b) Construction Photo Before Casting (Barnard et al. 2010). 39
Figure 3.5. Intermediate Diaphragm Details of FSEL Test Bridge (TxDOT 1996).................... 39
Figure 3.6. Typical Slab Section (TxDOT 2009). 40
Figure 3.7. Plan View of Tub Girder and Framing Plan (TxDOT 1996). 41
Figure 3.8. Elevation View of Tub Girder (TxDOT 1996)... 42
Figure 3.9. Tub Girder Cross-Section (TxDOT 1996). 43
Figure 3.10. Simulated HS-20 Truck Load on the FSEL Test Bridge (Neuman 2009). 46
Figure 3.11. Fractured and Intact Girder Deflections (adapted from Barnard et al. [2010])........ 47
Figure 3.12. Full-Depth Web Fracture and HS-20 Truck Load Positioning (Neuman 2009). 48
Figure 3.13. Scissor Jack with Explosive Tie Assembly (Neuman 2009)................................... 49
Figure 3.14. Fractured Girder Deflections Post Web Fracture (Neuman 2009).......................... 50
Figure 3.15. Bin Placement Diagram and Photo (Neuman 2009). 51
Figure 3.16. Constitutive Model for Steel Components (adapted from Barnard et al. [2010]).... 54
Figure 3.17. Concrete Compressive Strength from Cylinder Tests (Barnard et al. 2010)........... 55
Figure 3.18. Concrete Stress-Strain Behavior for Damaged Plasticity Model. 56
Figure 3.19. Mechanical Constitutive Model for Shear in Stud-Haunch Connections. 59
Figure 3.20. Stud Pullout Behavior under Tension (Barnard et al. 2010). 59
Figure 3.21. Finite Element Model of the STTG Test Bridge... 60
Figure 3.22. Comparison of FEM Deflection Profile with Test Results under Vehicle Loading. 62
Figure 3.23. Comparison of FEM Deflection Profile with Test Results After Bottom Flange Fracture. 63
Figure 3.24. FEM Deflection Profile Following the Fracture of the Web.................................. 64
Figure 3.25. Comparison of FEM Deflection Profile with Test Results After Web Fracture...... 65
Figure 3.26. FEM von Mises Stress Results Showing the Stress Concentration Web Fracture... 66
Figure 4.1. Distribution of Texas STTG Bridges by Maximum Span Length. 69
Figure 4.2. Distribution of Texas STTG Bridges by Curvature. 69
Figure 4.3. Distribution of Texas STTG Bridges by Number of Continuous Spans................... 70

Figure 4.4. Span vs. Curvature Scatter of Simple-Span STTG Bridges in Texas. 71
Figure 4.5. Span vs. Curvature Scatter of Two-Span STTG Bridges in Texas. 72
Figure 4.6. Span vs. Curvature Scatter of Three-Span STTG Bridges in Texas. 72
Figure 4.7. Mesh Details and Finite Element Types Shown on a Typical STTG Bridge............ 75
Figure 4.8. Constitutive Model for Steel Components (adapted from Barnard et al. [2010]). 76
Figure 4.9. Concrete Stress-Strain Behavior for Damaged Plasticity Model. 77
Figure 4.10. Constitutive Shear Model of Stud-Haunch Connection—Bridge 1. 78
Figure 4.11. Stud Pullout Behavior—Bridge 1.. 79
Figure 4.12. HL-93 Load Position for Two-Lane-Loaded Case.. 80
Figure 4.13. FEM Deflection Profile of Bridge 0 with Fractured Outside Girder....................... 83
Figure 4.14. FEM Results for Bridge 0.. 83
Figure 4.15. FEM Deflection Profile of Bridge 1 with Fractured Outside Girder....................... 85
Figure 4.16. FEM Results for Bridge 1.. 86
Figure 4.17. FEM Deflection Profile of Bridge 2 with Fractured Outside Girder....................... 88
Figure 4.18. FEM Results for Bridge 2.. 88
Figure 4.19. FEM Deflection Profile of Bridge 3 with Fractured Outside Girder....................... 90
Figure 4.20. FEM Results for Bridge 3.. 91
Figure 4.21. FEM Deflection Profile of Bridge 4, Span 1, with Fractured Outside Girder.......... 93
Figure 4.22. FEM Results for Bridge 4, Span 1... 94
Figure 4.23. FEM Deflection Profile of Bridge 4, Span 2, with Fractured Outside Girder.......... 94
Figure 4.24. FEM Results for Bridge 4, Span 2... 95
Figure 4.25. FEM Deflection Profile of Bridge 5 with Fractured Outside Girder....................... 97
Figure 4.26. FEM Results for Bridge 5, Spans 1 and 2. 98
Figure 4.27. FEM Deflection Profile of Bridge 6 with Fractured Outside Girder..................... 100
Figure 4.28. FEM Results for Bridge 6, Spans 1 and 2. 101
Figure 4.29. FEM Deflection Profile of Bridge 7, Span 1, with Fractured Outside Girder........ 104
Figure 4.30. FEM Results for Bridge 7, Span 1... 104
Figure 4.31. FEM Deflection Profile of Bridge 7, Span 2, with Fractured Outside Girder........ 105
Figure 4.32. FEM Results for Bridge 7, Span 2... 105
Figure 4.33. FEM Deflection Profile of Bridge 8, Span 1, with Fractured Outside Girder........ 108
Figure 4.34. FEM Results for Bridge 8, Span 1... 108
Figure 4.35. FEM Deflection Profile of Bridge 8, Span 2, with Fractured Outside Girder........ 109
Figure 4.36. FEM Results for Bridge 8, Span 2... 109
Figure 4.37. FEM Deflection Profile of Bridge 9, Span 1, with Fractured Outside Girder........ 112
Figure 4.38. FEM Results for Bridge 9, Span 1... 112
Figure 4.39. FEM Deflection Profile of Bridge 9, Span 2, with Fractured Outside Girder........ 113
Figure 4.40. FEM Results for Bridge 9, Span 2... 113
Figure 4.41. FEM Deflection Profile of Bridge 9, Span 3, with Fractured Outside Girder........ 114
Figure 4.42. FEM Results for Bridge 9, Span 3... 114
Figure 4.43. FEM Deflection Profile of Bridge 10, Span 1, with Fractured Outside Girder...... 117
Figure 4.44. FEM Results for Bridge 10, Span 1... 118
Figure 4.45. FEM Deflection Profile of Bridge 10, Span 2, with Fractured Outside Girder...... 118
Figure 4.46. FEM Results for Bridge 10, Span 2... 119
Figure 4.47. FEM Deflection Profile of Bridge 10, Span 3, with Fractured Outside Girder...... 119
Figure 4.48. FEM Results for Bridge 10, Span 3... 120
Figure 4.49. FEM Deflection Profile of Bridge 11, Span 1, with Fractured Outside Girder...... 122

Figure 4.50. FEM Results for Bridge 11, Span 1 123
Figure 4.51. FEM Deflection Profile of Bridge 11, Span 2, with Fractured Outside Girder 123
Figure 4.52. FEM Results for Bridge 11, Span 2 124
Figure 4.53. FEM Deflection Profile of Bridge 11, Span 3, with Fractured Outside Girder 124
Figure 4.54. FEM Results for Bridge 11, Span 3 125
Figure 4.55. FEM Deflection Profile of Bridge 12, Span 1, with Fractured Outside Girder 127
Figure 4.56. FEM Results for Bridge 12, Span 1 128
Figure 4.57. FEM Deflection Profile of Bridge 12, Span 2, with Fractured Outside Girder 128
Figure 4.58. FEM Results for Bridge 12, Span 2 129
Figure 4.59. FEM Deflection Profile of Bridge 12, Span 3, with Fractured Outside Girder 129
Figure 4.60. FEM Results for Bridge 12, Span 3 130
Figure 4.61. FEM Deflection Profile of Bridge 13, Span 1 and 3, with Fractured Outside Girder. 133
Figure 4.62. FEM Results for Bridge 13, Span 1 and 3. 133
Figure 4.63. FEM Deflection Profile of Bridge 13, Span 2, with Fractured Outside Girder 134
Figure 4.64. FEM Results for Bridge 13, Span 2 134
Figure 4.65. FEM Deflection Profile of Bridge 14, Span 1, with Fractured Outside Girder 137
Figure 4.66. FEM Results for Bridge 14, Span 1 137
Figure 4.67. FEM Deflection Profile of Bridge 14, Span 2, with Fractured Outside Girder 138
Figure 4.68. FEM Results for Bridge 14, Span 2 138
Figure 4.69. FEM Deflection Profile of Bridge 15, Span 1, with Fractured Outside Girder 141
Figure 4.70. FEM Results for Bridge 15, Span 1 141
Figure 4.71. FEM Deflection Profile of Bridge 15, Span 2, with Fractured Outside Girder 142
Figure 4.72. FEM Results for Bridge 15, Span 2 142
Figure 5.1. Different Probable Yield Line Mechanisms to Study the Model that Best Represents Collapse Mechanism Taking Place in Experimental Sand Loading Test. 153
Figure 5.2. Minimization Curves of Ultimate Static Load Generated for Sand Load on TxDOT Research Project 9-5498. 154
Figure 5.3. Probable Mechanisms Postulated. 155
Figure 5.4. Bridge Properties. 157
Figure 5.5. Critical Mechanism with the Inclined Negative Yield Lines Passing through Exterior Flange of the Outside Girder at the Supports 159
Figure 5.6. Folded Plate Mechanism for N Diagonal Yield Lines Showing (a) Plan View and Side Elevation Showing Deflection Profiles along D-D, E-E, and F-F; (b) Side Elevation Showing Deflection Profile along Sections A-A, B-B, and C-C; (c) Plan View Focusing on Half Bridge with N Diagonal Yield Lines and Side Elevation with Transverse Angular Deflection; and (d) Side View Showing Deflection Profiles with Longitudinal Deflections along Profile C-C. 164
Figure 5.7. Variation of Distributed Load with Number of Diagonal Yield Lines. 168
Figure 5.8. Strip Equivalent Mechanism. 171
Figure 5.9. Layout of a Generic Curved Bridge in Plan. 172
Figure 5.10. HL-93 Load Position for Two-Lane Loaded Case. 173
Figure 5.11. Critical Yield Line Mechanism for a Fractured Single-Span (9-5498). 174
Figure 5.12. Collapse Load Analysis of Interior Span of Continuous Bridges. 177
Figure 5.13. Collapse Load Analysis of End-Spans of Continuous Bridges. 179

Figure 5.14. Different Scenarios Used to Determine the Location of Maximum Positive Moment for Collapse Analysis. 181
Figure 5.15. Cumulative Distribution for λ = 0.4 and λ = 0.5. 183
Figure 5.16. Plan, Cross-Section, and Side Elevation with HL-93 Loading for Single-Span Bridges. 184
Figure 6.1. Constitutive Model for Steel Members (from SAP2000). 198
Figure 6.2. Constitutive Model of Concrete (from SAP2000). 199
Figure 6.3. Representative Longitudinal Grillage Members. 200
Figure 6.4. Representative Transverse Grillage Members. 201
Figure 6.5. Representative Grillage Schematic. 201
Figure 6.6. Representative Plastic Hinge Property (SAP2000). 203
Figure 6.7. HL-93 Loading Diagram for Two-Lane Loaded Case. 204
Figure 6.8. Grillage Deflection Profile of FSEL Bridge with Activated Hinges. 208
Figure 6.9. Grillage Analysis Results of FSEL Bridge. 208
Figure 6.10. Grillage Deflection Profile of Bridge 1 with Activated Hinges. 210
Figure 6.11. Grillage Analysis Results of Bridge 1. 210
Figure 6.12. Grillage Deflection Profile of Bridge 2 with Activated Hinges. 212
Figure 6.13. Grillage Analysis Results of Bridge 2. 212
Figure 6.14. Grillage Deflection Profile for Bridge 3 with Activated Hinges. 214
Figure 6.15. Grillage Analysis Results of Bridge 3. 214
Figure 6.16. Grillage Deflection Profile for Span 2 of Bridge 4 with Activated Hinges. 216
Figure 6.17. Grillage Analysis Results of Bridge 4, Span 1. 217
Figure 6.18. Grillage Analysis Results of Bridge 4, Span 2. 217
Figure 6.19. Grillage Deflection Profile for Span 1 of Bridge 5 with Activated Hinge. 220
Figure 6.20. Grillage Analysis Results of Bridge 5, Spans 1 & 2. 221
Figure 6.21. Grillage Deflection Profile for Spans 1 & 2 of Bridge 6 with Activated Hinges... 223
Figure 6.22. Grillage Analysis Results of Bridge 6, Spans 1 & 2. 223
Figure 6.23. Grillage Deflection Profile for Span 2 of Bridge 7 with Activated Hinges. 225
Figure 6.24. Grillage Analysis Results of Bridge 7, Span 1. 226
Figure 6.25. Grillage Analysis Results of Bridge 7, Span 2. 226
Figure 6.26. Grillage Deflection Profile for Span 2 of Bridge 8 with Activated Hinges. 229
Figure 6.27. Grillage Analysis Results of Bridge 8, Span 1. 229
Figure 6.28. Grillage Analysis Results of Bridge 8, Span 2. 230
Figure 6.29. Grillage Deflection Profile for Span 2 of Bridge 9 with Activated Hinges. 232
Figure 6.30. Grillage Analysis Results of Bridge 9, Span 1. 233
Figure 6.31. Grillage Analysis Results of Bridge 9, Span 2. 233
Figure 6.32. Grillage Analysis Results of Bridge 9, Span 3. 234
Figure 6.33. Grillage Deflection Profile for Span 2 of Bridge 10 with Activated Hinges. 236
Figure 6.34. Grillage Analysis Results of Bridge 10, Span 1. 237
Figure 6.35. Grillage Analysis Results of Bridge 10, Span 2. 237
Figure 6.36. Grillage Analysis Results of Bridge 10, Span 3. 238
Figure 6.37. Grillage Deflection Profile for Span 2 of Bridge 11 with Activated Hinges. 240
Figure 6.38. Grillage Analysis Results of Bridge 11, Span 1. 241
Figure 6.39. Grillage Analysis Results of Bridge 11, Span 2. 241
Figure 6.40. Grillage Analysis Results of Bridge 11, Span 3. 242
Figure 6.41. Grillage Deflection Profile for Span 2 of Bridge 12 with Activated Hinges. 244

Figure 6.42. Grillage Analysis Results of Bridge 12, Span 1. 245
Figure 6.43. Grillage Analysis Results of Bridge 12, Span 2. 245
Figure 6.44. Grillage Analysis Results of Bridge 12, Span 3. 246
Figure 6.45. Grillage Deflection Profile for Span 2 of Bridge 13 with Activated Hinges. 248
Figure 6.46. Grillage Analysis Results of Bridge 13, Spans 1 and 3... 249
Figure 6.47. Grillage Analysis Results of Bridge 13, Span 2. 249
Figure 6.48. Grillage Deflection Profile for Span 2 of Bridge 14 with Activated Hinges. 251
Figure 6.49. Grillage Analysis Results of Bridge 14, Spans 1 and 3... 252
Figure 6.50. Grillage Analysis Results of Bridge 14, Span 2. 252
Figure 6.51. Grillage Deflection Profile for Span 2 of Bridge 15 with Activated Hinges. 254
Figure 6.52. Grillage Analysis Results of Bridge 15, Spans 1 and 3... 255
Figure 6.53. Grillage Analysis Results of Bridge 15, Span 2. 255
Figure 7.1. Single Span with Zero Fixity at Supports... 260
Figure 7.2. Results for Short Single-Span (Simply Supported) Fractured Twin Tub Bridges ... 261
Figure 7.3. Results for Long Single-Span (Simply Supported) Fractured Twin Tub Bridges. .. 262
Figure 7.4. Interior Span with Fixities at Both Supports. 263
Figure 7.5. Results for Average Interior Spans of Fractured Twin Tub Bridges....................... 264
Figure 7.6. Results for Average Interior Spans of Fracture Twin Tub Bridges......................... 266
Figure 7.7. Results for Long Interior Spans of Fracture Twin Tub Bridges.............................. 267
Figure 7.8. Results for Very Long Interior Span of Fracture Twin Tub Bridges. 268
Figure 7.9. Exterior Span with Fixity at One Support. 269
Figure 7.10. Results for Short Exterior Spans of Fracture Twin Tub Bridges. 270
Figure 7.11. Results for Short Exterior Spans of Fracture Twin Tub Bridges. 271
Figure 7.12. Results for Short Exterior Spans of Fracture Twin Tub Bridges. 272
Figure 7.13. Results for Short Exterior Spans of Fracture Twin Tub Bridges. 273
Figure 7.14. Results for Short Exterior Span of Fracture Twin Tub Bridges. 274
Figure 7.15. Results for Average Exterior Spans of Fracture Twin Tub Bridges. 275
Figure 7.16. Results for Average Exterior Spans of Fracture Twin Tub Bridges. 276
Figure 7.17. Results for Average Exterior Spans of Fracture Twin Tub Bridges. 277
Figure 7.18. Results for Long Exterior Spans of Fracture Twin Tub Bridges........................... 278
Figure 7.19. Results for Long Exterior Spans of Fracture Twin Tub Bridges........................... 279
Figure 7.20. Results for Very Long Exterior Spans of Fracture Twin Tub Bridges.................. 280

LIST OF TABLES

Page

Table 3.1. FSEL Test Bridge Properties. 35
Table 3.2. Steel Reinforcing Bar Properties (Neuman 2009). 44
Table 3.3. Concrete Properties of Deck Slab and Railings (Neuman 2009). 44
Table 3.4. FSEL Test Bridge Steel Member Sizes. 45
Table 3.5. Mechanical Properties of Concrete at Different Ages. 57
Table 4.1. Range of Parameters Considered for the Bridge Selection. 70
Table 4.2. Main Geometric Properties of Selected Texas STTG Bridges. 73
Table 4.3. Geometric Properties and Member Dimensions of Bridge 1. 84
Table 4.4. Geometric Details of Steel Tub Girders for Bridge 1. 85
Table 4.5. Geometric Details of Steel Tub Girders for Bridge 2. 86
Table 4.6. Geometric Properties and Member Dimensions of Bridge 2. 87
Table 4.7. Geometric Properties and Member Dimensions of Bridge 3. 89
Table 4.8. Geometric Details of Steel Tub Girders for Bridge 3. 90
Table 4.9. Geometric Properties and Member Dimensions of Bridge 4. 92
Table 4.10. Geometric Details of Steel Tub Girders for Bridge 4. 92
Table 4.11. Geometric Details of Steel Tub Girders for Bridge 5. 96
Table 4.12. Geometric Properties and Member Dimensions of Bridge 5. 96
Table 4.13. Geometric Properties and Member Dimensions of Bridge 6. 99
Table 4.14. Geometric Details of Steel Tub Girders for Bridge 6. 99
Table 4.15. Geometric Details of Steel Tub Girders for Bridge 7. 102
Table 4.16. Geometric Properties and Member Dimensions of Bridge 7. 103
Table 4.17. Geometric Properties and Member Dimensions of Bridge 8. 106
Table 4.18. Geometric Details of Steel Tub Girders for Bridge 8. 107
Table 4.19. Geometric Properties and Member Dimensions of Bridge 9. 110
Table 4.20. Geometric Details of Steel Tub Girders for Bridge 9. 111
Table 4.21. Geometric Properties and Member Dimensions of Bridge 10. 115
Table 4.22. Geometric Details of Steel Tub Girders for Bridge 10. 116
Table 4.23. Geometric Properties and Member Dimensions of Bridge 11. 121
Table 4.24. Geometric Details of Steel Tub Girders for Bridge 11. 121
Table 4.25. Geometric Properties and Member Dimensions of Bridge 12. 126
Table 4.26. Geometric Details of Steel Tub Girders for Bridge 12. 126
Table 4.27. Geometric Properties and Member Dimensions of Bridge 13. 131
Table 4.28. Geometric Details of Steel Tub Girders for Bridge 13. 132
Table 4.29. Geometric Properties and Member Dimensions of Bridge 14. 135
Table 4.30. Geometric Details of Steel Tub Girders for Bridge 14. 136
Table 4.31. Geometric Properties and Member Dimensions of Bridge 15. 139
Table 4.32. Geometric Details of Steel Tub Girders for Bridge 15. 140
Table 4.33. Overstrength Factors for Single-Span STTG Bridges. 144
Table 4.34. Overstrength Factors for Exterior Spans of STTG Bridges. 145
Table 4.35. Overstrength Factors for Interior Spans of STTG Bridges. 146
Table 5.1. Internal Work Done Due to Deck Slab, Fractured Outside Girder, and Rail. 162
Table 5.2. Comparison of Overstrength Factors for Exterior Spans, Ω. 183

Table 5.3. Summary of Overstrength Factors for Single-Span Bridges. 185
Table 5.4. Summary of Overstrength Factors for Exterior Spans... 190
Table 5.5. Summary of Overstrength Factors for Interior Spans.. 190
Table 5.6. Overstrength Factors for 15 Selected STTG Bridges. 193
Table 6.1. Geometric Details of Steel Tub Girders for Bridge FSEL (0)................................... 206
Table 6.2. General Geometric Properties of Bridge FSEL (0). 207
Table 6.3. Geometric Details of Steel Tub Girders for Bridge 1.. 209
Table 6.4. General Geometric Properties of Bridge 1. 209
Table 6.5. Geometric Details of Steel Tub Girders for Bridge 2.. 211
Table 6.6. General Geometric Properties of Bridge 2. 211
Table 6.7. Geometric Details of Steel Tub Girders for Bridge 3.. 213
Table 6.8. General Geometric Properties of Bridge 3. 213
Table 6.9. Geometric Details of Steel Tub Girders for Bridge 4.. 215
Table 6.10. General Geometric Properties of Bridge 4. 216
Table 6.11. Geometric Details of Steel Tub Girders of Bridge 5. 218
Table 6.12. General Geometric Properties of Bridge 5. 219
Table 6.13. Geometric Details of Steel Tub Girders of Bridge 6. 222
Table 6.14. General Geometric Properties of Bridge 6. 222
Table 6.15. Geometric Details of Steel Tub Girders of Bridge 7. 224
Table 6.16. General Geometric Properties of Bridge 7. 225
Table 6.17. Geometric Details of Steel Tub Girders of Bridge 8. 228
Table 6.18. General Geometric Properties of Bridge 8. 228
Table 6.19. General Geometric Properties of Bridge 9. 231
Table 6.20. Geometric Details of Steel Tub Girders of Bridge 9. 232
Table 6.21. Geometric Details of Steel Tub Girders of Bridge 10. 235
Table 6.22. General Geometric Properties of Bridge 10. 236
Table 6.23. Geometric Details of Steel Tub Girders of Bridge 11. 239
Table 6.24. General Geometric Properties of Bridge 11. 240
Table 6.25. Geometric Details of Steel Tub Girders of Bridge 12. 243
Table 6.26. General Geometric Properties of Bridge 12. 244
Table 6.27. Geometric Details of Steel Tub Girders of Bridge 13. 247
Table 6.28. General Geometric Properties of Bridge 13. 248
Table 6.29. Geometric Details of Steel Tub Girders of Bridge 14. 250
Table 6.30. General Geometric Properties of Bridge 14. 251
Table 6.31. Geometric Details of Steel Tub Girders of Bridge 15. 253
Table 6.32. General Geometric Properties of Bridge 15. 254
Table 6.33. Overstrength Factors for Single-Span Bridges Utilizing Grillage Analysis............ 257
Table 6.34. Overstrength Factors for End Spans Utilizing Grillage Analysis............................ 257
Table 6.35. Overstrength Factors for Interior Spans Utilizing Grillage Analysis. 258
Table 7.1. Overstrength Results for Single-Span Twin Tub Girder Bridges.............................. 260
Table 7.2. Overstrength Results for Interior Span Twin Tub Girder Bridges. 265
Table 7.3. Overstrength Results for Exterior Span Twin Tub Girder Bridges. 281

1 INTRODUCTION

Twin tub girder bridges have the potential to serve as an engineering solution to the problem of long-span, curved bridges with tight radii of curvature. Particularly in the state of Texas, these bridges are becoming an alternative in lieu of the curved I-girder bridges. However, the major deterrent in the widespread reliance of these bridges is the classification of these bridges as fracture critical by the *Federal Highway Administration* (FHWA). The fracture critical designation leads to long term costs associated with hands-on inspections and fabrication of the fracture critical members (FCMs) according to the *American Welding Society* (AWS) Fracture Control Plan (FCP). There have been disastrous consequences in cases of failure of fracture critical bridges, that have elicited the need for rigorous hands-on inspections to avoid such terrible losses of life and property in the future. The *American Association of State Highway and Transportation Officials* (AASHTO) *Load and Resistance Factor Design* (LRFD) Bridge Design Specifications (AASHTO 2017)defines a FCM as a "component in tension whose failure is expected to result in the collapse of the bridge or the inability of the bridge to perform its function." Therefore, hands-on inspections are required to ensure the structure is safeguarded against fracture and fatigue failures. The hands-on inspection of these bridges are costing the Texas Department of Transportation (TxDOT) large sums of funds that could be allocated to address other problems since not all the twin tub girder bridges are truly fracture critical. The current definition of FCMs, based on only load path redundancy, is highly conservative, which deems all bridges as requiring elaborate and expensive inspections that deplete money and time. Instead of an elastic analysis that may be grossly underestimating the reserve capacity of the redundant structural members, a more realistic and exact elasto-plastic analysis is recommended for this research.

It is imperative to initiate an investigation to assess the relevance of the current classification of the twin tub girder bridges as fracture critical. A thorough analysis is needed to carry out the investigation aimed at reclassifying a bridge from its fracture critical status by proving sufficient reserve strength due to the structural redundancy of the superstructure. To execute an investigation, it is proposed that researchers conduct three independent analyses and compare the results to comprehend the behavior of these bridge superstructure systems in detail. The aim of all three methods is to find the overstrength of the twin tub girder bridges selected from the Texas Bridge inventory. The overstrength reflects the amount of reserve capacity the structural members possess when applied with factored design loads. The decision regarding the reclassification from the fracture critical status may be conclusively drawn if the scope of this research all three methods converge to a reasonable degree. Once it is identified that the three methods consistently predict sufficient reserve capacity, one or more methods may be recommended for implementation in the industry depending on the trends, if any, emerging from this research project. The three methodologies that are implemented are:

- An accurate and thorough computational finite element analysis.
- A yield line analysis based on the classical plastic theory.
- A lower-bound computational grillage method.

The finite element analysis implements the use of advanced elasto-plastic nonlinear elements to accurately simulate the material behavior and loading. The results generated from this method are considered the most accurate because the program utilizes advanced computational accuracy to model the system with high precision. Consequently, the procedure requires time and sophisticated computational resources. The plastic methods are employed to develop upper-bound (yield line theory) and lower-bound (strip method) solutions to calculate the reserve capacity manually. This gives a range of the overstrength factors to quickly compare with the computational methods. The grillage analysis (based on a lower-bound strip method) is conducted using nonlinear elasto-plastic material and hinge properties to model the behavior of the bridge under design vehicular loading. The computational push-down grillage analysis is carried out using the matrix methods of structural analysis in SAP2000. The grillage analysis can be considered as a practical blend of the advanced computational finite element analysis and the plastic method due to its nonlinear elasto-plastic modeling approach and its evolution from the lower-bound strip method.

The three methods are independently studied via extensive parametric studies and the veracity of each method is checked by validating the analytical results with those obtained experimentally from the TxDOT 9-5498 Project. The next stage of analyses involve the assessment of the overstrength factors of these bridges when analyzed under AASHTO load and resistance factor design (LRFD) loading. This research was aimed at equipping professional bridge engineers to apply the analytical methods to investigate the inherent reserve strength of the twin tub girder bridges so as to eliminate the FCM designation of the steel tub girders and reclassify them as system redundant members (SRMs) as defined by Federal Highway Administration (FHWA) memorandum HIBT-10 FHWA (2012). Since these are to be used on a large scale in the transportation industry, at least two of the three methods are meant to be practically feasible in terms of their economy and time commitment for industry standards. Thus, it is suggested that the simpler methods be used first to assess the overstrength of the bridges. In case of a large disparity between the methods, a more advanced and rigorous finite element analysis must be considered.

2 LITERATURE REVIEW

2.1 INTRODUCTION

Steel twin tub girder (STTG) bridges have become increasingly popular in Texas because they offer an engineering solution for long-span and/or curved highway bridges. STTG bridges appear in many different designs, and they vary in number of spans, span length, and degree of horizontal curvature. The twin box bridge superstructure has become more common due to reduced number of girder lines, higher torsional stiffness and more aesthetic superstructure option compared to curved I-girders. However, according to the AASHTO (2012) *Guide Specification for Fracture Critical Nonredundant Steel Bridge Members*, the choice of twin steel tub superstructures comes with additional inspection and fabrication cost due to their fracture critical designation. Fracture critical or nonredundant designation requires strict fatigue detail and design consideration, substantial testing during fabrication, and in-depth hands-on inspections compared to nonfracture critical structures because they consist of theoretically nonredundant structural systems. The rigorous frequent inspection requirement increases the life cycle cost of this class of bridge superstructure significantly.

STTG bridges require hands-on inspection every two years, which costs TxDOT about $2 million every two years, including the traffic control costs. Therefore, removing the fracture critical designation of some or all of these bridges may significantly lower the inspection cost of this bridge system. To be able to designate a two-girder bridge as redundant, it is necessary to show that the bridge has sufficient reserve capacity after the fracture of one of the girders. This outcome can be achieved through rigorous analysis techniques.

This chapter documents the state of the art and practice for the analysis of bridges and redundancy studies of fracture critical bridges. The opening subsection introduces the fracture critical twin tub girder bridges and describes the motivation for this research. In the second subsection, different methods of analysis are listed and briefly summarized. The third subsection presents the definition of fatigue and fracture and discusses several bridge failures due to fatigue and fracture. The fourth subsection introduces the concept of redundancy and the motivation for the initiation of fracture critical protocol. Different definitions provided in the design codes and specifications, along with different sources of redundancy, are also discussed in this subsection.

In the final subsection, relevant research about fracture critical bridges and modeling approaches for evaluating the redundancy of steel twin tub bridges are presented.

2.2 APPROACHES TO ANALYZING THE BEHAVIOR OF BRIDGE STRUCTURES

In structural engineering, physical phenomena are simulated using mathematical models that can represent the actual behavior of a structural system. Over the previous centuries, methods of structural analysis have developed and become more sophisticated as the ability to compute solutions has also improved. Indeterminate structural systems require solutions that concurrently deal with both equilibrium and compatibility of deformations. In contrast, if the compatibility condition is violated due to inelastic behavior but equilibrium is maintained, plastic solutions that provide collapse loads may be obtained. This subsection first describes historic to modern methods of elastic structural analysis. Next, plastic methods for both frames and slabs are discussed. The third and final part to this subsection describes nonlinear methods of analysis whereby computational solutions can give the entire solution from the initial elastic behavior to the plastic collapse load.

2.2.1 Elastic Structural Analysis

Linear analysis simply assumes that the load is proportional to displacement. Robert Hooke first introduced this principle in 1678, and it remains well known today as Hooke's law. Essentially, the Hooke's law stipulates that as force is related to stress and displacement to strains, they are also proportional to each other. Linear elastic analysis is based on the original undeformed geometry and elastic material properties. Analysis of structures using the mechanics of materials approach or the theory of elasticity are analytical formulations using linear elastic behavior; therefore, closed-form solutions may be obtained. Although most structural systems involve material and geometric nonlinearity, elastic analysis has been widely used due to its simplicity. Engineers still use linear elastic methods by some modification to consider nonlinearities. When predicting the ultimate strength or in-service deformations, the results of linear elastic analysis are adjusted, permitting a prescribed amount of moment redistribution. While it remains valid to use superposition for linear elastic analysis and then apply a measure of moment redistribution, it is not possible to assess the actual collapse load. However, if the provided capacity is greater than the load demands, some reserve capacity remains. Elastic solutions together with a limited amount of moment redistribution are lower-bound limit state solutions.

Linear elastic analysis may be used to estimate the actions and deflections of reinforced concrete structures under service loads, but care must be taken for reduced stiffness due to cracking resulting from loading or restraint to thermal and shrinkage effects. These additional reasons of material nonlinearity complicate the design process using linear elastic methods.

2.2.1.1 Beams and Frames

The simplified approach of using linear elastic behavior defined by Hooke's law enabled scientists to formulate mathematical models for many engineering problems. Bernoulli and Euler (1750) formulated differential equations for the deflection calculation of a beam. Euler derived equations to calculate deflection of beams and buckling load of beams, and his approach could be extended to calculate flexural stresses. The Euler-Bernoulli beam theory (EBT) for flexural behavior and stiffness was developed and evolved over some 300 years. In EBT, it is assumed that plain sections transverse to the longitudinal axis of the beam remain plane (straightness) and perpendicular to the axis after deformation (normality). In this so-called straight line theory, the transverse deflection of a beam is governed by a fourth-order differential equation. Although the derivation of analytical formulas originated back in 1700s, the results of EBT were not commonly used until the 19th century when wrought iron and later steel started to be used in large structures (Timoshenko 1953).

The theory of elasticity developed further in the second half of the 18th and throughout the 19th century. These developments made it possible to design and build relatively simple structures such as bridges. However, finding analytical solutions for mathematical models for complicated (indeterminate) structures led to large numbers of equations that were not easy to manage without modern computational methods. One of the early methods for analyzing statically indeterminate elastic structures was the force method, or flexibility method, that was initially developed by James Clerk Maxwell in 1874 and later improved upon by Heinrich Müller-Breslau. A breakthrough was made when Hardy Cross (1932) first introduced the iterative moment distribution method.

A significant development that led to computational analysis of structural systems was the development of matrix structural analysis (MSA). MSA was first used in the aerospace industry in the 1930s with formulations developed by Duncan and Collar (1934). Turner (1959) proposed the direct stiffness method (DSM) that created the framework for the finite element method. Later, Argyris and Kelsey (1960) described contrasting force and displacement-based matrix methods. These methods became solvable with early digital computers and were popular in the 1960s and beyond. MSA basically discretize the mathematical model and create the matrix formulation for an assembly of bar, beam, and/or beam-column members, which is then solved by computational tools.

2.2.1.2 Plates and Shells

In two-dimensional elasticity, the most basic member behavior is membrane that has in-plane stiffness only. This behavior is analogous to the bar element in one-dimension elasticity, in which the membrane cannot resist any bending moment. A plate is defined as a structural member that is thin, and its thickness is much smaller than its length or width. Like the beams, the transverse loads are carried by the bending actions of the plate. Plate behavior models out-of-plane bending stiffness only, and the member can resist bending moments. Various plate theories differ by their simplifying assumptions. The most commonly used one is the classical plate theory (Kirchhoff plate theory), which is a generalization of the Euler-Bernoulli beam theory. There are three main assumptions: (a) sections perpendicular to the mid-surface remain straight (straightness), (b) these sections also remain perpendicular to the mid-surface (normality), and (c) the thickness does not change during deflection (inextensibility). Based on these assumptions, the normal stresses in the transverse direction vanish (plane stress), and the transverse shear strains are neglected. However, for thick plates, significant shear strains may contribute to transverse stresses. The Mindlin plate theory includes the effect of transverse shear strains by removing the normality assumption, which is analogous to the Timoshenko beam theory (Timoshenko and Woinowsky-Krieger 1959). Shell behavior considers both in-plane stiffness (membrane behavior) and out-of-plane stiffness (plate bending) for modeling a two-dimensional structural member.

It is possible to simulate the behavior of a bridge superstructure as an orthotropic plate in order to get an analytical solution for the displacements and stresses and the eigenfrequencies (Hurlebaus 2007; Hurlebaus et al. 2001). An orthotropic plate is the common name for plates that have uniform but different elastic properties in the two orthogonal directions. In this method, the bridge superstructure is represented by an equivalent orthotropic plate with uniform thickness. Longitudinal stiffnesses are calculated based on the composite beam and slab section. Transverse stiffnesses are calculated based on the deck stiffness alone. This geometric simplification requires that the beams are equally spaced, which is generally the case in practice (Sanders and Elleby 1970). Based on these assumptions, the orthotropic plate behavior satisfies a fourth-order partial differential equation (Timoshenko and Woinowsky-Krieger 1959). Although this method is a way of obtaining the solution, it requires many approximations to reduce the three-dimensional complex bridge superstructure to a two-dimensional constant thickness plate.

2.2.2 Plastic Methods of Analysis (Limit Analysis)

Traditionally, the theory of elasticity has been widely used because it is relatively simple due to the assumption of proportional stress and strain. However, this approach cannot estimate the real behavior or safety at the limit state. Structural materials, especially steel, may withstand considerable strains beyond their initial yield strain. As a structural member is loaded beyond yield, the material behaves in a plastic fashion. Once a section reaches its load capacity, it deforms at almost constant load. This ultimate load capacity of the section is calculated from the material properties in the plastic range. The first critical section reaches the yield moment while other sections of the structure remain elastic. This state of the structure results in elastic-plastic deformations that eventually reach full plasticity as the loads are increased. When a full mechanism is achieved, the collapse load is reached.

In formulating plastic methods of analysis, there are two main theorems: (a) the lower-bound theorem that commonly uses graphical means or simplifying assumptions; and (b) the upper-bound theorem, where various mechanisms are assumed with the correct mechanism having the lowest load (least energy).

2.2.2.1 Beams and Frames

In using the LRFD approach, beams and frames are analyzed using elastic methods, while the reinforcement for beams and frames is calculated by strength methods that consider the inelastic properties at the ultimate load. Limit analysis does not have this inconsistency and accounts for redundancies and redistribution, thereby allowing more practical reinforcement design. The limit analysis of beams and frames can be achieved through either lower-bound graphical methods or upper-bound mechanism analysis. In either case, all plastic hinges must have adequate rotation capacity.

2.2.2.1.1 Lower-Bound Equilibrium Solution by Graphical Methods

The lower-bound analysis implies that the estimated capacity is smaller or equal to the true load capacity. The starting point of lower-bound graphical methods consists of (a) drawing moment diagrams for a statically determinate structure; (b) assigning fixing moments (the redundant actions); and (c) determining the required plastic capacity that is the largest moment. Note that this may not lead to a complete mechanism; thus, the solution is said to be lower bound.

2.2.2.1.2 Upper-Bound Plastic Mechanism Analysis by Virtual Work

The upper-bound method is used as follows: (a) various statically admissible mechanisms are postulated; (b) for each mechanism, the collapse load is determined using the principle of virtual work; and (c) the correct mechanism is that solution with the lowest collapse load. If the correct solution is not found, the obtained solution will be an upper bound to the true solution.

2.2.2.2 Slabs

Plastic analysis methods for estimating the ultimate capacity of beam and slab bridges have been used by many designers and researchers in the past. For example, the use of elastic analysis for estimating highly ductile, reinforced concrete bridge decks results in very conservative ultimate load predictions. The application of plastic analysis for slabs is relatively less tedious compared to beams and frames because slabs are generally under-reinforced and consequently have large rotational capacity. Practical techniques have been developed for the application of plastic methods to slabs by using limit analyses such as the upper-bound yield line analysis and the lower-bound strip method (Park and Gamble 2000).

Plastic methods of analysis for the analysis and design of bridge decks have long been available but rarely used in the United States. Limit analysis is particularly useful for investigating the possible failure modes, behavior beyond yielding, and residual capacity of in-service or deficient bridges. By investigating certain collapse mechanisms, it is possible to detect undesirable collapse mechanisms—such as shear failure, which is a sudden brittle failure mode—and adjust the design to get a more ductile behavior and get flexure mechanism at the ultimate load.

Jackson and Middleton (2013) recently developed a rigorous technique to obtain a yield line solution using an automated plastic lower-bound solution. This method eliminates the disadvantage of yield line analysis, which may result in unsafe capacity estimate if applied carelessly. The authors combined a safe lower-bound plastic analysis approach with a simpler yield line analysis. In this technique, the collapse load is estimated using an automatic analysis, where the viable moment field is calculated utilizing an optimization technique in which the moments are in equilibrium and do not violate yield condition, thus providing a lower-bound estimate. The locations that are close to yielding are marked, which eventually creates a yield line indicator diagram. Since the yield line indicators are found through a rigorous lower-bound method, the yield line analysis using this mechanism provides a realistic upper bound to the true collapse load.

2.2.2.2.1 Upper-Bound Yield Line Analysis

Ingerslev (1923) first demonstrated yield line behavior through experiments and analysis in the inaugural paper published by the *Journal of the Institution of Structural Engineers*. Later in Denmark, Johansen (1943) generalized a yield line theory. While linear elastic analysis can only predict the first yield at the section, yield line analysis gives more realistic ultimate capacity estimates for slabs. The only concern about yield line analysis is that it may estimate a higher, or at best equal, capacity to the true load carrying capacity. Thus, it requires experience to be able to establish reasonable or valid yield line mechanisms. In addition, the knowledge of reinforcement distribution is necessary at the start of the analysis, which means iterative procedure may be required for a specific design. However, this method can be very useful for analyzing existing structures. This principle can be also utilized for estimating the reserve capacity and redundancy of bridge decks for existing bridges. Because yield line theory generally provides upper-bound capacity estimates, it is essential to analyze a wide variety of possible kinematically admissible mechanisms in order to identify the critical yield line failure mode (Park and Gamble 2000).

Mander et al. (2011) utilized yield line analysis to estimate the failure mechanism for the interior portion of stay-in-place (SIP) precast panels with a cast-in-place (CIP) bridge deck under

a monotonic load that was representative of a tandem axle effect. When monotonically increasing path loads were applied, delamination occurred between the CIP concrete and the SIP panels, resulting in a compound shear-flexure mechanism. The authors derived an additive model of flexural yield line failure in the lower SIP precast prestressed panels and punching shear in the upper CIP-reinforced concrete. Three modes of failure in bridge decks were identified:
(a) flexure in CIP slabs common in thin slabs, (b) shear in CIP slabs that is a potential mode of failure in slabs without transverse reinforcement, and (c) membrane action that is considered a common failure mode in thick slabs with rigid boundary conditions. Based on the evaluation of the experimental results, a compound flexure-shear mechanism was proposed to explain the failures observed in dual, reinforced prestressed concrete bridge decks. The proposed additive shear-flexure model was able to model the experimental results well. However, the authors also noted that the mixed shear-flexure mode of failure that was observed in the laboratory experiments was not likely to occur in the field since the unrealistically high test pressures observed beneath the load plates cannot be achieved with rubber tire equipment. Still, the theory is useful to estimate the capacity and to aid in improved design and efficiency of SIP-CIP composite decks.

Pirayeh Gar et al. (2014) utilized yield line theory to analyze the ultimate load capacity of bridge deck slabs with precast panels prestressed with aramid fiber-reinforced polymer (AFRP) bars. The authors proposed equivalent plastic moment capacity for concrete sections with FRP to be used in the yield line analysis since the FRP concrete section does not have a distinct yield plateau. The results obtained from the experiment confirmed that the yield line theory is applicable to this new bridge deck system, and it was able to predict collapse loads within 3 percent of the observed test results.

2.2.2.2.2 Lower-Bound Strip Method

Hillerborg (1956) first developed strip methods for slabs. Strip methods provide lower-bound solutions that satisfy equilibrium and yield conditions (moments are always smaller than or equal to the plastic moment) everywhere in the slab. In contrast to yield line analysis, strip methods provide conservative (safe) capacity predictions. The strip method is a practical design method in which the reinforcement can be designed without any iterative process. Wood et al. (1968) later evaluated and improved the method regarding continuity conditions. Armer (1968) conducted an experimental study that tested half-scale slab specimens designed using the strip method. It was concluded that strip methods consistently produce safe designs.

2.2.3 Computational Nonlinear Finite Element Solutions

Physical systems are generally modeled using differential equations and corresponding boundary conditions. For real-world problems, such as complex structural shapes that include material nonlinearity, it is usually impossible to get a closed form analytical solution. It is a common practice to seek solutions using approximate and computational methods, such as finite difference, finite volume, and finite elements. The finite element method (FEM) is the most widely used technique due to its generality, versatility, and applicability to various differential equations. FEM is particularly useful for analyzing complex geometries, loadings, and material properties, which generally apply in real physical problems. In an FEM modeling approach, the structure is approximated with sets of elements having simple geometries such as triangles and rectangles. Each element satisfies the differential equation of the problem in hand and has the material properties of the structure, which forms the element stiffness relation. These elements are connected at their nodes to form the global stiffness relation for the whole structure by creating a set of algebraic relations.

Although it is not possible to clearly identify the inventor of FEM, Turner et al. (1956) generalized the direct stiffness method and created the FEM that was used in everyday engineering problems, starting with aerospace engineering. Later, E. L. Wilson (1958) developed the first open source computer program in FOR-TRAN II using IBM 704. Wilson`s work provided the basis for most of the early FEM programs (Felippa 2004). In the 1950s and 1960s, the FEM technology was transferred from aerospace engineering to a wide range of engineering applications by J. H. Argyris, R. W. Clough, H. C. Martin, and O. C. Zienkiewicz (Felippa 2004).

2.3 FATIGUE AND FRACTURE IN BRIDGES

Traffic loads on bridges cause stress cycling. Repeated stress cycling accumulates damage that may initiate fatigue cracks. If left unrepaired, the fatigue-induced cracks grow and lead to unstable growth and eventually fracture the material. Fatigue damage is prevalent in metal structures, particularly steel bridges. High-cycle fatigue failure is common in or near the connection of metal bridge components. Older metal bridges, whether constructed from wrought iron or steel, commonly show signs of distress at riveted connections. More modern steel bridge structures have the highest probability for fatigue failure at or near welded connections. This subsection outlines some classical fatigue and fracture failures and then goes on to describe how fatigue problems are categorized by design in accordance with AASHTO (2014) LRFD specifications. The subsection discusses fracture critical structural systems and how such systems are dealt with by design.

2.3.1 Fatigue and Fracture Failures in Bridge Structures

Figure 2.1 shows the infamous collapse of a typical fracture critical bridge, the Point Pleasant Bridge. Scheffey (1971) investigated the failure of the collapse of the Point Pleasant Bridge in December 1967 and reported that the collapse was due to failure of a single eye-bar connecting the suspension chain. The Point Pleasant Bridge, also known as Silver Bridge because of its silver-painted aluminum color, was opened in West Virginia over the Ohio River in 1928. The Silver Bridge was reported to be a “two-lane, 1760-foot-long eye-bar suspension bridge with a 700-foot main span 102 ft above the bottom of the Ohio River channel and two 380-foot anchor spans”, by the West Virginia Department of Transportation (WVDOT) on their webpage that mentions the facts about “Modern Bridges” (WVDOT 2016). The bridge design first called for conventional wire cables but was later modified to use eye-bar chains since they were less expensive. The Silver Bridge was the first eye-bar suspension bridge in the United States, and after nearly 40 years in use and a significant change in vehicle loads, the bridge collapsed during evening rush hour, killing 46 people and injuring nine. The Silver Bridge was inspected several times before the collapse, and even in the year of the collapse, two inspections occurred in the summer, with a final visit of the commission’s area maintenance engineer only nine days before the fatal failure (WVDOT 2016). Although the bridges that were constructed before 1985 did not have strict fatigue and fracture prevention requirements, there are very few examples of failure in the United States, including the Silver Bridge.

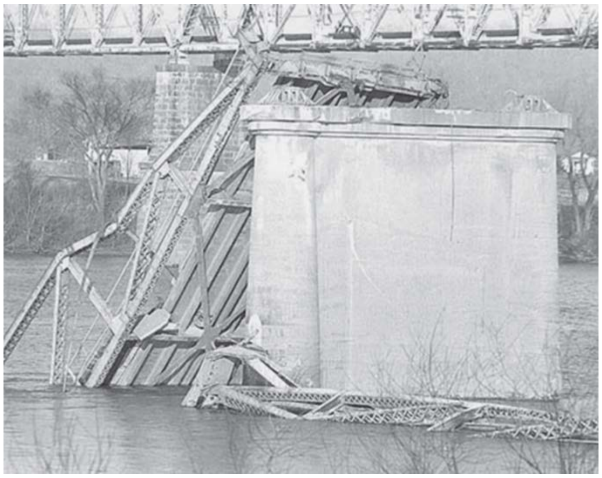

Figure 2.1. Silver Bridge After the Collapse in 1967 (NTSB 1971).

Barker and Puckett (2013) described the significant fracture critical bridge collapses that led to the development of more strict code provisions, namely the Silver Bridge and the Mianus River Bridge. All the other bridge collapses since 1950 were because of other unforeseen events such as accidents involving vehicles, ships, or natural disasters. The total collapse of the Silver Bridge had a significant influence on the design, selection of materials, and fabrication of future bridges and on the inspection of nonredundant bridges in the United States. In 1968, the National Bridge Inspection Standards (NBIS) were inaugurated under the Federal-Aid Highway Act, which prescribed that the time lag of an inspection of a bridge should not exceed two years.

In 1983, the Mianus River Bridge collapsed due to fatigue of the material, as shown in Figure 2.2 (Barker and Puckett 2013). The Mianus River Bridge was a “pin and hanger” bridge design that was commonly used in the year of construction because of the cheaper construction costs. The bridge collapsed after 25 years of service. Due to corrosion of storm drains that were installed 10 years before the collapse, the pin and hanger assemblies moved and shifted the weight to the outside hanger, which then had to carry all the weight, resulting in a fatigue crack. This fatigue crack caused the hanger to separate from the upper pin, and subsequently, the span of the bridge collapsed, and the span fell into the river. The Mianus River Bridge disaster should have been avoided because it had regular, but insufficient inspections. After the collapse of the Silver Bridge over the Ohio River, the Mianus River Bridge was inspected 12 times, with the last inspection only one year before the collapse. The inspectors only inspected the bridge visually from the ground with binoculars, so they could not identify the lateral displacement of the hangers. They noted “heavy rust on the top pins from water leaking through the expansion joints,” (Barker and Puckett 2013) but this was not relevant enough to foresee the collapse.

Figure 2.2. Collapse of the Mianus River Bridge (Fisher 1997).

After the publication of AASHTO guidelines for FCMs, the steel manufacturing industry and structural engineers adopted them successfully. Therefore, fatigue and fracture failures have been very rare in the last 35 years (Connor et al. 2005). Note, however, that both the Point Pleasant Bridge and the Mianus River Bridge were constructed before the implementation of the fracture critical bridge (FCB) inspection program. Several FCBs have experienced partial or full-depth fracture in the last 40 years. They were generally identified during periodic inspection but did not result in a collapse or loss of life. Apparently, secondary elements such as the deck, cross-bracing, or diaphragm helped to redistribute the load to other members.

Several total member failures of twin-girder bridges indicated that two-girder bridges offer somewhat of a redundant load path even though they are all declared fracture critical because of their composition. In May 1975, the Minnesota Department of Highways inspection personnel (now Minnesota Department of Transportation) discovered that one of the main girders of the Lafayette Street Bridge over the Mississippi River in St. Paul, Minnesota, had a full-depth fracture (Fisher et al. 1977). The crack was due to a fatigue crack; as a result, the bridge sagged 6.5 in. (165 mm) but did not collapse (Connor et al. 2005).

In January 1977, a tugboat captain discovered a large crack in a girder of the I-79 Glenfield Bridge, a two-girder tied arch bridge, over the back channel of the Ohio River (Fisher et al. 1980). After spotting the damage, observers watched the crack move up the web to the bottom of the flange in about one hour. Figure 2.3 shows the full-depth fracture of the girder. Obviously, the bridge had a redundant member that carried the load of the broken girder.

Figure 2.3. Cracked Girder of the I-79 Glenfield Bridge in 1977 (Fisher 1984).

However, none of these two given examples of girder bridges resulted in a collapse and provide evidence that two-girder bridges feature some redundancy in load path even though they are classified as fracture critical.

2.3.2 Addressing Fatigue Problems by Design

Fatigue is the structural damage of the material due to repeatedly applied loads. The damage occurs when the material is exposed to cyclic loadings, and the maximum load that initiates such damage may be much less than the capacity of the material, which is usually called yield stress limit. The material may experience progressive brittle cracking far below its yield stress due to the cyclic loadings. Cyclic loading is the repeated loading and unloading of the material, and the first microscopic brittle cracks develop where there are stress concentrations.

Much experimental research has been conducted to identify crack initiation (fatigue) and fracture propagation (fracture mechanics). However, all research and simulations on crack initiation are modeled on a macroscopic scale, and the first voids become visible at the size of 1 µm (Belak 1998), which indicates that the nucleation of tiny voids during the fatigue process has a microscopic start long before they may be identified. Fatigue has a significant influence on the lifetime of the structure because if the crack reaches a critical size, the crack size may increase rapidly, and the structure will fracture.

Fracture is the separation of a structural member into two or more independent pieces due to excessive stress or fatigue, and is of two types: ductile and brittle. The first type, the ductile fracture is the extensive permanent plastic deformation ahead of the crack, and the deformation is stable during the applied stress unless the load is increased. Most metal fractures may exhibit ductile characteristics when the applied load is increased continuously. First, the metal will deform elastically and will return to its original state when the applied load is removed until the yield point is reached. After exceeding the yield point, the curve typically decreases due to dislocation (Cottrell and Bilby 1949), and then the material will deform plastically until the ultimate strength is attained. The rupture of structural steel occurs after reaching the ultimate strength and passing the necking period, where the strain concentrates disproportionally in a small region of the material. The second type of fracture is the brittle fracture, which is how ceramics, cold metals, and ice break. Brittle fractures are characterized by possessing little or no plastic deformation. The crack appears quickly without an increase of an applied load and propagates rapidly.

A fracture initiated via fatigue stress cycling may also mean that brittle failure has progressed to unstable fracture propagation with the maximum (average) stress well below the yield stress limit. Therefore, fatigue design specifications for steel bridges were developed in the 1970s as a result of research studies conducted as part of an NCHRP project (Fisher 1970; Fisher et al. 1974). The use of floor beams or diaphragm plates connected to the flanges became a requirement in fatigue design specifications by 1985. These fatigue design specifications were adopted into AASHTO (1998) LRFD specifications in 1998. Modern steel bridges built after 1985 possess a high level of reliability in terms of fatigue due to current design and detailing requirements according to fatigue design specifications. Fatigue problems in bridges that were built according to current fatigue design provisions were typically due to design errors or unintended behavior.

The improved design specifications for modern steel bridges have two main aspects: (a) strict controls during the design and construction to prevent structural flaws and to assure sufficient material toughness, and (b) detailed inspection requirements to ensure that the defects are detected and repaired on time. The requirements for the manufacturing of steel girders and material toughness specifications assures high standards for modern bridges. In addition, high performance steel offers superior toughness that could reduce the need for some strict provisions for FCMs (Dexter et al. 2004). On the other hand, FHWA hands-on inspection requirements contain highly restrictive provisions even for newly built steel bridges. Although this inspection protocol may be necessary for older bridges built before 1985, the current inspection requirement does not differentiate between modern bridges and old bridges. Because of the restrictive fracture critical definition, numerous modern steel twin I-girder or twin tub girder bridges fall into the fracture critical category.

2.4 REDUNDANCY

The structural engineering community realized the importance of redundancy in steel bridges after the total collapse of the Silver Bridge in West Virginia in 1967 due to the failure of a single eye-bar connecting the suspension chain (Scheffey 1971). Code provisions and safety requirements were then modified for bridges susceptible to a fracture critical condition, where the failure of one member may lead to total collapse of the bridge. The concept of redundancy and definition of fracture critical members was first introduced into the AASHTO (1979) *Standard Specifications for Highway Bridges* after the release of the AASHTO (1978) *Guide Specification for Fracture Critical Nonredundant Steel Bridge Members*. However, the definition of redundancy and fracture critical members was vague and there remains no clear guidance on quantifying the level of redundancy. A fracture critical member is defined as a “component in tension whose failure is expected to result in the collapse of the bridge or the inability of the bridge to perform its function” in the current AASHTO (2017) *LRFD Bridge Design Specification*, but there are many other definitions, such as “a steel member in tension, or with a tension element, whose failure would probably cause a portion of or the entire bridge to collapse” in the NBIS (Lwin 2012).

Most of the U.S. and Canadian departments of transportation (DOTs) use the AASHTO or the NBIS definition for redundancy (Connor et al. 2005). In general, slab-on-girder type bridge superstructures are considered redundant when they have at least three girders, which is based on a load path consideration. This approach is quite conservative and does not take into account lateral distribution of loads through secondary elements from a damaged member to an undamaged member. In addition, internal redundancy and structural redundancy has not been taken into account for redundancy assessment. Early redundancy studies between the 1970s and late 1990s were conducted to develop tools for evaluating and measuring the redundancy levels in structural systems. This section summarizes several early studies conducted following the release of the AASHTO (1978) guide specifications, in which nonredundant bridges were defined as “structures where the failure of one member could cause collapse.” However, no objective way of measuring or defining redundancy was introduced.

Some twin girder bridges are likely to withstand service loads after the fracture of one member due to internal redundancy or alternate load paths such as bracings and bridge decks. One of the earliest studies about internal redundancy was carried out by Sweeney (1979). The author pointed out that riveted built-up members may provide internal redundancy; riveted members are not as critical as welded members in case of a fracture. Therefore, these differences should be identified to better quantify postfracture redundancy. Sweeney (1979)suggested that providing a redundant load path or a component redundant structure, such as in the case of riveted built-up structures, may be required to avoid fracture fractures.

Numerous other studies have focused on postfracture behavior by considering the alternative load path provided by bracing. Heins and Hou (1980) and Heins and Kato (1982) evaluated two girder steel bridge behavior after the major fracture of a girder. The findings suggest lateral bottom bracing and cross-bracing effectively transfer load to intact members, creating additional postfracture redundancy. Sandare (1983) investigated the redundancy of a steel truss bridge after the fracture of one mid-span truss. The bracing system was effective for transferring the loads, and all the members remained elastic under full service load with four HS-20 trucks including impact.

In the 1980s, researchers tried to develop guidelines and provisions to better define the redundancy of a bridge in the event of a full-depth fracture of a member. One of the early attempts was the study by Parmelee and Sandberg (1987). They suggested that more objective criteria and provisions should be developed to define redundant live load levels, allowable stress, and deflection limits after the fracture of a member in a nonredundant system.

Frangopol and Curley (1987) performed an analytical study to identify the effect of redundancy on the reliability of a bridge system. The authors defined redundant factors, *R*, for intact and damaged structures in order to quantify residual capacity. Equations (2.1) to (2.3) are used to find the overall strength of the system.

$$R_2 = \frac{L_{intact}}{L_{design}} \tag{2.1}$$

$$R_3 = \frac{L_{damaged}}{L_{intact}} \tag{2.2}$$

$$\Omega = R_2 R_3 = \frac{L_{damaged}}{L_{design}} \tag{2.3}$$

where R_2 = reserve redundant factor; R_3 = residual redundant factor; L_{intact} = load carrying capacity of the intact structure; L_{design} = design load; and $L_{damaged}$ = load carrying capacity of the damaged structure. The product of the reserve capacity and the residual capacity is a measure of the structure's reliability. It was suggested that R-factors may provide a deterministic way of measuring overall system strength.

Daniels et al. (1989) carried out a detailed analytical study investigating the redundancy of simple-span and continuous steel twin girder bridges with bracing systems. A fracture was assumed emanating from the bottom flange up the entire depth of the webs, but not into the compression flange. The postfracture behavior of twin girder steel bridges was evaluated in significant detail, using guidelines provided for assessing the redundancy through 3D analytical models or FEM analysis of an as-built structure with properly modeled bracings. It was concluded that twin girder steel bridges with properly designed bracing can provide significant redundancy following a near full-depth failure of one of the girders. Although the bracing may not be designed for redundancy, the bracing may provide a secondary load path following the fracture of one girder. The authors suggested that a redundancy rating based on 3D analytical models or computational FEM analysis may be used to develop a redundancy rating.

Ghosn and Moses (1998) defined redundancy as "the capability of a bridge superstructure to continue to carry loads after the damage or the failure of one of its members." A bridge system may be declared safe if it satisfies four criteria. First, the system must provide an appropriate safety level against member failure. Second, the system capacity of the bridge must not reach its maximum under extreme loading conditions. Third, the bridge must not deform largely under expected loading conditions, and fourth, the bridge must be able to carry some traffic loads after the failure of one of its members.

Ghosn and Moses (1998) also set objective criteria for estimating the residual capacity of bridges and provided guidelines accordingly. Their proposed approach utilizes statistical system factors to assess the level of redundancy of a member. Therefore, the overall system behavior is considered rather than the behavior of individual components. Current code requirements generally ignore the system effect and consider load path redundancy, which results in a conservative consideration. Their research suggested system factors that provide a sufficient level of redundancy for structural safety under service load conditions when the system reserve ratio for damaged condition is greater than 0.5, which means that the bridge capacity must be more than 50 percent of the capacity of the critical member. Equation (2.4) gives the formula for determining the reserve ratio for the system in damaged condition.

$$R_d = \frac{Lf_d}{LF_1} \tag{2.4}$$

where R_d = system reserve ratio for the damaged condition; LF_1 = the capacity of the bridge before failure of any member using elastic analysis; and Lf_d = the capacity of the damaged bridge before reaching ultimate load. Although different agencies and bridge designers have used the proposed approach, it has not been adopted into national bridge design specifications.

Connor et al. (2005) carried out a synthesis study as part of the *National Cooperative Highway Research Program (NCHRP) Report 354*, which focused on the inspection and maintenance of fracture critical bridges since the manufacturing costs were found to be small compared to mandated fracture critical inspection. As of 2005, they noted that around 76 percent of all FCBs were built prior to 1978. Eleven percent of all bridges in the United States have an FCM designation, and 83 percent of these bridges are two girder bridges or two line trusses, and 43 percent of the FCM are riveted members (Connor et al. 2005). The authors suggested that designers focus on a target reliability level rather than a redundancy level. They suggested that it is possible to achieve target reliability for a nonredundant bridge by providing about 17 percent conservatism in the design. One of the major contributions of this synthesis study was the compiled field information about the fracture incidents. Only two bridges, the Point Pleasant Bridge (constructed in 1928) and the Mianus River Bridge (constructed in 1957), had a total collapse due to fracture.

A technical memo entitled “Clarification of Requirements for Fracture Critical Members” (Lwin 2012b) pointed out the shortcomings of current redundancy definitions and recognized the system level performance as a way of evaluating redundancy. The concept of redundancy is critical for bridges because nonredundant bridges are classified as fracture critical. Although the term redundant is very intuitive for most structural engineers, there is no clear definition for measuring the redundancy level of a bridge superstructure. The AASHTO LRFD describes redundancy as “the quality of a bridge that enables it to perform its design function in a damaged state.”

Three different types of redundancy are defined (FHWA NBIS 2012):

- Load path redundancy.
- Structural redundancy.
- Internal redundancy.

A structure may be classified as redundant if it satisfies one or more of these redundancy criteria. Each of these are discussed in the following paragraphs.

Load path redundancy is relatively straightforward to identify because bridges having more than two girders are designated redundant, but some agencies even require four or more load carrying girders to be considered as load path redundant. If one of the girders would completely fracture or be unable to carry load, the load would be redistributed to the neighboring girders, and the bridge would be safe from a total collapse. Load path redundancy simply considers parallel primary load carrying members, which may be girders or trusses.

Structural redundancy is a function of static indeterminacy of the entire structure, which may be due to continuity of the bridge over interior supports or sometimes due to secondary members such as the deck. Continuous multi-span bridges possess structural redundancy and in case of a failure of one beam member, some load is redistributed from one span to another so that a total collapse of the bridge may be prevented.

Internal redundancy may be provided by member detailing to prevent fracture propagation through the entire cross-section. Internal redundancy exists in built-up members that have multiple parallel plates and other structural components within a member. A member is internally redundant if it has three or more similar elements connected together. If one of the elements fail, the load may be redistributed to the other elements, and the member will not fail. Internal redundancy ceases to exist when the member is repaired by welding the elements together. Welded members carry the load path from one element to the other and may be considered as one single member. In general, redundancy is determined by considering alternative load paths to identify FCBs. However recent experimental and analytical research has shown that certain bridges identified as nonredundant may have sufficient reserve capacity due to 3D system behavior and transverse load distribution through secondary load paths, such as the deck slab and/or cross-frames.

FCB designations have two main aspects: (a) design/fabrication requirement, and (b) inspection protocol. Currently, FHWA requires strict hands-on inspections for fracture critical bridges and FCBs have stricter fabrication requirements to meet the American Welding Society (AWS) Bridge Welding Code requirements. Although FHWA (2012) allows the use of rigorous analysis and consideration of system level redundancy for the inspection of in-service bridges, this approach is not allowed for fabrication protocols of steel twin tubs. Therefore, for fabrication, redundancy should be decided based on load path redundancy, and nonredundant tension members should conform to AASHTO LRFD, FCP, and AWS. This new classification is defined as a system redundant member, which is “a member that requires fabrication according to the AWS FCP, but need not be considered a FCM for in-service inspection,” as stated on the aforementioned FHWA technical memo webpage (Lwin 2012a).

2.5 FRACTURE CRITICAL INVESTIGATIONS ON SLAB-ON-STEEL GIRDER BRIDGES

Steel twin I-girder bridges are a popular system of construction used for both straight and curved bridges; this bridge system is designated as fracture critical due to a lack of load path redundancy (having less than three girder lines). Fasl et al. (2016) investigated the fatigue response of a fracture critical steel twin I-girder bridge that was built in 1935 over the Medina River and carry I-35 in Texas. The bridge features fatigue cracks along the weld at the top flange and lateral beam connections. The bridge was instrumented using strain gage and crack propagation gauges along the existing fatigue cracks. The behavior and crack propagation was monitored during rush hours. Due to the extent of the fatigue cracks, the girders were strengthened by installing bolted cover plates at critical locations, and the behavior was also monitored after the installation of those plates. The authors monitored the bridge for more than two months before strengthening and estimated the residual fatigue life of the structure. The bridge was also monitored during and after the strengthening. The authors reported that the built-up sections provide some level of internal redundancy because the fatigue cracks did not propagate into the webs. They also concluded that the strengthening method reduced the fatigue damage by providing composite action with the deck, and this procedure may be a potential rehabilitation for old bridges that exceed their original design life expectancy.

2.6 FRACTURE CRITICAL STEEL TWIN TUB GIRDER BRIDGES

Figure 2.4 presents a typical STTG bridge of the type that has become popular in Texas because they offer a solution for long-span and/or curved highway bridges in addition to providing an aesthetic structural option. STTG bridges consist of two steel girders that are the primary members for transmitting the dead load and live load to the substructure. On the other hand, concrete decks and stringers are secondary members that create a load path between girders (Daniels et al. 1989). Because of their fracture critical designation, STTG bridges require a hands-on inspection every two years. This rigorous inspection may include the testing of welds, nondestructive evaluation, and visual assessment. Procedures of nondestructive evaluation of steel members may “include dye penetrant, magnetic particle, or ultrasonic techniques” (TxDOT 2013a).

Most fracture critical designated bridges in the Texas Bridge inventory are steel twin tub girders, which automatically fall into the fracture critical category because they contain only two girder lines. Field testing of in-service bridges and experimental testing of full-scale bridges under controlled loading help to build up experimental data in order to assess the reliability level after the fracture of a load carrying member. Furthermore, these data enable researchers to verify different modeling approaches and develop modeling standards for evaluating redundancy levels due to internal redundancy, structural redundancy, or alternative load distributions through secondary members.

Coletti et al. (2005) provided guidelines and preliminary design suggestions for the design of steel tub girder bridges, including preliminary sizing and spacing considerations. They also discussed possible design issues, available analysis tools, and detailing of tub girders. The authors stated that steel twin tub girders are economical between a span range of 150 to 500 ft and also permit tight radius of curvature solutions and good aesthetics owing to the simple clean lines.

Figure 2.4. STTG Bridge, I-35/US 290 Interchange, Austin, Texas (Coletti et al. 2005).

Hunley and Harik (2012) investigated the effect of various secondary structural components for developing load transfer paths when one member of a twin steel tub bridge fails using a parametric, non-linear, finite element analysis. The variables that were studied in this investigation included location of damage, continuity, and span length. A load transfer mechanism from a fractured girder to the intact girder should develop in order to have a measure of redundancy. Figure 2.5 shows that for steel twin tub superstructures, it is only possible through concrete decks and/or external cross-frames. If the deck fails progressively following the failure of a girder, one should not rely only on the deck for lateral load transfer.

Hunley and Harik (2012) analyzed 33 bridge configurations to investigate reserve load capacities following the fracture of one member. The fracture of one of the girders was modeled by reducing the stiffness of the bottom flange line element and the web shell element. The damaged condition of the deck was modeled by reducing the stiffness of the individual finite element when it reached crushing strain. Redundancy levels of the analyzed bridges were calculated using the damaged condition capacity, R_d, as defined in *NCHRP Report 406*. The authors determined the capacity of the damaged bridge should be at least 50 percent of the capacity of the undamaged bridge to be classified as redundant. Based on the assessment of redundancy levels of all analyzed bridge geometries, the authors concluded that a progressive failure of a bridge deck results in insufficient load capacity to meet the minimum redundancy level. It was also noted that girder continuity increases redundancy. The authors also concluded that the external bracing is the key parameter for providing sufficient redundancy.

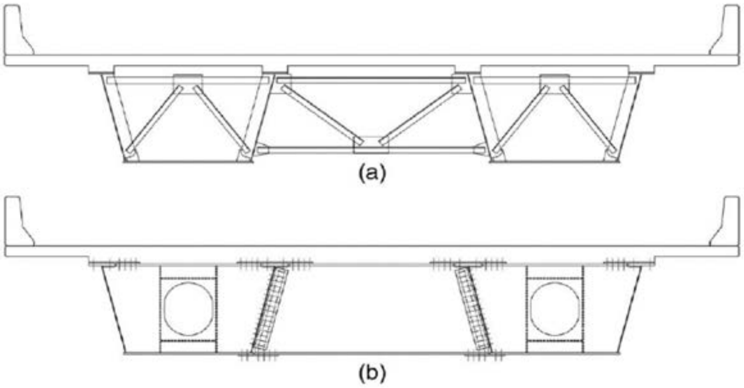

Figure 2.5. External Bracing Types: (a) K-type Cross-Frames; (b) Solid Diaphragms (Hunley and Harik 2012).

Barnard et al. (2010) recently investigated steel twin tub girders' performance as part of TxDOT Project 9-5498. The study included extensive laboratory testing, with the experimental investigation of a full-scale box-girder bridge together with comprehensive computational modeling. The major objective of the research was to evaluate the behavior of twin box-girder bridges after the fracture of one girder and provide guidelines for modeling the postfracture response. The tested bridge was simply supported; therefore, it did not have the structural redundancy that often exists for continuous multi-span (indeterminate) bridges. External braces that could contribute to load distribution in the damaged bridge were removed based on TxDOT practices. The authors conducted three tests at different damage states using different loading conditions. During the first test, a sudden fracture was created at the mid-span of the bottom flange of the exterior girder using charge explosives while an equivalent HS-20 load was placed directly above the fractured girder. The bridge deflected less than 1 in. The second test was conducted under similar loading, but this time a sudden full-depth fracture was created on the external girder. The fractured external girder deflected 7 in. but could still support the service load. The third test was an ultimate load test while the exterior girder had a full-depth fracture. The bridge could still carry more than five times the legal truck load. Barnard et al. concluded that the prominent failure mode was initiated by the pullout of shear studs in the deck followed by the crushing of the reinforced concrete deck.

The effect of different parameters, including radius of curvature, railing, and continuity, were also considered in the tests and analysis. The effect of the railing significantly reduced the deflection while increasing the tensile forces on the stud connections. Therefore, ignoring the railing is not necessarily conservative in a redundancy analysis. The results also showed that the decrease in the radius of curvature resulted in an increase in the vertical deflection of the damaged girder. Based on experimental testing, it was observed that the damaged bridge performed with sufficient redundancy to redistribute and continue to carry the very high applied loads.

Samaras et al. (2012) proposed a simplified method for evaluating the redundancy of twin steel box-girder bridges based on the work conducted as part of TxDOT Project 9-5498. The suggested method proposed an initial strength check and yield line analysis for evaluating the remaining strength of the damaged bridge. A three-level redundancy check was recommended:

1. The initial strength check (ISC) of the bridge with an intact girder is conducted. If the moment and shear strength is adequate and the deck has adequate shear capacity, the bridge can be called redundant.
2. If the initial strength check is not satisfied, a yield line analysis (YLA) can be performed. ISC cannot be used if the shear studs pull out from the deck concrete. Figure 2.6 depicts the surveyed deck deflections and assumed elastic plate displacements based on the actual failure shape. A yield line pattern was developed based on the observed failure shape. It was concluded that the assumed yield line could be used for fractured steel twin box-girder bridges for estimating the ultimate load if shear studs pull out. Both ISC and YLA are conservative and convenient methods to quickly evaluate the redundancy level of fracture critical bridges. It was concluded this method can provide information about the mode of failure that can help identify the remaining capacity of the bridge with a fractured girder.
3. If YLA also shows inadequate capacity, then more sophisticated nonlinear computational methods, such as finite element, must be used.

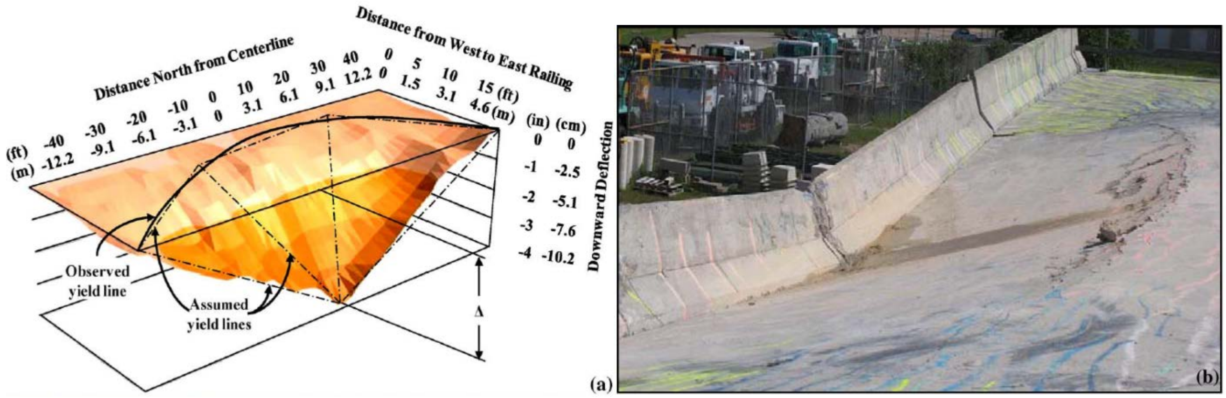

Figure 2.6. FSEL Bridge Test: (a) Surveyed Deflections and Assumed Yield Line; (b) Damaged Deck After Test (Samaras et al. 2012).

Kim and Williamson (2014) developed finite element modeling guidelines for evaluating the redundancy level of steel twin tub bridges. This study was also conducted as part of TxDOT Project 9-5498. Their proposed modeling approach considers nonlinearity due to concrete cracking and crushing, as well as steel yielding. In addition, the shear stud connection failure mechanism was also considered in the FEM model because stud connection failure may significantly affect redundancy. The pullout behavior of the embedded shear studs was evaluated through laboratory tests (Mouras et al. 2008; Sutton et al. 2014). A shear stud failure mode where the girder had a full-depth fracture was observed during the second test. The FEM models successfully estimated the bridge component failures. Both the test and FEM analysis suggested that the bridge had greater redundancy than defined by current code provisions.

After verifying the modeling approach, Kim and Williamson (2014) analyzed several other bridge configurations using the same modeling approach to investigate the remaining load capacity following a full-depth failure of one member. They concluded that the shear stud connection behavior is one of the important parameters for capturing the failure mode correctly and evaluating the redundancy level.

2.7 RESEARCH QUESTIONS ARISING FROM LITERATURE REVIEW

Based on the foregoing survey of the state-of-the-art and state-of-the-practice for fracture critical bridges in general and STTG bridges in particular, the following questions remain that will be addressed in this research:

- Is it possible to identify redundancy levels of existing and future STTG bridges in order to classify them as nonfracture critical?
- Do existing STTG bridges have adequate capacity following the fracture of one box member?
- Are there any currently available analysis techniques that may be utilized for fast and reliable capacity estimates for STTG bridges?
- Is it possible to develop reliable and easy to implement analysis criteria using yield line method and/or grillage analysis?

2.8 RECENT RELATED RESEARCH

To provide some insight into the methods and approaches used to answer the above questions, members of the research team recently conducted experimental and analytical studies on developing a new class of bridge for TxDOT. Although not fracture critical in nature, the analytical approach is instructive.

Recently, (Jiang 2015) adopted the yield line theory and strip methods (a lower-bound plastic method) to estimate the overstrength capacity of slab-on-beam bridges. This study was conducted as a continuation of TxDOT Project 0-6722 (Hueste et al. 2015; Terzioglu 2015; Terzioglu et al. 2016a; Terzioglu et al. 2016b). Different failure modes—including beam-only, slab-only, and mixed mechanisms—were considered. Plastic overstrength factors were determined using an upper-bound yield line analysis (Figure 2.7), and a lower-bound strip method was used for two different spread slab beam bridges. It was found that the two bridge designs evaluated are sufficiently safe at their ultimate limit states, and the plastic overstrength analyses provide important information regarding the balance of each design with respect to the hierarchy of failure mechanisms. Local flexural failure is more likely when wheel loads are applied to the slab at the end of the bridge deck. To remove this undesirable feature, strengthening the end region of the deck slab by adding more reinforcing steel to rebalance the design is suggested.

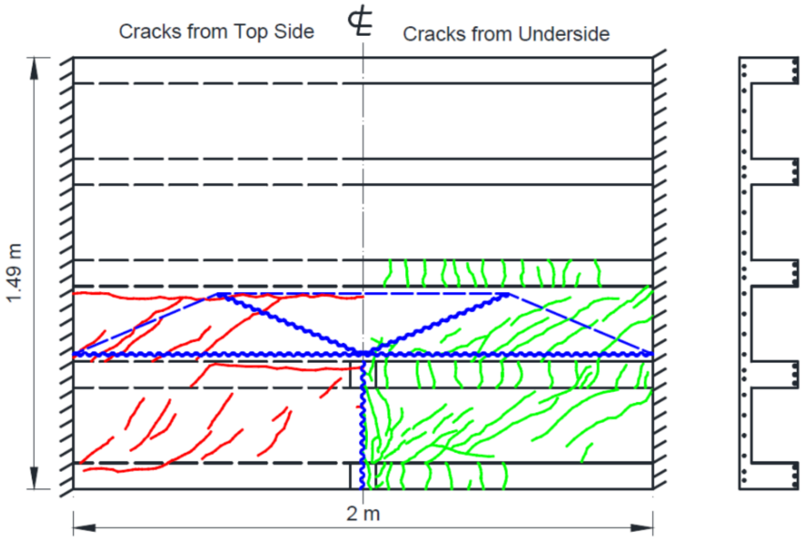

Figure 2.7. Yield Line Model Adapted from Jackson and Middleton (2013) Showing Observed Cracks as Tested by Hazell (1999).

Figure 2.8 presents the mid-span deflections of each slab beam in the Texas A&M University's RELLIS campus bridge and US 69 bridge under monotonic loads from initial elastic conditions until collapse. The overstrength factors were over 2.0 for both bridges. The estimated values from yield line and strip methods of analysis gave upper- and lower-bound values respectively. Apart from the slab-only failure mechanism, yield line theory generally provides upper-bound solutions, strip methods generate lower-bound results, and those values converge to be similar to each other.

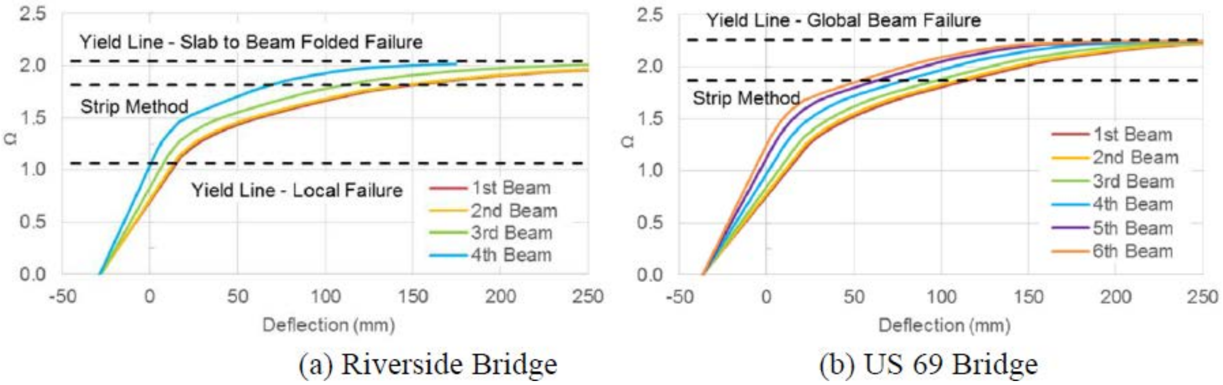

(a) Riverside Bridge (b) US 69 Bridge

Note: Ω = overstrength factor.

Figure 2.8**. Beam Deflections Due to Scaled Ultimate Design Loads (Jiang 2015).**

3 COMPUTATIONAL MODELING OF FRACTURE CRITICAL STEEL TWIN TUB GIRDER BRIDGES

3.1 INTRODUCTION

This task of the “Fracture Critical Steel Twin Tub Girder Bridges Project” includes the creation of an FEM model for a single-span fracture critical twin tub bridge and its verification using data collected in TxDOT Research Project 0-6937.

In this phase of research, a model has been created using the commercial software package Abaqus, a general purpose FEM code that can be used to solve a wide range of advanced engineering problems representative of the materials and geometry of the TxDOT bridge from Project 9-5498. This model includes the use of nonlinear elasto-plastic elements that adequately represent the nonlinear material behavior of crushing concrete and yielding of steel.

The FEM model has been used to simulate and analyze a sudden partial and a full-depth fracture of one of the tub girders. This FEM model allows for the evaluation of the residual capacity of the girder postfailure, and it considers the load path redistribution of the lateral load through the secondary load paths such as the bridge decks.

The accuracy of the above-stated FEM model has been evaluated using test data from the TxDOT research project. This research project involved the full-scale testing of a fracture critical steel box-girder bridge in August of 2009. This bridge was tested under four loading conditions, the first of which was an undamaged girder under an HS-20 truck load. The second loading condition consisted of a sudden fracture of one of the girder flanges under an HS-20 truck load. The third loading condition was a full-depth flange and web fracture under an HS-20 truck load. The fourth and final load case was the ultimate loading of a full-depth fracture. All four of the load cases were run using the FEM model, and the results from the various loading situations were compared to the full-scale test bridge results to verify the model’s ability to adequately assess the redundancy. Once the test results were compared, it was determined the model was successful in replicating the behavior of the full-scale test. This finding is promising for the future task of using FEM models in parametric studies to evaluate fracture critical twin tub girder bridges for redundancy.

The next section of this chapter describes the Ferguson Structural Engineering Laboratory (FSEL) test bridge, including the geometric parameters, material properties, test setup, and research procedure. It also details the four different loading scenarios and behavioral results. The following section details the development and test results for the various load cases of the FEM model. The fourth and final section of this chapter includes a comparison of the FEM model results to those acquired out in the field from the FSEL test bridge and an assessment of the FEM's ability to be used as realistic method of evaluating redundancy of in-use and future-construction fracture critical bridges.

3.2 DESCRIPTION OF THE TEST BRIDGE USED FOR MODEL VERIFICATION

The FSEL test bridge was constructed as a TxDOT and FHWA research initiative to evaluate the redundancy of twin box-girder steel bridges. The twin box-girder steel bridge is a fracture critical bridge, and the details of that study are in TxDOT Technical Report 9-5498. This type of bridge construction has received the fracture critical designation because it only has two tension flanges in the positive moment region of the bridge, and if one girder fails, the second girder may not be capable of supporting the required full-factored design loads.

The FSEL test bridge was originally used as a section of an exit ramp in Houston, TX. After taken out of service a portion of the bridge was used for the FSEL test bridge. The FSEL test bridge was designed to represent the worst case configuration, with respect to redundancy. The bridge was set up in a simply supported manner and all external braces that could have assisted in load transfer following a girder failure were also removed according to common TxDOT practice. Furthermore, the railing was constructed with expansion joints that significantly reduce any load carrying capability that might contribute to stiffening the girders. Finally, the bridge was constructed with a tight radius of curvature in the horizontal plan; an equivalent HS-20 truck load was applied on the exterior girder at the location of the mechanically induced girder fracture. An image of the full-scale destructive test setup of the twin steel box-girder bridge is located in Figure 3.1.

In subsequent sub-sections of this section, the geometry, material properties, test methods, and various load cases and failure modes are discussed.

Figure 3.1. The FSEL Test Bridge (Barnard et al. 2010).

3.2.1 Geometric and Material Properties

A typical cross-section of the FSEL test bridge is depicted in Figure 3.2. Figure 3.3 shows the plan view of the bridge, while the haunch detailing is shown in Figure 3.4. The FSEL test bridge was originally used as a section of the exit ramp on the IH 10/Loop 610 interchange in Houston, Texas. The bridge was configured in a simply supported fashion, with a total bridge span length of 120 ft. The top and bottom flange thickness did not change along the entire length of the bridge. The total width of the bridge deck was 23 ft 4 in., with a roadway width of 21 ft 4 in. A standard T501 section railing was used on both sides of the roadway over the entire length of the bridge. The bridge had a tight radius of curvature of 1365 ft. A summary of the bridge properties is shown in Table 3.1.

Table 3.1. FSEL Test Bridge Properties.

Property	**Measurement**
Length	120'
Deck Width	23' 4"
Roadway Width	21' 4"
Radius of Curvature	1365'
Shear Stud Spacing	22"
Diaphragm Spacing	12'

The bridge also had shear studs welded to the top girder flanges located in groups of three spaced at 22 in. on center. There was also a 3 in. unreinforced concrete haunch added above the top flanges of the steel girders.

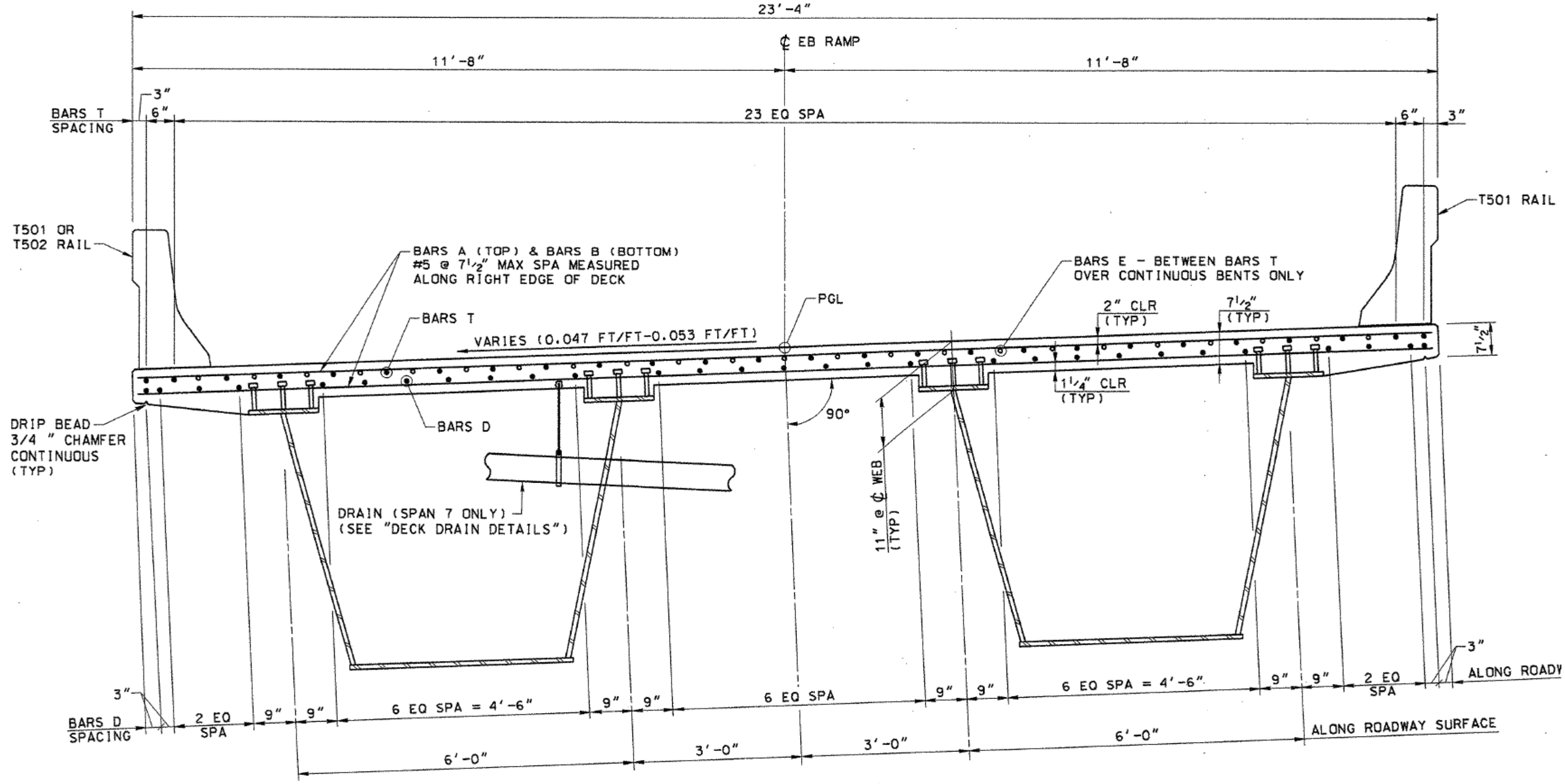

Figure 3.2. Typical Cross-Section of FSEL Test Bridge (TxDOT 1996).

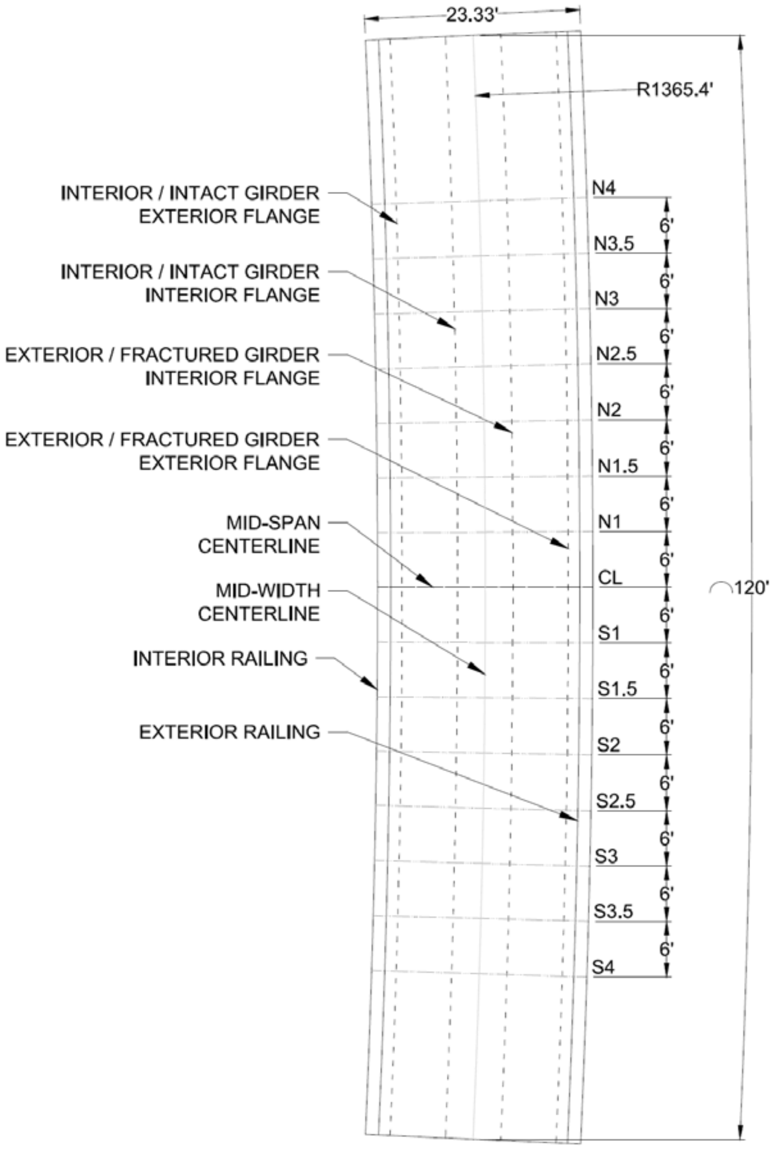

Figure 3.3. Plan View of FSEL Test Bridge with Cross-Bracing Stations (Neuman 2009).

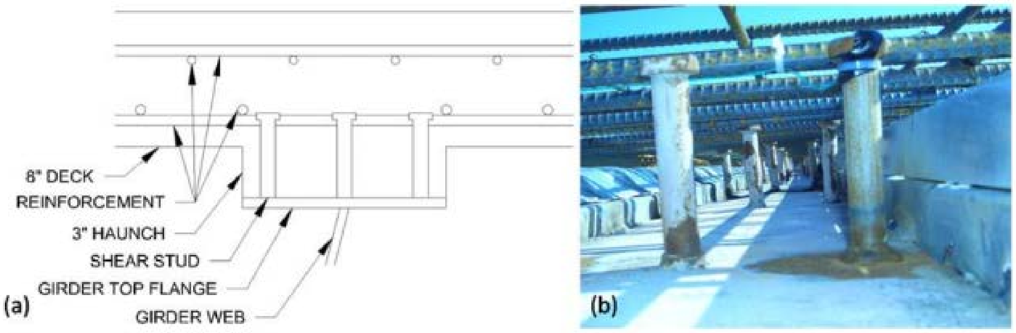

Figure 3.4. Haunch Detail: (a) Cross-Section of Haunch; (b) Construction Photo Before Casting (Barnard et al. 2010).

The FSEL test bridge also contained diaphragms between the girders at 12 ft increments on each side of the centerline. Figure 3.3, a plan view of the bridge, shows that half stations are the locations of the cross-bracing, and whole station numbers represent halfway points between cross-bracing.

The detailing of the intermediate diaphragm can be seen in Figure 3.5 and is comprised of a 5 in. by 5 in. by 3/8 in. angle to connect the top together and two 3 in. by 3 in. by 1/4 in. angles to connect the top angle to the girder.

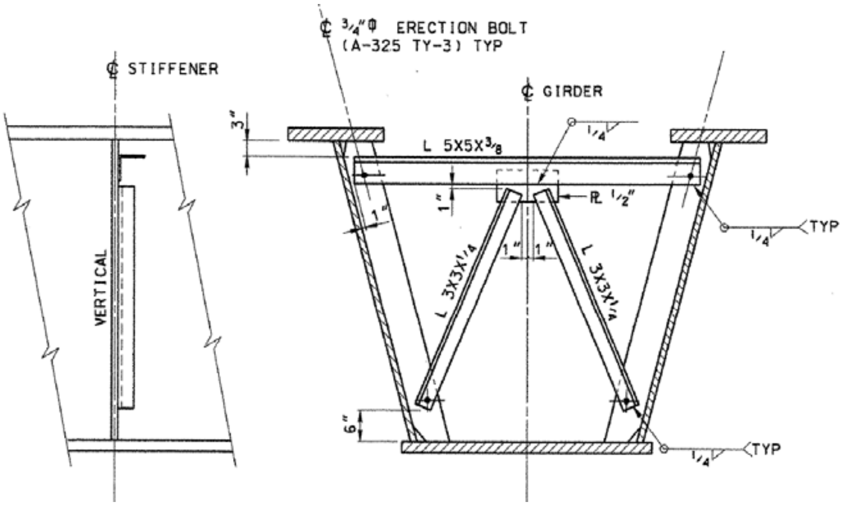

Figure 3.5. Intermediate Diaphragm Details of FSEL Test Bridge (TxDOT 1996).

A typical section showing the detail of the bridge span is shown in Figure 3.6. The bridge deck was 8 in. thick, with 2 in. and 1.25 in. of concrete cover over the upper and lower layer rebars. The deck consisted of two layers of longitudinal steel reinforcing bars: the top layer bars are labeled T bars and are size #4, and the bottom layer bars are labeled D bars and are size #5. Both layers of bars have a spacing of 6 in. The deck also contained two layers of transverse rebars: the top layer rebars are labeled A bars and are size #5, and the bottom layer rebars are labeled B bars and are size #5. Both layers of bars have a spacing of 6 in.

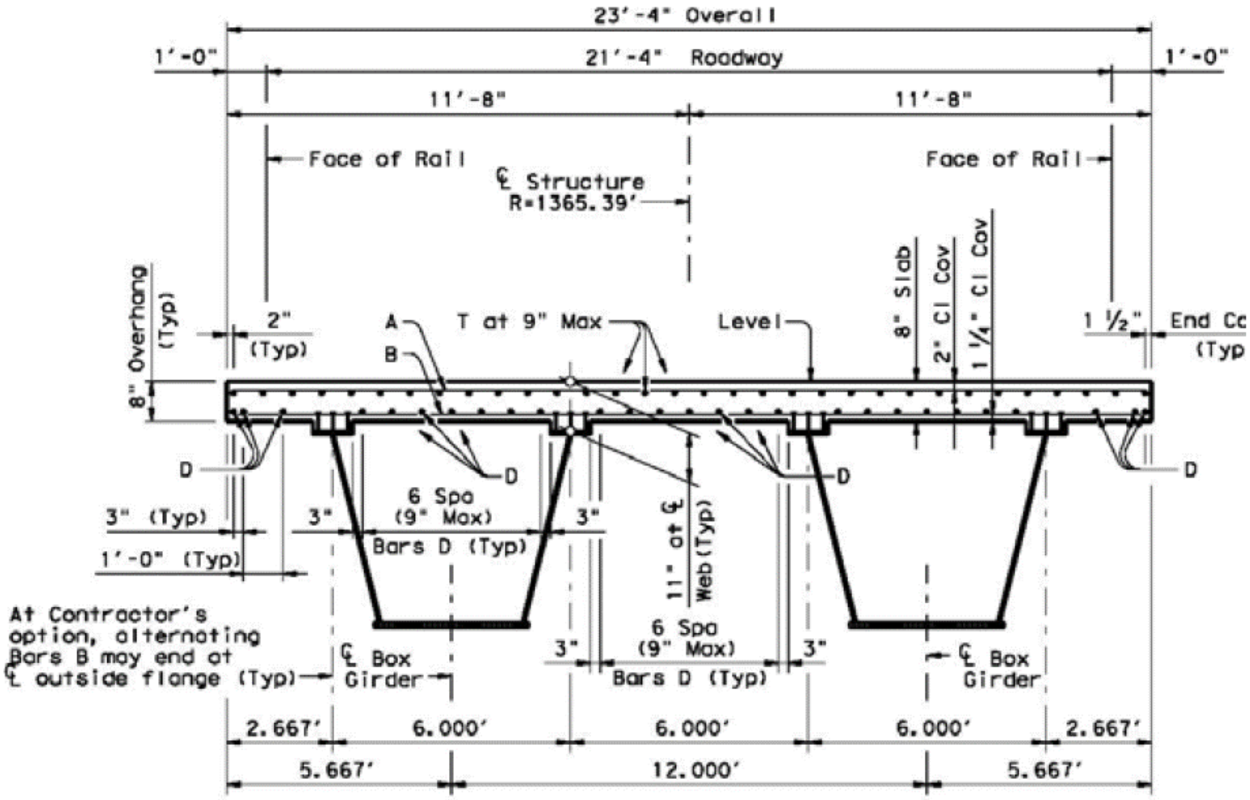

Figure 3.6. Typical Slab Section (TxDOT 2009).

The flanges and webs of the steel girder were constructed out of steel plates. The bottom flange of the girder was a 47 in. wide, 3/4 in. thick steel plate. The top flange of the girder was constructed of two 12 in. wide, 5/8 in. thick steel plates. The web of the girder was composed of two 1/2 in. plates on a 1 to 4 slope rise from the bottom flange to the top flanges over a vertical height of 57 in. The details of the girder are shown in Figure 3.7 through Figure 3.9.

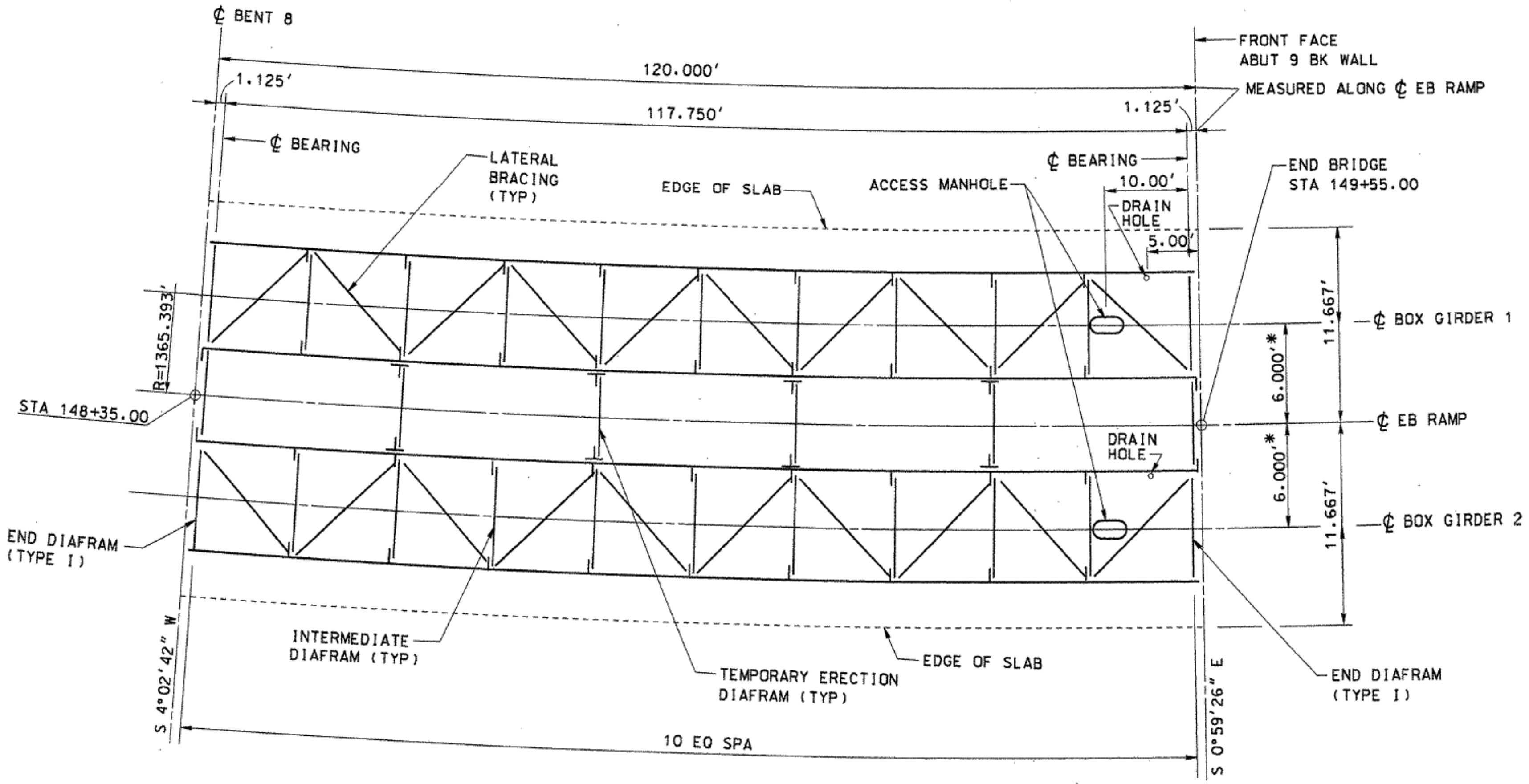

Figure 3.7. Plan View of Tub Girder and Framing Plan (TxDOT 1996).

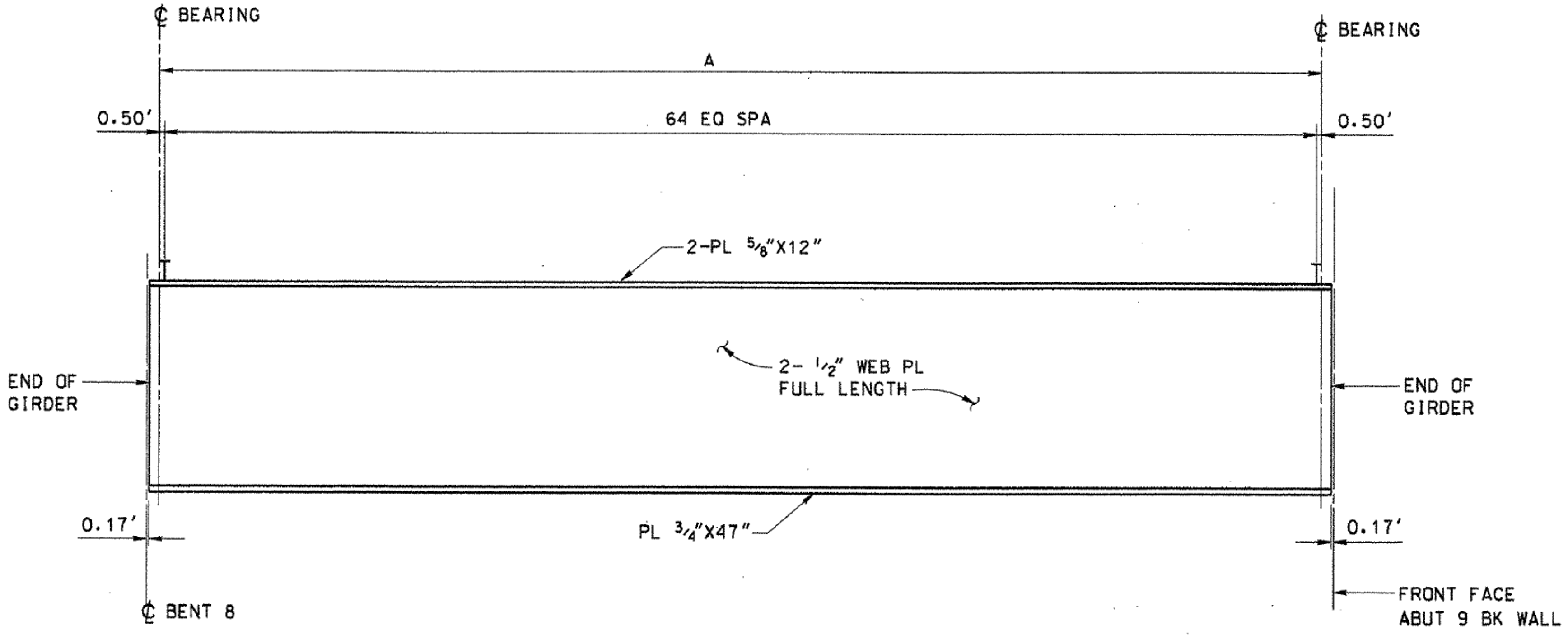

Figure 3.8. Elevation View of Tub Girder (TxDOT 1996).

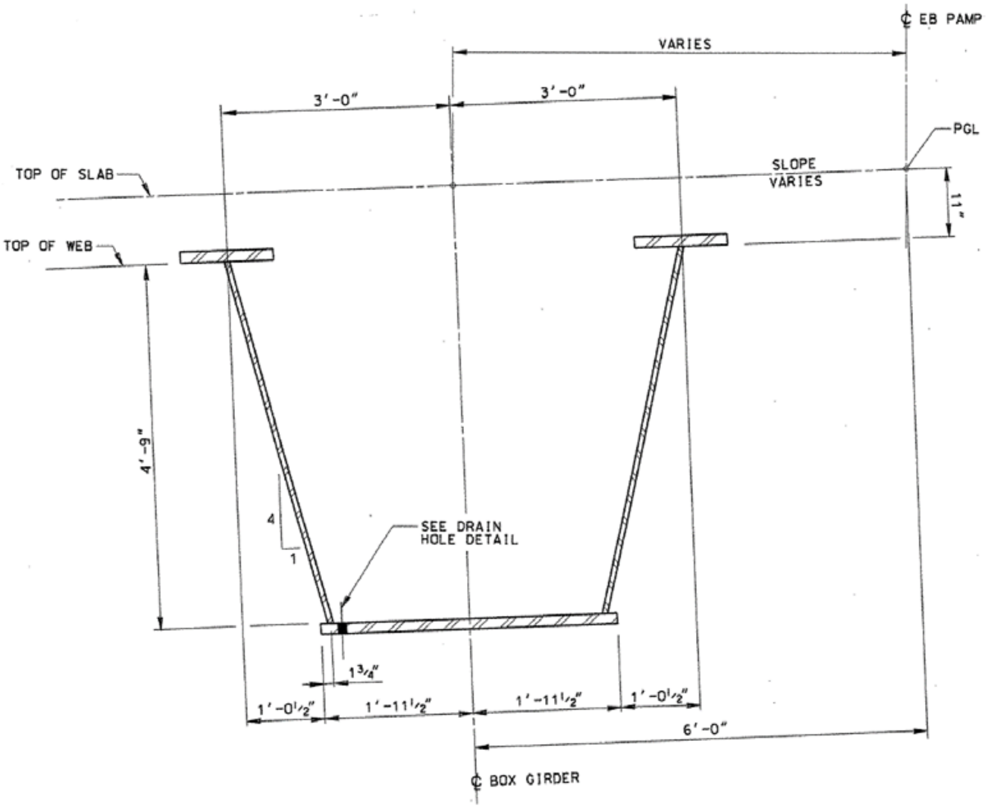

Figure 3.9. Tub Girder Cross-Section (TxDOT 1996).

The flanges and webs of the twin box-girder were comprised of A572 Grade 50 steel with yield strength of 50 ksi and an ultimate strength of 65 ksi. The lateral bracing was constructed using A36 steel with yield strength of 36 ksi and an ultimate strength of 58 ksi. The shear studs used on the top flange for the girder to engage the concrete deck were 7/8 in. in diameter and were 5 in. tall and were constructed from the A108 cold-drawn bar.

The bridge deck consisted of both steel reinforcing bars and concrete. Both the #4 and the #5 reinforcing bars were made of Grade 60 steel (Table 3.2). The actual values obtained in testing are the values used in the modeling phase of this research.

The concrete in the bridge deck, the interior railing, and the exterior railing was specified to have a compressive strength of 4 ksi. The actual 28-day compressive strength of the deck was 4.84 ksi. The interior railing's compressive strength was 5.34 ksi, and the exterior railing's was 4.74 ksi. However, the maximum recorded strength of the deck, interior railing, and exterior railing was 6.26 ksi, 6.63 ksi, and 6.27 ksi, respectively. Table 3.3 lists the strengths of the deck, interior railing, and exterior railing.

Table 3.2. Steel Reinforcing Bar Properties (Neuman 2009).

Bar Designation	Nominal Yield Strength Fy (ksi) (specified)	Nominal Yield Strength Fy (ksi) (measured)	Nominal Ultimate Strength Fu (ksi) (measured)
#4	60	60	102
#5	60	68	101

Table 3.3. Concrete Properties of Deck Slab and Railings (Neuman 2009).

Deck Slab—Cast 8/17/06 TxDOT Class S-Type (4 ksi)		
Test Date	**Age (days)**	**Average f'c (ksi)**
9/14/2006	28	4.84
10/24/2006	68	5.37
8/16/2008	669	6.26
4/2/2009	898	6.26
Interior Railing—Cast 8/22/06 Austin Class S-Type (4 ksi)		
Test Date	**Age (days)**	**Average f'c (ksi)**
9/19/2006	28	5.34
10/24/2006	63	5.95
8/16/2008	664	6.63
Exterior Railing—Cast 8/24/06 Austin Class S-Type (4 ksi)		
Test Date	**Age (days)**	**Average f'c (ksi)**
9/19/2006	26	4.74
10/24/2006	61	4.90
8/16/2008	662	6.27
4/2/2009	891	5.49

In Table 3.3, it appears that on April 2, 2009, the ultimate strength decreases. However, according to Neuman (2009), the samples used for testing on April 2, 2009, had poor endcap surfaces that may account for this inconsistency.

Important steel members and dimensions are listed in Table 3.4, which contains the member type, dimensions, and steel type.

Table 3.4. FSEL Test Bridge Steel Member Sizes.

3.2.1.1.1.1.1 Member		Dimension	Steel Type
Girder	Bottom Flange Plate	47" x 3/4"	A572 Gr.50
	Web Plates (2)	1/2"	
	Top Flange Plates (2)	12" x 5/8"	
Shear Studs (group of 3) per flange	Diameter	7/8"	A108 @ 22" Spacing
	Length	5"	
Diaphragm	Top Angle	5" x 5" x 3/8"	A36 Gr.36
	Cross Angles	3" x 3" x 1/4"	
Reinforcing Bar	Bar A—Top Transverse	#5	Gr. 60 @ 6" Spacing
	Bar B—Bottom Transverse	#5	
	Bar T—Top Longitudinal	#4	
	Bar D—Bottom Longitudinal	#5	

3.2.2 Experimental Methodology and Test Results

The FSEL test bridge was observed under four different load cases. The first loading case was just after construction under the HS-20 truck load. The second load case was just after flange fracture under the HS-20 truck loading. The third load case was just after flange and web fracture under the HS-20 truck loading. The fourth and final load case was after the flange and web fracture under ultimate loading conditions.

The following subsections will discuss instrumentation, testing methods, and test results of the previously discussed load cases.

3.2.2.1 Applying Approximate Service Loading to Intact Bridge and After Removing the Bottom Flange of One Girder

During the construction phase of the twin tub girder bridge, various structural components were instrumented to determine the strains and deflections of critical members. Uniaxial strain gages were placed on strategic shear studs near the mid-span of the single-span bridge to observe the induced tensile force. Rosset strain gages were affixed on specific reinforcing bars within the concrete deck.

Traditional surveying methods were used to determine deflections by shooting 1/10th points along the length of the interior and exterior girders. A straight line between the north and south end supports was used as the zero deflection, or base line. It should be noted that the researchers assumed the supported ends of the girder had zero deflection, even though the ends of the girders were supported by elastomeric bearing pads.

The induced fracture was strategically placed at the location of maximum damage potential—the mid-span of the bridge on the exterior girder. The fracture of flange was induced by a linear explosive charge affixed to the 47 in. tension flange to most accurately simulate a sudden and abrupt failure, as would be expected in in-situ conditions. A blast shield was attached to the girder prior to the flange fracture, specially designed to protect the underside of the deck from steel debris projectiles that were generated because of the fracture simulation.

The maximum standard truck load (the TxDOT standard HS-20 truck load) was chosen as the loading condition for Phases 2 and 3 of the project. The standard HS-20 truck load is 76 kip, with the front, middle, and rear axles separated by 14 ft. To generate the maximum moment the truck is placed on the exterior girder with the middle truck axle located at the exact midpoint, the middle and rear axles have a standard load of 33.9 kip, and the front axle has a load of 8.2 kip. Under this loading condition, a maximum moment of 1985 kip-ft is induced at the mid-span of the bridge at the location of the fracture for the HS-20 truck load.

In the research, the HS-20 truck load was simulated using five concrete girders that had a total weight of 76 kip supported by wooden cribbing to simulate axle loading. The middle axle was located 3.67 ft from the mid-span of the bridge, with all 3 axles separated by 14 ft. As per AASHTO standards, the exterior girder was placed 2 ft from the interior edge of the T501 concrete railing. A precise loading diagram of the HS-20 truck load in relation to the bridge fracture is shown in Figure 3.10.

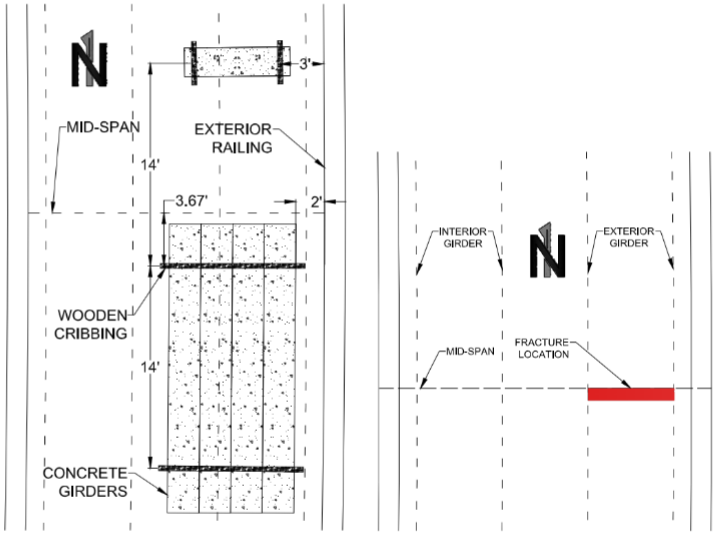

Figure 3.10. Simulated HS-20 Truck Load on the FSEL Test Bridge (Neuman 2009).

After the bridge was constructed, deflection measurements were collected at tenth points. The maximum deflection was observed at the mid-span of the bridge. The fractured girder initially deflected downward 5.55 in. under the HS-20 truck load, and a deflection of 5.64 in. was recorded upon flange fracture. The intact girder initially deflected downward 5.03 in. under the HS-20 truck load and deflected 4.94 in. after flange fractures. Note that these deflection measurements also include the initial upward deflection due to camber. The measurements were taken over several days by several different surveyors. Ambient temperature conditions changed during this time. Figure 3.11 shows the deflections of the fractured and intact girder after the HS-20 truck load application and after the girder flange was fractured.

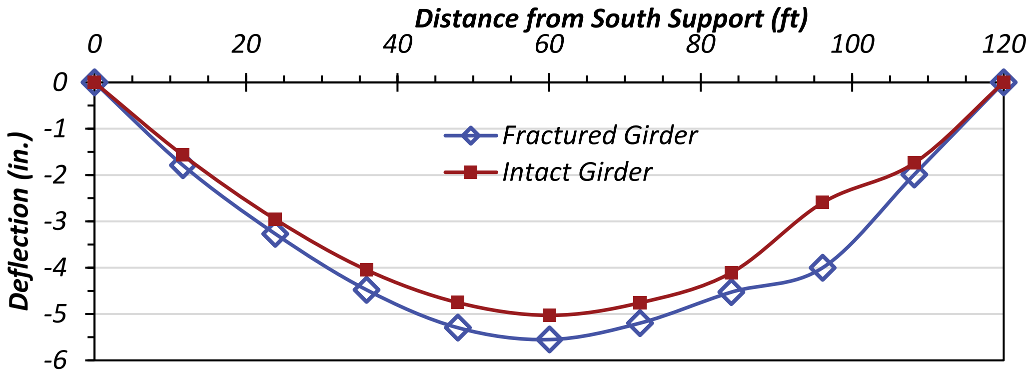

(a) Pre Flange Fracture

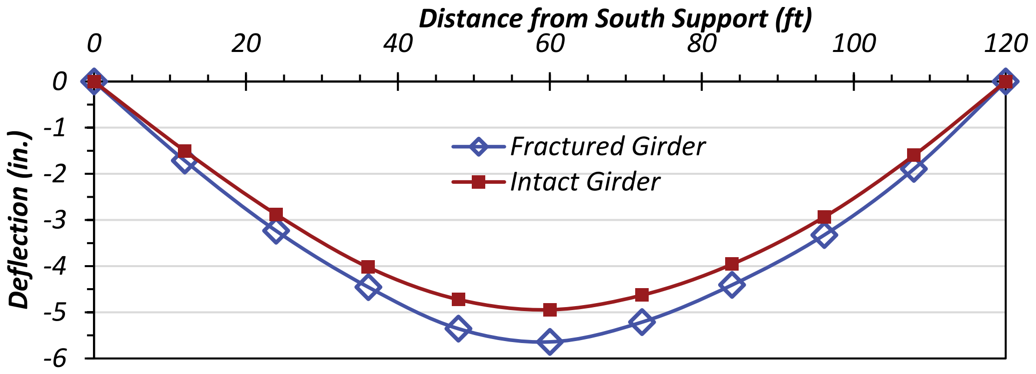

(b) Post Flange Fracture

Figure 3.11. Fractured and Intact Girder Deflections (adapted from Barnard et al. [2010]).

Upon failure of the girder flange, the bridge was able to withstand the HS-20 truck load without failure. Therefore, this finding promotes the idea that that twin tub bridges may have a measure of redundancy leading to further load carrying capability despite a fracture.

3.2.2.2 Removing the Webs of the Fractured Girder

The first step in testing the third load case involved repositioning the bridge to the approximate height of where it stood prior to the bottom flange being fractured during the second load case. In the fully supported position, an oxy-acetylene torch was used to extend the fracture from the bottom flange, and it was terminated 10 in. below the top flange weld. Following the cutting of the web, the concrete girders and wooden underpinning were once again strategically placed on the bridge per AASHTO standards at a location of maximum moment, with the outer girder 2 ft from the interior edge of the T501 railing, as shown in Figure 3.12. To appropriately simulate a sudden fracture of the tension flange and web, a special support system had to be installed that could quickly and simultaneously collapse, which was accomplished by using a scissor jack with cross tie supports, or tension tie assemblies, equipped with an explosive charge that would simultaneously fail. The tension tie assembly can be seen in Figure 3.13.

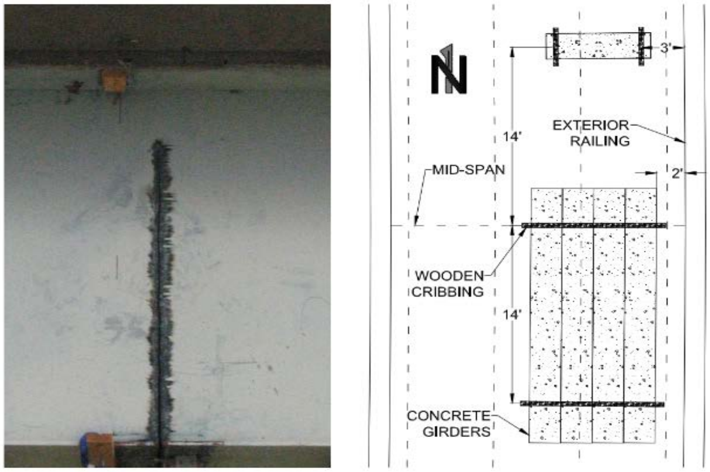

Figure 3.12. Full-Depth Web Fracture and HS-20 Truck Load Positioning (Neuman 2009).

Figure 3.13. Scissor Jack with Explosive Tie Assembly (Neuman 2009).

Before and after important stages in the testing procedure, surveys of the interior and exterior girders were taken at tenth points. The three main stages included after the HS-20 truck loading but prior to the scissor jack release, after the scissor jack release, and after unloading the HS-20 truck loading. Once again, the zero deflection line was taken as a straight line from the bottom of the girder at the north and south support.

The deflected shape of the fractured girder varied significantly from that of the intact girder. After the HS-20 truck load was applied to the bridge, the scissor jacks were released, and all dynamic energy was dissipated. The mid-span of the girder deflected downward a total of 7.02 in. for the fractured girder and 4.09 in. for the intact girder. It should be noted that the measurement also included the initial deflection due to camber. The overall appearance of the girder resembled that of “two partially restrained cantilevers pinned at the center” (Neuman, 2009). The deflections of the fractured and intact girders at the tenth points during the HS-20 truck load can be seen in Figure 3.14.

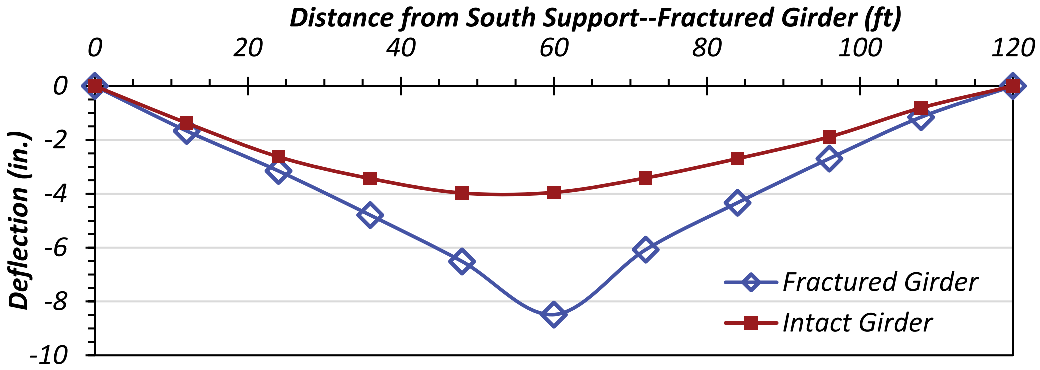

Figure 3.14. Fractured Girder Deflections Post Web Fracture (Neuman 2009).

Even though the fractured girder deflected significantly, the bridge did not fail and was able to carry the HS-20 truck load. These results indicate potential redundancy in the structure.

3.2.2.3 Applying the Ultimate Load

Upon completion of testing the bridge with the exterior girder's web fractured under HS-20 loading, the bridge had not collapsed and was able to resist load. To test for the ultimate loading condition, the five girders from the previous tests as well as an additional sixth girder were arranged in 40 ft by 8 ft bays centered on the mid-span of the bridge. The total weight of all six concrete girders was 82.1 kip. Once again, the outer concrete block was placed 2 ft from the interior railing as per AASHTO recommendations. The diagram of the loading bay can be seen in Figure 3.15.

Once again, the bridge deck, girders, diaphragms, studs, and railing were instrumented by many strain gages and potentiometers.

When the concrete girders were appropriately arranged, the bridge load was increased by using raw material to fill the bin. The raw material used for the loading was roadway base material. The roadway base material was brought onto the construction site via trucks and dumped into a holding area. The roadway base material was then loaded into a 1-cubic-yd concrete hopper and transferred to the bin by way of crane. To ensure that there was an accurate record of the load on the bridge, a load cell was attached to the crane. Each hopper was subsequently unloaded in a symmetric pattern in the bin and centered about the mid-span of the bridge. There was a concrete bedding placed below the fracture of the exterior girder to catch the bridge as it failed.

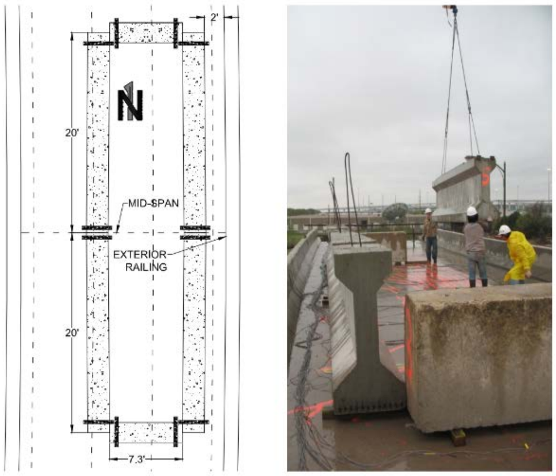

Figure 3.15. Bin Placement Diagram and Photo (Neuman 2009).

The bridge was incrementally loaded over the course of two weeks. A total of 104 concrete hoppers of roadway base material were added to the bridge prior to its failure. The total weight of concrete girders plus the base roadway material was 363.3 kip, meaning that the bridge, with a completely fractured tension flange and web, held more than four times the weight of the largest legal truck load of 80 kip.

Again, this final load case suggests that a so-called fracture critical twin tub girder bridge may have redundancy attributes that require further investigation.

3.3 NONLINEAR FINITE ELEMENT MODEL OF THE TEST BRIDGE

The FEM provides a versatile computational approach for correctly modeling the geometry of the bridge, thereby requiring few (if any) simplifying assumptions, particularly if three-dimensional (3D) modeling is adopted. A realistic representation of actual bridge geometry of slab-on-girder bridges may require significant mesh refinement and use of correct element types. The choice of element depends on the disposition of the bridge geometry. Commercial FEM programs provide a wide variety of element types to choose from depending on the relevant characteristic of the member, such as beam, shell, or isoparametric solid brick elements. Numerous guidelines and recommendations appropriately modeling different bridge types may be found in the literature (Barnard et al. 2010; Puckett et al. 2011; Puckett et al. 2005; Sotelino et al. 2004; Zokaie et al. 1991).

The appropriateness and accuracy of the selected modeling approach was verified through a comparison of field test results from TxDOT Project 9-5498 (Barnard et al. 2010) to the estimated response from the FEM model. A contemporary commercial software package, Abaqus v 6.14 (Dassault Systems 2014), which is a general-purpose FEM code used for solving a broad range of advanced problems in various fields of engineering, was used for simulating the response of the FSEL test bridge. A detailed nonlinear elasto-plastic finite element model was developed utilizing material nonlinearity due to crushing and cracking of concrete and yielding of rebar and steel plates. To achieve material nonlinearity, a concrete damaged plasticity model, which allows definition of dilation angle and yield surface, was used to represent the concrete components, and steel components were modeled using a metal plasticity model with isotropic hardening. The connection between steel tub girders and the reinforced concrete deck slab was modeled implicitly using nonlinear connector elements, which represent the load-deformation behavior of the haunch and shear studs. The pullout and shear load displacement behavior of shear studs were adopted from a study conducted on small-scale lab specimens, including the haunch (Mouras et al. 2008).

The superstructure of a STTG bridge consisted of two steel tub girders and a cast-in-place reinforced concrete deck slab plus the normal railings. The concrete deck and railings were modeled using 3D eight-node linear continuum elements (C3D8). 3D two-node straight truss elements (T3D2), which use linear interpolation, were used to represent the reinforcement; they were modeled as embedded within the concrete. The main members of a steel tub girder are steel plates for the bottom flange, webs, top flanges, and end diaphragms. In addition, intermediate diaphragm members connect the top and bottom flanges every 12 ft, with lateral brace members connecting the top flanges at the same points. Steel plates of the tubs were modeled using eight-node quadrilateral shell elements with reduced integration (S8R). All internal brace members were modeled using first-order 3D beam elements (B31). The effect of haunch was incorporated in the pullout behavior of shear stud connections, which was modeled implicitly using 3D two-node connector elements (CONN3D2).

The steel girders were seated on 3 in. thick elastomeric bearing pads that were 22 in. long and 11 in. wide. The bearing pads were located at the transverse center at both ends of each girder. Simulating the mechanical properties of a bearing pad is important because the boundary conditions may have a significant effect on the overall behavior of the bridge. Compressive and shear stiffness of the pads was adopted from other research (Hueste et al. 2015) that used similar bearing pad geometry. The compressive stiffness of 6000 k/in and shear stiffness of 20 k/in. (G = 100.6 psi) were used.

A steel twin tub bridge consists of two main components—steel tub girders and a reinforced concrete deck slab. Another key component of STTG bridges is the shear stud and haunch connection. Although this connection is made from steel studs and concrete haunch, it is not easy to model this connection explicitly. Therefore, this connection was also modeled using a nonlinear plasticity constitutive model.

The accurate modeling of a bridge superstructure is highly dependent on accurately defining the material behavior. Both steel and concrete may be modeled as an isotropic, linear elastic material so long as the structure is not under any critical loading beyond service loads. However, since this research aimed to investigate the behavior at loads much higher than at service level, both steel plates of the tub girders and reinforced concrete deck underwent significant deformations. When a structural component is subjected to severe overload, it is important to define how it may behave under such a load and whether it may possess sufficient ductility to withstand such a load without a catastrophic collapse. This type of behavior may be defined using nonlinear material models that include strain hardening effects. For both steel and concrete, there is wide range of constitutive models discussed in the literature, and the most common are available under the materials within the Abaqus software library. The mechanical constitutive relations were modeled considering both linear elastic and inelastic response. The inelastic response was simulated using available plasticity models. Damage mechanics were not included in the steel and concrete material constitutive models because the stiffness degradation and local failures are complex and create numerical convergence problems for complex behavior of reinforced concrete.

3.3.1 Inelastic Steel Model

The tub girders of the test bridge consisted of built-up members constructed using Grade 50 structural steel. Inelastic, mechanical constitutive behavior of steel plates and reinforcing bars were modeled using classical metal plasticity with an isotropic strain hardening rule. Plastic stress-strain behavior was modeled as rate independent. Perfectly plastic behavior was assumed once the equivalent stress reached the yield strength point based on the von Mises yield criteria.

Structural steel for webs and flanges, interior and end diaphragms, and lateral cross-bracings were also constructed using Grade 50 steel. ASTM A615 Grade 60 steel was used for all reinforcing bars in the deck slab and railings. Figure 3.16 shows the stress-strain behavior of steel components from uniaxial tension tests of the structural steel that was used for the tub girders and as reinforcing bars of the deck slab.

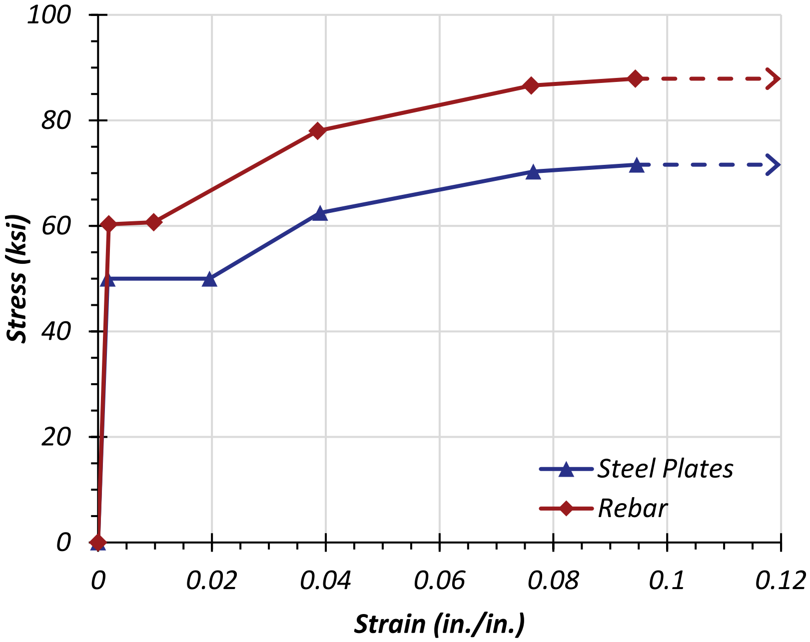

Figure 3.16. Constitutive Model for Steel Components (adapted from Barnard et al. [2010]).

3.3.2 Nonlinear Concrete Model

The deck slab of the test bridge was constructed using TxDOT Class S-Type concrete with a specified strength of f'c = 4 ksi at 28 days. The actual compressive strength is generally higher than the specified value. To accurately define the mechanical constitutive behavior of the concrete, compressive strength obtained from the laboratory tests should be used. Figure 3.17 shows the concrete compressive strength of deck and railing concrete at different ages measured from the concrete cylinder tests. Although the concrete compressive strength was slightly different for the deck and railing, the same compressive strength was used for all concrete components for simplicity. A compressive strength value of f'c = 5.37 ksi was used for the first fracture test (bottom fracture), and f'c = 6.23 ksi was used for the second and third tests.

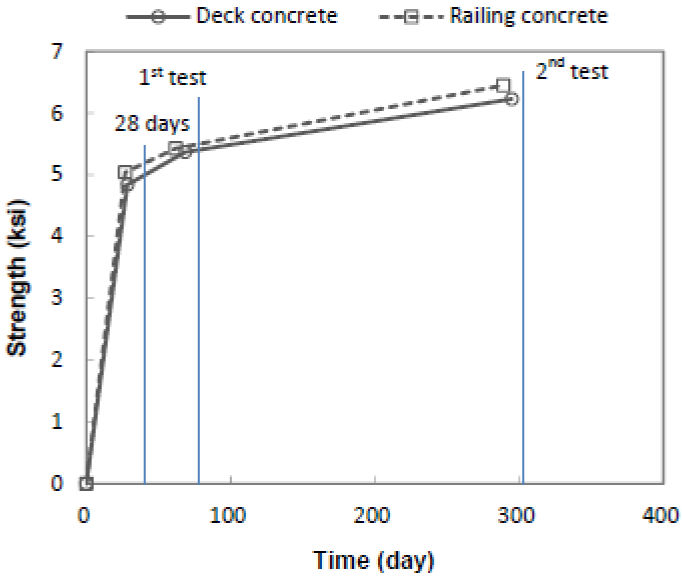

Figure 3.17. Concrete Compressive Strength from Cylinder Tests (Barnard et al. 2010).

The concrete components were modeled using 3D eight-node solid brick elements. The damaged plasticity model was used to simulate the behavior of the concrete. The concrete damaged plasticity model provides general capabilities to capture inelastic behavior of concrete due to cracking in tension and crushing in compression and defines different tensile and compressive strengths. This model is suitable for concrete under low confining pressures, where the main failure criteria is tension cracking or compression crushing. The confinement effect in the concrete deck of the STTG bridge is limited since the thickness is very small compared to width and length. The concrete damaged plasticity model uses isotropic compression and tension plasticity in combination with isotropic damaged elasticity to define the inelastic behavior of concrete. The concrete compressive hardening curve was defined using Equation (3.1) as given by the Kent and Park (1971) model for two different compressive strengths at different ages of concrete. Tensile behavior is defined using the initial stiffness of the stress-strain curve in compression. The behavior after reaching the tensile and compressive strength was assumed to be perfectly plastic.

$$f_c = f_c' \left[\frac{2\varepsilon_c}{\varepsilon_{co}} - \left(\frac{\varepsilon_c}{\varepsilon_{co}} \right)^2 \right] \tag{3.1}$$

where f_c = concrete compressive stress at specified strain (ksi); f_c' = concrete compressive strength at 28 days (ksi); ε_c = strain; and ε_{co} = strain at maximum stress (taken herein as ε_{co} = 0.002).

Figure 3.18 shows the adopted stress-strain behavior of concrete for Test 1, 2, and 3 depending on the measured compressive strength and the Kent and Park model. No test data are available regarding the tensile strength or modulus of elasticity of concrete. Therefore, the guidelines provided in American Concrete Institute (ACI) 318-14 (2014) Section 19.2 were used. Tensile strength of the concrete was calculated using the empirical relation provided in AASHTO LRFD (2014) Article 5.4.2.6, which is Equation (3.2), as follows:

$$f_r = 0.2\sqrt{f_c'} \tag{3.2}$$

where f_r = the modulus of rupture (ksi) and f_c' = the compressive strength of concrete (ksi). The modulus of elasticity of concrete for different ages of concrete were also calculated using an empirical relation provided in AASHTO LRFD (2014) Article 5.4.2.4, expressed in Equation (3.3):

$$E_c = 33000K_1 w_c^{1.5}\sqrt{f_c'} \tag{3.3}$$

where K_1 = the correction factor for the source of aggregate, which is taken to be 1.0 unless determined by physical test; w_c = unit weight of concrete (kcf)—use 0.145 kcf for normal weight concrete; and f_c' = compressive strength of concrete (ksi).

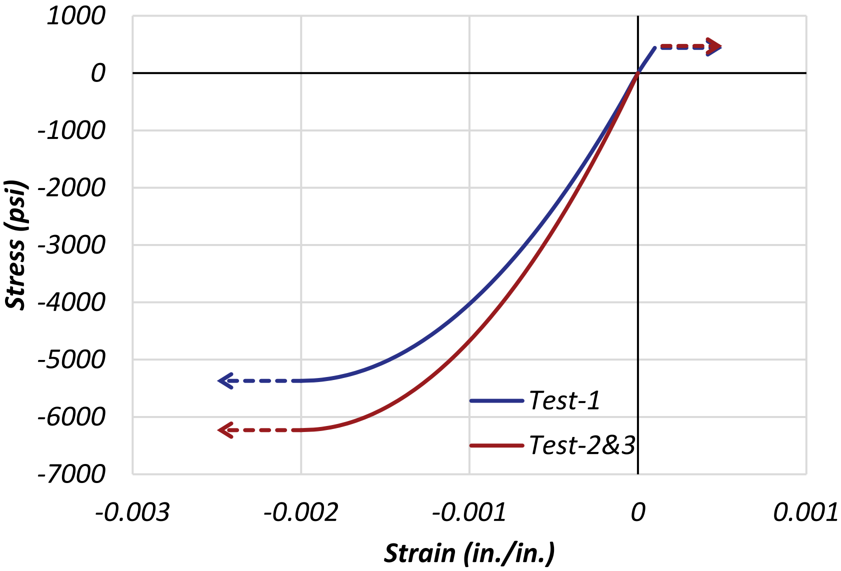

Figure 3.18. Concrete Stress-Strain Behavior for Damaged Plasticity Model.

Table 3.5 lists the tensile strength, compressive strength, and modulus of elasticity for the deck and railing concrete that was used to simulate the test bridge. Although the third test was conducted later, the concrete properties were assumed to be same as the second test because no cylinder test data were available. Also, the additional strength increase after the second test was not expected to be significant.

The concrete damaged plasticity model requires definition of various mechanical parameters to define the inelastic behavior of concrete. In addition to providing the compression hardening and tension stiffening behavior, the dilation angle, the flow potential eccentricity, and the ratio of biaxial compression to uniaxial compression, the ratio of the second stress invariant in the tensile meridian to the one in the compression meridian must be provided. Because of the absence of detailed material properties, default values that are common for normal concrete were used.

Table 3.5. Mechanical Properties of Concrete at Different Ages.

Test No.	**Age of Concrete (days)**	**Compressive Strength, f'_c (ksi)**	**Tensile Strength (ksi)**	**Modulus of Elasticity (ksi)**
1	66	5.37	0.46	4222
2	293	6.23	0.5	4550
3	940	6.23	0.5	4550

Note: Compressive strength values were obtained from laboratory tests; tensile strength and MOE values were calculated using empirical AASHTO LRFD formulas.

3.3.3 Modeling Shear Stud and Haunch Behavior

Slabs on steel girder bridges are typically constructed with shear studs to transfer longitudinal interface shear stresses between the deck and girders. Thus, shear studs are welded to the top flanges of the girders and are required to extend at least 2 in. above the deck slab soffit (AASHTO 2014). In general, tub girders are constructed with initial camber. Therefore, variable haunch is provided to obtain uniform deck thickness. (TxDOT 2013b) *Bridge Design Manual* limits the haunch thickness to 3 in. when there is no reinforcement provided within the haunch. Shear studs are key elements for developing composite action between girders and a reinforced concrete deck. Mechanical properties due to composite action were simulated through modeling of pullout and shear behavior for the stud-haunch connection. Simulating this connection is key to the successful modeling of a damaged girder because the stud-haunch connection is under significant pullout and shear force following the fracture of one tub girder.

Topkaya et al. (2004) investigated the horizontal shear transfer for curved steel girder bridges and developed a load-slip relationship model for shear studs using experimental observations. The authors provided Equation (3.4) to model the load versus slip behavior for a stud or group of studs:

$$\frac{Q}{Q_d} = \frac{3(\Delta/0.03)}{1 + 2(\Delta/0.03)} \tag{3.4}$$

in which Δ = slip (in.); and Q_d = the design strength of shear studs (kip) and is defined as the point where the shear displacement reaches 0.003 in., and is defined in Equation (3.5) as:

$$Q_d = 1.75A_{sc}(f_c'E_c)^{0.3} \tag{3.5}$$

in which f_c' = the compressive strength of concrete (ksi); E_c = the modulus of elasticity of concrete (ksi); and A_{sc} = the cross-sectional area of shear studs at a section (in^2).

The test bridge used in this research had three 5 in. long and 7/8 in. diameter shear studs installed on the top flanges every 2 ft. A group of three studs ($A_{sc} = 1.804$ in^2) at a section were simulated using one connector element having the same behavior as the three studs combined. Figure 3.19 shows the shear force slip behavior of a set of three studs at a section for two different compressive strengths. This constitutive relation was utilized to represent the horizontal shear behavior of connector elements that are used to model stud-haunch interface between the concrete deck and steel girders.

The pullout behavior of shear studs was modeled using the recommendations of Sutton (2007) and Mouras et al. (2008). The authors conducted experimental research on ductility characteristics and the strength of shear studs embedded in reinforced concrete decks. Experimental pullout strengths of test specimens with haunch were found to be lower compared to the values predicted by ACI 318 equations because ACI does not take into account the presence of haunch. Mouras et al. (2008) developed modification factors for ACI equations to account for the haunch thickness.

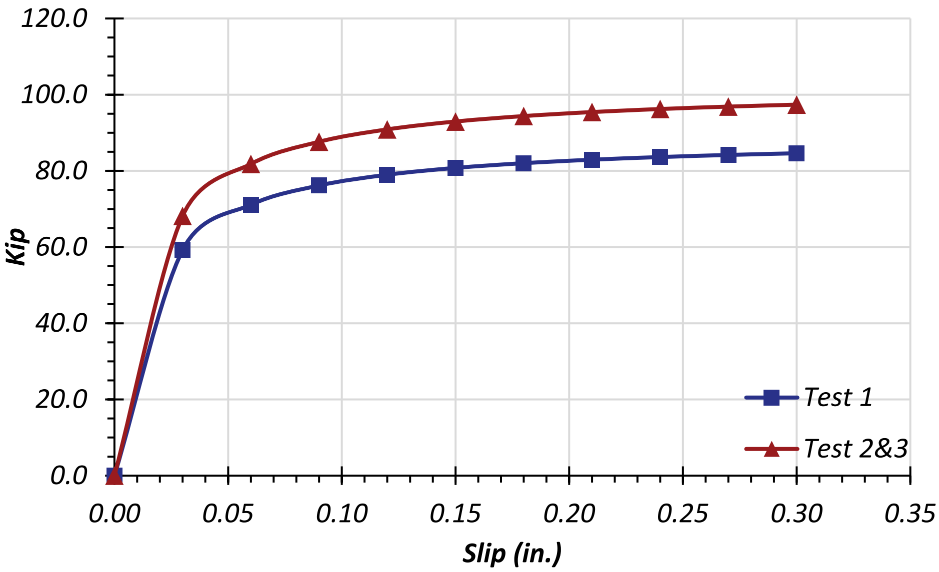

Figure 3.19. Mechanical Constitutive Model for Shear in Stud-Haunch Connections.

Barnard et al. (2010) developed a simplified load deformation behavior for connector elements using regression analysis of the test results from Sutton (2007) and Mouras et al. (2008). Figure 3.20 shows typical pullout behavior from experiments and assumed behavior for the connector elements of the FEM model.

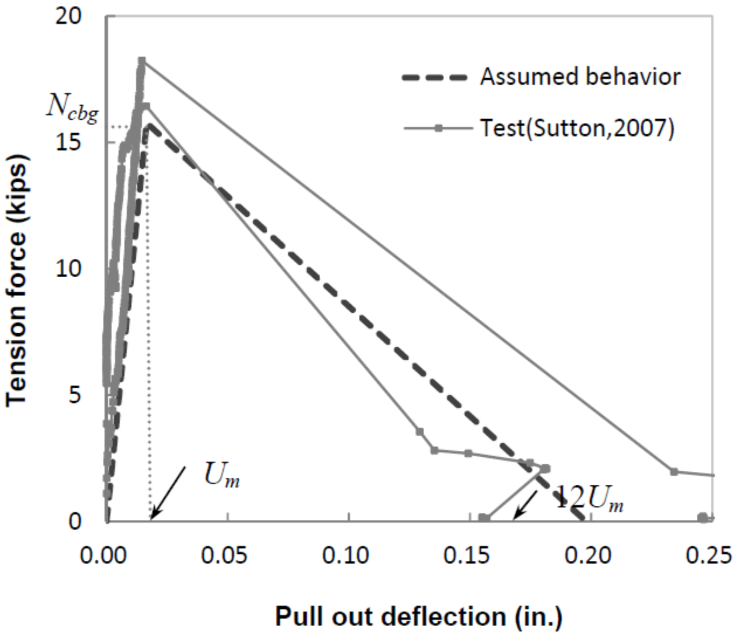

Figure 3.20. Stud Pullout Behavior under Tension (Barnard et al. 2010).

3.4 VERIFICATION OF FINITE ELEMENT MODELING APPROACH

A full 3D non-linear elasto-plastic finite element model of the full scale test bridge described above was created using the commercial software Abaqus (Dassault Systemes 2014). The bridge deck and rails were modeled using 3D brick elements and divided into uniform 4 in. meshes throughout the deck. For the tub girders, a 6 in. mesh size was adopted. Figure 3.21 shows the finite element model of the bridge superstructure.

Various load and damage conditions were simulated to create the actual loading conditions that were conducted during the test program. Before the first test, which is the fracture of the bottom flange, the bridge was loaded with concrete block to simulate vehicle loading. Next, three simulations were conducted: (a) simulation of the bottom flange fracture, (b) simulation of the web and bottom flange fracture, and (c) simulation of the ultimate load capacity of the fractured bridge.

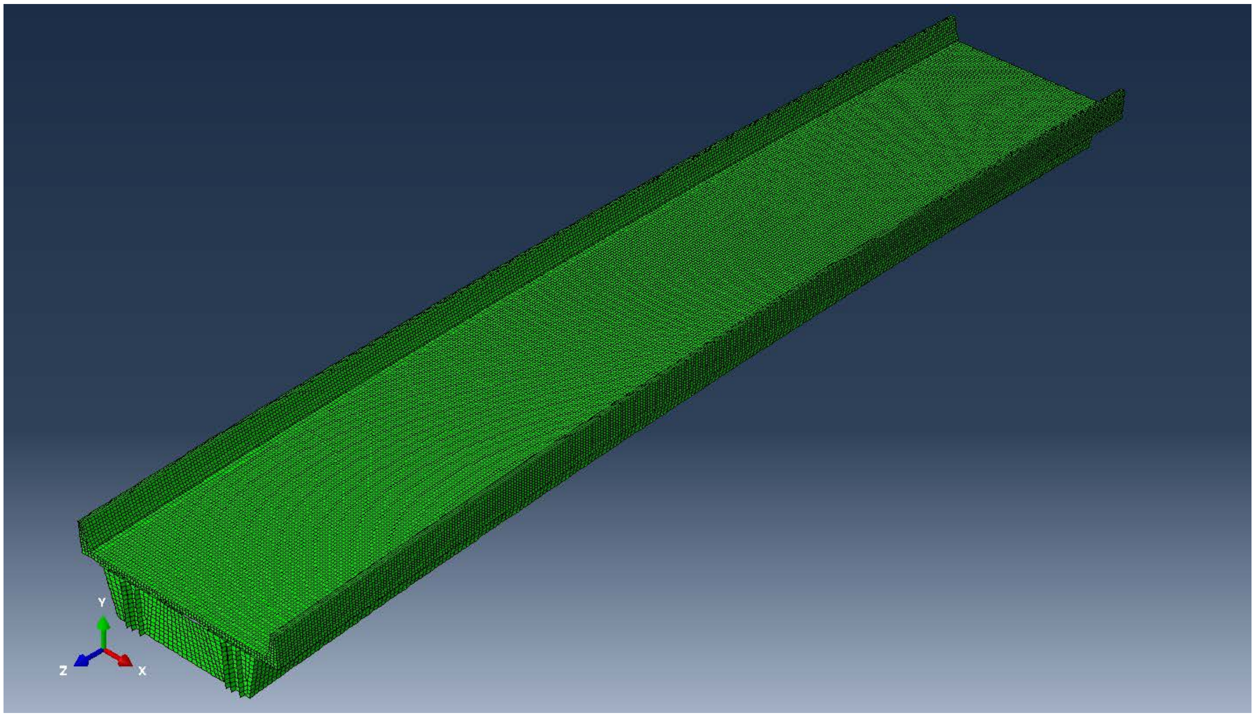

Figure 3.21. Finite Element Model of the STTG Test Bridge.

3.4.1 Simulating the Vehicle Loading

Initial testing was conducted on the intact bridge without any damage. The bridge was loaded with concrete block having a total weight of 76.2 kip. The concrete blocks were arranged such that the loading represented an HS-20 design truck load with three axles 14 ft apart. Detailed weights of each load and position of the loads were described in Section 1.2.

The finite element simulation for the vehicle loading was achieved in two steps: (1) the application of deck and railing weight on the top flanges of tub girders only, and (2) the application of vehicle load on top of the deck, which was carried by the composite girder and deck section. The objective was to represent the locked-in stresses developed during construction. To achieve such a loading simulation in Abaqus, a mock deck and railing (with very small stiffness and mass) were defined and tied to the actual deck and railing. The purpose of mock sections was to keep track of the deflected shape so that the actual deck could be correctly positioned once the concrete hardens. During the first step, the deck, the railing, and the reinforcement were all removed from the model, and their weight was applied on the top flange. They were later reactivated with self-weight, and the initial applied load was removed from the top flanges. Since there is a tie constraint between the mock and the actual deck and railing, the deck and railing positioned at the right location following the reactivation.

As the load simulation strategy implies, the baseline for the girder deflections is the undeformed shape of the girder before casting the deck and railings. Non-composite girders deflected due to weight of the unhardened concrete. Then the vehicle load was applied after the concrete hardened, at which point the composite girders deflected an additional amount. Figure 3.22 shows the comparison of experimental deflection profiles for east and west girders with the FEM predictions.

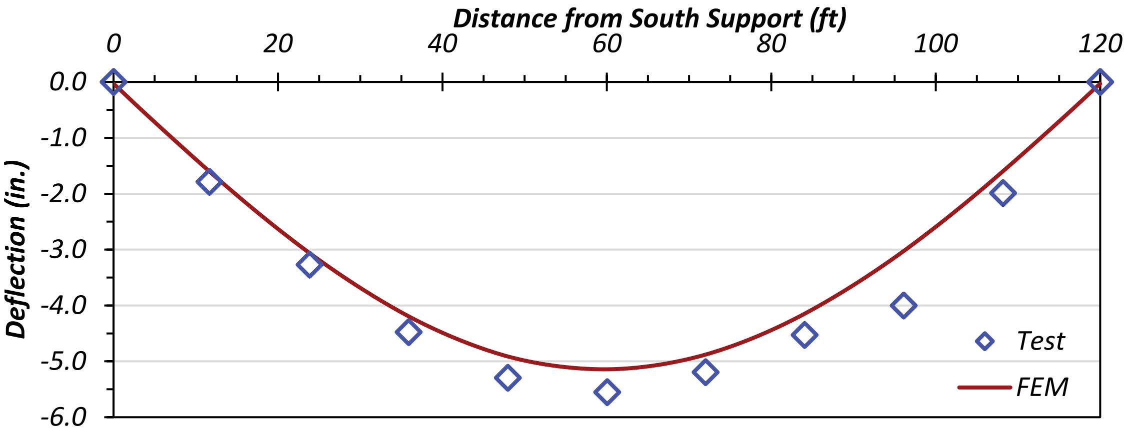

(a) Fractured East Girder

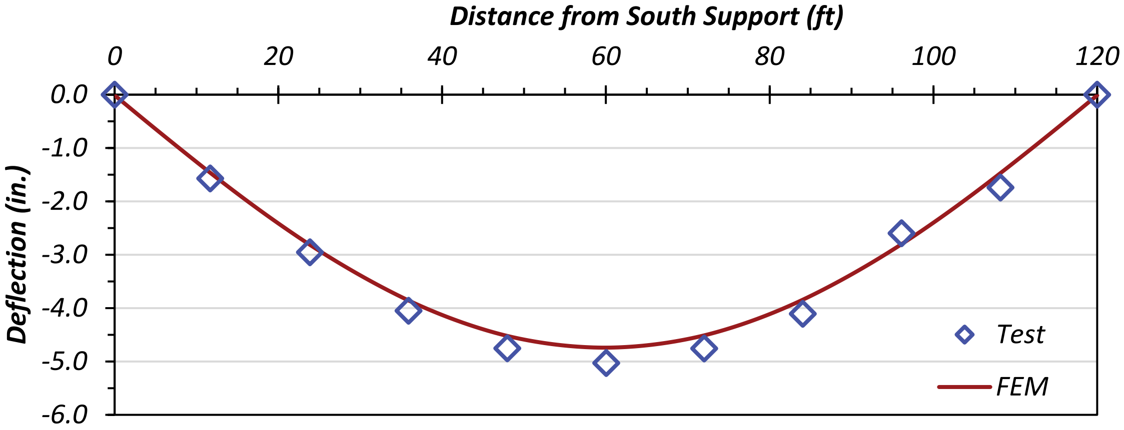

(b) Intact West Girder

Figure 3.22. Comparison of FEM Deflection Profile with Test Results under Vehicle Loading.

3.4.2 Simulating the First Test (Bottom Flange Removal)

The main objective of this analysis was to evaluate the behavior of the STTG bridge for the case of a partial and full fracture of one girder. Partial fracture of the east girder (outer girder) was created using explosives to create sudden failure of the entire bottom flange. To achieve such a load simulation in a finite element model, two halves of the east girder were tied together using weld connector elements (CONN3D2) along the predefined line at the mid-span. The loading steps and analysis procedures were followed as described in the previous section. Construction loads and the vehicle load were applied in a single static analysis step. In the final step, the connectors of the bottom flange only deactivated as a dynamic analysis step.

Figure 3.23(a) shows the comparison of test deflections for the fractured girder with the FEM predictions of the current study to the FEM predictions from Barnard et al. (2010). Figure 3.23(b) shows the estimated deflection profiles from FEM analysis and corresponding experimental deflections for the intact girder. While both predictions are in good agreement with test results, the estimated deflections for the intact girder were relatively closer to the intact measured ones.

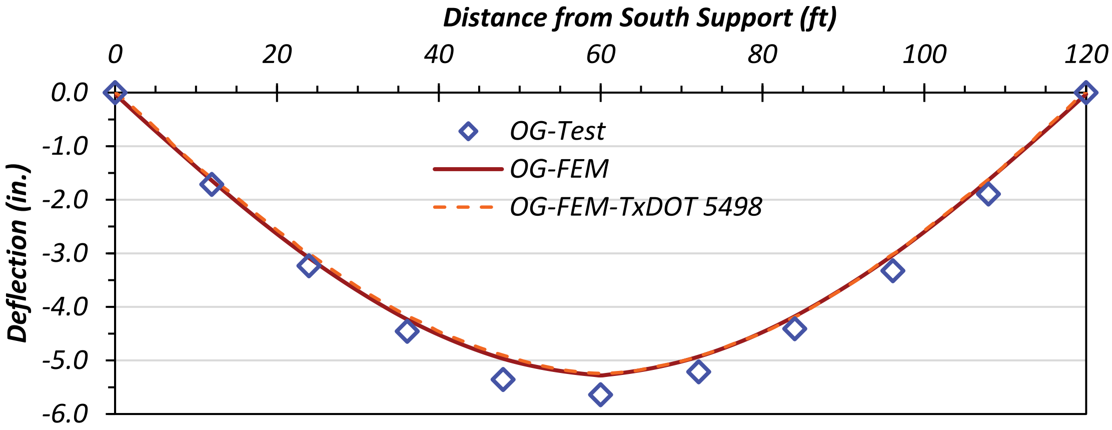

(a) Fractured East Girder

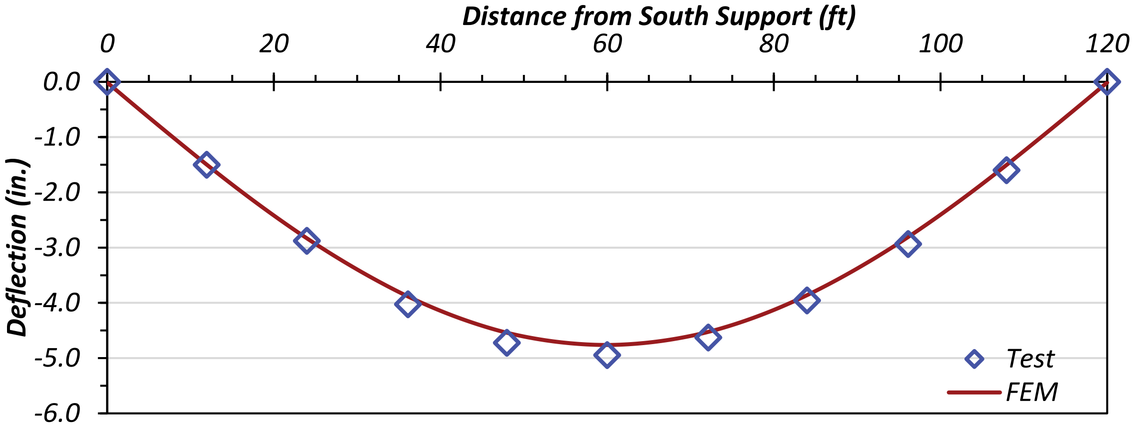

(b) Intact West Girder

Figure 3.23. Comparison of FEM Deflection Profile with Test Results After Bottom Flange Fracture.

3.4.3 Simulating the Second Test (Removal of the Webs of the Fractured Girder)

One of the main objectives of the project was to evaluate the behavior of the bridge following a full-depth fracture of a girder. Barnard et al. (2010) manually created a full-depth crack by extending the bottom flange fracture of the exterior girder using an acetylene torch. Temporary truss supports were provided during the cutting process so that the introduced fracture damage could be released suddenly to account for the dynamic effects. The concrete blocks were placed at the locations described in Figure 3.12 while the truss supports were still in place. Then, the supports were suddenly released.

The simulation process for the construction step was carried out like the first test in order to capture the locked-in stresses that develop during the construction. In the second static step, temporary boundary conditions fixing the vertical degree of freedom were applied 2.5 ft away on both sides from the centerline of the exterior girder. Vehicle loads were applied, and predefined connector elements joining the bottom flange and webs of the east girder were deactivated. The third step was removal of the temporary boundary conditions, which was applied as a transient dynamic analysis. Figure 3.24 shows the deflected shape of the bridge superstructure following the full-depth fracture of the east girder.

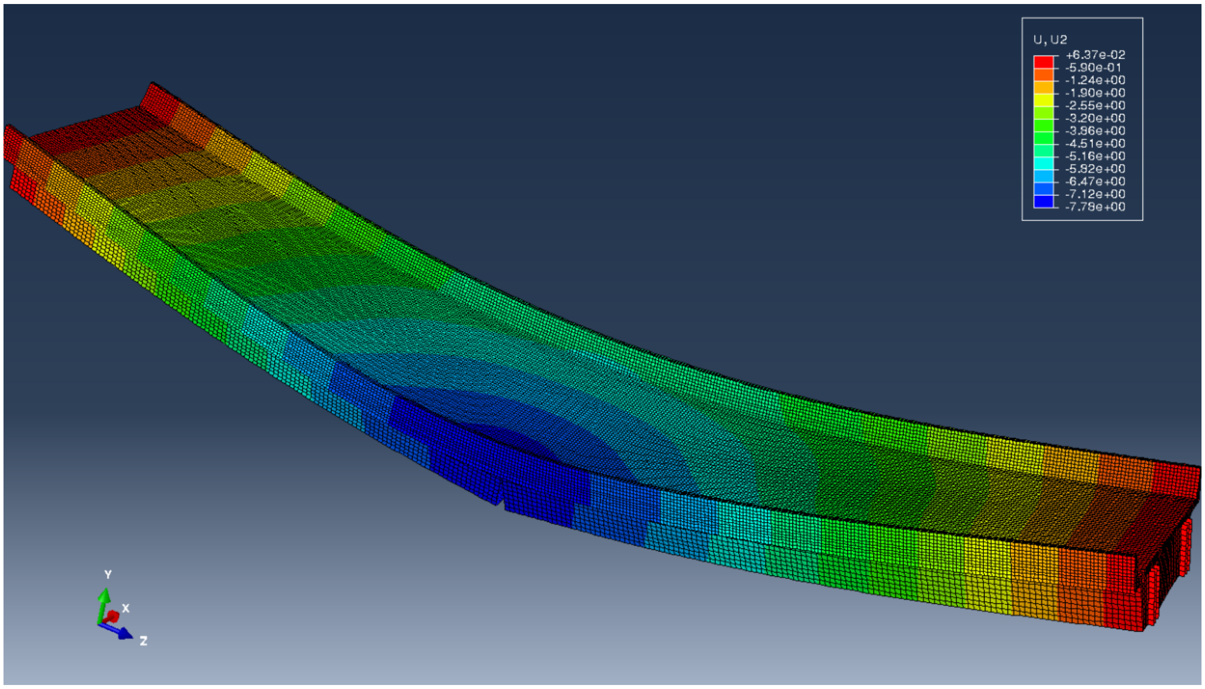

Figure 3.24. FEM Deflection Profile Following the Fracture of the Web.

Figure 3.25 shows the comparison of estimated and measured deflection profiles along the bottom flange of the fractured girder and intact girder, respectively. The measured mid-span deflection of the fractured girder was 7.02 in., and the FEM model predicted a value of 7.8 in. (11 percent higher). On the other hand, the estimated maximum deflection for the intact girder was about 30 percent higher than the measured value.

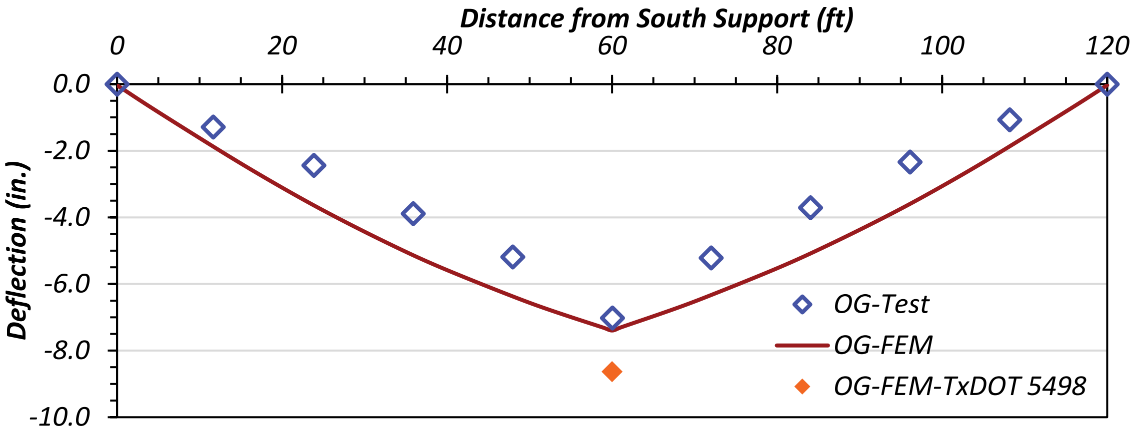

(a) Fractured East Girder

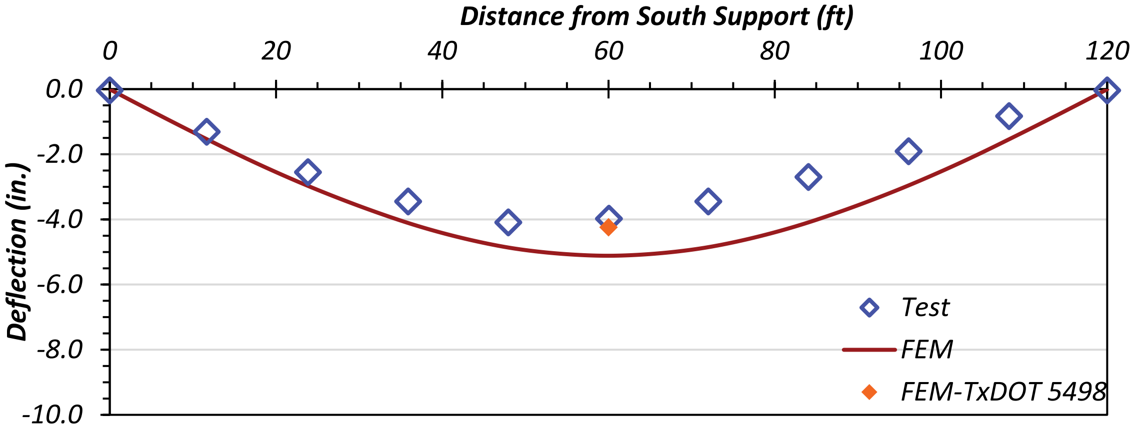

(b) Intact West Girder

Figure 3.25. Comparison of FEM Deflection Profile with Test Results After Web Fracture.

Figure 3.26 shows the stress distribution throughout the bridge and stress concentration at the end of the web fracture. The fracture extends almost the whole depth of both webs and stops 10 in. below the top flange, which is where the torch cut was stopped for the test bridge.

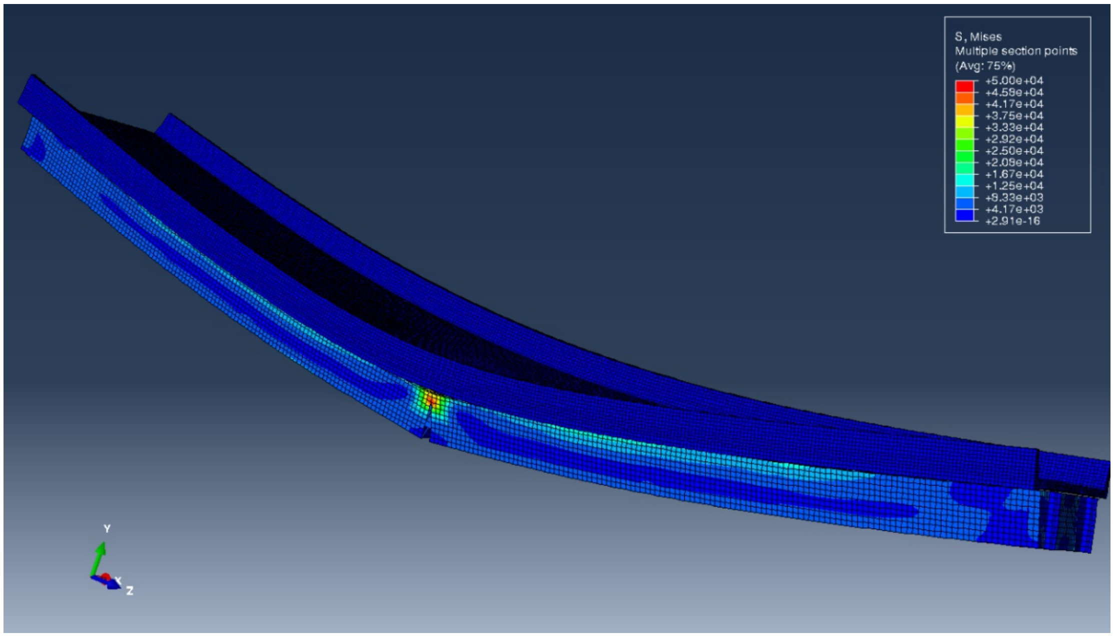

Figure 3.26. FEM von Mises Stress Results Showing the Stress Concentration Web Fracture.

3.5 CONCLUDING REMARKS

The current finite element model in this study used a constant mesh density throughout the bridge. The steel tub girders utilized 6 in. mesh, while the concrete was modeled using a 4 in. mesh size. This initial choice of the mesh size was justified based on similar studies in the literature and engineering judgment. A detailed convergence study was conducted to evaluate the mesh sensitivity of the key parameters.

The accuracy of the FEM results in this phase of the research project, when compared to the field data of the FSEL test bridge, gives confidence to the use of FEM in determining deflections and failure loads of so-called fracture critical bridges. In the following research phase, numerous geometric variations of the FEM model were created that consider the effect of different span lengths, different degrees of curvature, and continuity on redundancy. After the development of the different FEM models, simplified upper-bound plastic yield line theory and lower-bound Grillage methods were explored for determining the ultimate loading condition. The results from both the yield line theory and the grillage method were compared to the results from the various FEM bridge models for accuracy. Last, a set of guidelines for implementing design/analysis and estimating the redundancy levels and reserve strength capacity for twin tub girder bridges was generated.

4 PARAMETRIC STUDY FOR STEEL TWIN TUB GIRDER BRIDGES USING NONLINEAR FINITE ELEMENT ANALYSIS

4.1 INTRODUCTION

The current task deals with a parametric study that includes the selection of 15 typical STTG bridges from the Texas bridge inventory and computational modeling of the selected bridges using FEM. FEM models of the selected bridges were created following the same procedures as the verified FEM model that was tested as part of a previous TxDOT research project (Barnard et al. 2010). The TxDOT 5498 Research Project involved full-scale testing of a fracture critical steel box-girder bridge under static HS-20 truck load and at ultimate load levels following full-depth fracture of the outside girder. The previous chapter presented all the details of the FEM modeling approach and comparative results of different static tests of the test bridge with the simulation results obtained from nonlinear FEM analysis.

The current study investigates the performance of existing fracture critical STTG bridges in the case of a full-depth fracture of one of the girders. Therefore, a total of 15 STTG bridges were selected by considering different span lengths, different degrees of curvature, and the effect of continuity. These parameters are critical geometric parameters for evaluating the bridges' response in terms of load distribution between girders.

FEM models were created using the commercial software package Abaqus, which is a general purpose FEM software that is used to solve a wide range of advanced engineering problems. All bridge models used nonlinear elasto-plastic elements that adequately represent the nonlinear material behavior of crushing concrete and yielding of steel. FEM models were analyzed under the factored HL-93 live load model that includes HS-20 truck loading plus uniform distributed lane loading. Factored load demands were calculated, such as those in the AASHTO LRFD Bridge Design Specifications (AASHTO 2014), using 1.25DL +1.75 (LL + IM), where DL, LL, and IM represent dead load, live load, and impact factor, respectively.

All bridge models were analyzed to identify residual capacity before and after the full-depth fracture (bottom flange, web, and top flange) of the outside girder. Therefore, a quantitative redundancy measure was defined to identify the overstrength of an intact and damaged bridge superstructure to demonstrate the sufficient load carrying capacity under critical flexural conditions. 3D FEM modeling provided more realistic capacity estimations of the bridge by considering the load path redistribution of the lateral load through secondary load paths such as the bridge decks.

The next section presents the Texas STTG bridge inventory and shows distribution of span lengths and curvatures for all STTG bridges. It also describes the selection methodology and lists the 15 selected bridges. The following section provides details about the material and load models used for all FEM models. The fourth and final section of this chapter presents load displacement results for all 15 bridges and lists the overstrength factors.

4.2 EVALUATION OF TXDOT STEEL TWIN TUB BRIDGE INVENTORY

4.2.1 General

It is important that selected bridges represent existing STTG bridge inventory. This selection was done using a range of critical parameters that represent current STTG bridges in Texas. Based on literature and input from TxDOT, the critical parameters were identified as span length, radius of curvature, and continuity. The distribution of these three key parameters were investigated while selecting the 15 bridges for the parametric study.

4.2.2 Distribution of Texas STTG Bridges

Span length is one of the key parameters that can affect postfracture behavior, overall flexural demand, and load distribution. The relatively high flexural strength of steel tub girders offers long-span ranges up to 500 ft. An efficient lower span length is limited to 150 ft due to the 5 ft minimum web depth suggestion, which provides accessibility during inspection. Although very long spans have been achieved, most of the steel twin tub bridges are typically between 150–300 ft in length. Figure 4.1 presents the histogram of maximum span lengths for Texas STTG bridges. the majority of STTG bridges have between 150–300 ft span lengths with a median value of 210 ft.

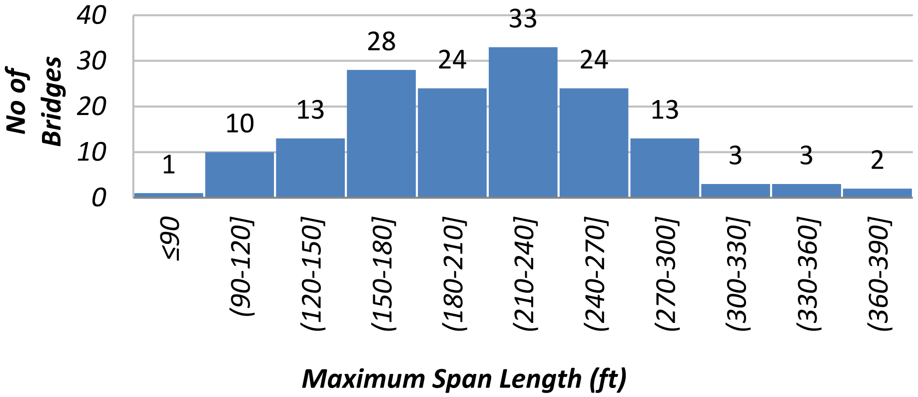

Figure 4.1. Distribution of Texas STTG Bridges by Maximum Span Length.

Another important parameter is the horizontal curvature. Although steel tub girders can be used for straight bridges, they offer a great advantage for curved bridges due to their superior torsional stiffness. They can achieve extremely tight curvatures, up to 6.7E-03. The range of horizontal curvature may be considered from tangential to a 150 ft radius. The flexural bending load demand on the outside girder increases as the curvature increases. Therefore, curvatures of STTG bridges were considered as one of the key parameters for the bridge selection process. Figure 4.2 shows the distribution of Texas STTG bridges by curvature. Most STTG bridges in Texas have curvature values between 7E-04–1.6E-03 with a mean curvature of 1.2E-03.

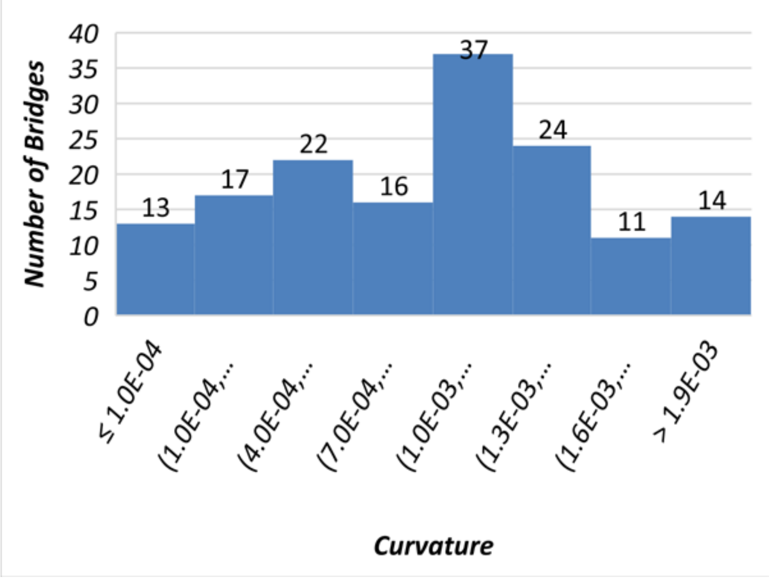

Figure 4.2. Distribution of Texas STTG Bridges by Curvature.

The third parameter of importance is continuity, which generally improves residual capacity due to structural redundancy inherent to continuous bridges. Most STTG bridges are

classified as fracture critical based on load path redundancy that only considers lateral load distribution; thus, all bridges with less than three girders are categorized as fracture critical. However, structural redundancy due to continuity can contribute significantly to longitudinal distribution of the load, thereby improving the flexural capacity. Therefore, different numbers of continuous spans—including simply supported, two-span continuous, and three-span continuous bridges—were considered to assess the effect of continuity on the level of redundancy.
Figure 4.3 provides a histogram for the distribution of STTG bridges in terms of number of continuous spans. Most STTG bridges have three continuous spans; next in frequency are two-span continuous bridges.

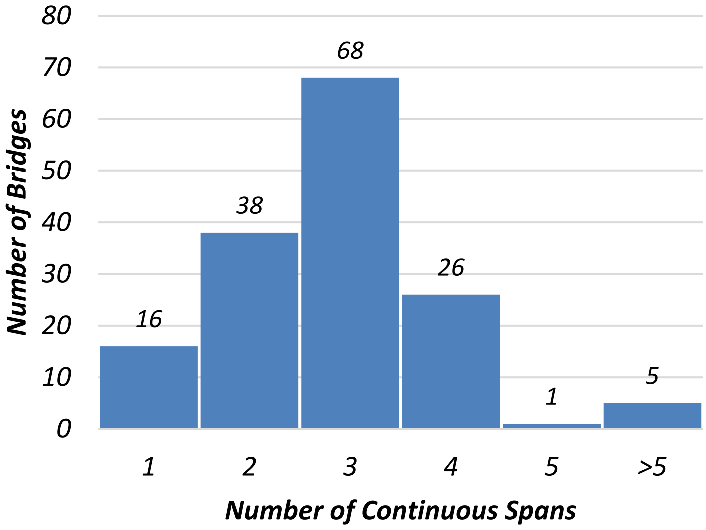

Figure 4.3. Distribution of Texas STTG Bridges by Number of Continuous Spans.

The above listed three key parameters were evaluated to come up with a range of radii of curvatures, span lengths, and number of continuous spans that represent most Texas STTG bridges. Table 4.1 lists the range of selected parameters that were considered for the FEM models for the parametric study.

Table 4.1. Range of Parameters Considered for the Bridge Selection.

Parameter	Range
Span Length, *L*	100–300 ft
Curvature, *R*	0–6E-03
Continuity	Simple, Two, and Three Spans

4.2.3 Selection of Fifteen Representative Steel Twin Tub Girder Bridges

The investigation of the histogram for number of continuous spans suggests that a majority of selected bridges should be three-span continuous followed by two-span continuous and simple-span bridges. These three groups represent all that is necessary to evaluate the structural behavior because they cover simple-span, exterior, and interior spans of continuous bridges. A total of 7 three-span continuous, 5 two-span continuous, and 3 simple-span bridges were selected based on the distribution of Texas STTG bridges by number of spans.

Span length versus curvature scatter plots were created for simple, two-span, and three-span bridges (Figure 4.4, Figure 4.5, and Figure 4.6). The scatter plots were then grouped using k-means clustering, which groups data points using the squared Euclidean distance measured. Clustering scattered data points helps to identify different data groups with multiple parameters. The solid red line shows where the span length to radius ratio is equal to 0.3 ft. For closed box and tub girders, the effect of curvature may be ignored in the analysis for determination of the major-axis bending moments and bending shears if for all spans the arc span divided by radius is less than 0.3 radians, girders are concentric, and bearings are not skewed (AASHTO 2014). The black circled points are the selected bridges for that specific category. The selection procedure followed two main criteria: (a) bridges from different clusters having similar curvature values but different span lengths, and (b) bridges from the same cluster having similar span lengths but different curvatures.

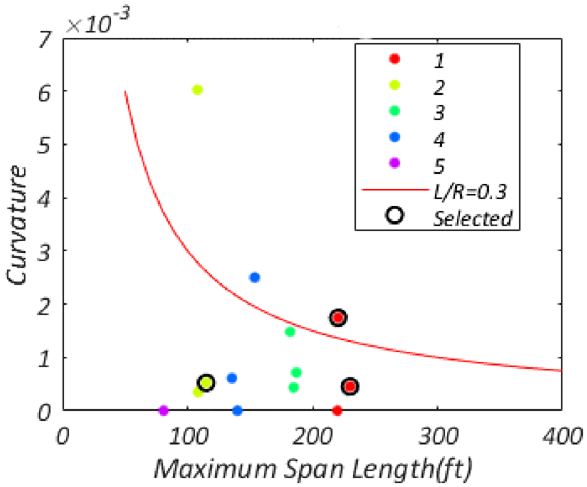

Figure 4.4. Span vs. Curvature Scatter of Simple-Span STTG Bridges in Texas.

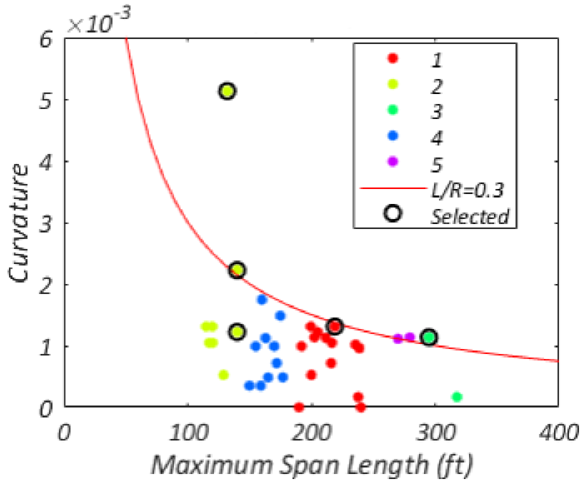

Figure 4.5. Span vs. Curvature Scatter of Two-Span STTG Bridges in Texas.

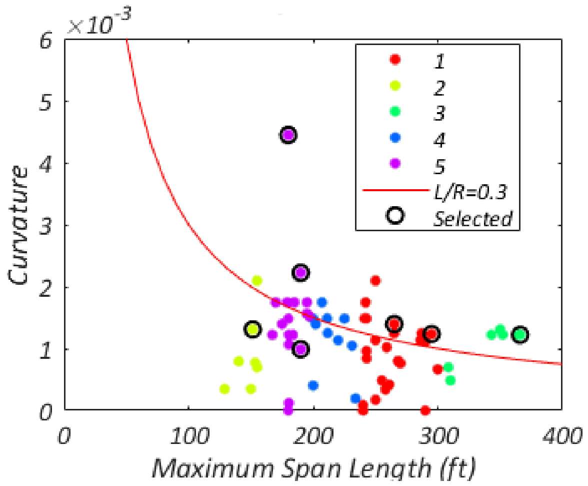

Figure 4.6. Span vs. Curvature Scatter of Three-Span STTG Bridges in Texas.

Figure 4.4 shows the scatter plot with selected bridges for simple-span STTG bridges. Three simple-span bridges were selected for the parametric study: one bridge with a small curvature from the short-span cluster and two bridges with small and large curvatures from the long-span cluster. Similarly, Figure 4.5 presents the scattered distribution of span length-curvature data and selected bridges for two-span STTG bridges. A total of five two-span bridges were selected for the parametric study from different span length groups having various curvature values. Figure 4.6 presents the clustered scatter of span-curvature data and selected bridges for three-span STTG bridges. Four bridges from different span clusters ranging from short to long spans and another three bridges from the medium-span cluster having small, medium, and large curvatures were selected. Table 4.2 lists the selected Texas STTG bridges with their span length radius of curvature and continuity information.

Table 4.2. Main Geometric Properties of Selected Texas STTG Bridges.

Bridge No.	Bridge ID	Span 1 (ft)	Span 2 (ft)	Span 3 (ft)	Radius of Curvature (ft)
1	12-102-3256-01-403	220.5	−	−	573.0
2	12-102-0271-17-530	115.0	−	−	1909.9
3	12-102-3256-01-403	230.0	−	−	2207.3
4	12-102-0271-07-637	132.0	128.2	−	195.0
5	14-227-0-0015-13-452	140.0	139.6	−	450.0
6	12-102-0271-07-575	140.0	140.0	−	818.5
7	12-102-0177-07-394	218.9	189.7	−	763.9
8	12-102-0271-06-661	265.0	295.0	−	881.5
9	12-102-0177-07-394	139.5	151.4	125.6	763.9
10	14-227-0-0015-13-450	148.0	265.0	189.6	716.2
11	12-102-0271-07-593	223.0	366.0	235.0	818.5
12	12-102-0271-07-639	140.0	180.0	145.0	225.0
13	14-227-0-0015-13-452	151.5	190.0	151.5	450.0
14	18-057-0-0009-11-460	150.0	190.0	150.0	1010.0
15	12-102-0271-06-689	200.0	295.0	200.0	809.0
Note: − indicates that data is “not available” or “not applicable.”					

4.3 NONLINEAR FINITE ELEMENT MODEL OF STEEL TWIN TUB GIRDER BRIDGES

4.3.1 General

3D FEM models of all 15 selected bridges were created and analyzed using Abaqus (Dassault Systemes 2017) finite element software. 3D nonlinear finite element analysis enables correct modeling of the geometry and accurate representation of the material properties with very few simplifying assumptions. The selection of mesh size and element type is critical for realistic representation of the bridge geometry and numerical accuracy of computational FEM analysis. In addition, using appropriate material models that can capture the nonlinear behavior of steel and concrete ensures accurate prediction of load displacement behavior at high load levels. Two subsections present finite element types, mesh size, and material models that were used for all bridge models in the parametric study. The third subsection describes the application of the HL-93 load model, load factors, and loading positions that were applied to simulate vehicular design loads.

4.3.2 Element Type and Mesh Size

Depending on the degree of assumptions, one can chose a variety of finite elements ranging from one-dimensional truss and beam elements, to two-dimensional shell elements, to three-dimensional solid brick elements. There are many previous studies, guidelines, and recommendations for appropriately modeling various structural components. Generally, shell elements are the appropriate choice for thin steel plates, while solid elements provide more accurate results for concrete members (Barnard et al. 2010; Puckett et al. 2011; Puckett et al. 2005; Sotelino et al. 2004; Zokaie et al. 1991). Based on those parameters, the concrete deck and railings were modeled using C3D8. The reinforcement was provided using embedded rebars that are modeled as T3D2. Rebar behavior is modeled using metal plasticity that is superposed on the mesh of C3D8 concrete elements. Steel plates of the bottom flanges, webs, top flanges, and end diaphragms use four-node quadrilateral shell elements with reduced integration (S4R), while intermediate diaphragm members and lateral brace members were modeled using B31. The effect of the concrete haunch was incorporated in the pullout behavior of the shear stud connections that were modeled implicitly using CONN3D2.

A mesh size of 8 in. was selected based on a mesh sensitivity study that was conducted on the FSEL test bridge, the details of which were reported in the previous chapter, except that the deck thickness (8 or 8.5 in.) was divided into four elements in the vertical direction to provide improved accuracy and reduce the numerical convergence issues around ultimate load levels due to the cracking of concrete. The effect of deck mesh in the vertical direction was also investigated by using two and four elements for FEM analysis of the FSEL bridge. It was found that both choices provide good ultimate load estimates. However, refined deck mesh in the vertical direction gives slightly better stiffness degradation prediction around ultimate load levels and slightly conservative ultimate load estimate. Therefore, the use of four elements for the deck thickness was adapted for all bridges in the parametric study. Figure 4.7 shows the finite element types and mesh details on a typical STTG bridge (FSEL test bridge).

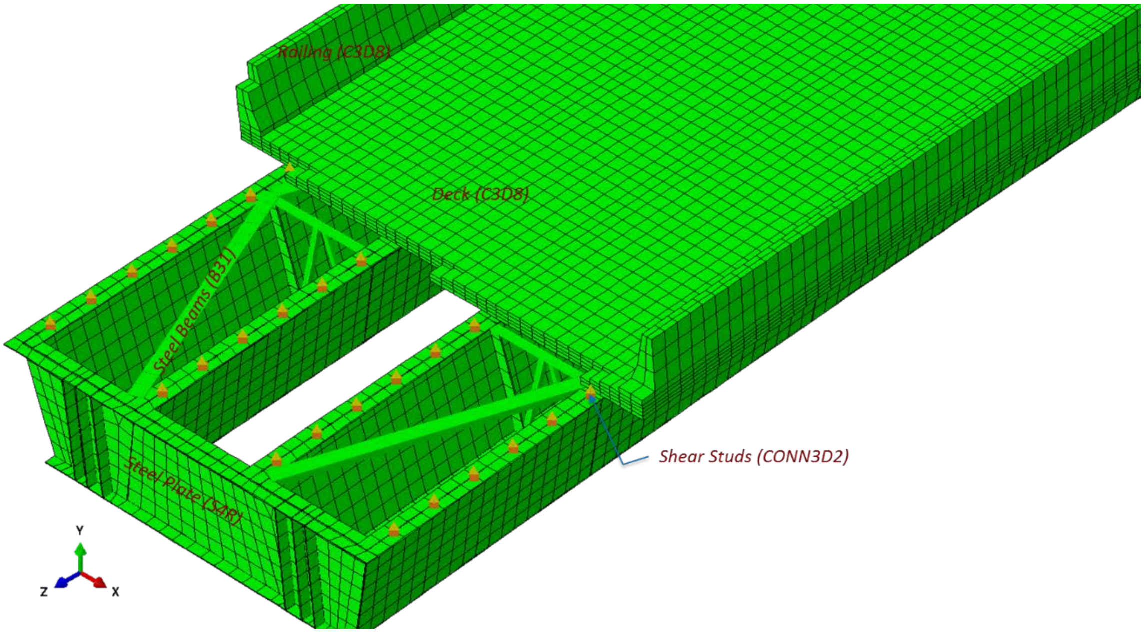

Figure 4.7. Mesh Details and Finite Element Types Shown on a Typical STTG Bridge.

The steel girders were considered to be seated on 3 in. thick elastomeric bearing pads that were 22 in. long and 11 in. wide. The bearing pads were located at the transverse center at both ends of each girder. Simulating the mechanical properties of a bearing pad is important because the boundary conditions may have a significant effect on the overall behavior of the bridge. A compressive stiffness value of 6000 k/in was adapted from other research (Hueste et al. 2015) that used similar bearing pad geometries. The shear stiffness was calculated as 12 k/in. using a manufacturer-provided shear modulus, G = 100.6 psi.

4.3.3 Constitutive Material Models

FEM models for the parametric study used the same constitutive material models as the verified FEM model of the FSEL test bridge. The FEM models were developed utilizing material nonlinearity due to the crushing and cracking of concrete and the yielding of rebar and steel plates. Concrete behavior was modeled using a concrete damaged plasticity model that assumed tensile cracking and compressive crushing as the main failure mechanisms. A 28-day design compressive strength of 4000 psi that is provided in structural drawings was used for all selected STTG bridges. Steel components used classical metal plasticity model with isotropic hardening. Structural drawings provided the design yield strength as 60 ksi and 50 ksi for mild steel reinforcement and steel plates, respectively. The haunch was not modeled explicitly; instead, pullout and shear behavior of studs were modeled implicitly. The behavior of shear studs was modeled using formulas provided by Mouras et al. (2008). Damage mechanics were not included in the steel and concrete material constitutive models because the stiffness degradation and local failures are complex and create numerical convergence problems for the complex behavior of reinforced concrete.

4.3.3.1 Steel Components

All tub girders of selected STTG bridges are built-up members using Grade 50 structural steel. The constitutive behavior of steel plates and reinforcing bars were modeled using classical metal plasticity with the isotropic strain hardening rule and without rate dependency. Perfectly plastic behavior was assumed once the equivalent stress reached the yield strength point based on the von Mises yield criteria. ASTM A615 grade 60 steel was used for all reinforcing bars in deck slabs and railings. Figure 4.8 shows the stress-strain model of steel that was adapted from Barnard et al. (2010).

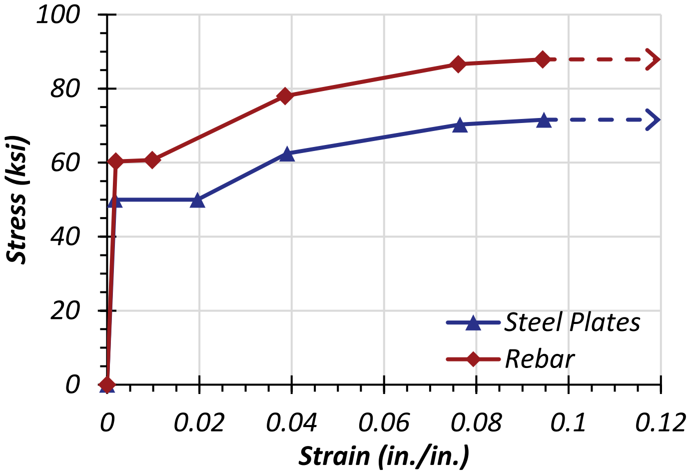

Figure 4.8. Constitutive Model for Steel Components (adapted from Barnard et al. [2010]).

4.3.3.2 Reinforced Concrete

The constitutive behavior of concrete was simulated with the concrete damaged plasticity model that uses the concept of isotropic damaged elasticity together with tensile and compressive plasticity to represent the inelastic behavior of concrete. This model is intended primarily for reinforced concrete structures and suitable for concrete under low confining pressures in which the main failure criteria is tension cracking or compression crushing. The constitutive behavior of concrete was defined using the Kent and Park (1971) model, with a design compressive strength of 4000 psi. The behavior after reaching the tensile and compressive strength was assumed to be perfectly plastic.

Figure 4.9 shows the adopted stress-strain behavior of concrete. The tensile strength of the concrete was calculated using the empirical relation provided in AASHTO LRFD (2014) Article 5.4.2.6, as follows in Equation (4.1):

$$f_r = 0.2\sqrt{f_c'} \tag{4.1}$$

where, f_r = the modulus of rupture (ksi) and f_c' = the compressive strength of concrete (ksi). The modulus of elasticity of concrete for different ages of concrete were also calculated using an empirical relation provided in AASHTO LRFD (2014) Article 5.4.2.4, in Equation (4.2):

$$E_c = 33000K_1 w_c^{1.5}\sqrt{f_c'} \tag{4.2}$$

where K_1 = the correction factor for the source of aggregate, which is taken to be 1.0 unless determined by physical test; w_c = the unit weight of concrete (kcf), using 0.145 kcf for the normal weight of concrete; and f_c' = compressive strength of concrete (ksi).

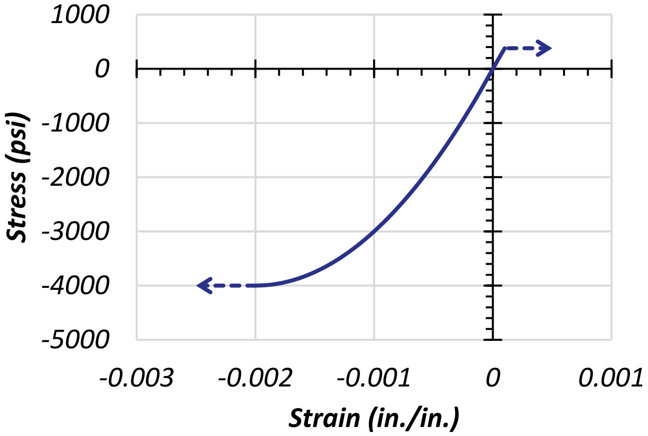

Figure 4.9. Concrete Stress-Strain Behavior for Damaged Plasticity Model.

The concrete damaged plasticity model requires the definition of various mechanical parameters to define the inelastic behavior of concrete. In addition to the compression hardening and tension-stiffening behavior, the dilation angle, the flow potential eccentricity, and the ratio of biaxial compression to uniaxial compression, the ratio of second stress invariant in tensile meridian to that of the compression meridian must be provided. In the absence of detailed material properties, default values that are common for normal concrete were used.

4.3.3.3 Modeling Shear Stud and Haunch Behavior

Shear studs develop composite action between steel girders and the reinforced concrete deck. Simulating mechanical behavior of this composite action is critical to capturing the ultimate load behavior of STTG bridges because the stud-haunch connection is under significant pullout and shear force following the fracture of one tub girder. Similar to the verified FEM model of the FSEL test bridge, the parametric study used load displacement expressions provided in Topkaya et al. (2004) for horizontal shear behavior for all STTG bridges. These equations model the load versus horizontal slip behavior for a stud or group of studs as a function of the total cross-sectional area of shear studs and the compressive strength and modulus of elasticity of concrete. Detailed equations for the horizontal shear model of the studs are provided in Chapter 3. Figure 4.10 shows a typical shear model for a group of studs that has 1.8 in^2 total cross-sectional area in 4 ksi concrete.

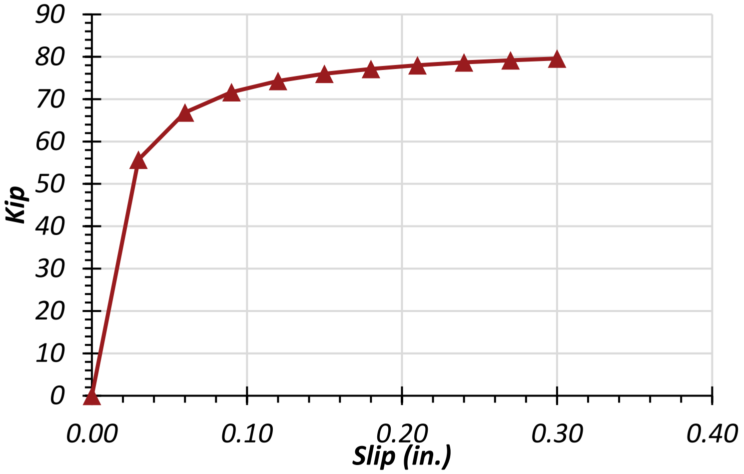

Figure 4.10. Constitutive Shear Model of Stud-Haunch Connection—Bridge 1.

Similar to the verified FEM model, the pullout behavior of shear studs was modeled using the recommendations of Sutton (2007) and Mouras et al. (2008), which include modification factors for ACI equations to account for the haunch thickness. Figure 4.11 shows typical pullout behavior from experiments and assumed behavior for connector elements of the FEM model.

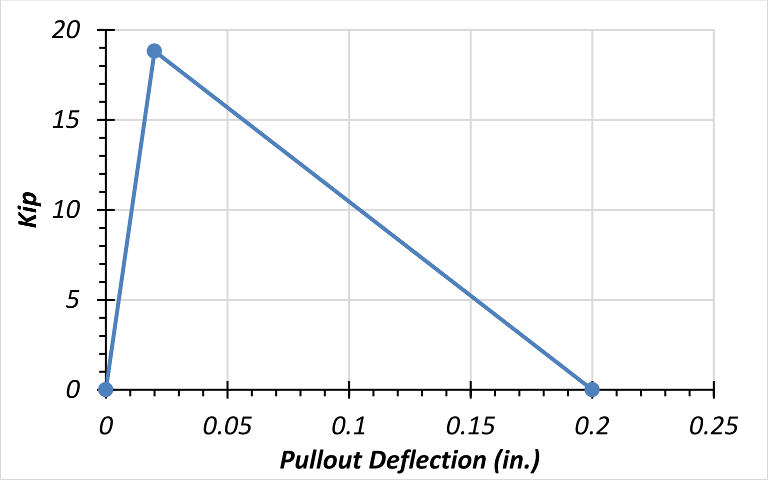

Figure 4.11. Stud Pullout Behavior—Bridge 1.

4.3.4 Simulating the Design Loading

A full three-dimensional non-linear elasto-plastic finite element model of all 15 bridges was created using the commercial software Abaqus (Dassault Systemes 2017) by following the procedures described above. Prior to any vehicular loading, dead loads were applied to realistically capture any locked-in stresses that developed due to construction loads. These initial loads were simulated in five steps: Step 1 was taking the self-weight of steel twin tub girders to simulate the stresses induced during the erection of girders. Step 2 was the application of deck and railing weight on the top flanges of tub girders to simulate additional stresses on non-composite steel tub girders when the deck concrete is fresh. To achieve such a loading simulation in Abaqus, a mock deck and railing (with very small stiffness and mass) were defined and tied to the actual deck and railing. The purpose of the mock sections was to keep track of the deflected shape so that the actual deck could be correctly positioned once the concrete hardened. During the second step, the deck, the railing, and the reinforcement were all removed from the model, and their weight was applied on the top flange. Step 3 was the activation of the deck, railing, and reinforcement with self-weight and the removal of the applied distributed load from the top flanges. Step 4 included removal of temporary exterior diaphragms and removal of weld connectors mid-span of the outside girder for the span being analyzed. If the analysis is for the nonfractured case, the weld connectors are not removed. The fracture event is assumed to happen while the HL-93 load is on the structure (1.25DL + 1.0LL). Extreme event load factors for live loads are generally smaller than 1.0 to account for the very low joint probability of two events (such as an earthquake and live load). However, in the case of a fracture, the probability of having a fracture while the truck is on the bridge is more likely. Therefore, the load factor for live loads are 1.0.

All bridges were first analyzed without any fracture and then with a full-depth fracture crack mid-span of the outside girder under a factored HL-93 vehicular load model that consisted of an HS-20 truck load with impact plus a uniform distributed lane load (LL = 0.64 k/ft applied over a 10 ft width). In Step 5, the live load was updated to 2.33HS20 + 1.75LL to account for design load factors. The total load at Step 5 was equal to 1.25DL + 2.33HS20 + 1.75LL for a one-lane-loaded case, and the same amount of factored vehicular load (2.33HS20 + 1.75LL) was applied to the second lane for a two-lanes-loaded case. Figure 4.12 shows the longitudinal and transverse positions of an HS-20 truck and uniform distributed lane load for two-lane bridges. The first lane was defined 2 ft away from the nominal face of the outer rail, and the second lane was defined as adjacent to the first lane. The transverse positions of the HS-20 truck and uniform distributed lane loading was favored toward the outer rail to create a more critical loading condition because all bridges are curved, and the fracture was created mid-span of the outer girder. All selected STTG bridges are two-lane bridges; therefore, the analysis involved both one-lane-loaded and two-lanes-loaded cases. The same loading conditions as Step 5 were applied for the following steps until the structure lost 95 percent of initial stiffness of the intact bridge. The initial three steps were conducted using static analysis to capture locked-in construction stresses. The following steps were conducted using general nonlinear dynamic analysis that uses implicit time integration to obtain a quasi-static response in which inertia effects are introduced.

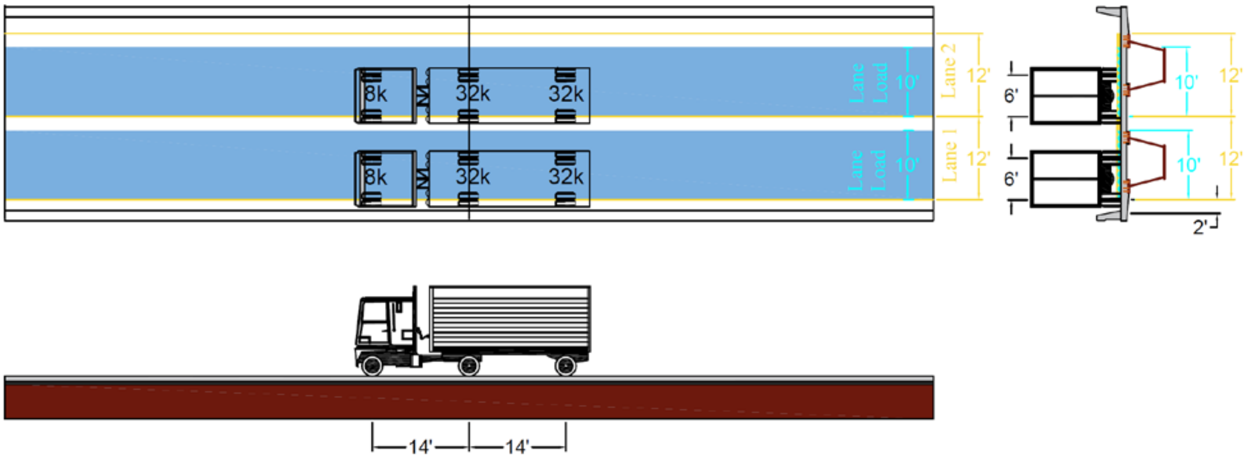

Figure 4.12. HL-93 Load Position for Two-Lane-Loaded Case.

4.4 FINITE ELEMENT ANALYSIS OF SELECTED STTG BRIDGES

In an investigation of the redundancy level (overstrength) of the damaged bridge superstructure, an overstrength factor is defined in Equation (4.3):

$$\Omega = R_d/Q_u \tag{4.3}$$

where R_d = the capacity of the damaged bridge and Q_u = the factored load demand. The bridge can be considered redundant with sufficient reserve capacity when $\Omega > 1.0$. Redundancy levels of each selected STTG bridge were evaluated based on the FEM results using nominal material properties. Factored load demands were the same as those in the AASHTO LRFD Bridge Design Specifications (2014): 1.25DL + 1.75 (HS20 + IM) +1.75LL, where DL , LL, and IM represent dead load, lane load, and impact factor, respectively.

It is important to define ultimate capacity to be able to evaluate the redundancy level of a bridge. Ghosn and Moses (1998), in *NCHRP Report 406*, defined ultimate capacity as the ultimate load that can be applied before the collapse of the bridge, and they defined collapse as the formation of a collapse mechanism. Long-span, highly ductile structures can experience significant deflections prior to formation of a collapse mechanism. Therefore, researchers have generally developed the ultimate limit state and the deflection limit states (Ghosn and Moses 1998; Hunley and Harik 2012). In this research, a similar approach was adopted, and the two-limit states are defined as (a) ultimate limit state, and (b) deflection limit states. Ultimate limit state is defined as the load that corresponds to formation of a collapse mechanism, and this point is explicitly defined as the point at which the bridge stiffness drops to 5 percent of the initial stiffness (SF) of an intact bridge. Deflection limit states are defined as the limit chord rotation along the outside girder and the transverse relative deck rotation. A chord rotation value equal to 2 degrees for simple and interior spans and 3 degrees for exterior spans is used as a deflection limit state in the longitudinal direction. The transverse deck rotation of 5 degrees is recommended as the second deflection limit state. At such longitudinal and transverse rotation levels, the bridge loses its functionality, becomes very uncomfortable for the bridge users, and provides sufficient damage indication to an observer.

The above described ultimate limit state and two deflection limit states were used to define the ultimate capacity of the analyzed bridges. The following subsections summarize the FEM models and the redundancy plots for the FSEL bridge and 15 selected bridges. The redundancy evaluation includes load displacement and load rotation charts.

4.4.1 Bridge 0—FSEL Bridge

The FSEL test bridge was originally used as a section of the exit ramp on the IH 10/Loop 610 interchange in Houston, Texas. The bridge girders were configured in a simply supported fashion, with a total bridge span length of 120 ft, and re-decked at the Ferguson Laboratory at UT Austin. The details of the geometry are provided as part of the previous chapter, in which the FEM model was analyzed under experimental loads. In this chapter, the same FEM model was analyzed under factored design loading to evaluate redundancy level with respect to design level loads. Because of its 23 ft deck width, it was analyzed as a one-lane bridge. This bridge is the only one-lane bridge that was analyzed as part of this research study; the remaining 15 bridges are two-lane bridges.

Figure 4.13 shows the deflection profile of Bridge 0 at the ultimate capacity, and Figure 4.14(a) illustrates the load displacement along the centerline of the outside and inside girders; the secondary x-axis on top depicts the chord rotations, and the secondary y-axis on the right shows the overstrength, which is the normalized load by the factored design load (1.25DL + 1.75(HS20 + IM) + 1.75LL). Solid lines represent the behavior of the outside girder, while dashed lines represent the inside girder. The blue lines show the results obtained from the FEM analysis of the fractured bridge where a full-depth fracture is induced at the maximum moment location of the outside girder. The green lines show the FEM results for the nonfractured bridge in its intact state. The ultimate load points are shown with diamond symbols. The ultimate load points are defined based on the stiffness degradation principle that is based on the initial stiffness of the intact bridge or the deflection limit state as described above.

Figure 4.14(b) shows the longitudinal deck rotation along the outer flange of the outside girder and transverse deck rotations at the cross-section corresponding to maximum deflections. Positive transverse deck rotation occurs at the interior top flange of the outside girder, while the negative transverse deck rotation corresponds to relative rotation at the interior top flange of the inside girder.

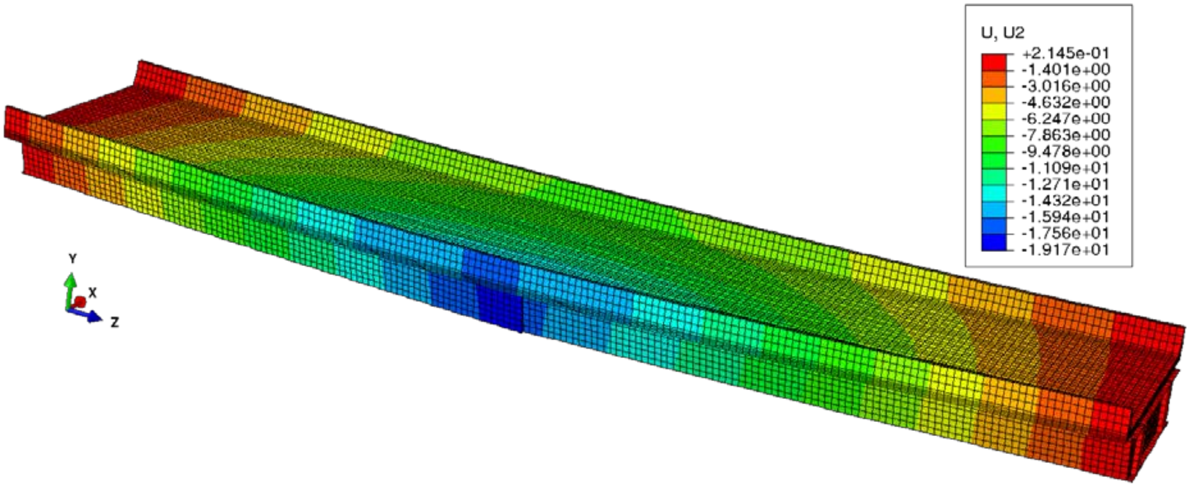

Figure 4.13. FEM Deflection Profile of Bridge 0 with Fractured Outside Girder.

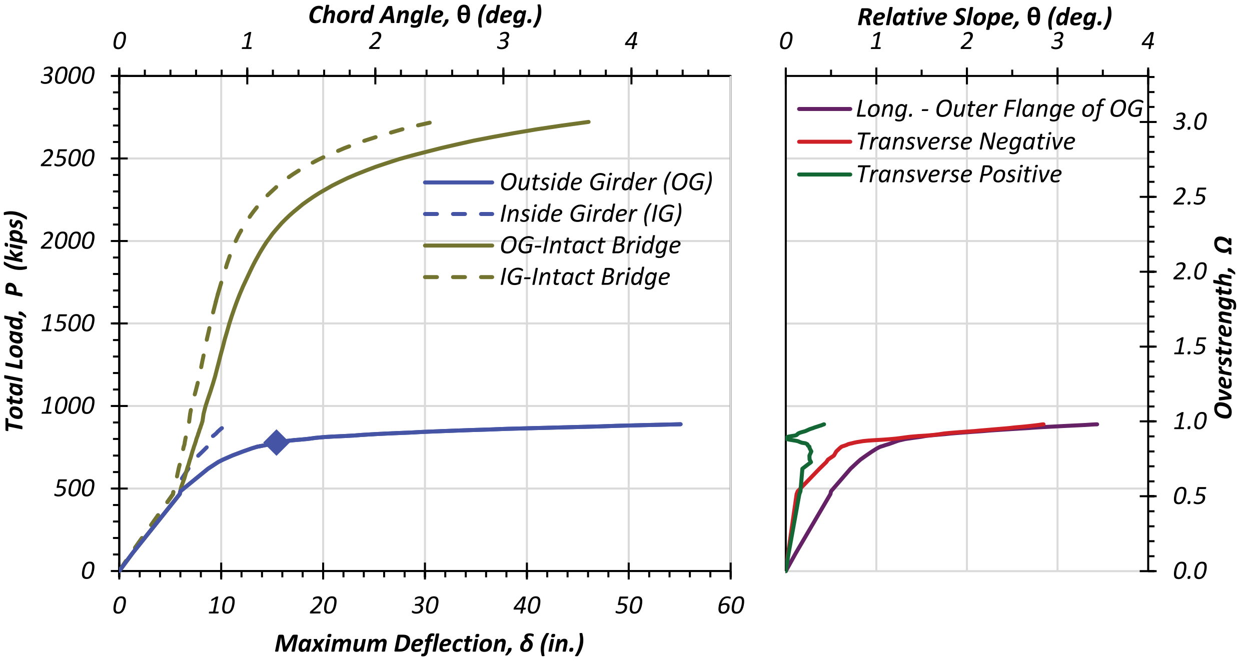

(a) Load displacement

(b) Deck rotations

Note: δ is along the centerline of the outside girder, Ω is the load normalized by factored design load.

Figure 4.14. FEM Results for Bridge 0.

4.4.2 Bridge 1—NBI #12-102-3256-01-403

Bridge 1 was built in 2007 in Houston on an IH 10 connector. It is a single-span simply supported bridge, 220.5 ft long, 32 ft 5 in. wide, with an 8 in. thick deck supported by two steel tub girders. A nonlinear FEM model of the bridge was created following the procedures described in Chapter 3. Table 4.3 and Table 4.4 provide tabulated information about overall geometry and member dimensions that are necessary for creating the FEM model. Further details about bridge geometry, member dimensions, reinforcement, diaphragm, and bracing details may be found in the structural drawings that are provided in Appendix A.

Table 4.3. Geometric Properties and Member Dimensions of Bridge 1.

Location	Parameter	Description/Value
Bridge	Location	Harris County, I-610
	Year Designed/Year Built	2004/2007
	Design Load	HS20
	Length, ft	220.46
	Spans, ft	220.46
	Radius of Curvature, ft	572.96
Deck	Width, ft	32.417
	Thickness, in.	8
	Haunch, in.	5
	Rail Type	SSTR
Studs	No. of Studs per row	3
	Length, in.	6
	Diameter, in.	0.875
Interior Intermediate Diaphragm	Top Angle	L 5 x 3 1/2 x 5/8
	Diagonal Angle	L 5 x 3 ½ x 5/8
	Stiffeners	5/8" x 7"
Exterior Erection Diaphragm	Top Shape	WT 7 x 34
	Diagonal Angle	L 5 x 3 ½ x 5/8
	Bottom Shape	WT 7 x 34
End Diaphragm	Interior Plate	1"
	Exterior Plate	1"
	Top Exterior Plate	1" x 18"
	Bottom Exterior Plate	1" x 18"
	Top Interior Plate	1" x 18"
	Stiffeners	1" x 9"
		1 1/4" x 9"

Note: Typical exterior, interior, and end diaphragms are listed. See Appendix A for other types.

Table 4.4. Geometric Details of Steel Tub Girders for Bridge 1.

Location ft	Top Flange		Web		Bottom Flange	
	Width in.	Thickness in.	Width in.	Thickness in.	Width in.	Thickness in.
0–52	18	1.50	84	2.625	72	1.000
52–167	18	2.25	84	2.625	72	1.500
167–220	18	1.50	84	2.625	72	1.000

Figure 4.15 shows the deflection profile of Bridge 1 at the ultimate load level, and Figure 4.16(a) illustrates the load displacement for both fractured and intact bridges along the centerline of the outside and inside girders. Figure 4.16(b) shows deck rotations in the longitudinal and transverse directions for fractured Bridge 1. Although stiffness drops to 5 percent of initial stiffness, at Ω = 0.88, the chord rotations and deck transverse rotation limits occurs at Ω = 0.82, which controls the ultimate capacity. Bridge 1 is one of the longest single-span bridges, with a 220 ft span length. FEM results indicate that the bridge cannot carry the factored design load when the outside girder has a full-depth fracture.

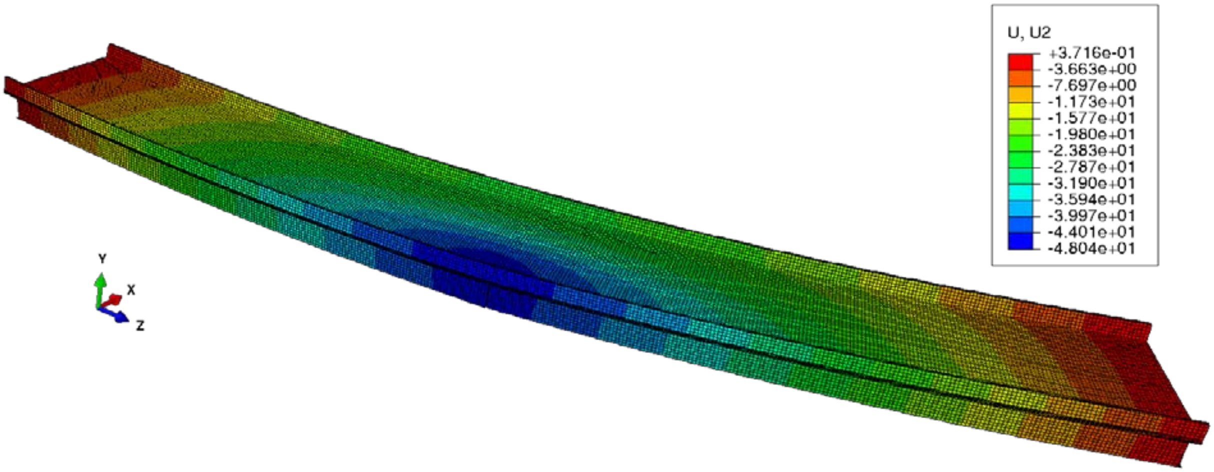

Figure 4.15. FEM Deflection Profile of Bridge 1 with Fractured Outside Girder.

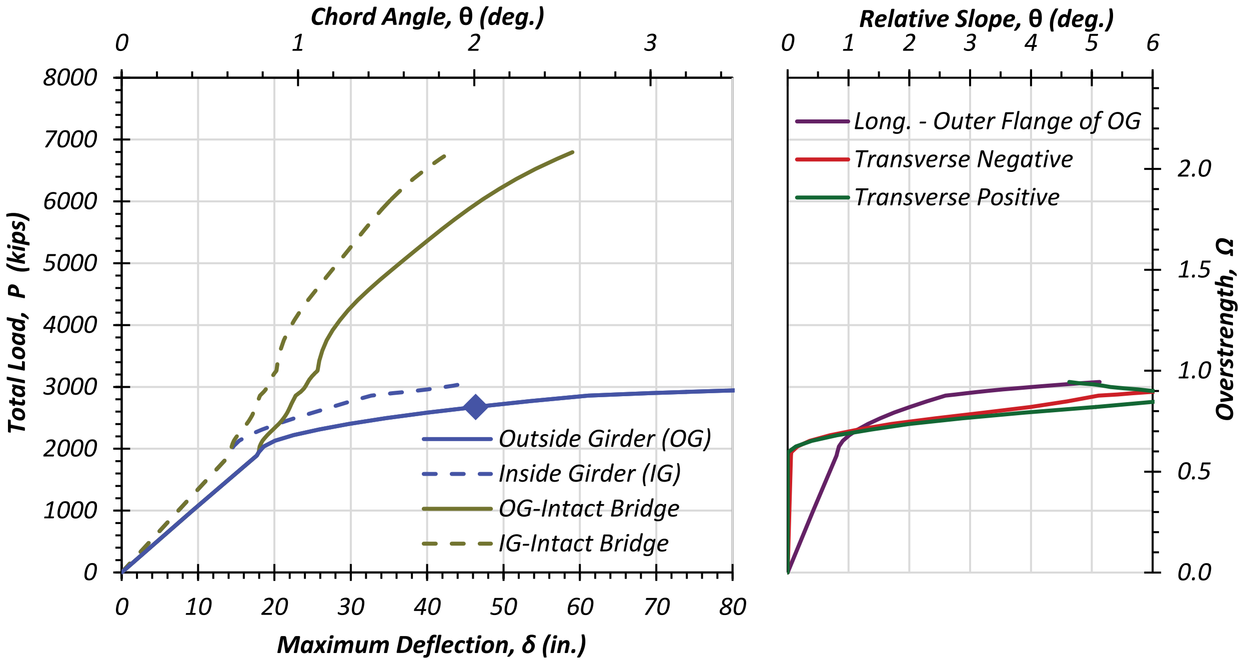

(a) Load displacement *(b) Deck rotations*

Note: δ is along the centerline of the outside girder, Ω is the load normalized by factored design load.

Figure 4.16. FEM Results for Bridge 1.

4.4.3 Bridge 2—NBI #12-102-0271-17-530

Bridge 2 was built in 2004 in Harris County on the I-610 connector. It is a single-span simply supported bridge 115 ft long, 26.6 ft wide, and has an 8 in. thick deck. The nonlinear FEM model of Bridge 2 follows similar procedures and loading conditions as described for Bridge 1. Table 4.5 and Table 4.6 provide member dimensions and tabulated information about overall geometry for Bridge 2. Further details about bridge geometry, member dimensions, reinforcement, diaphragm, and bracing details may be found in the structural drawings that are provided in Appendix A.

Table 4.5. Geometric Details of Steel Tub Girders for Bridge 2.

Location ft	Top Flange		Web		Bottom Flange	
	Width in.	Thickness in.	Width in.	Thickness in.	Width in.	Thickness in.
0–115	18	1.00	79	0.625	50	1.000

Table 4.6. Geometric Properties and Member Dimensions of Bridge 2.

Location	Parameter	Description/Value
Bridge	Location	Harris County, I-610
	Year Designed/Year Built	2002/2004
	Design Load	HS25
	Length, ft	115
	Spans, ft	115
	Radius of Curvature, ft	1909.86
Deck	Width, ft	26.625
	Thickness, in.	8
	Haunch, in.	4
	Rail Type	SSTR
Studs	No. of Studs per row	4
	Length, in.	7
	Diameter, in.	0.875
Interior Intermediate Diaphragm	Top Angle	L 5 x 3 ½ x 1/2
	Diagonal Angle	L 5 x 3 ½ x 1/2
	Stiffeners	5/8" x 7"
Exterior Erection Diaphragm	Top Shape	WT 7 x 21.5
	Bottom Shape	WT 7 x 21.5
	Diagonal Angle	L 5 x 3 ½ x 1/2
Exterior End Diaphragm	Top Plate	1" x 16"
	Solid Plate	3/4"
	Bottom Plate	1" x 16"
Interior End Diaphragm	Solid Plate	1"
	Top Plate	1" x 16"
	Stiffeners	1 1/2" x 8"

Note: Typical exterior, interior, and end diaphragms are listed. See Appendix A for other types.

Figure 4.17 shows the deflection profile of Bridge 2 at the ultimate load level, and Figure 4.18 illustrates the load displacement and deck rotation plots. FEM results indicate that Bridge 2 can carry 3.6 times the factored design load in its intact state. The FEM model of Bridge 2 was also analyzed by introducing a full-depth fracture mid-span of the outside girder while the HL-93 loading is located mid-span and 2 ft away from the face of the outside rail in the transverse direction. FEM results of the fractured Bridge 2 estimates the overstrength factor as 1.65, which is 55 percent lower than an intact Bridge 2. This single-span bridge has medium span length, and it can carry more than the factored design load in its fractured condition. Although stiffness drops to 5 percent of initial stiffness at Ω = 0.1.75, the chord rotation limits occurs at Ω = 1.65, which controls the ultimate capacity.

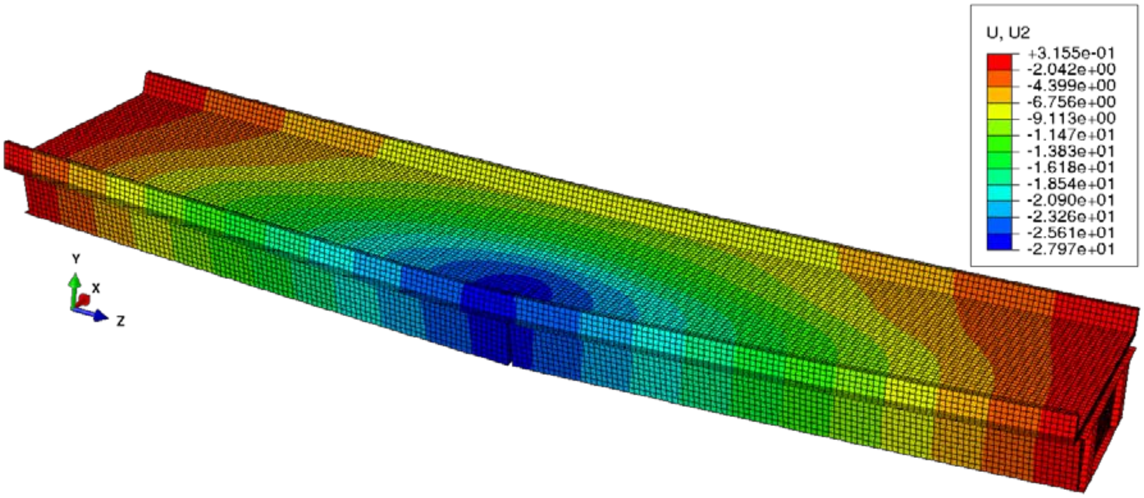

Figure 4.17. FEM Deflection Profile of Bridge 2 with Fractured Outside Girder.

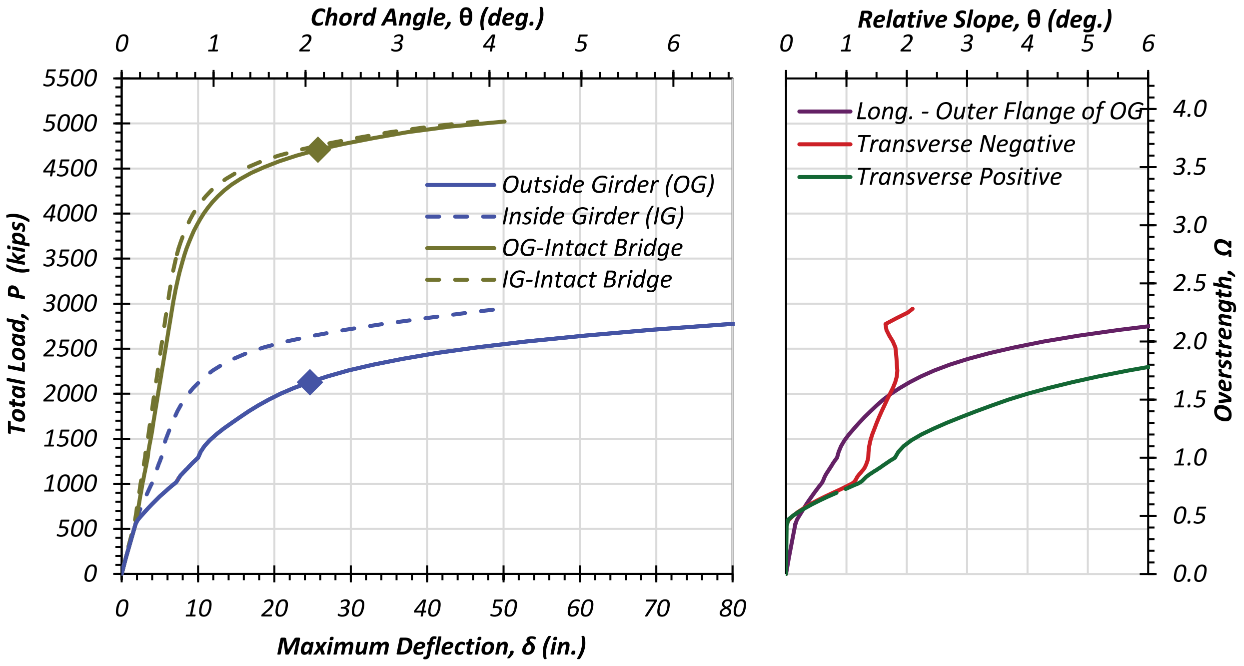

(a) Load displacement *(b) Deck rotations*

Note: δ is along the centerline of the outside girder, Ω is the load normalized by factored design load.

Figure 4.18. FEM Results for Bridge 2.

4.4.4 Bridge 3—NBI #12-102-0508-01-294

Bridge 3 was built in 2002 in Harris County. It is a single-span simply supported bridge with a 230 ft span length, 38.8 ft wide roadway, and a 9 in. thick deck. Table 4.7 summarizes the information about overall geometry and member dimensions for Bridge 3. Table 4.8 lists the geometric dimensions of steel tub girder components throughout the length of the bridge. The steel tub girders of the bridge have a constant web thickness, but the top and bottom flange thickness varies. Further details about bridge geometry, member dimensions, reinforcement, longitudinal stud spacing, other diaphragm types, and lateral bracing details may be found in the structural drawings that are provided in Appendix A.

Table 4.7. Geometric Properties and Member Dimensions of Bridge 3.

Location	Parameter	Description/Value
Bridge	Location	Harris County, FWY
	Year Designed/Year Built	1997/2002
	Design Load	HS20
	Length, ft	230
	Spans, ft	230
	Radius of Curvature, ft	2207.3
Deck	Width, ft	38.833
	Thickness, in.	9
	Haunch, in.	4
	Rail Type	T-501
Studs	No. of Studs per row	3
	Length, in.	6
	Diameter, in.	0.875
Interior Intermediate Diaphragm	Top Angle	L 5 x 5 x 1/2
	Diagonal Angle	L 5 x 5 x 1/2
	Stiffeners	3/4" x 8"
Exterior Erection Diaphragm	Top Shape	WT 8 x 33.5
	Bottom Shape	WT 8 x 33.5
	Diagonal Angle	L 5 x 5 x 1/2
Interior End Diaphragm	Top Plate	1" x 16"
	Solid Plate	2"
	Stiffeners	3/4" x 7"
Exterior End Diaphragm	Top Plate	1" x1 6"
	Solid Plate	3/4"
	Bottom Plate	1" x 16"

Note: Typical exterior, interior, and end diaphragms are listed. See Appendix A for other types.

Table 4.8. Geometric Details of Steel Tub Girders for Bridge 3.

Location ft	Top Flange		Web		Bottom Flange	
	Width in.	Thickness in.	Width in.	Thickness in.	Width in.	Thickness in.
0–21	24	1.50	102	0.75	63.5	1.250
21–42	24	2.50	102	0.75	63.5	1.750
42–185	24	3.00	102	0.75	63.5	2.750
185–207	24	2.50	102	0.75	63.5	1.750
207–230	24	1.50	102	0.75	63.5	1.250

Figure 4.19 shows the FEM deflection profile for Bridge 3 at the ultimate load level, Figure 4.20(a) presents load versus displacement results along the centerline of the outside and inside girders of Bridge 3, and Figure 4.20(b) provides deck rotation results. The FEM analysis of the nonfractured Bridge 3 resulted in a 2.3 overstrength factor, while the fractured case has a 0.85 overstrength factor that is a reduction of 37 percent due to a full-depth fracture of the outside girder. Overstrength factors of Bridge 3 can somewhat be compared to that of Bridge 1, which has a similar span length but a larger radius of curvature. The radius of curvature of Bridge 1 is 573 ft, while Bridge 3 has a 2207 ft radius. The radius of curvature of Bridge 3 is almost four times larger, but the overstrength factor is only slightly increased from 0.82 to 0.85 for the fractured case. Note that the radius of curvature is not the only variable between the two bridges; they also have different deck and girder geometries.

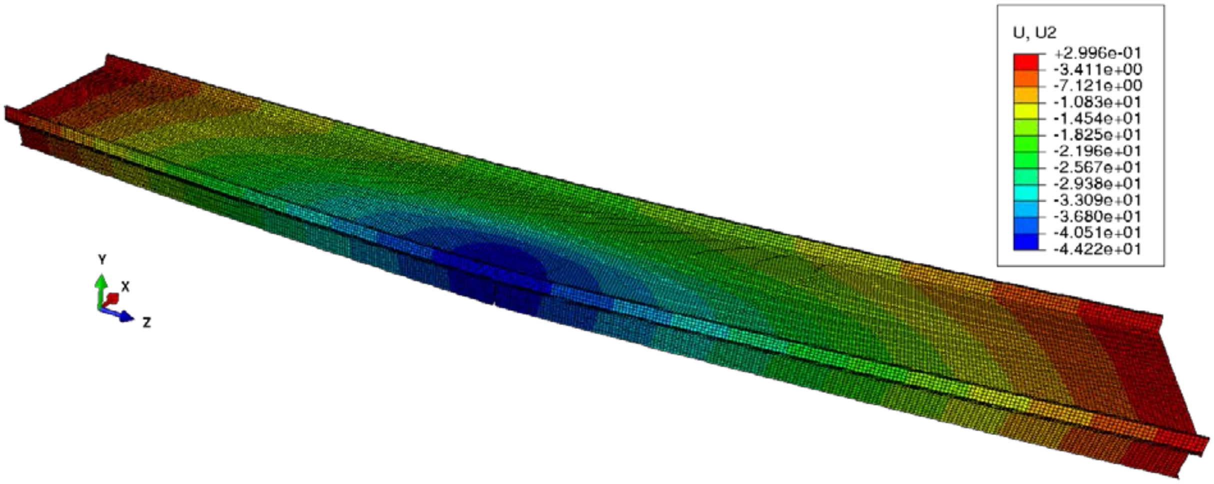

Figure 4.19. FEM Deflection Profile of Bridge 3 with Fractured Outside Girder.

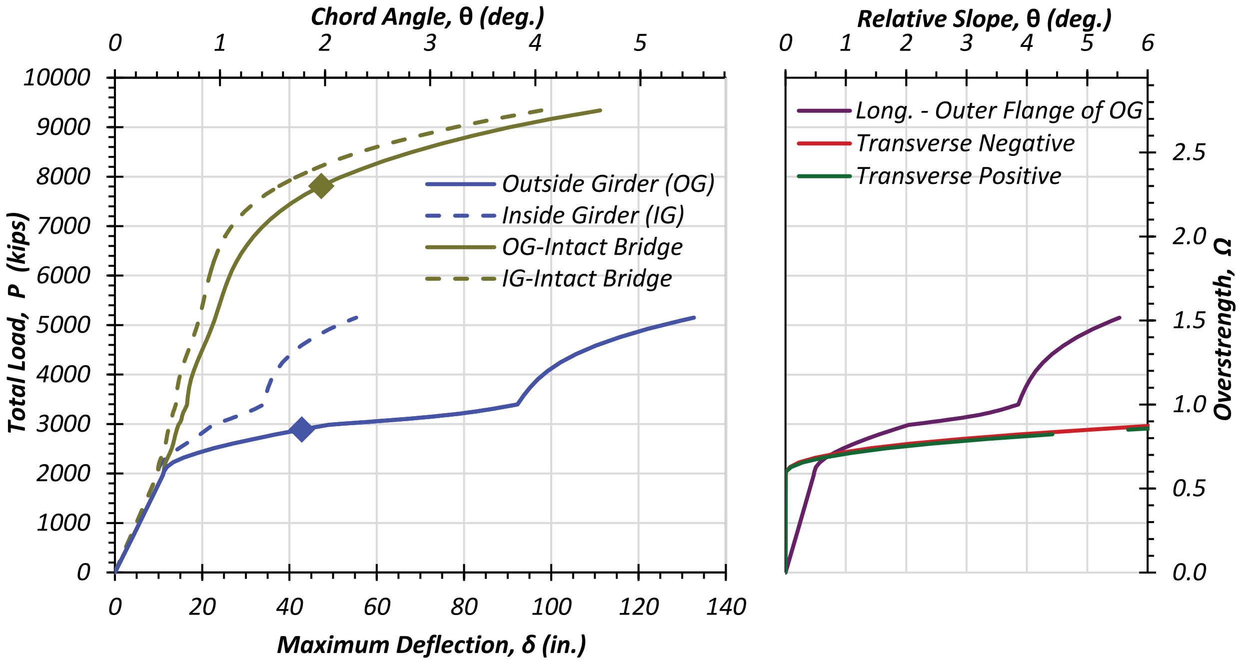

(a) Load displacement (b) Deck rotations

Note: δ is along the centerline of the outside girder, Ω is the load normalized by factored design load.

Figure 4.20. FEM Results for Bridge 3.

4.4.5 Bridge 4—NBI #12-102-0271-07-637

Bridge 4 was built in 2007 in Harris County. It is a two-span continuous STTG bridge having 132 ft and 128 ft span lengths; it is 28.4 ft wide and has an 8.5 in. thick deck. Table 4.9 summarizes the overall geometry properties and member details for Bridge 4. Table 4.10 lists the dimensional details of the steel tub girder components along the entire length of the bridge. The steel tub girders of the bridge have a constant web thickness, but the top and bottom flange thickness varies. Further details may be found in the structural drawings of Bridge 4 that are provided in Appendix A.

Table 4.9. Geometric Properties and Member Dimensions of Bridge 4.

Location	Parameter	Description/Value
Bridge	Location	Harris County, FWY
	Year Designed/Year Built	2004/2007
	Design Load	HS25
	Length, ft	260.27
	Spans, ft	132.03, 128.24
	Radius of Curvature, ft	195
Deck	Width, ft	28.417
	Thickness, in.	8.5
	Haunch, in.	3.5
	Rail Type	SSTR
Studs	No. of Studs per row	3
	Length, in.	7
	Diameter, in.	0.875
Interior Intermediate Diaphragm	Top Angle	L 5 x 5 x 1/2
	Diagonal Angle	L 5 x 5 x 1/2
	Stiffeners	1/2" x 8"
Exterior Erection Diaphragm	Top Shape	WT 7 x 21.5
	Diagonal Angle	L 5 x 3 x ½ x 1/2
	Bottom Shape	WT 7 x 21.5
End and Bent Diaphragm	Interior Top Plate	1" x 16"
	Interior Solid Plate	3/4"
	Interior Bottom Plate	1" x 16"
	Exterior Top Plate	1" x 16"
	Exterior Solid Plate	3/4"
	Stiffeners	1" x 8"

Note: Typical exterior, interior, and end diaphragms are listed. See Appendix A for other types.

Table 4.10. Geometric Details of Steel Tub Girders for Bridge 4.

Location ft	Top Flange		Web		Bottom Flange	
	Width in.	Thickness in.	Width in.	Thickness in.	Width in.	Thickness in.
0–82	20	1.00	54	0.5	72	0.875
82–110	20	1.50	54	0.5	72	1.750
110–130	20	2.75	54	0.5	72	1.750
130–150	20	2.75	54	0.5	72	1.750
150–177	20	1.50	54	0.5	72	1.750
177–260	20	1.00	54	0.5	72	0.875

Nonlinear FEM analyses were performed separately for the fractured and nonfractured cases for both spans of Bridge 4 by placing the design vehicular live load at mid-span of the span under consideration. The fractured condition was created by removing the welded connectors of the bottom flange and both webs and top flanges of the outside girder at the moment-critical location. Figure 4.21 shows the meshed superstructure and deflection profile of Span 1 for Bridge 4 at ultimate load level and Figure 4.22 shows the load versus displacement plots for Span 1 of Bridge 4 along the centerline of the outside and inside girders.

Figure 4.23 shows the meshed superstructure and deflection profile of Span 2 for Bridge 4 at ultimate load level and Figure 4.24 shows the load versus displacement plots of Span 2 of Bridge 4 along the centerline of the outside and inside girders. Nonlinear FEM analyses were conducted for the fractured and nonfractured conditions while the loading was located at mid-span of the corresponding span. The two spans have similar lengths, resulting in very close overstrength factors of around 1.7 when analyzed with a full-depth fracture at the moment-critical position of the outside girder of the loaded span. Similarly, FEM analysis of the nonfractured span gave very close overstrength factors of around 2.7 for both spans.

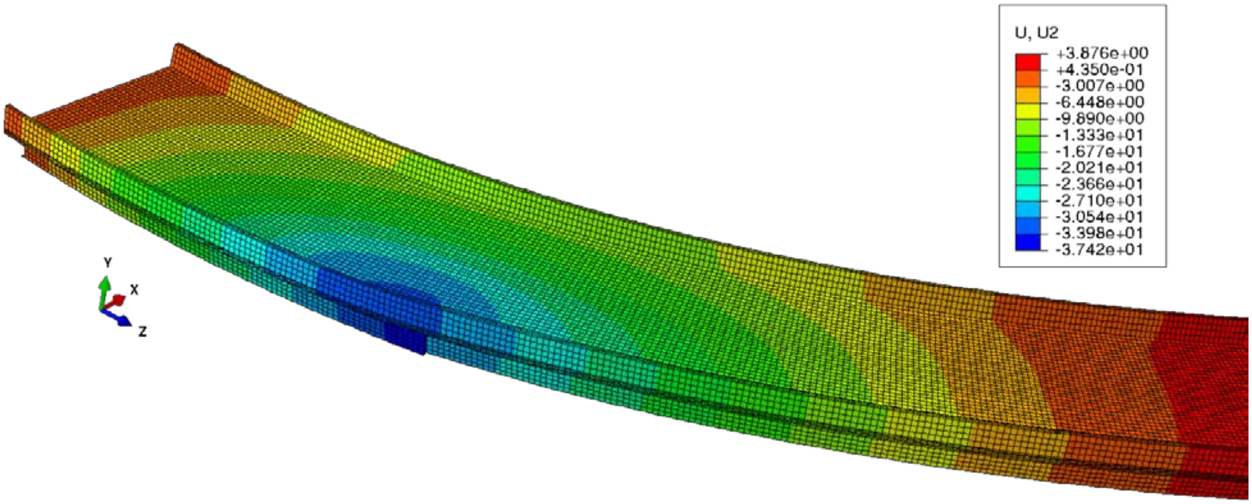

Figure 4.21. FEM Deflection Profile of Bridge 4, Span 1, with Fractured Outside Girder.

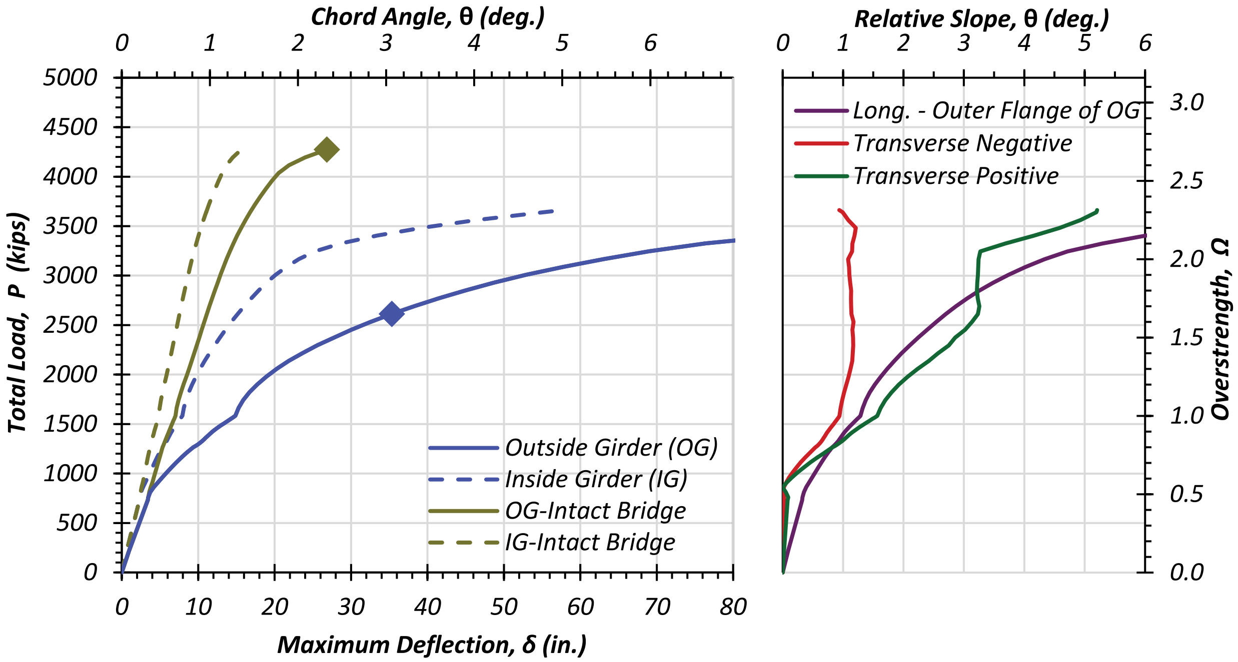

(a) Load displacement (b) Deck rotations

Note: δ is along the centerline of the outside girder, Ω is the load normalized by factored design load.

Figure 4.22. FEM Results for Bridge 4, Span 1.

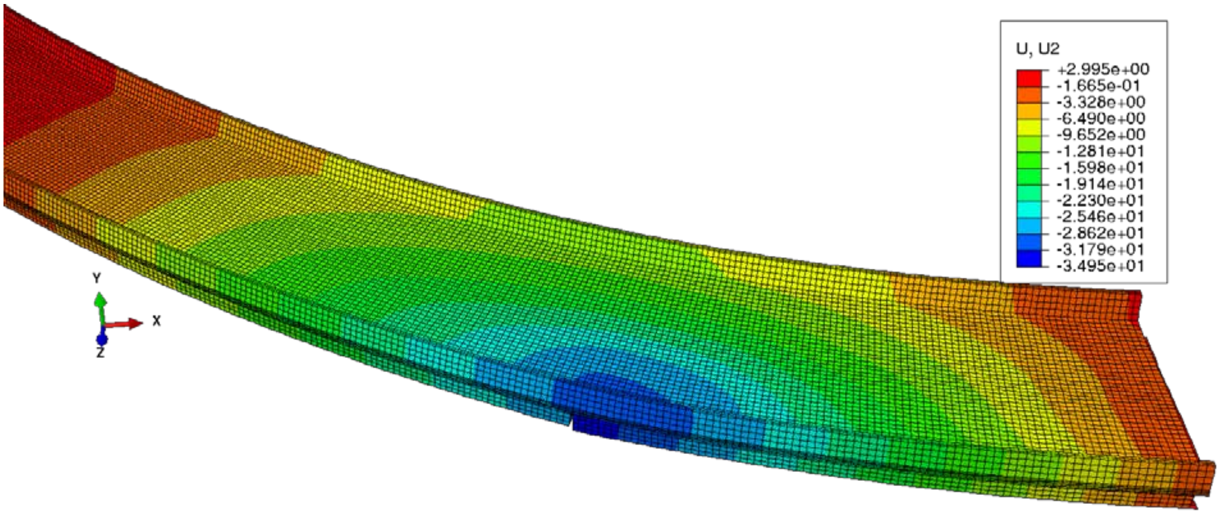

Figure 4.23. FEM Deflection Profile of Bridge 4, Span 2, with Fractured Outside Girder.

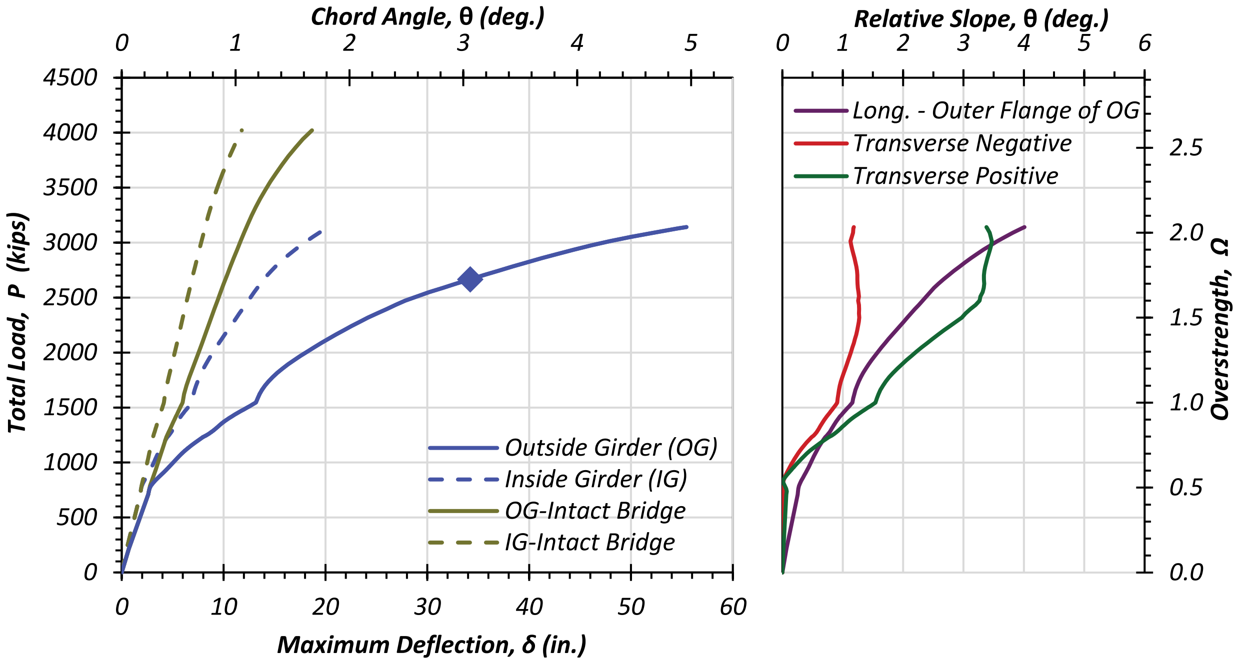

(a) Load displacement *(b) Deck rotations*

Note: δ is along the centerline of the outside girder, Ω is the load normalized by factored design load.

Figure 4.24. FEM Results for Bridge 4, Span 2.

4.4.6 Bridge 5—NBI #14-227-0-0015-13-452

Bridge 5 was built in 2002 in Travis County along I-35. It is a two-span continuous STTG bridge having 140 ft and 139.6 ft span lengths, with a 30 ft wide, 8 in. thick deck. Table 4.11 provides dimensional details of steel tub girder components along the entire length of the bridge. Table 4.12 summarizes the overall geometric properties and member details for Bridge 5. The steel tub girders of the bridge have variable web and flange thickness along the length of the bridge. Further details may be found in Appendix A.

Both spans were modeled following the actual geometry of the bridge to simulate the exact geometry and boundary conditions. However, only Span 1 was loaded and analyzed because the lengths of the spans were almost equal. The loaded span was first analyzed when there was no fracture in both the outside and inside steel tub girders, and the second analysis was carried out under the same loading conditions but with a full-depth fracture (bottom flange and both webs) mid-span of the outside girder. Figure 4.25 shows the meshed superstructure and deflection profile of Bridge 5 at ultimate load level when analyzed with a fracture in the outside girder of Span 1.

Table 4.11. Geometric Details of Steel Tub Girders for Bridge 5.

Location ft	Top Flange		Web		Bottom Flange	
	Width in.	Thickness in.	Width in.	Thickness in.	Width in.	Thickness in.
0–105	18	1.00	54	0.5	56	0.750
105–122	18	1.00	54	0.5625	56	1.250
122–140	18	1.75	54	0.5625	56	1.250
140–157	18	1.75	54	0.5625	56	1.250
157–174	18	1.75	54	0.5625	56	1.250
174–192	18	1.00	54	0.5625	56	0.750
192–280	18	1.00	54	0.5	56	0.750

Table 4.12. Geometric Properties and Member Dimensions of Bridge 5.

Location	Parameter	Description/Value
Bridge	Location	Travis County, I-35
	Year Designed/Year Built	1998/2002
	Design Load	HS20
	Length, ft	279.58
	Spans, ft	140, 139.58
	Radius of Curvature, ft	450
Deck	Width, ft	30
	Thickness, in.	8
	Haunch, in.	4
	Rail Type	T4(S)
Studs	No. of Studs per row	3
	Length, in.	7
	Diameter, in.	0.875
Interior Intermediate Diaphragm	Top Angle	L 4 x 4 x 1/2
	Diagonal Angle	L 4 x 4 x 1/2
	Stiffeners	5/8" x 8"
Exterior Erection Diaphragm	Top Angle	L 5 x 5 x 1/2
	Diagonal Angle	L 5 x 5 x 1/2
	Bottom Angle	L 5 x 5 x 1/2
End Diaphragm	Interior Top Plate	3/4" x 12"
	Interior Solid Plate	1/2"
	Interior Bottom Plate	3/4" x 12"
	Exterior Top Plate	3/4" x 12"
	Exterior Solid Plate	1/2"
	Stiffeners	5/8" x 5"
Pier Diaphragm	Interior Top Plate	1" x 18"
	Interior Solid Plate	1/2"
	Interior Bottom Plate	1" x 18"
	Exterior Top Plate	1" x 18"
	Exterior Solid Plate	7/8"
	Stiffeners	3/4" x 7"

Note: Typical exterior, interior, and end diaphragms are listed. See Appendix A for other types.

Figure 4.26 shows the load versus displacement and deck rotation plots for Span 1 and 2 of Bridge 5. The overstrength factor was estimated to be 2.2 for the nonfractured bridge while the overstrength factor reduces by 45 percent to 1.2 when analyzed with a full-depth fracture at the moment-critical location of the outside girder. The design vehicular load was also located at the moment-critical longitudinal position favored toward the outside rail for the FEM analysis of the fractured and nonfractured bridges.

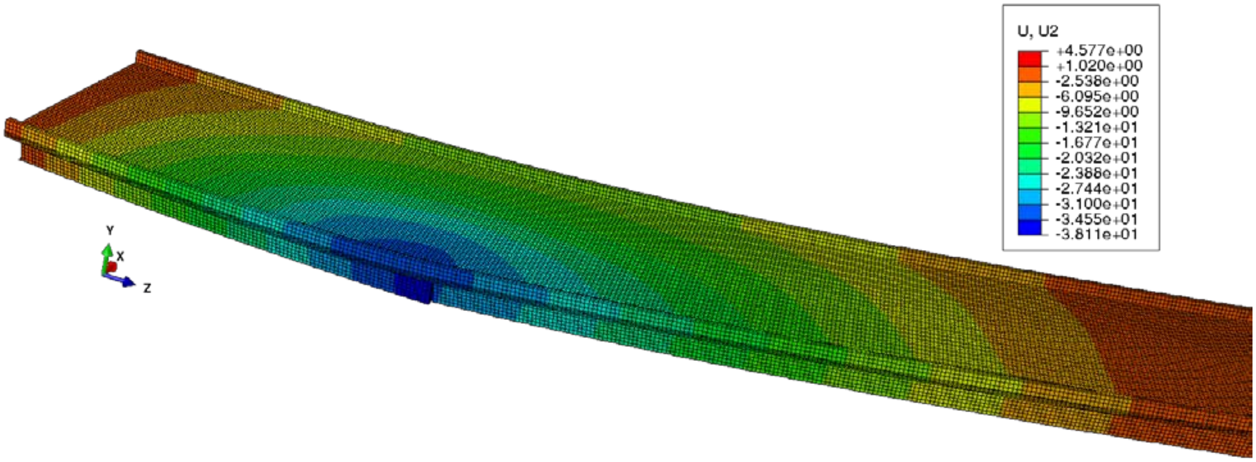

Figure 4.25. FEM Deflection Profile of Bridge 5 with Fractured Outside Girder.

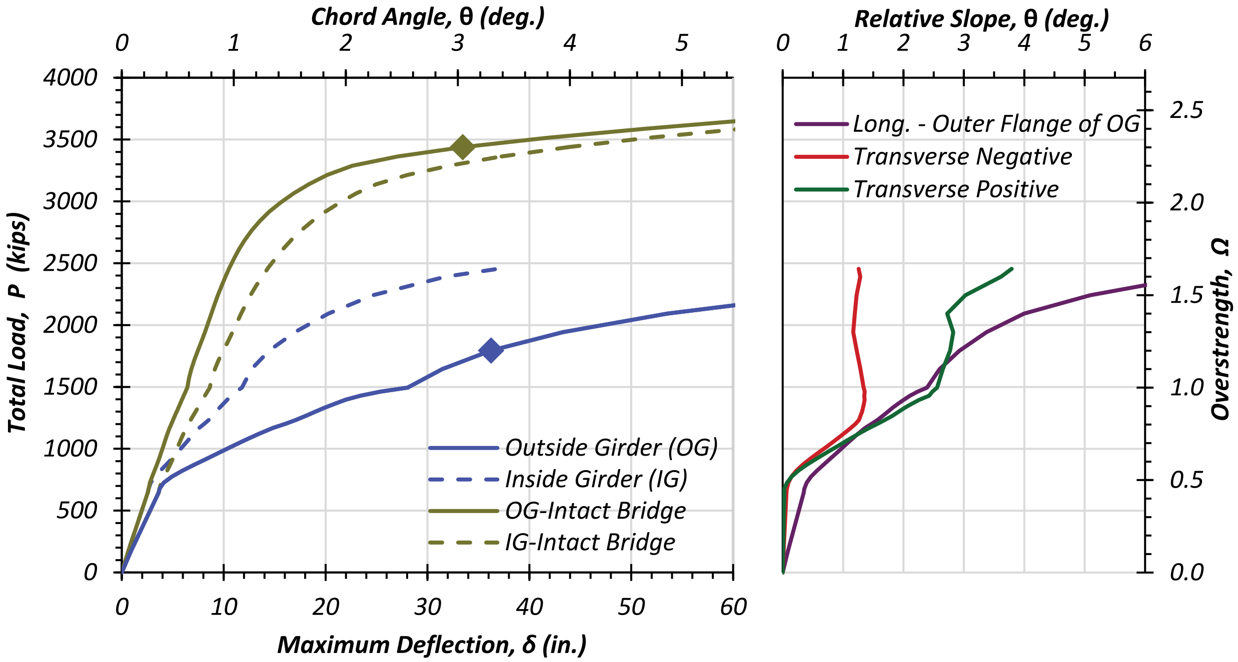

(a) Load displacement *(b) Deck rotations*

Note: δ is along the centerline of the outside girder, Ω is the load normalized by factored design load.

Figure 4.26. FEM Results for Bridge 5, Spans 1 and 2.

4.4.7 Bridge 6—NBI #12-102-0271-07-575

Bridge 6 was built in 2005 in Harris County along IH 10. It is a two-span continuous STTG bridge having 140 ft span lengths, with a 30 ft wide, 8 in. thick deck supported by two steel tub girders. Table 4.13 provides some of the overall geometric properties and member details for Bridge 6. Table 4.14 provides dimensional details of steel tub girder components along the entire length of the bridge. The steel tub girders of the bridge have variable top and bottom flange thickness as well as a variable top flange width along the length of the bridge. All variable geometric properties were incorporated into the FEM model. Further details may be found in the structural drawings of Bridge 6 that are provided in Appendix A.

Table 4.13. Geometric Properties and Member Dimensions of Bridge 6.

Location	Parameter	Description/Value
Bridge	Location	Harris County, IH 10
	Year Designed/Year Built	2003/2005
	Design Load	HS25
	Length, ft	280
	Spans, ft	140,140
	Radius of Curvature, ft	818.51
Deck	Width, ft	38.417
	Thickness, in.	8.25
	Haunch, in.	4.5
	Rail Type	SSTR
Studs	No. of Studs per row	4
	Length, in.	7
	Diameter, in.	0.875
Interior Intermediate Diaphragm	Top Angle	L 5 x 3 ½ x 1/2
	Diagonal Angles	L 5 x 3 ½ x 1/2
	Stiffeners	11/16" x 7 1/2"
Exterior Erection Diaphragm	Top Shape	WT 7 x 21.5
	Bottom Shape	WT 7 x 21.5
	Diagonal	L 5 x 3 ½ x 1/2
Interior End Diaphragm	Solid Plate	1 1/2"
	Top Plate	1 1/2" x 16"
	Stiffeners	1 1/2" x 8"
Exterior End Diaphragm	Top Plate	1" x 16"
	Solid Plate	1"
	Bottom Plate	1" x 16"

Note: Typical exterior, interior, and end diaphragms are listed. See Appendix A for other types.

Table 4.14. Geometric Details of Steel Tub Girders for Bridge 6.

Location ft	Top Flange		Web		Bottom Flange	
	Width in.	Thickness in.	Width in.	Thickness in.	Width in.	Thickness in.
0–110	18	1.00	76	0.6875	60	1.000
110–130	22	1.00	76	0.6875	60	1.875
130–150	22	1.88	76	0.6875	60	1.875
150–170	22	1.00	76	0.6875	60	1.875
170–280	18	1.00	76	0.6875	60	1.000

The entire length of Bridge 6 was modeled as a two-span bridge, where the intermediate pier bend was modeled using the same boundary conditions as the end piers. Since both spans are exterior spans having the same span length, only Span 1 was loaded with a factored HL-93 vehicular load and analyzed. The first simulation was carried out with no fracture, and the second simulation was conducted with the same loading conditions but with a full-depth fracture mid-span of the outside girder. Figure 4.27 shows the superstructure mesh and deflection profile of Bridge 6 at the ultimate load level when analyzed with a fracture in the outside girder of Span 1 and two-lanes-loaded case. Maximum deflection of the fractured girder was around 40 in., which is well above acceptable serviceability limits.

Figure 4.28 shows the load versus displacements and deck rotation for Span 1 and Span 2 of Bridge 6. The FEM prediction for the overstrength factor was 3.3 for the nonfractured bridge, but the overstrength factor reduces by 45 percent to 1.8 when analyzed with a full-depth fracture at the moment-critical location of the outside girder.

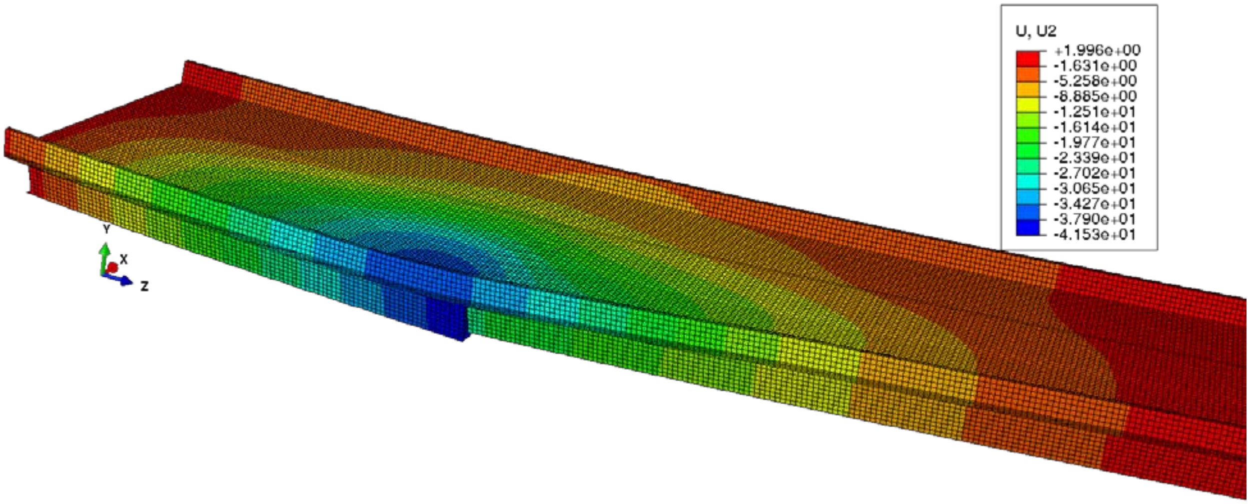

Figure 4.27. FEM Deflection Profile of Bridge 6 with Fractured Outside Girder.

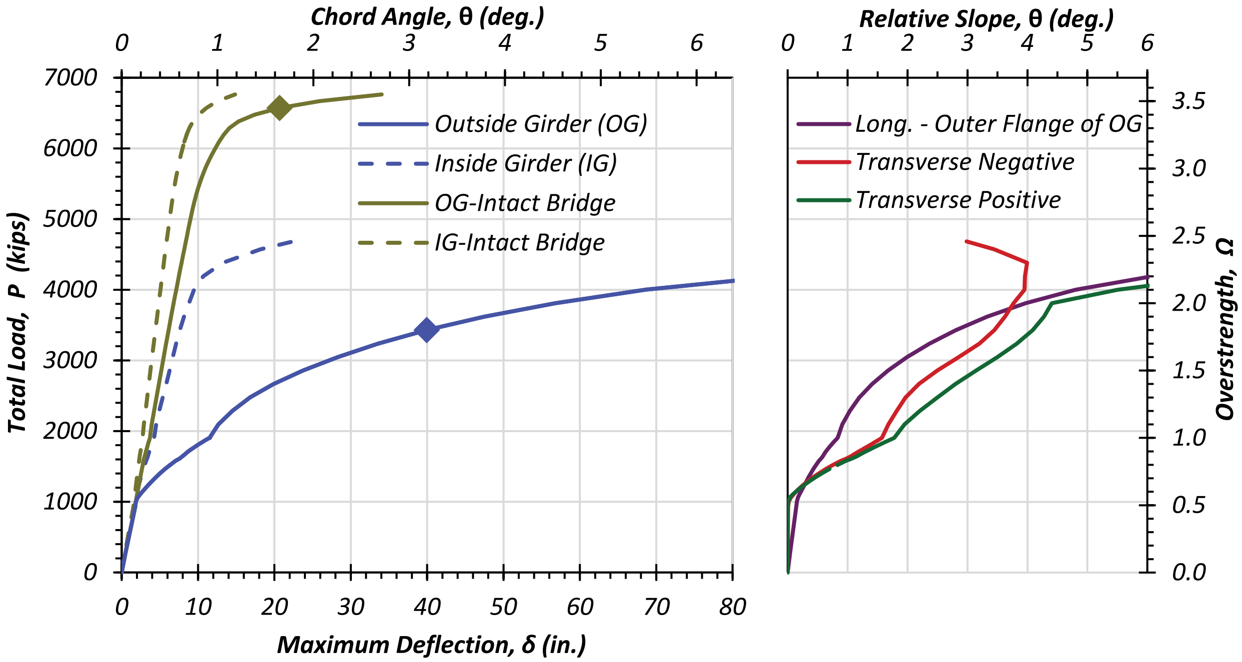

(a) Load displacement *(b) Deck rotations*

Note: δ is along the centerline of the outside girder, Ω is the load normalized by factored design load.

Figure 4.28. FEM Results for Bridge 6, Spans 1 and 2.

4.4.8 Bridge 7—NBI #12-102-0177-07-394

Bridge 7 was built in 2004 in Harris County along IH 10. It is a two-span continuous STTG bridge having 219 ft and 190 ft span lengths, with a 28.4 ft wide, 8 in. thick deck supported by two steel tub girders. Table 4.15 lists dimensions of steel tub girder components that vary along the length of the bridge.

The simulation of a factored HL-93 vehicular load was done for both spans separately, and both spans were analyzed under fractured and nonfractured conditions. The HS-20 truck load was placed at the moment-critical position starting 2 ft away from the outside rail for the span being simulated while the other span sustained a factored dead load only. The fractured condition was also created in the span under consideration by removing the weld connectors of the bottom flange, both webs, and top flanges of the outside girder at the moment-critical location. Figure 4.29 presents deflection profiles for Span 1 of Bridge 7 at ultimate capacity and Figure 4.30 shows the load versus displacement and deck rotation plots for Span 1 of Bridge 7.

Table 4.16 summarizes some of the key characteristics of Bridge 7, including the overall geometry, age, and location information, stud, and diaphragm details. The top flanges' have variable widths and thicknesses, while the bottom flanges have variable thicknesses; these factors were incorporated into the FEM model. Further geometric and material details may be found in the structural drawings of Bridge 7 that are provided in Appendix A.

Table 4.15. Geometric Details of Steel Tub Girders for Bridge 7.

Location ft	Top Flange		Web		Bottom Flange	
	Width in.	Thickness in.	Width in.	Thickness in.	Width in.	Thickness in.
0–17	20	1.10	63	0.625	60	1.000
17–141	20	2.36	63	0.625	60	2.362
141–162	20	1.77	63	0.625	60	1.772
162–193	30	1.77	63	0.625	60	1.772
193–219	30	3.15	63	0.625	60	3.150
219–247	30	3.15	63	0.625	60	3.150
247–292	30	1.77	63	0.625	60	1.772
292–381	20	1.10	63	0.625	60	1.102
381–408	20	1.10	63	0.625	60	1.000

Table 4.16. Geometric Properties and Member Dimensions of Bridge 7.

Location	Parameter	Description/Value
Bridge	Location	Harris County, IH 10
	Year Designed/Year Built	2002/2004
	Design Load	HS20
	Length, ft	408.62
	Spans, ft	218.92,189.7
	Radius of Curvature, ft	763.96
Deck	Width, ft	28.417
	Thickness, in.	7.9
	Haunch, in.	5.5
	Rail Type	T501
Studs	No. of Studs per row	3
	Length, in.	7
	Diameter, in.	0.866
Interior Intermediate Diaphragm	Top Plate	L 5 x 3 ½ x 1/2
	Diagonal Angle	L 5 x 3 ½ x 1/2
	Stiffeners	5/8" x 8"
Exterior Erection Diaphragm	Top Section	WT 7 x 32
	Diagonal Angle	L 5x 3 ½ x 1/2
	Bottom Plate	WT 8 x 50
Exterior End Diaphragm	Top Plate	3/4" x 12"
	Solid Plate	3/4"
	Bottom Plate	3/4"x 12"
Interior End Diaphragm	Solid Plate	3/4"
	Top Plate	3/4" x 12"
	Stiffeners	1 1/4" x 5"
		1 1/2" x 5"

Note: Typical exterior, interior, and end diaphragms are listed. See Appendix A for other types.

Figure 4.31 presents deflection profile for Span 2 of Bridge 7 at ultimate capacity and Figure 4.32 shows the load versus displacement and deck rotation plots for Span 2 of Bridge 7. When simulated with a fractured girder, the 220 ft long span reaches load levels 1.2 times the factored design load, while the 190 ft Span 2 can achieve a 1.45 overstrength factor. These governing overstrength values correspond to 2 degrees longitudinal chord rotation limit, while the overstrength factors corresponding to 95 percent stiffness degradation are 1.4 and 1.75 for Span 1 and Span 2, respectively.

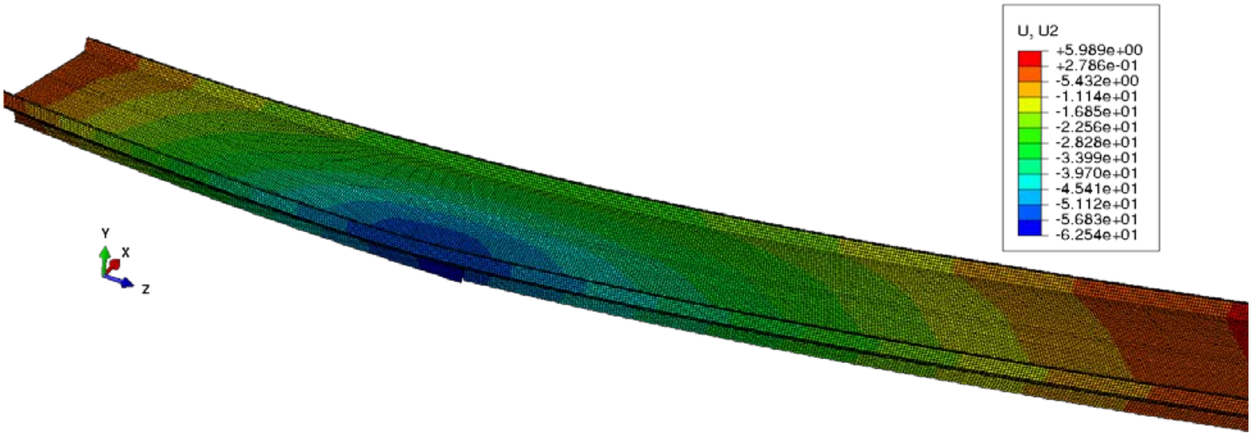

Figure 4.29. FEM Deflection Profile of Bridge 7, Span 1, with Fractured Outside Girder.

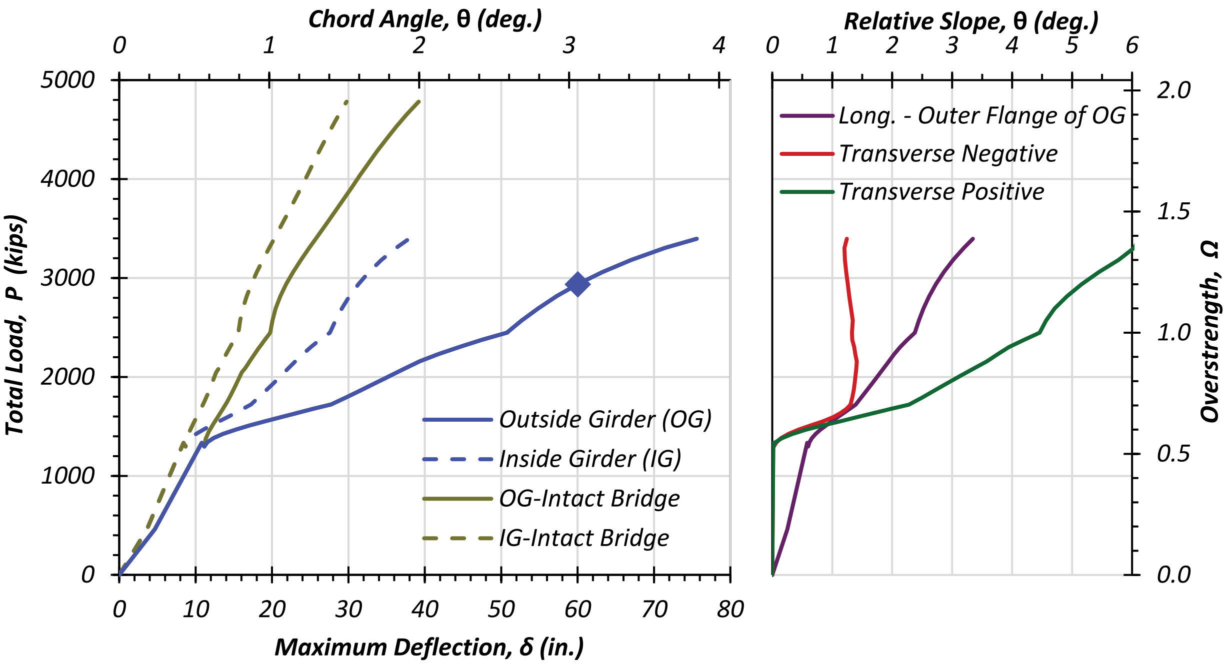

(a) Load displacement *(b) Deck rotations*

Note: δ is along the centerline of the outside girder, Ω is the load normalized by factored design load.

Figure 4.30. FEM Results for Bridge 7, Span 1.

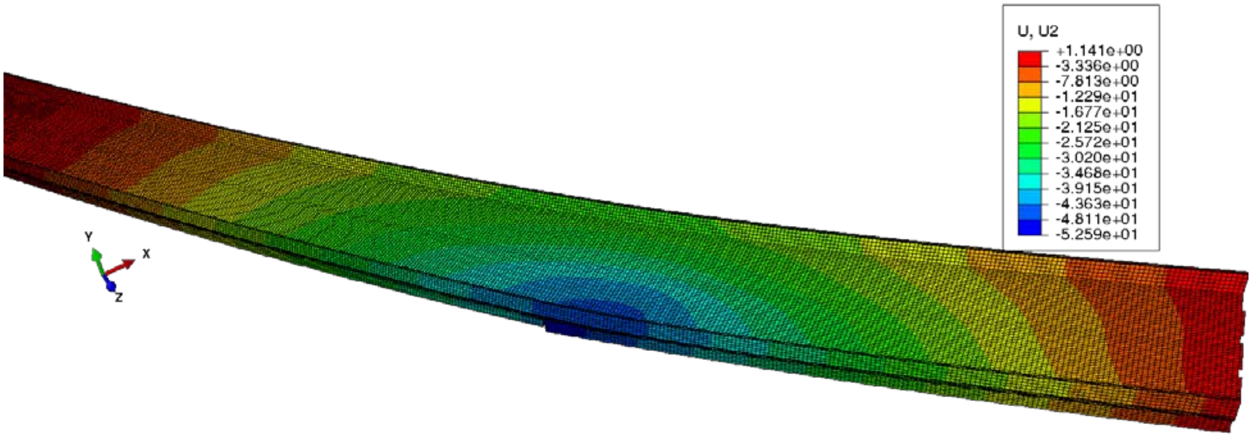

Figure 4.31. FEM Deflection Profile of Bridge 7, Span 2, with Fractured Outside Girder.

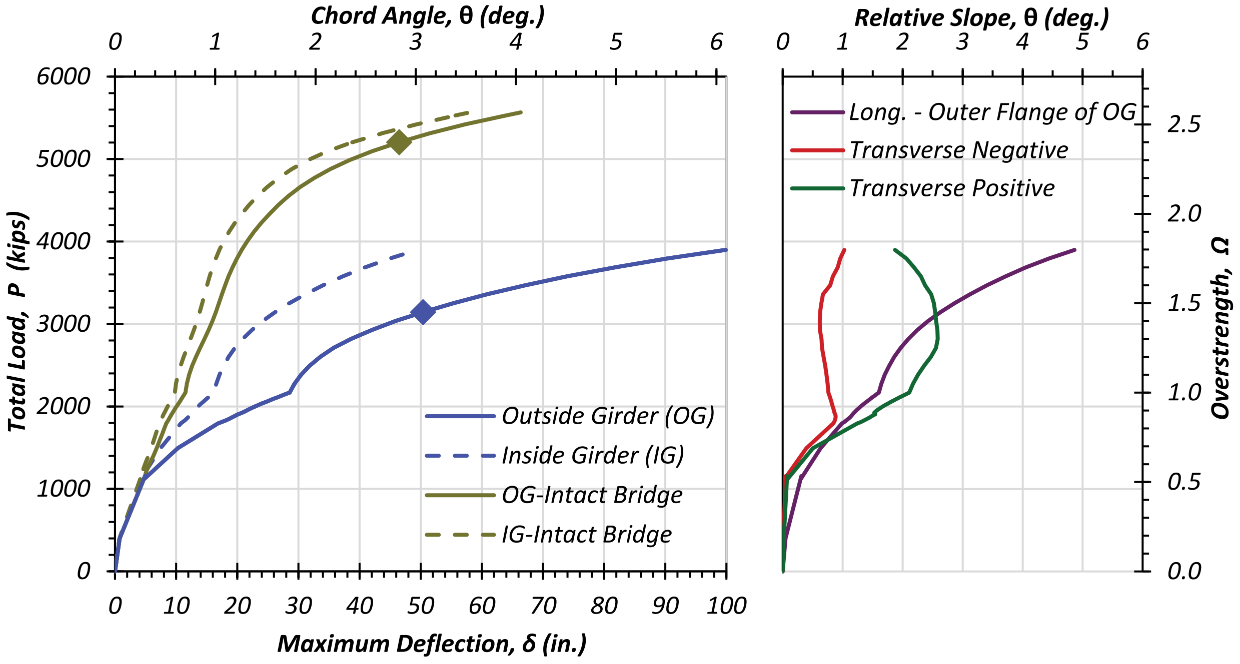

(a) Load displacement

(b) Deck rotations

Note: δ is along the centerline of the outside girder, Ω is the load normalized by factored design load.

Figure 4.32. FEM Results for Bridge 7, Span 2.

4.4.9 Bridge 8—NBI #12-102-0271-06-661

Bridge 8 was built in 2011 in Harris County along IH 10. It is a two-span continuous STTG bridge having 265 ft and 295 ft spans, with a 28.4 ft wide, 8 in. thick deck. Table 4.17 summarizes key characteristics, including overall geometry, age, location information, stud, and diaphragm details. Table 4.18 lists the dimensions of steel tub girder components. The thickness of both the top and bottom flanges varies along the length of the girder, and that element was adapted into the FEM model. Further geometric and material details may be found in the structural drawings of Bridge 8 that are provided in Appendix A.

Table 4.17. Geometric Properties and Member Dimensions of Bridge 8.

Location	Parameter	Description/Value
Bridge	Location	Harris County, IH 10
	Year Designed/Year Built	2011/NA
	Design Load	NA
	Length, ft	560
	Spans, ft	265, 295
	Radius of Curvature, ft	881.47
Deck	Width, ft	28.417
	Thickness, in.	8
	Haunch, in.	4
	Rail Type	SSTR
Studs	No. of Studs per row	3
	Length, in.	7 1/2
	Diameter, in.	0.875
Interior End Diaphragm	Solid Plate	1"
	Top Plate	1" x 16"
	Stiffeners	1 1/2" x 8"
Interior Intermediate Diaphragm	Top Angle	L 5 x 3 ½ x 1/2
	Diagonal Angle	L 5 x 3 ½ x 1/2
	Stiffeners	3/4" x 8"
Exterior End Diaphragm	Top Plate	1" x 16"
	Solid Plate	1"
	Bottom Plate	1" x 16"
Exterior Erection Diaphragm	Top Shape	WT 7 x 21.5
	Diagonal Angle	L 5 x 3 ½ x 1/2
	Bottom Shape	WT 7 x 21.5

Note: Typical exterior, interior, and end diaphragms are listed. See Appendix A for other types.

Table 4.18. Geometric Details of Steel Tub Girders for Bridge 8.

Location ft	Top Flange		Web		Bottom Flange	
	Width in.	Thickness in.	Width in.	Thickness in.	Width in.	Thickness in.
0–30	24	1.25	93	0.75	53.5	1.250
30–71	24	1.50	93	0.75	53.5	1.500
71–142	24	1.50	93	0.75	53.5	2.000
142–183	24	1.50	93	0.75	53.5	1.500
183–214	24	1.25	93	0.75	53.5	1.500
214–234	24	2.00	93	0.75	53.5	2.000
234–307	24	2.50	93	0.75	53.5	2.500
307–338	24	1.25	93	0.75	53.5	1.500
338–370	24	1.50	93	0.75	53.5	1.500
370–391	24	1.50	93	0.75	53.5	2.000
391–496	24	2.00	93	0.75	53.5	2.500
496–528	24	1.50	93	0.75	53.5	2.000
528–560	24	1.25	93	0.75	53.5	1.250

The entire superstructure of Bridge 8 was modeled by FEM utilizing the same material properties and boundary conditions as other FEM models. Both spans were analyzed under a factored HL-93 vehicular load while keeping only a factored dead load on the other span. Two lanes were defined starting 2 ft away from the face of outside rail. Both HS-20 truck and uniform distributed lane loads were favored toward the outside edge of the defined lanes to illustrate the most critical flexural loading condition. Figure 4.33 shows the deflection profiles for Span 1 of Bridge 8 when two lanes are loaded and Figure 4.34 presents the load versus displacement and deck rotation plots for Span 1 of Bridge 8. The ultimate load is located on the span that is being analyzed, and a full-depth fracture is induced at the moment-critical location of the outside girder. Figure 4.35 shows the deflection profiles for Span 2 of Bridge 8 when two lanes are loaded and Figure 4.36 presents the load versus displacement and deck rotation plots for Span 2 of Bridge 8. When simulated with a fractured girder, Span 1 (265 ft) has an overstrength factor of 1.0, while its second span (30 ft longer) can only achieve a 0.9 overstrength factor. The governing overstrength factors for both spans correspond to ultimate load capacities at 5 percent of initial stiffness.

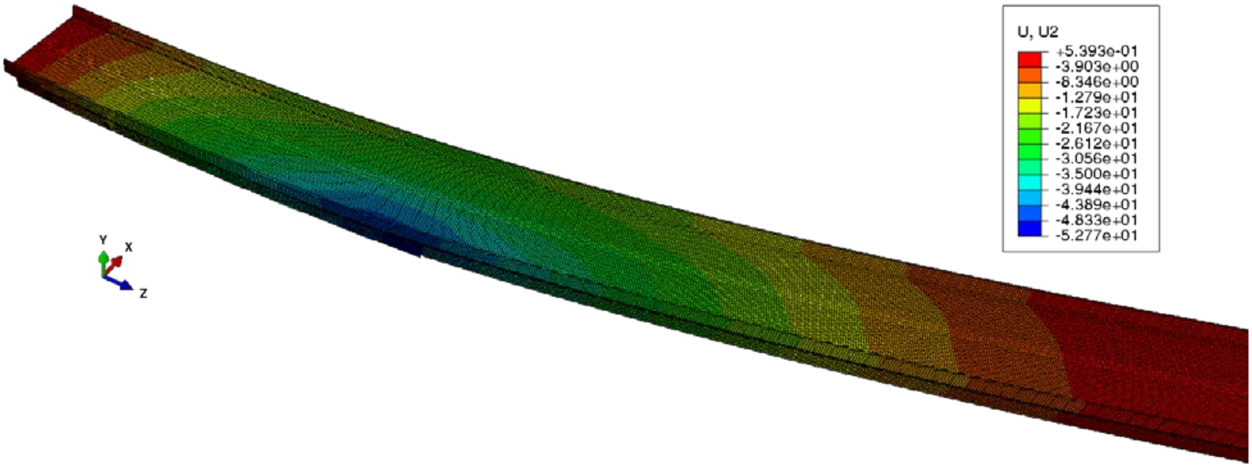

Figure 4.33. FEM Deflection Profile of Bridge 8, Span 1, with Fractured Outside Girder.

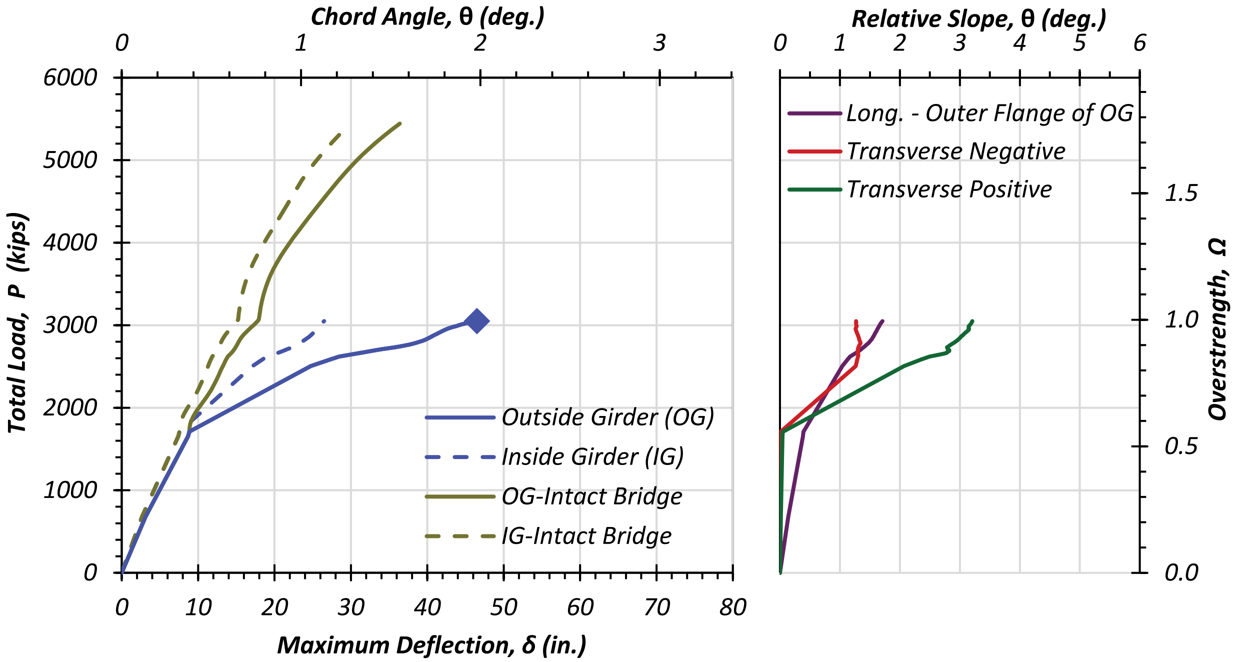

(a) Load displacement *(b) Deck rotations*

Note: δ is along the centerline of the outside girder, Ω is the load normalized by factored design load.

Figure 4.34. FEM Results for Bridge 8, Span 1.

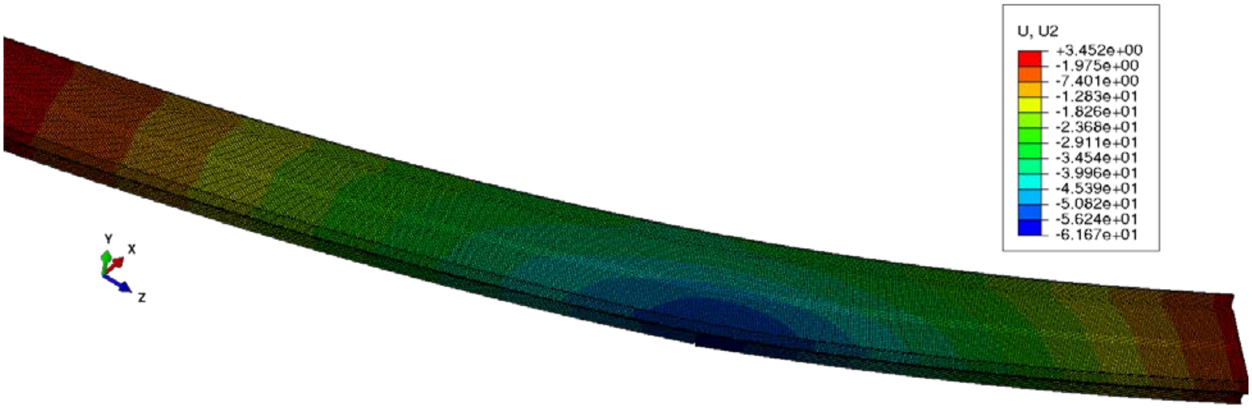

Figure 4.35. FEM Deflection Profile of Bridge 8, Span 2, with Fractured Outside Girder.

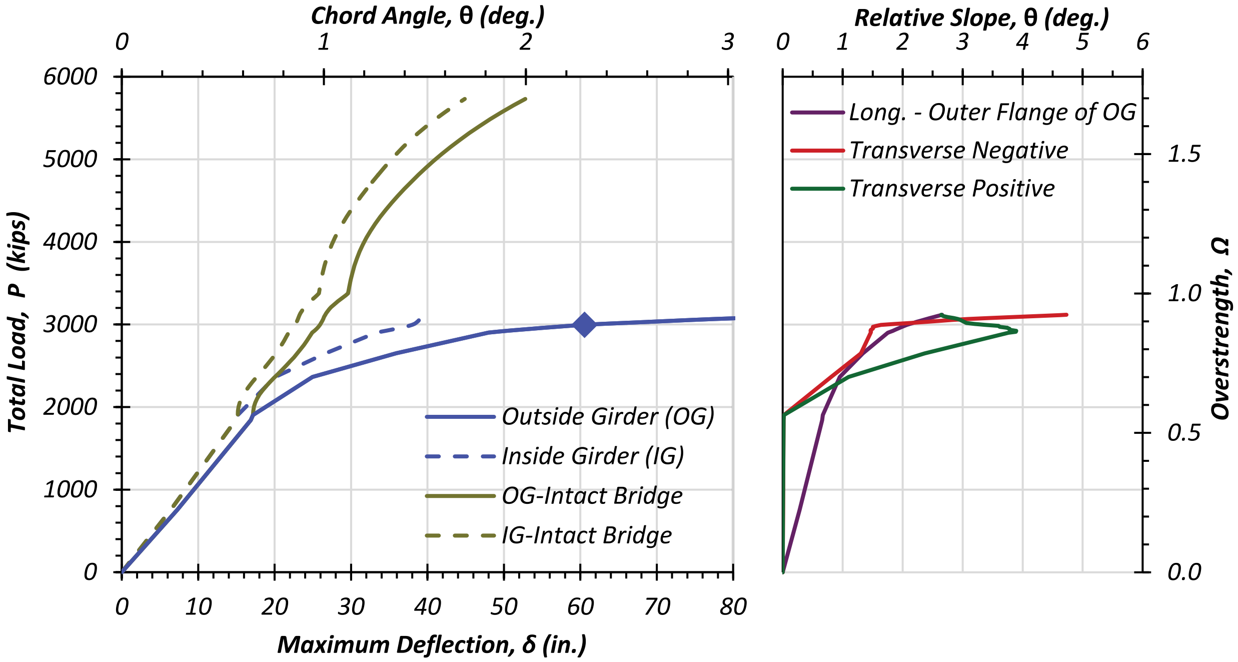

(a) Load displacement *(b) Deck rotations*

Note: δ is along the centerline of the outside girder, Ω is the load normalized by factored design load.

Figure 4.36. FEM Results for Bridge 8, Span 2.

4.4.10 Bridge 9—NBI #12-102-0177-07-394

Bridge 9, a three-span continuous bridge, was built in 2004 in Harris County along IH 10. Bridge 9 has 139.5 ft, 151.4 ft, and 125.6 ft long spans, with a 28.4 ft wide, 7.9 in. thick deck. Bridge 9 is part of the same bridge as Bridge 7 and has the same deck geometry and reinforcement and similar steel tub girder dimensions. Table 4.19 summarizes key characteristics of Bridge 9, including overall geometry, age, location information, stud, and diaphragm details. Table 4.20 lists dimensions of the steel tub girder components. The thickness of both top and bottom flanges varies along the length of the girder, and that element was incorporated into the FEM model. Further geometric and material details may be found in the structural drawings of Bridge 9 that are provided in Appendix A.

Table 4.19. Geometric Properties and Member Dimensions of Bridge 9.

Location	Parameter	Description/Value
Bridge	Location	Harris County, IH 10
	Year Designed/Year Built	2002/2004
	Design Load	HS20
	Length, ft	416.66
	Spans, ft	139.5,151.44,125.62
	Radius of Curvature, ft	763.93
Deck	Width, ft	28.417
	Thickness, in.	7.9
	Haunch, in.	4
	Rail Type	T501
Studs	No. of Studs per row	3
	Length, in.	7
	Diameter, in.	0.866
Interior End Diaphragm	Solid Plate	3/4"
	Top Plate	3/4" x 14"
	Stiffeners	1 1/2" x 5"
		1 1/4" x 5"
Interior Intermediate Diaphragm	Top Angle	L 5 x 3 ½ x 1/2
	Diagonal Angle	L 5 x 3 ½ x 1/2
	Stiffeners	8" x 5/8"
Exterior End Diaphragm	Top Plate	3/4" x 12"
	Solid Plate	3/4"
	Bottom Plate	3/4" x 12"
		L 5 x 3 ½ x 1/2
Exterior Erection Diaphragm	Top Shape	WT 7 x 32
	Diagonal Angle	L 5 x 3 ½ x 1/2
	Bottom Shape	WT 7 x 32

Note: Typical exterior, interior, and end diaphragms are listed. See Appendix A for other types.

Table 4.20. Geometric Details of Steel Tub Girders for Bridge 9.

Location ft	Top Flange		Web		Bottom Flange	
	Width in.	Thickness in.	Width in.	Thickness in.	Width in.	Thickness in.
0–104	20	1.10	63	0.625	59	1.000
104–127	20	1.10	63	0.625	59	1.250
127–152	20	1.58	63	0.625	59	1.500
152–177	20	1.10	63	0.625	59	1.250
177–240	20	1.10	63	0.625	59	1.000
240–265	20	1.10	63	0.625	59	1.250
265–278	20	1.10	63	0.625	59	1.500
278–316	20	1.58	63	0.625	59	1.500
316–341	20	1.10	63	0.625	59	1.250
341–416	20	1.10	63	0.625	59	1.000

A nonlinear FEM model of Bridge 9 was created for the entire bridge length using the same material properties and boundary conditions as previous bridge models. All three spans were analyzed separately under simulated HL-93 design vehicular loading while keeping only a factored dead load on the other spans. Figure 4.37 shows the deflection profiles for Span 1 of Bridge 9 when two lanes of ultimate loading are located on the analyzed span, and a full-depth fracture is induced at the moment-critical location of the outside girder in the same span, and Figure 4.38 presents the load versus displacement and deck rotation plots for Span 1 of Bridge 9. Span 1 and Span 3 were also analyzed under the same loading conditions for fractured and nonfractured conditions. The fracture was always located in the loaded span, and the other spans were considered intact. Figure 4.39 shows the deflection profiles for Span 2 of Bridge 9 when two lanes of ultimate loading are located on the analyzed span, and a full-depth fracture is induced at the moment-critical location of the outside girder in the same span, and Figure 4.40 presents the load versus displacement and deck rotation plots for Span 2 of Bridge 9.

Figure 4.41 shows the deflection profiles for Span 3 of Bridge 9 when two lanes of ultimate loading are located on the analyzed span, and a full-depth fracture is induced at the moment-critical location of the outside girder in the same span, and Figure 4.42 presents the load versus displacement and deck rotation plots for Span 3 of Bridge 9. When simulated with a fractured girder, the 140 ft Span 1 obtains an overstrength factor of 1.7, while the 126 ft long Span 3 can achieve a 1.8 overstrength factor. The predicted overstrength factor for the longer 151 ft interior span is 2.45 because the interior span has redundancy due to continuity from both ends.

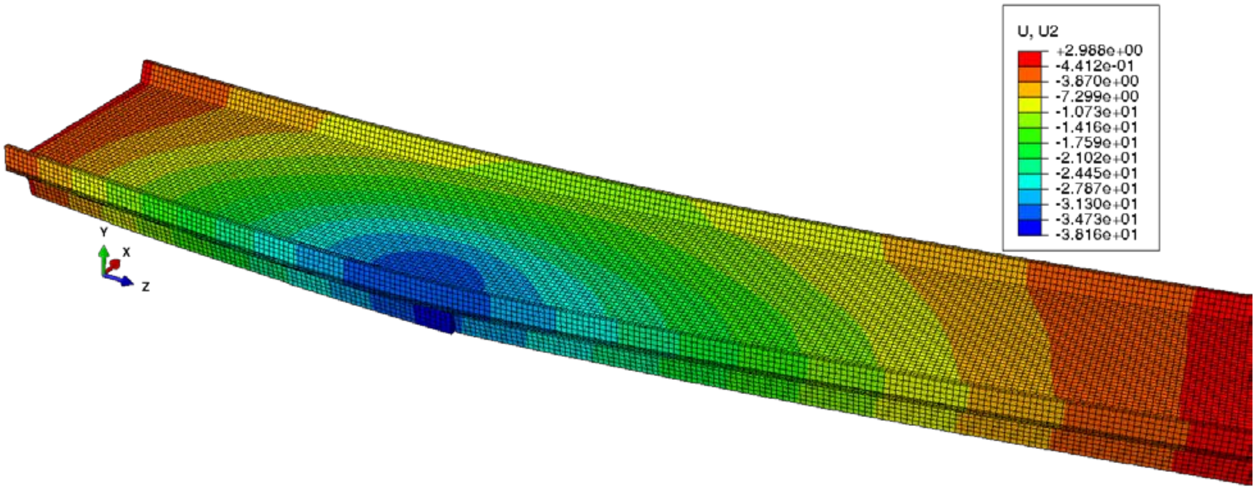

Figure 4.37. FEM Deflection Profile of Bridge 9, Span 1, with Fractured Outside Girder.

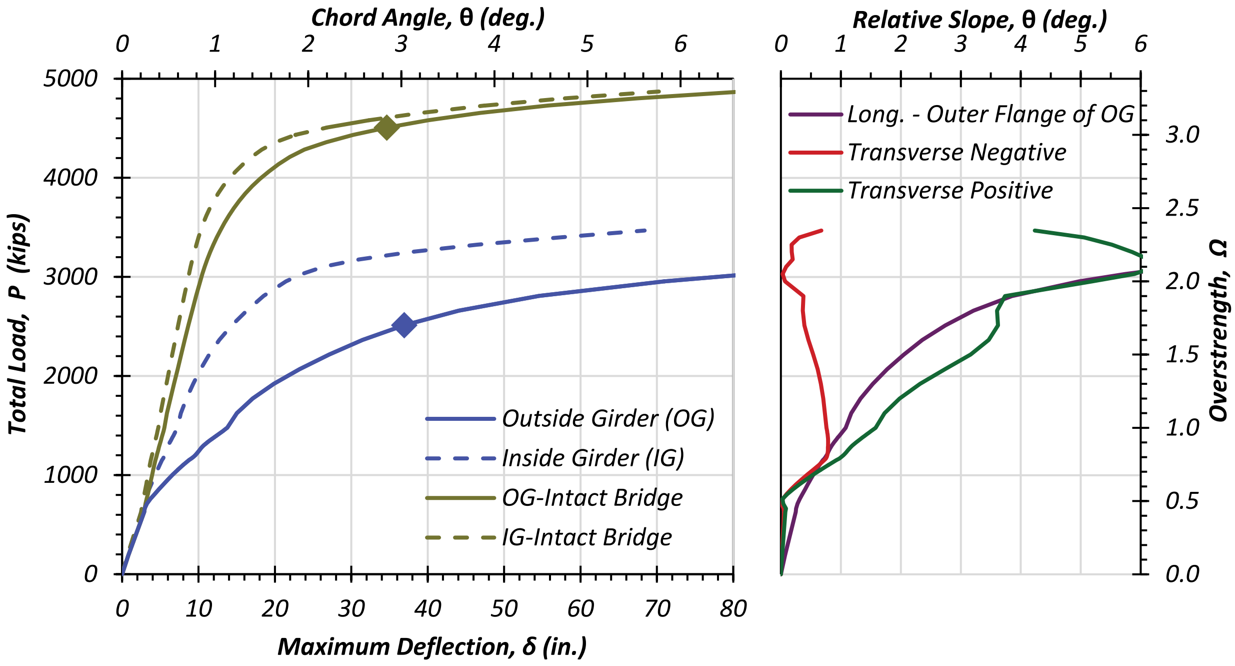

(a) Load displacement *(b) Deck rotations*

Note: δ is along the centerline of the outside girder, Ω is the load normalized by factored design load.

Figure 4.38. FEM Results for Bridge 9, Span 1.

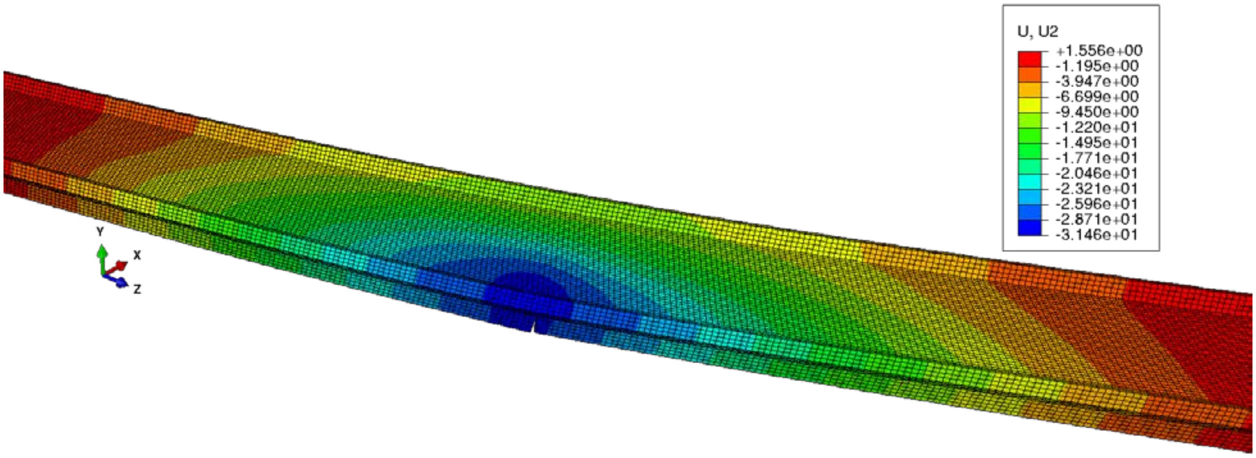

Figure 4.39. FEM Deflection Profile of Bridge 9, Span 2, with Fractured Outside Girder.

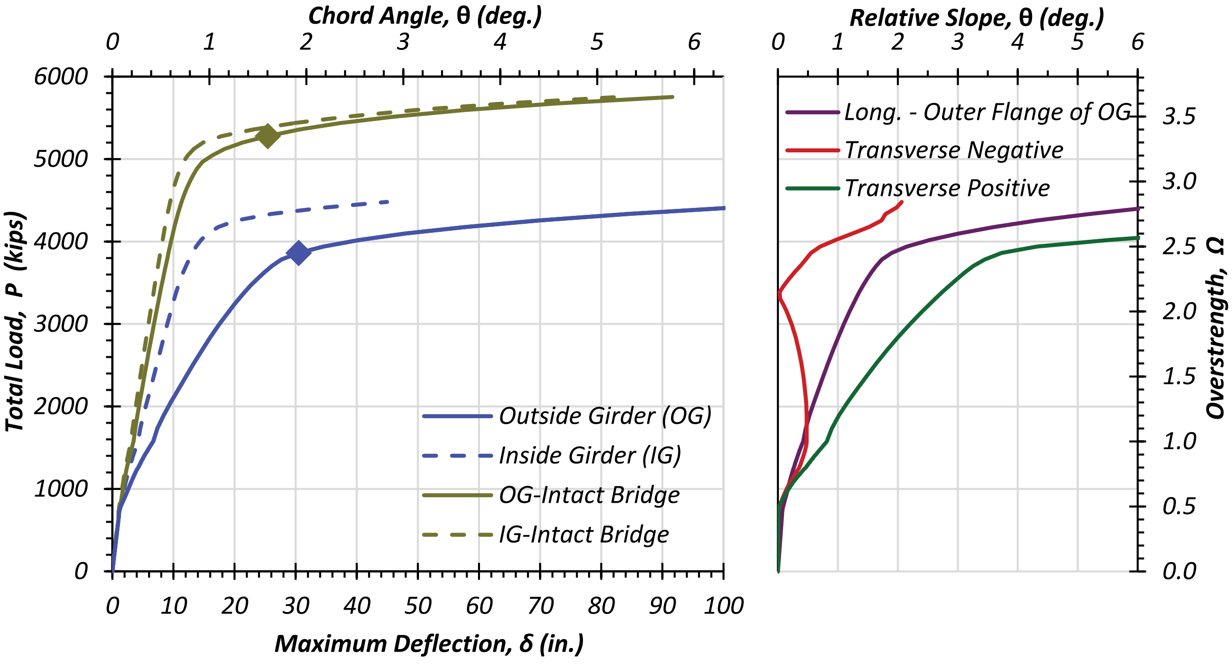

(a) Load displacement

(b) Deck rotations

Note: δ is along the centerline of the outside girder, Ω is the load normalized by factored design load.

Figure 4.40. FEM Results for Bridge 9, Span 2.

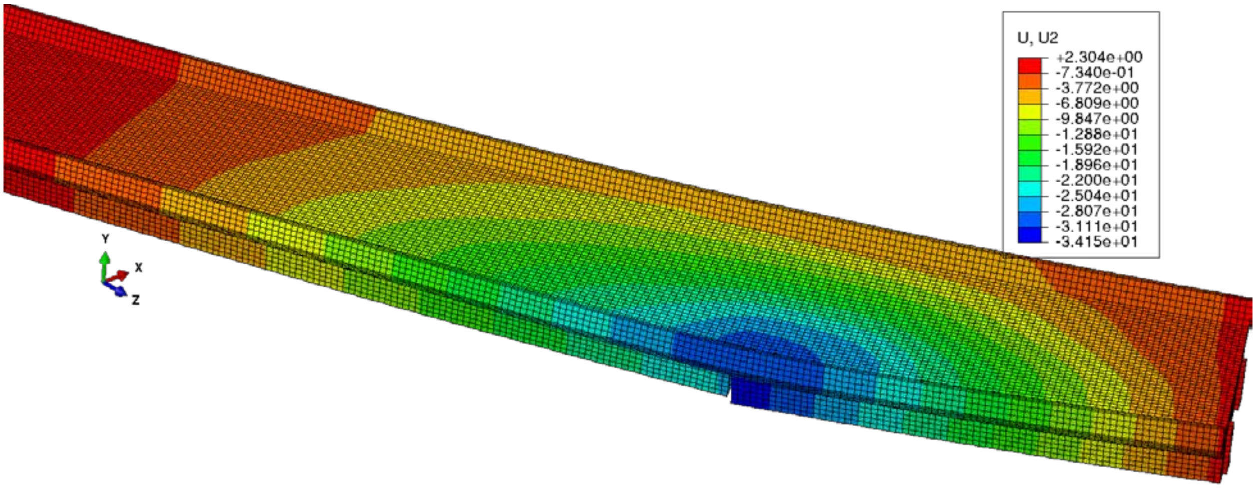

Figure 4.41. FEM Deflection Profile of Bridge 9, Span 3, with Fractured Outside Girder.

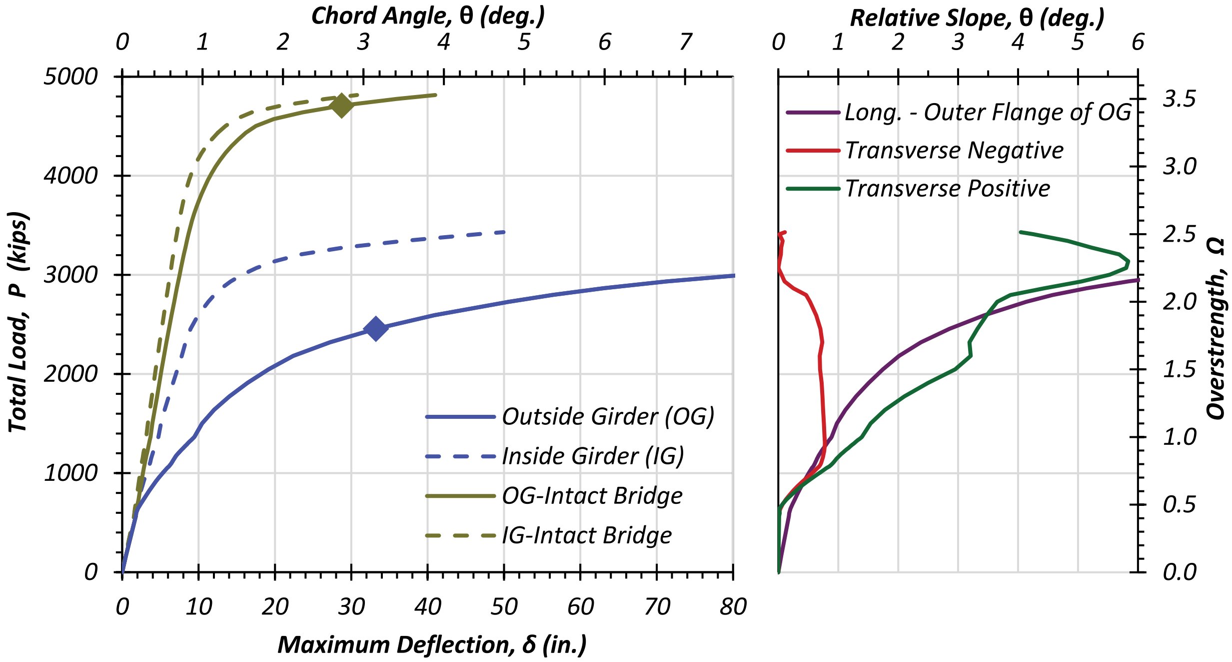

(a) Load displacement (b) Deck rotations

Note: δ is along the centerline of the outside girder, Ω is the load normalized by factored design load.

Figure 4.42. FEM Results for Bridge 9, Span 3.

4.4.11 Bridge 10—NBI #14-227-0-0015-13-450

Bridge 10 is a three-span continuous bridge that was built in 2002 in Harris County along IH 10. Bridge 10 has 148 ft, 265 ft, and 189.6 ft long spans, with a 716 ft radius of curvature and a 30 ft wide, 8 in. thick deck. Table 4.21 lists several main key characteristics of Bridge 10 that include overall geometry, age, location information, studs, and diaphragm details.

Table 4.22 provides dimensional details of the steel tub girder components. Along the length of the girders, top and bottom flanges and webs have variable thicknesses that were incorporated into the FEM model. Other details about geometry, member dimensions, reinforcement layout, and other diaphragm types may be found in the structural drawings of Bridge 10 that are provided in Appendix A.

Table 4.21. Geometric Properties and Member Dimensions of Bridge 10.

Location	Parameter	Description/Value
Bridge	Location	Harris County, IH 10
	Year Designed/Year Built	1998/2002
	Design Load	HS20
	Length, ft	602.58
	Spans, ft	148, 265, 189.58
	Radius of Curvature, ft	716.2
Deck	Width, ft	30
	Thickness, in.	8
	Haunch, in.	5
	Rail Type	T4(s)
Studs	No. of Studs per row	3
	Length, in.	7
	Diameter, in.	0.875
Interior Intermediate Diaphragm	Top Angle	L 4 x 4 x 1/2
	Diagonal Angles	L 4 x 4 x 1/2
	Stiffeners	5/8" x 8"
Exterior Erection Diaphragm	Top Shape	L 5 x 5 x 1/2
	Diagonal Angles	L 5 x 5 x 1/2
	Bottom Shape	L 5 x 5 x 1/2
Interior End Diaphragm	Solid Plate	5/8" x 78"
	Stiffeners	7/8" x 8"
	Top Plate	1" x 16"
Exterior End Diaphragm	Top Plate	1 1/4" x 24"
	Solid Plate	3/4"
	Bottom Plate	1 1/4" x 24"

Note: Typical exterior, interior, and end diaphragms are listed. See Appendix A for other types.

Table 4.22. Geometric Details of Steel Tub Girders for Bridge 10.

Location ft	Top Flange		Web		Bottom Flange	
	Width in.	Thickness in.	Width in.	Thickness in.	Width in.	Thickness in.
0–50	24	1.00	78	0.625	59	0.750
50–98	24	1.00	78	0.625	59	1.250
98–131	24	2.00	78	0.75	59	2.000
131–181	24	3.00	78	0.875	59	2.000
181–230	24	1.00	78	0.875	59	1.250
230–247	24	1.00	78	0.75	59	1.000
247–297	24	1.00	78	0.75	59	1.250
297–330	24	1.00	78	0.75	59	1.000
330–380	24	1.00	78	0.875	59	1.250
380–396	24	2.00	78	0.875	59	1.250
396–430	24	3.00	78	0.875	59	2.000
430–447	24	3.00	78	0.875	59	2.000
447–464	24	2.00	78	0.75	59	1.250
464–499	24	1.00	78	0.75	59	1.250
499–602	24	1.00	78	0.625	59	0.750

A nonlinear 3D FEM model of Bridge 10 was created for the entire bridge length using the material properties that are provided in structural drawings. The boundary conditions were modeled as spring stiffness (described in Chapter 3). The results herein present load displacement behavior after the initiation of a full-depth fracture crack at the moment-critical location of the outside girder for the loaded span. The factored dead load was applied on all three spans while the factored HL-93 design vehicular load was only applied on the span being simulated with a fracture crack. Figure 4.43, shows the colored deflection contours of Span 1 of Bridge 10 when two lanes of ultimate loading are located on the corresponding span with a full-depth fracture crack at the moment-critical location of the outside girder and Figure 4.44 presents the load versus displacement and deck rotation plots for Span 1 of Bridge 10. The behavior of the other two spans were also simulated under the same loading conditions for fractured and nonfractured conditions. The fracture was always located in the loaded span, and the other spans were considered intact. Figure 4.45, shows the colored deflection contours of Span 2 of Bridge 10 when two lanes of ultimate loading are located on the corresponding span with a full-depth fracture crack at the moment-critical location of the outside girder and Figure 4.46 presents the load versus displacement and deck rotation plots for Span 2 of Bridge 10. Figure 4.47, shows the colored deflection contours of Span 3 of Bridge 10 when two lanes of ultimate loading are located on the corresponding span with a full-depth fracture crack at the moment-critical location of the outside girder and Figure 4.48 presents the load versus displacement and deck rotation plots for Span 3 of Bridge 10.

When simulated with a fractured girder, the 148 ft exterior Span 1 obtains an overstrength factor of 1.7, which is 46 percent lower than the nonfractured case. 265 ft long interior Span 2 can achieve a 1.45 overstrength factor when simulated with a fracture in the outside girder, while the same span could achieve a 2.2 overstrength factor when the girders are intact. The interior span is almost two times longer than the first span and therefore has a lower overstrength factor and gains its ultimate strength at a larger maximum displacement. The predicted overstrength factor for the longer 190 ft exterior Span 3 is 1.45, which is 42 percent lower than the nonfractured simulation of the same span. Although the interior span is 40 percent longer than exterior Span 3, the estimated overstrength factors are the same because the interior span has additional redundancy due to continuity from both ends. This observation shows that the structural redundancy due to continuity contributes significantly to the redistribution of the loads, thereby providing additional distribution path. The redundancy evaluations must consider longitudinal distribution between spans in addition to load path redundancy for lateral distribution between girders to be able to accurately predict the overstrength factors. For all three spans, the longitudinal chord rotation limit governs the ultimate capacity values. The ultimate limit state corresponding to 5 percent initial stiffness value is 1.7, 2.05, and 1.6 for Spans 1, 2, and 3, respectively.

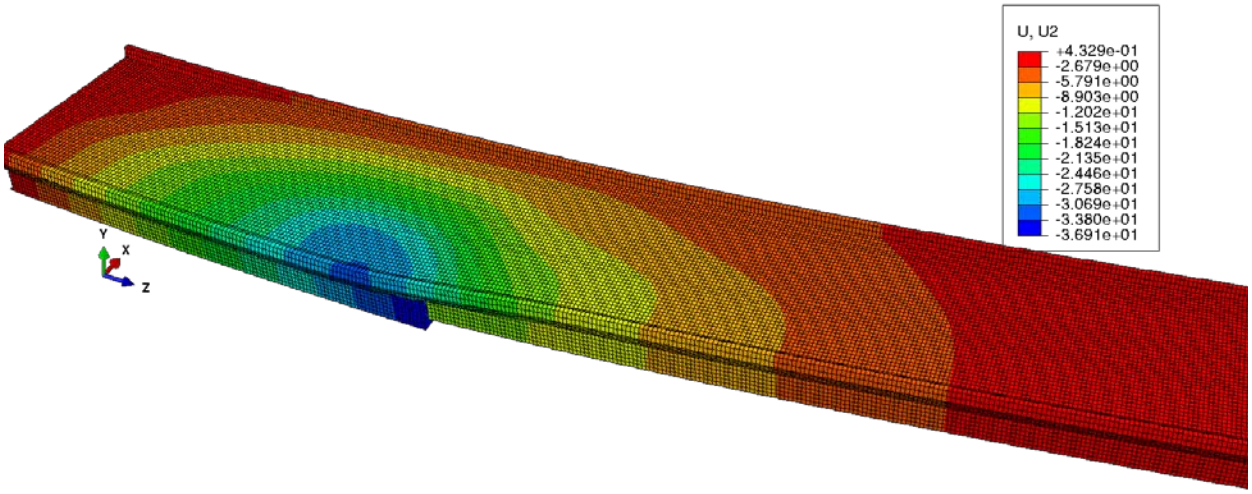

Figure 4.43. FEM Deflection Profile of Bridge 10, Span 1, with Fractured Outside Girder.

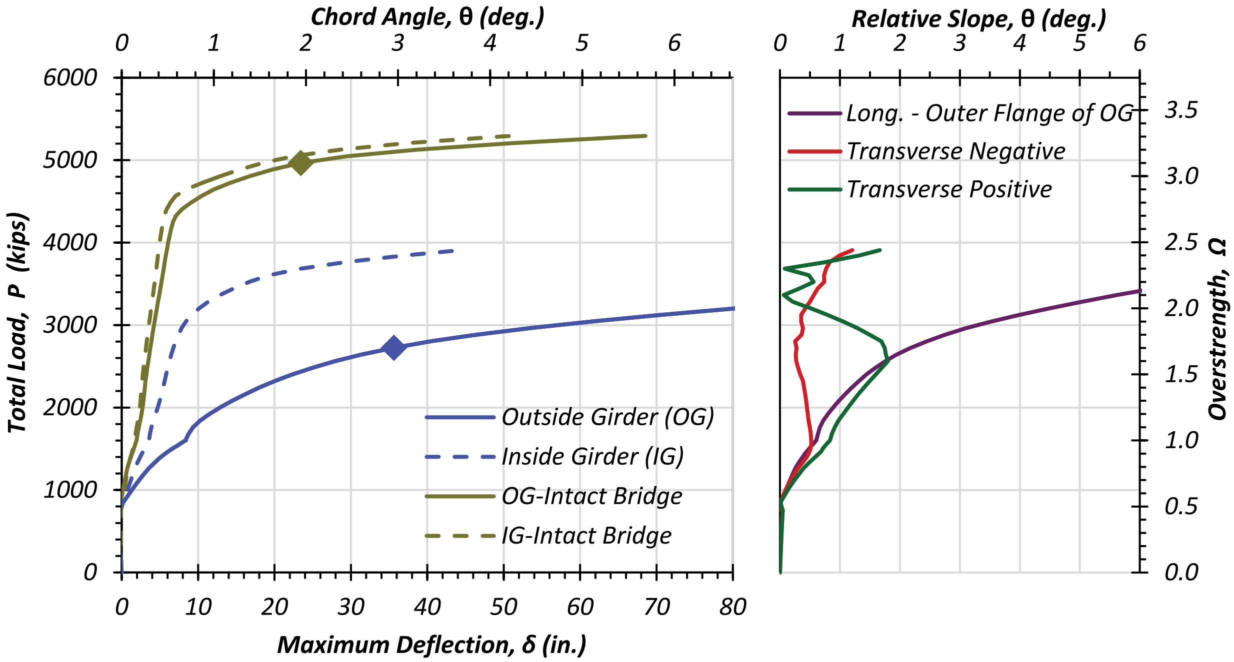

(a) Load displacement *(b) Deck rotations*

Note: δ is along the centerline of the outside girder, Ω is the load normalized by factored design load.

Figure 4.44. FEM Results for Bridge 10, Span 1.

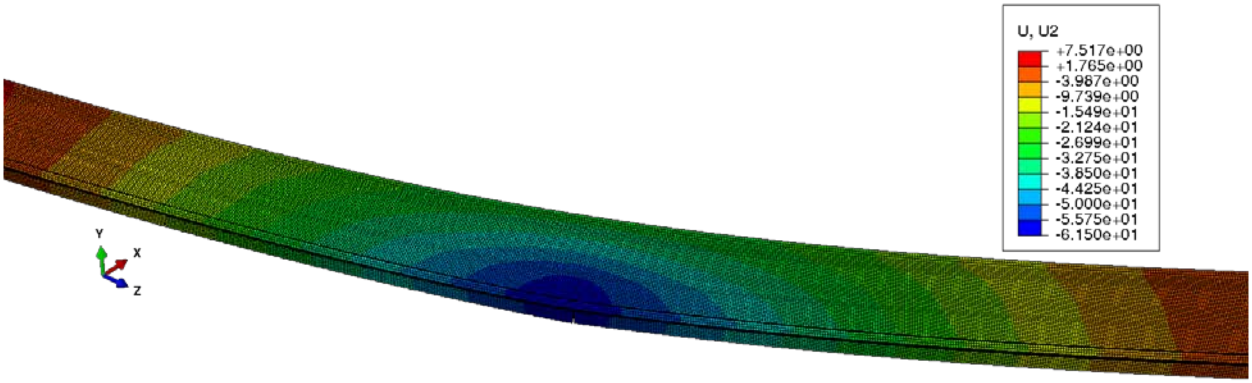

Figure 4.45. FEM Deflection Profile of Bridge 10, Span 2, with Fractured Outside Girder.

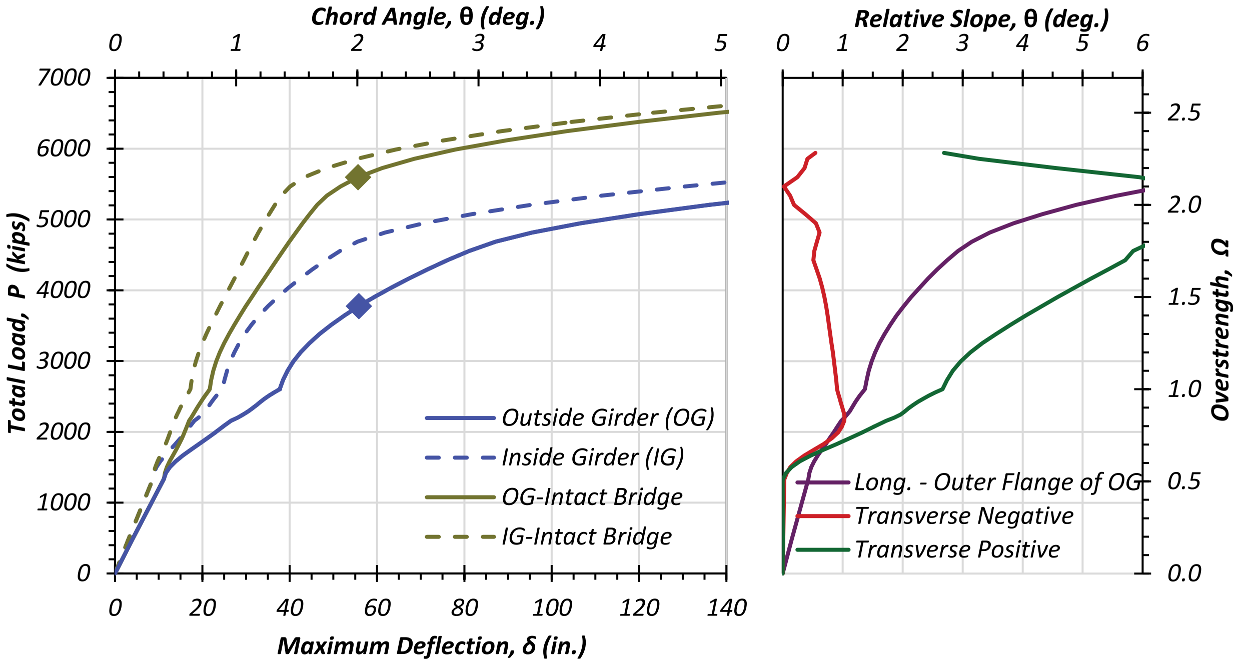

(a) Load displacement (b) Deck rotations

Note: δ is along the centerline of the outside girder, Ω is the load normalized by factored design load.

Figure 4.46. FEM Results for Bridge 10, Span 2.

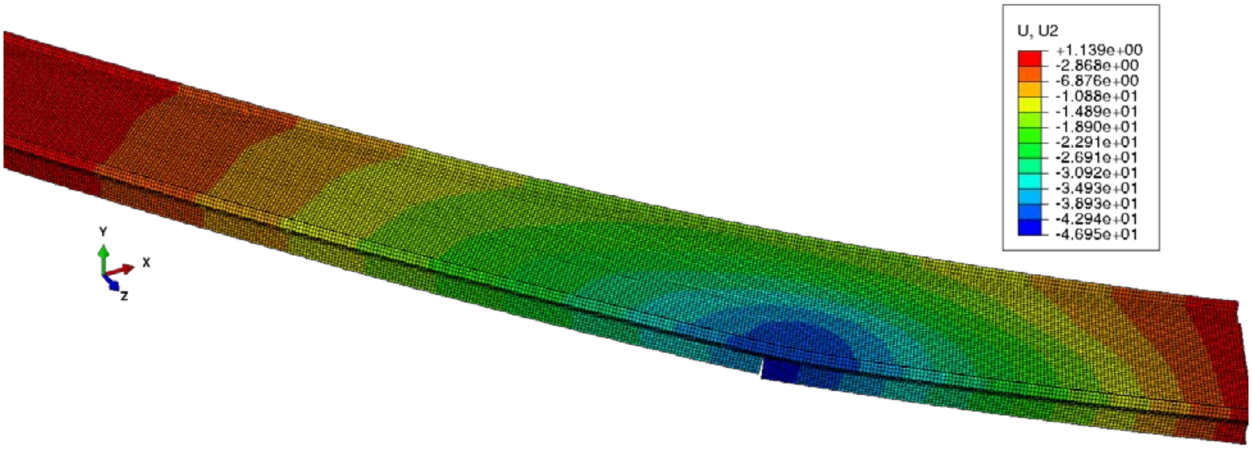

Figure 4.47. FEM Deflection Profile of Bridge 10, Span 3, with Fractured Outside Girder.

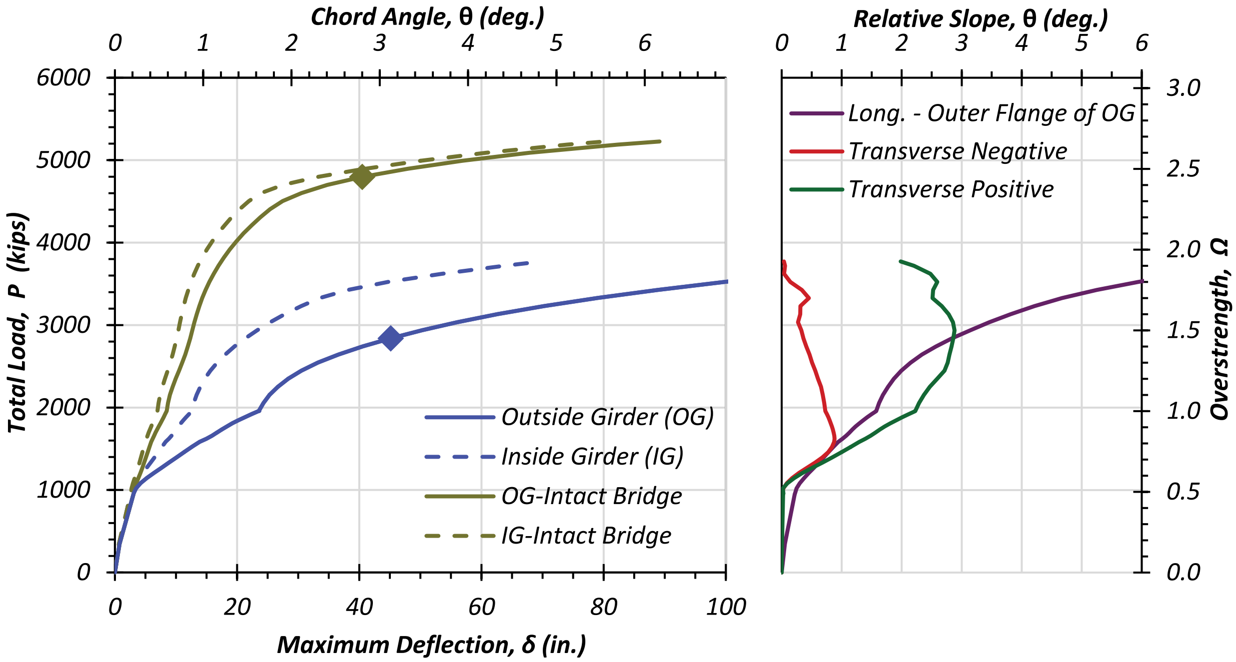

(a) Load displacement (b) Deck rotations

Note: δ is along the centerline of the outside girder, Ω is the load normalized by factored design load.

Figure 4.48. FEM Results for Bridge 10, Span 3.

4.4.12 Bridge 11—NBI #12-102-0271-07-593

Bridge 11, a three-span continuous bridge, was built in 2007 in Harris County along IH 10. Bridge 11 has 223 ft, 366 ft, and 235 ft long spans, with an 818.5 ft radius of curvature and a 28.4 ft wide, 8 in. thick deck. Table 4.23 summarizes several main key characteristics of Bridge 11, including geometry, age, location, studs, and diaphragm details. Table 4.24 lists dimensions of the steel tub girder components along the length of the bridge. The webs and bottom flange have variable thicknesses along the length of the girders, while both the width and thickness of the top flange changes along the length. The variable geometric properties of the steel tub girder components were incorporated into the FEM model. Further details about geometry, member dimensions, reinforcement layout, and other diaphragm types may be found in the structural drawings of Bridge 11 that are provided in Appendix A.

Table 4.23. Geometric Properties and Member Dimensions of Bridge 11.

Location	Parameter	Description/Value
Bridge	Location	Harris County, IH 10
	Year Designed/Year Built	2004/2007
	Design Load	HS25
	Length, ft	824
	Spans, ft	223, 366, 235
	Radius of Curvature, ft	818.51
Deck	Width, ft	28.417
	Thickness, in.	8
	Haunch, in.	4
	Rail Type	SSTR
Studs	No. of Studs per row	4
	Length, in.	6
	Diameter, in.	0.875
Interior Intermediate Diaphragm	Top Angle	L 6 x 6 x 5/8
	Diagonal Angles	L 6 x 6 x 5/8
	Stiffeners	3/4" x 8"
Exterior Erection Diaphragm	Top Angle	WT 7 x 34
	Diagonal Angles	L 5 x 3 ½ x 1/2
	Bottom Shape	WT 7 x 34
Internal End Diaphragm	Top Plate	1"
	Solid Plate	1" x 18"
	Stiffeners	1" x 9"
External End Diaphragm	Top Plate	1" x 18"
	Solid Plate	1"
	Bottom Plate	1" x 18"

Note: Typical exterior, interior, and end diaphragms are listed. See Appendix A for other types.

Table 4.24. Geometric Details of Steel Tub Girders for Bridge 11.

Location ft	Top Flange		Web		Bottom Flange	
	Width in.	Thickness in.	Width in.	Thickness in.	Width in.	Thickness in.
0–128	18	1.00	102	2.875	66	1.0
128–154	18	1.00	102	2.875	66	1.5
154–180	30	1.75	102	2.875	66	1.5
180–247	30	3.00	102	2.875	66	3.0
247–256	30	3.00	102	2.875	66	1.5
256–281	30	1.75	102	2.875	66	1.5
281–522	18	1.75	102	2.875	66	1.5
522–555	30	1.75	102	2.875	66	1.5
555–630	30	3.00	102	2.875	66	3.0
630–647	30	1.75	102	2.875	66	1.5
647–681	18	1.00	102	2.875	66	1.5
681–824	18	1.00	102	2.875	66	1.0

The 3D FEM model of Bridge 11 was created for the entire bridge length of the three-span superstructure. Figure 4.49 show the deflection profiles for Span 1 of Bridge 11 when two lanes of ultimate loading are located on the corresponding span with a full-depth fracture crack at the moment-critical location of the outside girder and Figure 4.50 presents the load versus displacement and deck rotation plots for Span 1 of Bridge 11. Figure 4.51 show the deflection profiles for Span 2 of Bridge 11 when two lanes of ultimate loading are located on the corresponding span with a full-depth fracture crack at the moment-critical location of the outside girder and Figure 4.52 presents the load versus displacement and deck rotation plots for Span 2 of Bridge 11. Figure 4.53 show the deflection profiles for Span 3 of Bridge 11 when two lanes of ultimate loading are located on the corresponding span with a full-depth fracture crack at the moment-critical location of the outside girder and Figure 4.54 presents the load versus displacement and deck rotation plots for Span 3 of Bridge 11.

The behavior of all three spans were simulated under the same loading conditions for fractured and nonfractured conditions. For exterior spans, the ultimate limit state governs the capacity values. For the interior span transverse deck rotation limit governs the capacity. The ultimate limit state corresponding to 95% stiffness degradation is 1.6, 2.45, and 1.6 for Spans 1, 2, and 3, respectively.

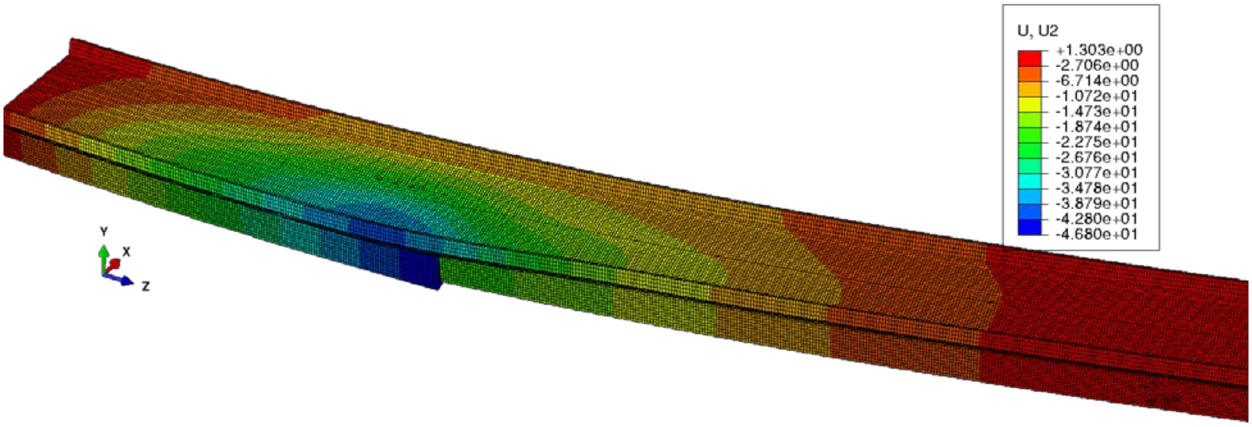

Figure 4.49. FEM Deflection Profile of Bridge 11, Span 1, with Fractured Outside Girder.

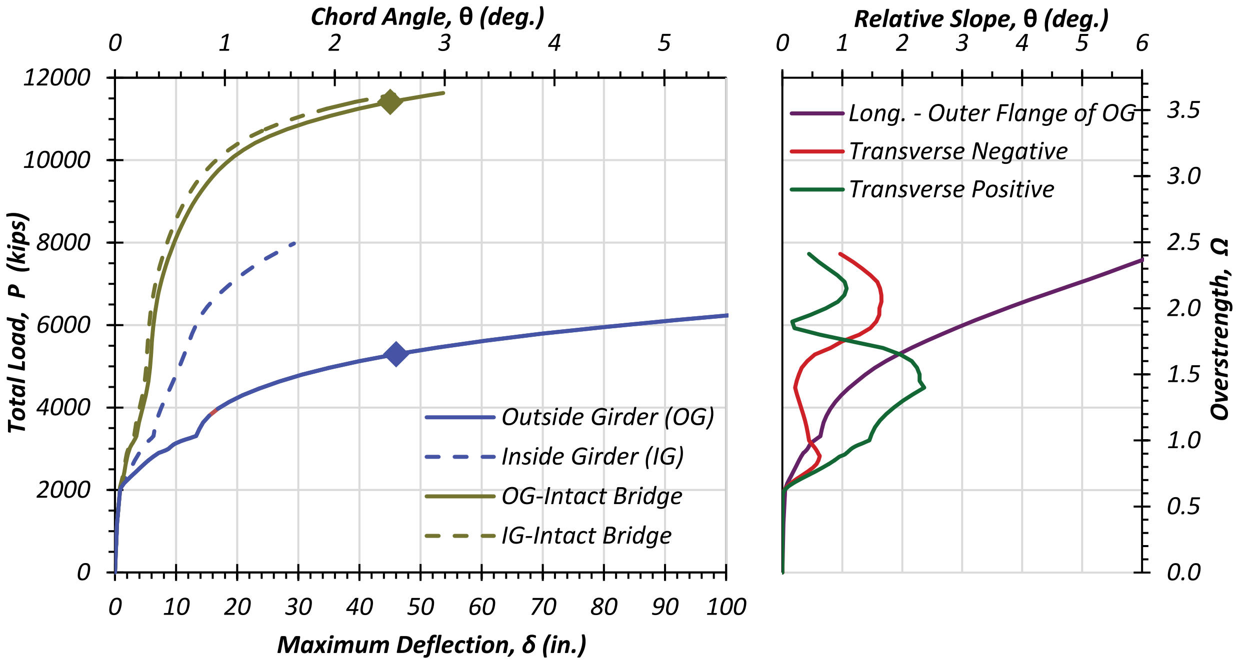

(a) Load displacement

(b) Deck rotations

Note: δ is along the centerline of the outside girder, Ω is the load normalized by factored design load.

Figure 4.50. FEM Results for Bridge 11, Span 1.

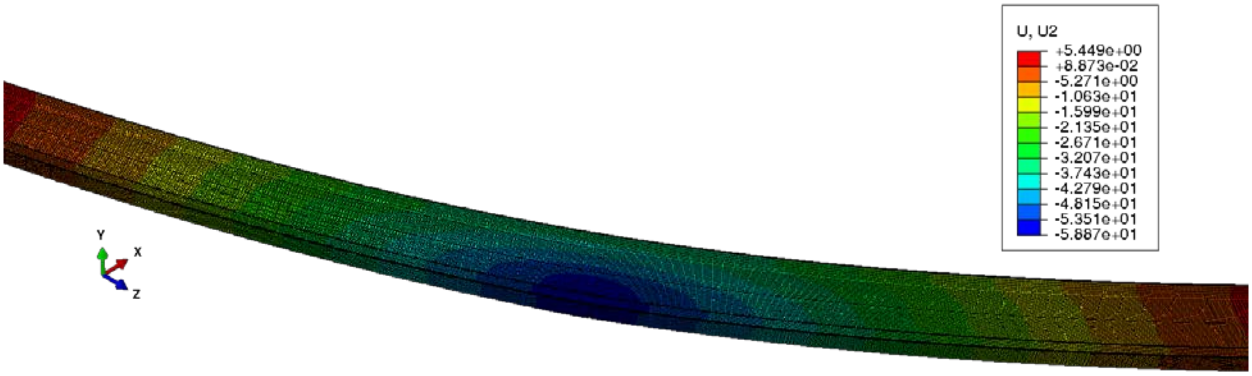

Figure 4.51. FEM Deflection Profile of Bridge 11, Span 2, with Fractured Outside Girder.

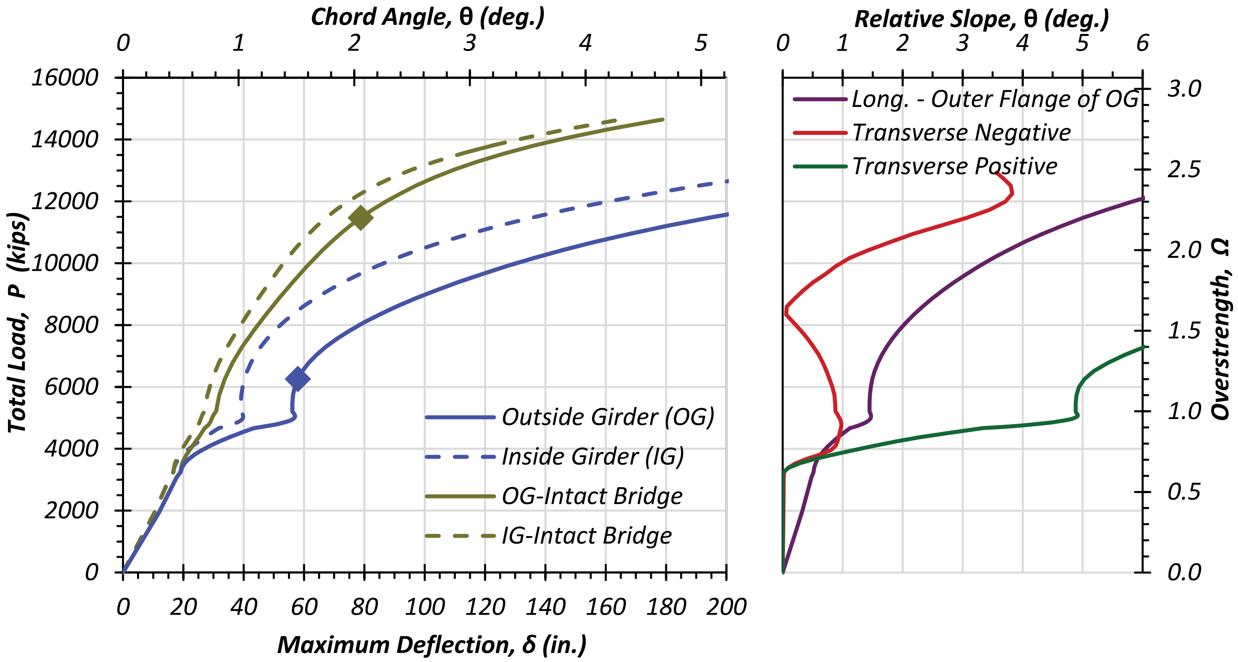

(a) Load displacement

(b) Deck rotations

Note: δ is along the centerline of the outside girder, Ω is the load normalized by factored design load.

Figure 4.52. FEM Results for Bridge 11, Span 2.

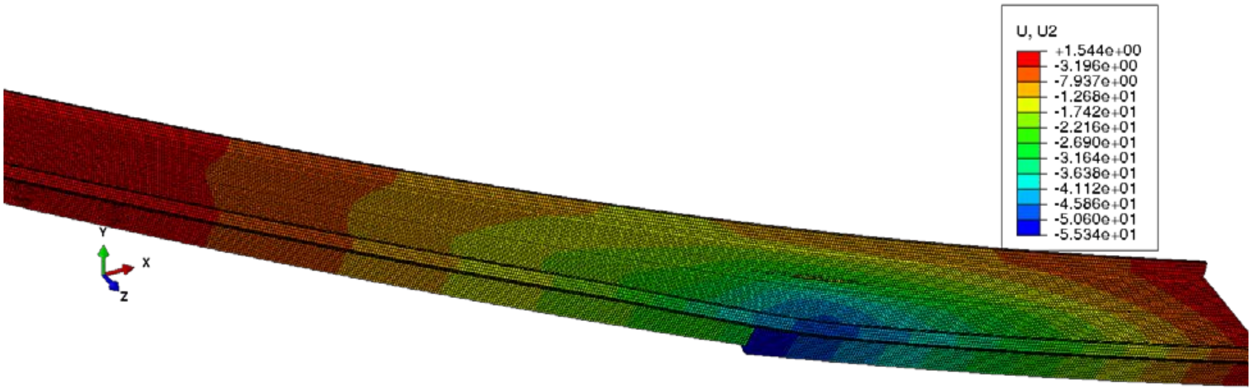

Figure 4.53. FEM Deflection Profile of Bridge 11, Span 3, with Fractured Outside Girder.

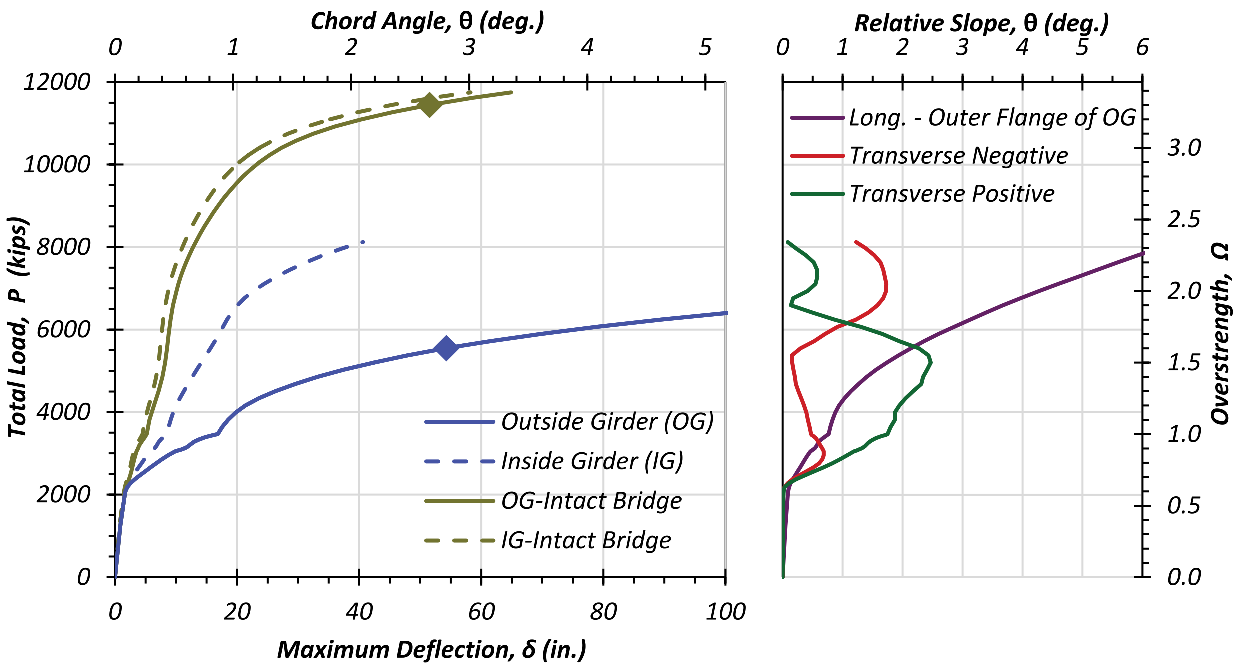

(a) Load displacement (b) Deck rotations

Note: δ is along the centerline of the outside girder, Ω is the load normalized by factored design load.

Figure 4.54. FEM Results for Bridge 11, Span 3.

4.4.13 Bridge 12—NBI # 12-102-0271-07-639

Bridge 12 is a three-span continuous bridge that was built in 2007 in Harris County along IH 10. Bridge 12 has 140 ft, 180 ft, and 145 ft long spans, with a 225 ft radius of curvature and a 28.4 ft wide, 8.5 in. thick deck. Table 4.25 provides various key characteristics of Bridge 12, including overall geometry, year built, location, stud information, and diaphragm details. Table 4.26 lists dimensional details of the steel tub girder components along the length of the bridge. Both top and bottom flanges of the tub girders have variable thicknesses along the length. The variation in the member thickness was incorporated into the FEM model. Further details about geometry, member dimensions, reinforcement layout, and other diaphragm types may be found in the structural drawings of Bridge 12 that are provided in Appendix A.

Table 4.25. Geometric Properties and Member Dimensions of Bridge 12.

Location	Parameter	Description/Value
Bridge	Location	Harris County, IH 10
	Year Designed/Year Built	2004/2007
	Design Load	HS25
	Length, ft	465
	Spans, ft	140, 180, 145
	Radius of Curvature, ft	225
Deck	Width, ft	28.417
	Thickness, in.	8.5
	Haunch, in.	3.5
	Rail Type	SSTR
Studs	No. of Studs per row	3
	Length, in.	7
	Diameter, in.	0.875
End Diaphragm	Interior Plate, in.	0.75
	Exterior Plate, in.	0.75
	Top Plate	1" x 16"
	Jacking Stiffener	1" x 8"
Intermediate Diaphragm	Top Angle	L 5 x 5 x 1/2
	Diagonal Angles	L 5 x 5 x 1/3
	Stiffeners	1/2" x 8"
	Lateral Bracing	WT8 x 44.5
Exterior Erection Diaphragm	Top Angle	WT7 x 21.5
	Bottom Angle	WT 7 x 21.5
	Diagonal Angles	L 5 x 3 ½ x 1/2

Note: Typical exterior, interior, and end diaphragms are listed. See Appendix A for other types.

Table 4.26. Geometric Details of Steel Tub Girders for Bridge 12.

Location ft	Top Flange		Web		Bottom Flange	
	Width in.	Thickness in.	Width in.	Thickness in.	Width in.	Thickness in.
0–90	20	1.00	54	0.5	72	0.875
90–116	20	1.75	54	0.5	72	1.750
116–138	20	3.25	54	0.5	72	1.750
138–160	20	3.25	54	0.5	72	1.750
160–189	20	1.75	54	0.5	72	1.750
189–267	20	1.00	54	0.5	72	0.875
267–296	20	1.75	54	0.5	72	1.750
296–318	20	3.25	54	0.5	72	1.750
318–340	20	3.25	54	0.5	72	1.750
340–371	20	1.75	54	0.5	72	1.750
371–465	20	1.00	54	0.5	72	0.875

Figure 4.55 show the deflection contour map for Span 1 of Bridge 12 when the analyzed span is simulated with a full-depth fracture crack at the moment-critical location of the outside

girder and with two lanes of ultimate loading favored toward the outside edge and Figure 4.56 presents the load versus displacement and deck rotation plots for Span 1 of Bridge 12.

Figure 4.57 show the deflection contour map for Span 2 of Bridge 12 when the analyzed span is simulated with a full-depth fracture crack at the moment-critical location of the outside girder and with two lanes of ultimate loading favored toward the outside edge and Figure 4.58 presents the load versus displacement and deck rotation plots for Span 2 of Bridge 12.

Figure 4.59 show the deflection contour map for Span 3 of Bridge 12 when the analyzed span is simulated with a full-depth fracture crack at the moment-critical location of the outside girder and with two lanes of ultimate loading favored toward the outside edge and Figure 4.60 presents the load versus displacement and deck rotation plots for Span 3 of Bridge 12.

The load-deflection behavior of the bridge was simulated for each span separately when the load is located on the corresponding span for fractured and nonfractured conditions. Similar length exterior spans achieve overstrength factors of 1.6, which is approximately 35 percent lower than the simulation of the same spans without a fracture. The 180 ft long interior span can achieve a 1.8 overstrength factor when simulated with a fracture in the outside girder. The interior span is about 30 percent longer than the exterior spans but could obtain slightly larger overstrength factor due to additional redundancy of the interior span. The governing overstrength factor that corresponds to the ultimate capacity for all three spans was the longitudinal chord rotation limit state. The ultimate limit state corresponding to 5 percent initial stiffness value is 1.9, 2.1, and 1.9 for Spans 1, 2, and 3, respectively.

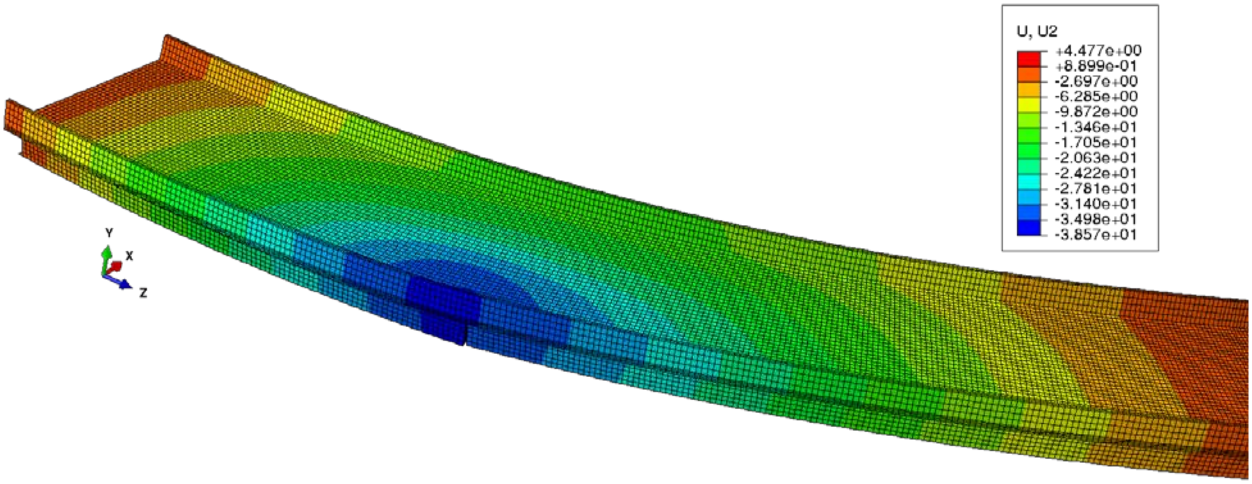

Figure 4.55. FEM Deflection Profile of Bridge 12, Span 1, with Fractured Outside Girder.

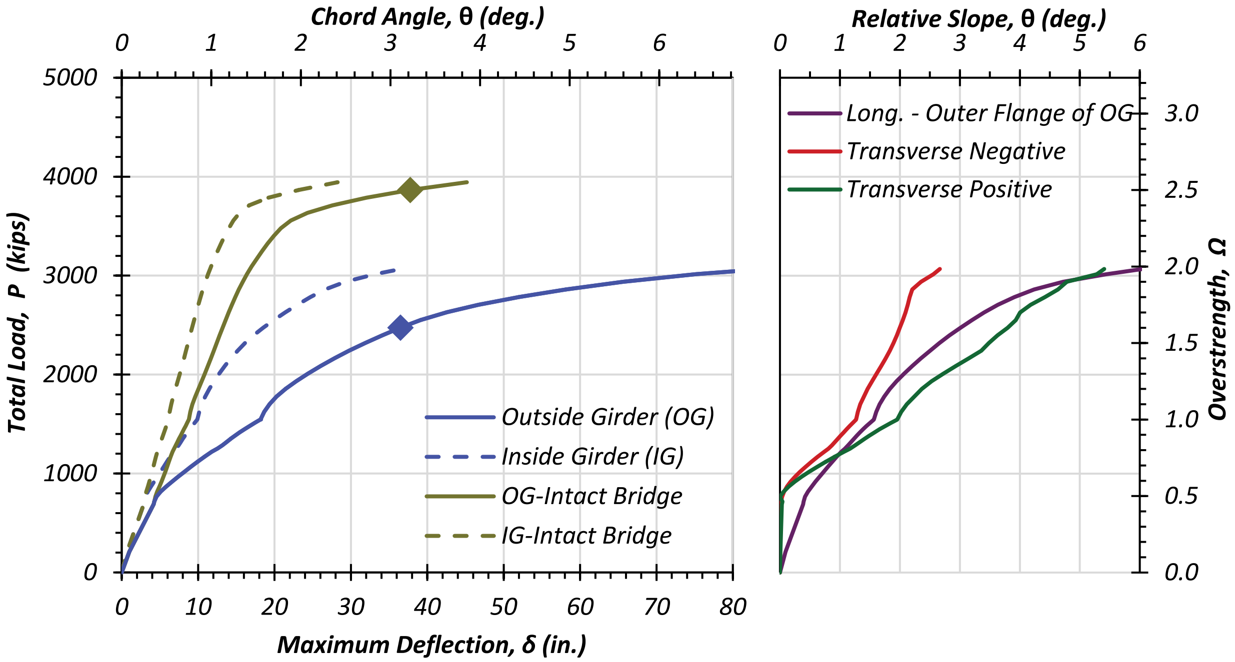

(a) Load displacement

(b) Deck rotations

Note: δ is along the centerline of the outside girder, Ω is the load normalized by factored design load.

Figure 4.56. FEM Results for Bridge 12, Span 1.

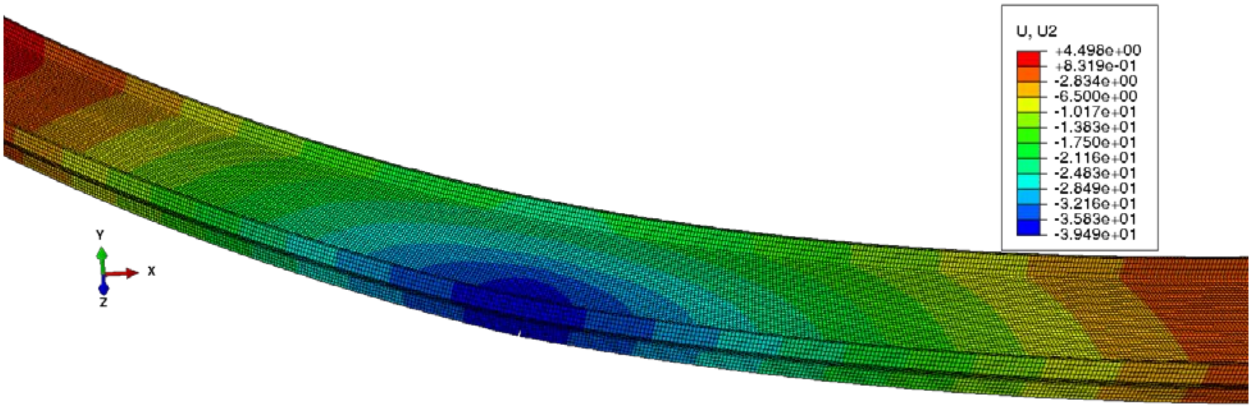

Figure 4.57. FEM Deflection Profile of Bridge 12, Span 2, with Fractured Outside Girder.

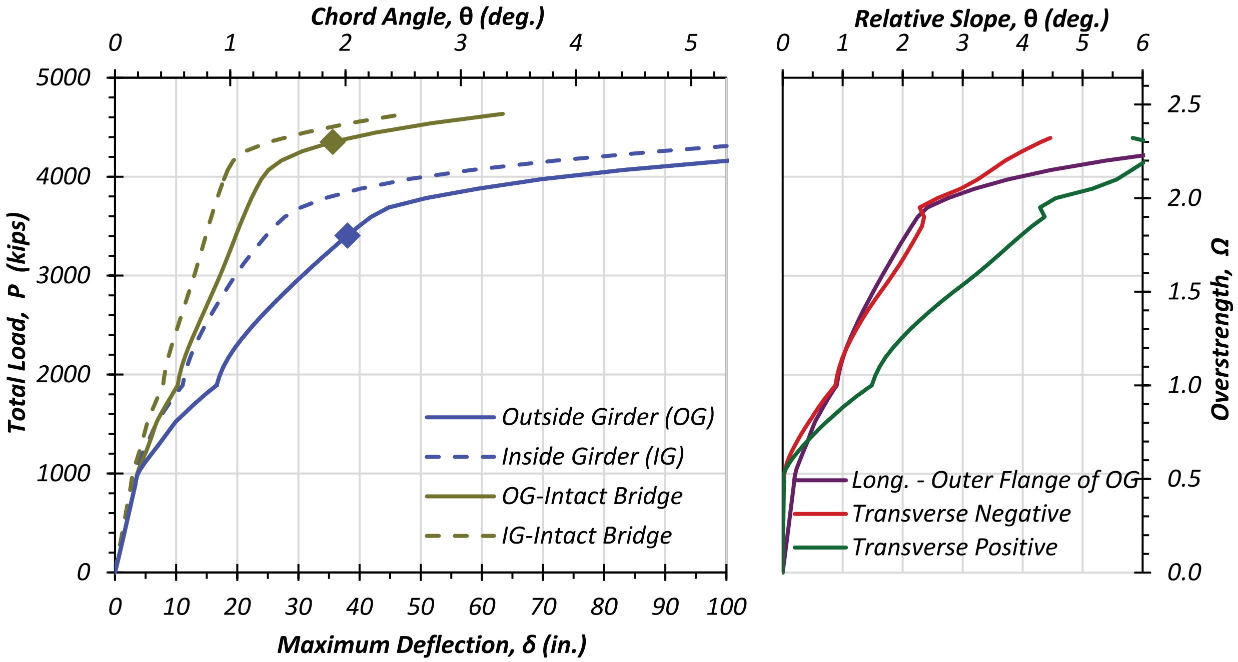

(a) Load displacement

(b) Deck rotations

Note: δ is along the centerline of the outside girder, Ω is the load normalized by factored design load.

Figure 4.58. FEM Results for Bridge 12, Span 2.

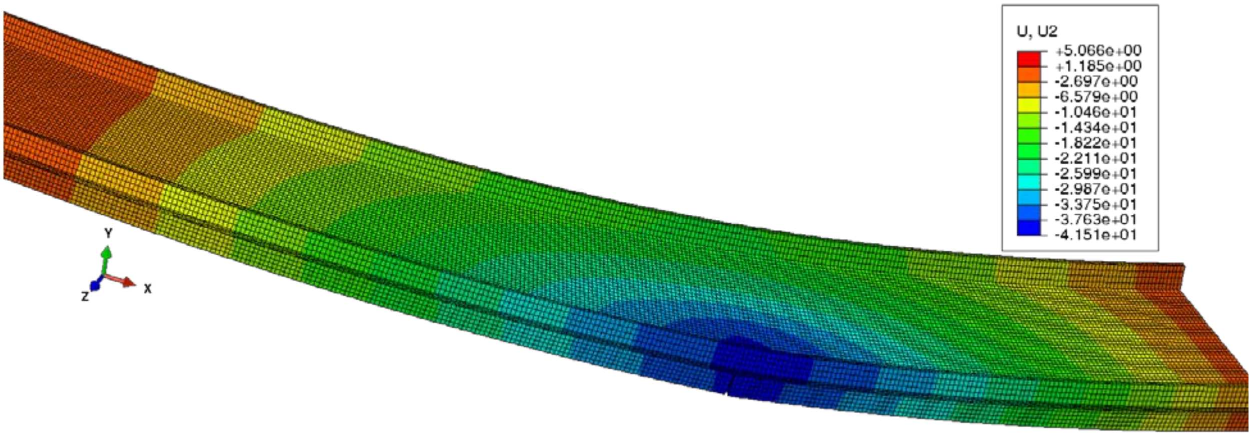

Figure 4.59. FEM Deflection Profile of Bridge 12, Span 3, with Fractured Outside Girder.

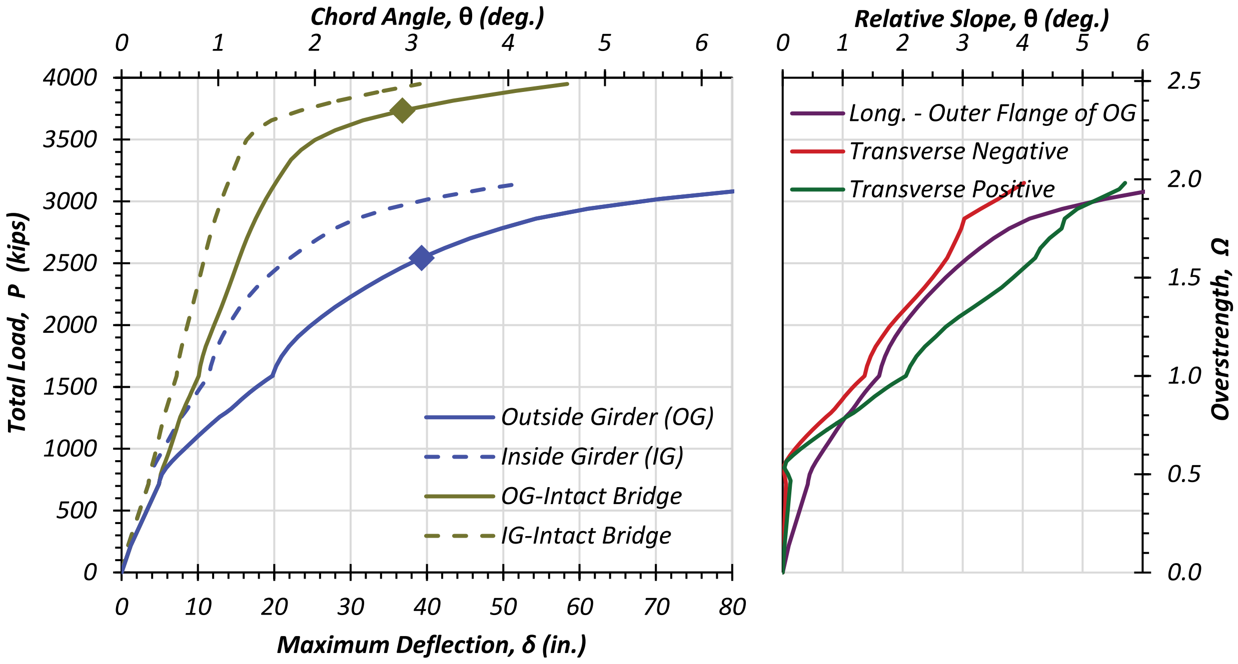

(a) Load displacement *(b) Deck rotations*

Note: δ is along the centerline of the outside girder, Ω is the load normalized by factored design load.

Figure 4.60. FEM Results for Bridge 12, Span 3.

4.4.14 Bridge 13—NBI #14-227-0-0015-13-452

Bridge 13, a three-span continuous bridge, was built in 2002 in Travis County along I-35. Bridge 13 has 151.5 ft, 190 ft, and 151.5 ft long spans, with a 450 ft radius of curvature and a 30 ft wide, 8 in. thick deck. Table 4.27 summarizes several key characteristics of Bridge 13, including overall geometry, year built, location information, studs, and diaphragm details. Table 4.28 provides dimensional details of the steel tub girder components along the length of the bridge. The thickness of the webs and top and bottom flanges of the tub girders varies along the length of the bridge. The variation in the member thickness was included in the FEM model. Further details about geometry, member dimensions, reinforcement layout, and other diaphragm types may be found in the structural drawings of Bridge 13 that are provided in Appendix A.

Table 4.27. Geometric Properties and Member Dimensions of Bridge 13.

Location	Parameter	Description/Value
Bridge	Location	Travis County, I-35
	Year Designed/Year Built	1998/2002
	Design Load	HS20
	Length, ft	493
	Spans, ft	151.5, 190, 151.5
	Radius of Curvature, ft	450
Deck	Width, ft	30
	Thickness, in.	8
	Haunch, in.	4
	Rail Type	T4(S)
Studs	No. of Studs per row	3
	Length, in.	7
	Diameter, in.	0.875
Interior Intermediate Diaphragm	Top Angle	4 x 4 x 1/2
	Diagonal Angles	4 x 4 x 1/2
	Stiffeners	5/8" x 8"
Exterior Erection Diaphragm	Top Angle	L 5 x 5 x 1/2
	Diagonal Angles	L 5 x 5 x 1/2
	Bottom Angle	L 5 x 5 x 1/2
Interior End Diaphragm	Top Plate	3/4" x 18"
	Solid Plate	1/2"
	Bottom Plate	3/4" x 18"
Exterior End Diaphragm	Top Plate	3/4" x1 8"
	Solid Plate	1/2"
	Stiffeners	5/8" x 5"

Note: Typical exterior, interior, and end diaphragms are listed. See Appendix A for other types.

Table 4.28. Geometric Details of Steel Tub Girders for Bridge 13.

Location ft	Top Flange		Web		Bottom Flange	
	Width in.	Thickness in.	Width in.	Thickness in.	Width in.	Thickness in.
0–18	24	1.25	54	0.625	60	0.75
19–94	24	1.25	54	0.500	60	0.75
94–113	24	1.25	54	0.625	60	0.75
113–132	24	1.25	54	0.625	60	1.25
132–151	24	1.75	54	0.625	60	1.50
151–170	24	2.75	54	0.625	60	2.00
170–189	24	1.75	54	0.625	60	1.50
189–208	24	1.25	54	0.625	60	1.25
208–284	24	1.25	54	0.500	60	0.75
284–303	24	1.25	54	0.625	60	0.75
303–322	24	1.25	54	0.625	60	1.25
322–341	24	1.75	54	0.625	60	1.50
341–360	24	2.75	54	0.625	60	2.00
360–379	24	1.75	54	0.625	60	1.50
379–398	24	1.25	54	0.625	60	1.25
398–474	24	1.25	54	0.500	60	0.75
474–493	24	1.25	54	0.625	60	0.75

Figure 4.61 shows the deflection profile for Spans 1 and 3 of Bridge 13 when simulated with a full-depth fracture in the outside girder of the corresponding span and with the HL-93 loading at a critical flexural position on the same span and Figure 4.62 presents load versus displacement and deck rotation plots for Spans 1 and 3 of Bridge 13. The behavior of the exterior Span 1 and interior Span 2 were simulated under the same loading conditions for fractured and nonfractured conditions. The fracture was always located in the loaded span, while the other spans were nonfractured and carried only a factored dead load.

Figure 4.63 shows the deflection profile for Span 2 of Bridge 13 when simulated with a full-depth fracture in the outside girder of the corresponding span and with the HL-93 loading at a critical flexural position on the same span while Figure 4.64 presents load versus displacement and deck rotation plots for Span 2 of Bridge 13.

The exterior spans have the same span length and therefore achieved the same overstrength factor of 1.0, which is 50 percent lower than the simulation of the same spans without a fracture. The 190 ft long interior Span 2 obtained a 1.4 overstrength factor when simulated with a fracture in the outside girder. Despite the 25 percent longer span length, the interior span has a bigger overstrength factor due to continuity from both ends of the span. The governing overstrength factor that corresponded, to the ultimate capacity for the exterior and interior spans was longitudinal chord rotation limit state. The ultimate limit state corresponding to 5 percent initial stiffness value is 1.5 and 1.75 for Spans 1 and 2, respectively.

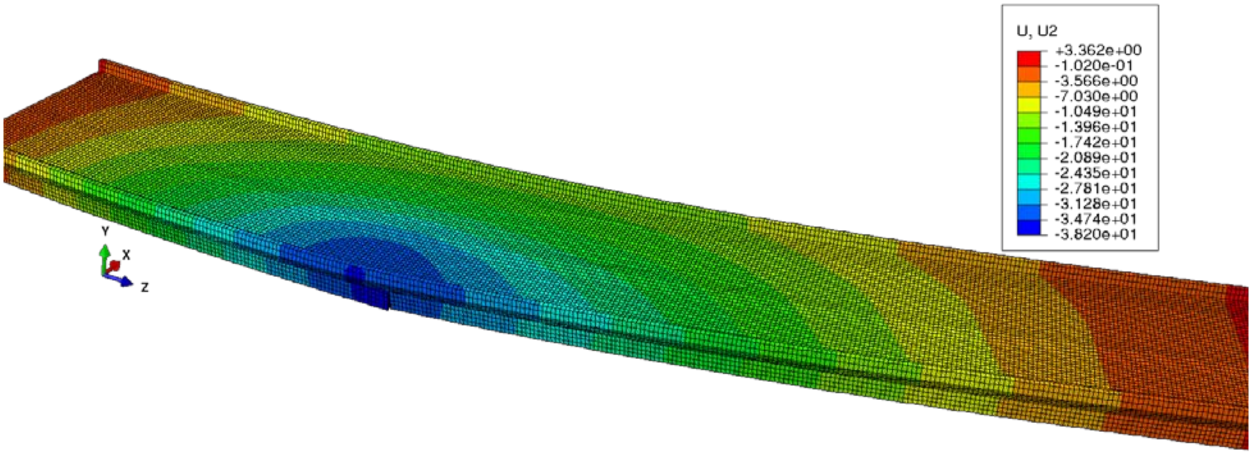

Figure 4.61. FEM Deflection Profile of Bridge 13, Span 1 and 3, with Fractured Outside Girder.

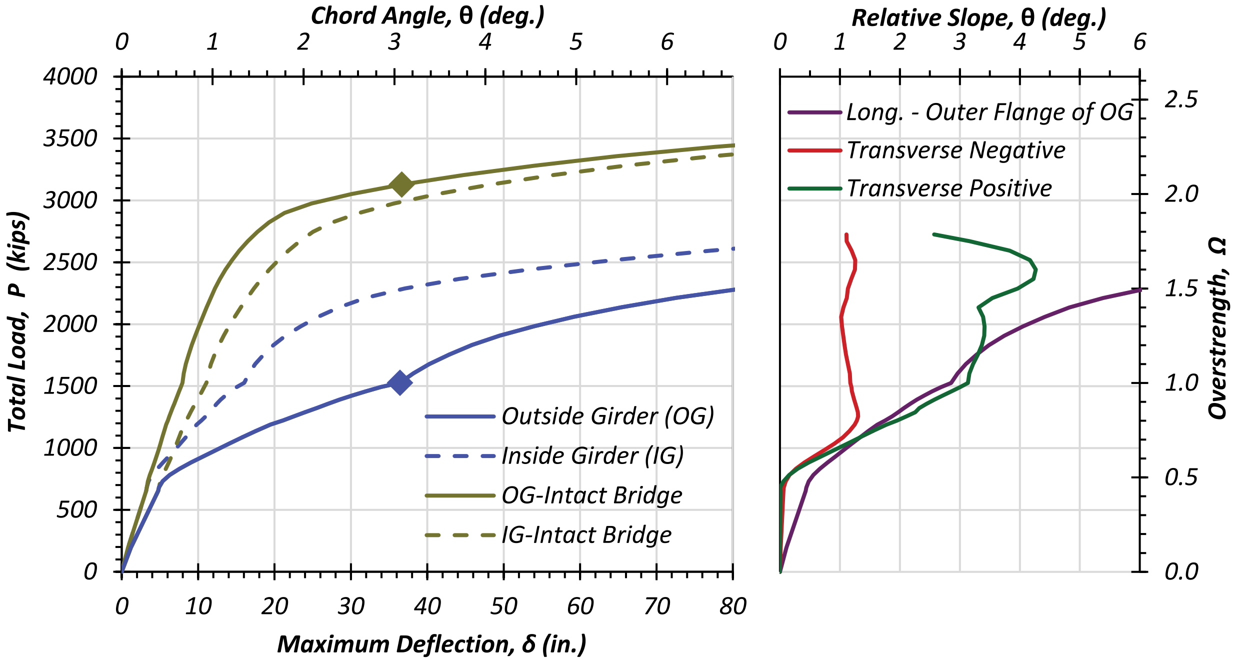

(a) Load displacement

(b) Deck rotations

Note: δ is along the centerline of the outside girder, Ω is the load normalized by factored design load.

Figure 4.62. FEM Results for Bridge 13, Span 1 and 3.

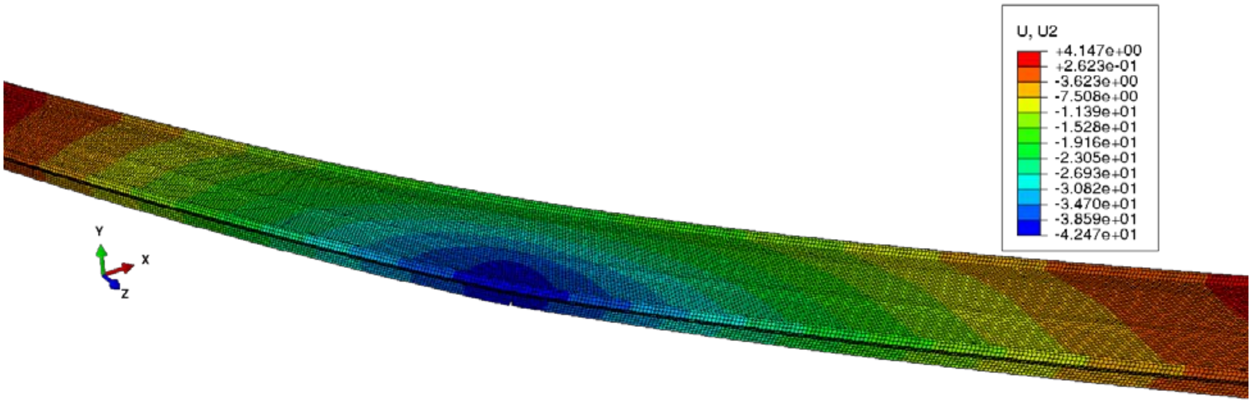

Figure 4.63. FEM Deflection Profile of Bridge 13, Span 2, with Fractured Outside Girder.

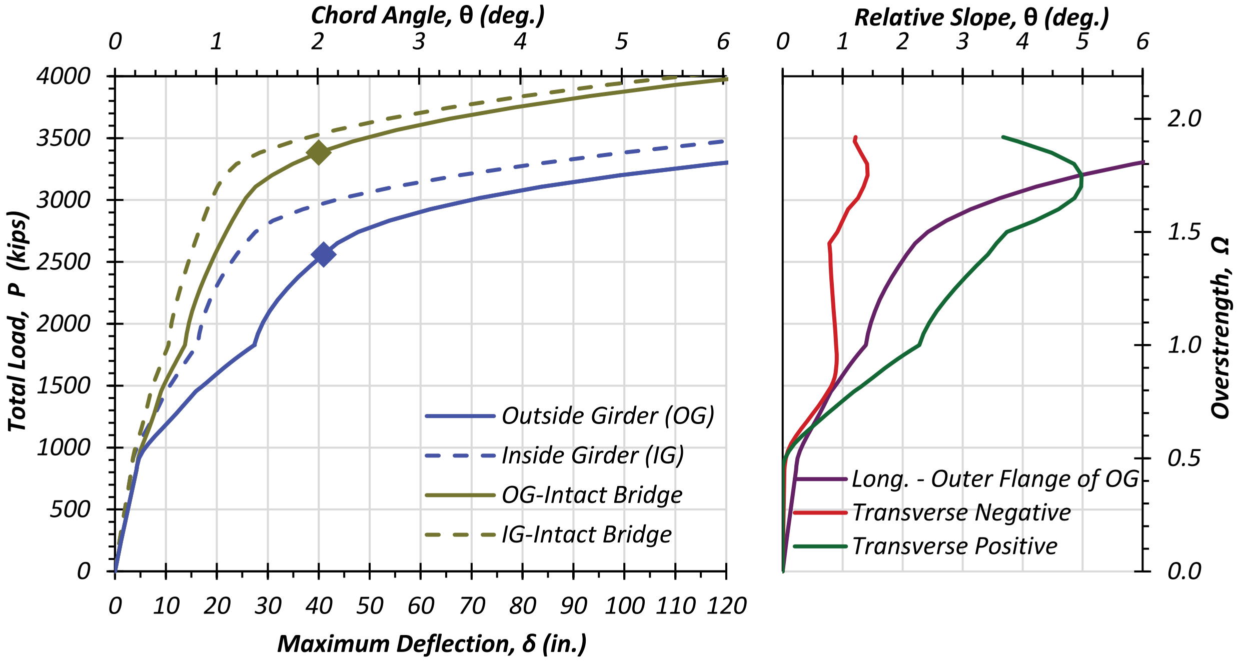

(a) Load displacement *(b) Deck rotations*

Note: δ is along the centerline of the outside girder, Ω is the load normalized by factored design load.

Figure 4.64. FEM Results for Bridge 13, Span 2.

4.4.15 Bridge 14—NBI #18-057-0-0009-11-460

Bridge 14 is a three-span continuous bridge that was built in 2012 in Dallas County along IH 30. Bridge 14 has 150 ft, 190 ft, and 150 ft long spans with a 1010 ft radius of curvature and a 28 ft wide, 8 in. thick deck. Table 4.29 provides key characteristics of Bridge 14, including overall geometry, year built, location information, studs, and diaphragm details. Table 4.30 provides dimensional details of the steel tub girder components along the length of the bridge. The webs and top and bottom flanges of the tub girders have variable thicknesses along the length of the bridge. The variation in the member thickness was included in the FEM model. The deck geometry and span lengths of Bridge 14 are very similar to that of Bridge 13. However, the more recently built Bridge 14 has deeper web sections and wider bottom flanges, which improves the capacity significantly. Further details about geometry, member dimensions, reinforcement layout, and other diaphragm types may be found in the structural drawings of Bridge 14 that are provided in Appendix A.

Table 4.29. Geometric Properties and Member Dimensions of Bridge 14.

Location	Parameter	Description/Value
Bridge	Location	Dallas County, IH 30
	Year Designed/Year Built	2008/2012
	Design Load	HS20
	Length, ft	490
	Spans, ft	150,190,150
	Radius of Curvature, ft	1010
Deck	Width, ft	28
	Thickness, in.	8
	Haunch, in.	4
	Rail Type	SSTR
Studs	No. of Studs per row	3
	Length, in.	7
	Diameter, in.	0.875
Internal Intermediate Diaphragm	Top Shape	WT 7 x 21.5
	Diagonal Angles	L 4 x 4 x 1/2
	Stiffeners	5/8" x 8"
Exterior Erection Diaphragm	Solid Plate	1/2"
	Top Plate	1/2" x 8 1/4"
	Bottom Plate	1/2" x 8 1/4"
Interior End Diaphragm	Solid Plate	1/2"
	Top Plate	3/4" x 12"
	Jacking Stiffeners	1 1/2" x 5"
	Cross Stiffeners	1/2" x 5"
Exterior End Diaphragm	Top Plate	1/2" x 8 1/4"
	Solid Plate	1/2"
	Bottom Plate	1/2" x 8 1/4"

Note: Typical exterior, interior, and end diaphragms are listed. See Appendix A for other types.

Table 4.30. Geometric Details of Steel Tub Girders for Bridge 14.

Location ft	Top Flange		Web		Bottom Flange	
	Width in.	Thickness in.	Width in.	Thickness in.	Width in.	Thickness in.
0–103	22	1.00	60	0.5625	70	0.750
103–112	22	1.00	60	0. 5625	70	1.125
112–131	22	1.00	60	0.625	70	1.125
131–169	22	1.75	60	0.625	70	1.500
169–198	22	1.00	60	0.625	70	1.125
198–302	22	1.00	60	0. 5625	70	0.750
302–321	22	1.00	60	0.625	70	1.125
321–358	22	1.75	60	0.625	70	1.500
358–386	22	1.00	60	0.625	70	1.125
386–490	22	1.00	60	0. 5625	70	0.750

A nonlinear 3D FEM model of Bridge 14 was created for the entire bridge length using the material properties that are provided in structural drawings. The boundary conditions were modeled as spring stiffness in the vertical and horizontal directions (as described in Chapter 3). Figure 4.65 shows the deflection contour map for Spans 1 and 3 of Bridge 14 when simulated with a full-depth fracture in the outside girder of the corresponding span and the HL-93 loading at a critical flexural position on the same span and Figure 4.66 presents the load versus displacement and deck rotation plots for the exterior spans of Bridge 14.

Figure 4.67 shows the deflection contour map for Span 2 of Bridge 14 when simulated with a full-depth fracture in the outside girder of the corresponding span and the HL-93 loading at a critical flexural position on the same span and Figure 4.68 presents the load versus displacement and deck rotation plots for the interior span of Bridge 14.

The behavior of both exterior Span 1 and interior Span 2 were simulated under the same loading conditions for fractured and nonfractured conditions. The fracture was always located in the loaded span, while the other spans were nonfractured and carried only a factored dead load. The exterior spans have the same lengths and therefore achieved the same overstrength factor of 1.65, which is 25 percent lower than the simulation of the same spans without a fracture. The 190 ft long interior span obtained a 1.8 overstrength factor when simulated with a fracture in the outside girder. Despite the 25 percent longer span length, the interior span has a slightly bigger overstrength factor due to continuity from both ends of the span. When compared with Bridge 13, Bridge 14 has about 20 percent higher overstrength factors for all three spans due to the deeper and stiffer steel tub girders of the more recently built Bridge 14.

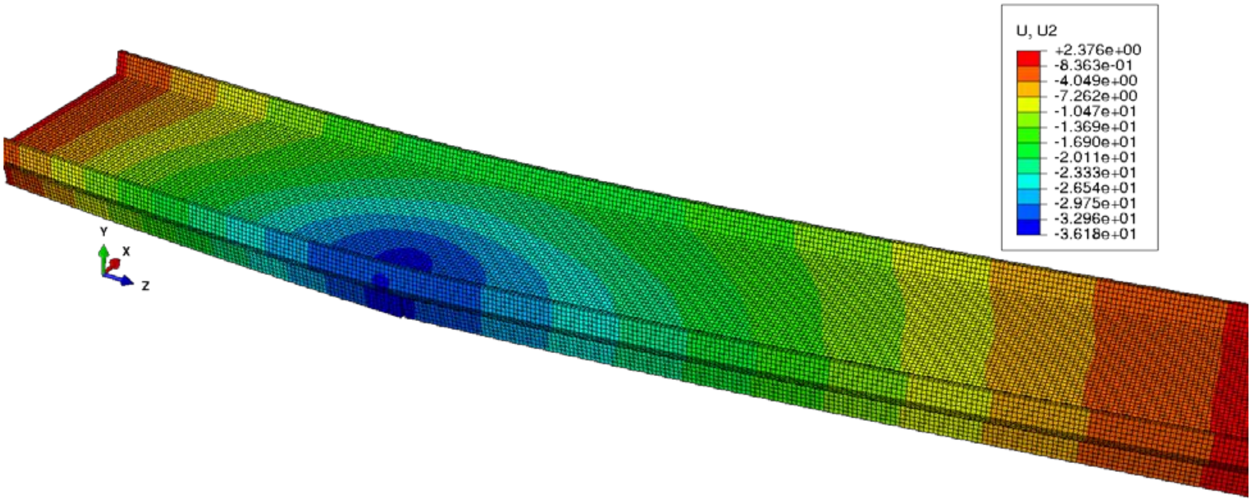

Figure 4.65. FEM Deflection Profile of Bridge 14, Span 1, with Fractured Outside Girder.

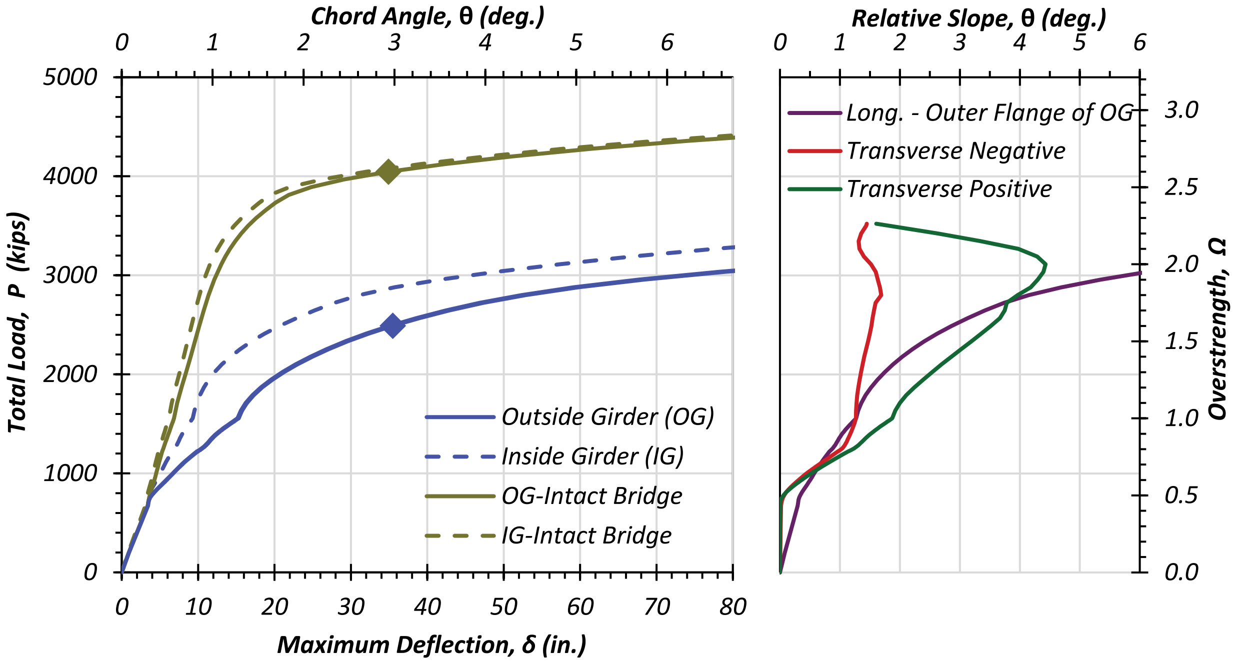

(a) Load displacement

(b) Deck rotations

Note: δ is along the centerline of the outside girder, Ω is the load normalized by factored design load.

Figure 4.66. FEM Results for Bridge 14, Span 1.

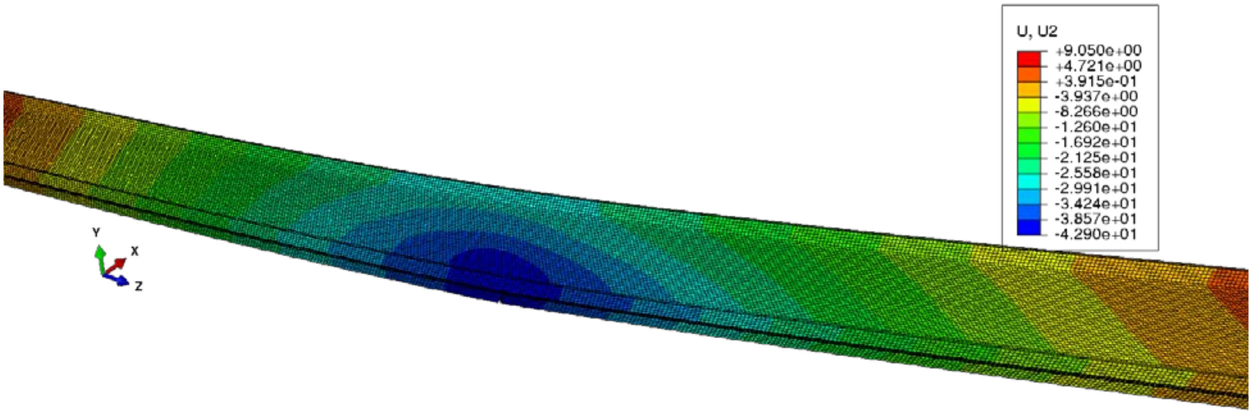

Figure 4.67. FEM Deflection Profile of Bridge 14, Span 2, with Fractured Outside Girder.

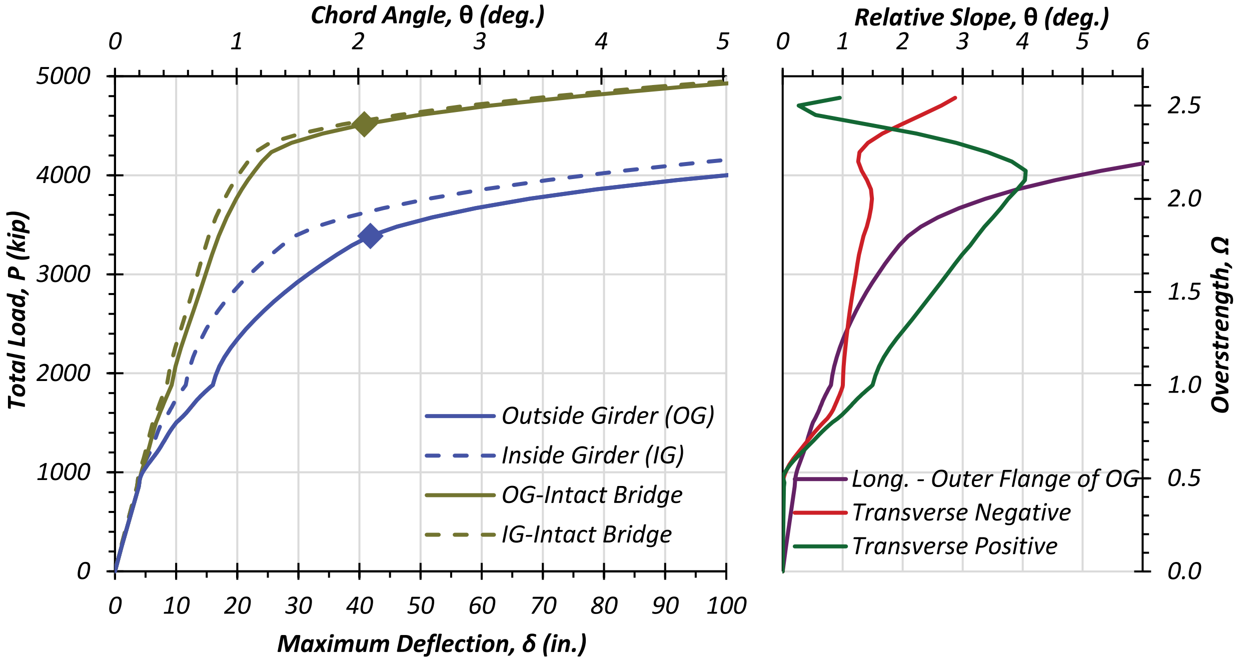

(a) Load displacement *(b) Deck rotations*

Note: δ is along the centerline of the outside girder, Ω is the load normalized by factored design load.

Figure 4.68. FEM Results for Bridge 14, Span 2.

4.4.16 Bridge 15—NBI #12-102-0271-06-689

Bridge 15, a three-span continuous bridge, was built in 2014 in Dallas County along IH 30. Bridge 14 has 200 ft, 295 ft, and 200 ft long spans, with an 809 ft radius of curvature and a 28.4 ft wide, 8 in. thick deck. Table 4.31 provides various key characteristics of Bridge 15, including geometry, year built, location information, studs, and diaphragm details. Table 4.32 provides dimensional details of the steel tub girder components along the length of the bridge. Both bottom and top flanges of the tub girders have variable thicknesses along the length of the bridge. The variation in the member thickness was incorporated in the FEM model. Further details about geometry, member dimensions, reinforcement layout, and other diaphragm types may be found in the structural drawings of Bridge 15 that are provided in Appendix A.

Table 4.31. Geometric Properties and Member Dimensions of Bridge 15.

Location	Parameter	Description/Value
Bridge	Location	Dallas County, IH 30
	Year Designed/Year Built	2012/2014
	Design Load	HL-93
	Length, ft	695
	Spans, ft	200,295,200
	Radius of Curvature, ft	809
Deck	Width, ft	28.417
	Thickness, in.	8
	Haunch, in.	4.5
	Rail Type	SSTR
Studs	No. of Studs per row	4
	Length, in.	7
	Diameter, in.	0.875
Interior Intermediate Diaphragm	Top Angle	L 5 x 3 ½ x 1/2
	Diagonal Angles	L 5 x 3 ½ x 1/2
	Stiffeners	11/16" x 7 1/2"
Exterior Erection Diaphragm	Top Shape	WT 7 x 21.5
	Bottom Shape	WT 7 x 21.5
	Diagonal Angles	L 5 x 3 ½ x 1/2
Interior End Diaphragm	Solid Plate	1"
	Top Plate	1" x 20"
	Stiffeners	1" x 16"
Exterior End Diaphragm	Solid Plate	1"
	Top Plate	1" x 16"
	Stiffeners	1" x 16"

Note: Typical exterior, interior, and end diaphragms are listed. See Appendix A for other types.

Table 4.32. Geometric Details of Steel Tub Girders for Bridge 15.

Location ft	Top Flange		Web		Bottom Flange	
	Width in.	Thickness in.	Width in.	Thickness in.	Width in.	Thickness in.
0–126	24	1.25	84	0.6875	53.5	1.250
126–147	24	1.50	84	0.6875	53.5	1.750
147–168	24	1.75	84	0.6875	53.5	2.000
168–189	24	2.25	84	0.6875	53.5	2.250
189–210	24	2.25	84	0.6875	53.5	2.250
210–231	24	2.50	84	0.6875	53.5	2.500
231–252	24	1.75	84	0.6875	53.5	2.000
252–284	24	1.25	84	0.6875	53.5	1.250
284–410	24	1.50	84	0.6875	53.5	1.750
410–422	24	1.25	84	0.6875	53.5	1.250
442–463	24	1.75	84	0.6875	53.5	2.000
463–484	24	2.25	84	0.6875	53.5	2.250
484–505	24	2.50	84	0.6875	53.5	2.500
505–526	24	2.25	84	0.6875	53.5	2.250
526–547	24	1.75	84	0.6875	53.5	2.000
547–568	24	1.50	84	0.6875	53.5	1.75
568–698	24	1.25	84	0.6875	53.5	1.25

A nonlinear 3D FEM model of Bridge 14 was created for the entire bridge length using the material properties that are provided in structural drawings. Figure 4.69 show the deflection profiles for Span 1 and Span 3 of Bridge 15 when simulated with a full-depth fracture in the outside girder of the corresponding span and the HL-93 vehicular load at a critical flexural position on the same span and Figure 4.70 presents the load versus displacement and deck rotation plots for the exterior spans of Bridge 15. The behavior of both spans was simulated under the same loading conditions for fractured and nonfractured conditions.

Figure 4.71 show the deflection profiles for Span 2 of Bridge 15 when simulated with a full-depth fracture in the outside girder of the corresponding span and the HL-93 vehicular load at a critical flexural position on the same span and Figure 4.72 presents the load versus displacement and deck rotation plots for the interior span of Bridge 15.

The exterior spans have the same lengths and therefore achieved the same overstrength factor of 1.7, which is 37 percent lower than the simulation of the same spans without a fracture. The 295 ft long interior span obtained a 1.4 overstrength factor when simulated with a fracture in the outside girder. The interior span length is 50 percent longer than the exterior spans and achieved 18 percent lower overstrength factor.

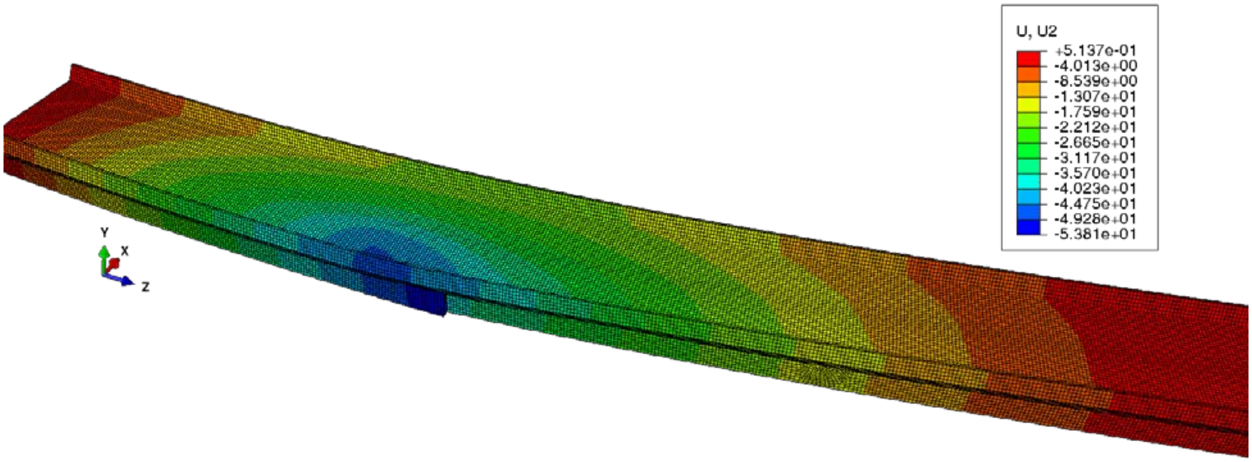

Figure 4.69. FEM Deflection Profile of Bridge 15, Span 1, with Fractured Outside Girder.

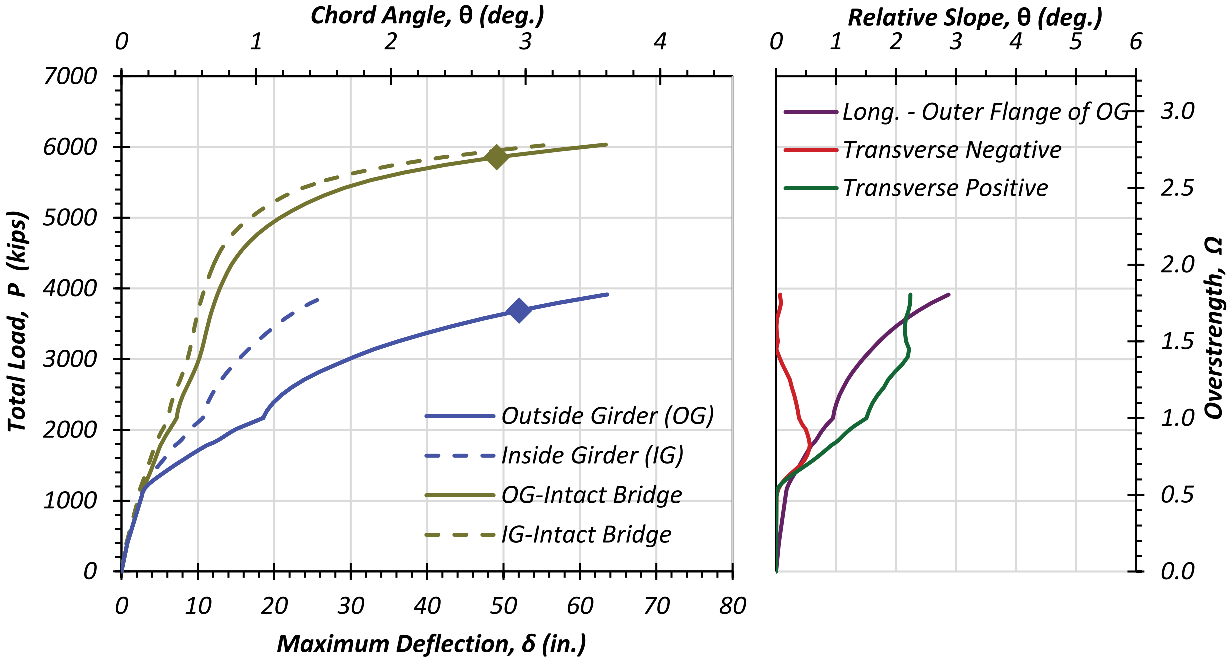

(a) Load displacement *(b) Deck rotations*

Note: δ is along the centerline of the outside girder, Ω is the load normalized by factored design load.

Figure 4.70. FEM Results for Bridge 15, Span 1.

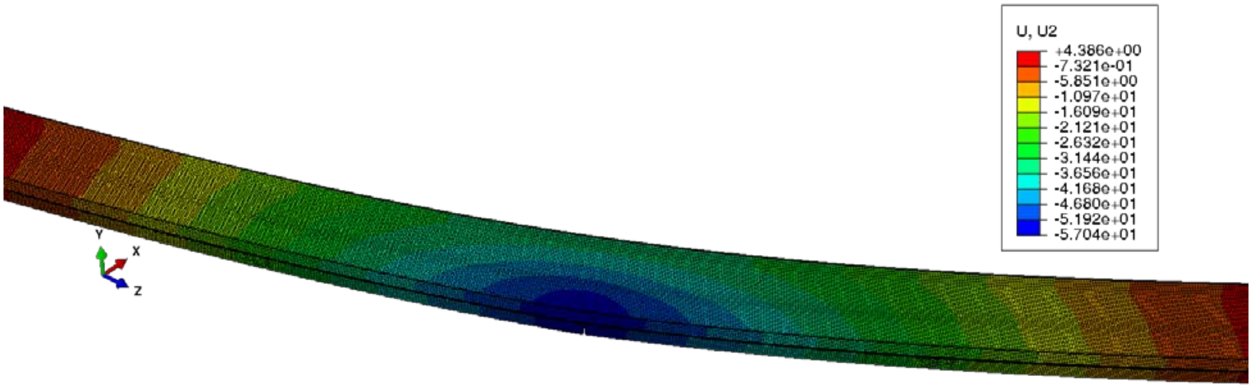

Figure 4.71. FEM Deflection Profile of Bridge 15, Span 2, with Fractured Outside Girder.

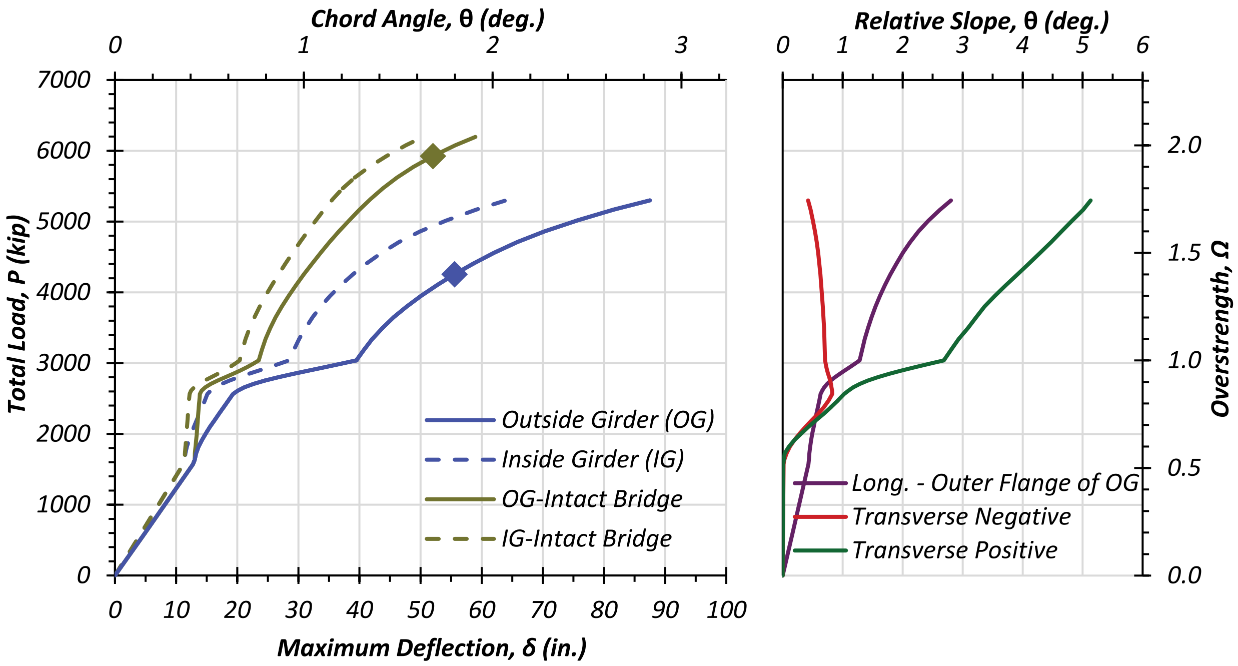

(a) Load displacement *(b) Deck rotations*

Note: δ is along the centerline of the outside girder, Ω is the load normalized by factored design load.

Figure 4.72. FEM Results for Bridge 15, Span 2.

4.5 CONCLUSIONS

The current chapter involved identifying 15 typical STTG Bridges from the Texas bridge inventory and evaluating the selected bridges in terms of their redundancy using FEM analysis and simulating the fractured condition under an HL-93 design vehicular load. All 15 selected STTG bridges were modeled in Abaqus following the same modeling procedures as the one used for verification of the FSEL test bridge. Table 4.33, Table 4.34, and Table 4.35 provide a brief summary of bridge geometries and FEM results for single-span bridges, exterior spans of continuous bridges, and interior spans of continuous bridges. The results presented include overstrength factors corresponding to the ultimate limit state (5 percent residual stiffness) and deflection limit states (longitudinal chord rotation and transverse deck rotation) for fractured STTG bridges. Based on the evaluation of FEM overstrength predictions, the following conclusions were drawn.

- Simple-span bridges generally obtain relatively low overstrength factors compared to continuous spans when simulated with a full-depth fracture at the mid-span of the outside girder. The overstrength factors (load normalized by factored design load) of modeled simple-span bridges range from 0.82 to 1.65 for fractured conditions although they can achieve 2.3 to 3.6 overstrength factors when both girders are intact. There is an average 37 percent reduction in ultimate load capacity when a fracture is induced in the outside girder.
- The overstrength factors of exterior spans (both spans of two-span bridges and exterior spans of three-span bridges) range between 1.0 and 1.8 when the outside girder of the simulated span has a full-depth fracture mid-span of the outside girder. (There is only one span with an 0.9 overstrength factor, which is the longest exterior span length of 295 ft). The average reduction in ultimate load carrying capacity due to the fracture of the outside girder is about 40 percent for the exterior spans of continuous bridges.
- The estimated overstrength factors of interior spans of three-span continuous bridges were the highest compared to exterior spans and simple spans. This effect can best be observed by comparing the exterior spans and interior span of the same three-span bridge. The interior spans of bridges 9, 10, 12, and 13 are 20 to 40 percent longer than their exterior spans. Despite the increase in the span length, the interior spans of these five 3-span continuous bridges have higher overstrength factors for both fractured and nonfractured analysis. The overstrength factors of interior spans of three-span continuous bridges ranges from 1.2 to 2.45 for fractured bridges, while it ranges from 1.9 to 3.4 for intact bridges. The average reduction in the ultimate load carrying

capacity due to a fracture of the outside girder is about 20 percent for the interior spans of continuous bridges.

- It is evident that structural redundancy due to continuity significantly increases the capacity by allowing load distribution between spans, thereby providing additional redundancy. Redundancy evaluation that only considers load path redundancy in the transverse direction between girders underestimates the overstrength factor for the continuous bridges.
- It is not possible to evaluate the effect of different parameters by comparing different bridges because multiple parameters vary between different bridges. However, it is possible to evaluate the effect of span length by observing the two different span lengths of the same two-span bridge or two different exterior span lengths of the same three-span bridge. The evaluation of Bridges 7, 9, and 10 indicate that an increase in the span length decreases the overstrength factors.
    - Bridge 7 has 219 ft and 190 ft exterior spans with a 764 ft radius of curvature. A 15 percent increase in the span length resulted in a 17 percent reduction in the overstrength factor for a fractured bridge.
    - Bridge 9 has 140 ft and 126 ft exterior spans with a 764 ft radius of curvature. An 11 percent increase in the span length resulted in only a 6 percent reduction in overstrength factor.
    - Bridge 10 has 190 ft and 148 ft long exterior spans with a 716 ft radius of curvature. A 28 percent increase in the span length resulted in a 15 percent reduction in overstrength factor.

Table 4.33. Overstrength Factors for Single-Span STTG Bridges.

ID	Span	R (ft)	L (ft)	B (ft)	S (ft)	5% SF	5° Trans.	2° Long.
0	1	1300	120	23	6.0	**0.86**	−	0.91
1	1	573	220	32	9.5	0.88	0.82	**0.82**
2	1	1910	115	26	6.1	1.75	1.70	**1.65**
3	1	2207	230	39	12.6	0.88	**0.85**	0.87

Note: L = length, B = breadth, R = radius of curvature, S = spacing between interior top flanges.
− indicates that data is “not available” or “not applicable.”

Table 4.34. Overstrength Factors for Exterior Spans of STTG Bridges.

ID	Span	R (ft)	L (ft)	B (ft)	S (ft)	5% SF	5° Trans.	3° Long.
4	1	195	132	28	7.6	2.00	2.30	**1.65**
4	2	195	128	28	7.6	2.03	−	**1.73**
5	1	450	140	30	9.7	1.50	−	**1.20**
5	2	450	140	30	9.7	1.50	−	**1.20**
6	1	819	140	38	9.8	1.90	2.10	**1.80**
6	2	819	140	38	9.8	1.90	2.10	**1.80**
7	1	764	219	28	7.4	1.40	1.20	**1.20**
7	2	764	190	28	7.4	1.75	−	**1.45**
8	1	882	265	28	8.4	**0.99**	−	**-**
8	2	882	295	28	8.4	**0.88**	−	0.91
9	1	764	140	28	7.4	1.80	2.00	**1.70**
9	3	764	126	28	7.4	1.90	2.15	**1.80**
10	1	716	148	30	7.7	1.70	−	**1.70**
10	3	716	190	30	7.7	1.60	−	**1.45**
11	1	819	223	28	7.0	**1.60**	−	1.70
11	3	819	235	28	7.0	**1.60**		1.65
12	1	225	140	28	7.6	1.90	1.95	**1.60**
12	3	225	145	28	7.6	1.90	1.90	**1.60**
13	1	450	152	30	9.3	1.50	−	**1.00**
13	3	450	152	30	9.3	1.50	−	**1.00**
14	1	1010	150	28	6.5	1.80	−	**1.65**
14	3	1010	150	28	6.5	1.80	−	**1.65**
15	1	809	200	28	8.0	1.80	−	**1.70**
15	3	809	200	28	8.0	1.80	−	**1.70**

Note: L = length, B = breadth, R= radius of curvature, S = spacing between interior top flanges.
− indicates that data is “not available” or “not applicable.”

Table 4.35. Overstrength Factors for Interior Spans of STTG Bridges.

ID	**Span**	**R (ft)**	**L (ft)**	**B (ft)**	**S (ft)**	**5% SF**	**5° Trans.**	**2° Long.**
9	2	764	151	28	7.0	**2.45**	2.55	2.50
10	2	716	265	30	7.7	2.05	1.60	**1.45**
11	2	819	366	28	7.0	2.45	**1.20**	1.55
12	2	225	180	28	7.6	2.10	2.05	**1.80**
13	2	450	190	30	9.3	1.75	−	**1.40**
14	2	1010	190	28	6.5	2.00	−	**1.80**
15	2	809	295	28	8.0	**1.40**	1.70	1.50

Note: L = length, B = breadth, R = radius of curvature, S = spacing between interior top flanges.
− indicates that data is “not available” or “not applicable.”

5 YIELD LINE ANALYSIS OF STEEL TWIN TUB GIRDER BRIDGES

This chapter gives a detailed explanation of the background, methodology and analysis used for implementing the yield line theory as an alternative analytical tool for assessing the overstrength factor of bridges. The chapter begins with an overview of the plastic analyses, which pertained to the yield line theory. The study for developing a yield line pattern based on specific bridge geometry and loading conditions is documented, as is validation of the solution with the experimental data. The implementation of the aforementioned techniques was extended to the wheel loading, and failure mechanisms were accordingly established. The specifications and results for each bridge are listed in the subsequent sections. The overstrength factors are summarized, and the reserve capacity of the selected bridges is examined based on the results.

5.1 INTRODUCTION

This chapter presents the results of the analysis of 15 typical STTG bridges selected from the Texas bridge inventory. The basis of the selection was discussed in detail in Chapter 4. The primary goal of yield line analysis is to validate the results from the static load test conducted experimentally during a previous TxDOT research project (Barnard et al. 2010). The full-scale testing of a typical STTG bridge was conducted as part of TxDOT Research Project 9-5498, and the experimental static ultimate load capacity of the bridge was reported. In the present task, the yield line analysis of the same bridge was undertaken to validate the failure mechanism with the experimental results. The failure mechanism of the bridge was studied in detail to analyze the load path when the exterior girder is fractured along the depth of its webs and its bottom flange. The problem was evaluated in light of various conditions, such as reduction in capacity due to the fracture of the outer girder, the contribution of the stud failure on the overall load carrying capacity, the capacity of the deck slab, and the impact of the external loads applied. The mechanism was further postulated to assess the behavior under live loads when the outside girder is fully fractured. The analysis procedures and results are discussed in the following sections.

5.2 YIELD LINE THEORY

The governing equation for the yield line analysis establishes the overstrength factor as follows in Equation (5.1):

$$\Omega EWD = IWD \tag{5.1}$$

where EWD = external work done by the factored loads based on 1.25DL + 1.75(LL + IM); IWD = internal work done on the yield lines in the deck, work done by plastic moments in the steel tub flanges (of the fractured girder), and work done by the pullout of shear studs between the tub flanges and reinforced concrete deck slab; and Ω is an overstrength factor necessary to give equivalence with IWD.

5.2.1 Internal Work Done

The internal work done due to the deck, flanges of the fractured girder, exterior guardrail, and the studs can be computed as the following in Equation (5.2):

$$IWD = \sum m_x \theta_x y + \sum m_y \theta_y x + \sum W_{\text{stud}} \delta_{\text{stud}} \tag{5.2}$$

where $\sum m_x \theta_x y$ = the summation of the internal work done due to the moment capacity of the deck in the longitudinal direction, the internal work done due to the guardrail, and the internal work done due to the fractured girder; $\sum m_y \theta_y x$ = the internal work done due to the moment capacity of the deck in the transverse direction; $\sum W_{\text{stud}} \delta_{\text{stud}}$ = the internal work done due to the studs; m_x and m_y = the longitudinal and the transverse moment capacity, respectively; θ_x and θ_y = the angular deflection of the plane segments of the deck slab along the longitudinal and transverse directions, respectively; y and x = the distances along which the moment capacities act in the longitudinal and transverse directions, respectively; W_{stud} = the internal work done by the group of studs connecting the deck slab and the twin tub girders; and δ_{stud} = the deflection of the center of gravity of that length along which the girder flanges are assumed to separate from the deck slab according to the geometry of the mechanism selected.

5.2.2 External Work Done

The loading that was applied in the experimental study of the bridge at the Ferguson Structural Engineering Laboratory, University of Texas at Austin, has been recreated in terms of distributed loads. The girders forming the boundary enclosure for the sand are termed as “sand bin," and the applied sand load increasingly added until failure of the bridge takes place has been modeled as accurately as possible from the data available. The applied sand load is known to exert a load of 363 kip from the experimental results.

The external work done due to the self-weight of each component, such as the deck slab, the fractured girder, and guardrail has been computed. The work done due to the sand bin girders and the sand has been computed using Equation (5.3):

$$EWD = \sum w_{\mathrm{d}} A_{\mathrm{d}} \delta_{\mathrm{d}} + \sum w_{\mathrm{load}} A_{\mathrm{load}} \delta_{\mathrm{load}} \tag{5.3}$$

in which $\sum w_{\mathrm{d}} A_{\mathrm{d}} \delta_{\mathrm{d}}$ = the total external work done due to the self-weight of the bridge components and $\sum w_{\mathrm{load}} A_{\mathrm{load}} \delta_{\mathrm{load}}$ = the total external work done due to the externally applied load of the sand bin girders and the sand; where w_{d} = the self-weight of the structure components expressed as an area load; A_{d} = the area of the respective components whose self-weight is w_{d}; δ_{d} = the deflection of the center of gravity of the region whose area is A_{d}; w_{load} = the external load applied due to the sand bin girders and the sand, expressed as an area load; A_{load} = the area of the applied load; and δ_{load} = deflection of the center of gravity of the region whose area is A_{load}.

Equations (5.2) and (5.3) are obtained in terms of the deflection (δ) that occurs at the location of maximum sagging. The principle of virtual work facilitates the computation of the load of sand needed to be added to reach the collapse of the bridge by equating Equations (5.2) and (5.3).

5.3 VALIDATION OF YIELD LINE ANALYSIS WITH EXPERIMENTAL RESULTS

This section gives a detailed analysis of the experimentally tested STTG bridge, which formerly was a single-lane, high-occupancy-vehicle (HOV) flyover exit-ramp of the interchange between IH 10 and Loop 610 in Houston, Texas. The yield line analysis was validated using the experimental results from the TxDOT Research Project 9-5498.

5.3.1 General Overview of Collapse Mechanism

An upper-bound yield line or plastic analysis solution may lead to a sufficient and economical treatment to address the reserve strength of bridges. A general treatise of plastic and yield line methods may be found in (Park and Gamble 2000). Plastic methods aim to identify the inherent reserve capacity of the structure that will be higher than the strength calculated from an elastic analysis. Elastic analysis is only able to identify the loads necessary to achieve first yield, whereas plastic methods provide the limit load that leads to a collapse mechanism. This rigid-plastic solution utilizes the equations of equilibrium or the virtual work equations; the former are generally used for lower-bound strip methods, whereas the latter are used for upper-bound solutions. The assumed virtual deflection eventually gets eliminated from the solution equations, thereby producing a single equation in terms of the collapse load. This solution provides the mechanism by which yield lines and plastic hinges form and significant plastic deformation occurs. Such a plastic analysis approach provides a rapid procedure in contrast with computational solutions like the FEM solutions since plastic methods are essentially hand-calculation methods. The success of the upper-bound plastic solutions, however, rests largely on identifying the correct yield line pattern forming the collapse mechanism.

5.3.2 Potential Collapse Mechanisms for the Experimental Bridge

Various yield line collapse mechanisms may be postulated, and the collapse load is determined using either a virtual work or an equilibrium analysis. The correct mechanism provides the minimum collapse load. The most admissible mechanism is identified from the various possibilities such that the boundary conditions of the bridge and the deck slab are suitably modeled. The loading of the bridge influences the formation of the yield line pattern. The concrete beams that form a rectangular bin at the mid-span along the outer edge of the bridge are formed to pour the sand in the critical region above the fractured girder. The barrier dimensions impact the crack formation and the governing mechanism due to the added stiffness from the concrete girders.

Consider the experimental twin tub bridge span tested at the University of Texas (Barnard et al. 2010; Neuman 2009). Figure 5.1 illustrates the few possible failure mechanisms that may occur due to the sand loading described in Neuman (2009) when the bending of the deck slab is on the longitudinal axis passing through the girder of the sand bin positioned at the nonfractured girder's interior flange. The different variables assigned for the dimensions of the bridge are needed for the computation of the load. The transverse dimensions are represented with b_e, b_g, b_s, b_r, and b'_y. The variables b_e, b_g, and b_s represent the width of the edge from the outer flange of the fractured girder, the overall width of each twin tub girder, and the spacing between interior flanges of the outer and inner girders, respectively; b_r = width assumed for the railing, and b'_y = the transverse distance from the outer edge of the bridge at which the horizontal yield line lies. The longitudinal dimensions are represented with X_x, a_e, a_s and a_b. X_x, a_e, a_s and a_b denote the distance of the point of intersection of the negative inclined yield line and the axis along the outer edge of the bridge from the mid-span, the length of half-span, the length of half of the negative horizontal yield line, and the length of half of the sand bin, respectively (Neuman 2009).

Solutions are presented for the variations of collapsed loads with the yield line geometry for different mechanisms and compared in Figure 5.1(a) (*Yield Line Mechanism [YLM] 1*). The graph shows the variation of the ultimate collapse load as the dimension of half of the horizontal negative yield line, a_s, varies from 0 ft to 60 ft. Figure 5.1(a) gives the overall minimum solution although it is eliminated as inadmissible because the girder is required to twist significantly, and this twist cannot be achieved unless the girder yields plastically. Figure 5.1(b) (*YLM 2*) assumes the girder is seated at the center of the tub. This feature was not strictly the case in the tests, so it is eliminated. Figure 5.1(c) (*YLM3*) assumes the fractured girder is seated over its entire width. Displacement compatibility along the length of the girder is violated, requiring some of the shear studs to pull out. Indeed, this was the case in the reported tests, and accordingly this work has been incorporated into the analysis.

Similarly, *YLM 4,* shown in Figure 5.1(d), requires stud pullout, but it should be noted that none of the *YLM 4* solutions in Figure 5.2(a) are critical, which leaves mechanism *YLM3* as the remaining viable mechanism. Among the various mechanisms, the case where the negative yield line passes through the exterior flange of the fractured outside girder is found to be the minimum. For this critical case, two of the values of a_s were short-listed such that the solutions resulting from these values encompass all possible mechanisms. Figure 5.2(b) illustrates the critical mechanism, with the loading for key a_s values indicated by red circles and pictorially represented in Figure 5.3(a), (b), (c), and (d), respectively.

Figure 5.3(a) and (b) illustrate two of the key mechanisms that form the extremities of the possible a_s values for *YLM3*. The parts (c) and (d) illustrate an intermediate case for a_s and a limiting case of X_x, which denotes the distance from mid-span to the location where diagonal negative yield lines intersect the point where the elevations meet at the zero-deflection datum. It is essential to carefully judge the admissibility of each mechanism in accordance with the boundary conditions and with the rules governing deformation compatibility. Several admissible collapse mechanisms were postulated in the given research. Since this is an upper-bound solution, the veracity of the critical collapse load must be thoroughly checked. Solution (b) shown in Figure 5.2(b), where a_s = 20 ft, which is the half-length of the stiff barrier at the back of the sand heap, was adopted because it constrained the mechanism shown in Figure 5.3(b).

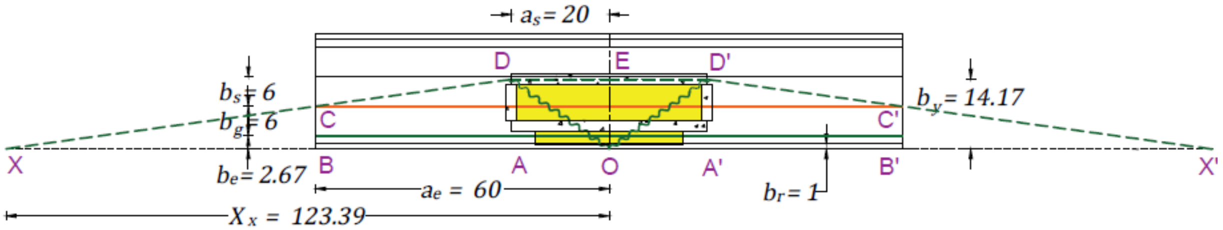

(a) YLM-1, Negative YL through interior flange of OG, Ultimate Collapse Load = 233 kip

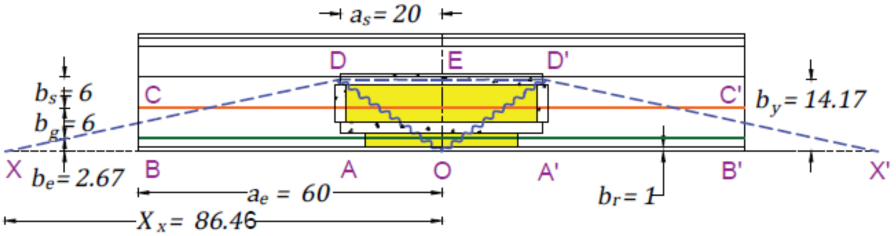

(b) YLM-2, Negative YL through mid-width of OG, Ultimate Collapse Load = 297 kip

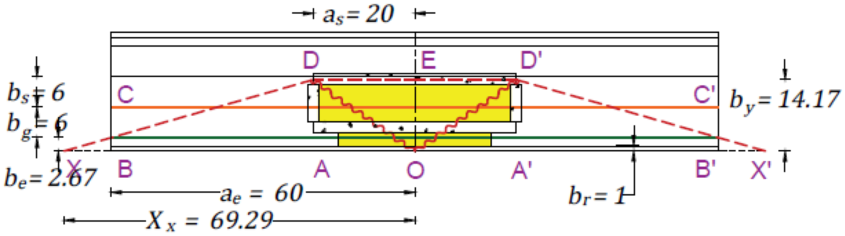

(c) YLM-3, Negative YL through exterior flange of OG, Ultimate Collapse Load = 353 kip

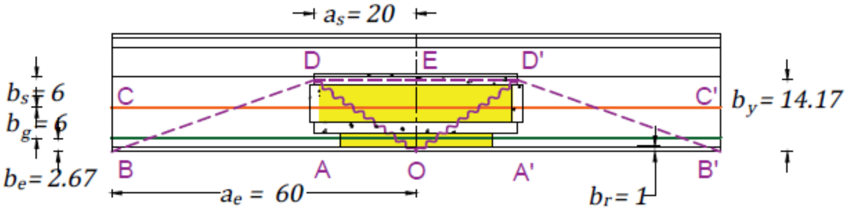

(d) YLM-4, Negative YL through edge of OG, Ultimate Collapse Load = 400 kip

Note: YLM = yield line mechanism; YL = yield lines; OG = outside girder.
The colors distinguish different locations through which diagonal negative YL pass:
Green: passing through interior flange of OG; Blue: passing through mid-width of OG;
Red: passing through exterior flange of OG; Purple: passing through mid-width of OG.

Figure 5.1. Different Probable Yield Line Mechanisms to Study the Model that Best Represents Collapse Mechanism Taking Place in Experimental Sand Loading Test.

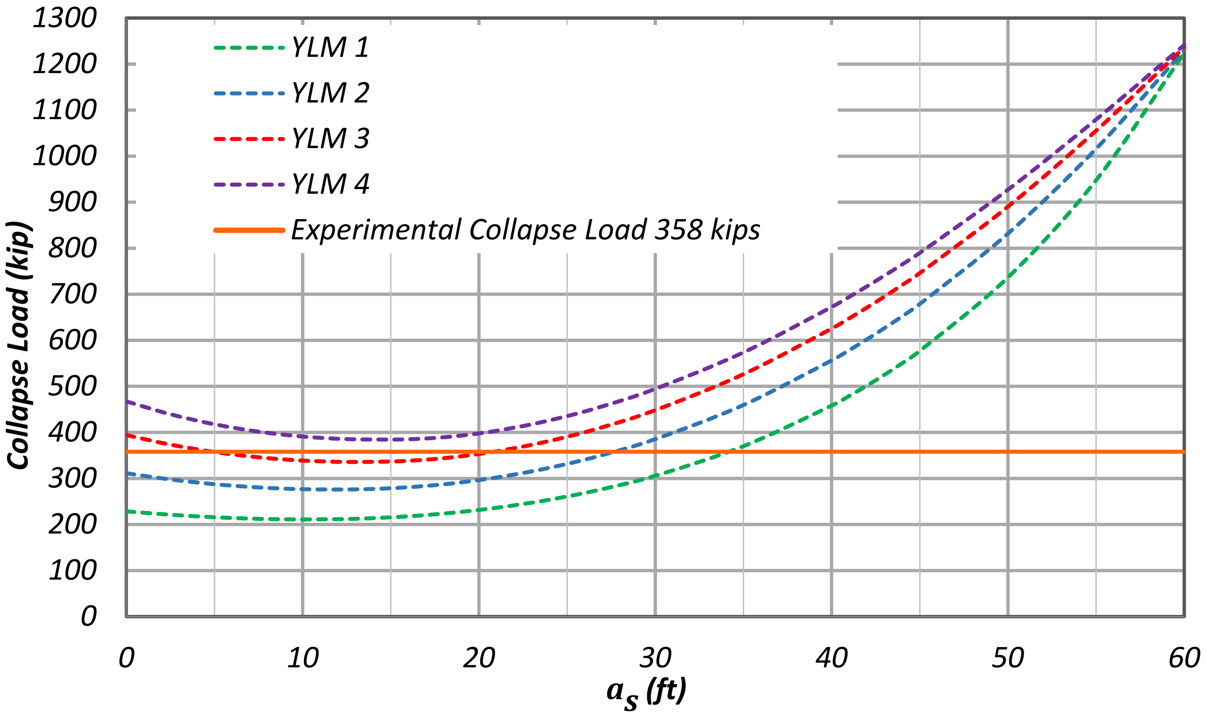

(a) Mechanisms 1 to 4, to be read in conjunction with Figure 5.1

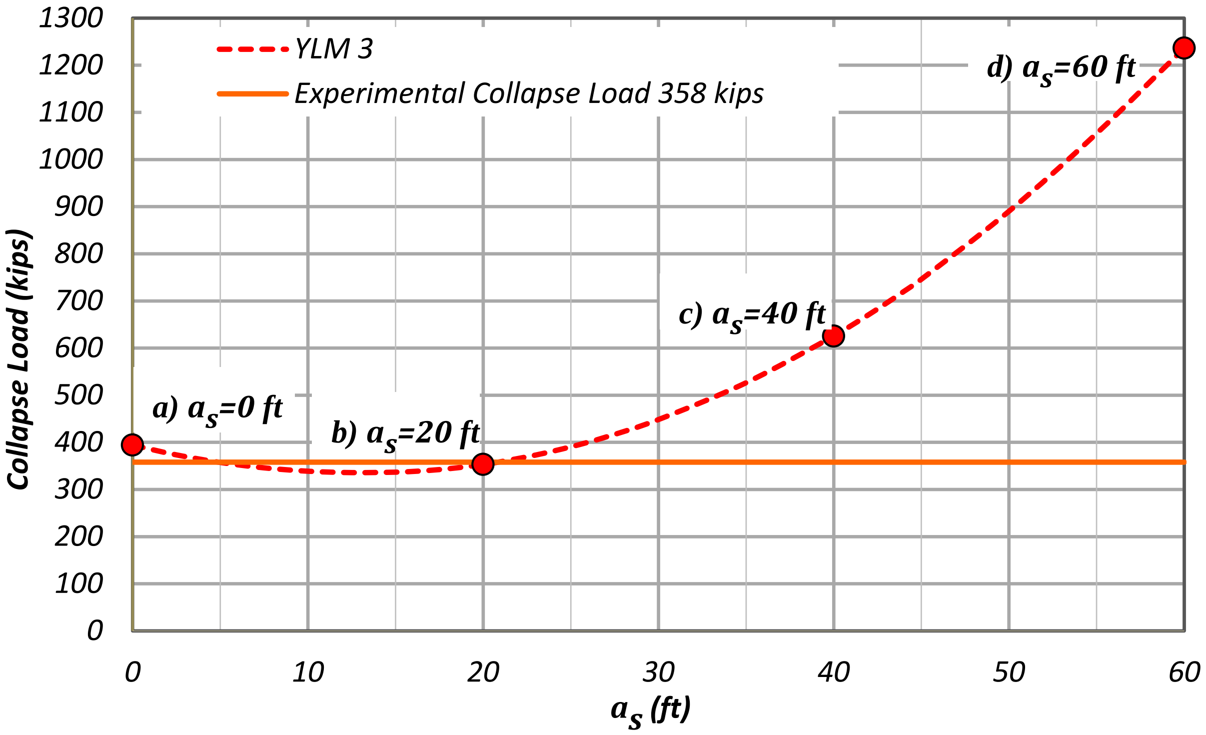

(b) Mechanism 3 showing the different solutions given in Figure 5.3

Figure 5.2. Minimization Curves of Ultimate Static Load Generated for Sand Load on TxDOT Research Project 9-5498.

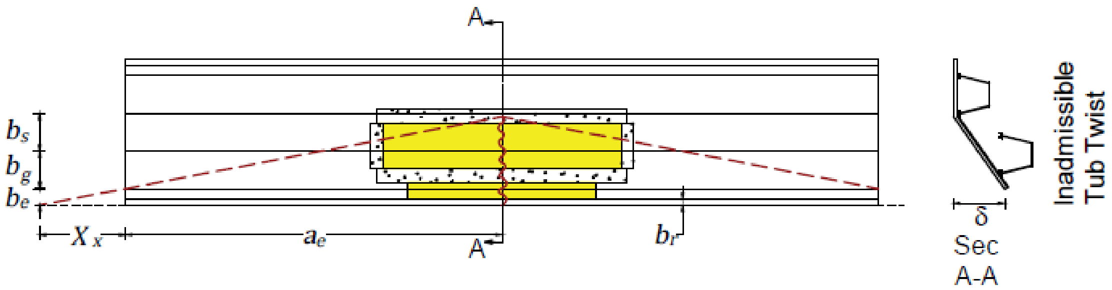

(a) Limiting case with $a_s = 0$ ft

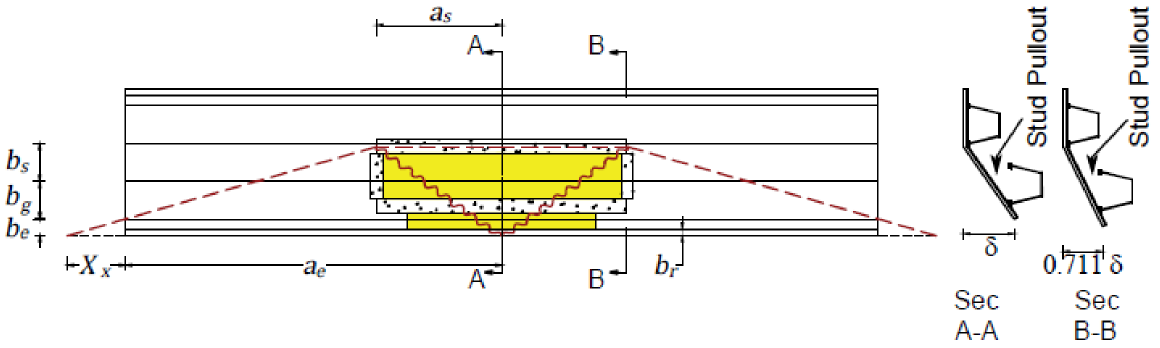

(b) Sand Bin constraint on a_s

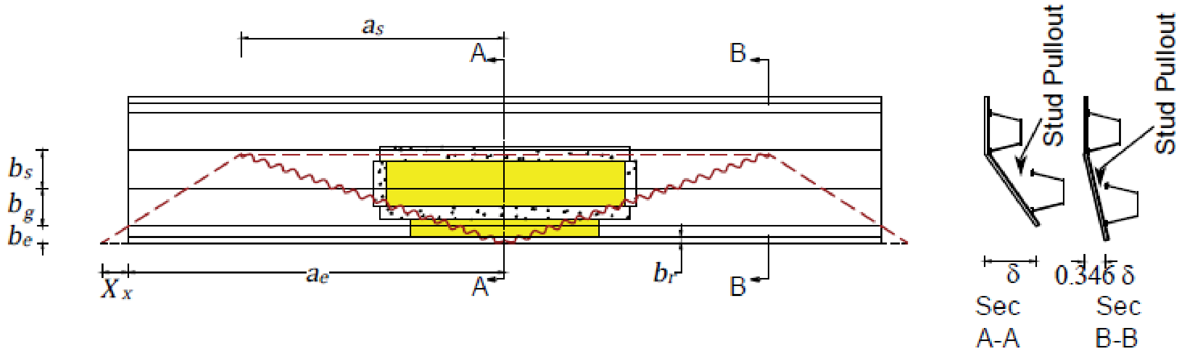

(c) Intermediate case encompassing all admissible values of a_s

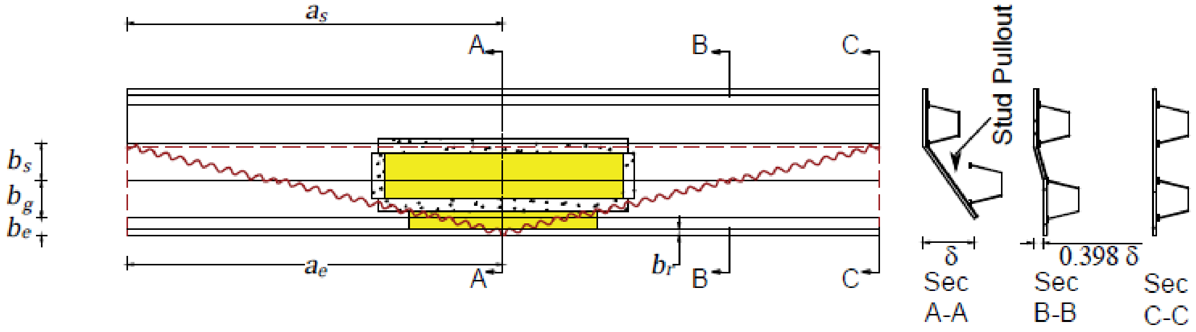

(d) Limiting case with a_s running along the span length

Figure 5.3. Probable Mechanisms Postulated.

5.3.3 Bridge Specifications and Details

This section describes the properties of the experimental test bridge under consideration used for the validation of the plastic limit analysis. Prior to the testing, this span was part of a single-lane, HOV flyover exit-ramp of the interchange between IH 10 and Loop 610 in Houston, Texas.

5.3.3.1 Material Properties

The deck slab was uniformly reinforced in each direction. The average cylindrical compressive strength of concrete in the deck slab was 6.26 ksi, and that in the exterior guardrail was also 6.26 ksi. The reinforcement in the longitudinal direction of the deck slab was provided with #4 bars at 9 in. on-center spacing with a nominal yield strength of 60 ksi at the top and #5 bars at 6 in. on-center spacing with a nominal yield strength of 68 ksi at the bottom. The reinforcement in the transverse direction of the deck slab was provided with #5 bars at 6 in. on-center spacing with a nominal yield strength of 68 ksi at top and bottom. The nominal yield strength of the steel twin tub girders was 50 ksi. The modulus of elasticity of the steel is taken as 29000 ksi Neuman (2009).

5.3.3.2 Bridge Properties

The bridge deck was 120 ft long, 23.22 ft wide, and 8 in. thick. Figure 5.4(a), (b), and (c) present the dimensions of the steel tub girder, the shear stud connection detail, and the guardrails, respectively. The web of the girder was 57 in. deep and 0.5 in. thick. The flanges were 12 in. wide and 0.625 in. thick, spaced at 6 ft on-center. The bottom flange steel plate was 47 in. wide and 0.75 in. thick. A 3 in. haunch was provided between the reinforced concrete deck, and the deck was flanked by T501 guardrails on both sides longitudinally Neuman (2009).

5.3.3.3 Member Capacity

The internal work done computations are based upon the moment capacities of the various member components engaged in the failure mechanism of the bridge, such as the transverse and longitudinal deck-slab sections of unit foot width, the guardrail, and the flanges.

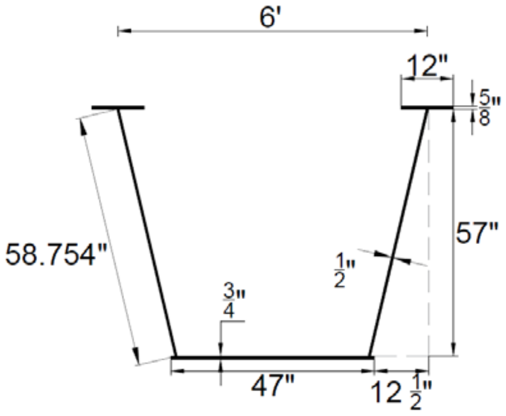

(a) Dimensions of steel tub girder

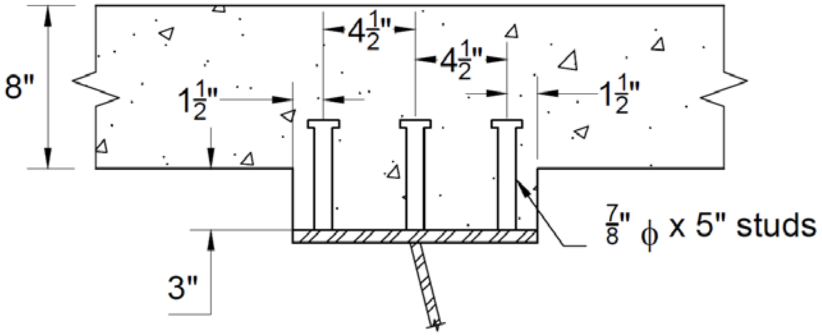

(b) Shear stud connection detail

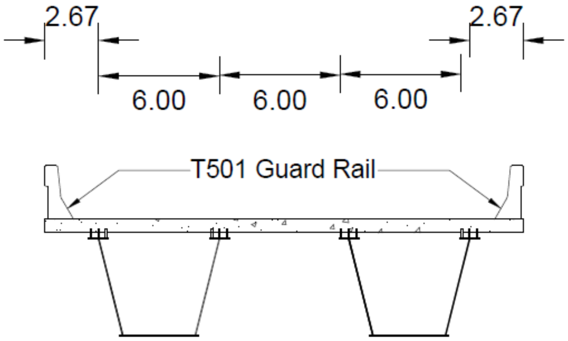

(c) Cross-section showing T501 guardrails

Figure 5.4. Bridge Properties.

These capacities are obtained using the standard U.S. code-based ultimate strength (Mn), using the yield strengths of steel and the characteristic strength of concrete as specified. These computations do not consider the effects of strain hardening. The flexural capacity of the railing was calculated by considering it as a regular doubly reinforced beam. The moment capacity of the flanges at the fractured section at mid-span was computed such that the compressive strength due to deck slab was not double counted.

The positive longitudinal moment capacity of the deck slab was m_x =16.18 k-in./in.; the negative longitudinal moment capacity per unit width of the deck slab was m'_x =10.69 k-in./in.; the positive transverse moment capacity per unit width of the deck slab was m_y =24.88 k-in./in.; and the negative transverse moment capacity per unit width of the deck slab was m'_y = 19.81 k-in./in. The moment capacity of the flanges of the fractured girder was M_f= 598 k-ft, and the moment capacity due to the T501 guardrail was M_{rail}= 485 k-ft. The pullout capacity of the shear studs was found to be 16 kip following the methods specified in ACI-318 (2017) and modified as per the recommendations from the experimental research conducted by Sutton (2007) and Mouras et al. (2008).

5.3.4 Ultimate Collapse Load

Figure 5.5 illustrates the yield line mechanism chosen for the sand loading. The negative yield lines follow a trapezoidal shape due to spreading of the sand load over the deck slab. This pattern is corroborated well by the crack lines observed during the experimental testing for TxDOT Research Project 9-5498. The loading was recreated for the manual analysis of the experimental bridge using yield line theory. The sand loading was modeled to capture the effects on deck slab as accurately as possible by accounting for the geometry in which the sand was accumulated around and inside the concrete girders forming the periphery. The load primarily affects the mid-span since it was concentrated within the sand bin area. To account for this sagging behavior, the positive yield lines (represented by the wiggly lines), form a V-shape at the mid-span region.

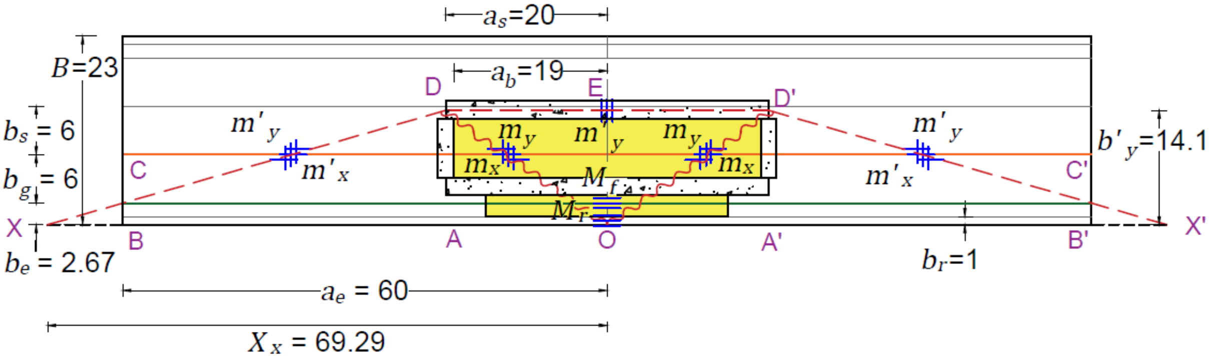

(a) Plan view of the bridge with the postulated yield line mechanism under experimental sand loading

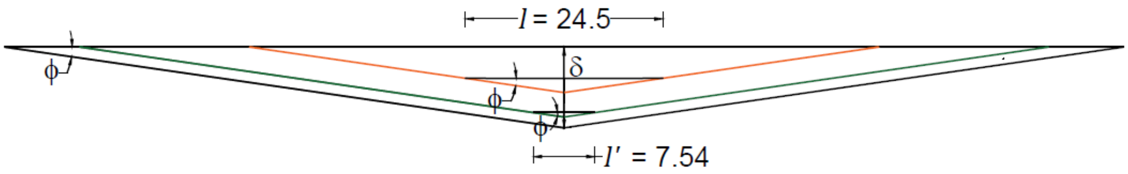

(b)Profile with angular deflections and assumed separation of the deck and flanges of outside girder (OG)

Figure 5.5. Critical Mechanism with the Inclined Negative Yield Lines Passing through Exterior Flange of the Outside Girder at the Supports.

The minimization trials conducted as mentioned in Section 5.3.2. resulted in the optimal mechanism in which the diagonal negative yield lines passes through the outer flange of the fractured outside girder before it terminates at the point where the elevations meet at the zero-deflection datum, located at a certain distance X_x on either side of the mid-span.The ultimate collapse load computation consists of the internal and external work done calculations.

The internal work done due to the slab (that has been divided into segments), the rail along the outer edge of the bridge, and the fractured outside girder are tabulated in Table 5.1. The internal work done due to the studs can be computed based on the assumption that the work is done due to the separation of the deck slab along the two flanges of the outside fractured girder following a constant angular deflection, ϕ, that can be expressed in terms of the deflection, δ as follows in Equation (5.4):

$$\phi = \frac{\delta}{X_x} \tag{5.4}$$

The design concrete breakout strength of the stud group N_{cbg} is computed to be 16 kip. The length of separation of the deck along the interior and exterior flanges of the outside fractured girder are denoted by l and l', respectively. The average separation between the deck slab and the interior and exterior flanges of the outside fractured girder are represented as δ_l and $\delta_{l'}$, given by Equations (5.5) and (5.6).

$$\delta_l = 0.5\frac{l}{2}\phi \tag{5.5}$$

$$\delta_{l'} = 0.5\frac{l'}{2}\phi \tag{5.6}$$

The stud spacing is denoted by $s_{stud}$and is considered in ft. The internal work done due to studs is given by Equation (5.7):

$$IWD_{stud} = N_{cbg}s_{stud}(\delta_l l + \delta_{l'}\, l') \tag{5.7}$$

The external virtual work done by the deck slab, the girder, the guardrail, the girders forming the concrete bin girders, and the applied sand load can be expressed in Equation (5.8) as:

$$EWD = w_d A_d \delta_d + W_g \delta_g + W_r \delta_r + W_{cbg}\delta_{cbg} + w_s A_s \delta_s \tag{5.8}$$

where w_d = weight of deck slab per unit area; W_g = weight force of the fractured outside girder; W_r = weight force of the outer rail; W_{cbg} = weight force of the concrete bin girders; w_s = weight of sand load per unit area; A_d = area of the deck slab that undergoes deflection for the assumed yield line mechanism; A_s = area of the region in which the sand is poured; δ_d = deflection of the center of gravity of the area A_d; δ_g = deflection of the center of gravity of the fractured outside girder; δ_r = deflection of the center of gravity of the outer rail; δ_{cbg} = deflection of the center of gravity of the concrete bin girders; and δ_s = deflection of the center of gravity of the area A_s.

The sand load, w_s, is the unknown that can be solved by equating the internal work done and the external work done. Using the critical mechanism from the minimization curves and applying the concepts discussed in Section 5.3, the ultimate collapse load is computed to be 353 kip. This compares well with the experimental collapse load of 363 kip. It is to be noted that the experimental value reported includes the total weight of the sand poured. However, for this analysis, the entire sand does not contribute to the work done in causing virtual deflection because some of the sand that is spilled out of the deflecting region of the deck slab does no work for the assumed yield line mechanism.

Deducting that volume of the sand load from the reported collapse load, the failure load is calculated as 358 kip. The analytical yield line result of W_{yield} = 353 kip is quite close to the experimental outcome of W_{yield} = 353 kip. The overall concept of the plastic yield line mechanism analysis is thus considered validated. The yield solution is expected to be an upper-bound solution, as suggested by (Park and Gamble 2000). However, the exception to this solution is that when deflections are extremely large and tensile, membrane forces may arise from a catenary action. For such action, the rigid-plastic theory adopted herein breaks down Pirayeh Gar et al. (2014).

Table 5.1. Internal Work Done Due to Deck Slab, Fractured Outside Girder, and Rail.

Segment	Angular Deflection		Internal Work Done	
	$\boldsymbol{\theta_x}$	$\boldsymbol{\theta_y}$	$(\boldsymbol{m_x})(\boldsymbol{\theta_x})(\boldsymbol{y})$	$(\boldsymbol{m_y})(\boldsymbol{\theta_y})(\boldsymbol{x})$
OABCD, OA'B'C'D'	$\frac{\delta}{X_x}$	$\frac{\delta}{b'_y} - \frac{a_s}{b'_y(Xx)}\delta$	$2\begin{Bmatrix}(m'_x)\left(\frac{\delta}{X_x}\right)(b'_y - b_e) \\ +(m_x)\left(\frac{\delta}{X_x}\right)(b'_y)\end{Bmatrix}$	$2\begin{Bmatrix}(m'_y)\left(\frac{\delta}{b'_y} - \frac{a_s}{b'_y X_x}\delta\right)(a_e - a_s) \\ +(m_y)\left(\frac{a_s}{b'_y X_x}\delta\right)(a_s)\end{Bmatrix}$
DOE, D'OE	0	$\frac{\delta}{b'_y}$	0	$2\left\{(m'_y)\left(\frac{\delta}{b'_y}\right)(a_s)\right\}$
Rail	$\frac{\delta}{X_x}$	0	$2\,M_r\frac{\delta}{X_x}$	0
Girder	$\frac{\delta}{X_x}$	0	$2M_f\frac{\delta}{X_x}$	0
Total Internal Work Done			$2\begin{Bmatrix}(m'_x)\left(\frac{\delta}{X_x}\right)(b'_y - b_e) \\ +(m_x)\left(\frac{\delta}{X_x}\right)(b'_y)\end{Bmatrix}+$ $2\left(\frac{\delta}{X_x}\right)(M_r + M_f)$	$2\begin{Bmatrix}(m'_y)\left(\frac{\delta}{b'_y} - \frac{a_s}{b'_y X_x}\delta\right)(a_e - a_s) \\ +(m_y)\left(\frac{a_s}{b'_y X_x}\delta\right)(a_s)\end{Bmatrix}+$ $2\left\{(m'_y)\left(\frac{\delta}{b'_y}\right)(a_s)\right\}$

5.4 GENERAL THEORY FOR FRACTURE CRITICAL SECTIONS

This section presents the theory behind postulated collapse mechanisms using the method of virtual work. A derivation is given for a critical folded plate yield-line mechanism that is representative of expected limit behavior in a certain class of bridge deck systems. General equations are then derived for the overstrength factor of fracture critical bridges.

5.4.1 Virtual Work Equations

Bridge decks supported by fracture critical girders are analyzed by yield-line theory using the equations of virtual work. In the upper-bound method of plastic collapse mechanism analysis, any kinematically admissible mechanism may be postulated. The mechanism with the lowest collapse load is then the theoretically correct mechanism.

Figure 5.6 presents a folded plate mechanism with N yield lines zigzagging between the unfractured and fractured girders, where N is an unknown number of diagonal yield lines but determined by a load minimization procedure. The degree of an equivalent distributed load that may be placed over the fractured girder, W_e, and its magnitude is found via a virtual work analysis.

Consider a folded plate mechanism supported on three sides, with the fourth side supported by a torsionally restrained beam with a central hinge, as shown in Figure 5.6(a). Note that negative (hogging) yield lines are dashed, while wiggly solid yield lines are positive (sagging) moments. The long edge with double hatching is fully fixed (clamped against rotation) while the ends are simply supported (free to rotate). The figure also shows the transverse angular deflections along the D-D, E-E, and F-F profiles.

Figure 5.6(b) depicts the side elevation illustrating the deflection profiles along Sections A-A, B-B, and C-C. Figure 5.6(c) and (d) show the geometry of the folded plate mechanisms with deflections, from which the internal work done is derived by considering the half-span of a bridge, as shown. Displacing the fractured girder downward by unit displacement (δ = 1) at mid-span, the external work done is given by Equation (5.9)

$$EWD = W_e L_x \frac{\delta}{2} = 0.5 W_e L_x \tag{5.9}$$

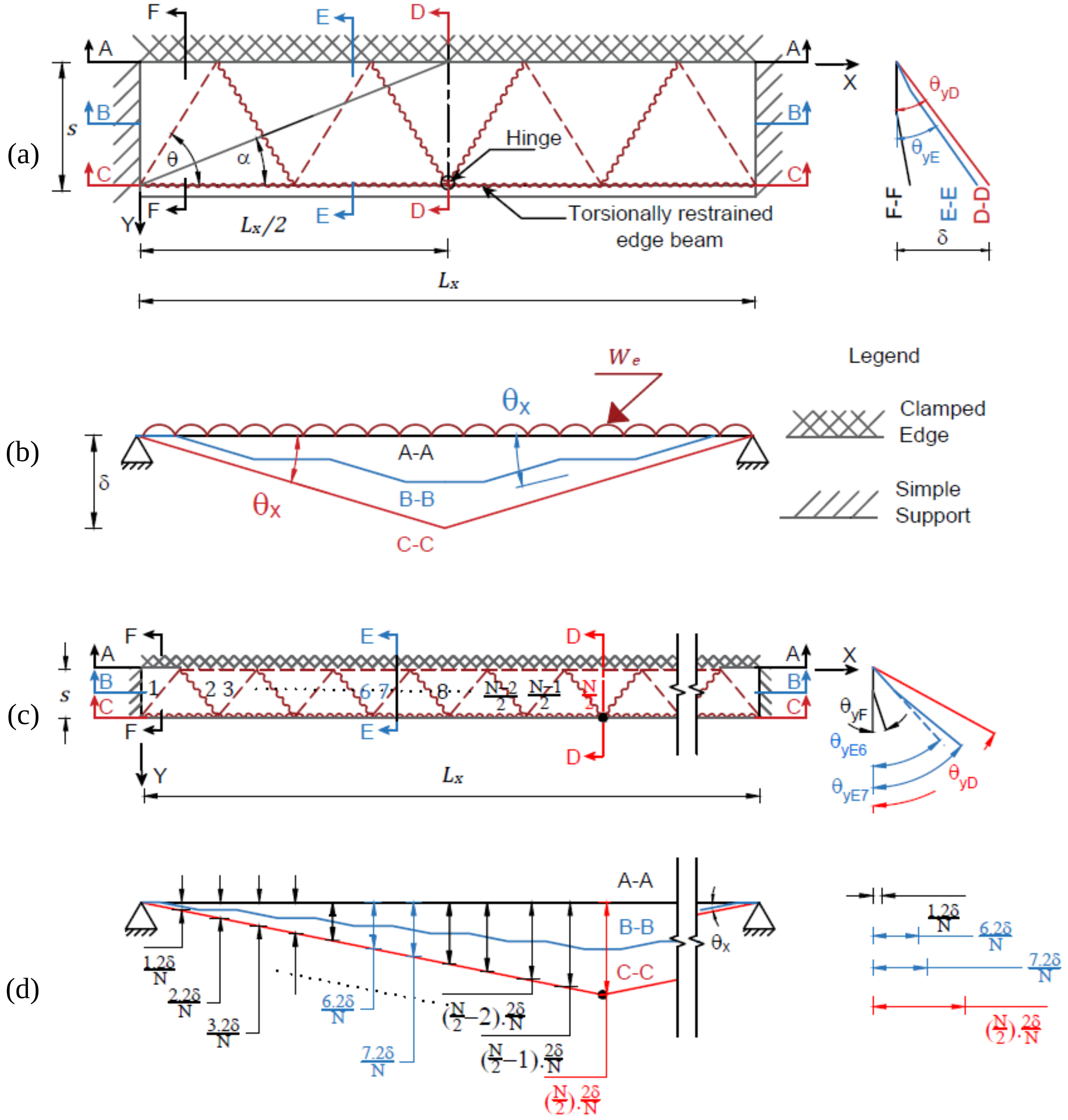

Figure 5.6. Folded Plate Mechanism for N Diagonal Yield Lines Showing (a) Plan View and Side Elevation Showing Deflection Profiles along D-D, E-E, and F-F; (b) Side Elevation Showing Deflection Profile along Sections A-A, B-B, and C-C; (c) Plan View Focusing on Half Bridge with N Diagonal Yield Lines and Side Elevation with Transverse Angular Deflection; and (d) Side View Showing Deflection Profiles with Longitudinal Deflections along Profile C-C.

The internal work done is computed for the cases obtained by incrementing the number of diagonal yield lines in multiples of four, and a pattern emerges that is used for expressing the internal work done in terms of N. The internal work done is thus expressed as Equation (5.10):

$$IWD = \sum (m'_x + m_x)(\theta_x)(y) + \sum (m'_y + m_y)(\theta_y)(x) \tag{5.10}$$

The deflection profile C-C shows a linear variation from zero at the supports to δ at the fracture location (mid-span). The angle of rotation in the longitudinal direction is a constant given by the slope of the section along C-C. Observing the section profile B-B, the section plateaus out between the alternate triangular segments formed between the zigzag yield lines. Therefore, the internal work done due to the longitudinal reinforcement for each of the triangular segment under consideration for half the span length is given by Equation (5.11). Since the rotation takes place alternately, the summation is carried out $N/4$ times for the half span of the bridge.

$$\frac{1}{2} IWD_x = \frac{N}{4}(m'_x + m_x)\left(\frac{2\delta}{L_x}\right)(s) \tag{5.11}$$

Twice the summation of the term in Equation (5.11) simplifies to the following expression for internal work done due to longitudinal reinforcement for the entire bridge in Equation (5.12):

$$IWD_x = (m'_x + m_x)\left(\frac{\delta}{L_x}\right)(sN) \tag{5.12}$$

The rotation of the slab in the transverse direction is not constant since it depends on the deflection of the slab along the C-C section, which linearly varies. Figure 5.6(c) and (d) show the deflection at every $1/N$ th segment, where each segment's length is L_x/N. It is observed that the deflection of the ith segment is the ith multiple of $2\delta/N$, which implies a maximum deflection at the mid-span when i = $N/2$. The angle of rotation in the transverse direction is the ratio of the ith deflection to the spacing, s. At section F-F, the rotation takes place once by the negative diagonal yield line and is calculated to be $(1 \times 2\delta)/sN$ over a distance of L_x/N. Along section E-E, the horizontal negative yield line rotates the slab by $(6 \times 2\delta)/sN$ over a distance of $2L_x/N$. The negative diagonal yield line causes a rotation of $(7 \times 2\delta)/sN$ over a distance of L_x/N. The horizontal positive yield line plateau the slab from a rotation of $(7 \times 2\delta)/sN$ over a distance of $2L_x/N$. Similar rotations take place for each section passing through the negative diagonal yield lines. Similarly, positive rotations pass through the sections with positive diagonal yield lines.

An exception is the triangle shown at D-D. Since this analysis solves the problem using symmetry, care must be taken that the horizontal negative yield line rotates the slab in a similar way, with a rotation of $(0.5N \times 2\delta)/\ sN$, but for a distance of $L_x/\ N$.

The internal work done is calculated along all the yield lines, and it is observed from the terms of the expression that the deflections form an arithmetic progression (AP) from 1 to $N/2$ terms. Using the result of the sum of first *"n"* natural numbers of an AP, *n*(*n*+1)/2 and substituting in terms of the problem parameters, the expression of the internal work done due to transverse reinforcement for each of the triangular segment under consideration for half the span length is given by Equation (5.13).

$$\sum IWD_{y.i} = \sum_{i=1}^{N/2} \left(m'_y + m_y\right)\left(\frac{i.\,2\delta}{sN}\right)\left(\frac{L_x}{N}\right) \tag{5.13}$$

Twice the summation then provides the internal work done due to the transverse reinforcement deck-slab reinforcement for the entire span as follows in Equation (5.14):

$$IWD_y = \left(\frac{m'_y + m_y}{2s}\right)\left(\frac{0.5N + 1}{0.5N}\right)\delta L_x \tag{5.14}$$

Substituting Equations (5.12) and (5.14) in Equation (5.10), the total internal work done due to the folded plate mechanism is given as the summation of IWD_x and IWD_y, thus expressed in Equation (5.15):

$$IWD = \left[\left(\frac{m'_y + m_y}{2s}\right)\left(1 + \frac{2}{N}\right)L_x + \left(\frac{m'_x + m_x}{L_x}\right)sN\right]\delta \tag{5.15}$$

where m'_y and m_y are the negative and positive moment capacities per unit width in the y-direction, respectively, and m'_x, and m_x are the negative and positive moment capacities per unit width in the x-direction, respectively; N = the number of diagonal yield lines in the area under consideration; L_x = the length of the span of the bridge; and s = the width of the area of the slab along which the mechanism under consideration is applied.

Equating the external and internal work, $EWD = IWD$, gives an expression for finding N, the derivation of which is shown in Equations (5.16) to (5.19):

$$W_e L_x \frac{\delta}{2} = \left[\left(m'_y + m_y\right)\left(\frac{L_x}{2s}\right) + \left(m'_y + m_y\right)\left(\frac{L_x}{sN}\right) + \left(m'_x + m_x\right)\left(\frac{sN}{L_x}\right)\right]\delta \tag{5.16}$$

from which the equivalent collapse load on the girder can be determined as follows:

$$W_e = \frac{2}{L_x}\left[\left(m_y' + m_y\right)\left(\frac{L_x}{2s}\right) + \left(m_y' + m_y\right)\left(\frac{L_x}{sN}\right) + \left(m_x' + m_x\right)\left(\frac{sN}{L_x}\right)\right]\delta. \tag{5.17}$$

The line load W_e, will have a minimum value when $\frac{dW_e}{dN} = 0$, as follows:

$$\frac{dW_e}{dN} = -\left(m_y' + m_y\right)\left(\frac{L_x}{sN^2}\right) + \left(m_x' + m_x\right)\left(\frac{s}{L_x}\right) = 0 \tag{5.18}$$

$$\frac{\left(m_y' + m_y\right)}{\left(m_x' + m_x\right)} = \left(\frac{s^2N^2}{{L_x}^2}\right) \tag{5.19}$$

Upon solving, the minimum value of N is obtained in Equation (5.20) :

$$N = \frac{L_x}{s}\sqrt{\frac{m'_y + m_y}{m'_x + m_x}} \tag{5.20}$$

Back-substituting N into Equation (5.17) gives the equivalent collapse line load in Equation (5.21):

$$W_{e\,min} = \frac{4}{L_x}\sqrt{\left(m_x' + m_x\right)\left(m_y' + m_y\right)} + \frac{\left(m_y' + m_y\right)}{s} \tag{5.21}$$

It is also of interest to note the geometry of yield lines. From Figure 5.6(a), the angle ϴ may be found using trigonometry, as shown in Equation (5.22):

$$\tan\theta = \frac{sN}{L_x} = \sqrt{\frac{m'_y + m_y}{m'_x + m_x}} \tag{5.22}$$

where θ is the angle of the diagonal yield lines with the horizontal. Therefore, Equation (5.21) may be further simplified to give alternate forms for expression for $W_{e\,min}$ represented by Equations (5.23a) and (5.23b)

$$W_{e\,min} = \frac{\left(m_y' + m_y\right)}{s} + 4\left(\frac{m_x' + m_x}{L_x}\right)\tan\theta \tag{5.23a}$$

or

$$W_{e\,min} = \frac{\left(m_y' + m_y\right)}{s}\left[1 + \frac{4s}{L_x}\cot\theta\right] \tag{5.23b}$$

Note that for isotropic reinforcement, $m_x = m_y$ and $m'_x = m_y'$, $\theta = 45^{\circ}$. A similar result to Equation (5.22) is given in (Park and Gamble 2000) based on the Affinity Theorem for orthotropic plates.

The aforementioned theory was applied to the test bridge from TxDOT Research Project 9-5498 and the minimum equivalent lane load was computed. Figure 5.7 presents a graph plotting the minimization of the distributed load, W_e, with respect to the number of diagonal yield lines, N.

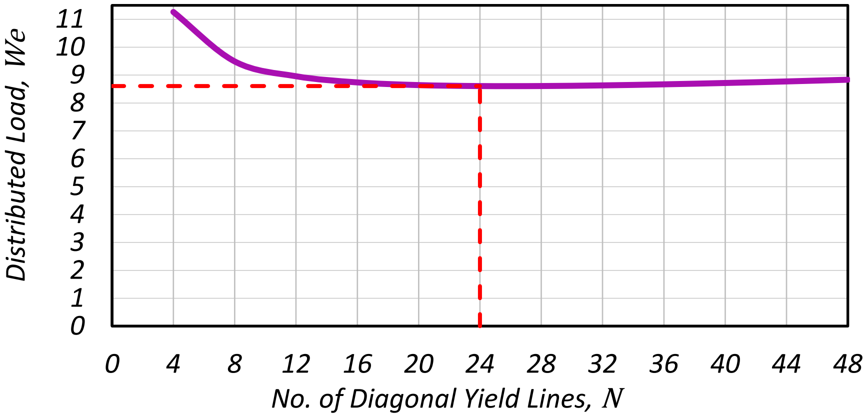

Figure 5.7. Variation of Distributed Load with Number of Diagonal Yield Lines.

Consider an area load of w acting on the trapezoidal region of the slab shown in Figure 5.6. The virtual work done by the load will be the product of the load, the area on which it acts, and the virtual deflections of the center of gravity of that area. From Figure 5.6(a), it can be observed that the diagonal yield lines divide the slab into triangular segments that undergo deflection. The virtual deflections of the triangular segments alternate as follows. Considering half the span, as shown in Figure 5.6(c), and starting from the supports, the centroidal deflection is the i^{th} multiple of 4/3N, where i = 1, 3, 5, … (0.5 N-1)—in other words, a set of odd integers from 1 to (0.5 N-1); and it is the j^{th} multiple of 2/3N, where i = 2, 4, 6, … (0.5 N-2), or a set of odd integers from 2 to (0.5 N-2). This encompasses the centroidal deflections of all the triangular segments from the support till the mid-span except the half triangle at section D-D. The areas of all these segments are Ns/L_x. As seen in the case of the internal work done, an exception is the triangle at section D-D, with an area of $Ns/2L_x$ and a centroidal deflection of 1/3. A pattern emerges from several computations of the external work done by incrementing the number of diagonal yield lines in multiples of 4, similar to that observed from the calculations of the internal work. The alternate centroidal deflections from the supports to the mid-span form two series of arithmetic progression, one of first $N/4$ odd numbers, from 1 to (0.5 N-1), and the other of first (.25N-1) even numbers, from 2 to (0.5 N-2). The sum of each series is obtained using the expression for the sum of first n terms of an AP, $0.5n\ (a_1\ +\ a_n)$, where a_1 and a_n are the first and n^{th} terms of the AP, respectively.

The summation of the product of the areas of each segment for half the span with their respective centroidal deflections is given as $sL/12$ for the odd numbered segments, $(N$-$4)\ sL_x/24N$ for the even numbered segments, and $sL/6\ N$ for the triangle at D-D section. For the full span, the summation of the product of slab segment and the centroidal deflection is $sL_x/4$. The external work done due to area load w is given by $EWD_{trapezium}$ in Equation (5.24):

$$EWD_{trapezium} = wsL_x/4 \tag{5.24}$$

5.4.1.1 Upper-Bound Solution

From the yield line solution from Equation (5.16), the total load on the girder can be set as $W_T = L_x W_e$. Then, equating external and internal work done (with δ = 1) yields the following Equation (5.25):

$$0.5W_T = \left[\left(m'_y + m_y\right)\left(\frac{L_x}{2s}\right) + \left(m'_y + m_y\right)\left(\frac{L_x}{sN}\right) + \left(m'_x + m_x\right)\left(\frac{sN}{L_x}\right)\right] \tag{5.25}$$

where W_T = total ultimate load at the bridge participating in the collapse mechanism.

The internal work done may be rewritten by substituting Equation (5.20) in Equation (5.15) and further simplified using Equation (5.22). For the next step, put in the $IWD = EWD$ format using Equation (5.23a) as shown in Equations (5.26) and (5.27).

$$\Omega 0.5W_T = \Omega 0.5W_e L_x = 2(m'_x + m_x)\tan\theta + \left(m'_y + m_y\right)\frac{L_x}{2s} \tag{5.26}$$

$$\Omega 0.5W_T = \left(m'_y + m_y\right)\frac{L_x}{2s}\left[1 + 2\left(\frac{2s}{L_x}\right)\left(\frac{m'_x + m_x}{m'_y + m_y}\right)\tan\theta\right] \tag{5.27}$$

Define angle α, as shown in Figure 5.6(a), in Equation (5.28):

$$\frac{s}{L_x/2} = \tan\alpha \tag{5.28}$$

Then, by using Equation (5.22), Equation (5.27) may be recast as Equation (5.29):

$$\Omega 0.5W_T \ = \left(m'_y + m_y\right)\cot\alpha\left[1 + 2\frac{\tan\alpha}{\tan\theta}\right] \tag{5.29}$$

Thus, the system upper-bound overstrength factor is given as Equations (5.30 a) and (5.30b) :

$$\Omega_{Upper} = \frac{IWD}{EWD} \ = \frac{\left(m'_y + m_y\right)[\cot\alpha + 2\cot\theta]}{0.5W_T} \tag{5.30a}$$

or

$$\Omega_{Upper} = \frac{\left(m'_y + m_y\right)\left(\frac{L_x}{2s}\right)\left[1 + 2\frac{\tan\alpha}{\tan\theta}\right]}{0.5W_T} \tag{5.30b}$$

5.4.1.2 Lower-Bound Solution

A lower-bound solution may also be formed using a strip method (Park and Gamble 2000). Figure 5.8 illustrates the lower-bound solution via strips in equilibrium in the x- and y-directions, respectively, where W_x and W_y are the uniformly distributed load on the longitudinal and transverse strips, respectively. Equations (5.31) to (5.38) show the steps leading to the lower-bound solution as follows:

Consider the W_y strips (assuming $L_x = s$):

$$\left(m'_y + m_y\right) = 2W_y\frac{L_x}{4} = 2W_y\frac{2s}{4} = W_y s \tag{5.31}$$

$$\therefore W_y = \frac{\left(m'_y + m_y\right)}{s} \tag{5.32}$$

Distributed load by W_x strips:

$$(m'_x + m_x) = \frac{W_x}{s}\frac{{L_x}^2}{8} \text{ Thus, } W_x = \frac{8s}{{L_x}^2}\ (m'_x + m_x) \tag{5.33}$$

$$W_e \ = W_x + W_y = \frac{8s}{{L_x}^2}(m'_x + m_x) + \frac{\left(m'_y + m_y\right)}{s} \tag{5.34}$$

$$\Omega 0.5W_T \ = \Omega 0.5W_e L_x = \left(m'_y + m_y\right)\frac{L_x}{2s} + \ \frac{4s}{L_x}(m'_x + m_x) \tag{5.35}$$

but, $\frac{s}{L_x/2} = \tan\alpha$, therefore by inversion it is substituted into Equation (5.35):

$$\Omega 0.5W_T \ = \left(m'_y + m_y\right)\cot\alpha + \ 2(m'_x + m_x)\tan\alpha \tag{5.36}$$

$$\Omega 0.5W_T \ = \left(m'_y + m_y\right)\left[\cot\alpha + \ 2\left(\frac{m'_x + m_x}{m'_y + m_y}\right)\tan\alpha\right] \tag{5.37}$$

$$\Omega 0.5W_T \ = \left(m_y' + m_y\right)[\cot\alpha + \ 2\cot^2\theta\tan\alpha] \tag{5.38}$$

Solving gives the lower-bound overstrength factor in Equations (5.39a) and (5.39b):

$$\Omega_{Lower} = \frac{\left(m_y' + m_y\right)[\cot\alpha + \ 2\cot^2\theta\tan\alpha]}{0.5W_T} \tag{5.39a}$$

or

$$\Omega_{Lower} = \frac{\left(m_y' + m_y\right)\left(\frac{L_x}{2s}\right)\left[1 + 2\frac{\tan^2\alpha}{\tan^2\theta}\right]}{0.5W_T} \tag{5.39b}$$

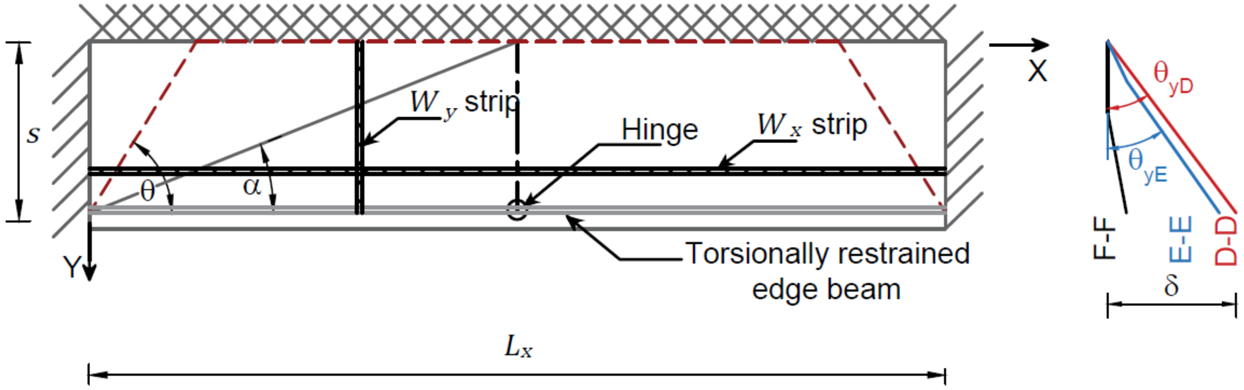

(a) Plan view of interior slab with a central fracture on the edge beam.

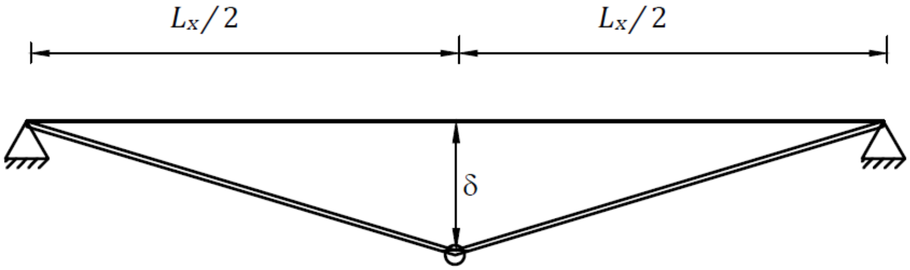

(b) Side elevation of the mechanism.

Figure 5.8. Strip Equivalent Mechanism.

5.4.1.3 Generalized Plastic Solution

By harmonizing the upper- and lower-bound solutions, a general solution covering the two distinct approaches is as follows in Equations (5.40) to (5.42):

$$\Omega = \frac{\left(m_y' + m_y\right)\left(\frac{L_x}{2s}\right)k_{bound}}{0.5W_T} \tag{5.40}$$

in which

$$k_{bound}^{upper} = \left[1 + 2\frac{\tan\alpha}{\tan\theta}\right] = 1 + \frac{4s}{L_x}\sqrt{\left(\frac{m'_x + m_x}{m'_y + m_y}\right)} \tag{5.41}$$

and

$$k_{bound}^{lower} = \left[1 + 2\frac{\tan^2\alpha}{\tan^2\theta}\right] = 1 + \frac{8s^2}{{L_x}^2}\left(\frac{m'_x + m_x}{m'_y + m_y}\right) \tag{5.42}$$

5.4.1.4 Accounting for the Effect of the Horizontal Curve of a Bridge

Figure 5.9 presents a schematic representation of a generic curved bridge in plan view. Since the bridges are curved in reality, with a centerline radius of curvature $R_{℄}$, arched at an angle ω, with a centerline length, L_x, and breadth, B, the length of the innermost edge progressively increases as a function of $R_{℄}$ and ω.

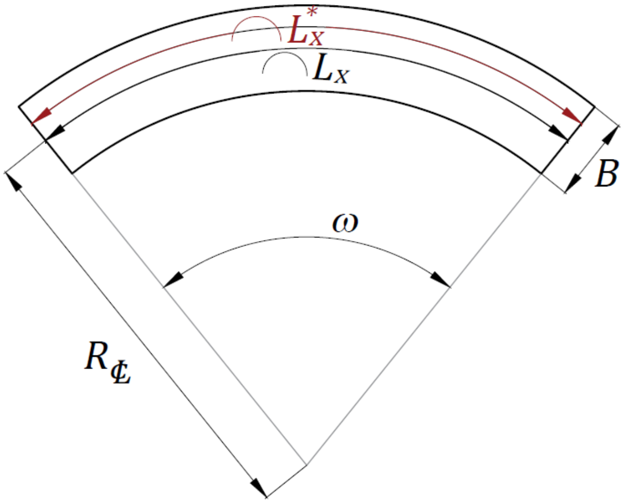

Figure 5.9. Layout of a Generic Curved Bridge in Plan.

Since the internal work done is primarily contributed by the trapezoidal band that is equidistant from the centerline of the bridge at a distance of $s/2$, the increase and decrease of the arc lengths of this folded plate mechanism are compensated. Therefore, the span length L_x used for the internal work done calculations for the trapezoidal region refers to the length of the centerline of the bridge span. However, since the outer region primarily contributes toward the external work done for the yield line mechanism under consideration and the internal work done by the region beyond the trapezoidal band, the span length used in those computations refers to the length of the outer region of the curved bridge, which is denoted in Equations (5.43) to (5.45) by:

$$L_x^* = (R_{℄} + 0.25B)\omega \tag{5.43}$$

$$\omega = \frac{L_x}{R_{℄}} \tag{5.44}$$

$$L_x^* = \left(1 + \frac{B}{4R_{℄}}\right) L_x \tag{5.45}$$

5.4.2 Overstrength Capacity for Factored Applied Loads for Single-Span Bridge

Figure 5.10 presents a generic bridge loaded with two HL-93 vehicular load models. The HL-93 loading consists of HS-20 trucks having 8 kip, 32 kip, and 32 kip axle loads spaced 14 ft apart along the bridge span and placed centrally such that the load is concentrated above the fracture.

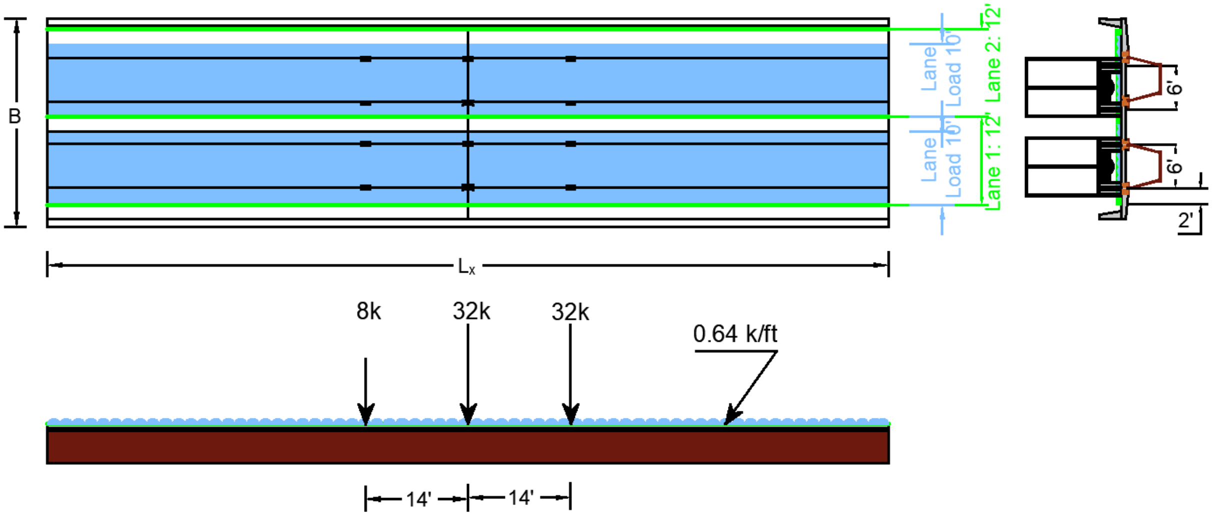

Figure 5.10. HL-93 Load Position for Two-Lane Loaded Case.

These concentrated point loads are the resultant load of each of the 6 ft wide axles. Additionally, a congested traffic load is applied as a uniformly distributed load of 0.64 kip/ft spread across a width of 10 ft. Each lane consists of a congested lane load and the truck, and each lane is specified to have an equivalent width of 12 ft according to AASHTO (2017) specifications.

Figure 5.11 presents the implementation of the yield line mechanism postulated for the HL-93 loading on a typical single-span bridge. The internal work done due to the trapezoidal region can be obtained from Equation (5.40). Assuming a unit virtual deflection and further simplifying gives Equation (5.46).

$$IWD = \left(m_y' + m_y\right)\left(\frac{L_x}{2s}\right)k_{bound} \tag{5.46}$$

The internal work done due to the rectangular part of the deck slab and the fractured outside girder is due to the hinge formation at the mid-span that causes a rotation of $4/L_x$ by the positive longitudinal reinforcement m_x along a width b as shown in Equation (5.47)

$$IWD = 4m_x\left(\frac{b}{L_x^*}\right) \tag{5.47}$$

rearranging more specifically, in terms of the moment at the central hinge region, is represented by Equation (5.48):

$$IWD = \frac{4}{L_x^*}(m_x b) \tag{5.48}$$

This constitutes the total internal work done for the assumed yield line mechanism when the outside girder is fully fractured.

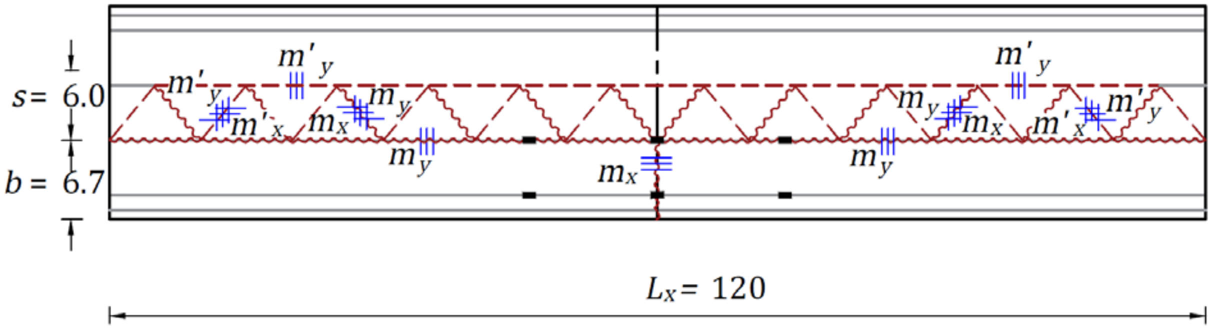

Figure 5.11. Critical Yield Line Mechanism for a Fractured Single-Span (9-5498).

The external work done is due to the virtual work done by the deck slab, the girder and the guardrail, and the HL-93 loading. The external work done due to the live load (HL-93) is considered due to the lane load that is increased by 75 percent to account for live load allowance and to the wheel loads of the trucks that are increased by 75 percent to account for the live load factor, and it increases by 33 percent to account for the impact factor as specified by AASHTO (2017).

For the sake of convenience, an approximation is implemented wherein the lane load is considered spread across the deck, similar to the self-weight per unit area. This measurement is achieved by applying the lane load for a width of the HL-93 lane of 12 ft. Thus, the distributed lane load is w_l of 0.0533 ksf and considered to act with the area load of reinforced concrete deck slab, w_c. The equivalent combined area load is denoted by w_u. This assumption is justified because the lane load is considered to act over an area beyond the actual loaded area. In accordance with the LRFD loads, (AASHTO (2017), the dead loads are increased by 25 percent.

The external work done due to an area load w_u in Equation (5.49) is derived using Equation (5.24):

$$EWD_{\,w_u} = w_u L_x^* \left(\frac{b}{2} + \frac{s}{4}\right) \tag{5.49}$$

The external work done due to the combined weight of the fractured outside girder and the outer guardrail, W_x, is given by Equation (5.50):

$$EWD_{W_x} = \frac{W_x L_x^*}{2} \tag{5.50}$$

The deflections under each wheel load are computed using similar triangles and are multiplied with the factored loads of each wheel to obtain the external virtual work done by the HS-20 truck, as given by Equation (5.51):

$$EWD_{HS20} = \left(168 - \frac{2613}{L_x^*}\right) \tag{5.51}$$

For a wider bridge, the second lane of trucks may participate (in part) in the collapse mechanism, as depicted in Figure 5.12(b). The axle loads are therefore required to be increased proportionally to their deflection with respect to the truck position over the fractured girder. Thus, the lane load requires modification through the scalar K_{lane}. For one line of truck wheels participating, the factor is given by Equation (5.52):

$$K_{lane} = 1 + 0.5\ \frac{y}{s} \tag{5.52}$$

in which y = distance measured from the intact (unfractured) girder to the line of wheels.

Equation (5.53) is used if both lines of wheels are participating in the mechanism:

$$K_{lane} = 1 + \frac{y}{s}\ ; K_{lane} \leq 2 \tag{5.53}$$

where y = distance to the centerline of the truck. Thus, the total external work done is given by Equation (5.54):

$$EWD = w_u L_x^* (0.5b + 0.25s) + 0.5 W_x L_x^* + \left(168 - \frac{2613}{L_x^*}\right) K_{lane} \tag{5.54}$$

and may be contracted to the following in Equation (5.55):

$$EWD = 0.5W_T \tag{5.55}$$

where W_T = total ultimate load at the bridge participating in the collapse mechanism, represented by Equation (5.56):

$$W_T = w_u L_x^*(b + 0.5s) + W_x L_x^* + \left(336 - \frac{5226}{L_x^*}\right) K_{lane}. \tag{5.56}$$

Solving for the overstrength factor $\Omega = IWD/EWD$ for the simply supported span is given by Equation (5.57):

$$\Omega = \frac{\left(m'_y + m_y\right)\left(\frac{L_x}{2s}\right) k_{bound} + (m_x b)\left(\frac{4}{L_x^*}\right)}{0.5W_T} \tag{5.57}$$

where m'_y and m_y are the negative and positive moment capacities per unit width in the y-direction, respectively, and m'_x, and m_x are the negative and positive moment capacities per unit width in the x-direction, respectively; L_x = the centerline length of the span of the bridge; L_x^* = the length of the outer region of the bridge, factored for curvature; s = the width of the area of the slab along which the mechanism under consideration is applied; b = the transverse distance of the interior flange of the fractured girder from the outer edge of the bridge; w_u = the area load consisting of self-weight of the reinforced concrete deck slab and the applied lane load; and W_x = the line load consisting of the self-weight of the fractured tub girder and the guardrail.

When implemented for the bridge of TxDOT Research Project 9-5498, the upper-bound and lower-bound overstrength factors are found—using Equation (5.57)—to be Ω_{Upper} = 1.46 and Ω_{Lower} = 1.28. Note that in that project, the bridge is narrow and can only accommodate a single HS-20 truck load alone.

5.4.3 Analysis for Spans with Plastic End Moments

Consider now the general case for spans that possess a measure of fixity at their ends due to the presence of continuity via the adjacent spans, as shown in Figure 5.12 (a).

Equating the factored external work done to the internal work done as shown in Equations (5.58) and (5.59):

$$\Omega\, 0.5W_T = 0.5M_{p1}^{-}\theta + 0.5M_{p2}^{-}\theta \tag{5.58}$$

$$\Omega\, 0.5W_T = \left(0.5M_{p1}^{-} + 0.5M_{p2}^{-}\right)\left(\frac{2}{L_x^*}\right) \tag{5.59}$$

Thus, the overstrength factor for the intact case is given by Equation (5.60):

$$\Omega = \frac{\left(0.5M_{p1}^{-} + 0.5M_{p2}^{-}\right)\left(\frac{2}{L_x^{*}}\right)}{0.5W_T} \tag{5.60}$$

where $0.5M_{p1}^{-}$ and $0.5M_{p2}^{-}$ are the plastic moment capacities of the composite deck participating in the overall plastic mechanism (0.5 is used since the outside girder alone takes part in the critical mechanism).

This result may now be incorporated into the overall solution for the fractured girder case. Thus, the overall effective weight, W_{ET}, used in the plastic analysis is given by Equation (5.61):

$$W_{ET} = w_u L_x^{*}(b + 0.5s) + W_x L_x^{*} + \left(336 - \frac{5226}{L_x^{*}}\right) K_{lane} \tag{5.61}$$

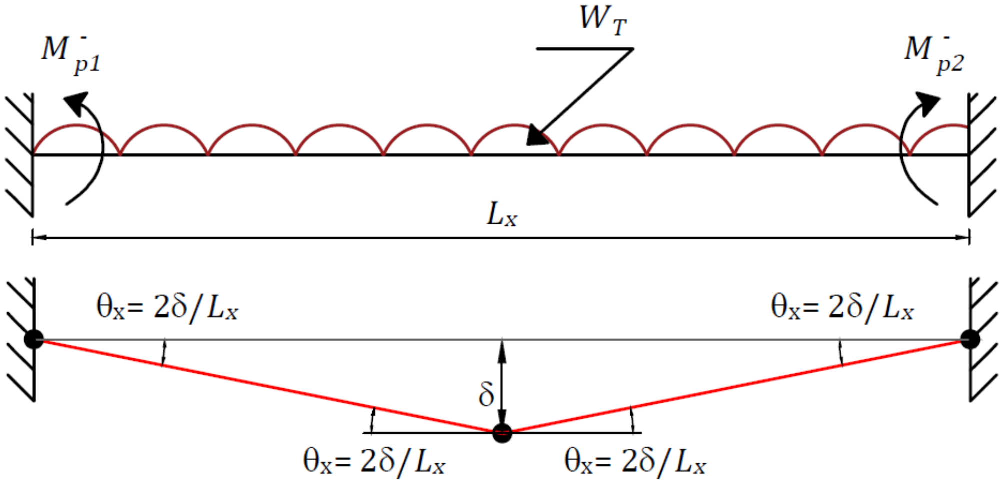

(a) Continuous Bridge Span with End Elastic Moments

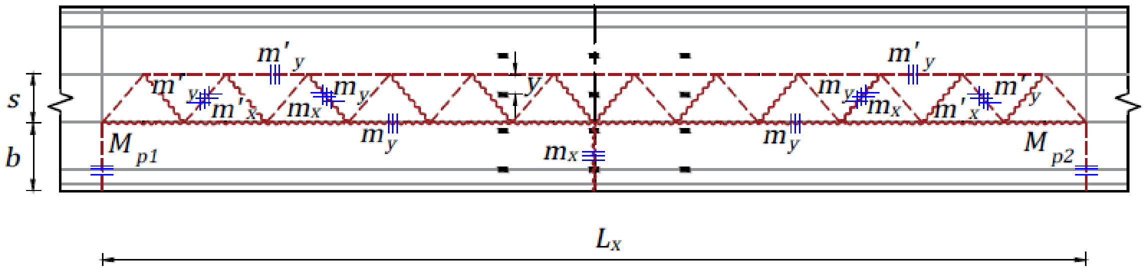

(b) Layout of a Typical Interior Span with Yield Line Mechanism

Figure 5.12. Collapse Load Analysis of Interior Span of Continuous Bridges.

Adding the effect of end moments, the overall collapse overstrength capacity is given by Equation (5.62):

$$\Omega = \frac{\left(m_y^{'} + m_y\right)\left(\frac{L_x}{2s}\right) k_{bound} + \left(\frac{4m_x b}{L_x^*}\right) + \left(0.5M_{p1}^{-} + 0.5M_{p2}^{-}\right)\left(\frac{2}{L_x^*}\right)}{0.5W_{ET}} \tag{5.62}$$

For the end-spans in multi-span bridges as well as two-span continuous bridges, either $0.5M_{p1}^{-}$ or $0.5M_{p2}$ is set to zero at the outermost abutments, as shown in Figure 5.13. The overstrength factor of the system due to the moment, $0.5M_p^{-}$, at the continuous interior support is given by Equation (5.63):

$$\Omega = \frac{\left(0.5M_p^{-}\right)\left(\frac{1}{(\lambda - 1)L_x^*}\right)}{0.5W_T} \tag{5.63}$$

where $0.5M_p^{-}$ = the plastic moment capacities of the composite deck participating in the overall plastic mechanism at the supports, and λ = fraction of span length from the simply supported end of the span at which the steel twin tub girder is fractured. The overall effective weight, W_{ET}, used in the plastic analysis, is given by Equation (5.64):

$$W_{ET} = w_u L_x^*(b + 0.5s) + W_x L_x^* + \left(336 - \frac{523}{\lambda L_x^*} - \frac{2091}{(1-\lambda)L_x^*}\right) K_{lane} \tag{5.64}$$

The critical case in which the external work done, $0.5W_{ET}$, is set to be the maximum by positioning the 8 kip load at the side of the fracture that is nearer to the simply supported end of the span is considered in Equation (5.64).

This result may now be incorporated into the overall solution for the fractured girder case and represented by Equation (5.65).

$$\Omega = \frac{\left(m_y^{'} + m_y\right)\left(\frac{L_x}{2s}\right) k_{bound} + \left(\frac{m_x b}{(\lambda - \lambda^2)L_x}\right) + \left(\frac{0.5M_p^{-}}{(1-\lambda)L_x}\right)}{0.5W_{ET}} \tag{5.65}$$

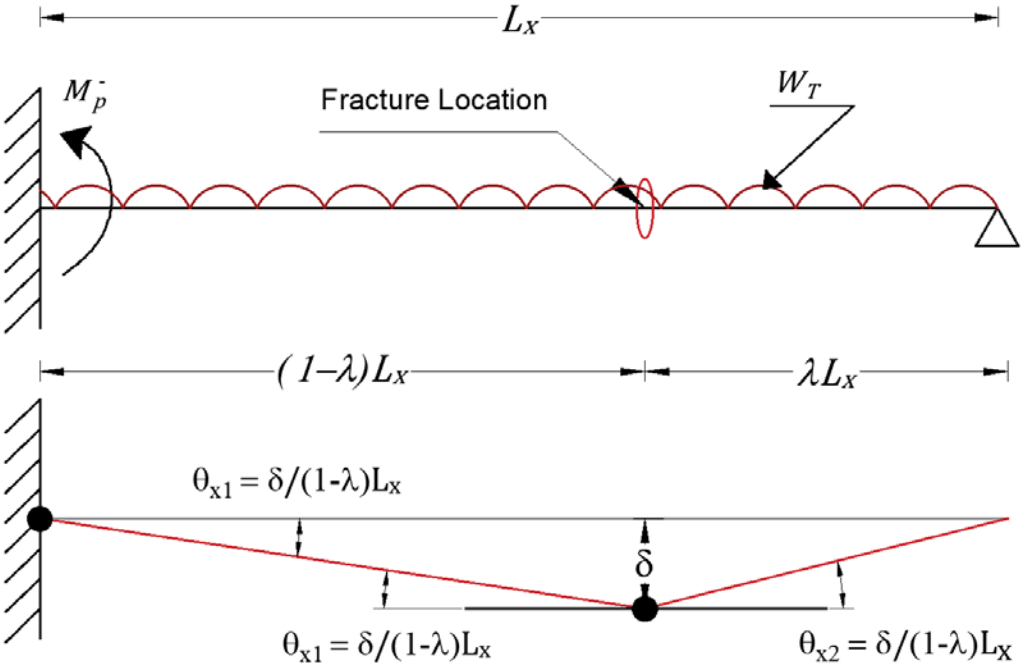

(a) End-Span of Bridge

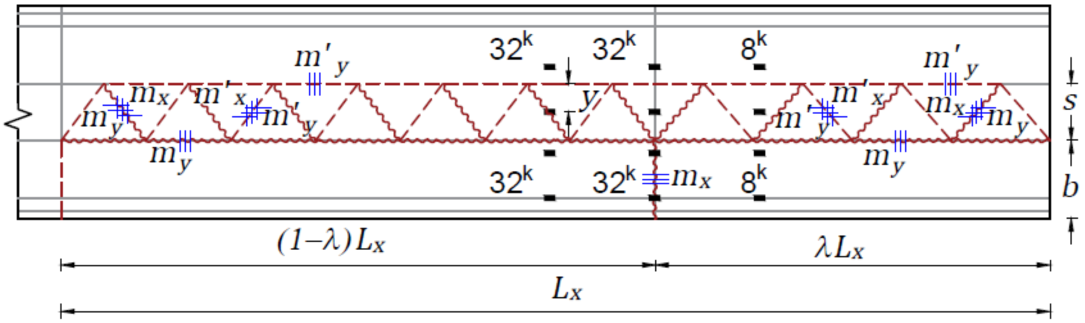

(b) Layout of a Typical Interior Span with Yield Line Mechanism

Figure 5.13. Collapse Load Analysis of End-Spans of Continuous Bridges.

5.4.4 Location of Maximum Positive Moment for Collapse Analysis of Fractured Girder

The location of the maximum positive moment within the end-span region of multi-span continuous bridge structures depends on several factors:

- The stiffness (length) of the adjoining span or spans.
- The relative positive to negative moment capacities, as designed and constructed.
- The relative proportion of distributed loads to point loads.

To illustrate the significance of the above, consider the following scenarios depicted in Figure 5.14 where the location of the maximum positive moment is expressed as a fraction of the span length, λ.

Figure 5.14(a) and (b) respectively show the extreme cases for a multi-span bridge with full fixity (where M^F=$wL^2/8$) and for a two-span structure with partial fixity where only one span is fully loaded. For an elastic design, moment capacities are proportionately tuned to the elastic bending moment diagram. Thus, for Figure 5.14(a) and (b), λ = 0.375 (full fixity) and λ = 0.4375 (partial fixity), respectively. Figure 5.14(c) and (d) present the location of the maximum positive moment under the moving concentrated load with full fixity (where M^F= $(\lambda - \lambda^3)PL/2$) and partial fixity for a two-span structure. The maximum positive moment occurs where λ = 0.366 (full fixity) and λ = 0.5536 (partial fixity).

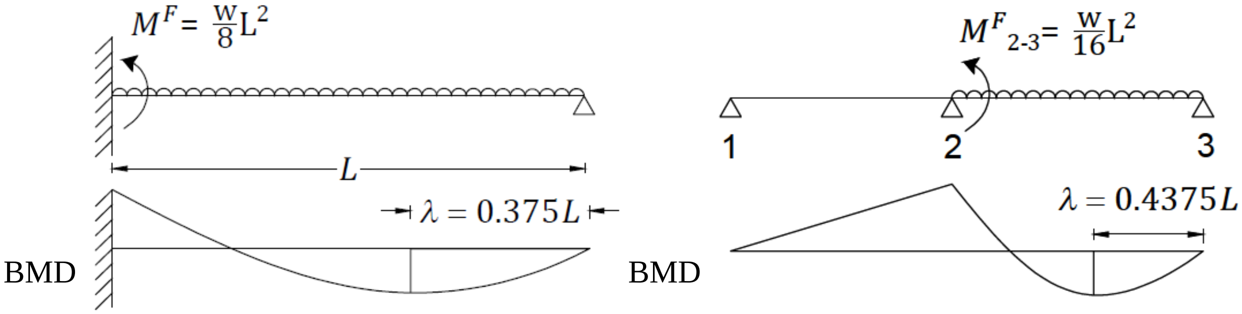

(a) Elastic Design Propped Cantilever

(b) Elastic Design of Two Spans

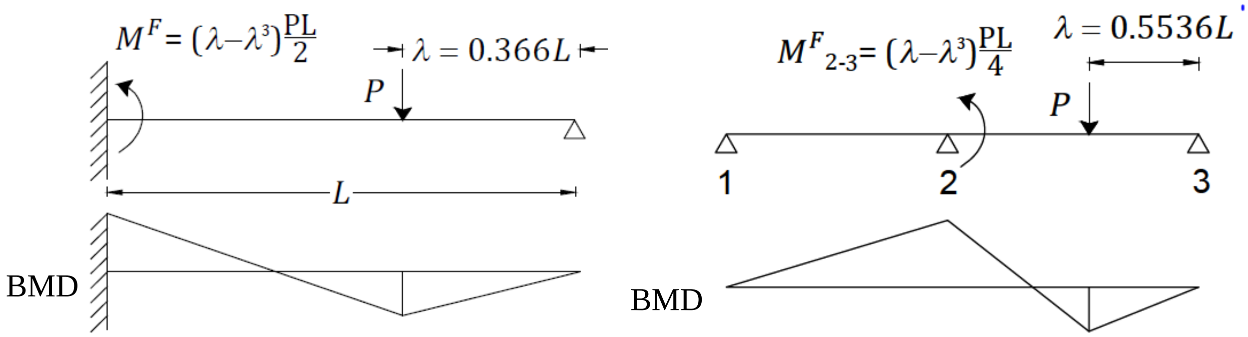

(c) Maximum Positive Moment Location under Moving Concentrated Load

(d) Two Span with Moving Load Case

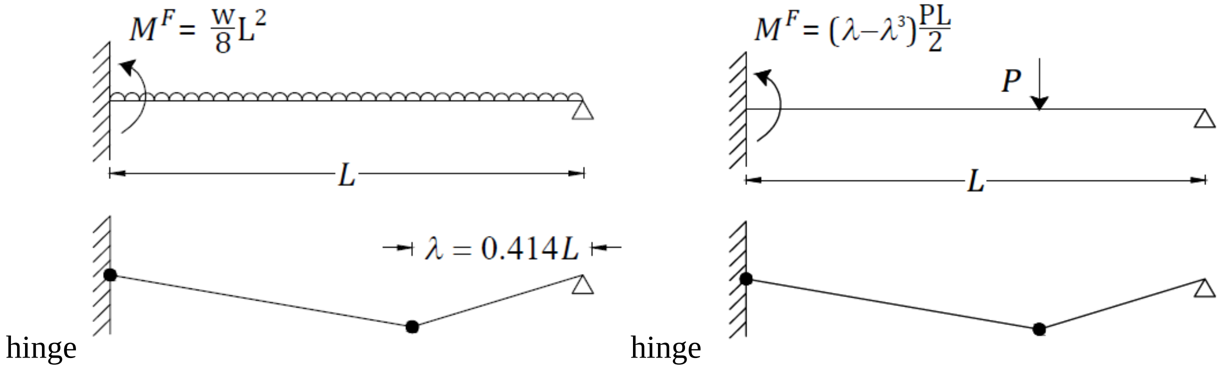

(e) Uniformly Distributed Load

(f) Concentrated Moving Load

Figure 5.14. Different Scenarios Used to Determine the Location of Maximum Positive Moment for Collapse Analysis.

For plastic analysis and design, in both the cases of Figure 5.14(a) and (b), λ = 0.414 if the beam has the same positive and negative moment capacity as shown in Figure 5.14(e). Figure 5.14(f) indicates that the maximum moment occurs at the location where the concentrated load acts. The critical location in the end spans in continuous bridges will be at that location where fracture critical (welded joint) details exist closest to the maximum positive moment region. Because this may vary from structure to structure, for simplicity it may be assumed to be in the vicinity of λ = 0.40. Such high moments are assumed to be capable of initiating fracture at that location. Therefore, for consistency, in this study the location of fractures in the end-spans of multi-span continuous bridges shall be taken herein as λ = 0.40.

To check the veracity of this assumption, the overstrength factors of the fifteen pre-selected bridges were calculated using the exact λ value found using the formula given in Equation (5.66):

$$\lambda = \frac{\sqrt{\mu+1}-1}{\mu} \tag{5.66}$$

where μ represents the ratio of the negative and positive bending moment ($\mu = M_p^- / M_p^+$) of the composite bridge section at support and at mid-span, respectively. These “exact” values of λ range from 0.37 to 0.42 for the different bridges under consideration and presented in Table 5.2. The overstrength factors have also been calculated by setting λ = 0.4 and λ = 0.5. To assess the significance of the differences in overstrength factors, ratios have been formed using Equation (5.67):

$$R = \frac{\Omega(\lambda)}{\Omega(\lambda_{exact})} \tag{5.67}$$

Results are shown for these ratios plotted as a cumulative distribution in Figure 5.15. A lognormal distribution has also been fitted to the data points for the two cases where λ = 0.4 and λ = 0.5. The median values of the distributions show that when λ = 0.4, there is only a very slight bias of 0.73 percent, whereas the bias (error) increases markedly to 11 percent when λ = 0.5. This simply means that λ = 0.5 is not the most appropriate or adverse location to assume the existence of a girder fracture in end-span positive moment regions. It is therefore evident that in lieu of a more precise minimization analysis, one can confidently adopt λ = 0.4 as being an appropriate location to assume fractures in end-spans of the continuous bridges. Using λ = 0.4 means that any error introduced into the Ω factor will be less than 3 percent.

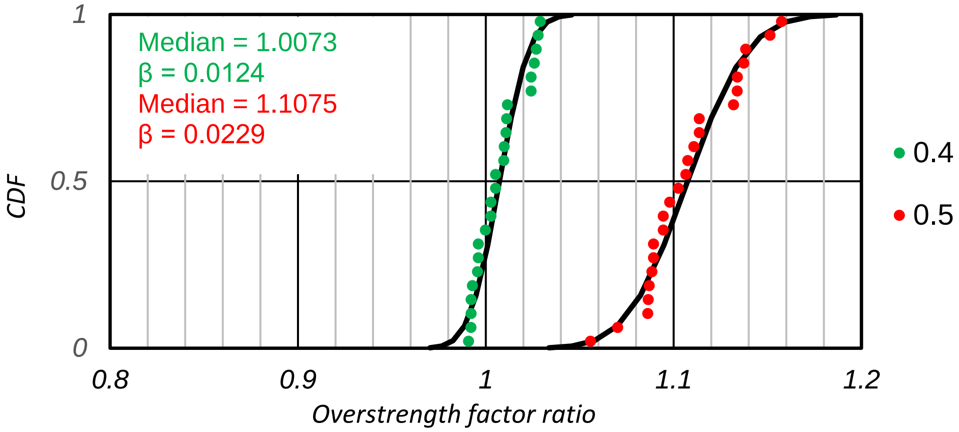

Figure 5.15. Cumulative Distribution for λ = 0.4 and λ = 0.5.

Table 5.2. Comparison of Overstrength Factors for Exterior Spans, Ω.

ID	L_x (ft)	λ_{exact}	B (ft)	Ω λ_{exact}	Ω at λ=0.4	Ω at λ=0.5
B4S1	132	0.39	28	1.79	1.80	1.98
B4S2	128	0.39	28	1.83	1.85	2.03
B5S1	140	0.41	30	1.41	1.40	1.53
B5S2	140	0.41	30	1.40	1.39	1.52
B6S1	140	0.40	38	1.63	1.62	1.81
B6S2	140	0.40	38	1.63	1.62	1.81
B7S1	219	0.40	28	1.45	1.45	1.57
B7S2	190	0.37	28	1.64	1.69	1.86
B8S1	265	0.41	28	1.35	1.34	1.44
B8S2	295	0.42	28	1.26	1.25	1.33
B9S1	140	0.41	28	1.57	1.56	1.71
B9S3	126	0.41	28	1.69	1.68	1.86
B10S1	148	0.39	30	1.96	1.98	2.23
B10S3	190	0.37	30	1.62	1.67	1.85
B11S1	223	0.37	28	1.71	1.75	1.97
B11S3	235	0.37	28	1.61	1.65	1.85
B12S1	140	0.38	28	1.73	1.75	1.91
B12S3	145	0.38	28	1.69	1.71	1.87
B13S1	152	0.37	30	1.38	1.41	1.57
B13S3	152	0.37	30	1.37	1.40	1.55
B14S1	150	0.40	28	1.63	1.63	1.77
B14S3	150	0.40	28	1.63	1.63	1.77
B15S1	200	0.39	28	1.69	1.70	1.85
B15S3	200	0.39	28	1.69	1.69	1.85

5.5 YIELD LINE ANALYSIS OF SELECTED STTG BRIDGES

This section discusses the yield line analysis conducted for the 15 pre-selected bridges. The mechanism that was formulated for the HL-93 loading case with the folded plate mechanism was implemented for the calculation of the overstrength factors of the bridges. The expressions for the overstrength factor derived in Section 5.4, modified according to the boundary conditions of the bridges, namely the simply supported, the pinned-fixed and the fixed-fixed condition, and for the trucks accommodated on the deck under HL-93 loading, are used to obtain the results reported in this section.

5.5.1 Bridge 1—NBI #12-102-3256-01-403

The yield line analysis for the first of the bridges is illustrated in Figure 5.16. This is a single-span bridge of 220 ft span length and 32 ft width. The upper-bound and lower-bound overstrength factors calculated using an appropriate factor explained in Equation (5.52) to modify Equation (5.57) to account for the addition of the external work done due to inner wheels of the second truck are Ω_{Upper} = 0.62 and Ω_{Lower} = 0.57 for this bridge. In fact, all the STTG bridges selected for this section are wide enough to accommodate two lanes of HL-93 loading, unlike the bridge of TxDOT Research Project 9-5498.

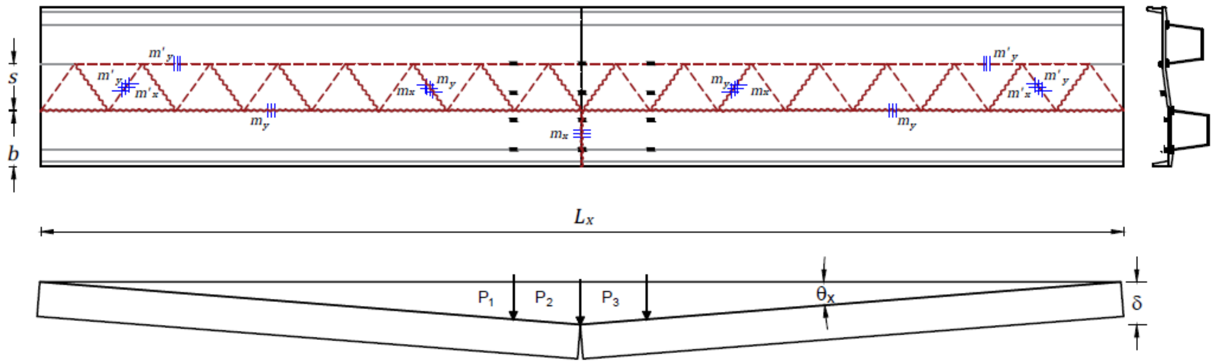

Figure 5.16. Plan, Cross-Section, and Side Elevation with HL-93 Loading for Single-Span Bridges.

5.5.2 Bridge 2—NBI #12-102-0271-17-530

This is a single-span bridge of 115 ft span length and 26.42 ft width. The upper-bound and lower-bound overstrength factors calculated using Equation (5.57) are Ω_{Upper} = 1.17 and Ω_{Lower} = 1.02 for this bridge. Since the span of this bridge is much less than that of Bridge 1, the overstrength factor is higher. It is to be noted that the dimensions of this bridge are comparable to that of the test bridge, and consequently, so is the overstrength factor.

5.5.3 Bridge 3—NBI #12-102-0508-01-294

This is a single-span bridge of 230 ft span length and 38.84 ft width. The upper-bound and lower-bound overstrength factors calculated using an appropriate factor explained in Equation (5.53) to modify Equation (5.56) to account for the addition of the external work done due to both the lines of wheels of the second truck are Ω_{Upper} = 0.51 and Ω_{Lower} = 0.44 for this bridge. Equation (5.53) is applied because the bridge is so wide that the outer wheels also cause a small amount of deflection and, therefore, external work. Since the span length of this bridge is very high, the overstrength factor is low.

Table 5.3 summarizes the input values and the results for the overstrength factors of the test bridge of TxDOT Research Project 9-5498 and single-span STTG bridges using the equations mentioned in Section 5.4.1.4.

Table 5.3. Summary of Overstrength Factors for Single-Span Bridges.

ID	**L_x** ft	**R** ft	**B** ft	**L_x^*** ft	**s** ft	**b** ft	**t** in	**m_x** kip	**m'_x** kip	**m_y** kip	**m'_y** kip	**w_u** ksf	**W_x** kip/ft	**IWD** k-ft	**EWD** k-ft	**Ω UB**	**Ω LB**
9-5498	120	1300	23	121	6.0	8.7	8	16	11	25	20	0.22	0.94	521	357	**1.46**	**1.28**
B1	220	573	32	224	9.5	11.4	8	10	5	27	21	0.22	3.44	605	980	**0.62**	**0.57**
B2	115	1910	26	115	6.1	10.2	8	15	13	23	19	0.22	1.42	478	409	**1.17**	**1.02**
B3	230	2207	39	231	12.6	13.1	9	18	15	27	23	0.23	2.50	543	1065	**0.51**	**0.44**

Note: UB and LB denote upper-bound and lower-bound overstrength factors, respectively.

5.5.4 Bridge 4—NBI #12-102-0271-07-637

Bridge 4 is a two-span bridge with an exterior critical span that is 132 ft long and 28.42 ft wide, and it has the upper-bound and lower-bound overstrength factors of Ω_{Upper} = 1.80 and Ω_{Lower}=1.67. The 128 ft span is not critical since the upper-bound and lower-bound overstrength factors are Ω_{Upper} = 1.85 and Ω_{Lower} = 1.71. Equation (5.52) was used to modify Equation (5.64).

The fixed-end moment causes negative yield line to occur vertically along the width b at the interior continuous support. There will also be additional hinge formation due to the negative moment of the steel tub girder. Both effects are accounted for by the plastic moment capacity of the composite deck at support, M_p^-.

5.5.5 Bridge 5—NBI #14-227-0-0015-13-452

This is a two-span bridge whose exterior span is 140 ft long and 30 ft wide. The upper-bound and lower-bound overstrength factors are Ω_{Upper} = 1.40 and Ω_{Lower} = 1.28 for this span. The other exterior span of 139.58 ft span length has critical upper-bound and lower-bound overstrength factors of Ω_{Upper} = 1.39 and Ω_{Lower} = 1.28. The calculations use the same procedure as that of Bridge 4.

5.5.6 Bridge 6—NBI #12-102-0271-07-575

This is a two-span bridge whose exterior critical spans are both 140 ft long and 38.42 ft wide. The upper-bound and lower-bound overstrength factors are Ω_{Upper} = 1.62 and Ω_{Lower} = 1.52. Equation (5.64) is modified using the appropriate factor mentioned in Equation (5.53) to account for the external work done due to the second truck since the bridge is so wide that the outer wheels of the second truck also cause a small amount of deflection and, consequently, external work. This modification factor is similar to that used for computing the overstrength factor of Bridge 3.

5.5.7 Bridge 7—NBI #12-102-0177-07-394

This is a two-span bridge whose exterior critical span is 219 ft long and 28.42 ft wide. The upper-bound and lower-bound overstrength factors calculated using Equation (5.65) and Equation (5.52) are Ω_{Upper} = 1.45 and Ω_{Lower} = 1.37 for this span. The upper-bound and lower-bound overstrength factors calculated using the same equation for the 190 ft span are Ω_{Upper} = 1.69 and Ω_{Lower} = 1.59.

5.5.8 Bridge 8—NBI #12-102-0271-06-661

This is a 28.42 ft wide two-span bridge whose exterior critical span is 295 ft long. The upper-bound and lower-bound overstrength factors calculated using Equation (5.65) are Ω_{Upper} = 1.25 and Ω_{Lower} = 1.18 for this span. The upper-bound and lower-bound overstrength factors calculated using Equation (5.65) for the 265 ft span are Ω_{Upper} = 1.34 and Ω_{Lower} = 1.27. The modification factor of Equation (5.52) was used.

5.5.9 Bridge 9—NBI #12-102-0177-07-394

This three-span bridge has a width of 28.42 ft and an exterior critical span 140 ft long. The upper-bound and lower-bound overstrength factors are calculated to be Ω_{Upper} = 1.56 and Ω_{Lower} = 1.44 for the exterior critical span and calculated to be Ω_{Upper} = 1.68 and Ω_{Lower} = 1.56 for the other exterior span of 126 ft. Equation (5.65) and Equation (5.61) were used by modifying with the factor explained in Equation (5.52) to find the overstrength factor of the interior span. The fixed-end moments cause negative yield line to occur vertically along a width of b at the two continuous supports of the interior span. There will also be additional hinge formation due to the negative moment of the steel tub girder. Both of these are accounted for by the plastic moment capacities of the composite deck, M_{p1}^{-} and M_{p2}^{-}, at the continuous supports at the left and right ends of the interior span, respectively. For Bridge 9, the interior continuous span, clamped on both ends, is 151 ft long and 28.42 ft wide. The upper-bound and lower-bound overstrength factors are Ω_{Upper} = 2.34 and Ω_{Lower} = 2.24.

5.5.10 Bridge 10—NBI # 14-227-0-0015-13-450

This three-span bridge is 30 ft wide and the exterior critical span is 190 ft long, and the other exterior span is 148 ft long. The upper-bound and lower-bound overstrength factors calculated using Equation (5.65) are Ω_{Upper} = 1.67 and Ω_{Lower} = 1.59 for the exterior critical span and Ω_{Upper} = 1.98 and Ω_{Lower} = 1.88 for the other exterior span. The interior span of length 265 ft and width 30 ft has upper-bound and lower-bound overstrength factors of Ω_{Upper} = 1.90 and Ω_{Lower} = 1.84 that were calculated using Equation (5.62).

5.5.11 Bridge 11—NBI #12-102-0271-07-593

This three-span bridge is 28.42 ft wide; the critical exterior span is 235 ft long and the other exterior span is 223 ft long. The upper-bound and lower-bound overstrength factors calculated using Equation (5.65) are Ω_{Upper} = 1.65 and Ω_{Lower} = 1.59 for the exterior critical span and Ω_{Upper} = 1.75 and Ω_{Lower} = 1.69 for the other exterior span. The interior span, 366 ft long and 30 ft wide, has upper-bound and lower-bound overstrength factors of Ω_{Upper} = 1.69 and Ω_{Lower} = 1.66 that were calculated using Equation (5.62).

5.5.12 Bridge 12—NBI # 12-102-0271-07-639

This three-span bridge is 28 ft wide, the critical exterior span is 145 ft long, and the other exterior span is 140 ft long. The upper-bound and lower-bound overstrength factors calculated using Equation (5.65) are Ω_{Upper} = 1.71 and Ω_{Lower} = 1.60 for the exterior critical span and Ω_{Upper} = 1.75 and Ω_{Lower} = 1.63 for the other exterior span. The interior span, 180 ft long and 28 ft wide, has upper-bound and lower-bound overstrength factors of Ω_{Upper} = 2.20 and Ω_{Lower} = 2.10 that were calculated using Equation (5.62).

5.5.13 Bridge 13—NBI #14-227-0-0015-13-452

This three-span bridge has a width of 30 ft. Both exterior spans are 151.5 ft long, but with differing girder dimensions. The upper-bound and lower-bound overstrength factors calculated using Equation (5.65) are Ω_{Upper} = 1.40 and Ω_{Lower} = 1.30 for the exterior critical span and Ω_{Upper} = 1.41 and Ω_{Lower} = 1.32 for the other exterior span. The 190 ft long, 30 ft wide interior span has upper-bound and lower-bound overstrength factors of Ω_{Upper} = 1.89 and Ω_{Lower} = 1.80 that were calculated using Equation (5.62).

5.5.14 Bridge 14—NBI #18-057-0-0009-11-460

This three-span bridge has a width of 28 ft; both the exterior spans are 150 ft long. The upper-bound and lower-bound overstrength factors calculated using Equation (5.65) are Ω_{Upper} = 1.63 and Ω_{Lower} = 1.52 for both. The 190 ft long, 28 ft wide interior span has upper-bound and lower-bound overstrength factors of Ω_{Upper} = 2.07 and Ω_{Lower} = 1.98 that were calculated using Equation (5.62).

5.5.15 Bridge 15—NBI #12-102-0271-06-689

This three-span bridge has a width of 28 ft, and both exterior spans are 200 ft long, but with differing girder dimensions. The upper-bound and lower-bound overstrength factors calculated using Equation (5.65) are Ω_{Upper} = 1.69 and Ω_{Lower} = 1.59 for the exterior critical span and Ω_{Upper} = 1.70 and Ω_{Lower} = 1.60 for the other exterior span. The 295 ft long, 28 ft wide interior span has upper-bound and lower-bound overstrength factors of Ω_{Upper} = 1.86 and Ω_{Lower} = 1.78 that were calculated using Equation (5.65).

It is to be noted that Bridges 9–15 use the modification factor defined in Equation (5.52) for both exterior and interior spans to account for the external work done by the HS-20 truck load of the second lane.

Table 5.4 and Table 5.5 summarize the input values and the results for the bridges to obtain the overstrength factors of the exterior and interior spans of the STTG bridges using the equations mentioned in Section 5.4.3.

Table 5.4. Summary of Overstrength Factors for Exterior Spans.

ID	L_x ft	R ft	B ft	L_x^* ft	s ft	b ft	t in	m_x kip	m'_x kip	m_y kip	m'_y kip	$0.5M_p^-$ k-ft	w_u ksf	W_x kip/ft	IWD k-ft	EWD k-ft	Ω UB	Ω LB
B4S1	132	195	28	137	8	10.4	9	14	13	25	21	34362	0.23	1.44	899	499	**1.80**	**1.67**
B4S2	128	195	28	133	8	10.4	9	14	13	25	21	34362	0.23	1.42	900	487	1.85	1.71
B5S1	140	450	30	142	10	10.2	8	12	9	23	19	26450	0.22	0.95	683	490	1.40	1.28
B5S2	140	450	30	142	10	10.2	8	12	9	23	19	26450	0.22	0.99	683	491	**1.39**	**1.28**
B6S1	140	819	38	142	10	14.3	8	15	13	29	24	52716	0.22	1.74	1087	671	**1.62**	**1.52**
B6S2	140	819	38	142	10	14.3	8	15	13	29	24	52716	0.22	1.74	1087	671	**1.62**	**1.52**
B7S1	219	764	28	221	7	10.5	8	15	11	20	17	60107	0.22	1.85	1060	733	**1.45**	**1.37**
B7S2	190	764	28	191	7	10.5	8	15	11	20	17	60107	0.22	1.53	1058	628	1.69	1.59
B8S1	265	882	28	267	8	10.0	8	15	12	23	19	69672	0.22	2.02	1177	876	1.34	1.27
B8S2	295	882	28	297	8	10.0	8	15	12	23	19	69672	0.22	2.13	1209	971	**1.25**	**1.18**
B9S1	140	764	28	141	7	10.5	8	15	11	20	17	29774	0.22	1.32	763	490	**1.56**	**1.44**
B9S3	126	764	28	127	7	10.5	8	15	11	20	17	29774	0.22	1.33	768	458	1.68	1.56
B10S1	148	716	30	150	8	11.2	8	12	9	21	17	58368	0.22	1.42	1070	541	1.98	1.88
B10S3	190	716	30	192	8	11.2	8	12	9	21	17	64603	0.22	1.46	1082	648	**1.67**	**1.59**
B11S1	223	819	28	225	7	10.7	8	14	11	21	17	150362	0.22	4.21	1770	1010	1.75	1.69
B11S3	235	819	28	237	7	10.7	8	14	11	21	17	150362	0.22	4.24	1745	1058	**1.65**	**1.59**
B12S1	140	225	28	144	8	10.4	9	13	10	25	21	35482	0.23	1.47	907	519	1.75	1.63
B12S3	145	225	28	150	8	10.4	9	13	10	25	21	35482	0.23	1.44	908	530	**1.71**	**1.60**
B13S1	152	450	30	154	9	10.3	8	12	9	21	17	35873	0.22	1.13	749	530	1.41	1.32
B13S3	152	450	30	154	9	10.3	8	12	9	21	17	35873	0.22	1.21	749	536	**1.40**	**1.30**
B14S1	150	1010	28	151	7	10.8	8	14	10	21	17	31546	0.22	1.40	839	515	**1.63**	**1.52**
B14S3	150	1010	28	151	7	10.8	8	14	10	21	17	31546	0.22	1.40	839	515	**1.63**	**1.52**
B15S1	200	809	28	202	8	10.2	8	16	14	25	21	61187	0.22	1.83	1164	685	1.70	1.60
B15S3	200	809	28	202	8	10.2	8	16	14	25	21	61187	0.22	1.85	1164	687	**1.69**	**1.59**

Table 5.5. Summary of Overstrength Factors for Interior Spans.

ID	L_x ft	R ft	B ft	L_x^* ft	s ft	b ft	t in	m_x kip	m'_x kip	m_y kip	m'_y kip	$0.5M_{p1}^-$ k-ft	$0.5M_{p2}^-$ k-ft	w_u ksf	W_x kip/ft	IWD k-ft	EWD k-ft	Ω UB	Ω LB
B9S2	151	764	28	153	7.4	10.5	8	15	11	20	17	29774	29774	0.22	1.37	1218	520	**2.34**	**2.24**
B10S2	265	716	30	268	7.7	11.2	8	12	9	21	17	58368	64603	0.22	1.61	1620	851	**1.90**	**1.84**
B11S2	366	819	28	369	7.0	10.7	8	14	11	21	17	150362	150362	0.22	4.41	2663	1573	**1.69**	**1.66**
B12S2	180	225	28	186	7.6	10.4	9	13	10	25	21	35482	35482	0.23	1.61	1384	629	**2.20**	**2.10**
B13S2	190	450	30	193	9.3	10.3	8	12	9	21	17	35873	35873	0.22	1.21	1180	625	**1.89**	**1.80**
B14S2	190	1010	28	191	6.5	10.8	8	14	10	21	17	31546	31546	0.22	1.45	1264	611	**2.07**	**1.98**
B15S2	295	809	28	298	8.0	10.2	8	16	14	25	21	61187	61187	0.22	1.97	1755	944	**1.86**	**1.78**

Note: UB and LB denote upper-bound and lower-bound overstrength factors, respectively.

5.6 CLOSURE

In this chapter, yield line theory was developed so that it can be applied to twin tub girder bridges with one tub completely fractured. First, the general yield line methodology was validated for a test bridge loaded to failure with a large load of sand on the mid-span region.

Second, the yield line theory was adapted using both upper- and lower-bound approaches for the class of curved twin tub bridges investigated herein. Finally, the theory was applied to the 15 bridges investigated in these results. The results were tabulated for each span type: (a) simply supported, (b) both ends continuous; and (c) one end continuous plus the abutment simply supported (free). Table 5.6 summarizes the overstrength factors for the test bridge of TxDOT Research Project 9-5498 and the 15 preselected STTG bridges with the overstrength factors of the critical spans presented in boldface.

Some of the conclusions drawn from the results of yield line analysis are as follows:

- The critical mechanism postulated to predict the capacity of the test bridge was validated using the experimental results. The collapse load calculated using the yield line analysis was 353 kip, while the experiment conducted during TxDOT Research Project 9-5498 gave a load of 358 kip. The yield line result is 1.40 percent lower than the reported collapse load.
- The analysis modified the yield line theory to account for the stud failure.
- The analysis of the bridges under the HL-93 loads results in a mechanism that makes use of torsional folded-plate action. This mechanism ensures the estimation of critical capacity after several trials.
- The simple-span bridges with the span lengths of 115 ft and 120 ft have upper-bound overstrength factors of 1.17 and 1.46, respectively, while those with the span lengths of 220 ft and 230 ft have upper-bound overstrength factors of 0.62 to 0.51, respectively.
- The exterior spans have upper-bound overstrength factors ranging from 1.25 to 1.98 depending on the length of the span and the variation of the girder geometry along the span.
- The interior spans have overstrength factors ranging from 1.69 to 2.34 depending on the length of the span.
- The redundancy due to the continuity at supports contributes to a greater strength, as evidenced by the higher overstrength factors of the exterior and interior spans when compared to those of the simply supported single spans. The general order is that the interior spans have the most load bearing capacity, the exterior spans have the next highest load bearing capacity, and the single-span bridges are weakest in comparison,

especially for long span bridges having span length greater than 120 ft, as seen in the case of Bridges 1 and 3.

- The width of the bridges, however, is observed to not have as substantial an impact as that of the length of the span and boundary conditions in the case of yield line analysis. This phenomenon is because the external work done due to the second truck considered for the computation of the overstrength factor of the wider bridges does not change the overall outcome significantly since the deflections under the second HS-20 truck are of smaller magnitude.
- The overall analysis is conservative because the guardrail is disengaged in this analysis. This assumption is reasonable since the guardrail is not constructed as a uniformly continuous entity due to the presence of expansion joints. Moreover, crushing of the guardrail under compression is reported to have taken place during the failure of the test bridge, as mentioned by Barnard et al. (2010). Therefore, it is reasonable to not count on any strength from the guardrail since it may lead to an incorrectly higher estimate of the strength of the bridge.

These results are further discussed and compared in Chapter 7.

Table 5.6. Overstrength Factors for 15 Selected STTG Bridges.

Bridge ID	**Radius of curvature ft**	**Width, B ft**	**Span, L_x ft**	**Overstrength Factor $\Omega_{\text{yield Line}}$**	
9-5498	1300	23	120	**1.46**	**1.28**
1	573	32	220	**0.62**	**0.57**
2	1910	26	115	**1.17**	**1.02**
3	2207	39	230	**0.51**	**0.44**
4-S1	195	28	132	**1.80**	**1.67**
4-S2		28	128	1.85	1.71
5-S1	450	30	140	1.40	1.28
5-S2		30	140	**1.39**	**1.28**
6-S1	819	38	140	**1.62**	**1.52**
6-S2		38	140	**1.62**	**1.52**
7-S1	764	28	219	**1.45**	**1.37**
7-S2		28	190	1.69	1.59
8-S1	819	28	265	1.34	1.27
8-S2		28	295	**1.25**	**1.18**
9-S1	764	28	140	**1.56**	**1.44**
9-S2		28	151	2.34	2.24
9-S3		28	126	1.68	1.56
10-S1	716	30	148	1.98	1.88
10-S2		30	265	1.90	1.84
10-S3		30	190	**1.67**	**1.59**
11-S1	819	28	223	1.75	1.69
11-S2		28	366	1.69	1.66
11-S3		28	235	**1.65**	**1.59**
12-S1	225	28	140	1.75	1.63
12-S2		28	180	2.20	2.10
12-S3		28	145	**1.71**	**1.60**
13-S1	450	30	151	1.41	1.32
13-S2		30	190	1.89	1.80
13-S3		30	151	**1.40**	**1.30**
14-S1	1010	28	150	**1.63**	**1.52**
14-S2		28	190	2.07	1.98
14-S3		28	150	**1.63**	**1.52**
15-S1	809	28	200	1.70	1.60
15-S2		28	295	1.86	1.78
15-S3		28	200	**1.69**	**1.59**

Note: The boldface type value for Ω is the critical (lowest Ω) case for the bridge concerned.

6 PARAMETRIC STUDY FOR STEEL TWIN TUB GIRDER BRIDGES USING GRILLAGE METHOD PUSH-DOWN ANALYSIS

6.1 INTRODUCTION

This task consisted of a parametric study involving a selection of 15 preselected typical STTG bridges from the Texas bridge inventory utilizing a Grillage Method Push-down Analysis. These 15 bridges are the same bridges evaluated using the FEM in Chapter 4. The grillage method employed was verified using the static ultimate load test results of the STTG bridge tested in TxDOT Research Project 9-5498 (Barnard et al. 2010). The TxDOT project consisted of testing a full-scale fracture critical steel box-girder bridge under simulated HS-20 truck loading and at ultimate loading with a full-depth fracture on the exterior girder.

This task evaluated the performance of existing fracture critical STTG bridges in the event of a full-depth web fracture of one of the girders. The 15 bridges under evaluation vary with respect to span lengths, degree of curvature, and continuity. These variables are the most critical geometric properties for determining the response of a bridge to load distribution between girders.

Grillage models were created using the commercial software package SAP2000, which is a structural analysis program that utilizes the matrix structural analysis approach to solve and evaluate structural engineering problems. All the grillage bridge models have used nonlinear elasto-plastic material and hinge properties due to the nonlinear behavior of the reinforcing bars, steel plates, and concrete during concrete crushing and steel yielding under ultimate loading conditions. The grillage models were analyzed under the factored HL-93 live loading model. This loading pattern consists of HS-20 truck loading as well as a uniformly distributed lane load. Per AASHTO LRFD Bridge Design Specifications AASHTO (2017), the load demands were 1.25DL + 1.75(LL + IM), where DL, LL, and IM represent respectively dead load, live load, and impact factor.

The bridges evaluated utilizing the grillage method were analyzed twice: (1) analysis of the bridge with the intact girder condition, and (2) analysis of the bridge with a full-depth girder fracture for one of the tub girders. The intact bridge analysis provides information about the initial stiffness of the intact bridge as well as the overstrength factor for the nonfractured case.

The second analysis is for simulating the ultimate load behavior when one of the girders are fractured. A predefined overstrength factor was determined for both the fully intact case and one fractured girder case to assess the load carrying capacity of both cases under critical loading. The grillage method allows for load redistribution from the fractured girder through the lateral deck slab members.

The next section describes the grillage method and material models used for all evaluated bridges. The following section gives the load displacement results of the grillage models as well as their respective overstrength factor results.

6.2 GRILLAGE METHOD PUSH-DOWN ANALYSIS

6.2.1 Introduction

The grillage method is a computational variation of the strip method, both of which are conservative lower-bound solutions. Designers have employed the strip method due to its ability to quickly generate solutions by hand. Like the strip method, the grillage method models the bridge deck and beam elements as a grillage of beams. The longitudinal grillage members consist of the steel tub girders, the concrete deck with longitudinal reinforcement, and the guardrail. The transverse grillage members are bridge deck components with transverse reinforcement.

The grillage method was originally developed in the 1950s by Lightfoot and Sawko (1959). Created in the primitive days of matrix structural analysis, the grillage method was utilized to divide a bridge deck into equivalent longitudinal and transverse beam members that resembled a grillage. Due to the increase in technological abilities through programs such as SAP2000, this method has increased in accuracy. Surana and Agrawal (1998) studied the grillage method of analysis as it applies to various bridge types. When compared with other methods of analysis, including FEM, the grillage method of analysis was found to be an accurate and valid modeling technique.

Grillage models of the preselected 15 bridges were created and analyzed using the structural analysis software SAP2000 Version 19 (Computers and Structures 2017). The grillage models were expected to capture the constitutive material behavior and boundary condition to be able to accurately predict load displacement behavior and the ultimate load capacity of the analyzed bridge. For all 15 bridges, the support conditions were modeled using springs with a lateral stiffness of 6 kip/in. and a vertical stiffness of 3050 kip/in. These values are conducive with the stiffness values used in the elastomeric bearing pads at the support locations in the bridges. Appropriate steel and concrete nonlinear material models were used to ensure appropriate modeling of bridge behavior under the ultimate loading conditions.

6.2.2 Material Models

Grillage models generated for the 15 bridges in the parametric study were created using similar material models utilized in the FEM modeling approach. Nonlinear material models were used for the grillage analysis of the bridges due to the concrete crushing and yielding of the steel plates and reinforcing bars. The steel model used for both reinforcing bars and steel plates assume nonlinear elastic-plastic behavior with strain hardening. The mechanical constitutive model of concrete considers nonlinear inelastic behavior up to peak stress level without damage mechanics. Therefore, it assumes perfectly plastic behavior beyond peak compressive and tensile stress.

6.2.2.1 Steel Material Model

The built-up plate components of the STTG bridges are comprised of Grade 50 structural steel. The classical metal plasticity models with strain hardening simulated the constitutive behavior of both the steel members and reinforcing bars. The nonlinear steel models assumed a perfectly plastic behavior once the yield stress was reached. The reinforcing bar in both the longitudinal and transverse directions, as well as in the railings, consists of Grade 60 ASTM A615 steel. Figure 6.1 shows the stress-strain relationship of both the plate steel and reinforcing bars. Both steel plate and rebar constitutive behavior were obtained from material tests conducted on actual specimens as part of TxDOT Research Project 9-5498 (Barnard et al. 2010)

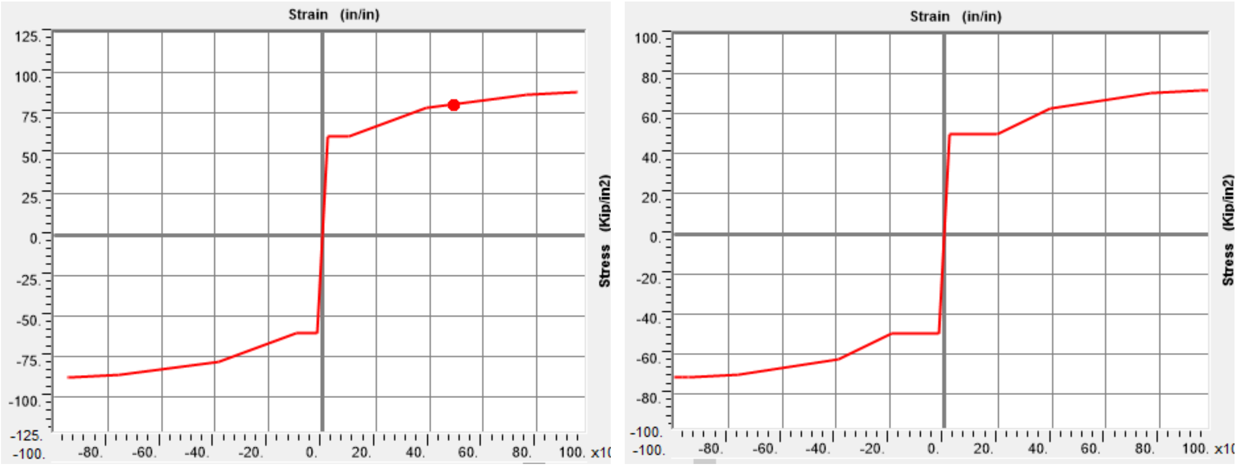

a) Reinforcing Bar *b) Steel Plate*

Figure 6.1. Constitutive Model for Steel Members (from SAP2000).

6.2.2.2 Concrete Material Model

The constitutive concrete behavior was defined using the Kent and Park (1971) model, the same model used in the FEM analysis, with a design strength of 4000 psi. After reaching ultimate compressive and tensile forces, the concrete behavior is assumed to be perfectly plastic.

Figure 6.2 shows the stress-strain behavior of the concrete used for the grillage models. The tensile strength of the concrete was calculated using the empirical equation in AASHTO (2017) Article 5.4.2.6 as:

$$f_r = 0.2\sqrt{f'_c} \tag{6.1}$$

where, f_r = the modulus of rupture (ksi) and f'_c = compressive strength of concrete (ksi). The modulus of elasticity of concrete for different strength capacities were calculated using an empirical equation from AASHTO (2017) Article 5.4.2.4 as:

$$E_c = 33000K_1 w_c^{1.5}\sqrt{f'_c} \tag{6.2}$$

where K_1 = correction factor for aggregate source, which is assumed to be 1.0 unless determined by physical test; w_c = unit weight of concrete (kcf)—0.145 is assumed for normal weight concrete; and f'_c = compressive strength of concrete (ksi).

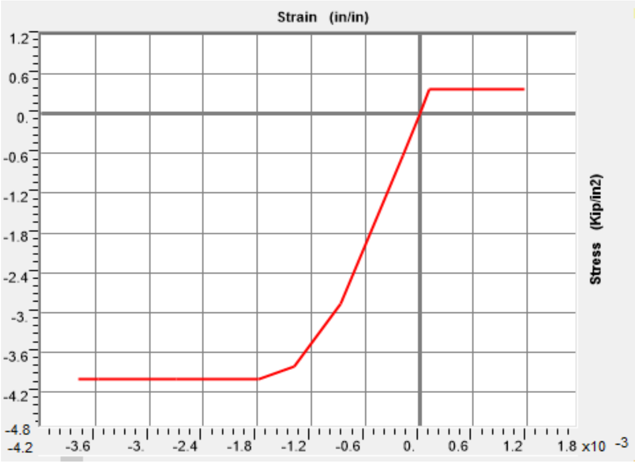

Figure 6.2. Constitutive Model of Concrete (from SAP2000).

The constitutive model from SAP2000 indicates that beyond compressive crushing and tensile rupturing, the strength is maintained. This behavior was utilized in order to be consistent with the FEM modeling approach and to avoid convergence issues in SAP2000.

6.2.3 Grillage Beam Elements

Hambly and Pennells (1975) and Barker and Puckett (2007) have established guidelines for the construction and location placement of beam elements. It is recommended that each grillage member take on the same bending and torsional properties of their representative bridge sections. For the case of slab-on-girder bridges, the longitudinal beam element should be placed along the centerline of the girder. Since the twin tub girders are so wide, in this grillage analysis they were divided in half, and the centerline of the top flange was used as the centerline for the placement of grillage elements. This process maintains the stiffness at the appropriate location within the bridge structure and appropriate load distribution. Lateral beam members should be placed at appropriate locations. Grillage members should be positioned in locations of high stress and forces. High force and stress locations could include interior and exterior supports and point load locations. To assure accurate load distribution, it is important that the longitudinal and transverse members are equally gaged in both directions.

The exterior longitudinal members (Figure 6.3a) consist of the guardrail, the deck from the outside edge to the center of the tub girder—including corresponding reinforcing bars, and half of the tub girder. The interior longitudinal members (Figure 6.3b) consist of the deck from the center of the tub girder to the centerline of the bridge, with corresponding reinforcing bars, and half of the tub girder. The transverse members (Figure 6.4a-b) consist of the deck slab and transverse reinforcing bars. The longitudinal members are placed along the centerline of each of the four top flange members of the tub girders. The transverse members are placed at 7 ft increments along the interior with varying spacing at the end supports. Figure 6.5 is a representative grillage schematic of a grillage model.

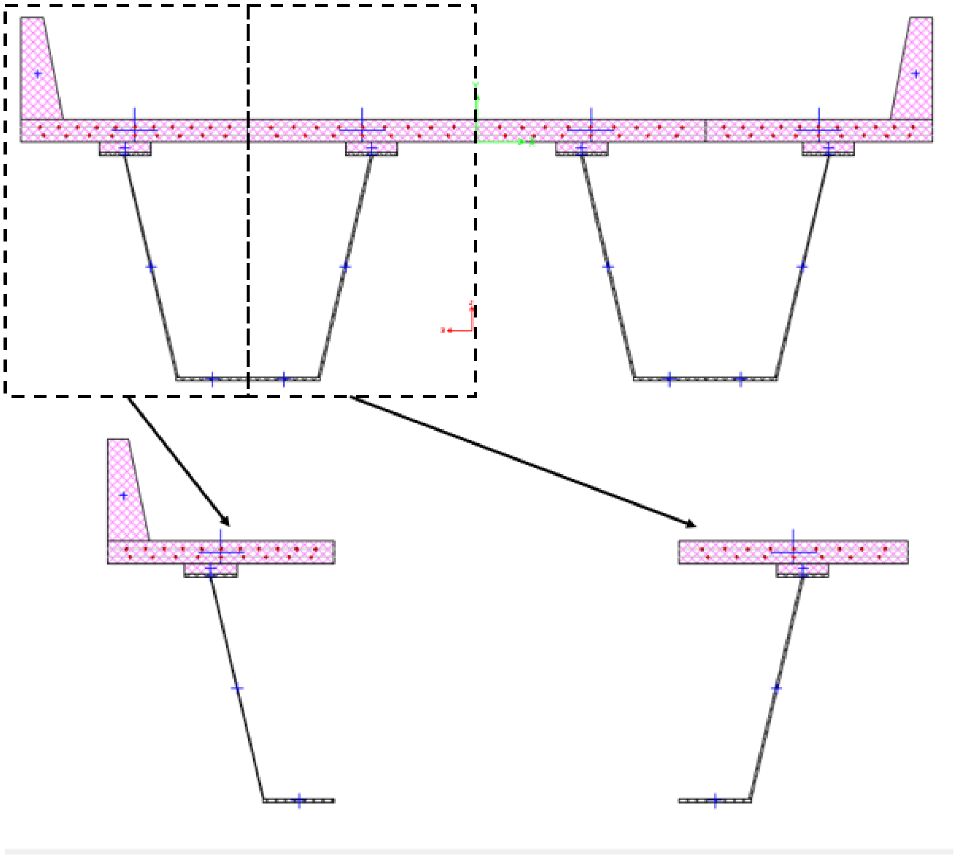

a) Exterior Longitudinal Member b) Interior Longitudinal Member

Figure 6.3. Representative Longitudinal Grillage Members.

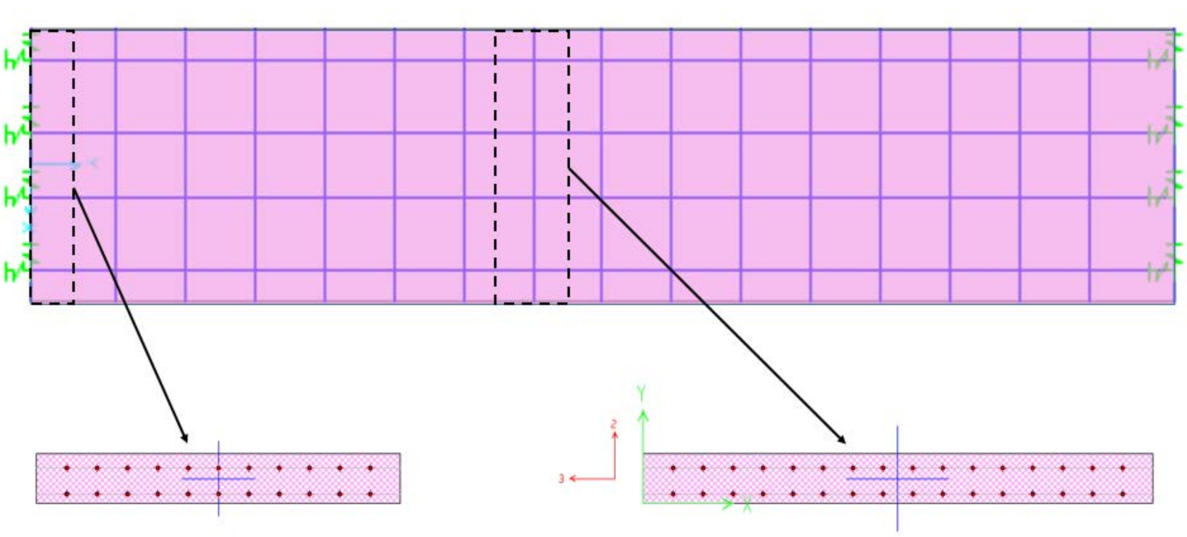

a) Exterior Transverse Member b) Interior Transverse Member

Figure 6.4. Representative Transverse Grillage Members.

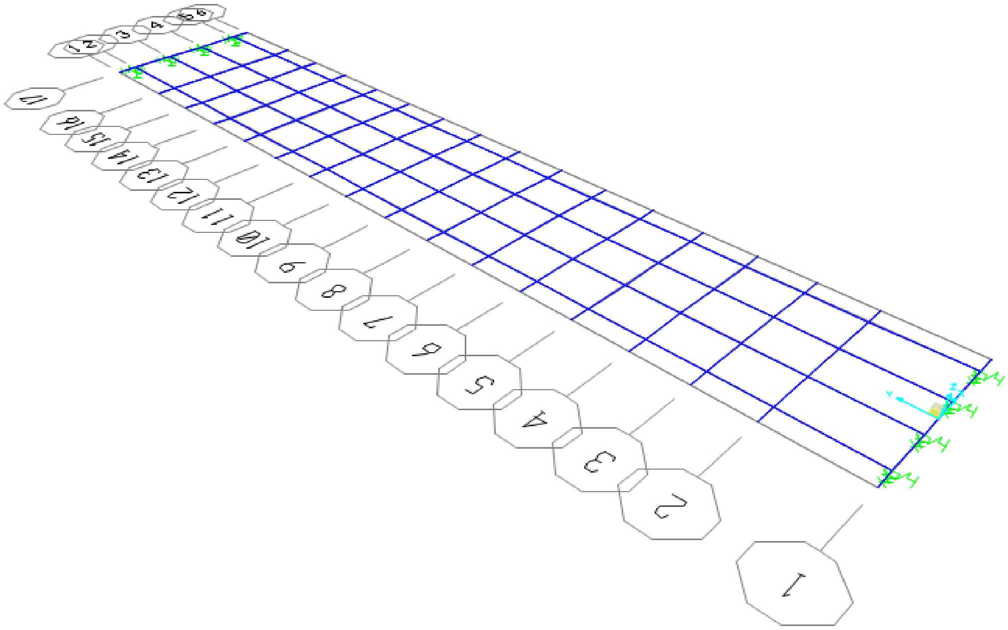

Figure 6.5. Representative Grillage Schematic.

6.2.4 Grillage Plastic Hinges

To capture the nonlinear behavior of the bridge during ultimate loading conditions, the nonlinear static analysis approach, also known as push-down analysis, was used. Incorporating this approach reduces the uncertainty and conservatism inherently existing in elastic analysis.

Since the bridge superstructure is modeled as grillage of beam elements, inelastic behavior is achieved by using plastic hinges at the anticipated hinge locations. The hinges used are moment controlled (M3) in the global Z (or gravitational) direction. Longitudinal and transverse hinges were developed using the moment curvature responses of the individual cross-sections. The individual cross-sections were generated using the section designer tool in SAP2000, which allows the user to combine the concrete, reinforcing bars, and steel plates into one composite grillage member. Once the member is created, SAP2000 has a moment curvature feature within the section designer that generates the moment curvature response of the composite section. In the case of the fractured longitudinal plastic hinge, the bottom flange and web were removed prior to generating the moment curvature diagram.

The length of the plastic hinge was taken to be half of the depth of the member in both the transverse and longitudinal directions. Two of the most prominent hinge length expressions for reinforced concrete beam elements in flexure were developed by Corley (1966) and Mattock (1967), represented as Equations (6.3) and (6.4) respectively:

$$l_p = 0.5d + 0.5\sqrt{d}(z/d) \tag{6.3}$$

$$l_p = 0.5d + 0.05(z) \tag{6.4}$$

where l_p = plastic hinge length, d = member depth, and z = distance from hinge to node location. For the purposes of this section, the hinge was located at the point of contra flexure, therefore driving the value of z to 0. The remaining portions of both expressions reduces to half the member depth value.

A representative external longitudinal intact plastic hinge is shown in Figure 6.6. For convergence requirements, once the maximum moment value was reached, a perfectly plastic assumption was made, and the maximum moment was maintained for all further rotation. Perfectly plastic assumption is acceptable because the aim was to identify the ultimate load, not the post-peak-load degradation of the structure.

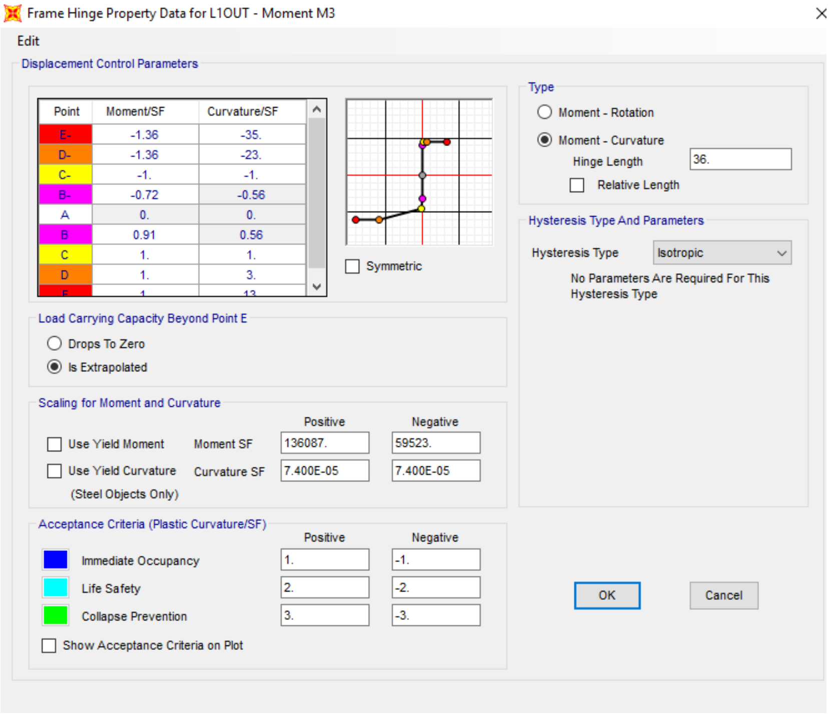

Frame Hinge Property Data for L1OUT - Moment M3

Edit

Displacement Control Parameters

Point	Moment/SF	Curvature/SF
E-	-1.36	-35.
D-	-1.36	-23.
C-	-1.	-1.
B-	-0.72	-0.56
A	0.	0.
B	0.91	0.56
C	1.	1.
D	1.	3.
E	1.	13.

☐ Symmetric

Load Carrying Capacity Beyond Point E

○ Drops To Zero

● Is Extrapolated

Scaling for Moment and Curvature

		Positive	Negative
☐ Use Yield Moment	Moment SF	136087.	59523.
☐ Use Yield Curvature	Curvature SF	7.400E-05	7.400E-05
(Steel Objects Only)			

Acceptance Criteria (Plastic Curvature/SF)

	Positive	Negative
Immediate Occupancy	1.	-1.
Life Safety	2.	-2.
Collapse Prevention	3.	-3.

☐ Show Acceptance Criteria on Plot

Type

○ Moment - Rotation

● Moment - Curvature

Hinge Length: 36.

☐ Relative Length

Hysteresis Type And Parameters

Hysteresis Type: Isotropic

No Parameters Are Required For This Hysteresis Type

Figure 6.6. Representative Plastic Hinge Property (SAP2000).

For the longitudinal members, the hinges were placed at both ends of the longitudinal beam elements. For the transverse members, the hinges were placed at the edge of the top flanges, or half a flange length from each node.

6.2.5 Simulating HL-93 Loading

In simulating the HL-93 loading, it was critical to place the HS-20 truck load and the uniform lane load at the appropriate critical locations (shown in Figure 6.7). The interior transverse grillage beams were placed at 7 ft increments to have a grillage member at locations corresponding to the axles of an HS-20 truck that has axle spacing of 14 ft. The center axle of the truck load was placed at the mid-span. An HS-20 truck consists of 32 kip middle and rear axles and 8 kip front axle for a total of 72 kip. The distance between wheel lines of the truck is 6 ft.

When the two-lane bridges were analyzed, the first lane, which is 12 ft wide, was defined as close as possible to the outside edge of the curved bridge to create the most adverse loading condition when the outside girder has a full-depth web fracture. AASHTO LRFD (2017) requires that a design lane should be at least 2 ft away from the nominal rail face, which is generally one ft away from the edge of the deck. To create the most adverse loading conditions, both the HS-20 truck and the uniform lane load were placed at the outside edge of the design lane. For the first lane loading, the first wheel line of the truck was placed 3 ft from the edge of the deck (at the outside edge of the first lane), and per the HS-20 definition, the second wheel line was located 6 ft from the first wheel line. The standard uniform lane load is distributed to 10 ft width and starts at 3 ft from the outside edge of the deck and ends at 13 ft from the deck edge. Therefore, the uniform lane load for the first lane was modeled by a lane load of 0.64 kip/ft along the longitudinal members located 8 ft from the outer edge of the bridge. Since the lane load generally occurred between two grillage members, an equivalent load was distributed appropriately to each of the grillage members. The second lane loading is the same as the first one; however, it begins at the edge of the second lane, which is 15 ft away from the outer edge of the deck.

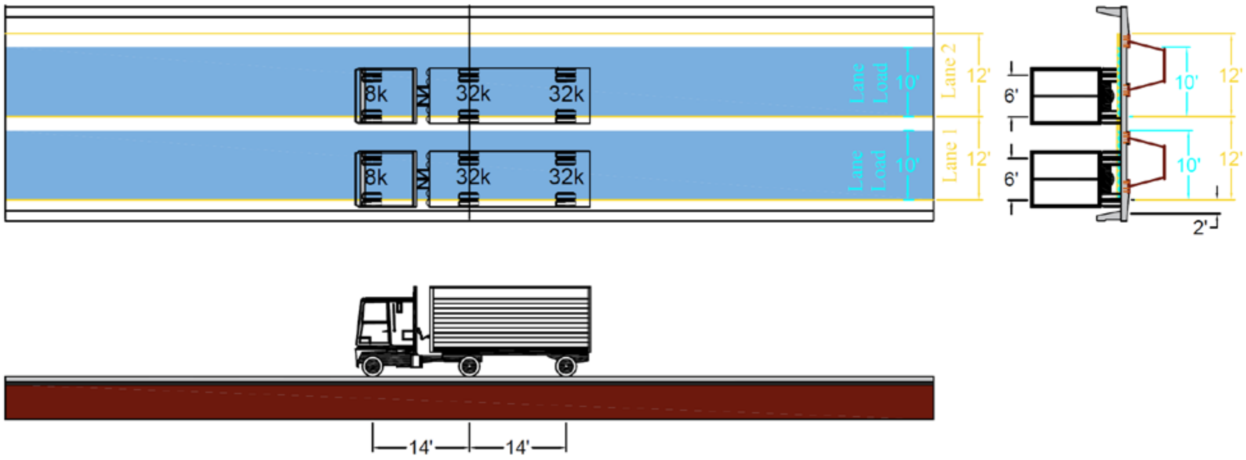

Figure 6.7. HL-93 Loading Diagram for Two-Lane Loaded Case.

Each bridge was first analyzed in its intact condition with no fractures. Subsequently, the fractured model for each bridge was analyzed. Load steps were generated for the two lanes loaded cases as follow: 1.25DL + 1.75LL + 1.75(HS-20 +IM), where DL is dead load, LL is lane load, IM = 33 percent impact load, and HS-20 is the HS-20 truck load.

The intact bridge was analyzed first. The grillage members were generated in SAP2000's section designer. Using the moment curvature feature within the section designer, researchers produced the moment curvature output for each of the transverse and longitudinal members in the bridge. Plastic hinges were developed for each of the intact members based on the moment curvature criteria produced from the section designer. The longitudinal and transverse grillage members were then arranged in a grillage array that adequately represented the geometry for the bridge. End spring supports were then added to represent the elastomeric bearing pads.

Appropriate section hinges were added to each node, or crossing, of longitudinal and transverse members. HS-20 truck loads and lane loads were appropriately defined and assigned to the correct grillage elements. The standard load case was then defined as 1.25DeadLoad + 1.75LaneLoad + 2.33HS-20Load. The first loading step began at a zero stress state, and each additional load case began at the final loading and displacement of the preceding load case. Each load step was applied to the bridge in 20 increments. Load steps were continually applied to the bridge until the stiffness reduced to 5 percent of the initial stiffness of the intact bridge.

After the analysis of the intact bridge, the bridge was evaluated in its fractured state. Once the analysis of the intact bridge was complete, a copy of both the exterior and interior longitudinal sections at mid-span were created. The bottom flanges and webs were removed in both sections to mimic a full web fracture. Researchers used the section designer to generate moment curvature plots for each of the sections and compatible hinges. At mid-span of the intact bridge, the exterior and interior longitudinal hinges were then replaced on the heavily loaded side of the bridge with the representative fractured hinges. The bridge was then analyzed under the same loading sequence as the intact bridge, starting from a state of zero stress with continuous additions of the standard load case in 1/20 th increments until either the stiffness was reduced to 5 percent of the stiffness of the intact bridge, the transverse rotation was greater than 5°, or the longitudinal rotation was greater than 3° for the exterior spans and greater than 2° for the interior spans.

SAP2000 has a load case feature called staged loading that allows certain loads to be applied to certain members during various stages of construction. An example is applying the dead load of the tub girder and the weight of the concrete slab to only the tub girder of the composite member while applying the live loads and impact loads to the composite deck and tub girder member. Staged loading would have allowed a more accurate representation of the true load displacement nature of both the intact and fractured bridge spans. However, it could not be utilized in the fractured bridge case because staged loading does not allow for frame section or plastic hinge substitutions during mid-loading. For comparative purposes, the intact and fractured bridges were loaded from a zero stress state in complete composite action.

6.3 GRILLAGE ANALYSIS OF SELECTED STTG BRIDGES

To successfully gage the redundancy of the 15 STTG bridges, it was important to establish a quantitative measurement of the remaining strength in the bridge beyond the factored design load demand. An overstrength factor was established to measure the residual strength and is defined as:

$$\Omega = R_d/Q_u \tag{6.5}$$

where R_d = capacity of the damaged bridge, and Q_u = factored load demand. Bridges where $\Omega > 1.0$ are considered redundant and have enough reserve capacity postfracture. In this section, redundancy levels are established via the grillage results using design material properties. The loading condition, as per AASHTO LRFD Bridge Design Specifications AASHTO (2017), used was 1.25DL + 1.75(HS20 + IM) + 1.75LL, where DL, LL, and IM are dead load, uniform lane load, and impact factor, respectively.

6.3.1 Grillage Analysis of Bridge 0—FSEL: TxDOT Project # 0-6937

The FSEL Test Bridge included in TxDOT Project 0-6937 is a simple-span straight bridge used for research purposes and for method verification earlier in this project. The FSEL test bridge has a span length of 120 ft, a bridge width of 23 ft 4 in, and an 8-in. deck. The FSEL test bridge was evaluated using the established grillage method. It should be noted that due to the narrow road width, only one lane of HL-93 loading was used to evaluate the postfracture redundancy.Table 6.1 and Table 6.2 list the necessary details for the Bridge FSEL (0).

Table 6.1. Geometric Details of Steel Tub Girders for Bridge FSEL (0).

Location ft	Top Flange		Web		Bottom Flange	
	Width in.	Thickness in.	Width in.	Thickness in.	Width in.	Thickness in.
0–120	12	0.625	57	0.5	47	0.75

Table 6.2. General Geometric Properties of Bridge FSEL (0).

Location	Parameter	Description/Value
Bridge	Length, ft	120
	Spans, ft	120
	Radius of Curvature, ft	-
	Width, ft	23.333
Deck	Thickness, in.	8
	Haunch, in.	4
	Rail Type	T501
Rebar	# of Bar Longitudinal Top Row (#4)	32
	# of Bar Longitudinal Bottom Row (#5)	30
	Transverse Spacing Top Row (#5)	6
	Transverse Spacing Bottom Row (#5)	6

Figure 6.8 depicts the displacement profile with activated hinges of the FSEL bridge. Figure 6.9 shows the grillage analysis results of the FSEL bridge. The solid lines indicate the behavior of the outside girder, and the dashed lines indicate the behavior of the inside girder. The blue color represents the load displacement results for the fractured model, and the green represents the load displacement results of the intact model. The ultimate load capacity of the fracture bridge model is indicated by a blue diamond symbol. The ultimate load capacity of the bridge is defined as the lowest of the following: when the stiffness of the bridge falls below 5 percent of the initial stiffness of the intact outside girder, or the transverse rotation is greater than 5 degrees, or the longitudinal rotation is greater than 2 degrees.

The fractured FSEL bridge fails under HL-93 loading at an overstrength factor of 1.07 via longitudinal rotation, and the intact bridge fails under stiffness control at an overstrength value of 2.55.

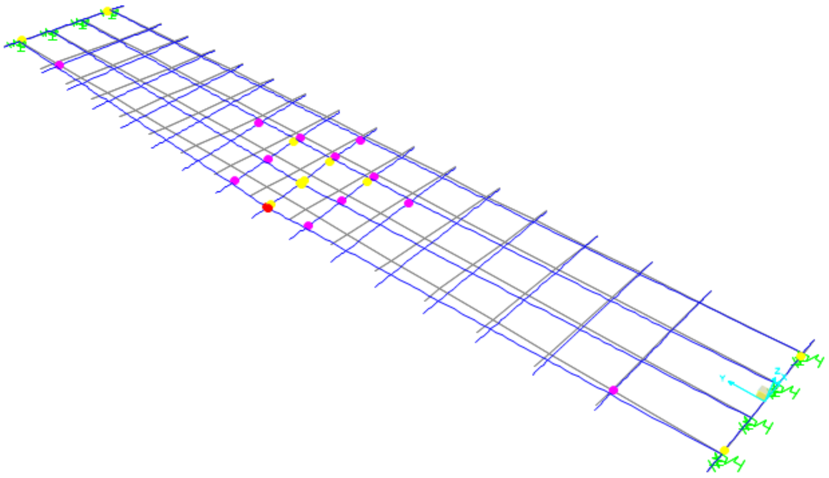

Note: The colors represent achieved curvature limits (magenta = yielding, yellow = beyond yielding, orange = beyond yielding close to failure, red = failure). Additional hinge data are located in Appendix B.

Figure 6.8. Grillage Deflection Profile of FSEL Bridge with Activated Hinges.

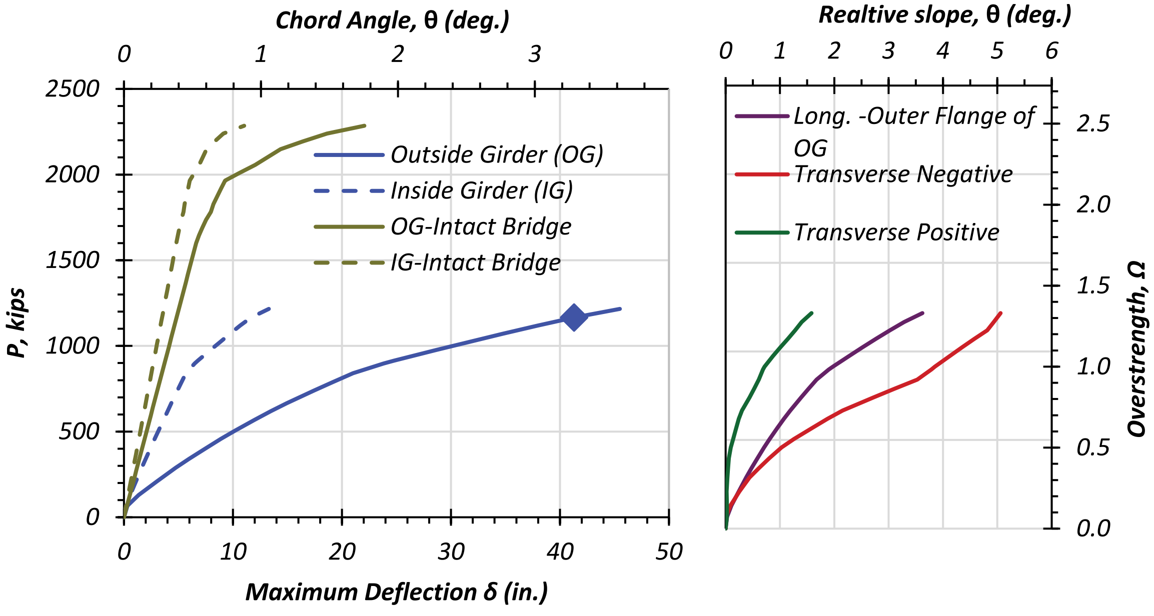

(a) Load displacement (b) Deck rotations

Note: δ is along the centerline of the girder, Ω is the load normalized by factored design load.

Figure 6.9. Grillage Analysis Results of FSEL Bridge.

6.3.2 Grillage Analysis of Bridge 1—NBI #12-102-3256-01-403

The simple-span, 220.5 ft long, 32 ft 5 in. wide Bridge 1, built along the IH 10 connector in 2007 in Houston, TX, is primarily supported by two steel tub girders and has an 8 in. thick deck. A comprehensive grillage model was generated following the procedure established in Section 1.2. Table 6.3 and Table 6.4 contain the necessary geometric information for generating an adequate grillage model.

Table 6.3. Geometric Details of Steel Tub Girders for Bridge 1.

Location ft	Top Flange		Web		Bottom Flange	
	Width in.	Thickness in.	Width in.	Thickness in.	Width in.	Thickness in.
0–52	18	1.50	84	0.625	72	1.00
52–167	18	2.25	84	0.625	72	1.50
167–220	18	1.50	84	0.625	72	1.00

Table 6.4. General Geometric Properties of Bridge 1.

Location	Parameter	Description/Value
Bridge	Location	Harris County, I-610
	Year Designed/Year Built	2004/2007
	Design Load	HS20
	Length, ft	220.46
	Spans, ft	220.46
	Radius of Curvature, ft	572.96
Deck	Width, ft	32.417
	Thickness, in.	8
	Haunch, in.	5
	Rail Type	SSTR
Rebar	# of Bar Longitudinal Top Row (#5)	38
	# of Bar Longitudinal Bottom Row (#5)	44
	Transverse Spacing Top Row (#5) in.	5
	Transverse Spacing Bottom Row (#5) in.	5

Figure 6.10 shows the grillage deflection profile of Bridge 1 with activated plastic hinges at the ultimate loading condition. Figure 6.11 depicts the load displacement plot of the bridge at the center of both the interior and exterior girders.

The intact bridge has an overstrength factor of 1.00, and the fractured bridge has an overstrength factor of 0.21 controlled by longitudinal rotation. Under the fractured condition, Bridge 1 is not considered redundant because its overstrength factor is less than 1.

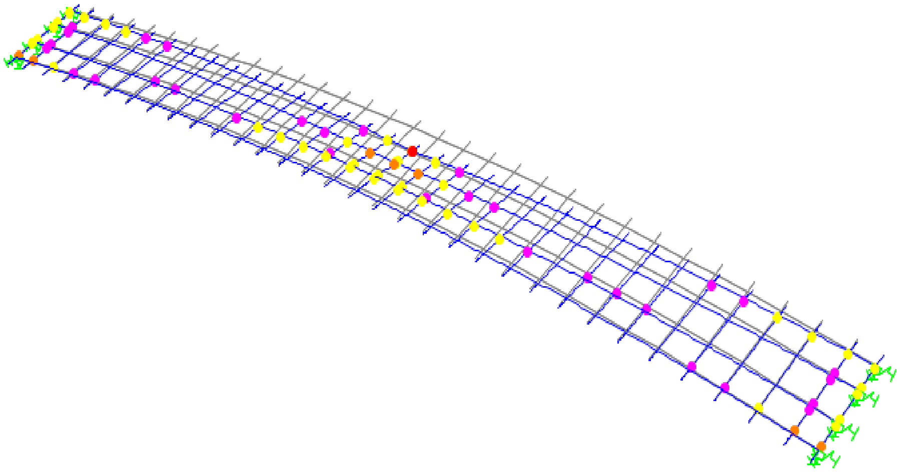

Note: The colors represent achieved curvature limits (magenta = yielding, yellow = beyond yielding, orange = beyond yielding close to failure, red = failure). Additional hinge data are located in Appendix B.

Figure 6.10. Grillage Deflection Profile of Bridge 1 with Activated Hinges.

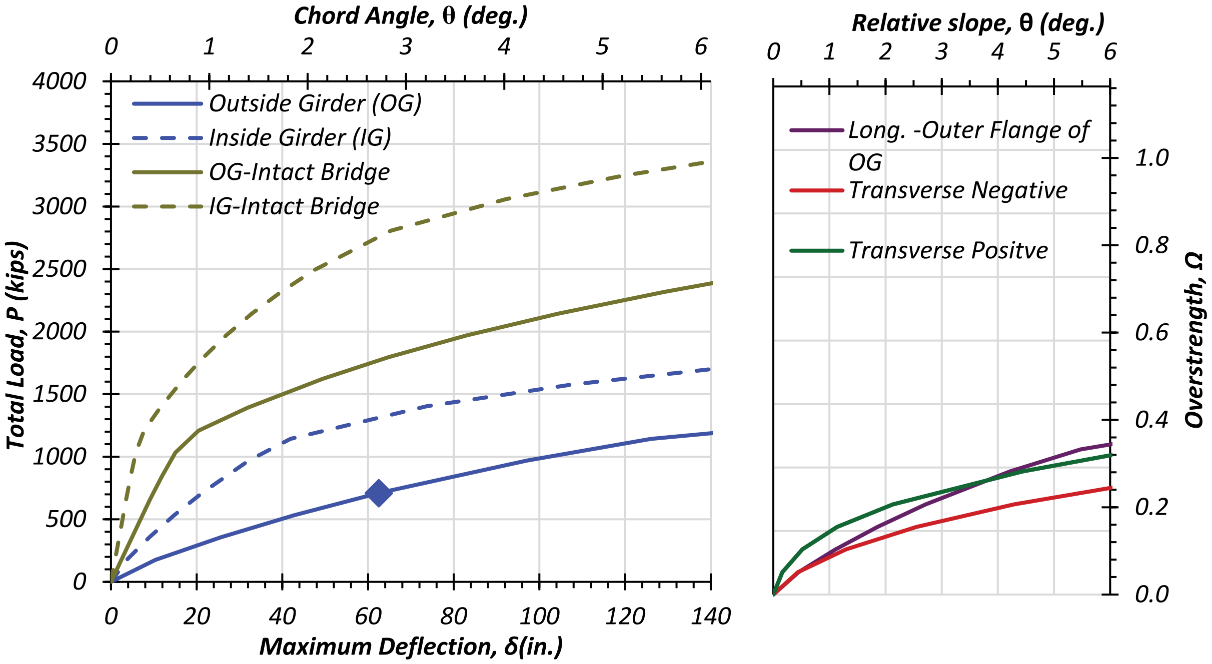

(a) Load displacement *(b) Deck rotations*

Note: δ is along the centerline of the girder, Ω is the load normalized by factored design load.

Figure 6.11. Grillage Analysis Results of Bridge 1.

6.3.3 Grillage Analysis of Bridge 2—NBI #12-102-0271-17-530

Bridge 2, built on the I-610 connector in 2004 and located in Harris County, is a simple-span bridge 115 ft in length, with a deck width of 26.6 ft and thickness of 8 in. The nonlinear model for Bridge 2 was developed using a similar process as Bridge 1. Table 6.5 and Table 6.6 contain the relative geometry information for Bridge 2 necessary to create a grillage model.

Table 6.5. Geometric Details of Steel Tub Girders for Bridge 2.

Location ft	Top Flange		Web		Bottom Flange	
	Width in.	Thickness in.	Width in.	Thickness in.	Width in.	Thickness in.
0–115	18	1.00	79	0.625	50	1.00

Table 6.6. General Geometric Properties of Bridge 2.

Location	Parameter	Description/Value
Bridge	Location	Harris County, I-610
	Year Designed/Year Built	2002/2004
	Design Load	HS25
	Length, ft	115
	Spans, ft	115
	Radius of Curvature, ft	1909.86
Deck	Width, ft	26.625
	Thickness, in.	8
	Haunch, in.	4
	Rail Type	SSTR
Rebar	# of Bar Longitudinal Top Row (#5)	40
	# of Bar Longitudinal Bottom Row (#5)	32
	Transverse Spacing Top Row (#5) in.	5
	Transverse Spacing Bottom Row (#5) in.	5

Figure 6.12 depicts the deflection profile of Bridge 2 at the ultimate loading condition with activated hinges. Figure 6.13 illustrates the load displacement along the centerline of the girders.

The fractured grillage model of Bridge 2 was run with a full web fracture at mid-span of the bridge. Under HL-93 loading, Bridge 2 has an intact overstrength factor of 3.42 and a fractured overstrength factor of 1.11 controlled by stiffness reduction. Since the overstrength value is greater than 1, Bridge 2 is redundant; however, there is a significant strength reduction caused by the fracture of the outside girder.

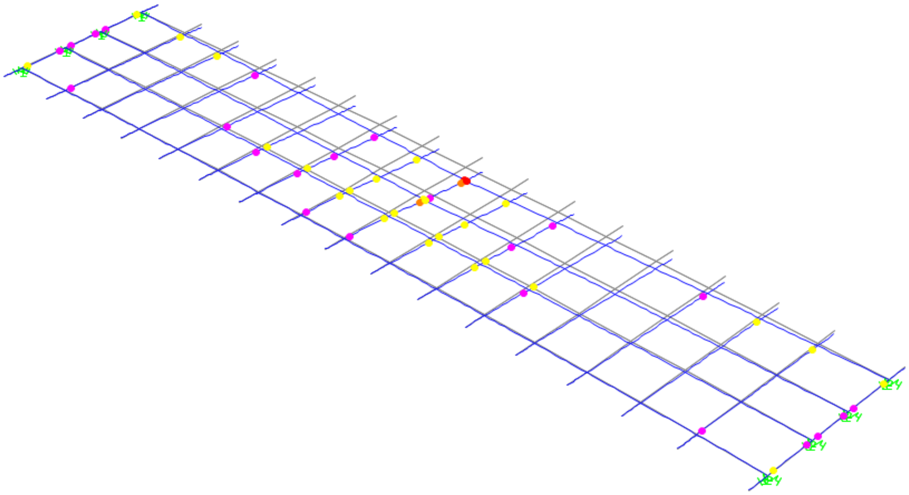

Note: The colors represent achieved curvature limits (magenta = yielding, yellow = beyond yielding, orange = beyond yielding close to failure, red = failure). Additional hinge data are located in Appendix B.

Figure 6.12. Grillage Deflection Profile of Bridge 2 with Activated Hinges.

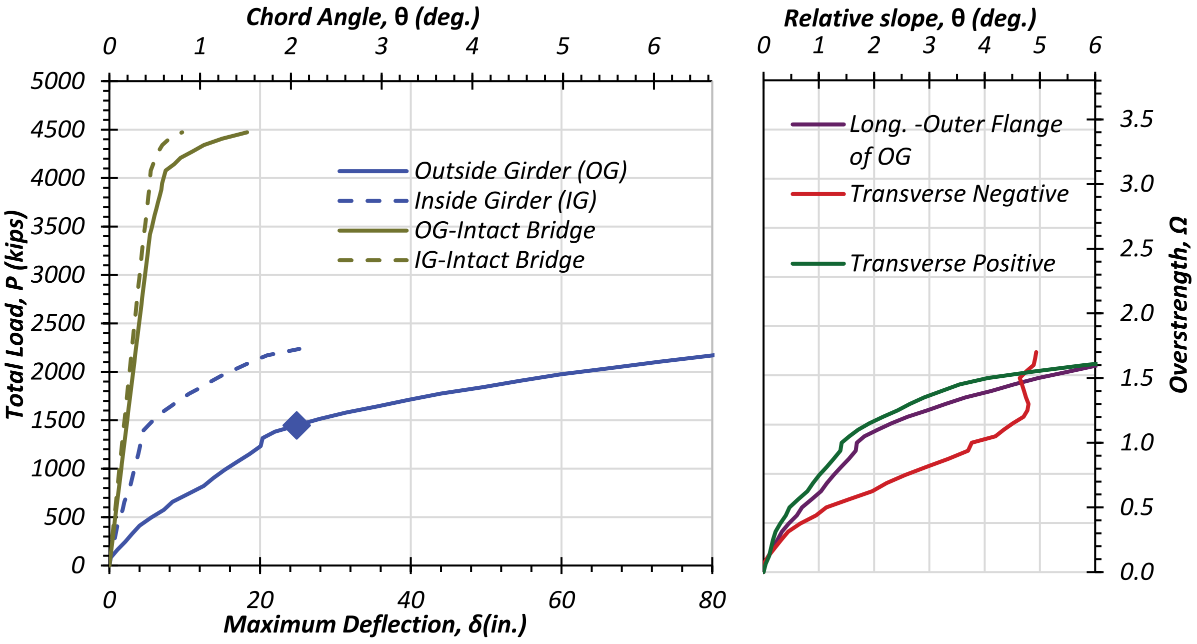

(a) Load displacement *(b) Deck rotations*

Note: δ is along the centerline of the girder, Ω is the load normalized by factored design load.

Figure 6.13. Grillage Analysis Results of Bridge 2.

6.3.4 Grillage Analysis of Bridge 3—NBI #12-102-0508-01-294

Bridge 3, built in 2002 in Harris County, has a span length of 230 ft, with a roadway width of 38.8 ft and a 9 in. deck slab thickness. Table 6.7 and Table 6.8 both contain geometric information on Bridge 3 that is necessary to create an accurate grillage model. The process by which the grillage model was created was the same used for the preceding bridges.

Table 6.7. Geometric Details of Steel Tub Girders for Bridge 3.

Location ft	Top Flange		Web		Bottom Flange	
	Width in.	Thickness in.	Width in.	Thickness in.	Width in.	Thickness in.
0–21	24	1.5	102	0.75	63.5	1.25
21–42	24	2.5	102	0.75	63.5	1.75
42–185	24	3	102	0.75	63.5	2.75
185–207	24	2.5	102	0.75	63.5	1.75
207–230	24	1.5	102	0.75	63.5	1.25

Table 6.8. General Geometric Properties of Bridge 3.

Location	Parameter	Description/Value
Bridge	Location	Harris County, FWY
	Year Designed/Year Built	1997/2002
	Design Load	HS20
	Length, ft	230
	Spans, ft	230
	Radius of Curvature, ft	2207.3
Deck	Width, ft	38.833
	Thickness, in.	9
	Haunch, in.	4
	Rail Type	T-501
Rebar	# of Bar Longitudinal Top Row (#5)	46
	# of Bar Longitudinal Bottom Row (#5)	64
	Transverse Spacing Top Row (#5), in.	5
	Transverse Spacing Bottom Row (#5), in.	5

Figure 6.14 shows the deflection profile of Bridge 3 along with the activated plastic hinges. The load displacement results from Bridge 3 are shown in Figure 6.15. Postfracture, the bridge has an overstrength factor of 0.16 controlled by transverse rotation and varies

significantly from the intact overstrength factor of 2.00. In its factored state, Bridge 3 has an overstrength factor less than 1 and is therefore not a redundant structure.

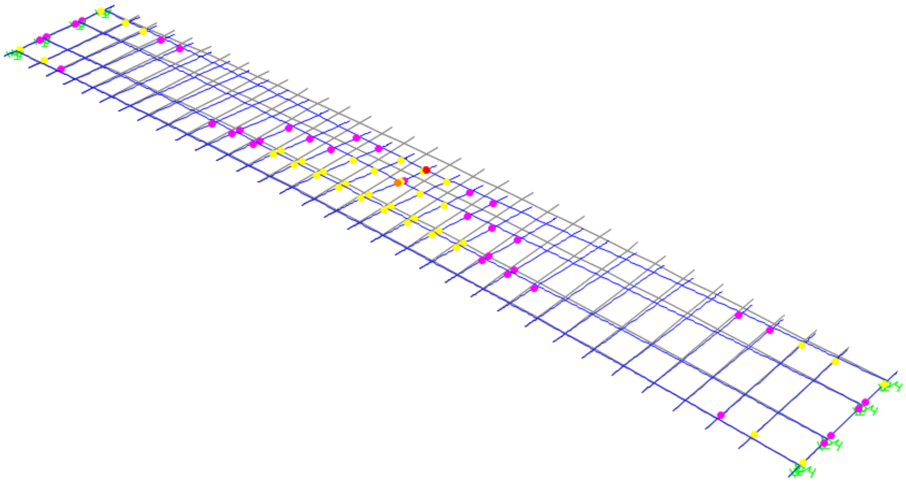

Note: The colors represent achieved curvature limits (magenta = yielding, yellow = beyond yielding, orange = beyond yielding close to failure, red = failure). Additional hinge data are located in Appendix B.

Figure 6.14. Grillage Deflection Profile for Bridge 3 with Activated Hinges.

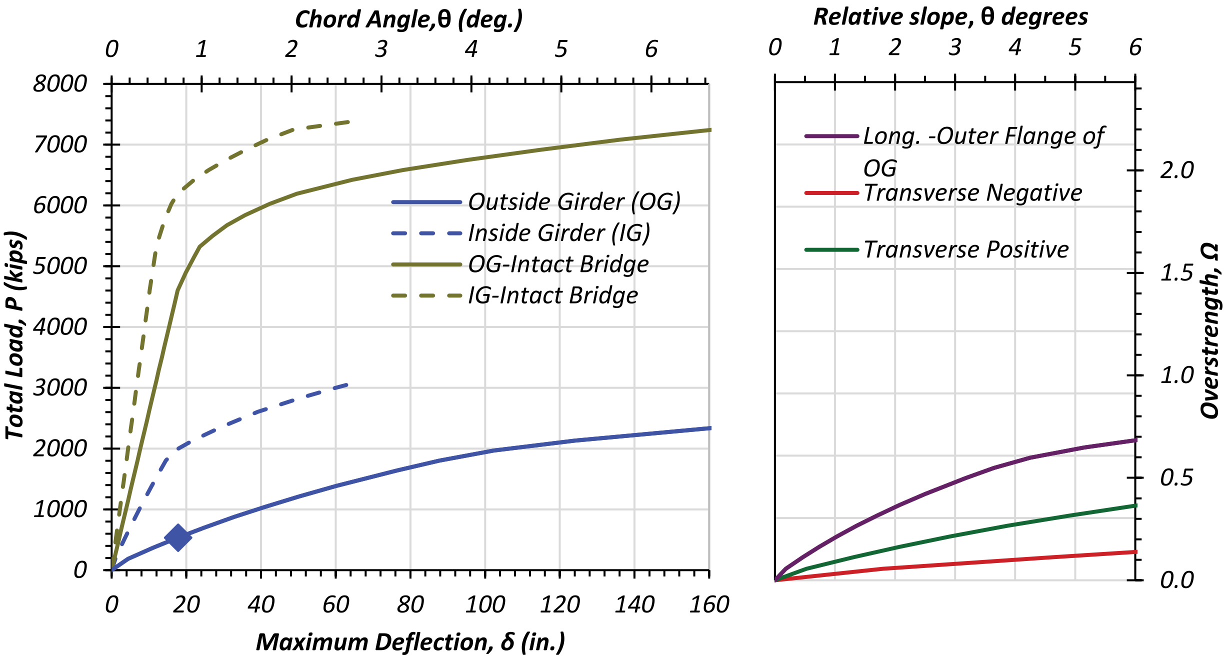

(a) Load displacement (b) Deck rotations

Note: δ is along the centerline of the girder, Ω is the load normalized by factored design load.

Figure 6.15. Grillage Analysis Results of Bridge 3.

6.3.5 Grillage Analysis of Bridge 4—NBI #12-102-0271-07-637

Bridge 4 is a two-span continuous STTG bridge built in 2007 in Harris County. Span 1 of Bridge 4 is 132 ft long, and Span 2 is 128 ft long. Bridge 4 has a deck width of 28.4 ft and a thickness of 8.5 in. Table 6.9 and Table 6.10 give the geometric properties for Bridge 4. It should be noted that although the top and bottom flanges do not vary in width, they do vary in thickness. It should also be noted that over the intermediate support and negative moment region there is an additional top reinforcing bar.

Table 6.9. Geometric Details of Steel Tub Girders for Bridge 4.

Location ft	Top Flange		Web		Bottom Flange	
	Width in.	Thickness in.	Width in.	Thickness in.	Width in.	Thickness in.
0–82	20	1.00	54	0.5	72	0.875
82–110	20	.50	54	0.5	72	1.750
110–130	20	2.75	54	0.5	72	1.750
130–150	20	2.75	54	0.5	72	1.750
150–177	20	1.50	54	0.5	72	1.750
177–260	20	1.00	54	0.5	72	0.875

Figure 6.16 shows the deflection profile of Bridge 4 with a fracture at 0.4*L of Span 2. Figure 6.17 and Figure 6.18 show the load versus displacement diagram for Spans 1 and 2, respectively, of Bridge 4. For an 0.4*L fracture, the overstrength factors are 1.30 for Span 1 and 1.32 for Span 2. Prior to fracture, Span 1 has an overstrength factor of 2.60, and Span 2 has an overstrength factor of 2.88. Under HL-93 loading, both spans are redundant under the fractured condition and are controlled by longitudinal rotation.

Table 6.10. General Geometric Properties of Bridge 4.

Location	Parameter	Description/Value
Bridge	Location	Harris County, FWY
	Year Designed/Year Built	2004/2007
	Design Load	HS25
	Length, ft	260.27
	Spans, ft	132.03, 128.24
	Radius of Curvature, ft	195
Deck	Width, ft	28.417
	Thickness, in.	8.5
	Haunch, in.	3.5
	Rail Type	SSTR
Rebar	# of Bar Longitudinal Top Row (#5)	38
	# of Bar Longitudinal Bottom Row (#5)	30
	# of Bar Longitudinal Top Row (#5) @support	78
	# of Bar Longitudinal Bottom Row (#5) @support	30
	Transverse Spacing Top Row (#5), in.	5
	Transverse Spacing Bottom Row (#5), in.	5

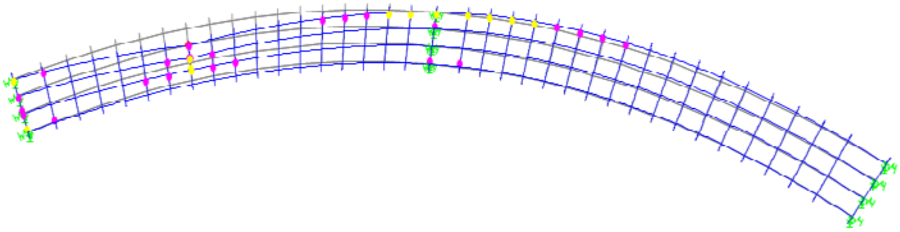

Note: The colors represent achieved curvature limits (magenta = yielding, yellow = beyond yielding, orange = beyond yielding close to failure, red = failure). Additional hinge data are located in Appendix B.

Figure 6.16. Grillage Deflection Profile for Span 2 of Bridge 4 with Activated Hinges.

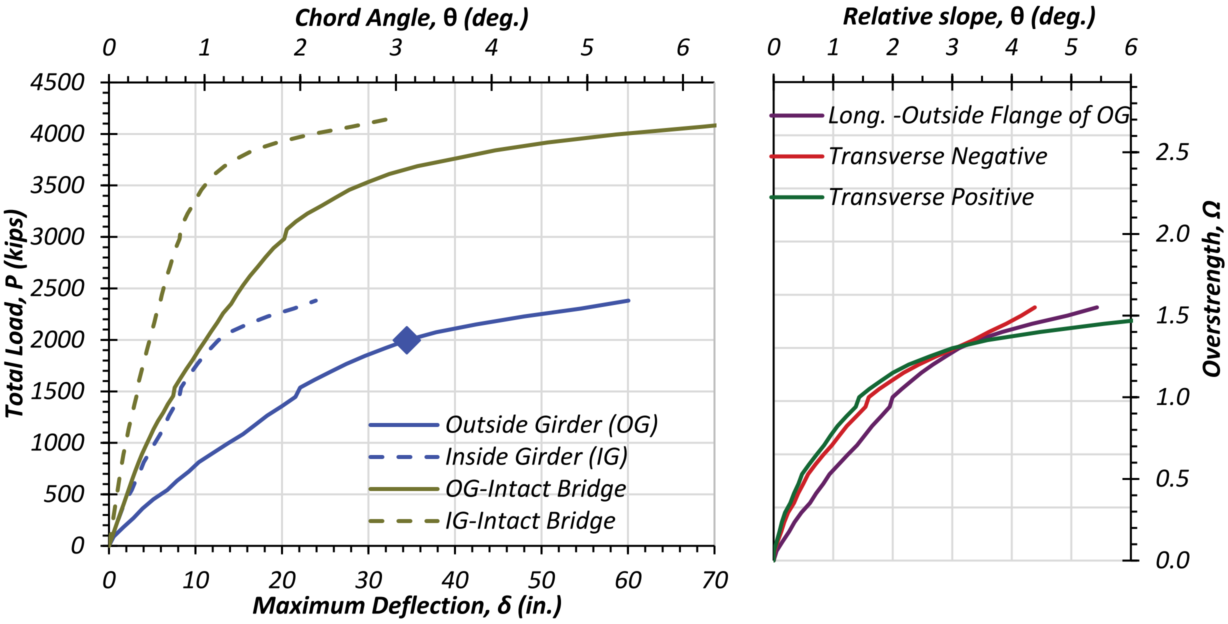

(a) Load displacement (b) Deck rotations

Note: δ is along the centerline of the girder, Ω is the load normalized by factored design load.

Figure 6.17. Grillage Analysis Results of Bridge 4, Span 1.

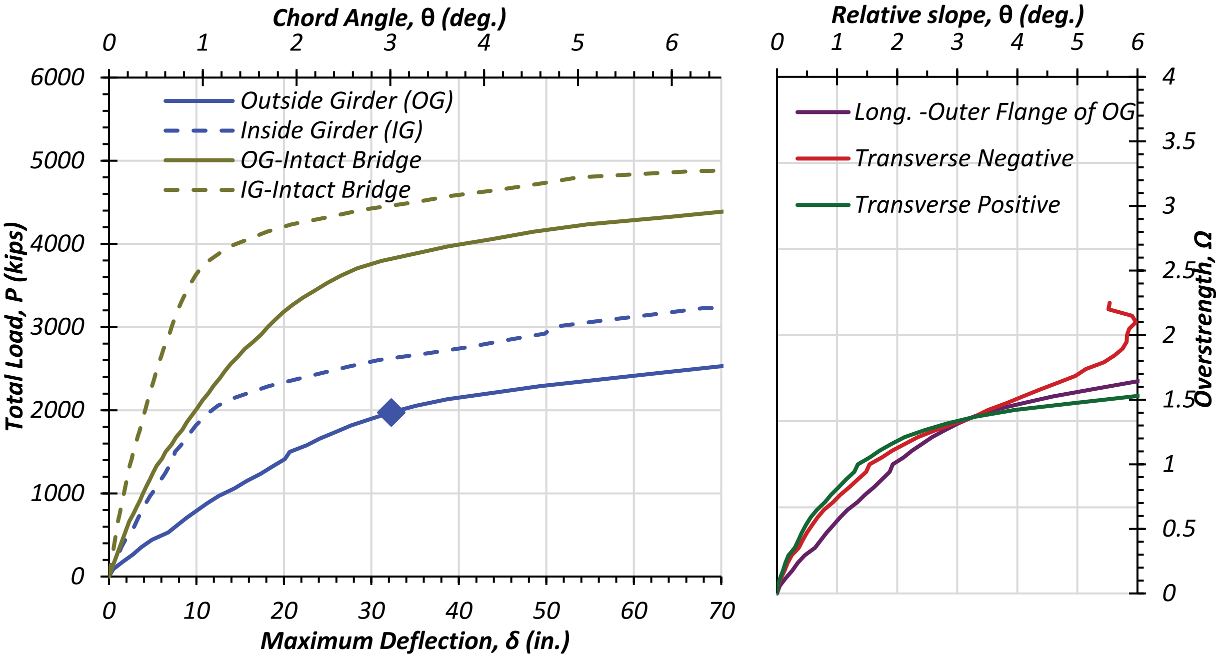

(a) Load displacement (b) Deck rotations

Note: δ is along the centerline of the girder, Ω is the load normalized by factored design load.

Figure 6.18. Grillage Analysis Results of Bridge 4, Span 2.

6.3.6 Grillage Analysis of Bridge 5—NBI #14-227-0-0015-13-452

Bridge 5 was built in 2002 in Travis County along I-35. It is a continuous two-span twin tub girder bridge. The first span of Bridge 5 has a span length of 140 ft, and the second span has a length of 139.6 ft. The bridge deck is 30 ft wide with a thickness of 8 in. Table 6.11 and Table 6.12 contain the geometric properties of Bridge 5 needed to construct an appropriate grillage model. Note that the top flange, web, and bottom flange thickness, as well as the rebar configuration, changes along the length.

Table 6.11. Geometric Details of Steel Tub Girders of Bridge 5.

Location ft	Top Flange		Web		Bottom Flange	
	Width in.	Thickness in.	Width in.	Thickness in.	Width in.	Thickness in.
0–105	18	1.00	54	0.5	56	0.75
105–122	18	1.00	54	0.5625	56	1.250
122–140	18	1.75	54	0.5625	56	1.250
140–157	18	1.75	54	0.5625	56	1.250
157–174	18	1.57	54	0.5625	56	1.250
174–192	18	1.00	54	0.5625	56	0.75
192–280	18	1.00	54	0.5	56	0.75

Table 6.12. General Geometric Properties of Bridge 5.

Location	Parameter	Description/Value
Bridge	Location	Travis County, I-35
	Year Designed/Year Built	1998/2002
	Design Load	HS20
	Length, ft	279.58
	Spans, ft	140, 139.58
	Radius of Curvature, ft	450
Deck	Width, ft	30
	Thickness, in.	8
	Haunch, in.	4
	Rail Type	T4(S)
Rebar	# of Bar Longitudinal Top Row (#4)	41
	# of Bar Longitudinal Bottom Row (#5)	36
	# of Bar Longitudinal Top Row (#4) @support	41
	# of Bar Longitudinal Top Row (#5) @support	40
	# of Bar Longitudinal Bottom Row (#5) @support	36
	Transverse Spacing Top Row (#5), in.	5
	Transverse Spacing Bottom Row (#5), in.	5

Figure 6.19 shows the deflection profile of Span 1 of Bridge 5. Figure 6.20 depicts the load displacement results for Spans 1 and 2 of Bridge 5. Prior to fracture, Bridge 5 has an overstrength factor of 2.15. With a controlling fractured overstrength value of 1.10, Bridge 5 is considered redundant. Since the bridge contains spans of almost equal lengths, there was no need to run a second analysis on Span 2. The fracture failure of Bridge 5 is controlled by longitudinal rotation.

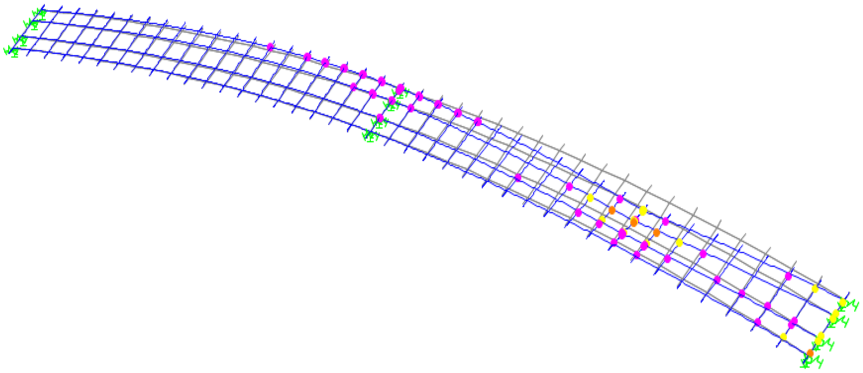

Note: The colors represent achieved curvature limits (magenta = yielding, yellow = beyond yielding, orange = beyond yielding close to failure, red = failure). Additional hinge data are located in Appendix B.

Figure 6.19. Grillage Deflection Profile for Span 1 of Bridge 5 with Activated Hinge.

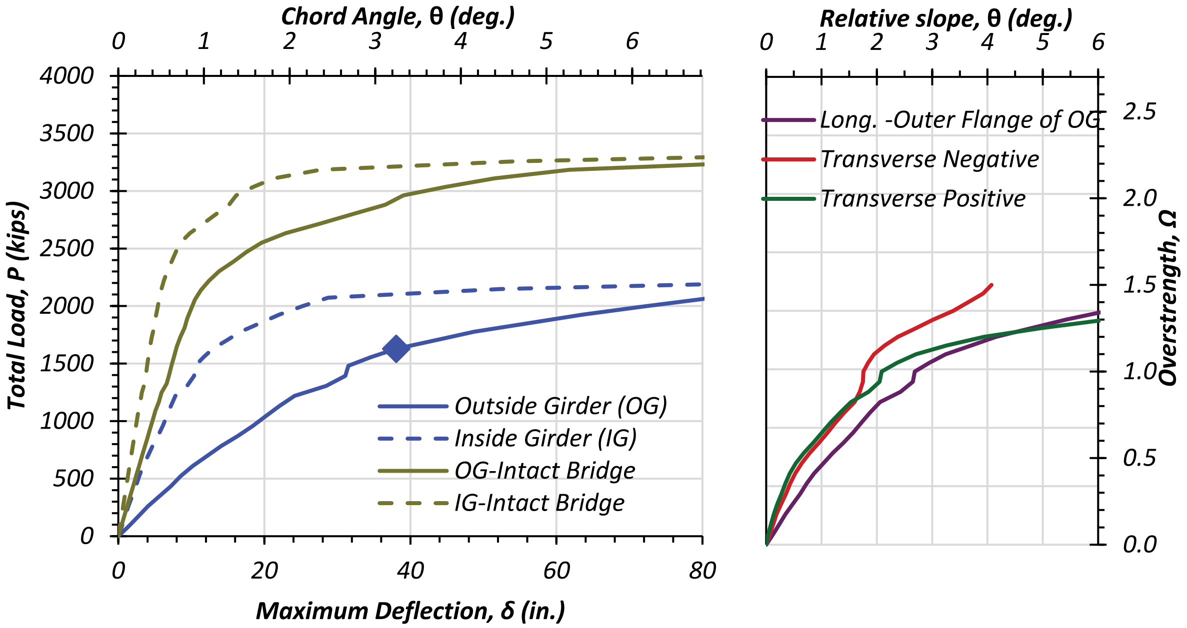

(a) Load displacement *(b) Deck rotation*

Note: δ is along the centerline of the girder, Ω is the load normalized by factored design load.

Figure 6.20. Grillage Analysis Results of Bridge 5, Spans 1 & 2.

6.3.7 Grillage Analysis of Bridge 6—NBI #12-102-0271-07-575

Bridge 6 is a two-span continuous twin tub girder bridge located in Harris County constructed along IH 10 in 2005. Both spans of Bridge 6 have a length of 140 ft, and it has a deck width of 30 ft with a thickness of 8.25 in. Table 6.13 contains the geometric details of the steel tubs. It should be noted that along the length of the girder, the top flange thickness changes. Table 6.14 provides general information about the overall geometric properties of the bridge. The grillage model for Bridge 6 was created using the same principles as for all the preceding bridges.

Table 6.13. Geometric Details of Steel Tub Girders of Bridge 6.

Location ft	Top Flange		Web		Bottom Flange	
	Width in.	Thickness in.	Width in.	Thickness in.	Width in.	Thickness in.
0–110	18	1.000	76	0.6875	60	1.000
110–130	22	1.000	76	0.6875	60	1.875
130–150	22	1.875	76	0.6875	60	1.875
150–170	22	1.000	76	0.6875	60	1.875
170–280	18	1.000	76	0.6875	60	1.000

Table 6.14. General Geometric Properties of Bridge 6.

Location	Parameter	Description/Value
Bridge	Location	Harris County, IH 10
	Year Designed/Year Built	2003/2005
	Design Load	HS25
	Length, ft	280
	Spans, ft	140,140
	Radius of Curvature, ft	818.51
Deck	Width, ft	38.417
	Thickness, in.	8.25
	Haunch, in.	4.5
	Rail Type	SSTR
Rebar	# of Bar Longitudinal Top Row (#5)	54
	# of Bar Longitudinal Bottom Row (#5)	48
	# of Bar Longitudinal Top Row (#5) @support	99
	# of Bar Longitudinal Bottom Row (#5) @support	48
	Transverse Spacing Top Row (#5), in.	4
	Transverse Spacing Bottom Row (#5), in.	4

Figure 6.21 depicts the deflection profile of Spans 1 and 2 of Bridge 6 under ultimate loading condition with activated plastic hinges. Figure 6.22 shows the load deflection data at 0.4*L of Bridge 6. Both spans of Bridge 6 have an intact overstrength factor of 3.38. After fracture of the outside girder, the overstrength factor is 1.43, yet the fracture overstrength factor is still greater than 1. This implies that the bridge is redundant..

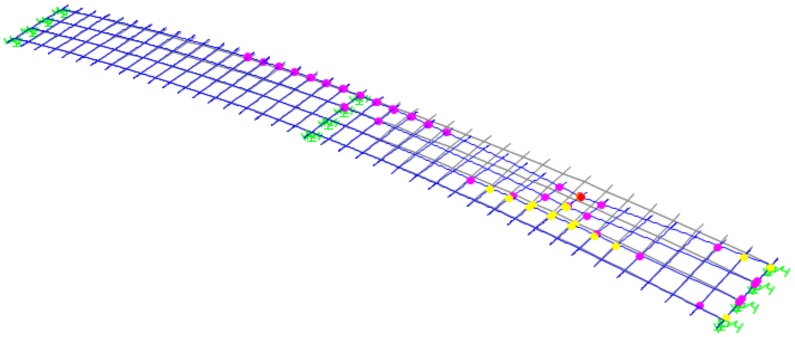

Note: The colors represent achieved curvature limits (magenta = yielding, yellow = beyond yielding, orange = beyond yielding close to failure, red = failure). Additional hinge data are located in Appendix B.

Figure 6.21. Grillage Deflection Profile for Spans 1 & 2 of Bridge 6 with Activated Hinges.

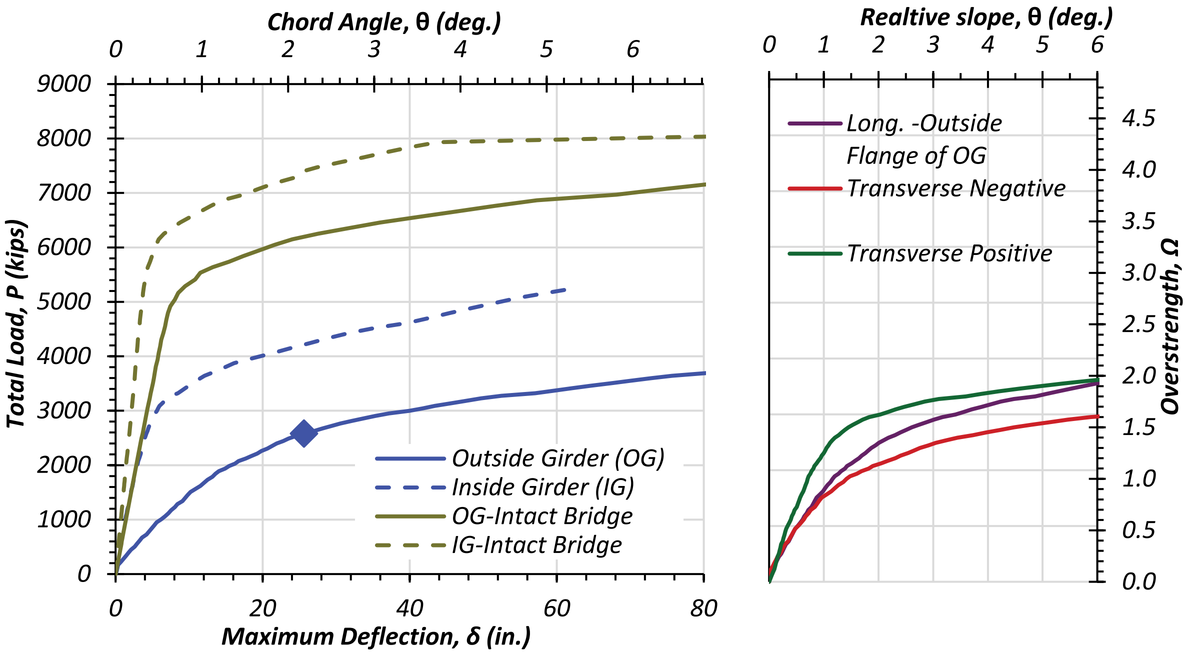

(a) Load displacement *(b) Deck rotation*

Note: δ is along the centerline of the girder, Ω is the load normalized by factored design load.

Figure 6.22. Grillage Analysis Results of Bridge 6, Spans 1 & 2.

6.3.8 Grillage Analysis of Bridge 7—NBI #12-102-0177-07-394

Bridge 7 is a two-span continuous twin tub bridge with two spans of length 219 ft and 190 ft, respectively, built in 2004 along IH 10 in Harris County. This bridge has an overall deck width of 28.4 ft and a thickness of 8 in. Table 6.15 contains the geometric information for the steel tub girder. It should be noted that the top and bottom flanges change thickness along the length of the girder and along the top flange width. Further geometric details of Bridge 7 are depicted in Table 6.16. This table includes details of the concrete deck and the reinforcing bars.

Figure 6.23 shows the grillage profile of Bridge 7 under ultimate loading condition on Span 2 with a fracture located mid-span of Span 2 with activated plastic hinges. Figure 6.24 and Figure 6.25 contain the load displacement results for both Spans 1 and 2, respectively for Bridge 7.

Table 6.15. Geometric Details of Steel Tub Girders of Bridge 7.

Location ft	Top Flange		Web		Bottom Flange	
	Width in.	Thickness in.	Width in.	Thickness in.	Width in.	Thickness in.
0–17	20	1.100	63	0.625	60	1.000
17–141	20	2.360	63	0.625	60	2.362
141–162	20	1.770	63	0.625	60	1.772
162–193	30	1.770	63	0.625	60	1.772
193–219	30	3.150	63	0.625	60	3.150
219–247	30	3.150	63	0.625	60	3.150
247–292	30	1.770	63	0.625	60	1.772
292–381	20	1.100	63	0.625	60	1.102
381–408	20	1.100	63	0.625	60	1.000

Table 6.16. General Geometric Properties of Bridge 7.

Location	Parameter	Description/Value
Bridge	Location	Harris County, IH 10
	Year Designed/Year Built	2002/2004
	Design Load	HS20
	Length, ft	408.62
	Spans, ft	218.92,189.7
	Radius of Curvature, ft	763.96
Deck	Width, ft	28.417
	Thickness, in.	7.9
	Haunch, in.	5.5
	Rail Type	T501
Rebar	# of Bar Longitudinal Top Row (#5)	30
	# of Bar Longitudinal Bottom Row (#5)	40
	# of Bar Longitudinal Top Row (#5) @support	59
	# of Bar Longitudinal Bottom Row (#5) @support	40
	Transverse Spacing Top Row (#5), in.	6
	Transverse Spacing Bottom Row (#5), in.	6

Spans 1 and 2 have intact overstrength factors of 1.85 and 2.15. Span 1 has a fractured overstrength factor of 0.94, and Span 2 has a fractured overstrength factor of 1.25. Span 1, having an omega less than 1, is not considered redundant, but Span 2 is redundant postfracture. Both Span 1 and Span 2 fail due to excess longitudinal rotation.

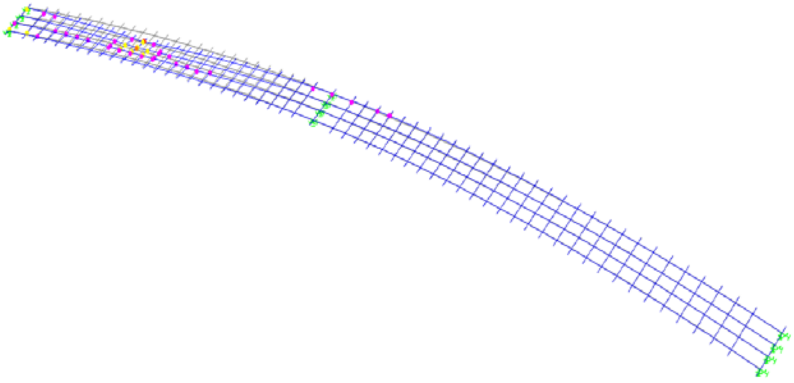

Note: The colors represent achieved curvature limits (magenta = yielding, yellow = beyond yielding, orange = beyond yielding close to failure, red = failure). Additional hinge data are located in Appendix B.

Figure 6.23. Grillage Deflection Profile for Span 2 of Bridge 7 with Activated Hinges.

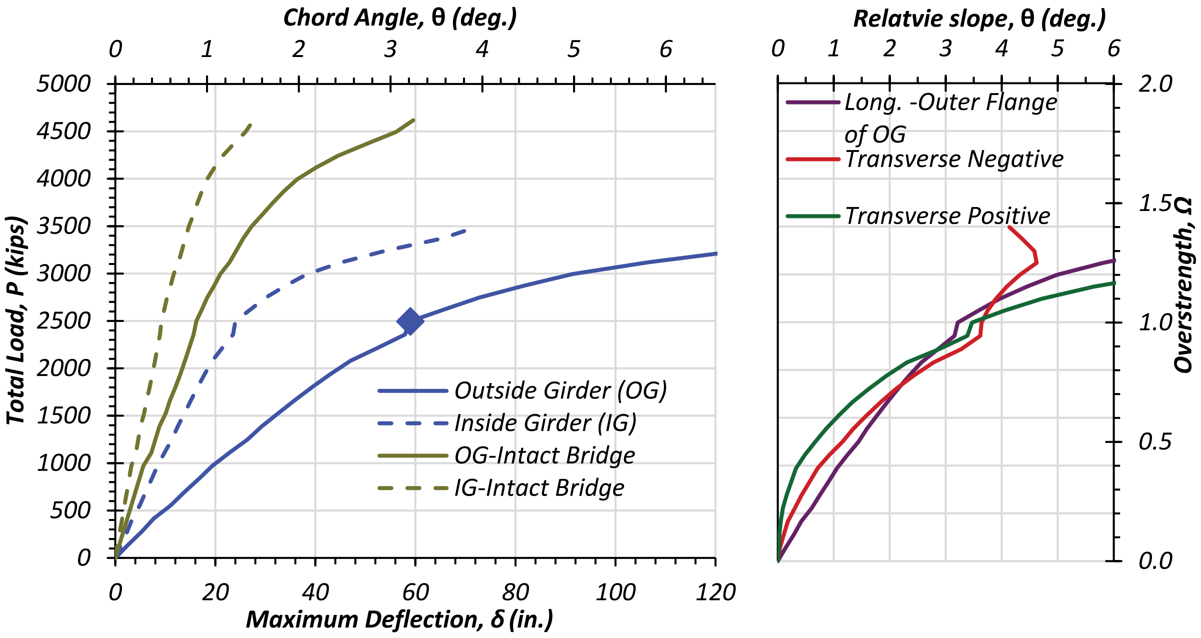

(a) Load displacement *(b) Deck rotation*

Note: δ is along the centerline of the girder, Ω is the load normalized by factored design load.

Figure 6.24. Grillage Analysis Results of Bridge 7, Span 1.

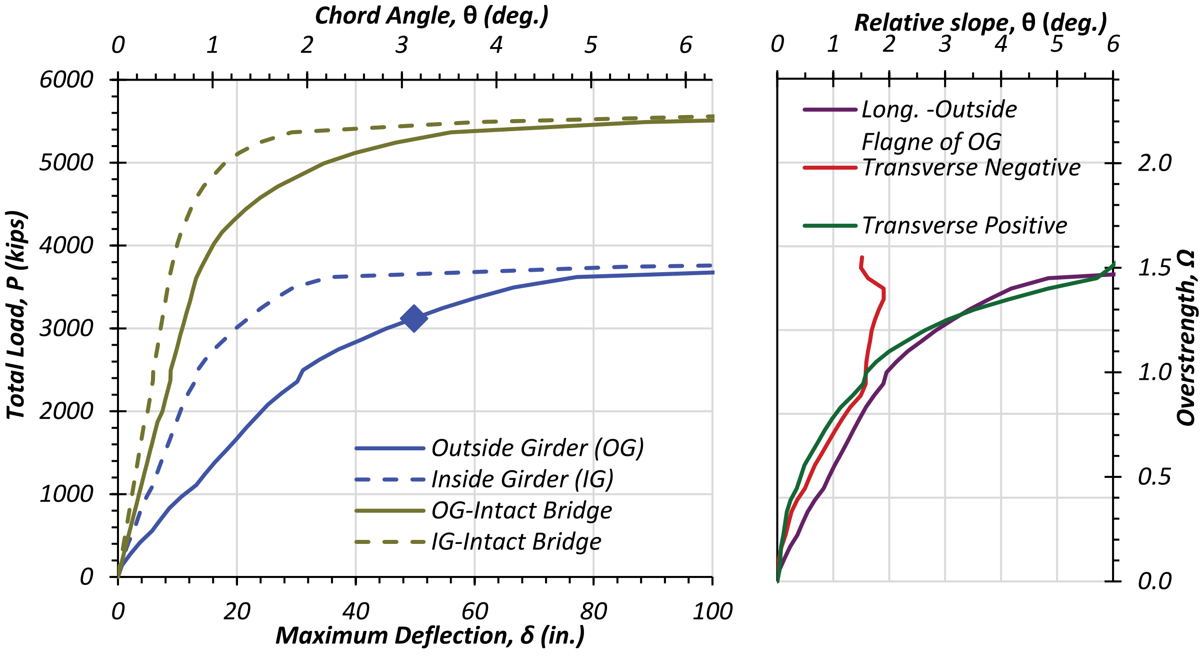

(a) Load displacement *(b) Deck rotation*

Note: δ is along the centerline of the girder, Ω is the load normalized by factored design load.

Figure 6.25. Grillage Analysis Results of Bridge 7, Span 2.

6.3.9 Grillage Analysis of Bridge 8—NBI #12-102-0271-06-661

Bridge 8 is a two-span twin tub girder continuous bridge built in Harris County along IH 10 in 2011. Bridge 8 is composed of a 265 ft span and a 295 ft span, with a 28.4 ft wide, 8 in. thick deck. Table 6.17 contains the geometric information for the steel tub portion for Bridge 8. It should be observed that the top flange and bottom flange of the tubs vary in thickness along the length of the girder. Table 6.18 provides further geometric information for Bridge 8, including concrete deck and reinforcing bar details.

Figure 6.26 depicts the grillage displacement profile of a fractured Span 1 under ultimate loading conditions. Figure 6.27 and Figure 6.28 contain the load versus displacement behavior of Spans 1 and Span 2. Span 1 has an intact overstrength factor of 1.75 and a fractured overstrength factor of 0.88. Span 2 has an intact overstrength factor of 1.45 and a fractured overstrength factor of 0.60. Both spans, with controlling overstrength factors of less than 1, do not exhibit redundant behavior and are controlled by transverse and longitudinal rotation.

Table 6.17. Geometric Details of Steel Tub Girders of Bridge 8.

Location ft	Top Flange		Web		Bottom Flange	
	Width in.	Thickness in.	Width in.	Thickness in.	Width in.	Thickness in.
0–30	24	1.25	93	0.75	53.5	1.250
30–71	24	1.50	93	0.75	53.5	1.500
71–142	24	1.50	93	0.75	53.5	2.000
142–183	24	1.50	93	0.75	53.5	1.500
183–214	24	1.25	93	0.75	53.5	1.500
214–234	24	2.00	93	0.75	53.5	2.000
234–307	24	2.50	93	0.75	53.5	2.500
307–338	24	1.25	93	0.75	53.5	1.500
338–370	24	1.50	93	0.75	53.5	1.500
370–391	24	1.50	93	0.75	53.5	2.000
391–496	24	2.00	93	0.75	53.5	2.500
496–528	24	1.50	93	0.75	53.5	2.000
528–560	24	1.25	93	0.75	53.5	1.250

Table 6.18. General Geometric Properties of Bridge 8.

Location	Parameter	Description/Value
Bridge	Location	Harris County, IH 10
	Year Designed/Year Built	2011/NA
	Design Load	NA
	Length, ft	560
	Spans, ft	265, 295
	Radius of Curvature, ft	881.47
Deck	Width, ft	28.417
	Thickness, in.	8
	Haunch, in.	4
	Rail Type	SSTR
Rebar	# of Bar Longitudinal Top Row (#5)	38
	# of Bar Longitudinal Bottom Row (#5)	38
	# of Bar Longitudinal Top Row (#5) @support	76
	# of Bar Longitudinal Bottom Row (#5) @support	38
	Transverse Spacing Top Row (#5), in.	5
	Transverse Spacing Bottom Row (#5), in.	5

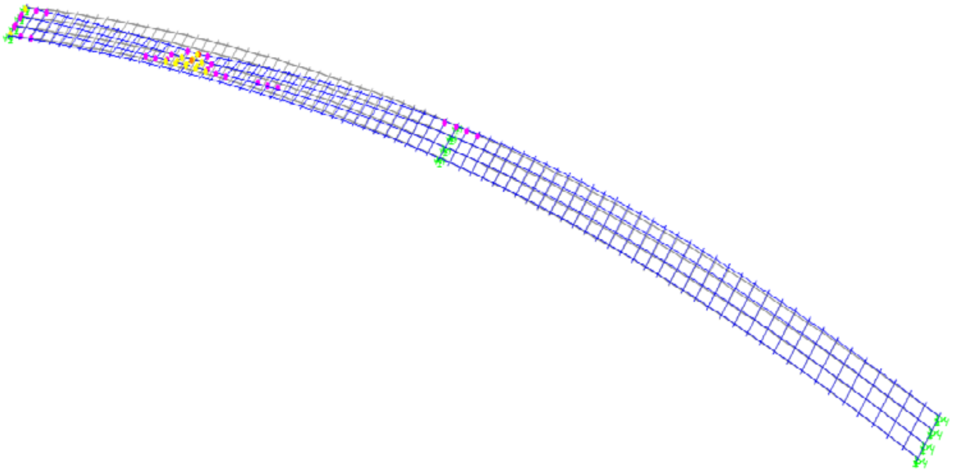

Note: The colors represent achieved curvature limits (magenta = yielding, yellow = beyond yielding, orange = beyond yielding close to failure, red = failure). Additional hinge data are located in Appendix B.

Figure 6.26. Grillage Deflection Profile for Span 2 of Bridge 8 with Activated Hinges.

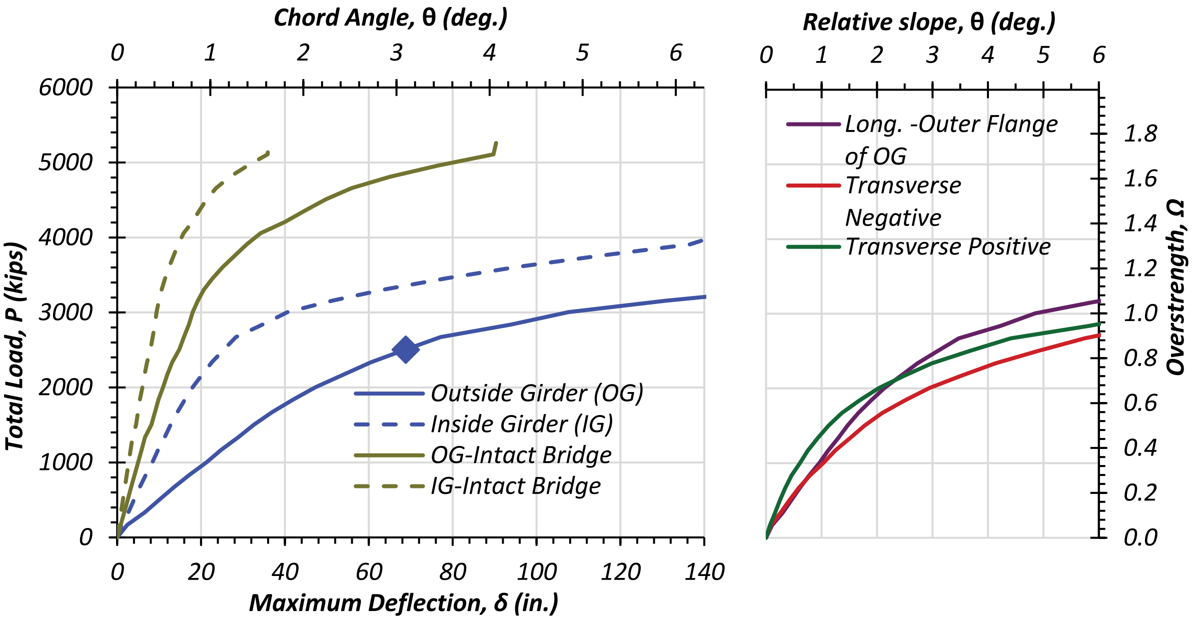

(a) Load displacement

(b) Deck rotation

Note: δ is along the centerline of the girder, Ω is the load normalized by factored design load.

Figure 6.27. Grillage Analysis Results of Bridge 8, Span 1.

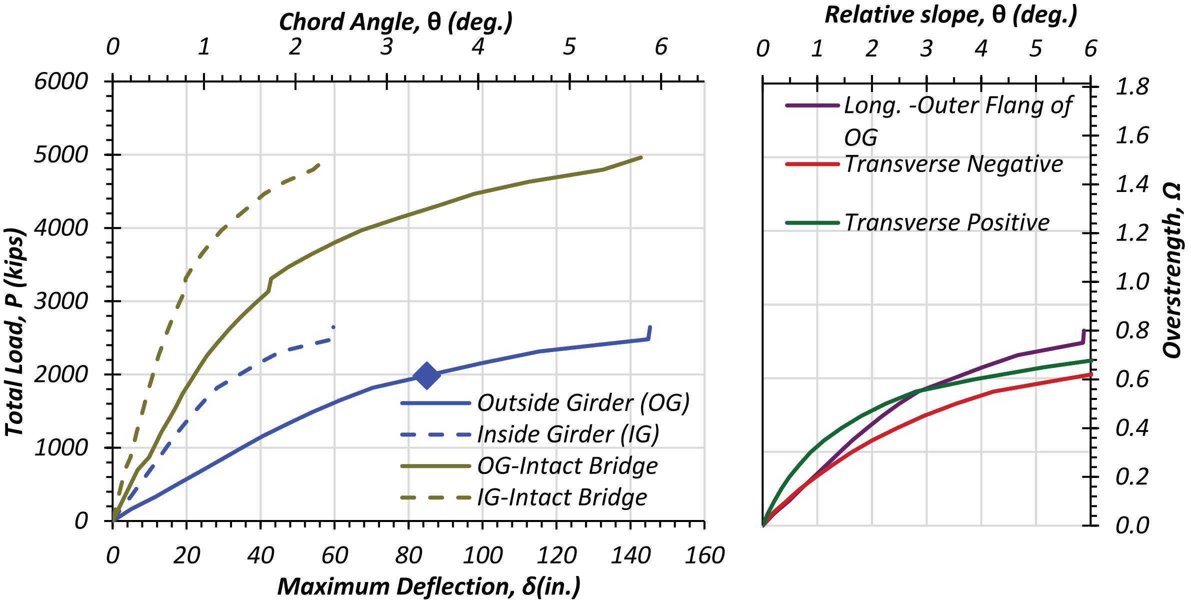

(a) Load displacement *(b) Deck rotation*

Note: δ is along the centerline of the girder, Ω is the load normalized by factored design load.

Figure 6.28. Grillage Analysis Results of Bridge 8, Span 2.

6.3.10 Grillage Analysis of Bridge 9—NBI #12-102-0177-07-394

The first three-span continuous bridge evaluated in this study is Bridge 9. Bridge 9 has spans of length 139.5 ft, 151.4 ft, and 125.5 ft. The overall deck width is 28.4 ft wide with a thickness of 8 in. It should be noted that Bridge 9 contains the same segment of bridges that contain Bridge 7. Table 6.19 and Table 6.20 contain relevant geometric properties to produce a grillage model for Bridge 9. It should be noted that the top and bottom flange thickness changes along the length of the tub girder.

Table 6.19. General Geometric Properties of Bridge 9.

Location	Parameter	Description/Value
Bridge	Location	Harris County, IH 10
	Year Designed/Year Built	2002/2004
	Design Load	HS20
	Length, ft	416.66
	Spans, ft	139.5,151.44,125.62
	Radius of Curvature, ft	763.93
Deck	Width, ft	28.417
	Thickness, in.	8
	Haunch, in.	4
	Rail Type	T501
Rebar	# of Bar Longitudinal Top Row (#5)	30
	# of Bar Longitudinal Bottom Row (#5)	40
	# of Bar Longitudinal Top Row (#5) @support	59
	# of Bar Longitudinal Bottom Row (#5) @support	30
	Transverse Spacing Top Row (#5), in.	5
	Transverse Spacing Bottom Row (#5), in.	5

Figure 6.29 depicts the displacement profile of Bridge 9 with HL-93 loading on the fractured Span 2. Figure 6.30, Figure 6.31, and Figure 6.32 depict the load displacement results of all three spans in Bridge 9. Span 1 has an intact overstrength factor of 2.82 and a fractured overstrength factor of 1.35. Span 2 has an intact overstrength factor of 3.10 and a fractured factor of 2.10. Span 3 has an intact overstrength factor of 3.05 and a fractured overstrength factor of 1.53. All spans of Bridge 9, even with the exterior girder fractured, have overstrength factors greater than 1 and are considered redundant and are controlled by stiffness.

Table 6.20. Geometric Details of Steel Tub Girders of Bridge 9.

Location ft	Top Flange		Web		Bottom Flange	
	Width in.	Thickness in.	Width in.	Thickness in.	Width in.	Thickness in.
0–104	20	1.10	63	0.625	59	1.000
104–127	20	1.10	63	0.625	59	1.250
127–152	20	1.58	63	0.625	59	1.500
152–177	20	1.10	63	0.625	59	1.250
177–240	20	1.10	63	0.625	59	1.000
240–265	20	1.10	63	0.625	59	1.250
265–278	20	1.10	63	0.625	59	1.500
278–316	20	1.58	63	0.625	59	1.500
316–341	20	1.10	63	0.625	59	1.250
341–416	20	1.10	63	0.625	59	1.000

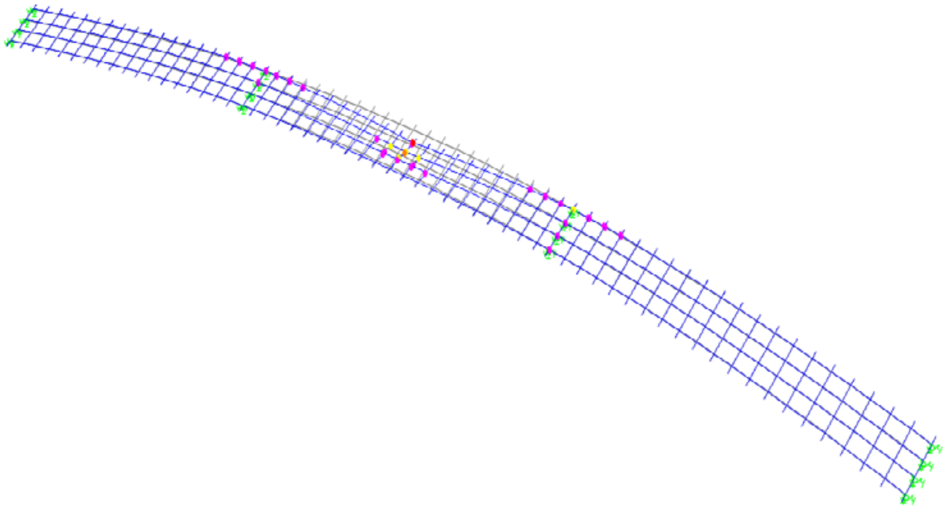

Note: The colors represent achieved curvature limits (magenta = yielding, yellow = beyond yielding, orange = beyond yielding close to failure, red = failure). Additional hinge data are located in Appendix B.

Figure 6.29. Grillage Deflection Profile for Span 2 of Bridge 9 with Activated Hinges.

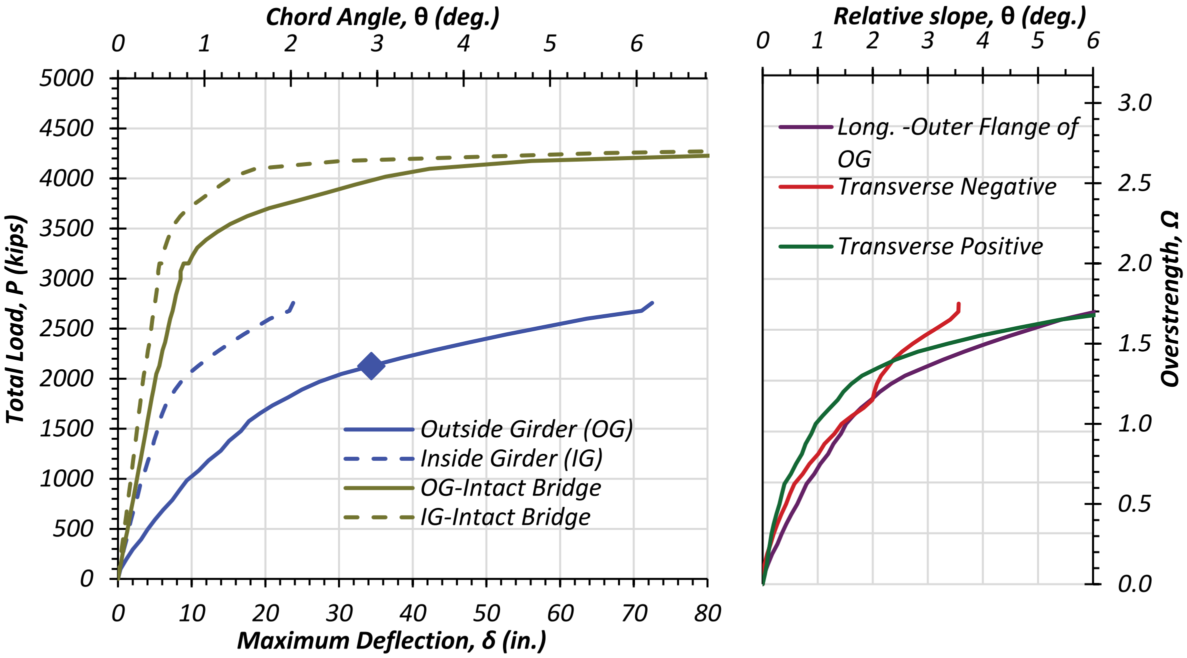

(a) Load displacement (b) Deck rotation

Note: δ is along the centerline of the girder, Ω is the load normalized by factored design load.

Figure 6.30. Grillage Analysis Results of Bridge 9, Span 1.

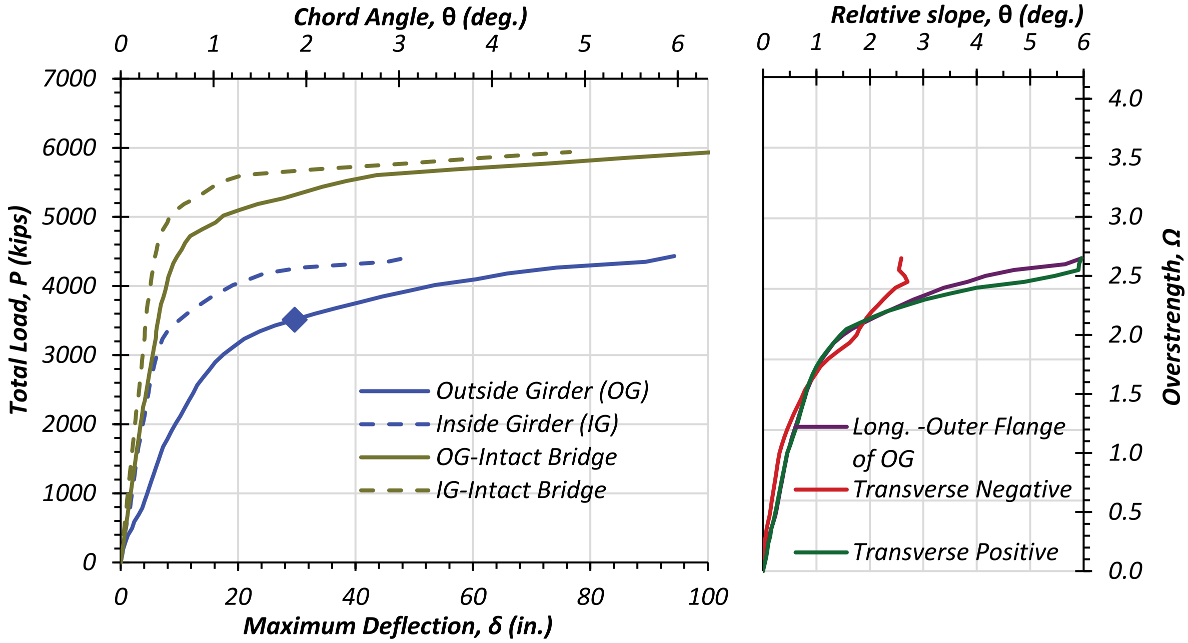

(a) Load displacement (b) Deck rotation

Note: δ is along the centerline of the girder, Ω is the load normalized by factored design load.

Figure 6.31. Grillage Analysis Results of Bridge 9, Span 2.

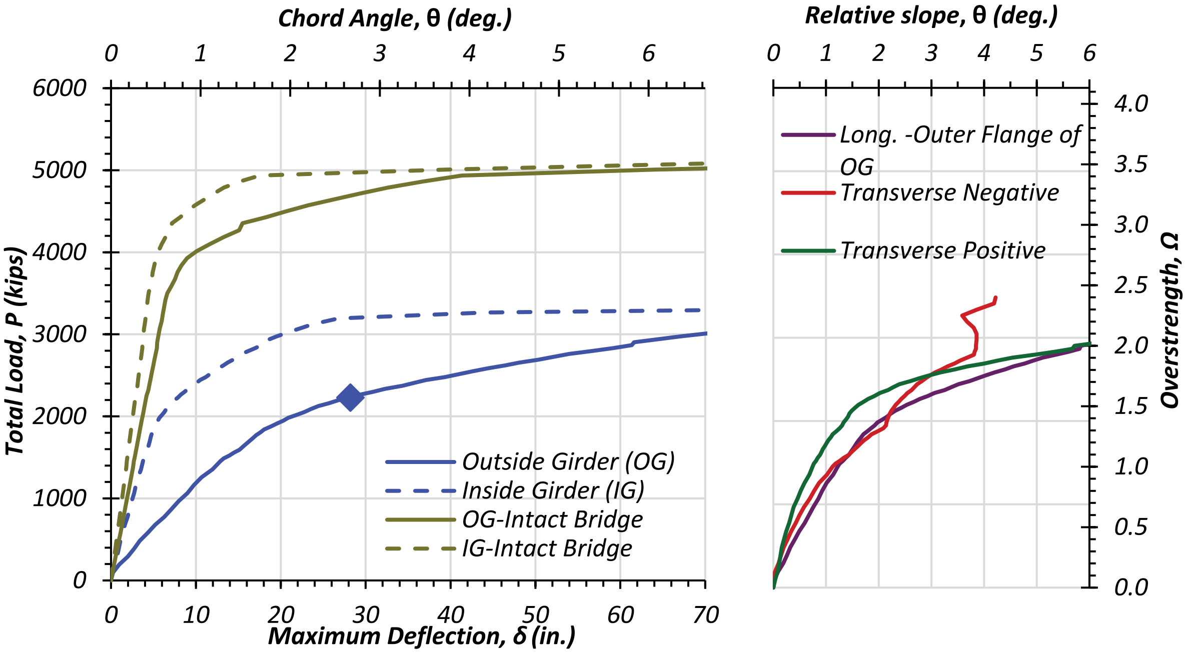

(a) Load displacement *(b) Deck rotation*

Note: δ is along the centerline of the girder, Ω is the load normalized by factored design load.

Figure 6.32. Grillage Analysis Results of Bridge 9, Span 3.

6.3.11 Grillage Analysis of Bridge 10—NBI #14-227-0-0015-13-450

Bridge 10, built in 2002 in Harris County along IH 10, is a continuous three-span bridge with span lengths of 148 ft, 265 ft, and 189.6 ft. It has a total deck width of 30 ft and thickness of 8 in. Table 6.21 and Table 6.22 contain the geometric property details of Bridge 10. It should be noted that the top flange, web, and bottom flange thickness changes over the length of the girders. The top reinforcing bars are a mixture of Number 4 and 5 bars over the support.

Table 6.21. Geometric Details of Steel Tub Girders of Bridge 10.

Location ft	Top Flange		Web		Bottom Flange	
	Width in.	Thickness in.	Width in.	Thickness in.	Width in.	Thickness in.
0–50	24	1.00	78	0.625	59	0.750
50–98	24	1.00	78	0.625	59	1.250
98–131	24	2.00	78	0.75	59	2.000
131–181	24	3.00	78	0.875	59	2.000
181–230	24	1.00	78	0.875	59	1.250
230–247	24	1.00	78	0.75	59	1.000
247–297	24	1.00	78	0.75	59	1.250
297–330	24	1.00	78	0.75	59	1.000
330–380	24	1.00	78	0.875	59	1.250
380–396	24	2.00	78	0.875	59	1.250
396–430	24	3.00	78	0.875	59	2.000
430–447	24	3.00	78	0.875	59	2.000
447–464	24	2.00	78	0.75	59	1.250
464–499	24	1.00	78	0.75	59	1.250
499–602	24	1.00	78	0.625	59	0.750

Figure 6.33 depicts the displacement profile of Bridge 10 with HL-93 loading and a fracture in Span 2. Figure 6.34, Figure 6.35, and Figure 6.36 illustrate the load displacement results for all spans of Bridge 10. Span 1 has a fractured overstrength factor of 1.71. Span 2 has a fractured overstrength factor of 1.25 and an intact overstrength factor of 1.85. Span 3 has a fractured factor of 1.25 and an intact factor of 2.10. Each of the spans has an overstrength factor greater than 1 and are therefore exhibiting a necessary level of redundancy for load redistribution postfracture. Span 1 is controlled by stiffness; however, Span 2 and Span 3 are controlled by longitudinal chord rotation.

Table 6.22. General Geometric Properties of Bridge 10.

Location	Parameter	Description/Value
Bridge	Location	Harris County, IH 10
	Year Designed/Year Built	1998/2002
	Design Load	HS20
	Length, ft	602.58
	Spans, ft	148, 265, 189.58
	Radius of Curvature, ft	716.2
Deck	Width, ft	30
	Thickness, in.	8
	Haunch, in.	5
	Rail Type	T4(s)
Rebar	# of Bar Longitudinal Top Row (#4)	42
	# of Bar Longitudinal Bottom Row (#5)	32
	# of Bar Longitudinal Top Row (#4) @support	42
	# of Bar Longitudinal Top Row (#5) @support	40
	# of Bar Longitudinal Bottom Row (#5) @support	32
	Transverse Spacing Top Row (#5), in.	6
	Transverse Spacing Bottom Row (#5), in.	6

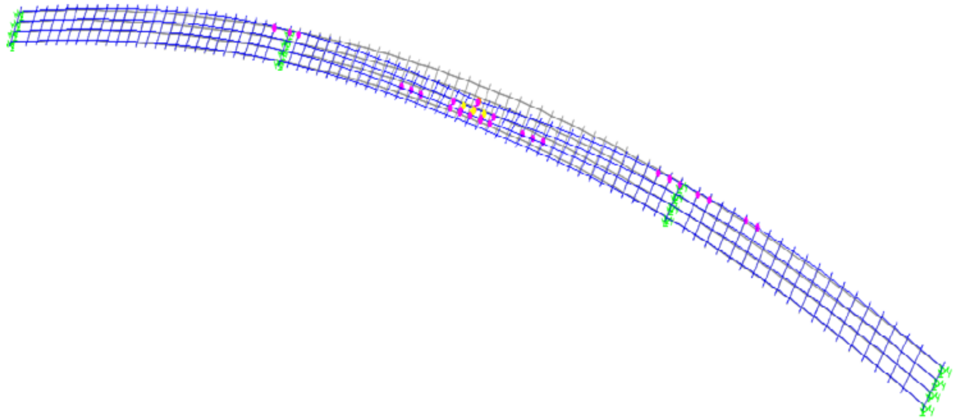

Note: The colors represent achieved curvature limits (magenta = yielding, yellow = beyond yielding, orange = beyond yielding close to failure, red = failure). Additional hinge data are located in Appendix B.

Figure 6.33. Grillage Deflection Profile for Span 2 of Bridge 10 with Activated Hinges.

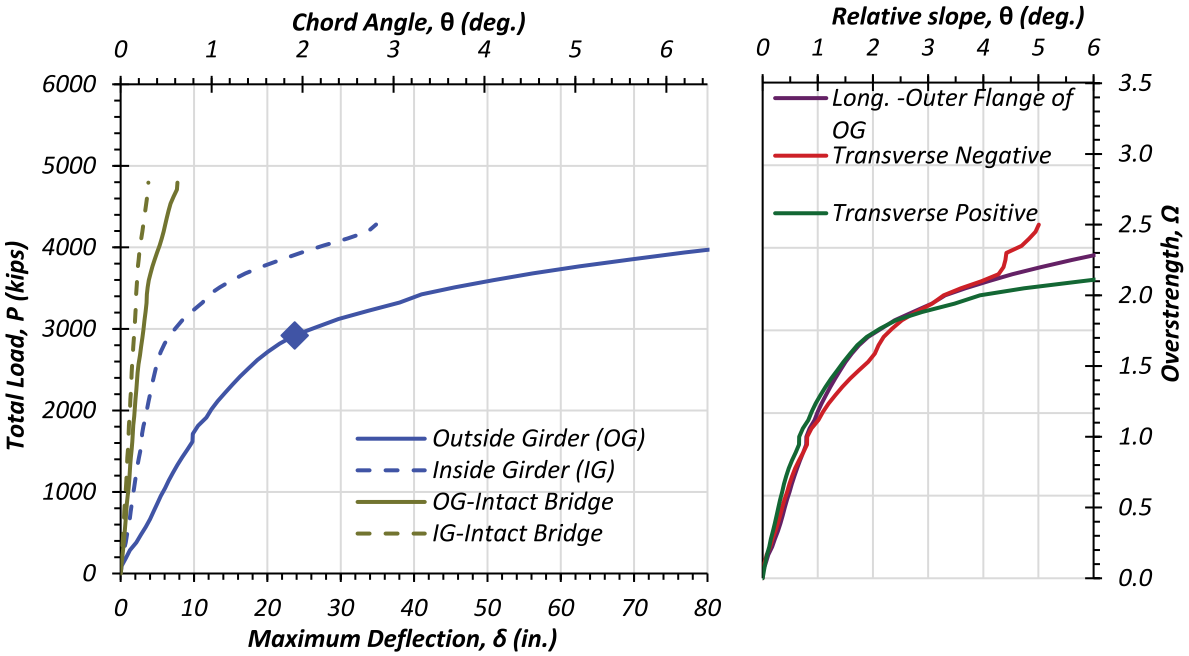

(a) Load displacement *(b) Deck rotation*

Note: δ is along the centerline of the girder, Ω is the load normalized by factored design load.

Figure 6.34. Grillage Analysis Results of Bridge 10, Span 1.

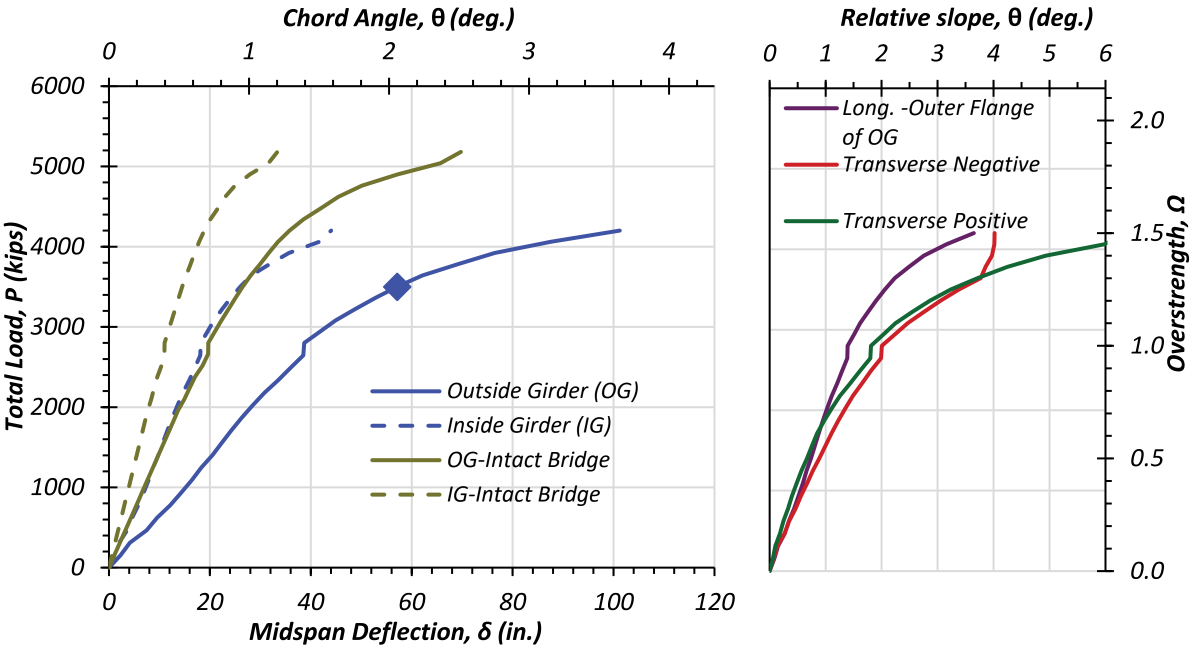

(a) Load displacement *(b) Deck rotation*

Note: δ is along the centerline of the girder, Ω is the load normalized by factored design load.

Figure 6.35. Grillage Analysis Results of Bridge 10, Span 2.

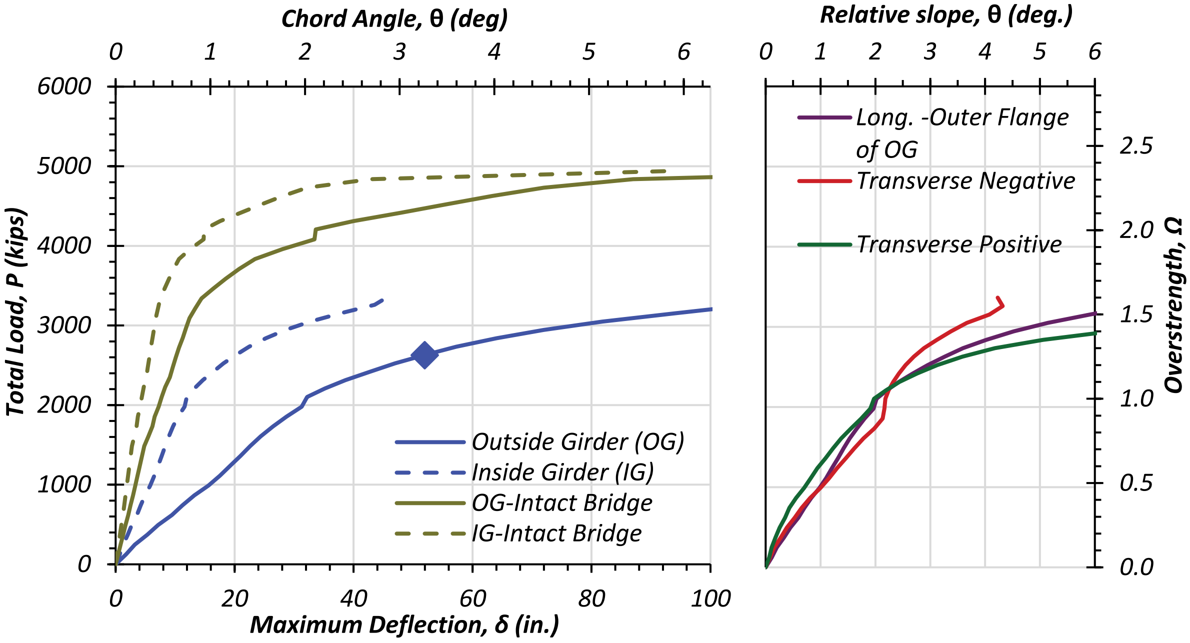

(a) Load displacement *(b) Deck rotation*

Note: δ is along the centerline of the girder, Ω is the load normalized by factored design load.

Figure 6.36. Grillage Analysis Results of Bridge 10, Span 3.

6.3.12 Grillage Analysis of Bridge 11—NBI #12-102-0271-07-593

Bridge 11, compared to Bridge 10, is a longer three-span continuous bridge located along IH 10 in Harris County. Bridge 11 consist of three spans with span lengths of 223 ft, 366 ft, and 235 ft, with an overall deck width of 28.4 ft and a deck thickness of 8 in. Table 6.23 and Table 6.24 contain the necessary geometric information to generate an accurate grillage model. It should be noted that both the top flange width and thickness change over the length of the girder, as does the bottom flange thickness.

Table 6.23. Geometric Details of Steel Tub Girders of Bridge 11.

Location ft	Top Flange		Web		Bottom Flange	
	Width in.	Thickness in.	Width in.	Thickness in.	Width in.	Thickness in.
0–128	18	1.00	102	0.875	66	1.000
128–154	18	1.00	102	0.875	66	1.500
154–180	30	1.75	102	0.875	66	1.500
180–247	30	3.00	102	0.875	66	3.000
247–256	30	3.00	102	0.875	66	1.500
256–281	30	1.75	102	0.875	66	1.500
281–522	18	1.75	102	0.875	66	1.500
522–555	30	1.75	102	0.875	66	1.500
555–630	30	3.00	102	0.875	66	3.000
630–647	30	1.75	102	0.875	66	1.500
647–681	18	1.00	102	0.875	66	1.500
681–824	18	1.00	102	0.875	66	1.000

Figure 6.37 illustrates the deflection profile of Span 2 for an HL-93 load. Figure 6.38, Figure 6.39, and Figure 6.40 show the load displacement response of all three spans of Bridge 11. Span 1 has a fractured overstrength factor of 1.35. Span 2 has a fractured overstrength factor of 1.00. Span 3 has a fractured overstrength factor of 1.30. Span 1 fails via stiffness, Span 2 fails via longitudinal rotation, and Span 3 is controlled by transverse rotation.

Table 6.24. General Geometric Properties of Bridge 11.

Location	Parameter	Description/Value
Bridge	Location	Harris County, IH 10
	Year Designed/Year Built	2004/2007
	Design Load	HS25
	Length, ft	824
	Spans, ft	223, 366, 235
	Radius of Curvature, ft	818.51
Deck	Width, ft	28.417
	Thickness, in.	8
	Haunch, in.	4
	Rail Type	SSTR
Rebar	# of Bar Longitudinal Top Row (#5)	30
	# of Bar Longitudinal Bottom Row (#5)	38
	# of Bar Longitudinal Top Row (#5) @support	59
	# of Bar Longitudinal Bottom Row (#5) @support	38
	Transverse Spacing Top Row (#5), in.	6
	Transverse Spacing Bottom Row (#5), in.	6

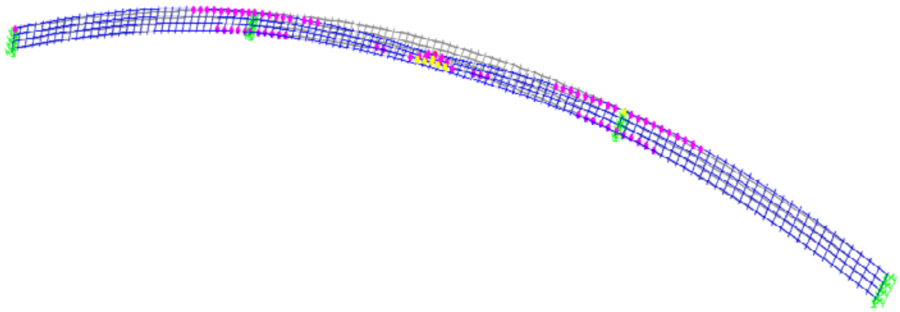

Note: The colors represent achieved curvature limits (magenta = yielding, yellow = beyond yielding, orange = beyond yielding close to failure, red = failure). Additional hinge data are located in Appendix B.

Figure 6.37. Grillage Deflection Profile for Span 2 of Bridge 11 with Activated Hinges.

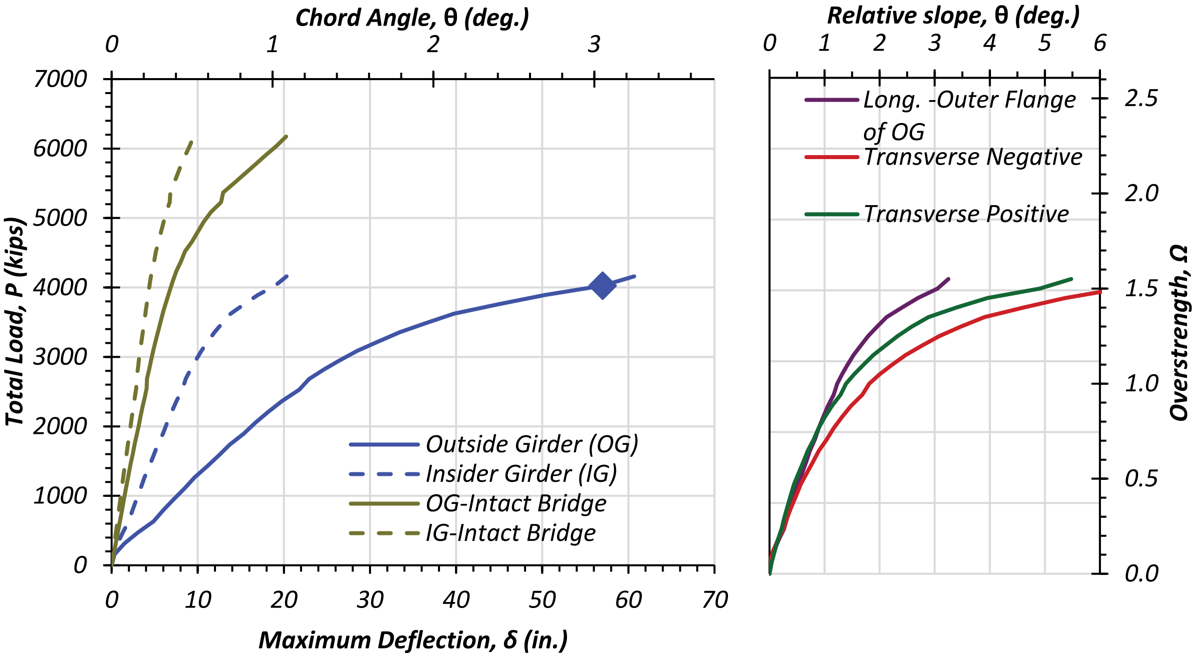

(a) Load displacement (b) Deck rotations

Note: δ is along the centerline of the girder, Ω is the load normalized by factored design load.

Figure 6.38. Grillage Analysis Results of Bridge 11, Span 1.

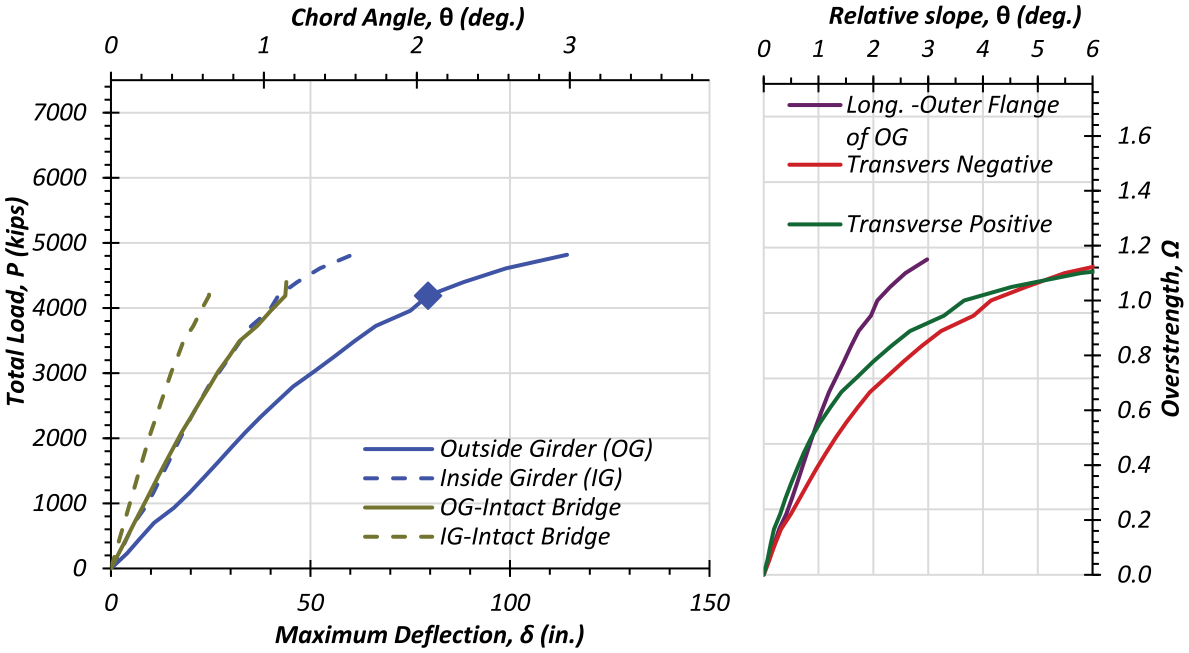

(a) Load displacement (b) Deck rotation

Note: δ is along the centerline of the girder, Ω is the load normalized by factored design load.

Figure 6.39. Grillage Analysis Results of Bridge 11, Span 2.

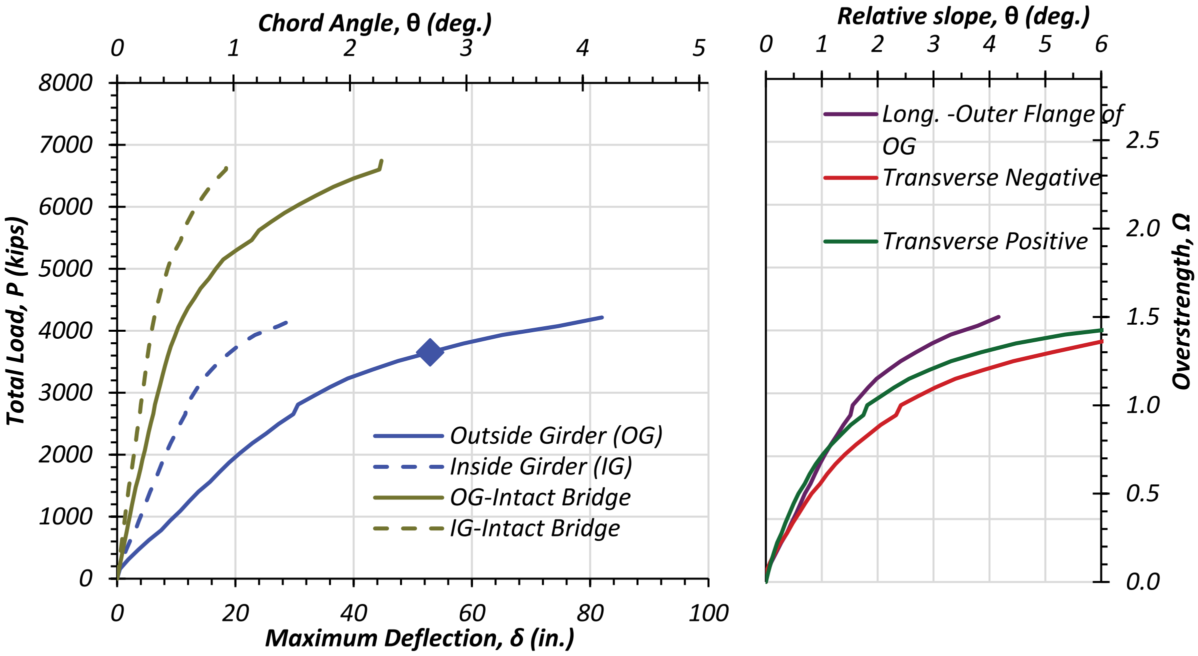

(a) Load displacement *(b) Deck rotation*

Note: δ is along the centerline of the girder, Ω is the load normalized by factored design load.

Figure 6.40. Grillage Analysis Results of Bridge 11, Span 3.

6.3.13 Grillage Analysis of Bridge 12—NBI #12-102-0271-07-639

Bridge 12, built in 2007 in Harris County along IH 10, is a three-span continuous bridge. The lengths of the spans that comprise Bridge 12 are 140 ft, 180 ft, and 145 ft, respectively. The overall bridge deck width is 28.4 ft, and the deck thickness is 8.5 in. Table 6.25 and Table 6.26 contain the geometric properties and information necessary for appropriately generating a grillage model to represent Bridge 12. Note that both the top and bottom flanges vary in thickness along the length of the member.

Table 6.25. Geometric Details of Steel Tub Girders of Bridge 12.

Location ft	Top Flange		Web		Bottom Flange	
	Width in.	Thickness in.	Width in.	Thickness in.	Width in.	Thickness in.
0–90	20	1.00	54	0.5	72	0.875
90–116	20	1.75	54	0.5	72	1.750
116–138	20	3.25	54	0.5	72	1.750
138–160	20	3.25	54	0.5	72	1.750
160–189	20	1.75	54	0.5	72	1.750
189–267	20	1.00	54	0.5	72	0.875
267–296	20	1.75	54	0.5	72	1.750
296–318	20	3.25	54	0.5	72	1.750
318–340	20	3.25	54	0.5	72	1.750
340–377	20	1.75	54	0.5	72	1.750
340–465	20	1.00	54	0.5	72	0.875

Figure 6.41 depicts the displacement profile for Bridge 12 under the ultimate HL-93 loading state. Figure 6.42, Figure 6.43, and Figure 6.44 illustrate the load displacement behavior of all spans of Bridge 12 under HL-93 loading. Span 1 has a fractured overstrength factor of 1.20 and an intact factor of 2.50. Span 2 has a fractured overstrength factor of 1.56 and an intact factor of 2.60. Span 3 has a fractured overstrength factor of 1.15 and an intact factor of 2.35. Once again, the longer spans have lower overstrength factors. Span 1 fails due to transverse rotation while Spans 2 and 3 fail due to longitudinal rotation.

Table 6.26. General Geometric Properties of Bridge 12.

Location	Parameter	Description/Value
Bridge	Location	Harris County, IH 10
	Year Designed/Year Built	2004/2007
	Design Load	HS25
	Length, ft	465
	Spans, ft	140, 180, 145
	Radius of Curvature, ft	225
Deck	Width, ft	28.417
	Thickness, in.	8.5
	Haunch, in.	3.5
	Rail Type	SSTR
Rebar	# of Bar Longitudinal Top Row (#5)	40
	# of Bar Longitudinal Bottom Row (#5)	30
	# of Bar Longitudinal Top Row (#5) @support	79
	# of Bar Longitudinal Bottom Row (#5) @support	30
	Transverse Spacing Top Row (#5), in.	5
	Transverse Spacing Bottom Row (#5), in.	5

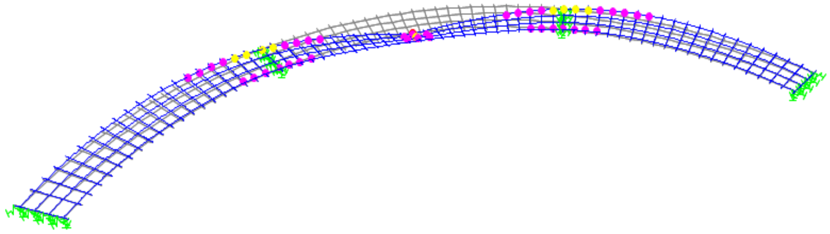

Note: The colors represent achieved curvature limits (magenta = yielding, yellow = beyond yielding, orange = beyond yielding close to failure, red = failure). Additional hinge data are located in Appendix B.

Figure 6.41. Grillage Deflection Profile for Span 2 of Bridge 12 with Activated Hinges.

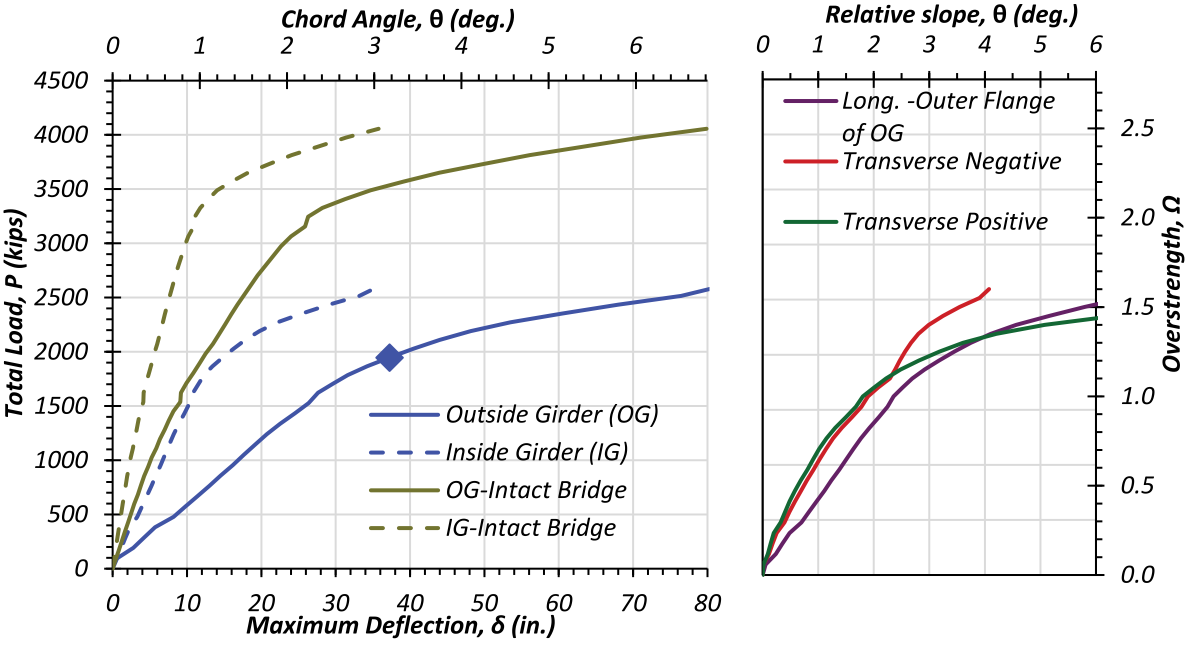

(a) Load displacement (b) Deck rotation

Note: δ is along the centerline of the girder, Ω is the load normalized by factored design load.

Figure 6.42. Grillage Analysis Results of Bridge 12, Span 1.

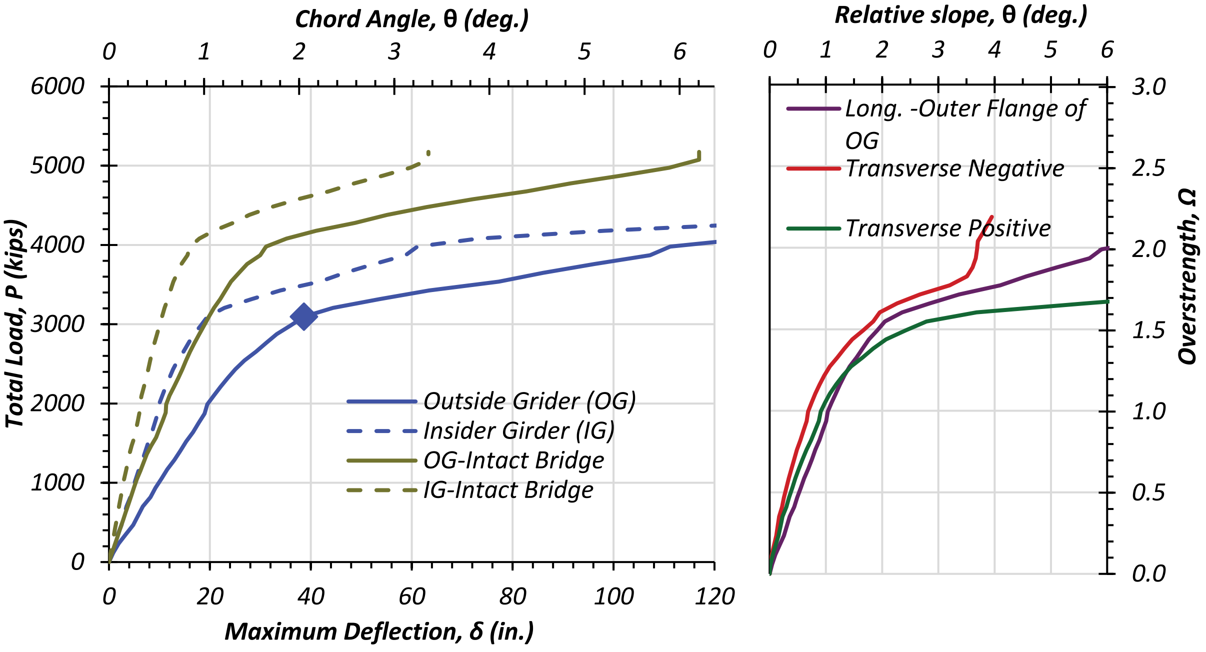

(a) Load displacement (b) Deck rotation

Note: δ is along the centerline of the girder, Ω is the load normalized by factored design load.

Figure 6.43. Grillage Analysis Results of Bridge 12, Span 2.

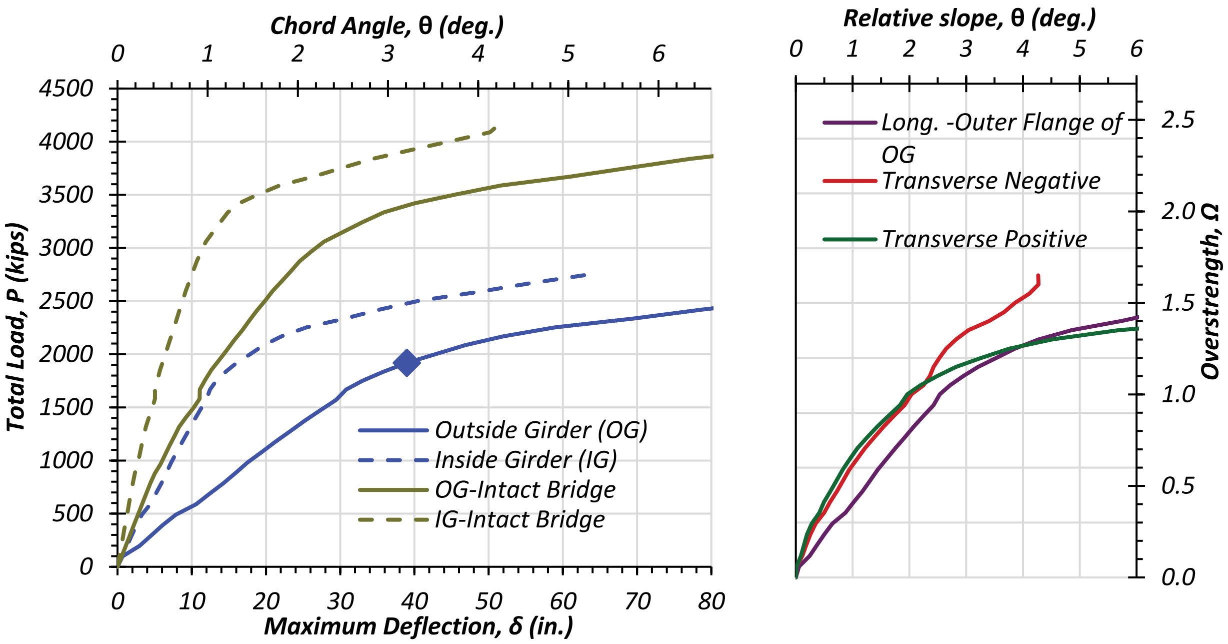

(a) Load displacement (b) Deck rotation

Note: δ is along the centerline of the girder, Ω is the load normalized by factored design load.

Figure 6.44. Grillage Analysis Results of Bridge 12, Span 3.

6.3.14 Grillage Analysis of Bridge 13—NBI #14-227-0-0015-13-452

Bridge 13, located in Travis County along I-35, is a three-span continuous bridge built in 2002. Bridge 13 has an overall deck width of 30 ft with a deck thickness of 8 in. and has 151.5 ft, 190 ft, and 151.5 ft long spans. Table 6.27 contains the geometric property details for the tub girders for Bridge 13. Table 6.28 details further geometric properties necessary for constructing an appropriate grillage model.

Table 6.27. Geometric Details of Steel Tub Girders of Bridge 13.

Location ft	Top Flange		Web		Bottom Flange	
	Width in.	Thickness in.	Width in.	Thickness in.	Width in.	Thickness in.
0–18	24	1.25	54	0.625	60	0.750
18–94	24	1.25	54	0.625	60	0.750
94–113	24	1.25	54	0.625	60	0.750
113–132	24	1.25	54	0.625	60	1.250
132–151	24	1.75	54	0.625	60	1.500
151–170	24	2.75	54	0.625	60	2.000
170–189	24	1.75	54	0.625	60	1.500
189–208	24	1.25	54	0.625	60	1.250
208–284	24	1.25	54	0.625	60	0.750
284–303	24	1.25	54	0.625	60	0.750
303–322	24	1.25	54	0.625	60	1.250
322–341	24	1.75	54	0.625	60	1.500
341–360	24	2.75	54	0.625	60	2.000
360–379	24	1.75	54	0.625	60	1.500
379–398	24	1.25	54	0.625	60	1.250
398–474	24	1.25	54	0.625	60	0.750
474–493	24	1.25	54	0.625	60	0.750

Figure 6.45 illustrates the deflection profile of Bridge 13 with a fractured second span and with the HL-93 load case. Figure 6.46 and Figure 6.47 depict the load displacement behavior of each span of Bridge 13. Spans 1 and 3 have an intact overstrength factor of 2.10 with a fractured overstrength factor of 1.10. Span 2 has an intact overstrength factor of 2.20 and a fractured overstrength factor of 1.35. All spans of Bridge 3 fail due to longitudinal rotation.

Table 6.28. General Geometric Properties of Bridge 13.

Location	Parameter	Description/Value
Bridge	Location	Travis County, I-35
	Year Designed/Year Built	1998/2002
	Design Load	HS20
	Length, ft	493
	Spans, ft	151.5, 190, 151.5
	Radius of Curvature, ft	450
Deck	Width, ft	30
	Thickness, in.	8
	Haunch, in.	4
	Rail Type	T4(S)
Rebar	# of Bar Longitudinal Top Row (#4)	40
	# of Bar Longitudinal Bottom Row (#5)	32
	# of Bar Longitudinal Top Row (#4) @support	39
	# of Bar Longitudinal Top Row (#5) @support	40
	# of Bar Longitudinal Bottom Row (#5) @support	32
	Transverse Spacing Top Row (#5), in.	6
	Transverse Spacing Bottom Row (#5), in.	6

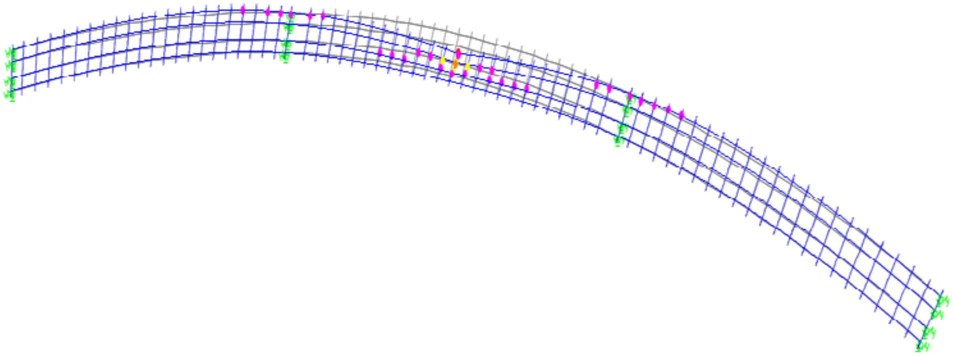

Note: The colors represent achieved curvature limits (magenta = yielding, yellow = beyond yielding, orange = beyond yielding close to failure, red = failure). Additional hinge data are located in Appendix B.

Figure 6.45. Grillage Deflection Profile for Span 2 of Bridge 13 with Activated Hinges.

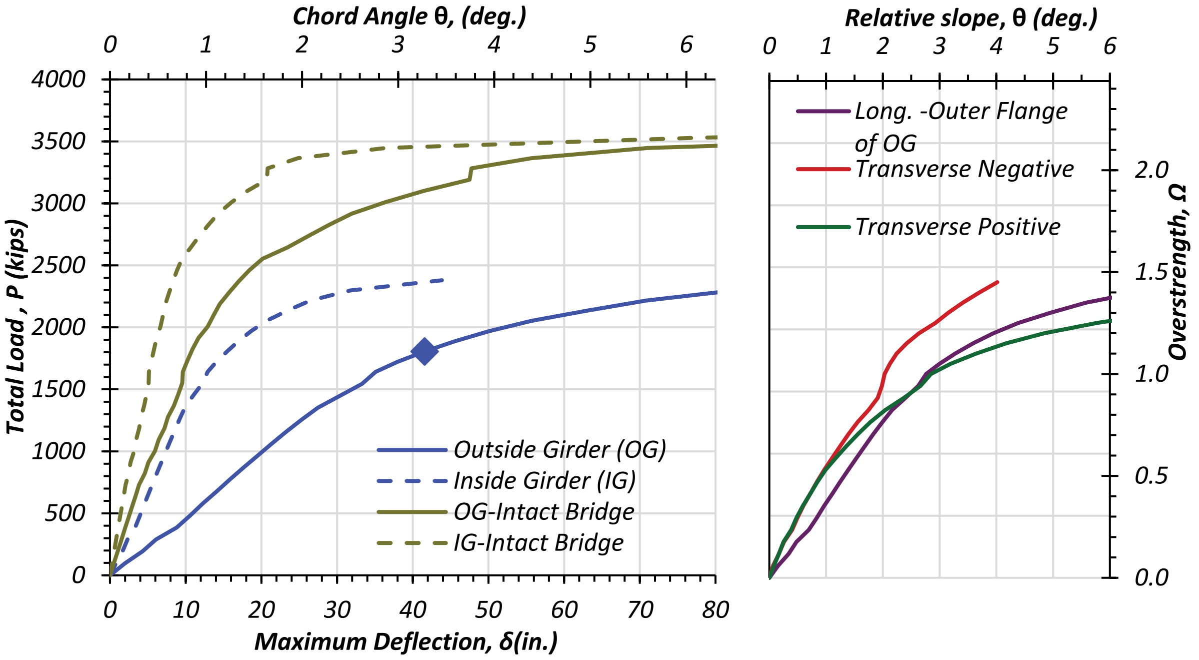

(a) Load displacement *(b) Deck rotation*

Note: δ is along the centerline of the girder, Ω is the load normalized by factored design load.

Figure 6.46. Grillage Analysis Results of Bridge 13, Spans 1 and 3.

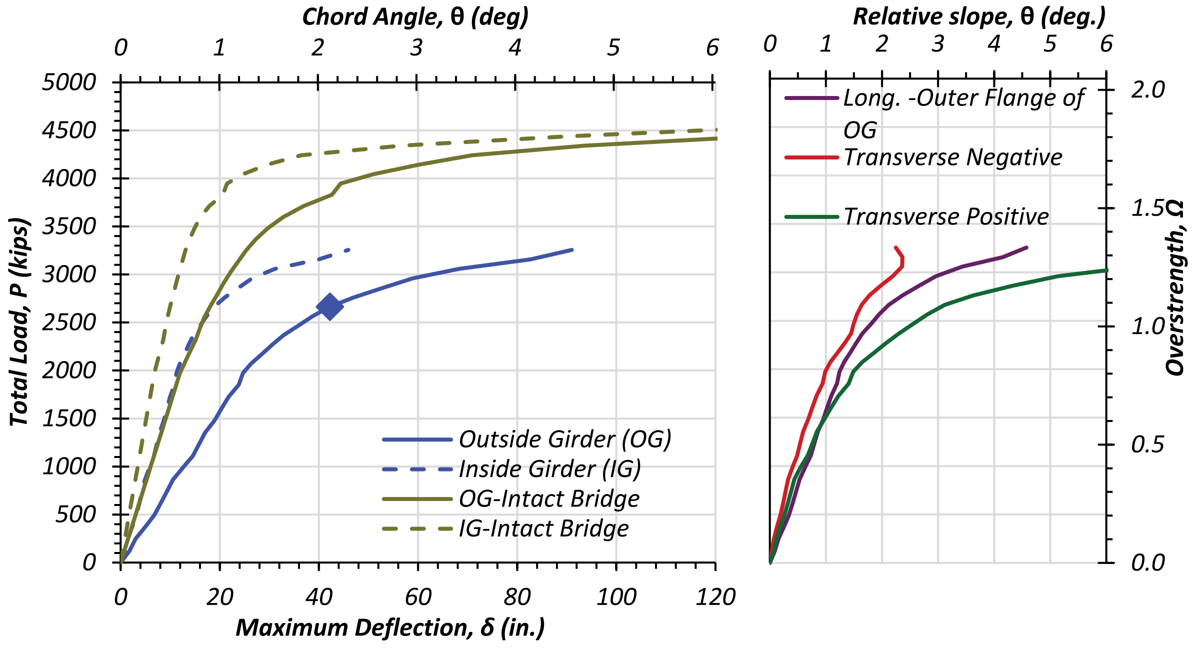

(a) Load displacement *(b) Deck rotation*

Note: δ is along the centerline of the girder, Ω is the load normalized by factored design load.

Figure 6.47. Grillage Analysis Results of Bridge 13, Span 2.

6.3.15 Grillage Analysis of Bridge 14—NBI #18-057-0-0009-11-460

Bridge 14, built in Dallas County in 2012, is a three-span continuous bridge built along IH 30. Bridge 14 consists of three spans with lengths of 150 ft, 190 ft, and 150 ft. It has a deck with an overall width of 28 ft and a thickness of 8 in. Table 6.29 contains the geometric information of the steel tub girders for Bridge 14. Note that the top flanges, web, and bottom flange vary in thickness along the length of the girder. Table 6.30 contains additional information needed to construct an accurate grillage model of Bridge 14.

Table 6.29. Geometric Details of Steel Tub Girders of Bridge 14.

Location ft	Top Flange		Web		Bottom Flange	
	Width in.	Thickness in.	Width in.	Thickness in.	Width in.	Thickness in.
0–103	22	1.00	60	0.5625	70	0.750
103–112	22	1.00	60	0.5625	70	1.125
112–131	22	1.00	60	0.625	70	1.125
131–169	22	1.75	60	0.625	70	1.500
169–198	22	1.00	60	0.625	70	1.125
198–302	22	1.00	60	0.5625	70	0.750
302–321	22	1.00	60	0.625	70	1.125
321–358	22	1.75	60	0.625	70	1.500
358–386	22	1.00	60	0.625	70	1.125
386–490	22	1.00	60	0.5625	70	0.750

Figure 6.48 shows the deflection profile of Span 2 under the ultimate HL-93 loading with a mid-span fracture and activated plastic hinge**.** Figure 6.49 and Figure 6.50 illustrate the load displacement behavior of all spans of Bridge 14. Spans 1 and 3 have an intact overstrength factor of 2.15 and a fractured overstrength factor of 1.25. Span 2 has an intact overstrength factor of 2.05 and a fractured overstrength factor of 1.35. All spans of Bridge 14 have fractured overstrength factors greater than 1 and are therefore redundant. All spans of Bridge 14 are controlled by the longitudinal rotation limit.

Table 6.30. General Geometric Properties of Bridge 14.

Location	Parameter	Description/Value
Bridge	Location	Dallas County, IH 30
	Year Designed/Year Built	2008/2012
	Design Load	HS20
	Length, ft	490
	Spans, ft	150,190,150
	Radius of Curvature, ft	1010
Deck	Width, ft	28
	Thickness, in.	8
	Haunch, in.	4
	Rail Type	SSTR
Rebar	# of Bar Longitudinal Top Row (#4)	38
	# of Bar Longitudinal Bottom Row (#5)	32
	# of Bar Longitudinal Top Row (#4) @support	38
	# of Bar Longitudinal Top Row (#5) @support	38
	# of Bar Longitudinal Bottom Row (#5) @support	32
	Transverse Spacing Top Row (#5), in.	6
	Transverse Spacing Bottom Row (#5), in.	6

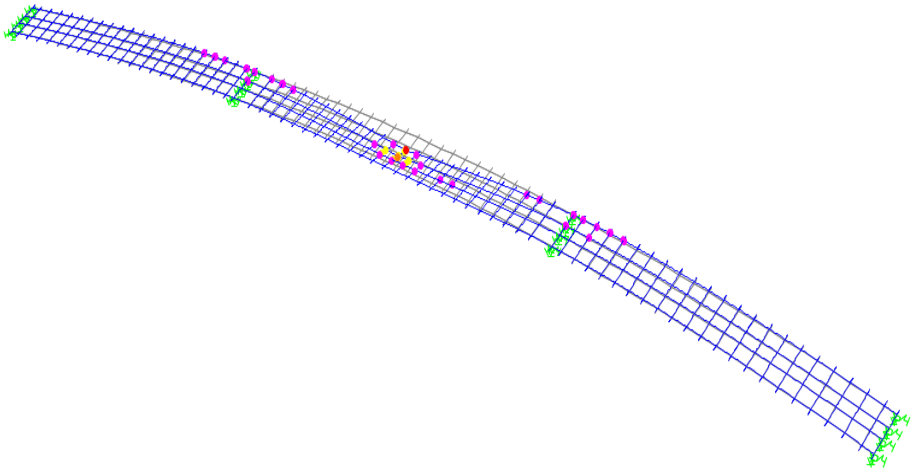

Note: The colors represent achieved curvature limits (magenta = yielding, yellow = beyond yielding, orange = beyond yielding close to failure, red = failure). Additional hinge data are located in Appendix B.

Figure 6.48. Grillage Deflection Profile for Span 2 of Bridge 14 with Activated Hinges.

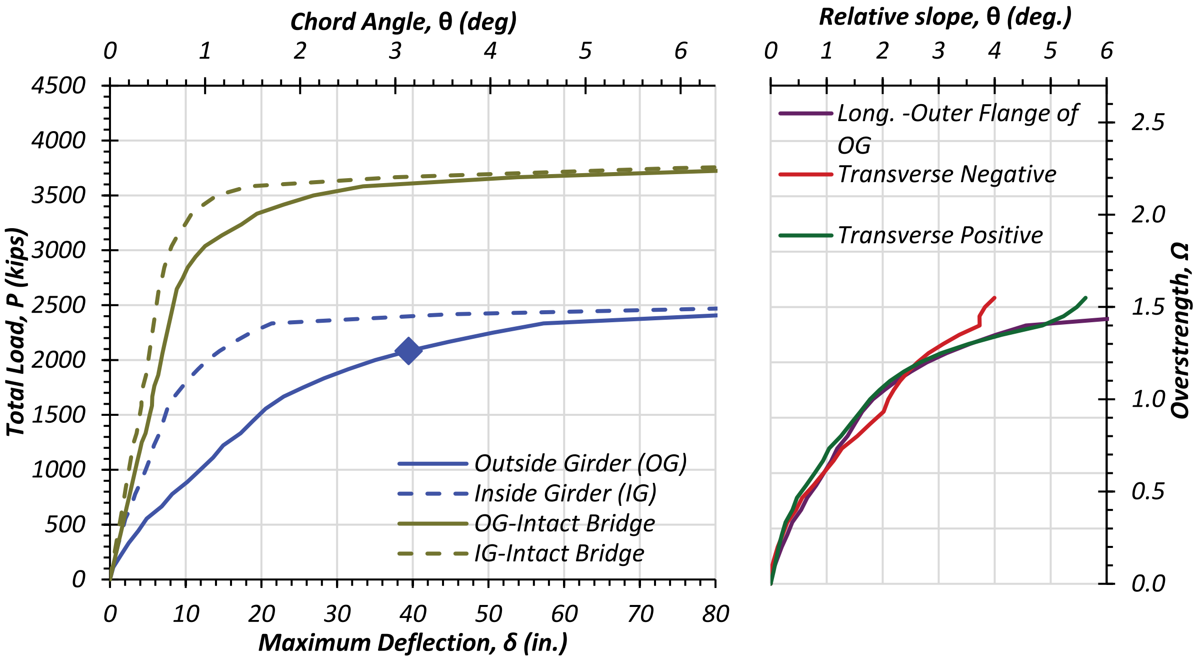

(a) Load displacement *(b) Deck rotation*

Note: δ is along the centerline of the girder, Ω is the load normalized by factored design load.

Figure 6.49. Grillage Analysis Results of Bridge 14, Spans 1 and 3.

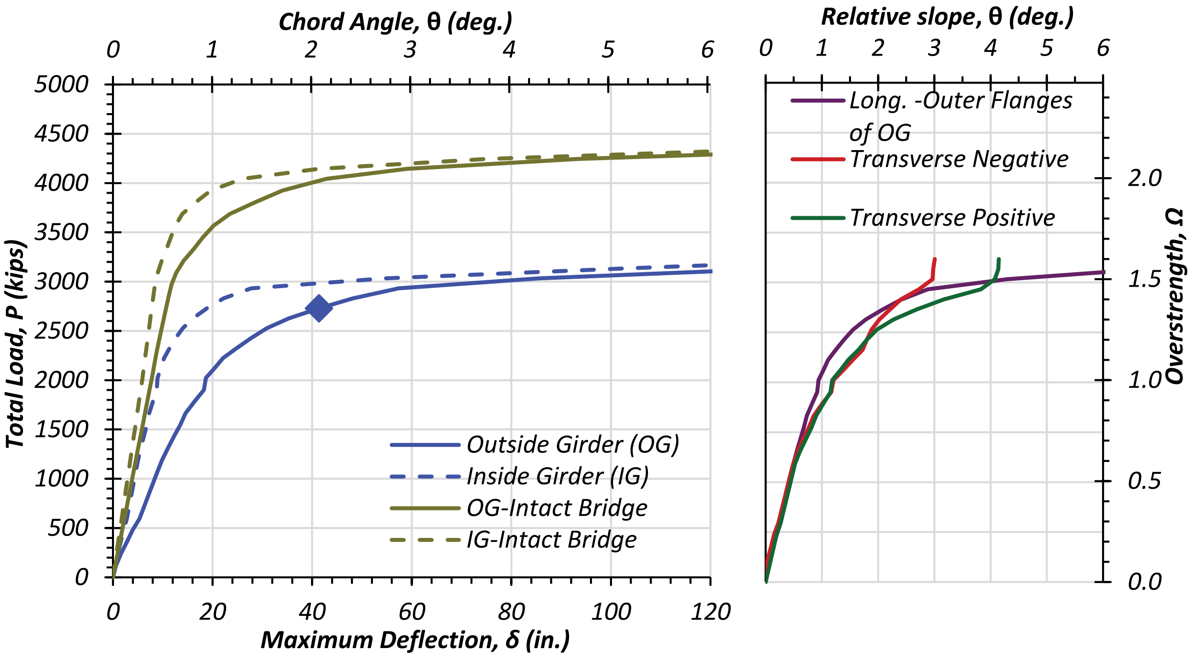

(a) Load displacement *(b) Deck rotation*

Note: δ is along the centerline of the girder, Ω is the load normalized by factored design load.

Figure 6.50. Grillage Analysis Results of Bridge 14, Span 2.

6.3.16 Grillage Analysis of Bridge 15—NBI #12-102-0271-06-689

The final bridge investigated in this study is Bridge 15. It is a three-span continuous bridge. Bridge 15 contains 200 ft, 295 ft, and 200 ft long spans, with an overall deck width of 28.4 ft and a thickness of 8 in. Table 6.31 details the geometric details of the tub girders in Bridge 15. It should be noted that the top and bottom flanges vary in thickness along the length of the girder. Table 6.32 outlines additional information regarding the geometric configuration of Bridge 15 needed to generate an appropriate grillage model.

Table 6.31. Geometric Details of Steel Tub Girders of Bridge 15.

Location ft	Top Flange		Web		Bottom Flange	
	Width in.	Thickness in.	Width in.	Thickness in.	Width in.	Thickness in.
0–126	24	1.25	84	0.6875	53.5	1.250
126–147	24	1.50	84	0.6875	53.5	1.750
147–168	24	1.75	84	0.6875	53.5	2.000
168–189	24	2.25	84	0.6875	53.5	2.250
189–210	24	2.25	84	0.6875	53.5	2.250
210–231	24	2.50	84	0.6875	53.5	2.500
231–252	24	1.75	84	0.6875	53.5	2.000
252–284	24	1.25	84	0.6875	53.5	1.250
284–410	24	1.50	84	0.6875	53.5	1.750
410–422	24	1.25	84	0.6875	53.5	1.250
422–463	24	1.75	84	0.6875	53.5	2.000
463–484	24	2.25	84	0.6875	53.5	2.250
484–505	24	2.50	84	0.6875	53.5	2.500
505–526	24	2.25	84	0.6875	53.5	2.250
526–547	24	1.75	84	0.6875	53.5	2.000
547–568	24	1.50	84	0.6875	53.5	1.750
568–698	24	1.25	84	0.6875	53.5	1.250

Figure 6.51 depicts the displacement profile of the fractured Span 2 under the ultimate HL-93 loading case. Figure 6.52 and Figure 6.53 show the load displacement response of all spans in Bridge 15. Spans 1 and 3 have an intact overstrength factor of 2.45 and a fractured overstrength factor of 1.40. Span 2 has a fractured overstrength factor of 1.25. All three spans of Bridge 15 have fractured omega factors greater than 1 and are considered redundant. Every span in Bridge 15 is controlled by longitudinal rotation.

Table 6.32. General Geometric Properties of Bridge 15.

Location	Parameter	Description/Value
Bridge	Location	Dallas County, IH 30
	Year Designed/Year Built	2008/2012
	Design Load	HS20
	Length, ft	490
	Spans, ft	150,190,150
	Radius of Curvature, ft	1010
Deck	Width, ft	28
	Thickness, in.	8
	Haunch, in.	4
	Rail Type	SSTR
Rebar	# of Bar Longitudinal Top Row (#5)	38
	# of Bar Longitudinal Bottom Row (#5)	36
	# of Bar Longitudinal Top Row (#5) @support	77
	# of Bar Longitudinal Bottom Row (#5) @support	36
	Transverse Spacing Top Row (#5), in.	5
	Transverse Spacing Bottom Row (#5), in.	5

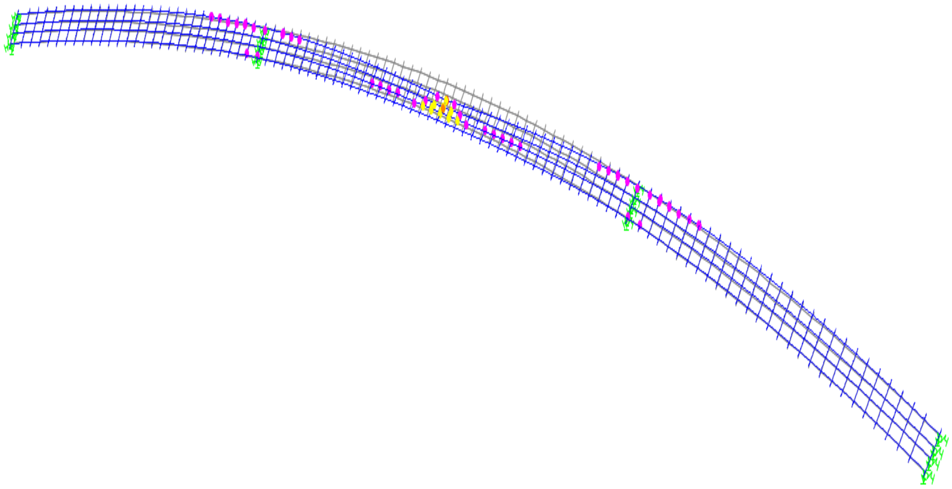

Note: The colors represent achieved curvature limits (magenta = yielding, yellow = beyond yielding, orange = beyond yielding close to failure, red = failure). Additional hinge data are located in Appendix B.

Figure 6.51. Grillage Deflection Profile for Span 2 of Bridge 15 with Activated Hinges.

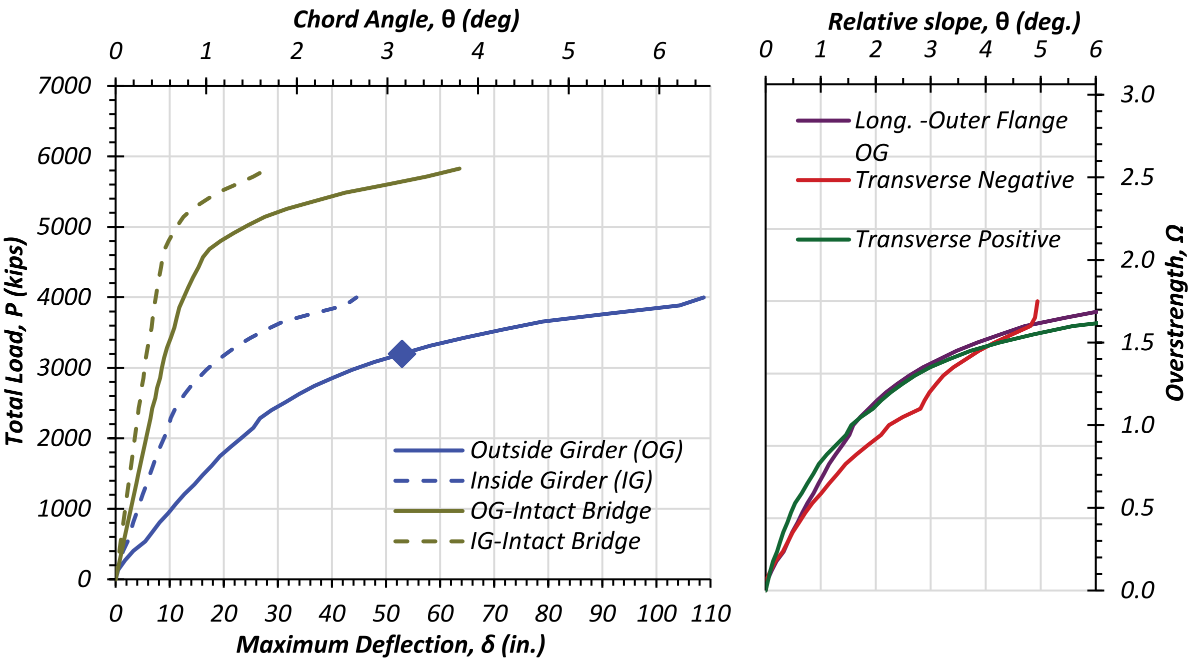

(a) Load displacement *(b) Deck rotation*

Note: δ is along the centerline of the girder, Ω is the load normalized by factored design load.

Figure 6.52. Grillage Analysis Results of Bridge 15, Spans 1 and 3.

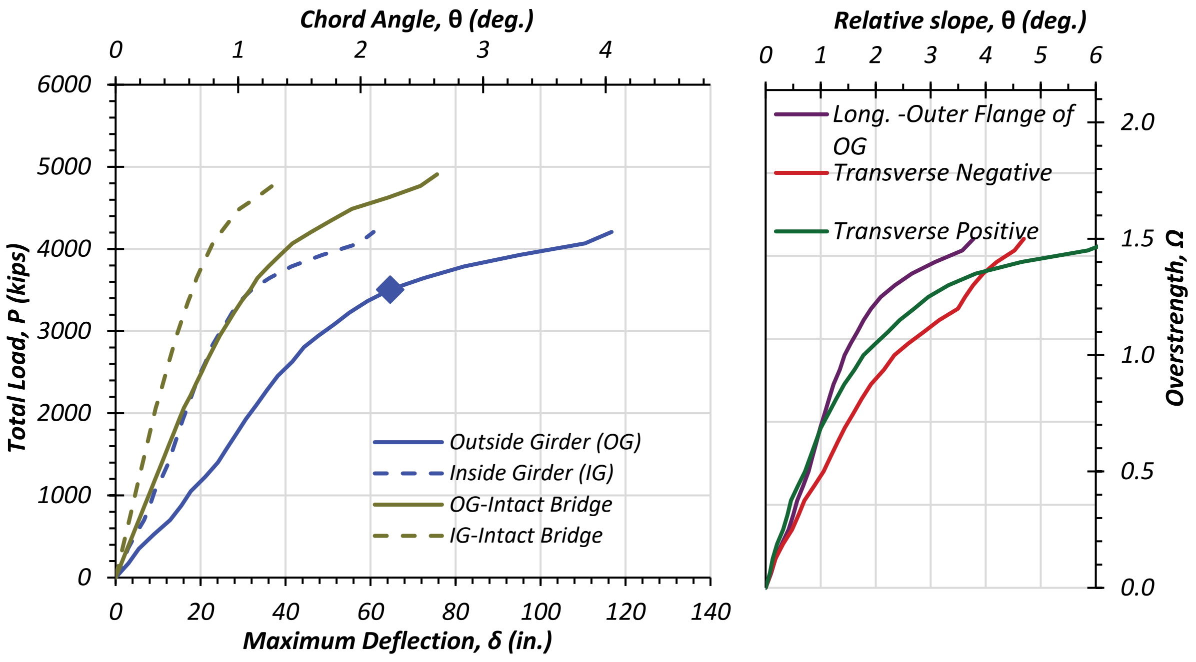

(a) Load displacement *(b) Deck rotation*

Note: δ is along the centerline of the girder, Ω is the load normalized by factored design load.

Figure 6.53. Grillage Analysis Results of Bridge 15, Span 2.

6.4 CONCLUSION

In the portion of the STTG study discussed in this chapter, 15 bridges from the Texas bridge inventory were evaluated to determine their strength and redundancy before and after a simulated fracture under HL-93 design load. The 15 bridges were modeled using the state-of-the-art structural analysis program SAP2000 based on matrix analysis methods and principles. These bridges were evaluated in a manner outlined in Section 6.2 of this report. Table 6.33, Table 6.34, and Table 6.35 offer a summary of the grillage analysis results gathered and include the normalized load for the fractured and nonfractured cases for each bridge. From the grillage analysis results, the following observations were seen:

- Overall, simple-span bridges have much lower fractured overstrength factors than their continuous-span counterparts. The fractured overstrength factors range from 0.16 to 1.11, while their intact overstrength factors range from 3.42 to 1.00. On average, after simulating a full web fracture, simple-span bridges experience a strength reduction of nearly 74 percent.
- In the case of exterior spans of continuous bridges (all spans in two-span bridges and the exterior span in three-span bridges), fractured overstrength factors range from 0.60 to 1.71. Their intact overstrength factors range from 1.45 to 3.38. However, overall, exterior spans lose an average of 46 percent of their initial strength post web fracture, which is significantly less than that of the single-span bridges.
- When compared to single-span bridges and the exterior spans, the interior spans of the three-span continuous bridge had the lowest strength reduction post full web fracture. This outcome can be seen by looking at the results of the continuous bridges. The intact overstrength factors range from 1.85 to 3.10. The fractured overstrength factors range from 1.00 to 2.10. However, the average strength reduction of the interior spans is only 35 percent, which is significantly lower than that of the simple spans and exterior spans.
- The results show some redundancy due to continuity because as the degree of continuity increases, the average strength reduction decreases. These results demonstrate that even though some transverse redundancy exists between the two

girders, there is some longitudinal redundancy and load redistribution between the spans of the same bridge.

Table 6.33. Overstrength Factors for Single-Span Bridges Utilizing Grillage Analysis.

ID	Span	R (ft)	L (ft)	B (ft)	S (ft)	5% SF	5° Trans.	2° Long.
0	1	1300	120	23	6.0	1.33	1.33	**1.07**
1	1	573	220	32	9.5	0.46	0.28	**0.21**
2	1	1910	115	26	6.1	**1.11**	1.65	1.11
3	1	2207	230	39	12.6	0.60	**0.16**	0.37

Note: L = length, B = breadth, R = radius of curvature, S = spacing between interior top flanges.

Table 6.34. Overstrength Factors for End Spans Utilizing Grillage Analysis.

ID	Span	R (ft)	L (ft)	B (ft)	S (ft)	5% SF	5° Trans.	3° Long.
4	1	195	132	28	7.6	1.50	1.45	**1.30**
4	2	195	128	28	7.6	1.58	1.53	**1.32**
5	1	450	140	30	9.7	1.25	1.30	**1.10**
5	2	450	140	30	9.7	1.25	1.30	**1.10**
6	1	819	140	38	9.8	**1.43**	1.58	1.58
6	2	819	140	38	9.8	**1.43**	1.58	1.58
7	1	764	219	28	7.4	1.30	1.15	**0.94**
7	2	764	190	28	7.4	1.50	1.45	**1.25**
8	1	882	265	28	8.4	0.94	0.88	**0.83**
8	2	882	295	28	8.4	0.80	0.60	**0.60**
9	1	764	140	28	7.4	**1.35**	1.65	1.40
9	3	764	126	28	7.4	**1.53**	1.95	1.61
10	1	716	148	30	7.7	**1.71**	2.10	1.94
10	3	716	190	30	7.7	1.40	1.35	**1.25**
11	1	819	223	28	7.0	**1.35**	1.45	1.50
11	3	819	235	28	7.0	1.40	**1.30**	1.40
12	1	225	140	28	7.6	1.55	**1.20**	1.40
12	3	225	145	28	7.6	1.50	1.35	**1.15**
13	1	450	152	30	9.3	1.40	1.25	**1.10**
13	3	450	152	30	9.3	1.40	1.25	**1.10**
14	1	1010	150	28	6.5	1.35	1.45	**1.25**
14	3	1010	150	28	6.5	1.35	1.45	**1.25**
15	1	809	200	28	8.0	1.55	1.60	**1.40**
15	3	809	200	28	8.0	1.55	1.60	**1.40**

Note: L = length, B = breadth, R = radius of curvature, S = spacing between interior top flanges.

Table 6.35. Overstrength Factors for Interior Spans Utilizing Grillage Analysis.

ID	Span	R (ft)	L (ft)	B (ft)	S (ft)	5% SF	5° Trans.	2° Long.
9	2	764	151	28	7.0	**2.10**	2.50	2.15
10	2	716	265	30	7.7	1.50	1.45	**1.25**
11	2	819	366	28	7.0	1.15	1.10	**1.00**
12	2	225	180	28	7.6	2.05	1.67	**1.56**
13	2	450	190	30	9.3	1.60	1.50	**1.35**
14	2	1010	190	28	6.5	1.45	1.60	**1.35**
15	2	809	295	28	8.0	1.50	1.45	**1.25**

Note: L = length, B = breadth, R = radius of curvature, S = spacing between interior top flanges.

7 DISCUSSION AND IMPLICATIONS

7.1 INTRODUCTION AND SCOPE

From the foregoing three chapters, it is evident that there are varying degrees of disparity between the results of the three analysis methods used in this investigation. This chapter discusses the significance of those observed differences and the implications going forward in professional practice. This chapter compares the bridges by dividing them into categories by degree of redundancy. First, simply supported bridges (Bridges 0 to 3) that have no longitudinal redundancy from end fixity are considered. Next, the center spans of the three-span bridges (Bridges 9 to 15) that have full moment restraint at each end of their span are compared. Last, the end spans of all multi-span bridges (Bridges 4 to 15) are considered. The end spans have 1 degree of longitudinal redundancy that provides some protection against span collapse in the event of fracture within one of the steel tubs.

7.2 SINGLE SPANS (ZERO FIXITY AT SUPPORTS)

Figure 7.1 shows a simply supported span with a central plastic hinge. Since this location is normally the location of the maximum bending moment, it is also assumed to be the most likely location for a sudden fracture. If a fracture occurs, the remaining capacity is comprised of transverse plastic yield in the deck plus a longitudinal folded plate mechanism that exists between the twin tubs. This plastic mechanism between the fractured and intact box girders is the only measure of redundancy that exists in restraining collapse of the fractured girder. This shall be referred to as longitudinal redundancy herein.

A comparison of the simply supported analysis is presented in Figure 7.2 and Figure 7.3 for short ($L < 120$ ft) and long ($L \geq 220$ ft) bridges, respectively. Table 7.1 presents the overstrength results of the single-span bridges tabulated in increasing order of their span lengths. As the length increases, the overstrength capacity of the spans decrease. For the two shorter-span simply supported bridges presented in Figure 7.2, it is evident that the overstrength factor above the normal design requirements can be maintained ($\Omega > 1$). In contrast, the two longer single-span bridges presented in Figure 7.3 do not, in general, meet the criteria of $\Omega \geq 1$. This result suggests that at the very least there should be a limitation of span length for bridges in order to be reclassified as nonfracture critical. As a general principle, there remain limitations on the restraint that can effectively be mobilized to prevent collapse from the longitudinal redundancy inherent in this single-span class of twin tub bridge structures.

In practice, a prudently conservative approach is to continue to classify all simply supported twin tub bridges as fracture critical unless it can be shown by advanced analysis or tests that sufficient redundancy remains after fracture (i.e., $\Omega > 1$). In this instance, advanced analysis means a full non-linear FEM analysis confirmed independently by the yield line theory. Note that the non-linear grillage analysis, while promising, cannot be used with confidence for simply supported bridges at this time due to the disparity between the two computational methods. However, continued use and refinement are encouraged because the effort required to obtain a result is substantially less than that required for an FEM solution.

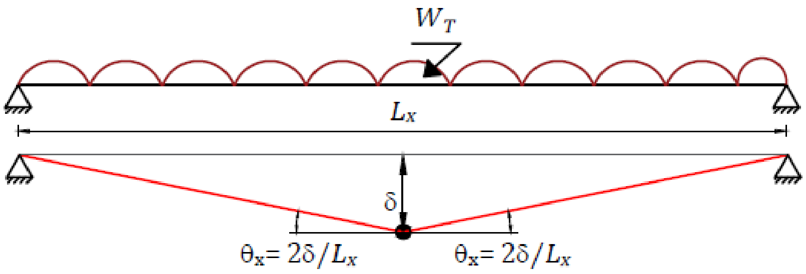

(a) Single-Span Support Conditions

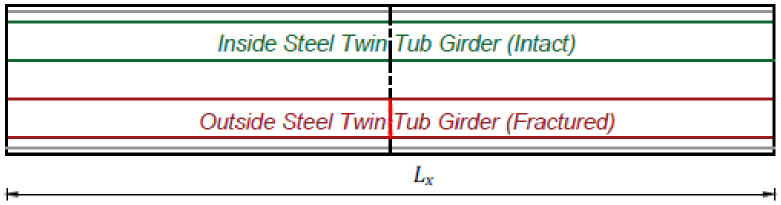

(b) Plan View of a Typical Single Span

Figure 7.1. Single Span with Zero Fixity at Supports.

Table 7.1. Overstrength Results for Single-Span Twin Tub Girder Bridges.

ID	Span	R (ft)	L (ft)	B (ft)	S (ft)	FEM	Yield Line		Grillage
							Upper Bound	Lower Bound	
2	1	1910	**115**	26	6.1	1.65	1.17	1.02	1.11
0	1	1300	**120**	23	6	0.86	1.46	1.28	1.07
1	1	573	**220**	32	9.5	0.82	0.62	0.57	0.21
3	1	2207	**230**	39	12.6	0.85	0.51	0.44	0.16

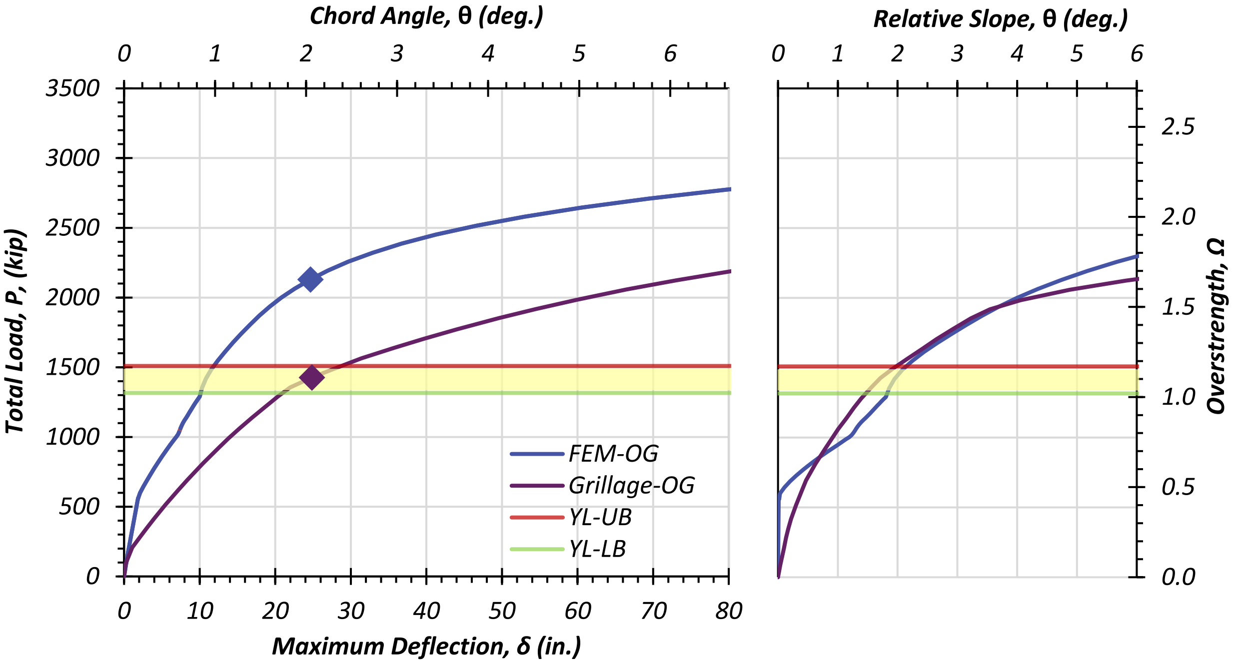

(i) Load displacement (ii) Deck rotations

(a) Comparison of the Results for Bridge 2, L = 115 ft

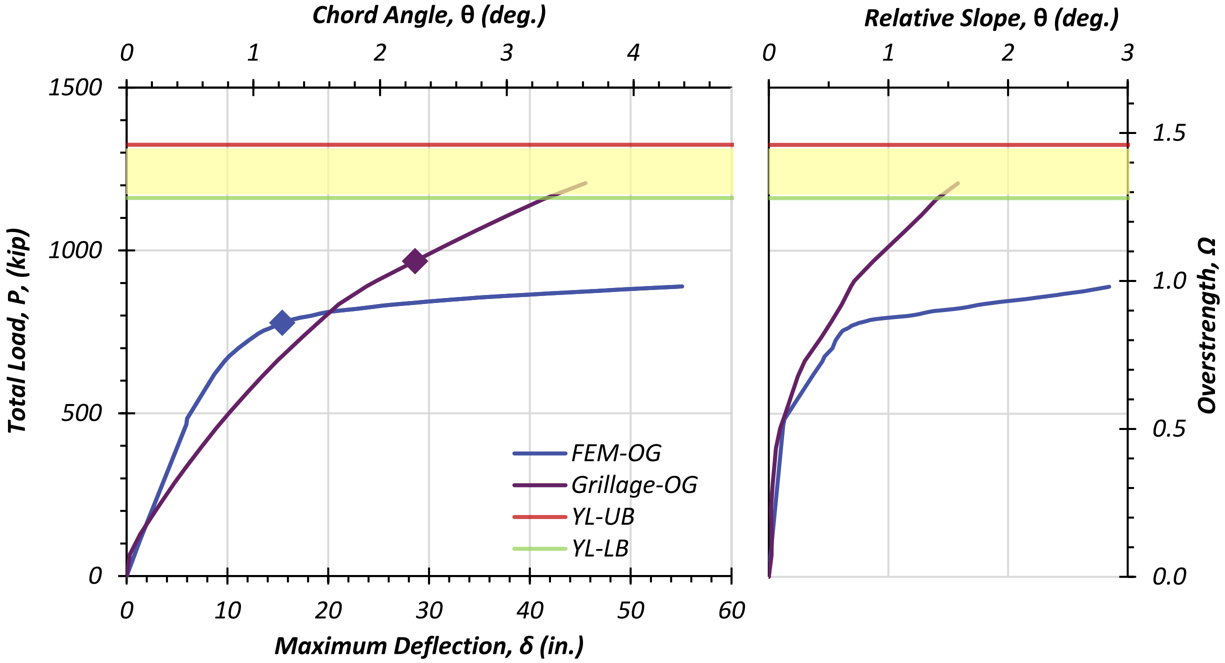

(i) Load displacement (ii) Deck rotations

(b) Comparison of the Results for Bridge 0, L = 120 ft

Figure 7.2. Results for Short Single-Span (Simply Supported) Fractured Twin Tub Bridges

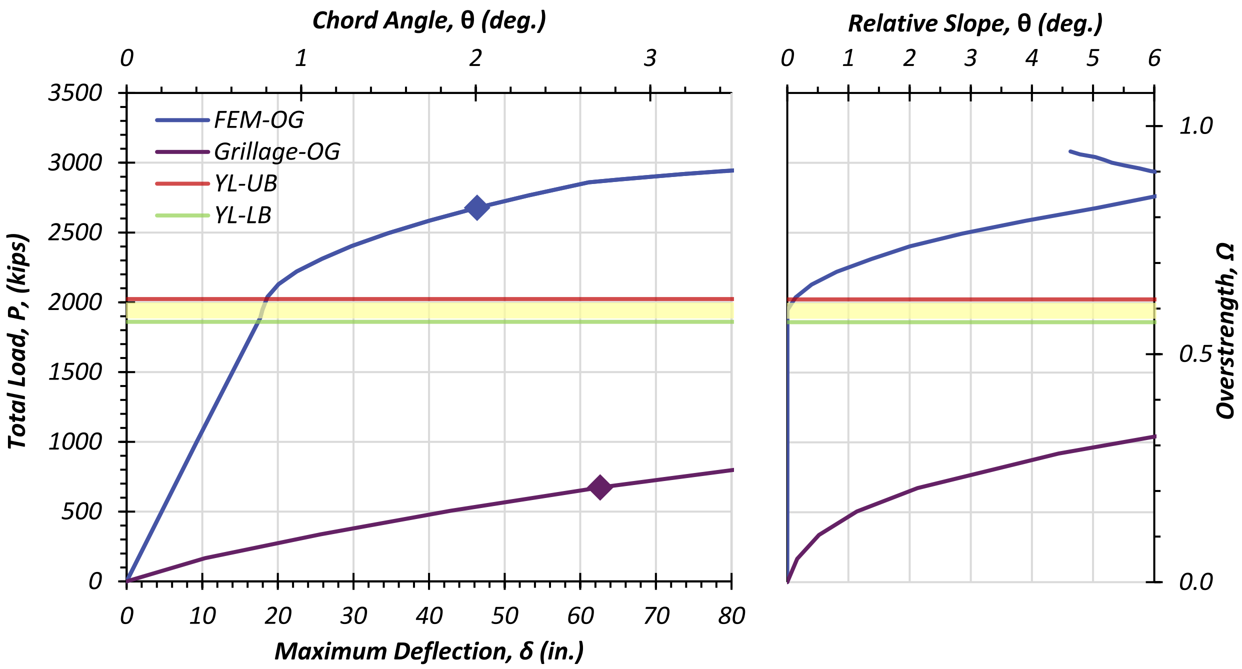

(i) Load displacement *(ii) Deck rotations*

(a) Comparison of the Results for Bridge 1, L = 220 ft

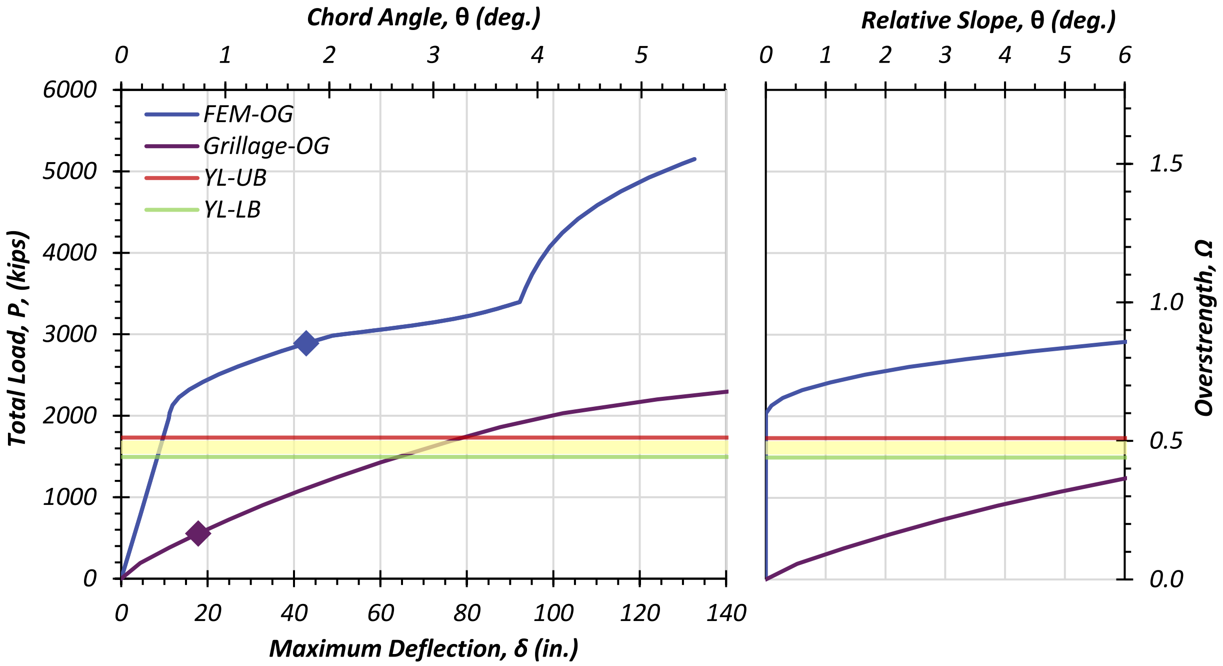

(i) Load displacement *(ii) Deck rotations*

(b) Comparison of the Results for Bridge 3, L = 230 ft

Figure 7.3. Results for Long Single-Span (Simply Supported) Fractured Twin Tub Bridges.

7.3 INTERIOR SPANS WITH TWO DEGREES OF LONGITUDINAL FIXITY

Figure 7.4 shows a typical interior span of a multi-span bridge structure. To form a plastic collapse mechanism, it is necessary to form three plastic hinges: one in the center of the span region where the positive moments are greatest, and one at each end of the span over the pier supports. For a fracture critical twin tub bridge, it is assumed that it is the interior hinge region that is prone to brittle fracture, leaving the deck alone to provide a transverse yield line at the fractured tub location.

Additional redundancy is then provided by the transverse hinge and yield lines at each span end over the bearing seats. Like their single-span counterparts, transverse redundancy is also provided if only one tub fractures by the formation of the longitudinal folded plate mechanism. As seen from the analysis of the simple-span bridges, the longitudinal redundancy provided by the folded plate mechanism becomes increasingly inefficient as the span length increases. This effect is also demonstrated with the interior span of the three-span bridges although it is not so pronounced since much of the reserve capacity (overstrength) is supplied by the formation of the plastic hinges at the supports. Figure 7.5 through Figure 7.8 show the results sorted into average, long, and very long (interior) span bridges, respectively.

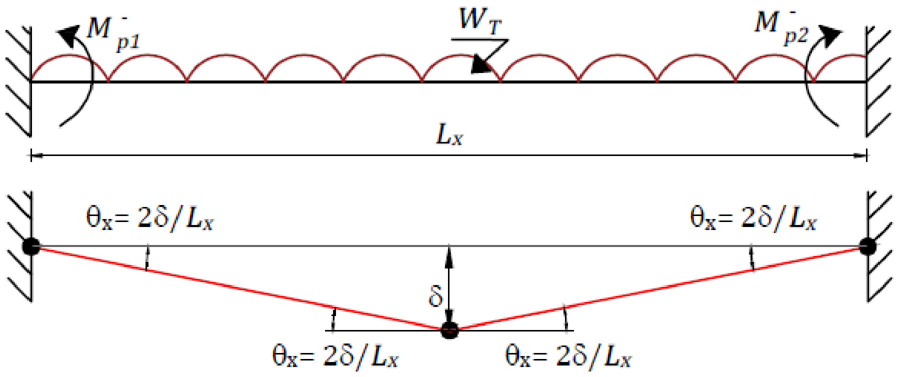

(a) Interior Span Support Conditions

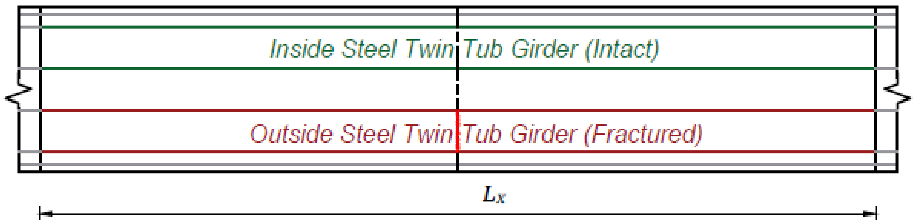

(b) Plan View of a Typical Interior Span

Figure 7.4. Interior Span with Fixities at Both Supports.

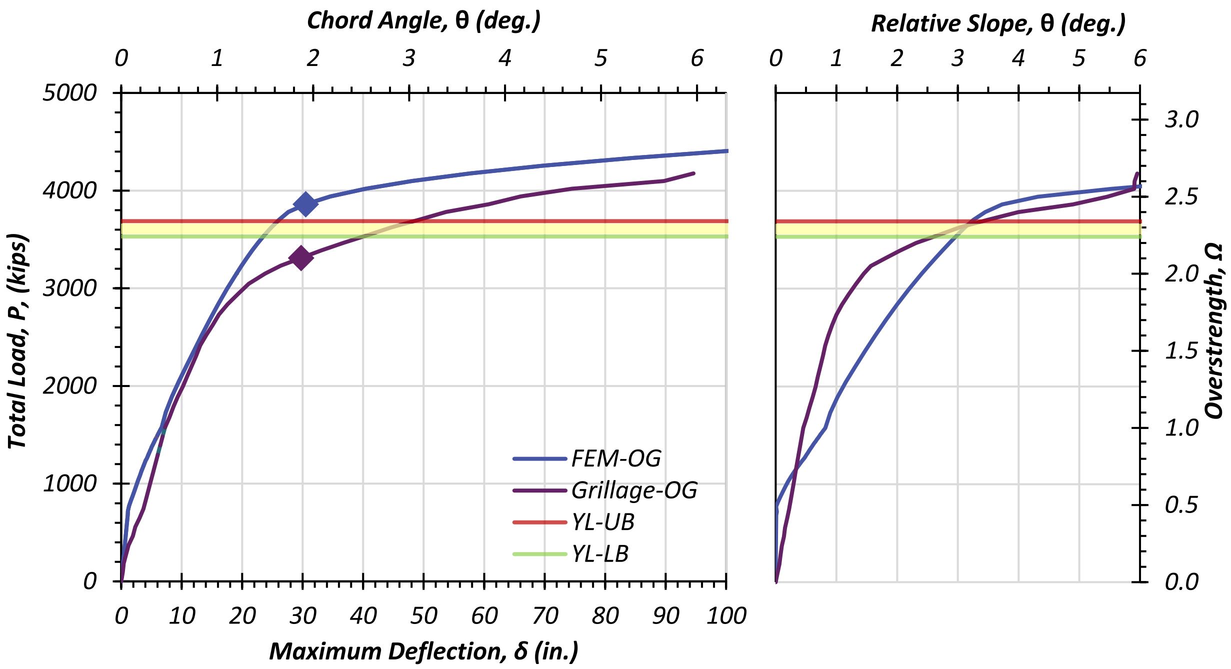

(i) Load displacement *(ii) Deck rotations*

(a) Comparison of the Results for Bridge 9, Span 2, L = 151 ft

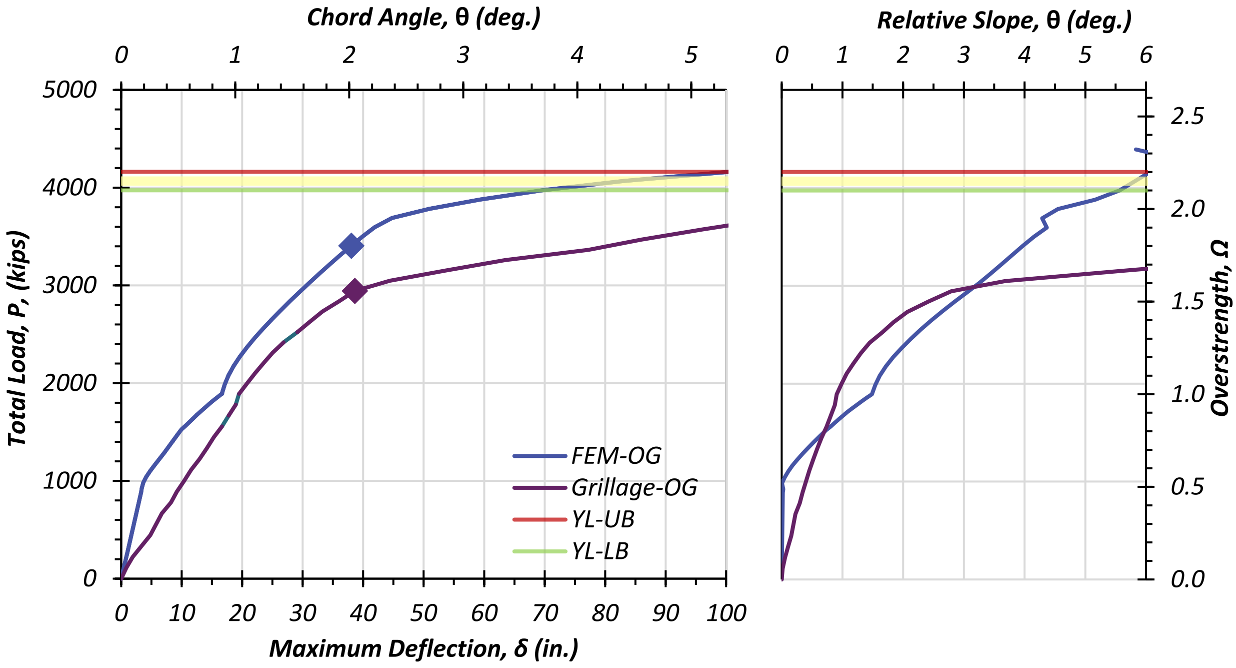

(i) Load displacement *(ii) Deck rotations*

(b) Comparison of the Results for Bridge 12, Span 2, L = 180 ft

Figure 7.5. Results for Average Interior Spans of Fractured Twin Tub Bridges.

It should be noted that in all cases the overstrength factor is greater than unity (Ω > 1), indicating that in the event of a complete fracture of a steel tub, sufficient redundancy and reserve capacity exist to sustain design loads. Table 7.2 shows the overstrength results sorted by ascending span length. It is evident that there is a reduction in overstrength as the span length increases.

Table 7.2. Overstrength Results for Interior Span Twin Tub Girder Bridges.

ID	Span	R (ft)	L (ft)	B (ft)	S (ft)	FEM	Yield Line Upper Bound	Yield Line Lower Bound	Grillage
9	2	764	151	28	7	2.45	2.34	2.24	2.10
12	2	225	180	28	7.6	1.80	2.20	2.10	1.56
13	2	450	190	30	9.3	1.40	1.89	1.80	1.35
14	2	1010	190	28	6.5	1.80	2.07	1.98	1.35
10	2	716	265	30	7.7	1.45	1.90	1.84	1.25
15	2	809	295	28	8	1.40	1.86	1.78	1.25
11	2	819	366	28	7	1.20	1.69	1.66	1.00

Figure 7.5 shows the analysis results for the shortest two average spans (Bridges 9 and 12) in this category (L < 180 ft). Reasonably good agreement is shown between the three different analysis approaches. It should be noted that when the FEMs and grillage methods exceed the upper-bound plastic (yield line) solutions, the effect is ascribed to membrane (catenary) action arising from the large vertical displacements. These two bridges have considerable overstrength ($\Omega > 2$).

Figure 7.6 shows the results for the longer of the medium-length central spans (Bridges 13 and 14, with L equivalent to 180 ft < L < 200 ft) where these spans have a moderate degree of overstrength ($1.4 < \Omega < 2.0$). While there is a disparity in the results between the two computational methods (see in particular Figure 7.6[b]), the grillage method still indicates sufficient overstrength to justify reclassifying the span as nonfracture critical. It is also worth noting that the deflections at mid-span govern at 2 degrees chord rotation, whereas $\delta \sim 42$ in. governs the overall result.

Figure 7.7 and Figure 7.8 present the results for three interior spans (Bridges 10, 15, and 11) herein defined as being long central spans (L > 200 ft) and very long central spans (L > 350 ft).

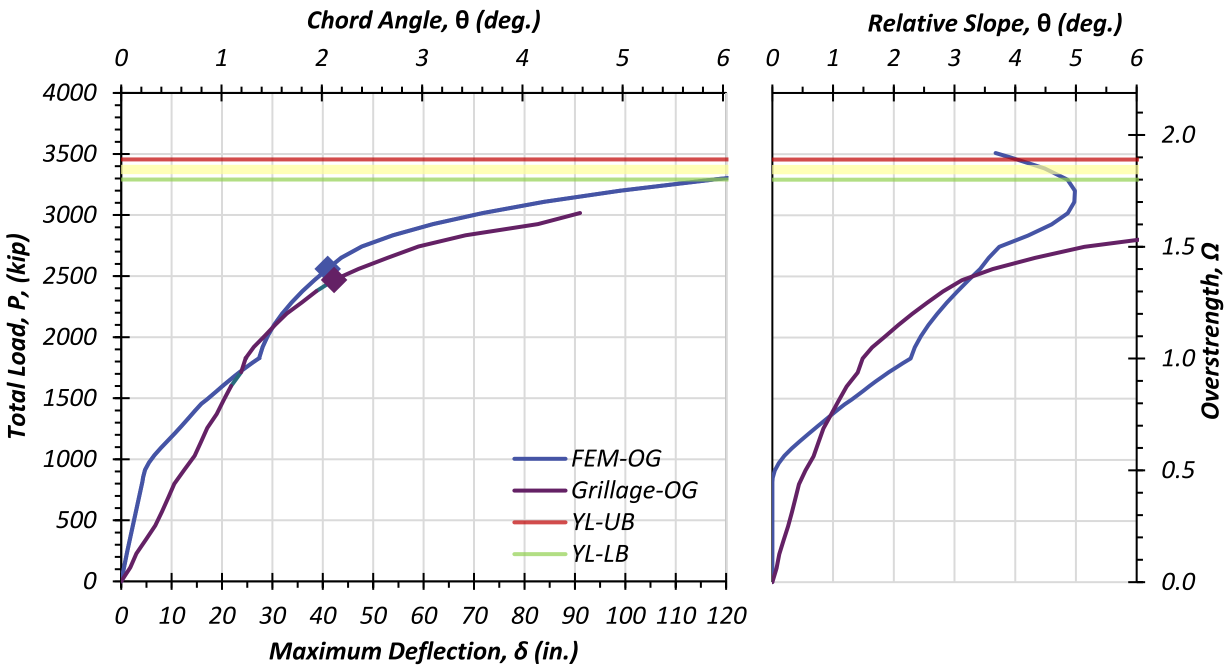

(i) Load displacement

(ii) Deck rotations

(a) Comparison of the Results for Bridge 13, Span 2, L = 190 ft

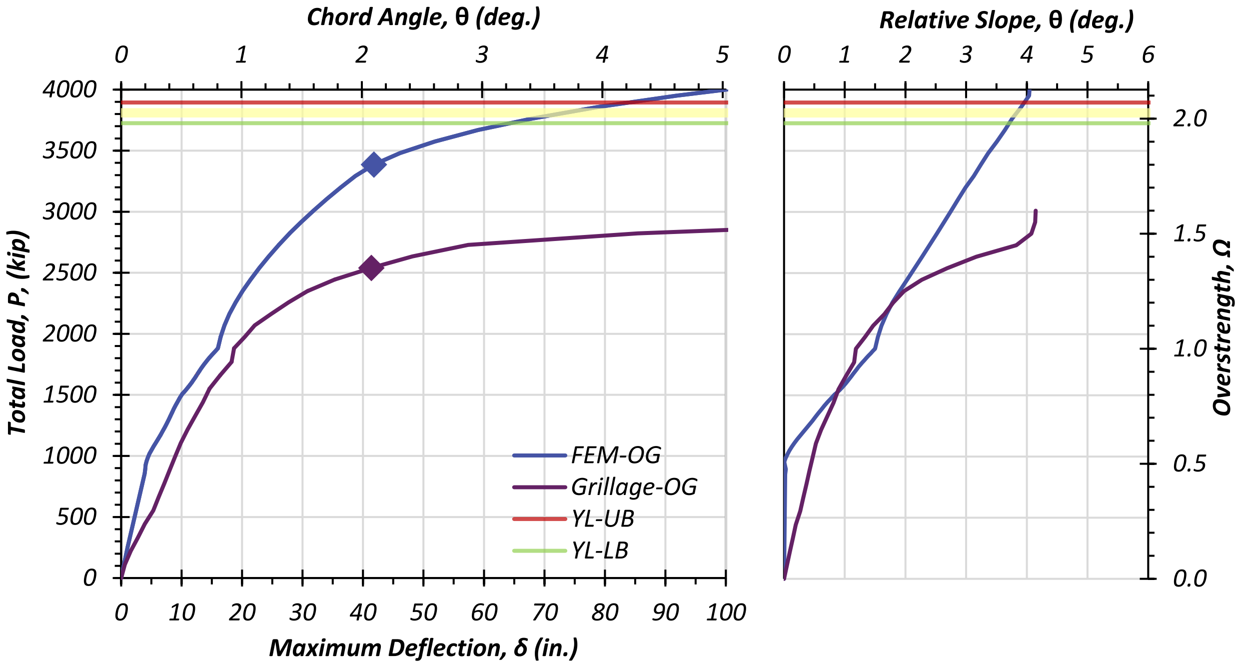

(i) Load displacement

(ii) Deck rotations

(b) Comparison of the Results for Bridge 14, Span 2, L = 190 ft

Figure 7.6. Results for Average Interior Spans of Fracture Twin Tub Bridges.

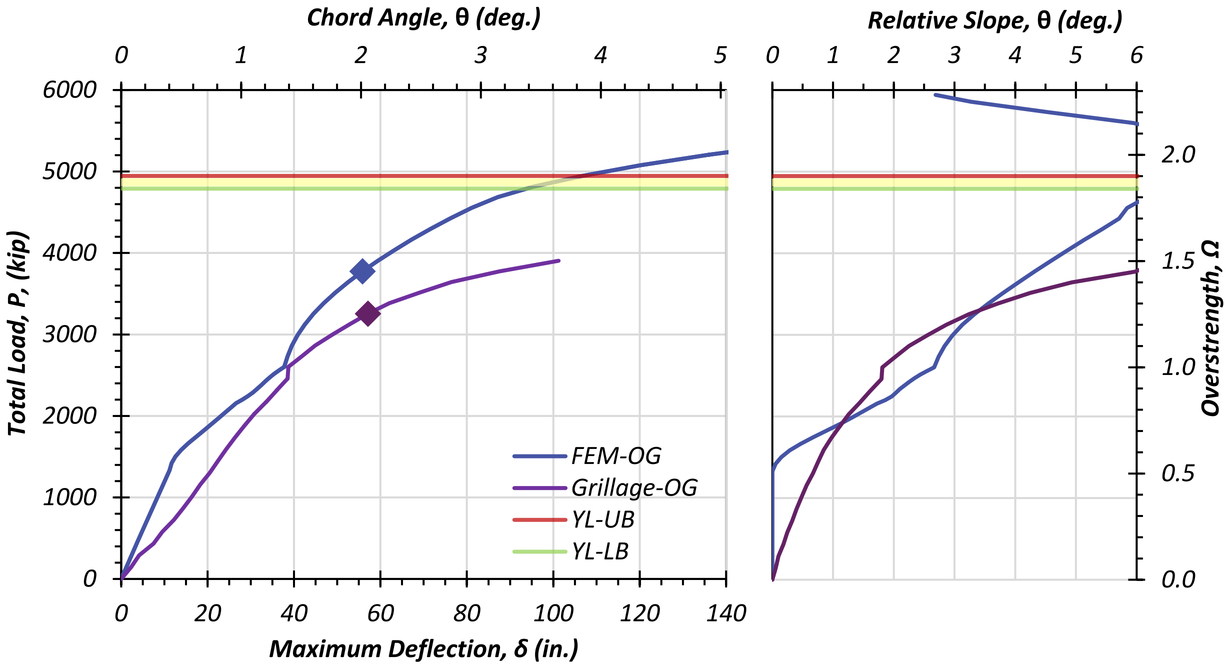

(i) Load displacement (i) Deck rotations

(a) Comparison of the Results for Bridge 10, Span 2, L = 265 ft

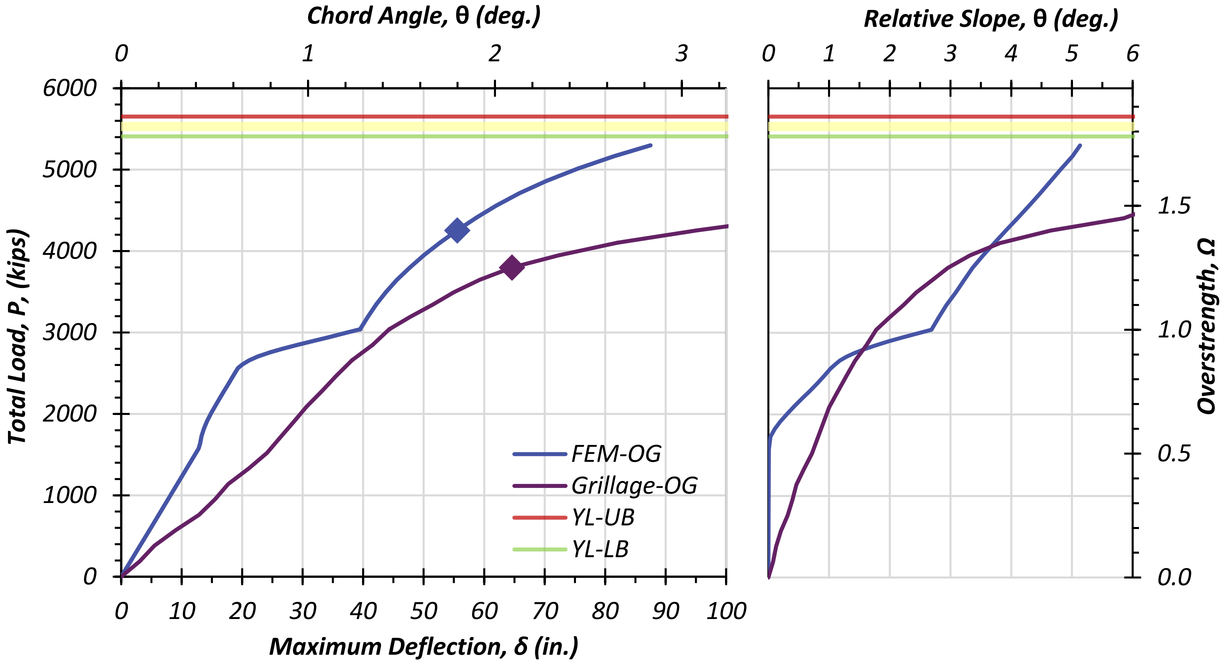

(i) Load displacement (ii) Deck rotations

(b) Comparison of the Results for Bridge 15, Span 2, L = 295 ft

Figure 7.7. Results for Long Interior Spans of Fracture Twin Tub Bridges.

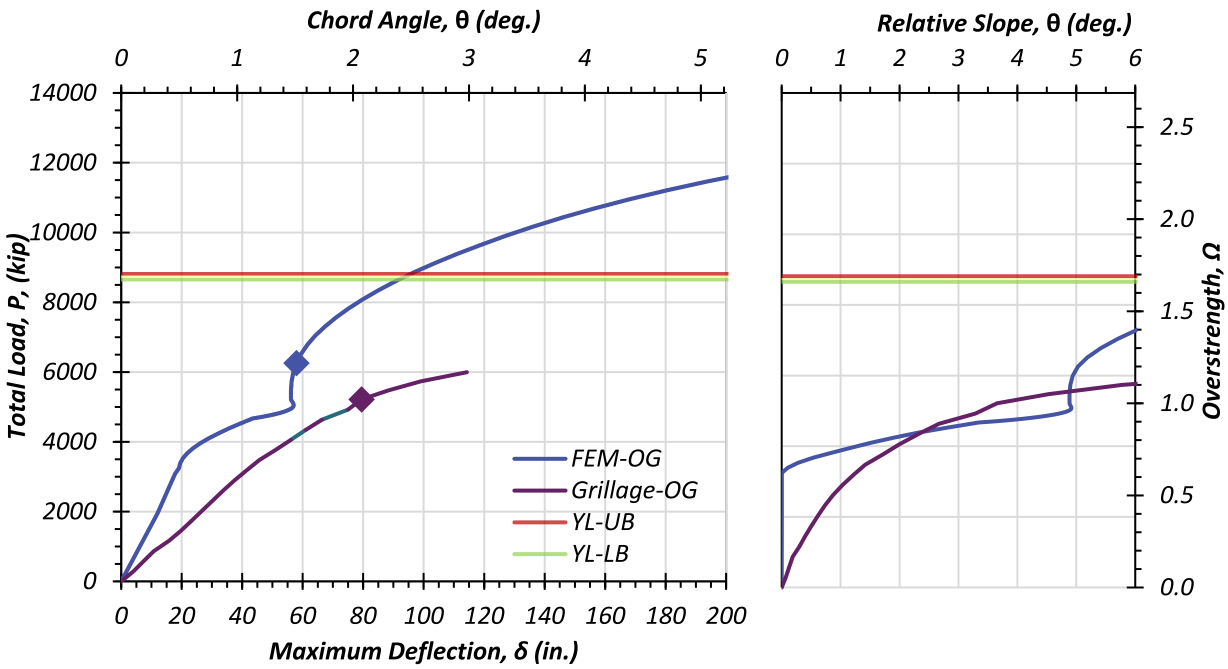

(i) Load displacement *(ii) Deck rotations*

Comparison of the Results for Bridge 11, Span 2, L = 366 ft

Figure 7.8. Results for Very Long Interior Span of Fracture Twin Tub Bridges.

While all the results show that Ω > 1, the overstrength decreases as the span length increases. The estimated overstrength factors are in good agreement between the FEM and grillage analysis, with the grillage method consistently providing the lower-bound solution. However, the disparity between the computational methods and yield line analysis becomes more pronounced for these longer spans. In part, the disparity is attributed to the three-dimensional member depth not accounted for in the yield line analysis. It is of interest to note that at a deflection of δ ~ 90 in., the capacity for both the FEM and the plastic limit analysis (yield line method) are in good agreement for each bridge.

7.4 EXTERIOR SPANS (ONE SUPPORT FIXED, ONE SUPPORT FREE)

Figure 7.9 shows a typical exterior span of a multi-span bridge structure. A plastic collapse mechanism is formed with two plastic hinges—one at the location of the maximum bending moment and one at the end of the span over the interior pier support. It is assumed that the interior hinge region is prone to brittle fracture. Section 5.4.4 explains the choice of the location of this brittle fracture at 40 percent of the span length from the exterior support. In case of a fracture, the deck alone provides a transverse yield line at the fractured tub location of the fracture critical twin tub girders. The interior support at one end of the span provides additional redundancy similar to the supports of the interior spans.

In the event of the fracturing of only one tub, transverse redundancy provided by the longitudinal folded plate mechanism is observed, like that of single and interior spans. This redundancy, too, becomes ineffectual with an increase in span length. However, the formation of the plastic hinges at the support makes up for this reduction in the system overstrength.

Figure 7.10 to Figure 7.14, Figure 7.15 to Figure 7.17, Figure 7.18 to Figure 7.19, and Figure 7.20 present the results of the exterior spans grouped as short, average, long, and very long spans, respectively. Figure 7.10(a) and (b) and Figure 7.11(a) present the shortest of the exterior spans ($L < 140$ ft) of Bridges 9 and 4, respectively. Figure 7.11(b), Figure 7.12, Figure 7.13, and Figure 7.14 present the results of those shorter spans falling under the category of 140 ft $\leq L < 150$ ft for Bridges 9, 6, 5, 12 and 10, respectively, all of which have a moderate degree of overstrength ($1.5 < \Omega < 2.0$).

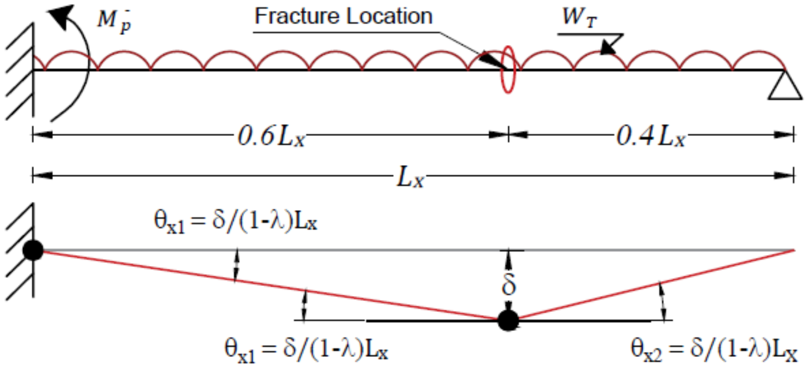

(a) Exterior Span Support Conditions

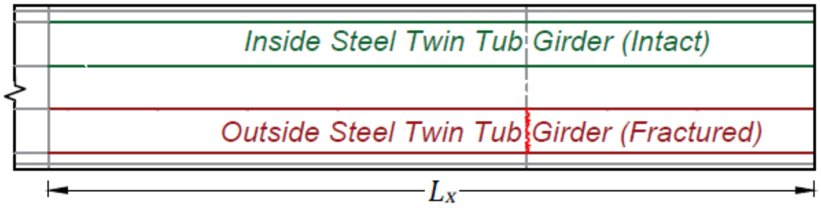

(b) Plan View of a Typical Exterior Span

Figure 7.9. Exterior Span with Fixity at One Support.

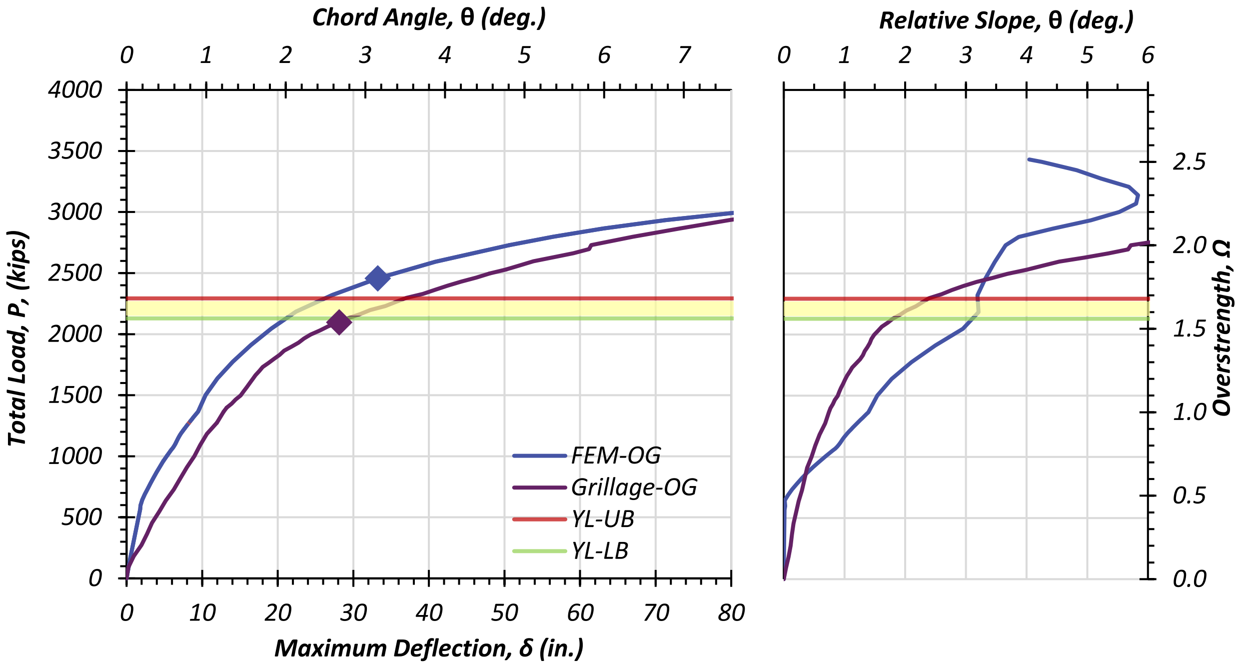

(i) Load displacement (ii) Deck rotations

(a) Comparison of the Results for Bridge 9, Span 3, L = 126 ft

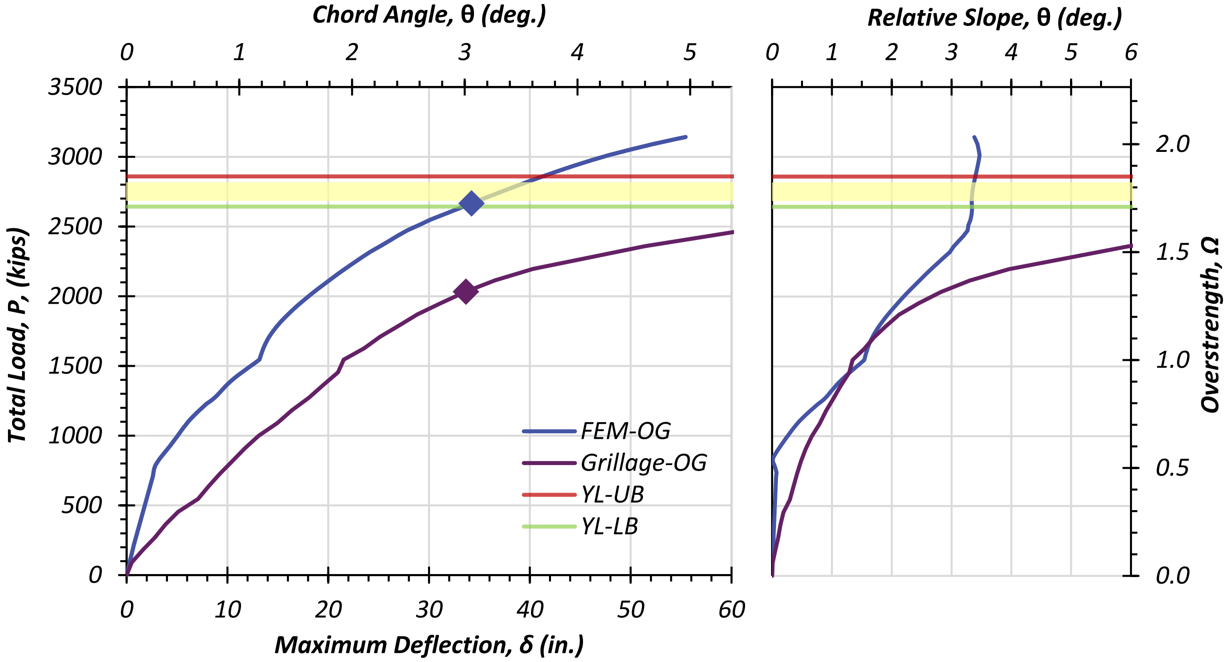

(i) Load displacement (ii) Deck rotations

(b) Comparison of the Results for Bridge 4, Span 2, L = 128 ft

Figure 7.10. Results for Short Exterior Spans of Fracture Twin Tub Bridges.

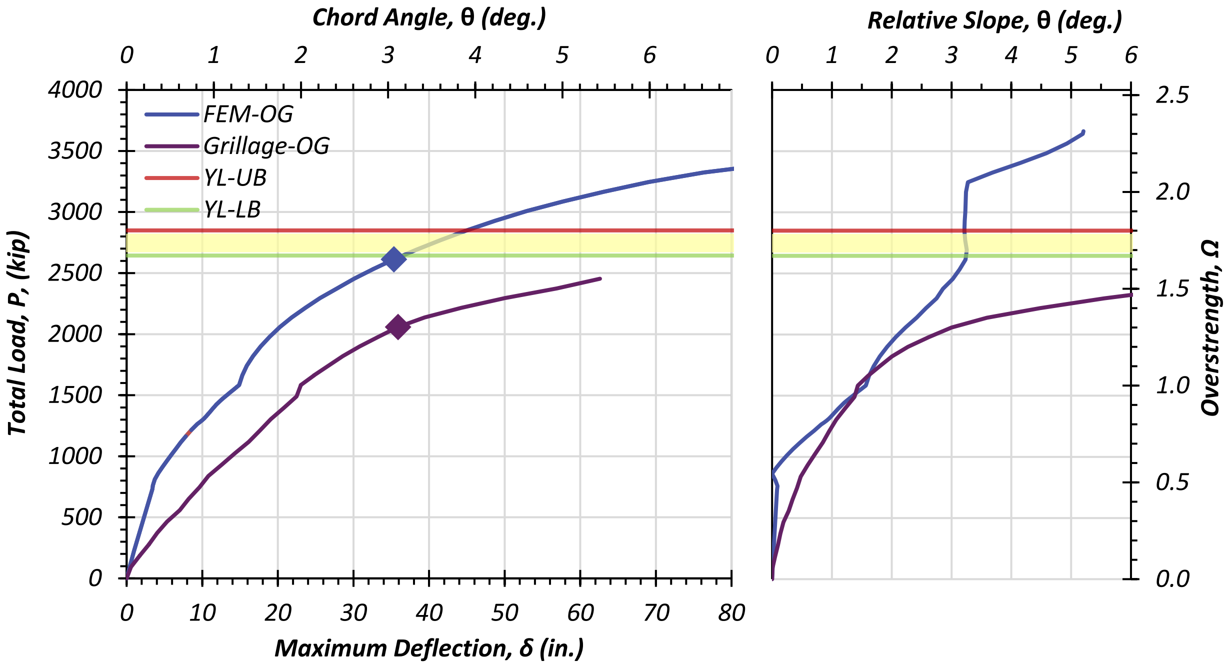

(i) Load displacement

(i) Deck rotations

(a) Comparison of the Results for Bridge 4, Span 1, L = 132 ft

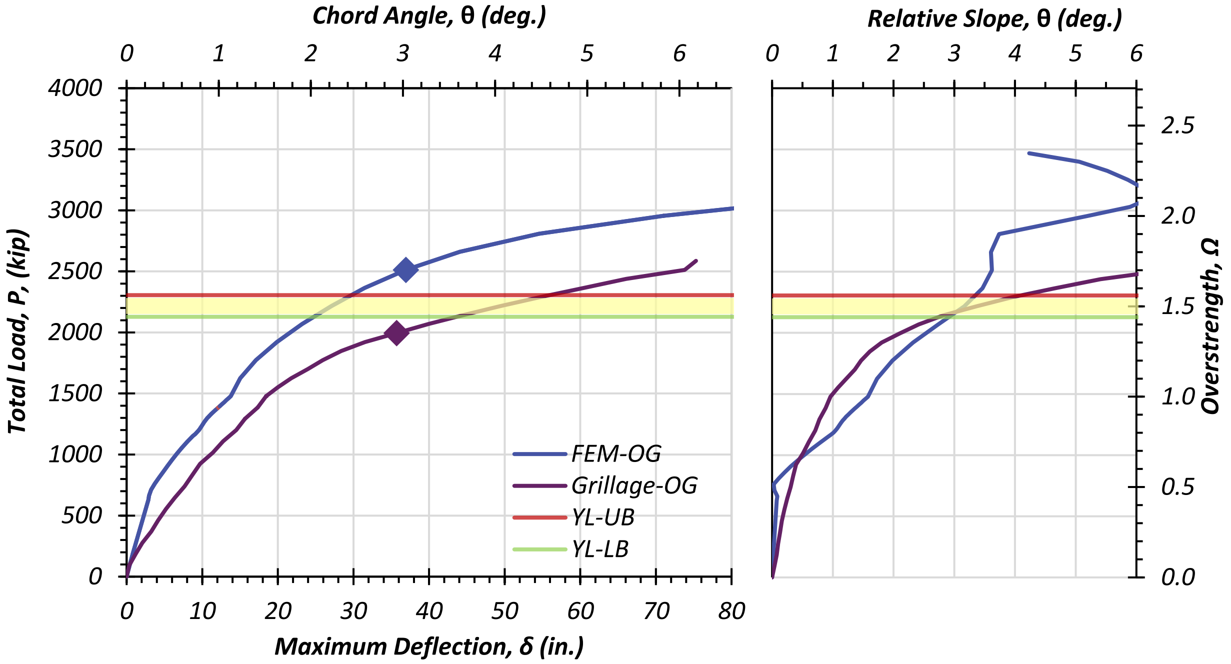

(i) Load displacement

(ii) Deck rotations

(b) Comparison of the Results for Bridge 9, Span 1, L = 140 ft

Figure 7.11. Results for Short Exterior Spans of Fracture Twin Tub Bridges.

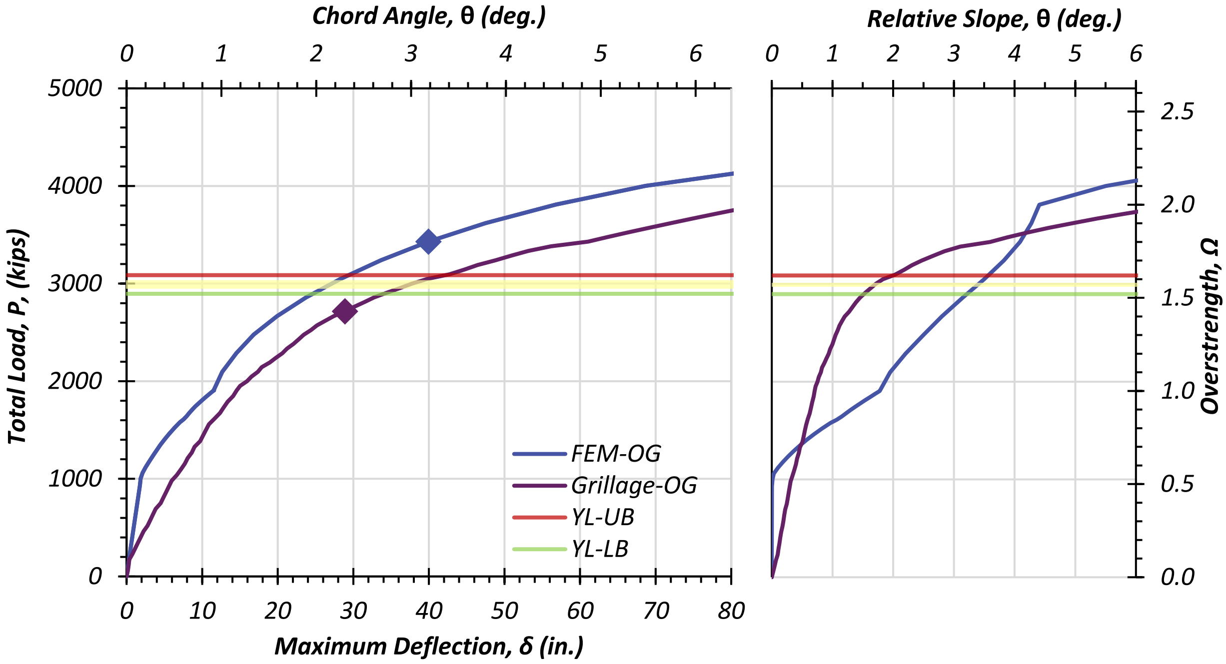

(i) Load displacement *(ii) Deck rotations*

(a) Comparison of the Results for Bridge 6, Spans 1 and 2, L = 140 ft

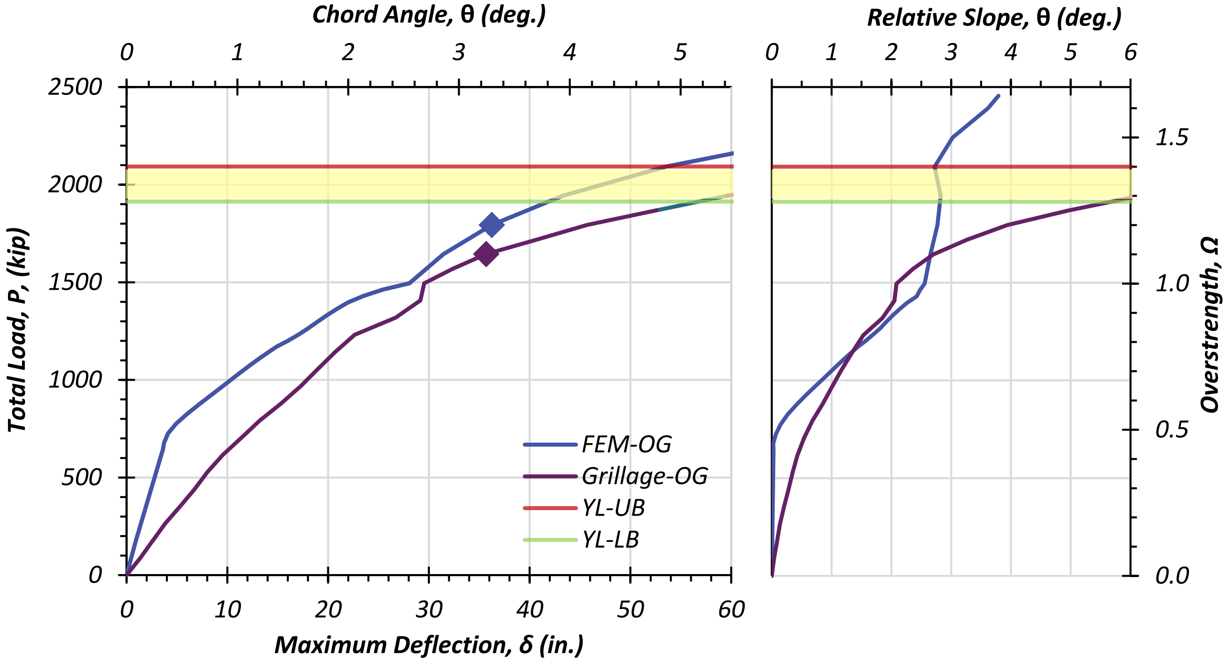

(i) Load displacement *(ii) Deck rotations*

(b) Comparison of the Results for Bridge 5, Spans 1 and 2, L = 140 ft

Figure 7.12. Results for Short Exterior Spans of Fracture Twin Tub Bridges.

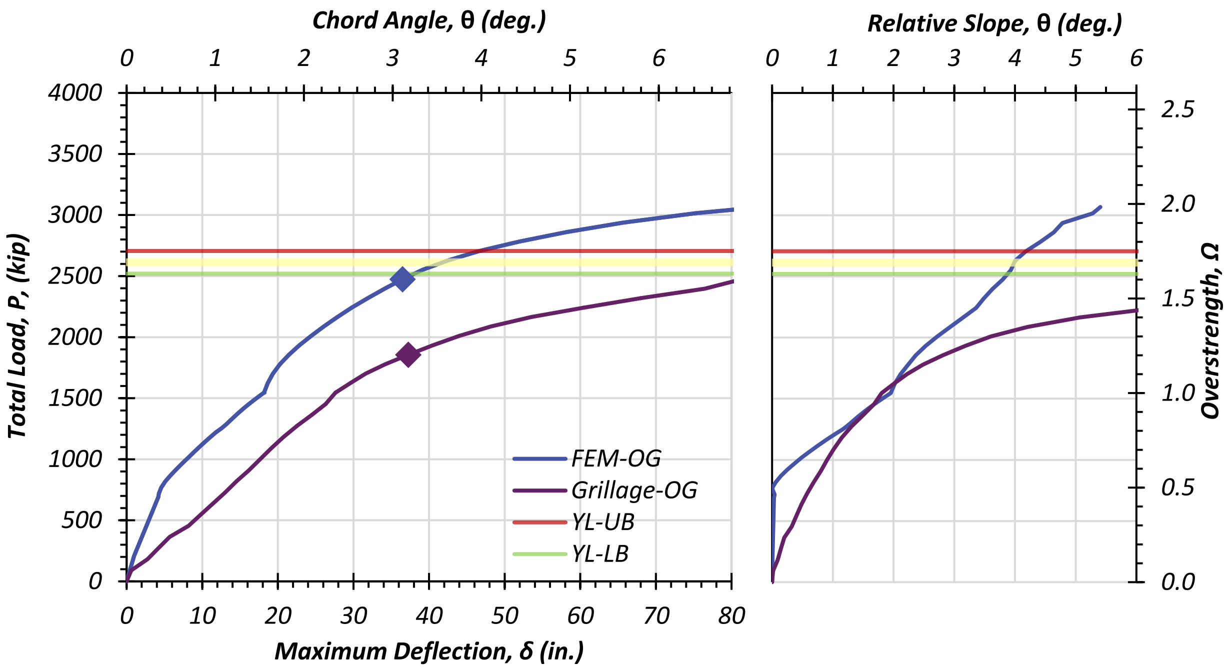

(i) Load displacement *(ii) Deck rotations*

(a) Comparison of the Results for Bridge 12, Span 1, L = 140 ft

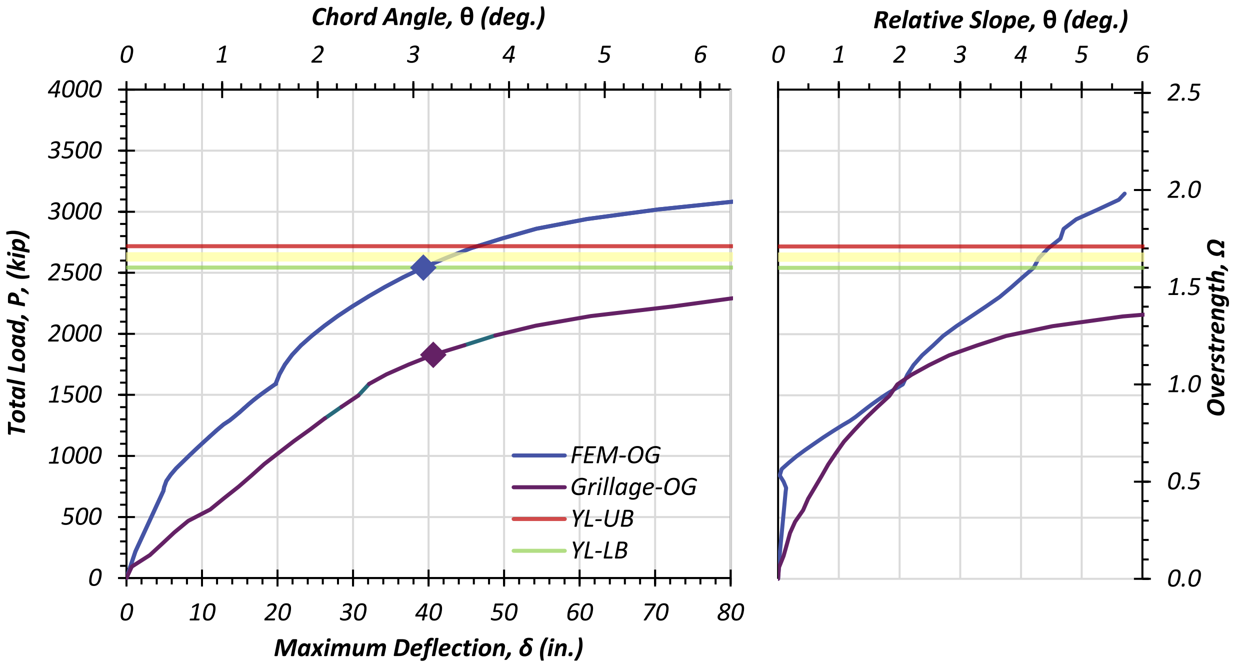

(i) Load displacement *(ii) Deck rotations*

(b) Comparison of the Results for Bridge 12, Span 3, L = 145 ft

Figure 7.13. Results for Short Exterior Spans of Fracture Twin Tub Bridges.

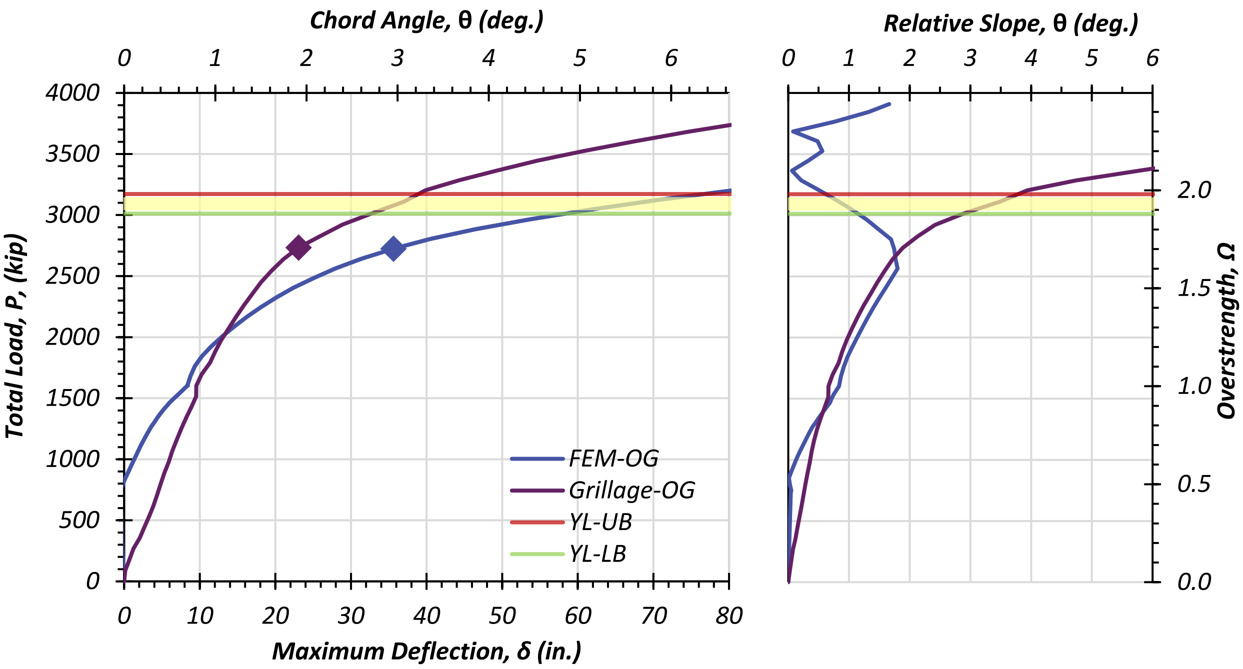

(i) Load displacement *(ii) Deck rotations*

Comparison of the Results for Bridge 10, Span 1, L = 148 ft

Figure 7.14. Results for Short Exterior Span of Fracture Twin Tub Bridges.

There appears to be good agreement between the FEM and the lower-bound plastic method for Bridges 4 and 12. While there is a disparity in the results between the two computational methods for Bridges 9, 6, and 10, the grillage method still indicates sufficient overstrength to justify reclassifying the spans as nonfracture critical. It is also worth noting that the deflections at mid-span govern at 2 degrees chord rotation, whereas δ ~ 30 to 40 in. governs the overall result.

Figure 7.12(b) presents the results for both the spans of Bridge 5. Although this is an exterior span bridge falling under the category of shorter spans (140 ft ≤ L < 150 ft), the overstrength (Ω = 1.2) is lower than that of the other spans in this category. The key difference between Bridge 5 and Bridge 6 is the radius of curvature (R = 450 ft) is much tighter in the former than in the latter (R = 819 ft). Similarly, the overstrength is lower for Span 1 of Bridge 12.

Figure 7.15, Figure 7.16, and Figure 7.17 present the exterior spans of average length (150 ft ≤ L ≤ 200 ft).

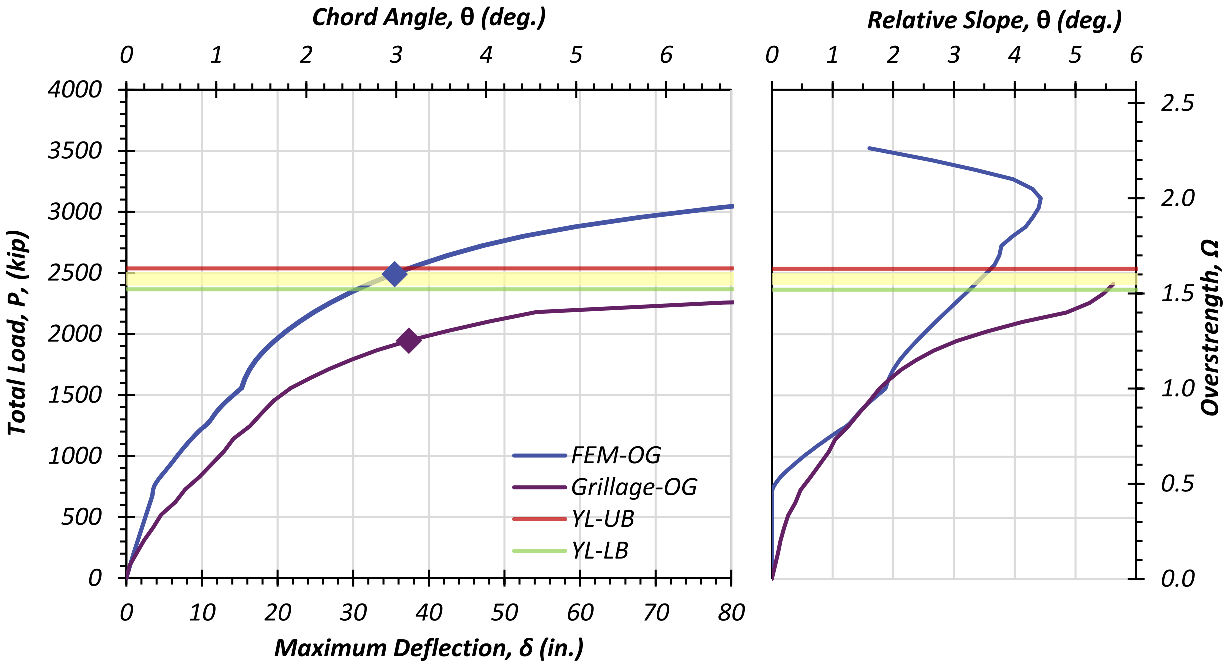

(i) Load displacement (ii) Deck rotations

(a) Comparison of the Results for Bridge 14, Span 1 and 3, L = 150 ft

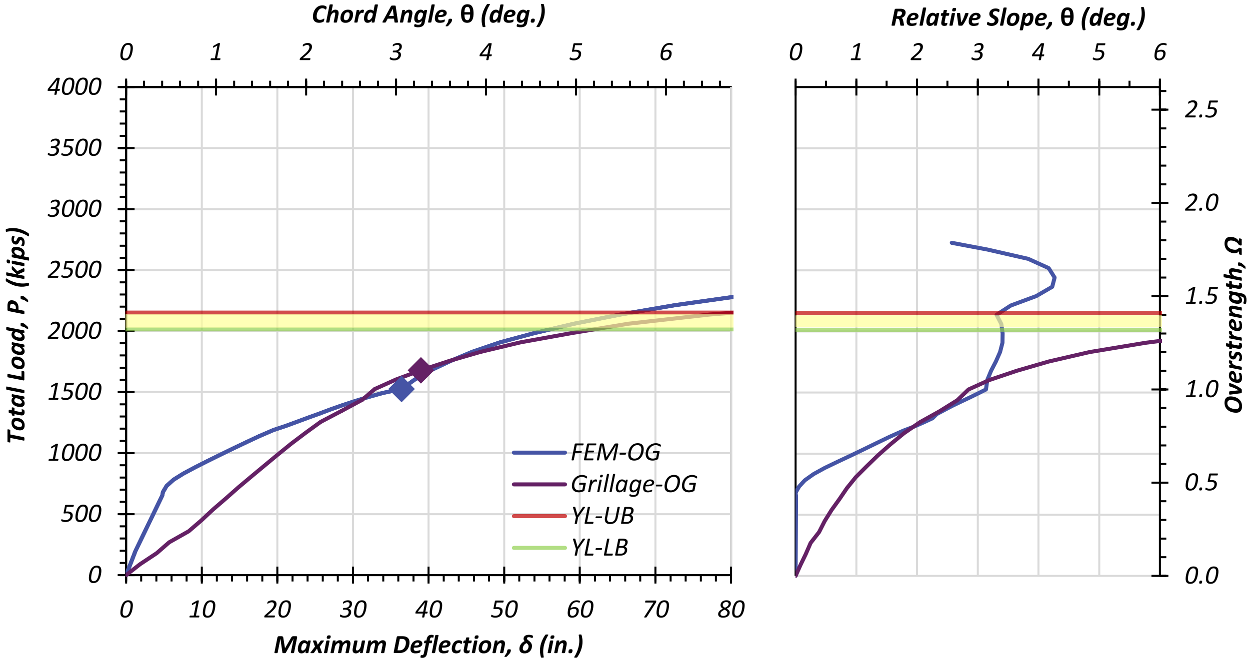

(i) Load displacement (ii) Deck rotations

(b) Comparison of the Results for Bridge 13, Spans 1 and 3, L = 152 ft

Figure 7.15. Results for Average Exterior Spans of Fracture Twin Tub Bridges.

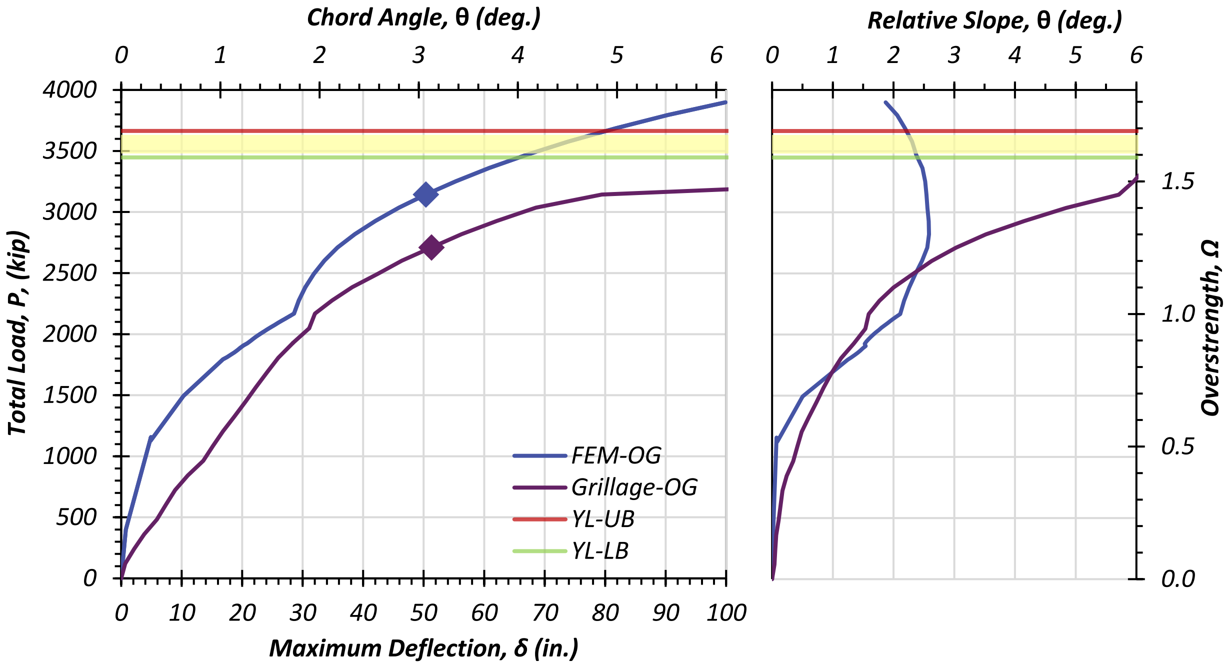

(i) Load displacement (ii) Deck rotations

(a) Comparison of the Results for Bridge 7, Span 2, L = 190 ft

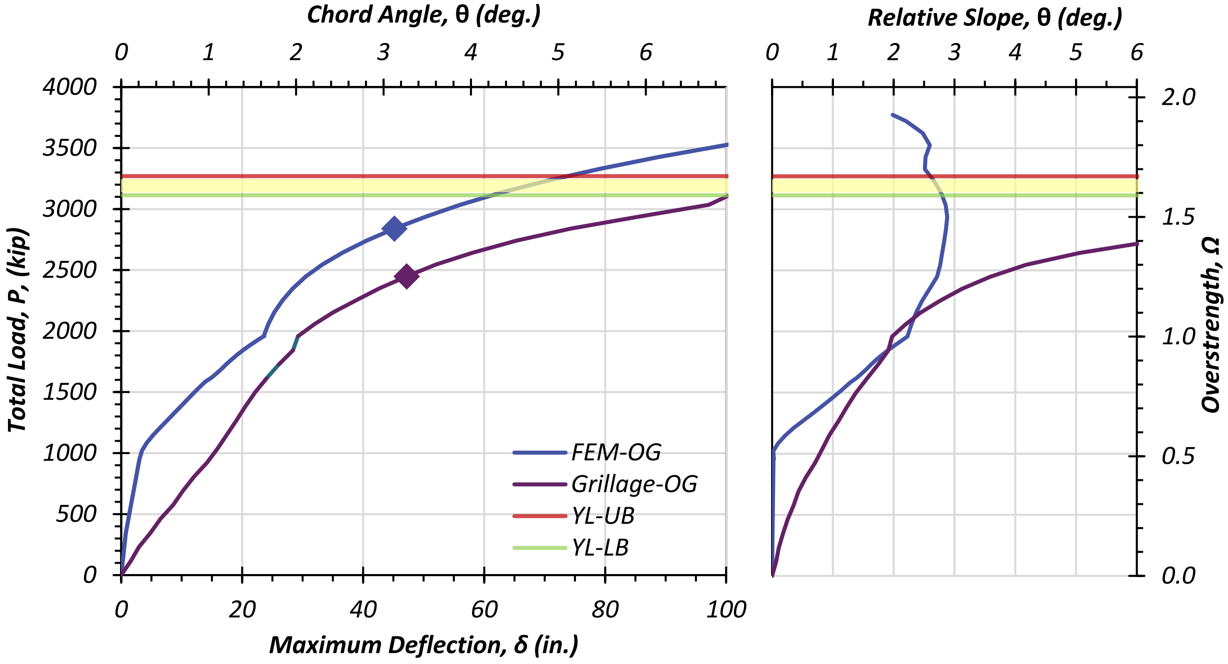

(i) Load displacement (ii) Deck rotations

(b) Comparison of the Results for Bridge 10, Span 3, L = 190 ft

Figure 7.16. Results for Average Exterior Spans of Fracture Twin Tub Bridges.

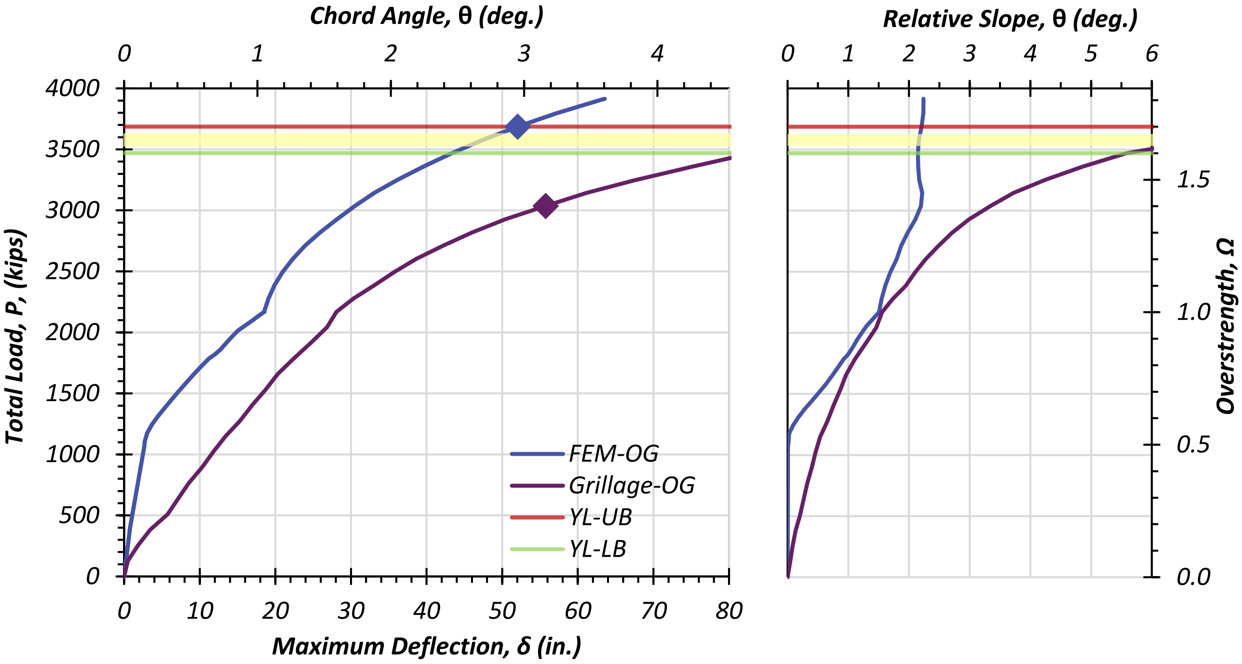

(i) Load displacement *(ii) Deck rotations*

Comparison of the Results for Bridge 15, Spans 1 and 3, L = 200 ft

Figure 7.17. Results for Average Exterior Spans of Fracture Twin Tub Bridges.

Figure 7.15(a) and Figure 7.17 present the results of Bridges 14 and 15, respectively, which exhibit a good agreement between the FEM and the upper-bound plastic method of analysis with a sufficient degree of overstrength (Ω > 1.60). Figure 7.16(a) and (b) show the results of those average spans falling under the category of 150 ft ≤ L ≤ 200 ft for Bridges 7 and 10, respectively. There appears to be a disparity in the results between the two computational methods (for Bridges 7 and 10). The grillage method still indicates sufficient overstrength to justify reclassifying the spans as nonfracture critical. It is also worth noting that the deflections at mid-span govern at 2 degrees chord rotation, where δ ~ 50 in. governs the overall result.

Figure 7.15(b) presents the results for both the spans of Bridge 13. Although this is an exterior span bridge falling under the category of average spans (150 ft ≤ L ≤ 200 ft), the overstrength (Ω ~ 1.00) is lower than the other spans of this category due to a tighter radius of curvature (R = 450 ft).

Figure 7.18 and Figure 7.19 present the exterior spans of long length (200 ft < L< 250 ft).

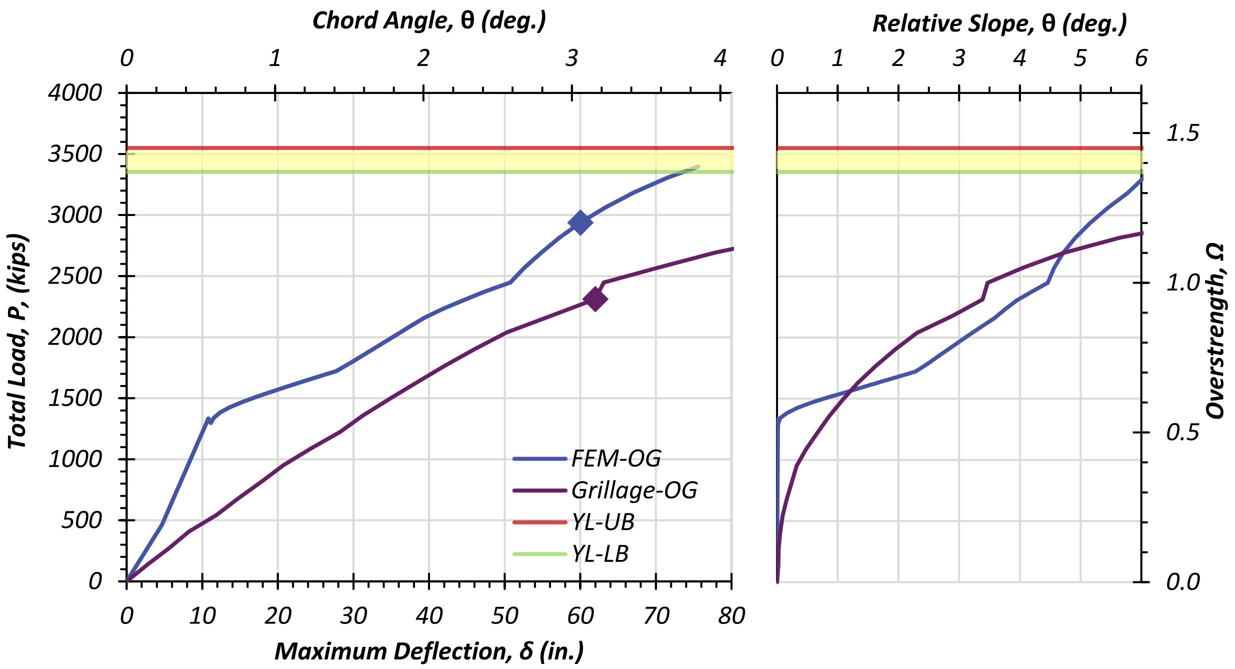

(i) Load displacement *(ii) Deck rotations*

Comparison of the Results for Bridge 7, Span 1, L = 219 ft

Figure 7.18. Results for Long Exterior Spans of Fracture Twin Tub Bridges.

Figure 7.18 shows a disparity between the results of Bridge 7 (Span 1) obtained from the three methods: the overstrength for the FEM is 1.20; the lower-bound plastic method is 1.37; and the grillage analysis is 0.94. This disparity may be due to the three-dimensional member depth not being fully accounted for in the grillage method. Figure 7.19 shows that both the spans exhibit a considerable overstrength (Ω > 1.00) with both the computational methods. It is of interest to note that at a deflection of δ ~ 60 in., the capacity for both the FEM and the plastic limit analysis (yield line method) are in good agreement for both the spans.

Figure 7.20 presents the results of Bridge 8, whose spans are classified as very long since both exceed 250 ft. Although there is a considerable disparity between the three results, both the FEM and the grillage method predict an overstrength less than unity. Therefore, this bridge may not be reclassified as nonfracture critical.

Like their interior span counterparts, all the exterior spans (except for Span 2 of Bridge 7 and both the spans of Bridges 8 and 13) exhibit sufficient redundancy and reserve capacity to bear the externally applied loads when experiencing a total fracture of the outer critical steel tub, owing to the overstrength factor exceeding unity.

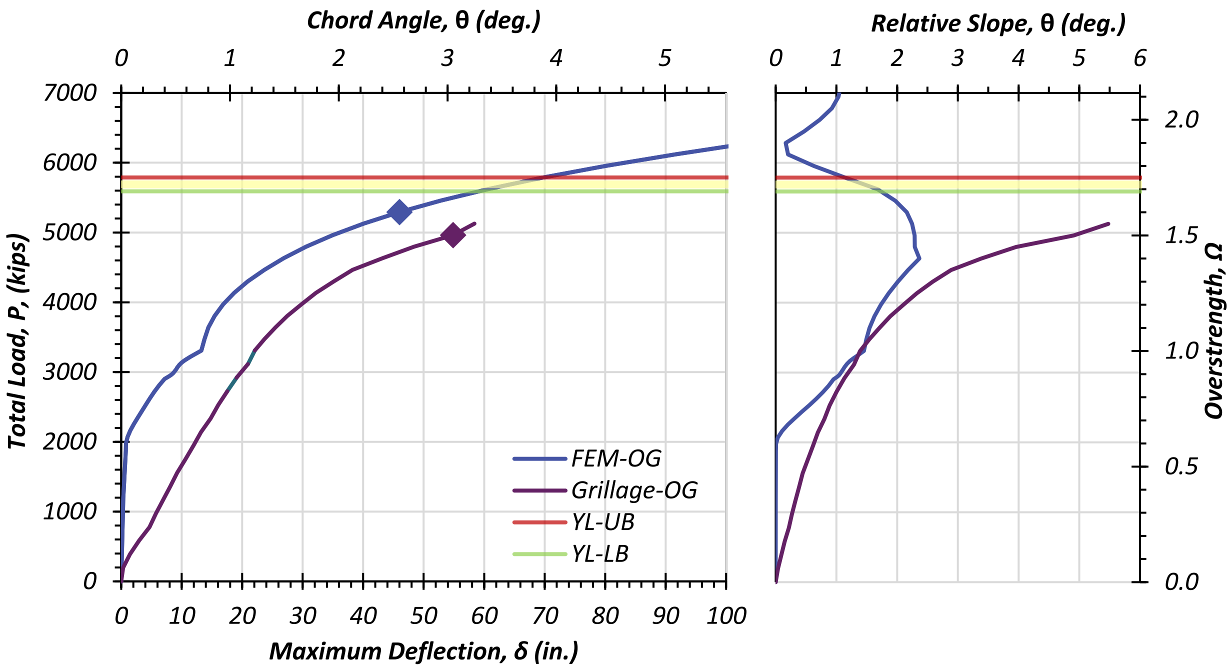

(i) Load displacement

(ii) Deck rotations

(a) Comparison of the Results for Bridge 11, Span 1, L = 223 ft

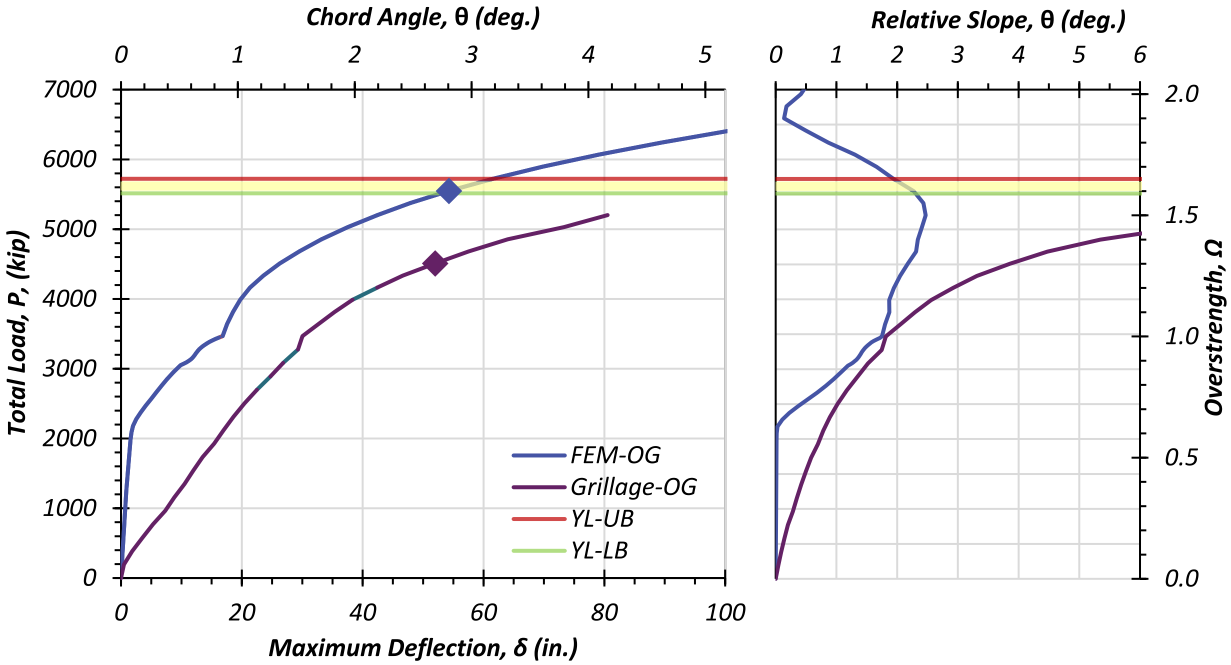

(i) Load displacement

(ii) Deck rotations

(b) Comparison of the Results for Bridge 11, Span 3, L = 235 ft

Figure 7.19. Results for Long Exterior Spans of Fracture Twin Tub Bridges.

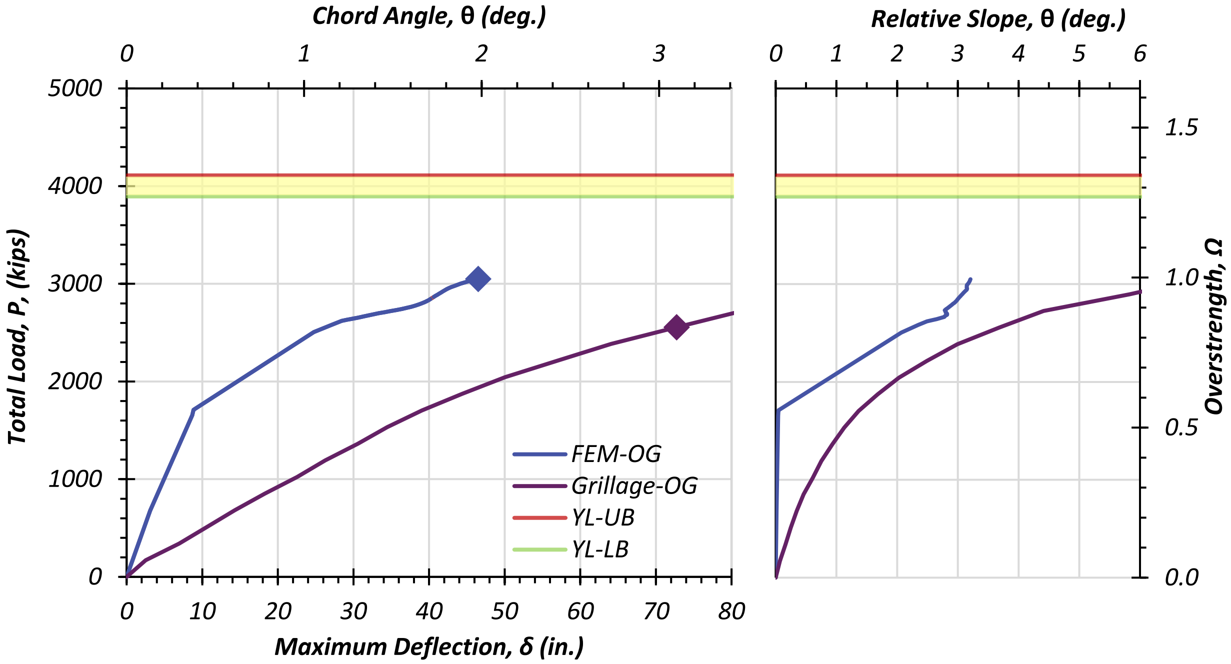

(i) Load displacement (ii) Deck rotations

(a) Comparison of the Results for Bridge 8, Span 1, L = 265 ft

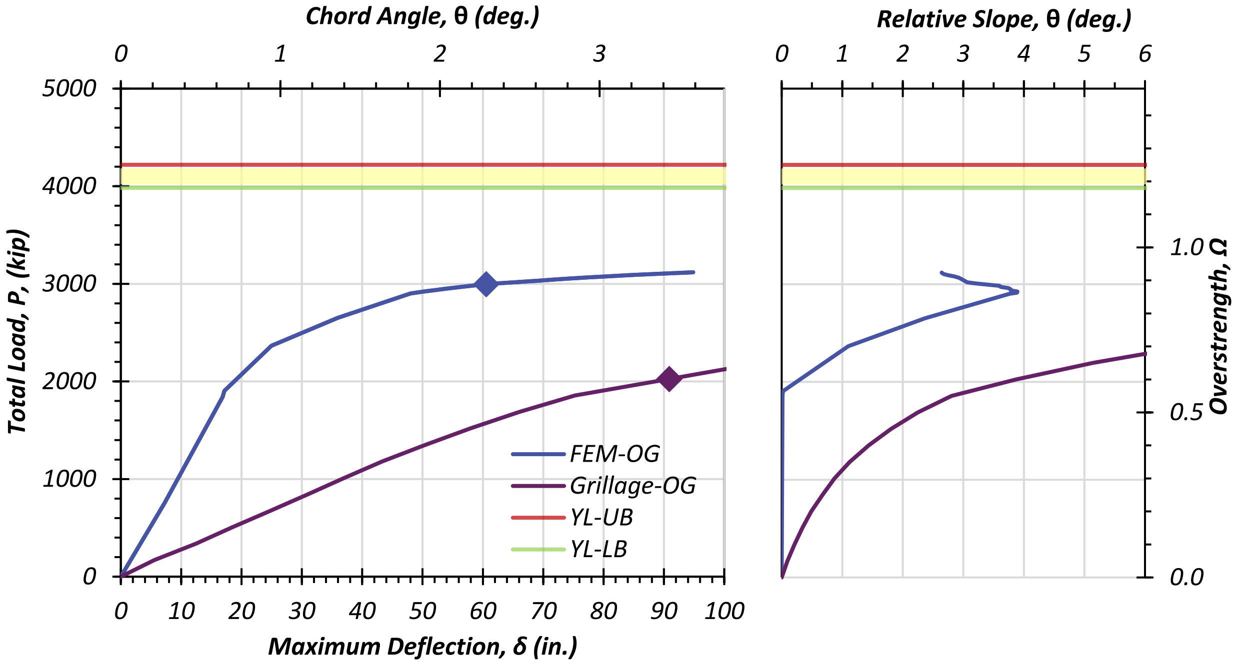

(i) Load displacement (ii) Deck rotations

(b) Comparison of the Results for Bridge 8, Span 2, L = 295 ft

Figure 7.20. Results for Very Long Exterior Spans of Fracture Twin Tub Bridges.

Table 7.3 lists the results of the exterior sorted spans based on their lengths—short, medium, long, and very long spans. It is observed that the yield line theory analysis shows a pattern among the overstrength factors of the bridges with respect to the boundary conditions and the length of the spans. The longer bridges with simple supports are susceptible to failure although the redundancy of continuous supports increases the strength, as evidenced from the higher overstrength factors of the exterior spans and an even higher strength of the interior spans.

Table 7.3. Overstrength Results for Exterior Span Twin Tub Girder Bridges.

							Yield Line		
ID	**Span**	**R (ft)**	**L (ft)**	**B (ft)**	**S (ft)**	**FEM**	**Upper Bound**	**Lower Bound**	**Grillage**
9	3	764	126	28	7.4	1.80	1.68	1.56	1.53
4	2	195	128	28	7.6	1.73	1.85	1.71	1.32
4	1	195	132	28	7.6	1.65	1.80	1.67	1.30
9	1	764	140	28	7.4	1.70	1.56	1.44	1.35
6	1	819	140	38	9.8	1.80	1.62	1.52	1.43
6	2	819	140	38	9.8	1.80	1.62	1.52	1.43
5	1	450	140	30	9.7	1.20	1.40	1.28	1.10
5	2	450	140	30	9.7	1.20	1.39	1.28	1.10
12	1	225	140	28	7.6	1.60	1.75	1.63	1.20
12	3	225	145	28	7.6	1.60	1.71	1.60	1.15
10	1	716	148	30	7.7	1.70	1.98	1.88	1.71
14	1	1010	150	28	6.5	1.65	1.63	1.52	1.25
14	3	1010	150	28	6.5	1.65	1.63	1.52	1.25
13	1	450	152	30	9.3	1.00	1.41	1.32	1.10
13	3	450	152	30	9.3	1.00	1.40	1.30	1.10
7	2	764	190	28	7.4	1.45	1.69	1.59	1.25
10	3	716	190	30	7.7	1.45	1.67	1.59	1.25
15	1	809	200	28	8	1.70	1.70	1.60	1.40
15	3	809	200	28	8	1.70	1.69	1.59	1.40
7	1	764	219	28	7.4	1.20	1.45	1.37	0.94
11	1	819	223	28	7	1.60	1.75	1.69	1.35
11	3	819	235	28	7	1.60	1.65	1.59	1.30
8	1	882	265	28	8.4	0.99	1.34	1.27	0.83
8	2	882	295	28	8.4	0.88	1.25	1.18	0.60

8 FINDINGS

Here is a summary of the major study findings:

- All bridges may be reclassified as not fracture critical if shown by two of the analysis methods (FEM, grillage, or yield line) that they possess sufficient overstrength ($\Omega > 1$) when analyzed under design loads with a fully fractured outside girder.
- In this study, all simply supported bridges that have a fully fractured outside girder either showed marginally acceptable overstrength capacity or as the spans grew beyond 115 ft were likely to be deficient in terms of overstrength. In general, single-span twin tub bridges lack redundancy and should remain classified as fracture critical.
- If bridges possess structural redundancy, which can be provided by continuity of girders over interior supports, they may be reclassified as nonfracture critical, providing the span lengths are not very long (see next item).
- If span lengths of continuous bridges exceed 250 ft for exterior spans or 350 ft for interior spans, special studies should be conducted to justify their reclassification to nonfracture critical.

REFERENCES

AASHTO (2014). "AASHTO LRFD Bridge Design Specifications." American Association of State Highway and Transportation Officials (AASHTO), Washington, DC.

AASHTO (2017). "AASHTO LRFD Bridge Design Specifications." American Association of State Highway and Transportation Officials (AASHTO), Washington, DC.

ACI-318 (2017). "Building code requirements for structural concrete (ACI 318-17) and commentary." ACI Committee, American Concrete Institute, and International Organization for Standardization.

Argyris, J. H., and Kelsey, S. (1960). "Energy Theorems and Structural Analysis: A Generalised Disclosure with Applications on Energy Principles of Structural Analysis Including the Effects of Temperature and Nonlinear Stress-Strain Relations."Butterworths, London, UK.

Armer, G. (1968). "Ultimate load tests of slabs designed by the strip method." *Proceedings of the Institution of Civil Engineers*, 41(2), 313-331.

Barker, M. R., and Puckett, J. (2007). "Design of Highway Bridges-An LRFD approach." John Wiley& Sons.

Barker, R. M., and Puckett, J. A. (2013). *Design of highway bridges: An LRFD approach*, John Wiley & Sons.

Barnard, T., Hovell, C. G., Sutton, J. P., Mouras, J. M., Neuman, B. J., Samaras, V. A., Kim, J., Williamson, E. B., and Frank, K. H. (2010). "Modeling the Response of Fracture Critical Steel Box-Girder Bridges." *Report No. FHWA/TX-10/9-5498*,1, Center for Transportation Research at the Univ. of Texas at Austin, Austin, TX.

Belak, J. (1998). "On the nucleation and growth of voids at high strain-rates." *Journal of computer-aided materials design*, 5(2-3), 193-206.

Computers and Structures, I. 2017. SAP2000, version 19.1.1Computers and Structures Inc., Berkeley, CA.

Connor, R. J., Dexter, R. J., and Mahmoud, H. (2005). "Inspection and Management of Bridges with Fracture-Critical Details." *NCHRP Synthesis 354*0309097614, National Cooperative Highway Research Program, Transportation Research Board, Washington, DC.

Corley, W. (1966). "Rotational capacity of reinforced concrete beams." *Journal of the Structural Division*, 92(5), 121-146.

Cottrell, A. H., and Bilby, B. (1949). "Dislocation theory of yielding and strain ageing of iron." *Proceedings of the Physical Society. Section A*, 62(1), 49.

Cross, H. (1932). "Analysis of continuous frames by distributing fixed-end moments." *American Society of Civil Engineers Transactions*.

Daniels, J. H., Kim, W., and Wilson, J. L. (1989). "Recommended Guidelines for Redundancy Design and Rating of Two-Girder Steel Bridges." *NCHRP Report 319*0309046165, National Cooperative Highway Research Program., Transportation Research Board, Washington, DC.

Dassault Systemes, S. A. 2014. Abaqus, version 6.14 Abaqus, Inc, Providence, RI, USA.

Dexter, R. J., Wright, W. J., and Fisher, J. W. (2004). "Fatigue and fracture of steel girders." *Journal of Bridge Engineering*, 9(3), 278-286.

Duncan, W., and Collar, A. (1934). "LXXIV. A method for the solution of oscillation problems by matrices." *The London, Edinburgh, and Dublin Philosophical Magazine and Journal of Science*, 17(115), 865-909.

Fasl, J., Helwig, T., and Wood, S. L. (2016). "Fatigue Response of a Fracture-Critical Bridge at the End of Service Life." *Journal of Performance of Constructed Facilities*, 04016019.

Felippa, C. A. (2004). "Introduction to finite element methods." *Course Notes, Department of Aerospace Engineeing Sciences, University of Colorado at Boulder, available at* http://www*. colorado. edu/engineering/Aerospace/CAS/courses. d/IFEM. d*.

FHWA (2012). "Clarification of Requirements for Fracture Critical Members." *Memorandum from Office of Bridge Technology*, Federal Highway Administration, Washington, DC.

FHWA NBIS (2012). *Bridge Inspector's Reference Manual*, U.S. Department of Transportation.

Fisher, J. (1997). "Evolution of fatigue-resistant steel bridges." *Transportation Research Record: Journal of the Transportation Research Board*(1594), 5-17.

Fisher, J., Pense, A., Wood, J., and Daniels, J. (1980). "Evaluation of the fracture of the I79 back channel girder and the electroslag welds in the I79 complex, October 1980, 101p."

Fisher, J. W. (1970). *Effect of weldments on the fatigue strength of steel beams*, TRB.

Fisher, J. W. (1984). *Fatigue and fracture in steel bridges. Case studies*.

Fisher, J. W., Albrecht, P., Yen, B. T., Klingerman, D. J., and McNamee, B. M. (1974). "Fatigue strength of steel beams with welded stiffeners and attachments." *NCHRP report*(147).

Fisher, J. W., Pense, A. W., and Roberts, R. (1977). "Evaluation of fracture of Lafayette Street bridge." *Journal of the Structural Division*, 103(ASCE 13051 Proceeding).

Frangopol, D. M., and Curley, J. P. (1987). "Effects of damage and redundancy on structural reliability." *Journal of Structural Engineering*, 113(7), 1533-1549.

Ghosn, M., and Moses, F. (1998). "Redundancy in highway bridge superstructures." *NCHRP Report 406*,406, 0309062578, National Cooperative Highway Research Program, Transportation Research Board, Washington, DC.

Hambly, E., and Pennells, E. (1975). "Grillage analysis applied to cellular bridge decks." *Structural Engineer*, 53(7).

Hazell (1999). "Strength Assessment of Concrete Beam-and-Slab Bridges." *MEng Report*, University of Cambridge.

Heins, C. P., and Hou, C. K. (1980). "Bridge redundancy: Effects of bracing." *Journal of the Structural Division*, 106(6), 1364-1367.

Heins, C. P., and Kato, H. (1982). "Load redistribution of cracked girders." *Journal of the Structural Division*, 108(8), 1909-1915.

Hueste, M. D., Mander, J. B., Terzioglu, T., Jiang, D., and Petersen-Gauthier, J. (2015). "Spread Prestressed Concrete Slab Beam Bridges." *Research Report No. FHWA/TX-14/0 6722-1*, Texas A&M Transportation Institute and Texas Department of Transportation.

Hunley, C. T., and Harik, I. E. (2012). "Structural Redundancy Evaluation of Steel Tub Girder Bridges." *Journal of Bridge Engineering*, 17(3), 481-489.

Hurlebaus, S. (2007). "Calculation of eigenfrequencies for rectangular free orthotropic plates–An overview." *ZAMM-Journal of Applied Mathematics and Mechanics/Zeitschrift für Angewandte Mathematik und Mechanik*, 87(10), 762-772.

Hurlebaus, S., Gaul, L., and Wang, J.-S. (2001). "An exact series solution for calculating the eigenfrequencies of orthotropic plates with completely free boundary." *Journal of Sound and Vibration*, 244(5), 747-759.

Jackson, A., and Middleton, C. (2013). "Closely correlating lower and upper bound plastic analysis of real slabs." *Structural Engineer*, 91, 34-40.

Jiang, D. (2015). "Experiments, Analysis and Design Models for Slab on Prestressed Concrete Girder Bridge Structures." Doctoral dissertation, Texas A&M University, College Station, TX.

Johansen, K. W. (1943). *Brudlinieteorier*, I kommission hos J. Gjellerup.

Kent, D. C., and Park, R. (1971). "Flexural members with confined concrete." *Journal of the Structural Division*.

Kim, J., and Williamson, E. B. (2014). "Finite-Element Modeling of Twin Steel Box-Girder Bridges for Redundancy Evaluation." *Journal of Bridge Engineering*, 20(10), 04014106.

Lightfoot, E., and Sawko, F. (1959). "Structural frame analysis by electronic computer: grid frameworks resolved by generalized slope deflection." *Engineering*, 187(1), 18-20.

Lwin, M. (2012a). "Clarification of Requirements for Fracture Critical Members." *FHWA Memorandum HIBT*, 10.

Lwin, M. M. (2012b). "Action: Clarification of Requirements for Fracture Critical Members." *HIBT-10*, FHWA, 5.

Mander, T. J., Mander, J. B., and Head, M. H. (2010). "Modified yield line theory for full-depth precast concrete bridge deck overhang panels." *Journal of Bridge Engineering*, 16(1), 12-20.

Mander, T. J., Mander, J. B., and Head, M. H. (2011). "Compound Shear-Flexural Capacity of Reinforced Concrete–Topped Precast Prestressed Bridge Decks." *Journal of Bridge Engineering*, 16(1), 4.

Mattock, A. H. (1967). "Discussion of" Rotation Capacity of Reinforced Concrete Beams" by WG Corley." *Journal of Structual Division ASCE*, 93, 519-522.

Mouras, J. M., Sutton, J. P., Frank, K. H., and Williamson, E. B. (2008). "The tensile capacity of welded shear studs." *Report No. FHWA/TX-09/9-5498-2*, Center for Transportation Research at the Univ. of Texas at Austin, Austin, TX.

Neuman, B. J. (2009). "Evaluating the redundancy of steel bridges: Full-scale destructive testing of a fracture critical twin box-girder steel bridge." M.S., The Ubiversity of Texas at Austin, Austin, TX.

NTSB (1971). "Collapse of U.S. 35 Bridge, Point Pleasant, West Virginia, December 15, 1967." National Transportation Safety Board, Washington, D.C.

Park, R., and Gamble, W. L. (2000). *Reinforced concrete slabs*, John Wiley & Sons.

Parmelee, R. A., and Sandberg, H. R. "Redundancy - A Design Objective." *Proc., AISC National Engineering Conference*.

Pirayeh Gar, S., Mander, J. B., Head, M., and Hurlebaus, S. (2014). "FRP slab capacity using yield line theory." *Journal of Composites for Construction*, 18(6), 04014021.

Puckett, J. A., Huo, S. X., Jablin, M., and Mertz, D. R. (2011). "Framework for Simplified live load distribution-factor computations." *Journal of Bridge Engineering*, 16(6), 777-791.

Puckett, J. A., Mertz, D., Huo, X. S., C., J. M., Peavy, M. D., and Patrick, M. D. (2005). "Simplified Live Load Distribution Factor Equations for Bridge DEsign." *Journal of the Transportation Research Board*, 11(S), 67-78.

Samaras, V. A., Sutton, J. P., Williamson, E. B., and Frank, K. H. (2012). "Simplified method for evaluating the redundancy of twin steel box-girder bridges." *Journal of Bridge Engineering*, 17(3), 470-480.

Sandare, M. (1983). "Computer Study of Redundancy of a 3-D Steel Deck Truss Bridge." Lehigh University, Bethlehem, PA.

Sanders, W. W., and Elleby, H. A. (1970). "Distribution of Wheel Loads on Highway Bridges." National Cooperative Highway Research Program, Highway Research Board.

Scheffey, C. F. (1971). "Point Pleasant Bridge Collapse: Conclusions of Federal Study." *Civil Engineering*, 41(7), 41.

Sotelino, E., Liu, J., Chung, W., and Phuvoravan, K. (2004). "Simplified Load Distribution Factor for Use in LRFD Design." *Joint Transportation Research Program*, 1-148.

Surana, C., and Agrawal, R. (1998). *Grillage analogy in bridge deck analysis*, Alpha Science Int'l Ltd.

Sutton, J. P. (2007). "Evaluating the redundancy of steel bridges: Effect of a bridge haunch on the strength and behavior of shear studs under tensile loading." MS Thesis. The University of Texas at Austin, Austin, TX.

Sutton, J. P., Mouras, J. M., Samaras, V. A., Williamson, E. B., and Frank, K. H. (2014). "Strength and ductility of shear studs under tensile loading." *Journal of Bridge Engineering*, 19(2), 245-253.

Sweeney, R. (1979). "Importance of redundancy in bridge-fracture control." *Transportation Research Record*(711).

Terzioglu, T. (2015). "Behavior and Design of Spread Prestressed Concrete Slab Beam Bridges." PhD, Texas A&M University, College Station, TX.

Terzioglu, T., Jiang, D., Hueste, M. B. D., and Mander, J. B. (2016a). "Design and Constructability of Spread Slab-Beam Bridges." *Journal of Bridge Engineering*, 04016089.

Terzioglu, T., Jiang, D., Hueste, M. B. D., Mander, J. B., and Fry, G. T. (2016b). "Experimental Investigation of a Full-Scale Spread Slab Beam Bridge." *Journal of Bridge Engineering*, 04016082.

Timoshenko, S. (1953). *History of strength of materials: with a brief account of the history of theory of elasticity and theory of structures*, Courier Corporation.

Timoshenko, S. P., and Woinowsky-Krieger, S. (1959). *Theory of Plates and Shells*, McGrawHill, New York.

Topkaya, C., Williamson, E. B., and Frank, K. H. (2004). "Behavior of curved steel trapezoidal box-girders during construction." *Engineering structures*, 26(6), 721-733.

Turner, M. (1959). *The Direct Stiffness Method of Structural Analysis*, Boeing Airplane Company.

TxDOT (1996). "Bridge Design Drawings for Northwest Transit Center/ Inner Katy Connector." *Project No: cc 912-71-403*, Texas Department of Transportation, Austin, TX.

TxDOT (2009). "Bridge Design Drawings of 120' Tub Girder Test Specimen." Texas Department of Transportation, Austin, TX.

TxDOT (2013a). *Bridge Inspection Manual - Revised August 2013*, Texas Department of Transportation.

TxDOT (2013b). "TxDOT Bridge Design Manual - LRFD." Texas Department of Transportation, http://onlinemanuals.txdot.gov/txdotmanuals/lrf/lrf.pdf.

Wood, R., Armer, G., and Hillerborg, A. (1968). "The Theory of the Strip Method for Design of Slabs.(Includes Appendix)." *Proceedings of the Institution of Civil Engineers*, 41(2), 285-311.

WVDOT (2016). "Transportation > Highways > Bridge Facts > Modern Bridges > Silver Bridge." <http://www.transportation.wv.gov/highways/bridge_facts/Modern-Bridges/Pages/Silver.aspx>. (2016).

Zokaie, T., Imbsen, R. A., and Osterkamp, T. A. (1991). "Distribution of Wheel Loads on Highway Bridges." *NCHRP Project Report 12-26*12-26, Transportation Research Board, Washington, DC.

APPENDIX A. STRUCTURAL DRAWINGS

Bridge 1: 12-102-3256-01-403

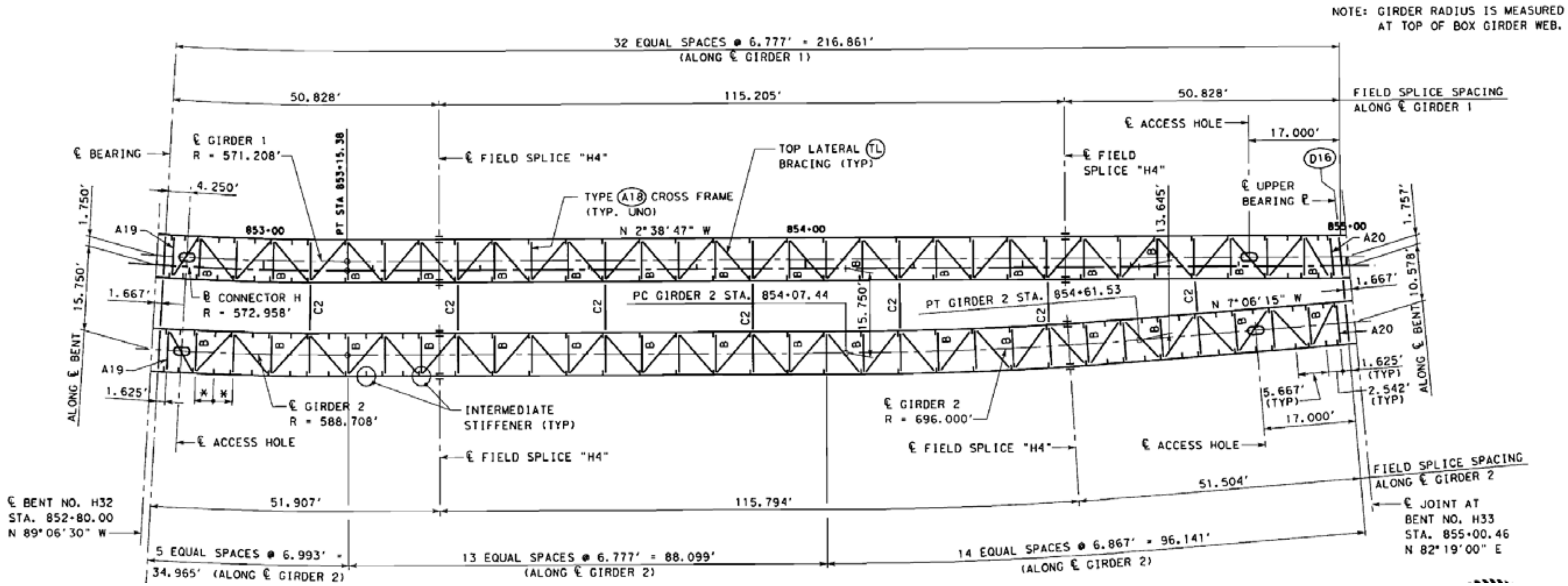

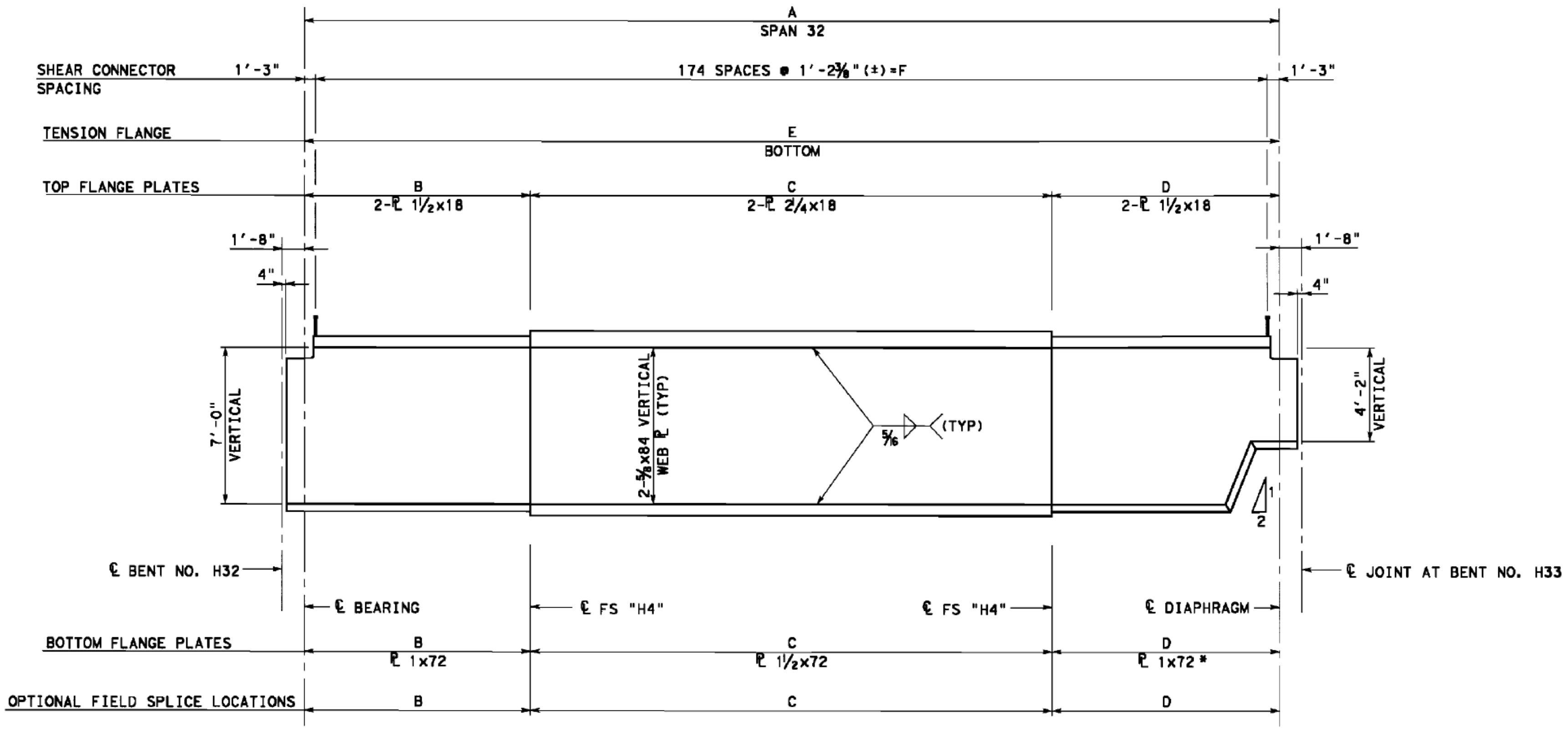

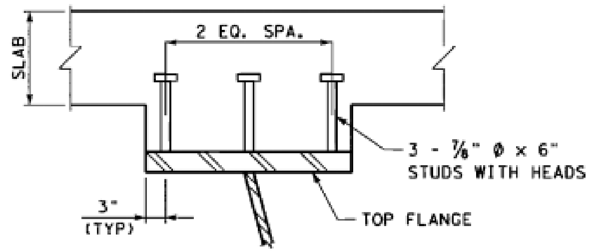

SHEAR CONNECTOR STUD DETAIL

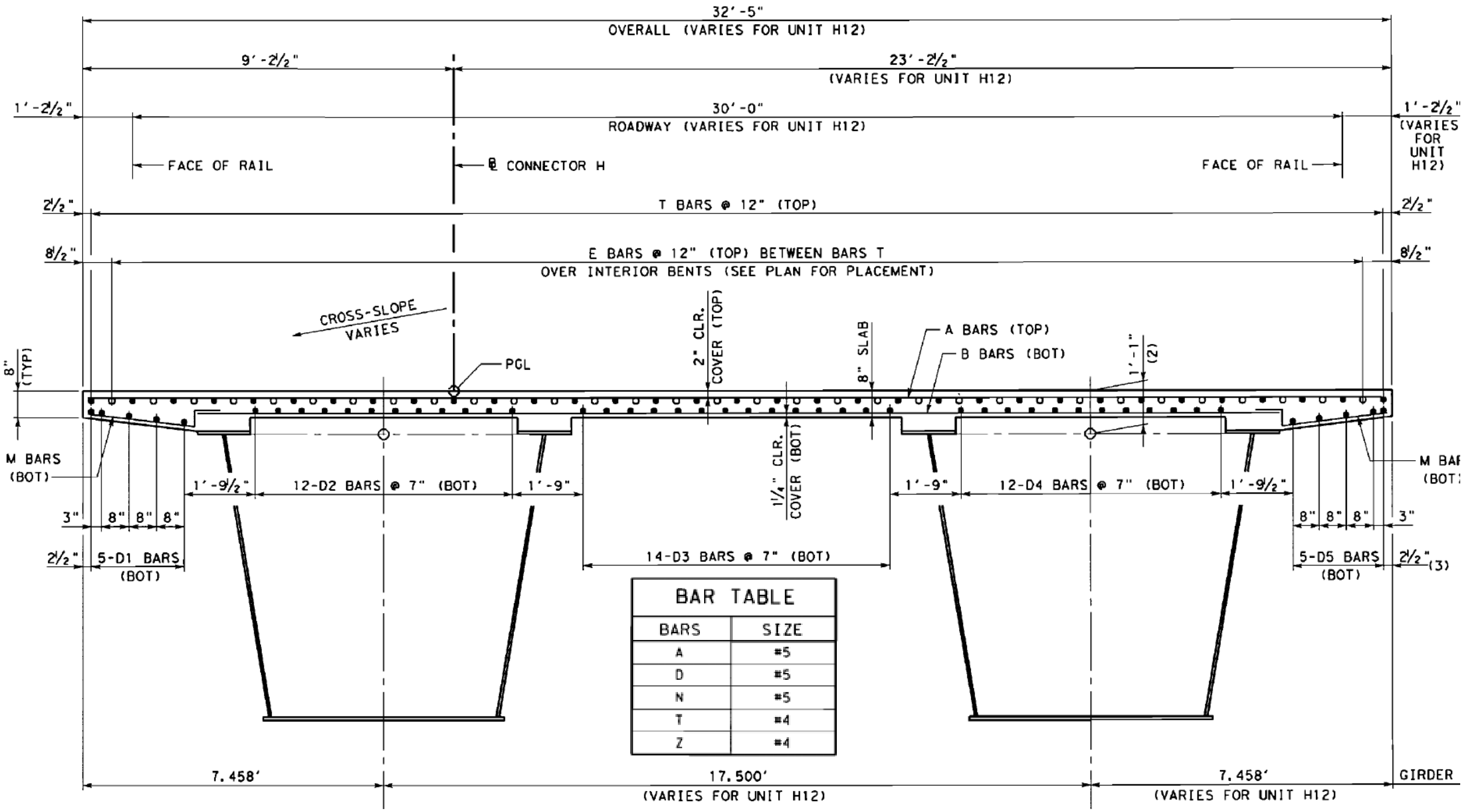

BAR TABLE

BARS	SIZE
A	#5
D	#5
N	#5
T	#4
Z	#4

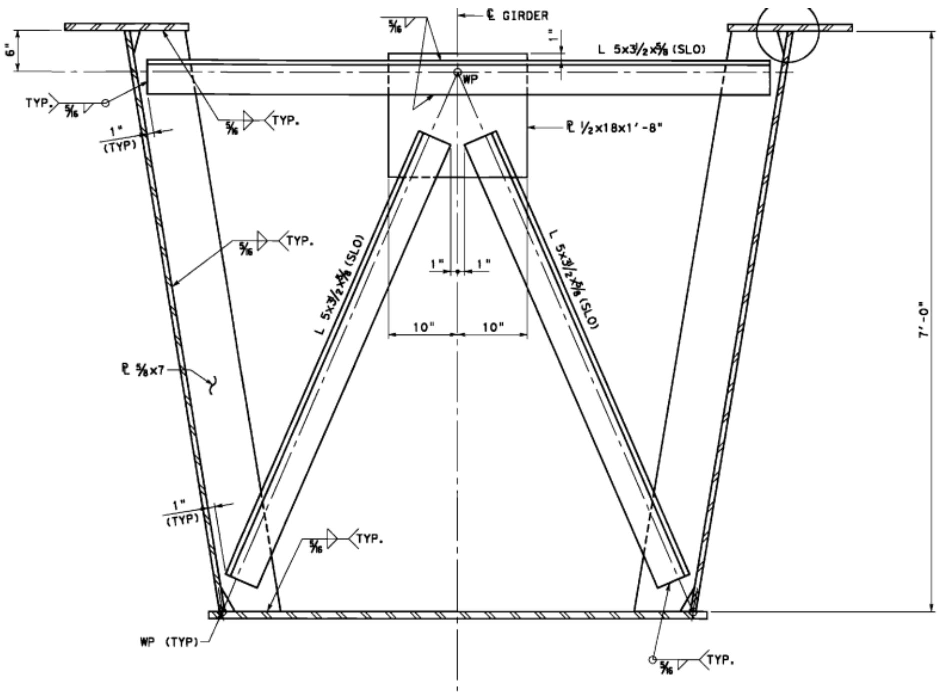

CROSS FRAME - TYPE A18

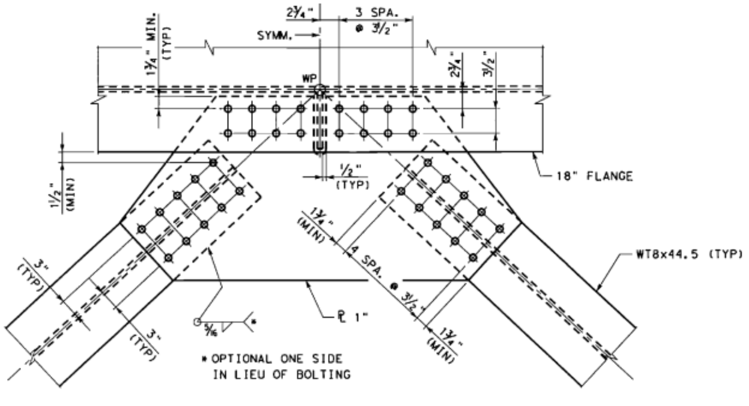

TOP LATERAL BRACING CONNECTION

DETAIL - UNIT H12

(18" TOP FLANGE)

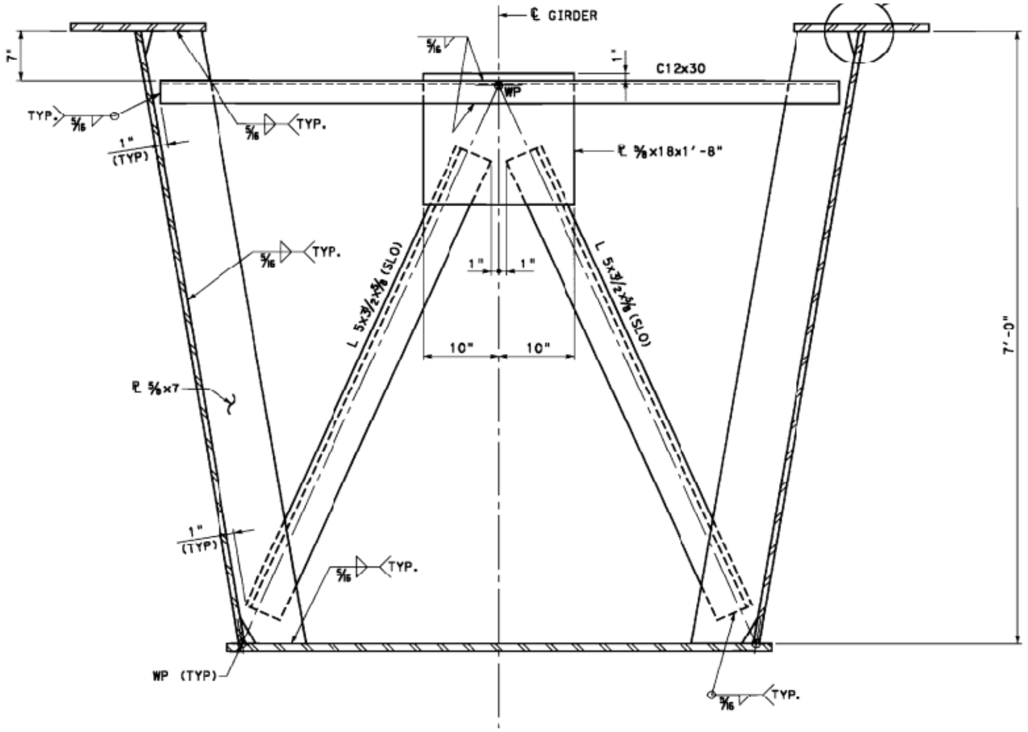

CROSS FRAME - TYPE A19

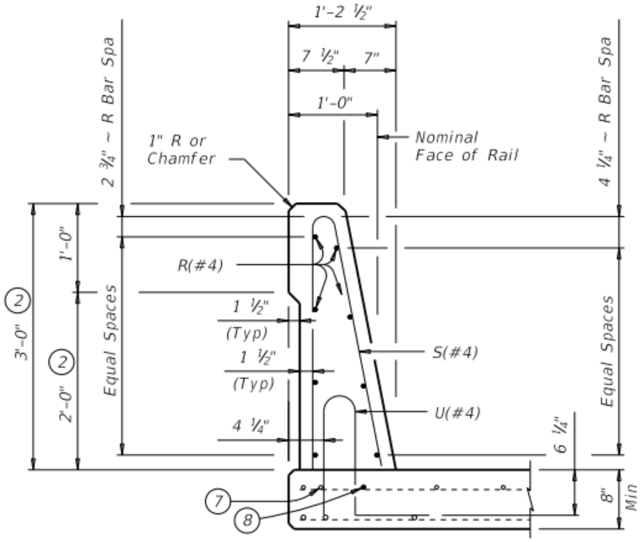

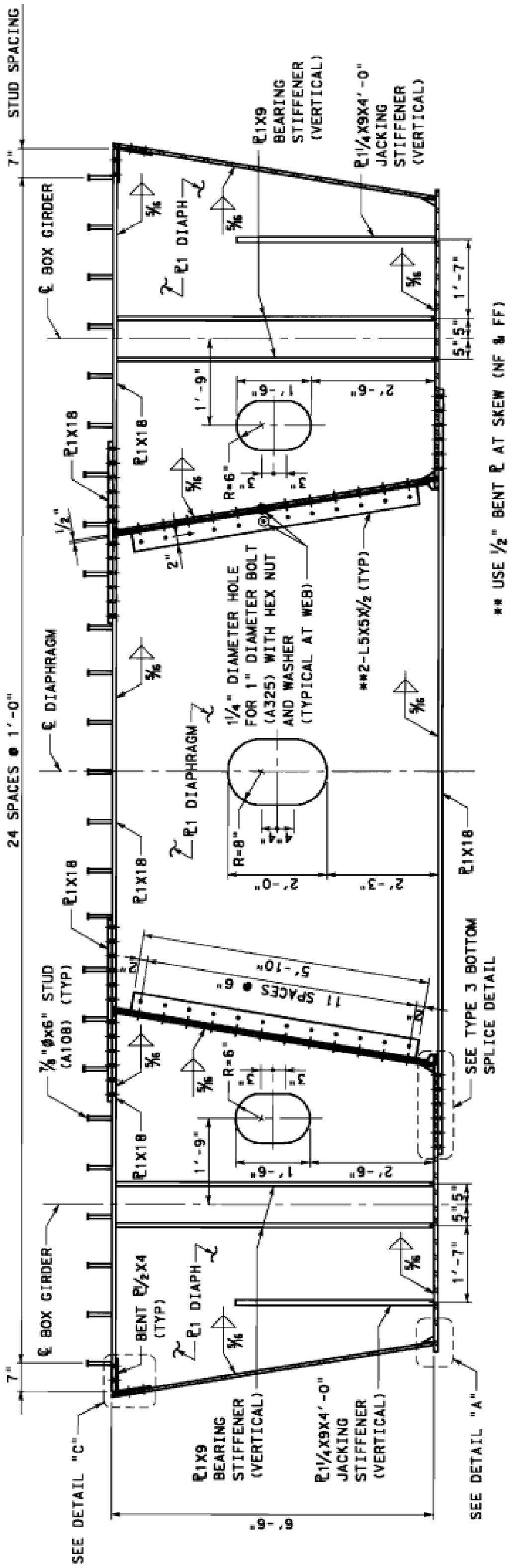

** USE 1/2" BENT PL AT SKEW (NF & FF)

DIAPHRAGM - TYPE D13

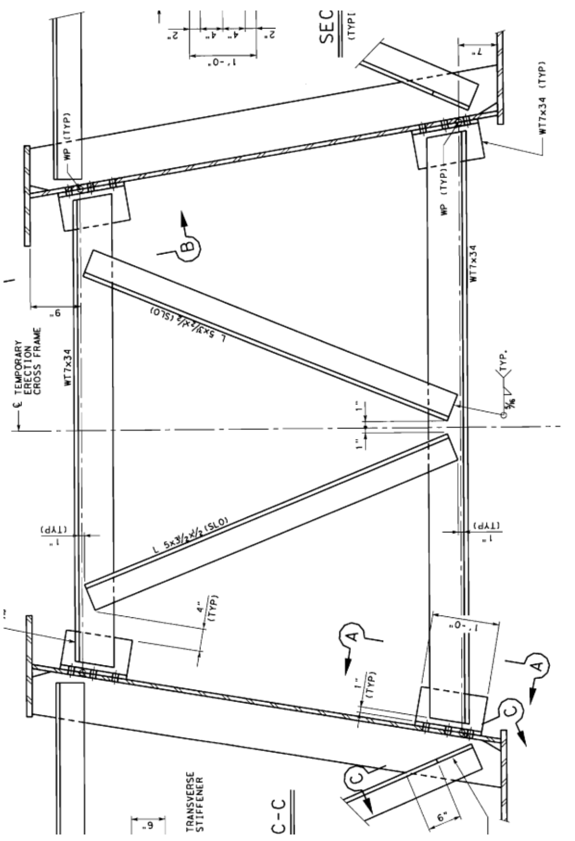

TEMPORARY ERECTION CROSS FRAME TYPE C2

Bridge 2: 12-102-0271-17-530

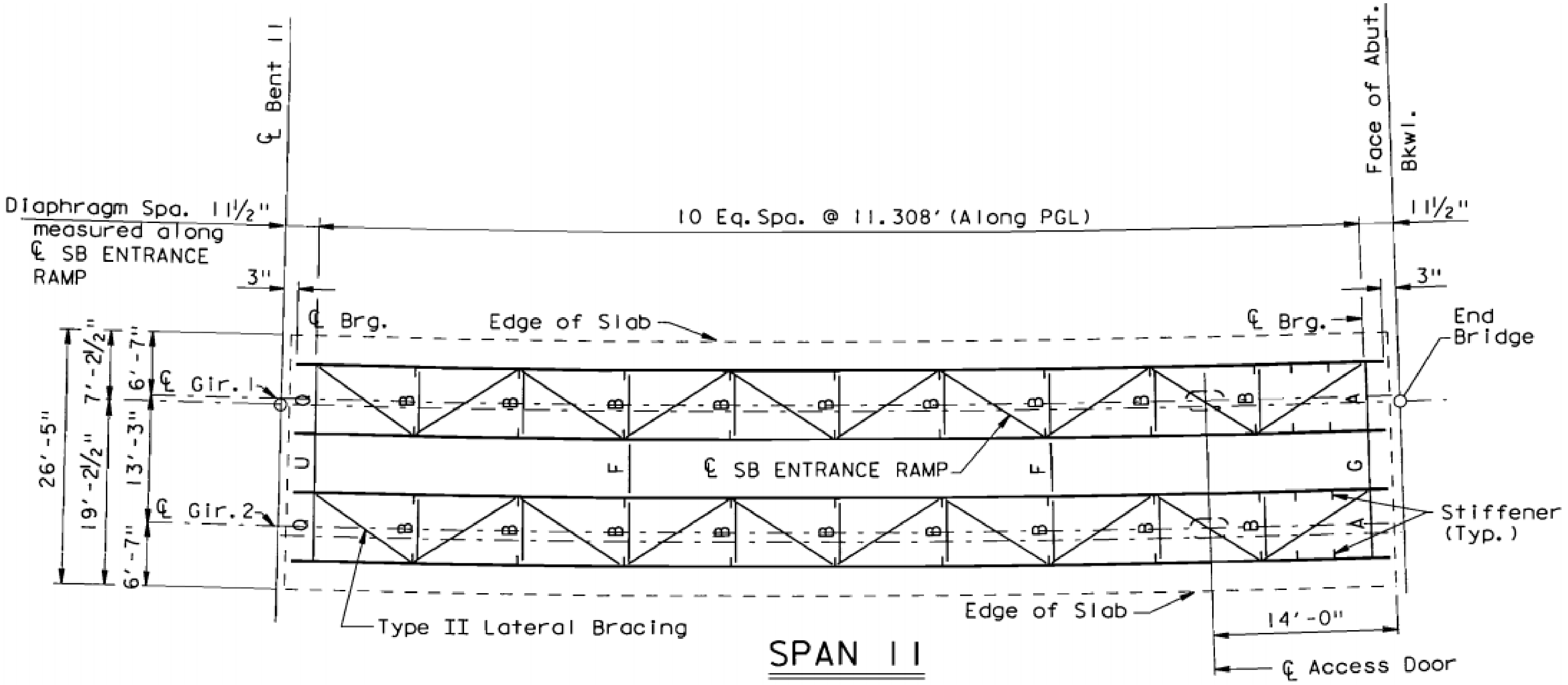

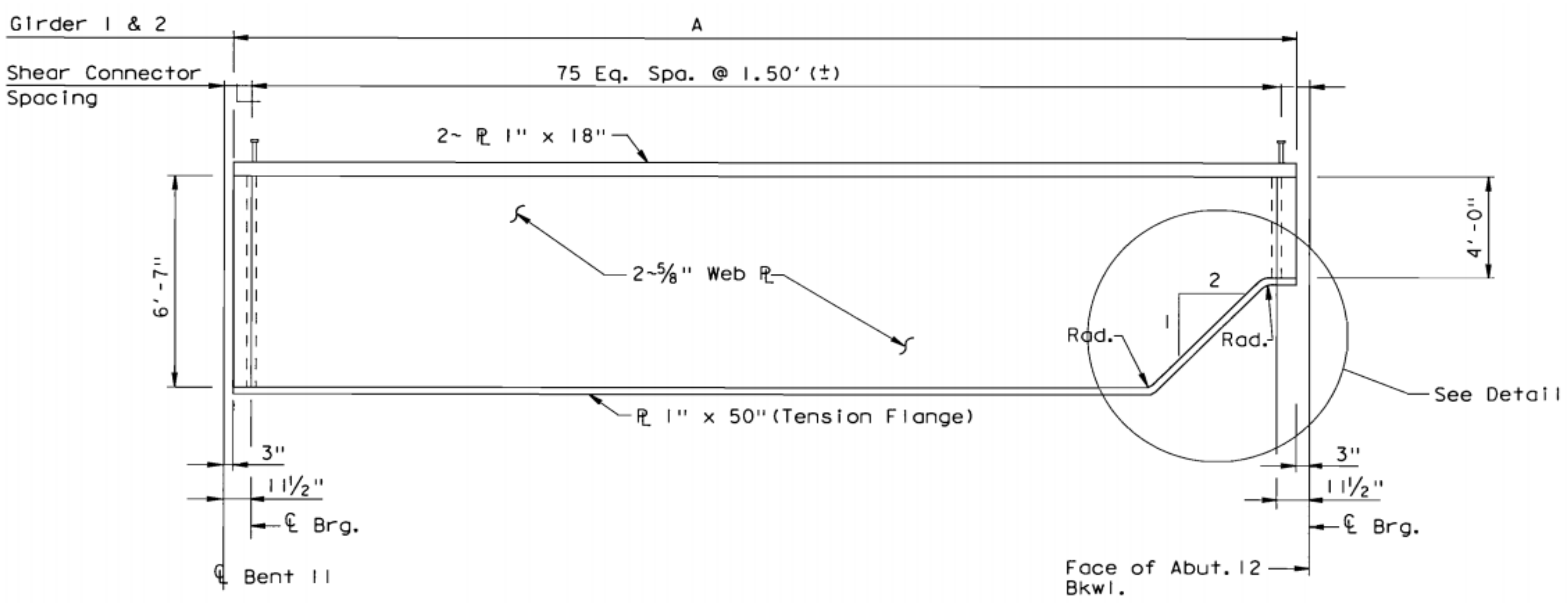

BOX GIRDER ELEVATION (TYP)

(DIMENSIONS SHOWN ARE ALONG ℄ GIRDER)

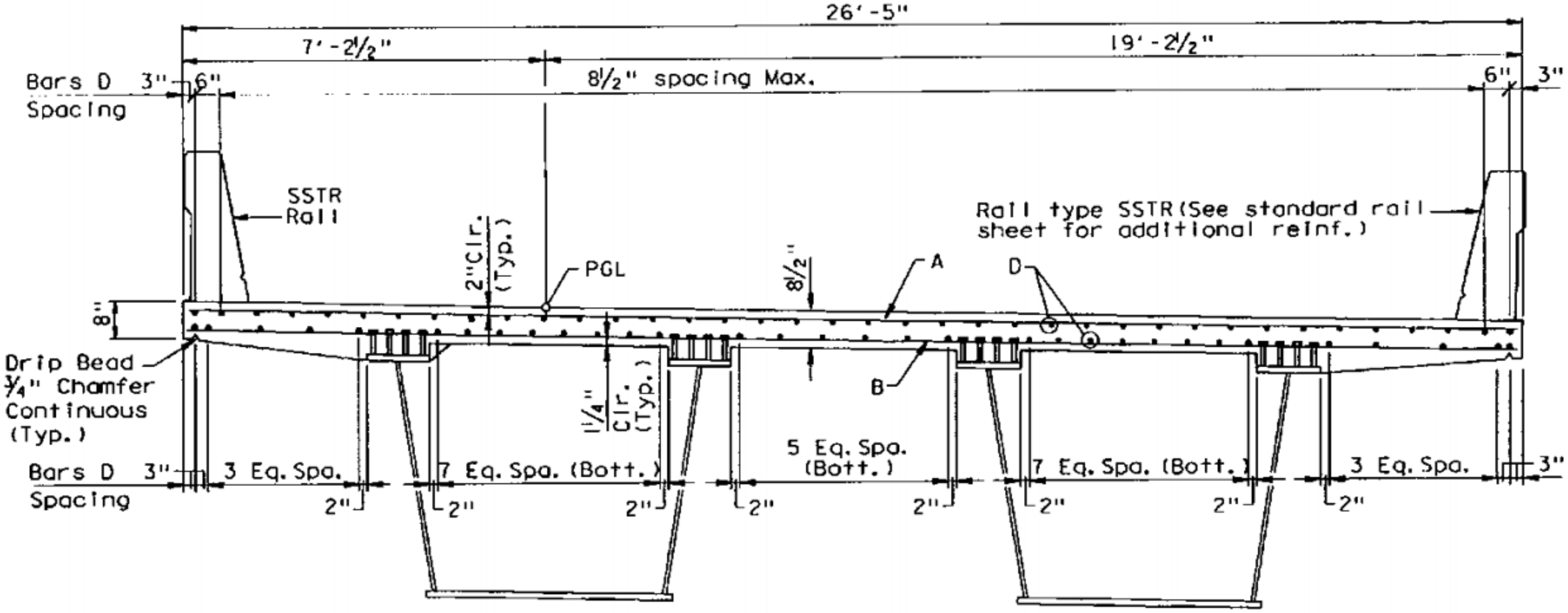

BOX GIRDER ELEVATION (TYP)

(DIMENSIONS SHOWN ARE ALONG ℄ GIRDER)

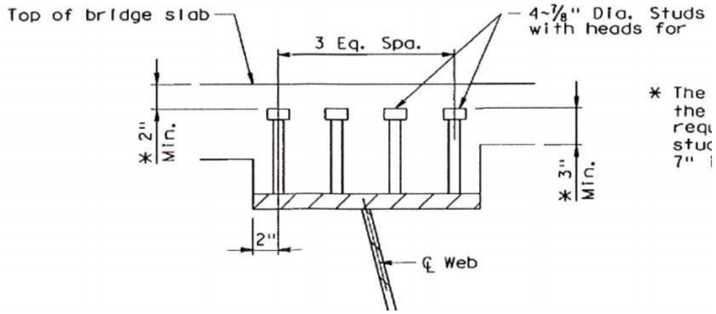

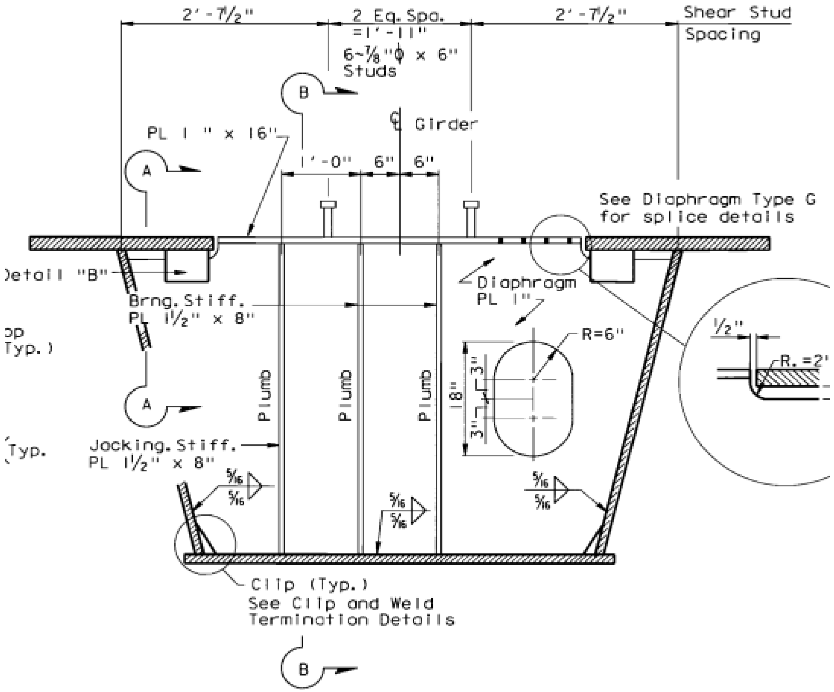

DIAPHRAGM ~ TYPE A

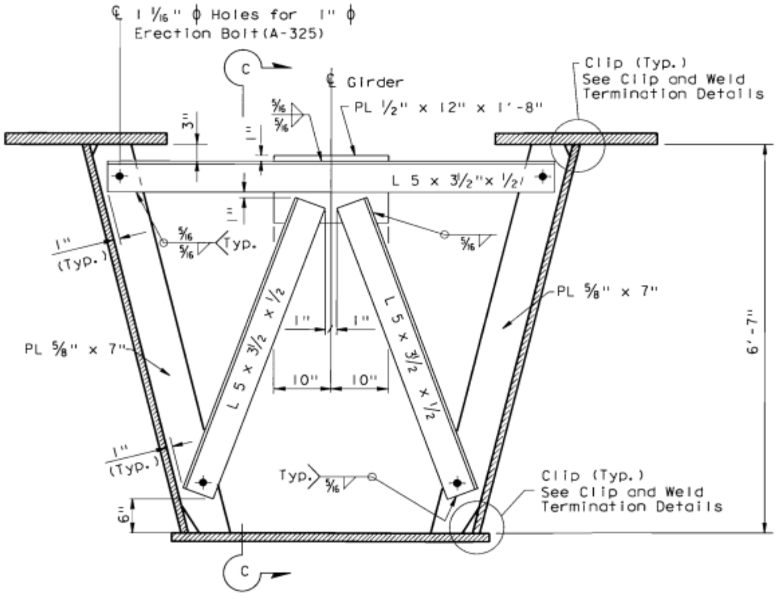

DIAPHRAGM ~ TYPE B

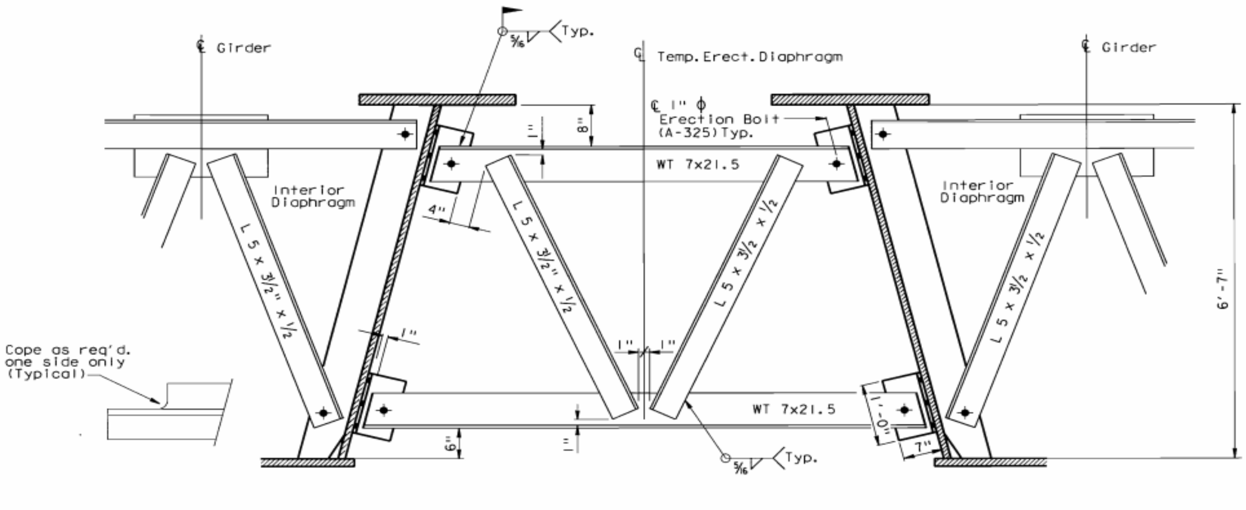

DIAPHRAGM ~ TYPE F (Temporary)

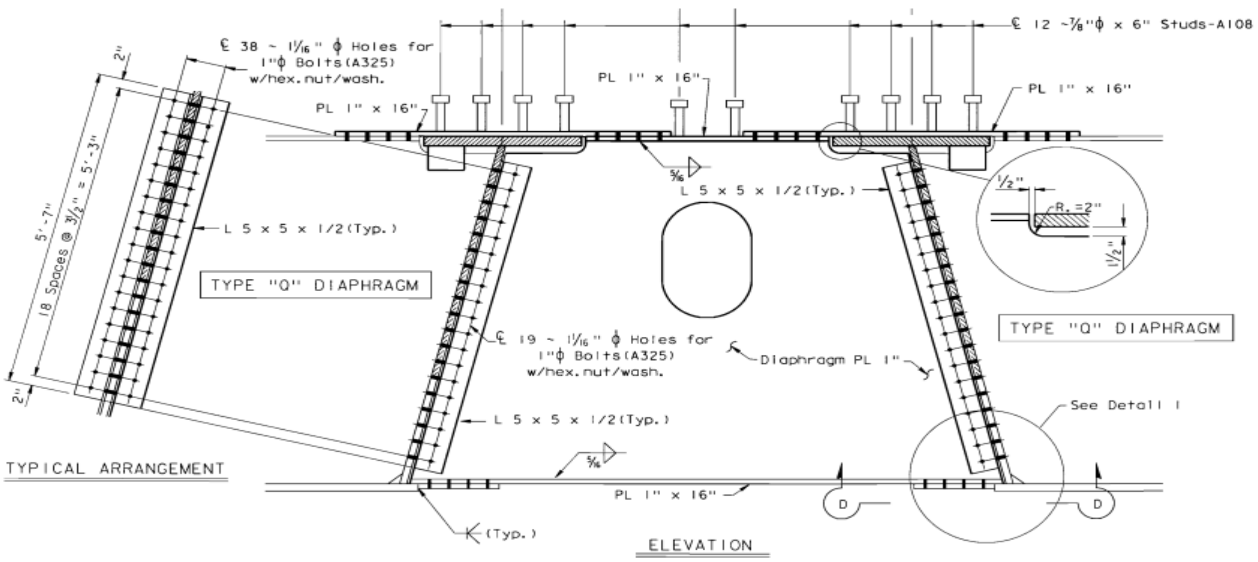

DIAPHRAGM ~ TYPE U

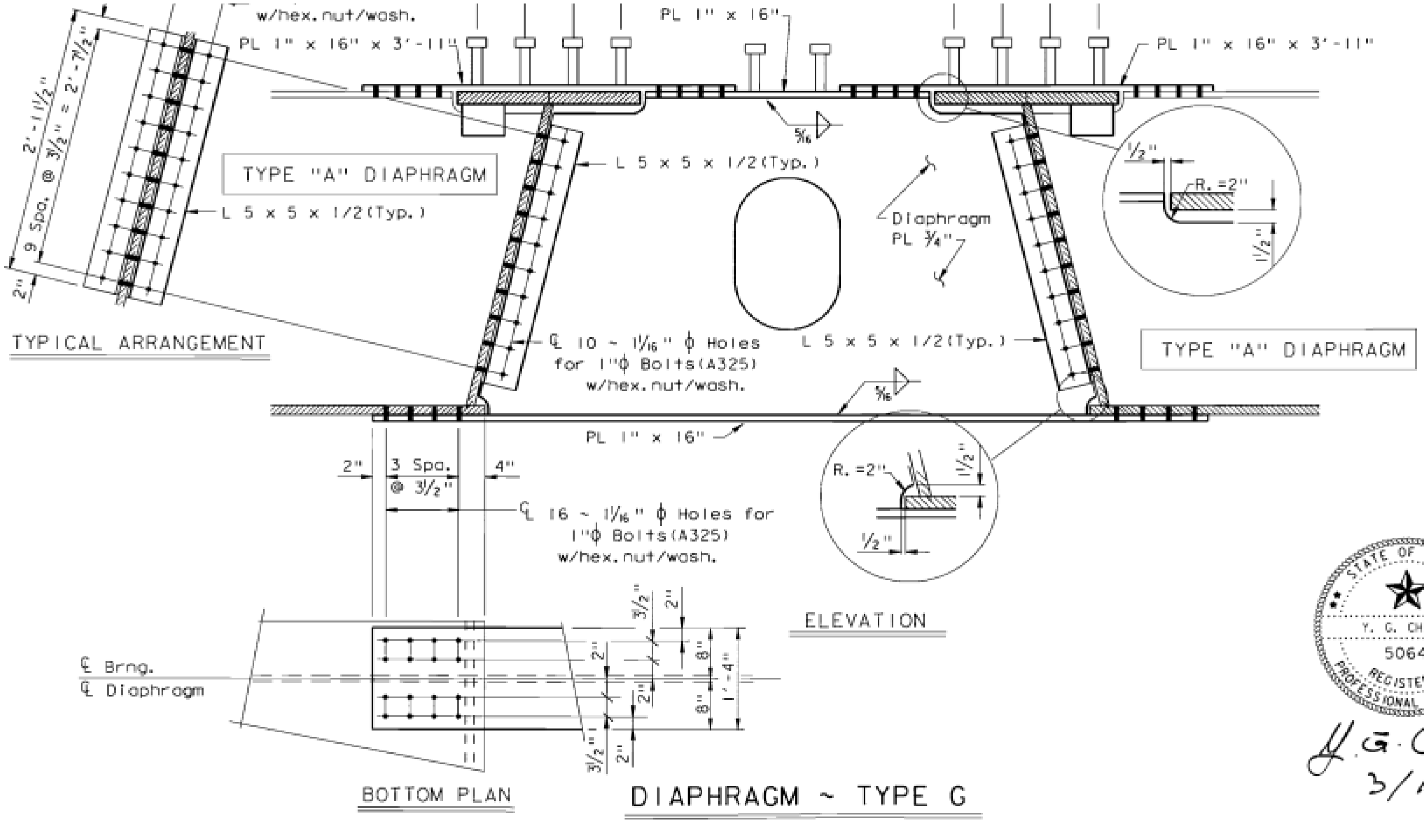

DIAPHRAGM ~ TYPE G

Y. G. CH
5064

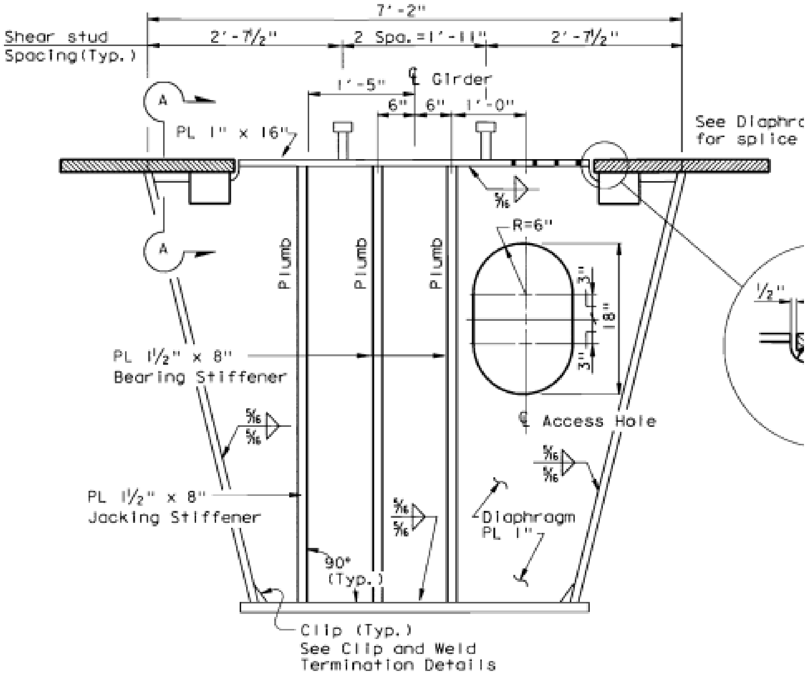

DIAPHRAGM ~ TYPE Q

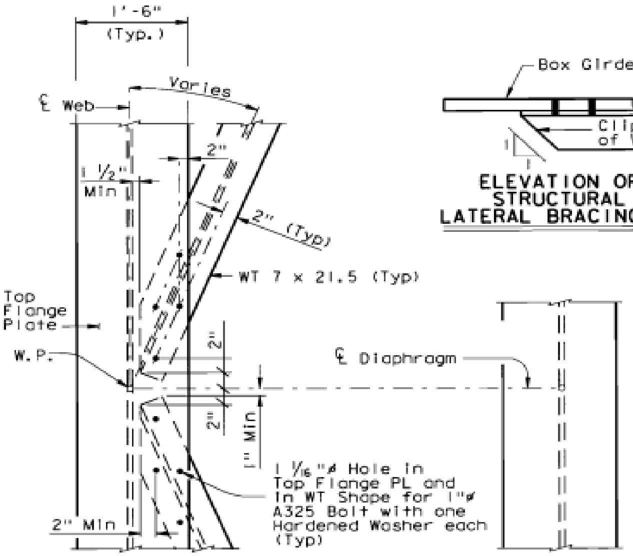

TYPICAL PLAN VIEW OF LATERAL BRACING TYPE "II"

Installed in shop except at locations spanning a field splice, which shall be installed in the field.

ELEVATION OF END OF STRUCTURAL TEE OF LATERAL BRACING TYPE "II"

Bridge 3: 12-102-0508-01-294

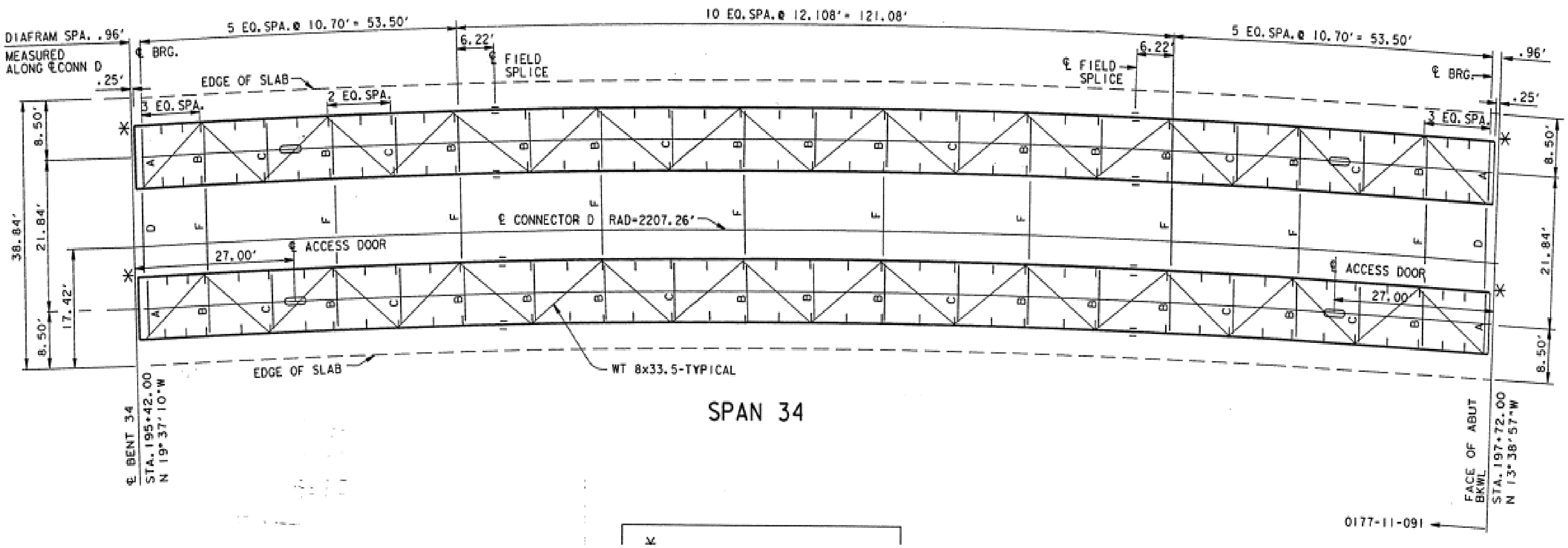

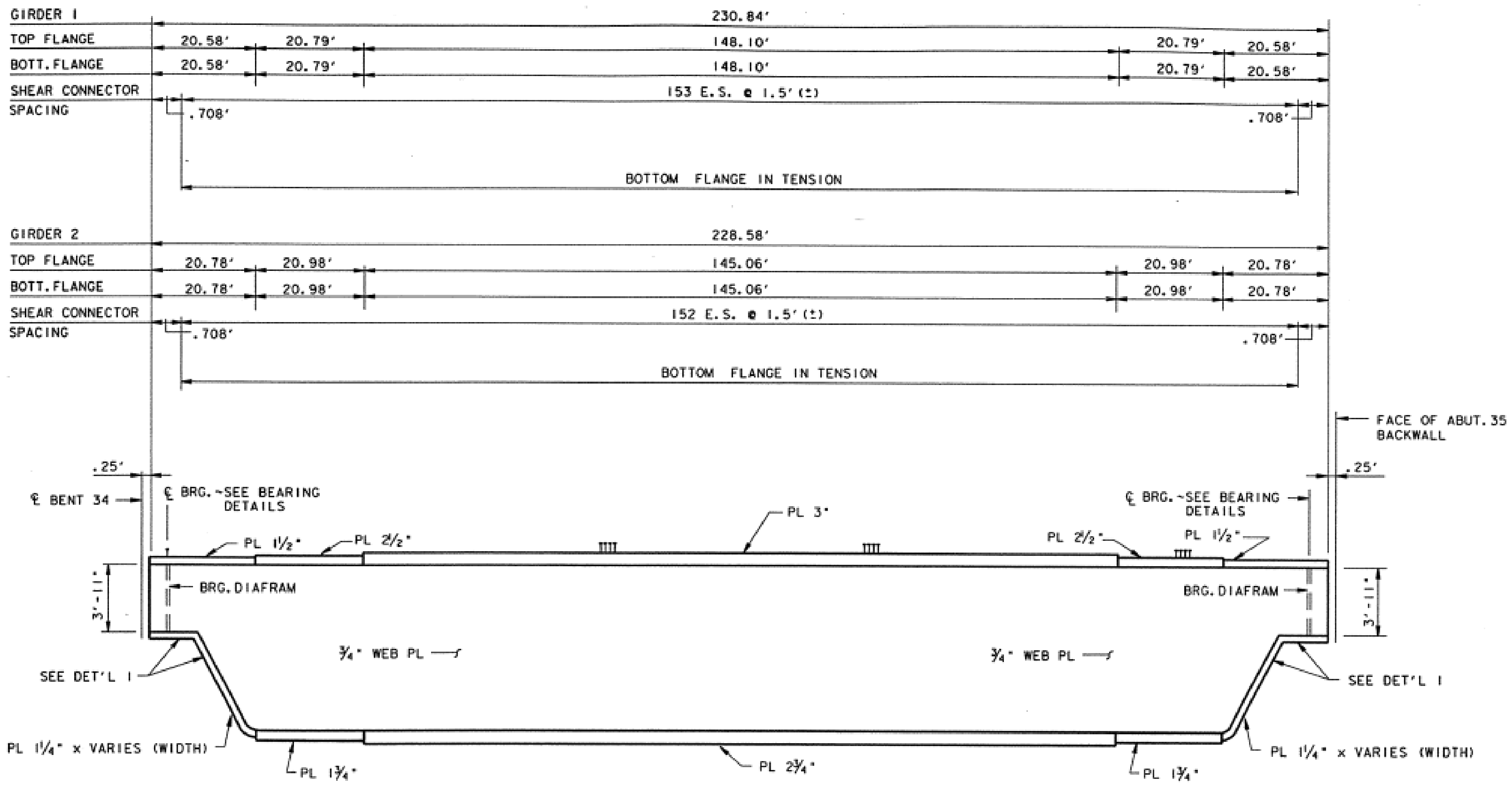

SPAN 34

ELEVATION

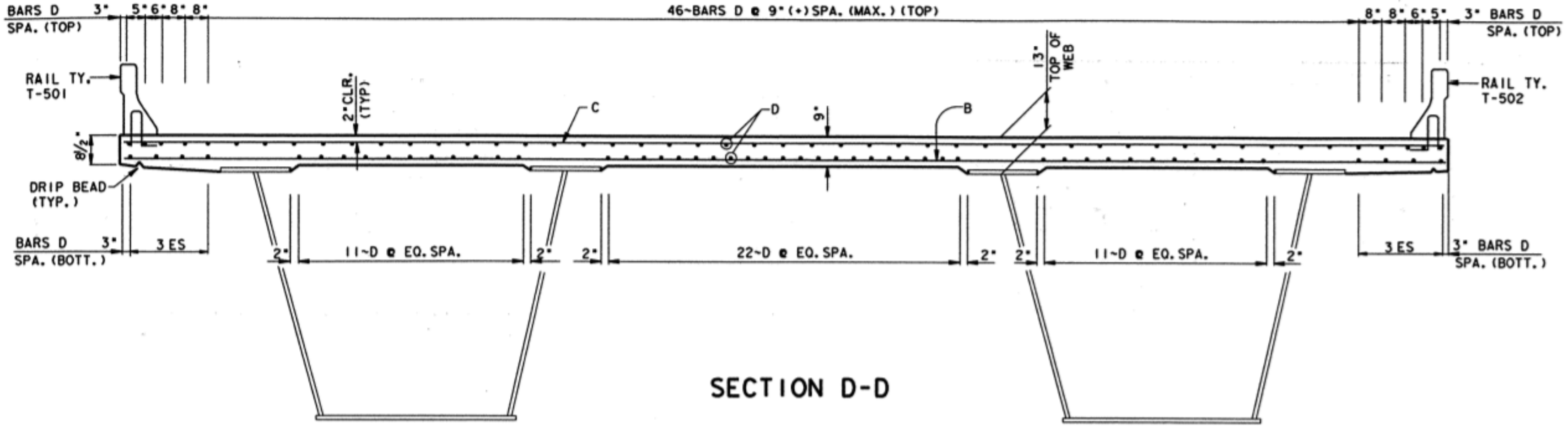

SECTION D-D

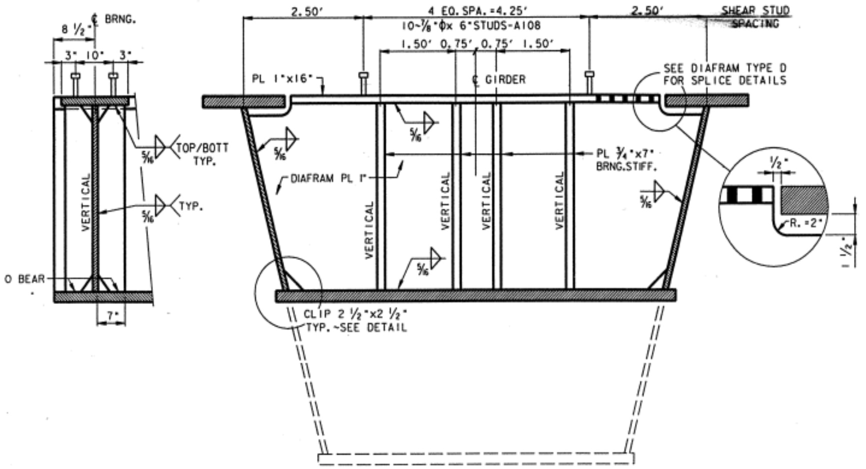

DIAFRAM ~ TYPE A

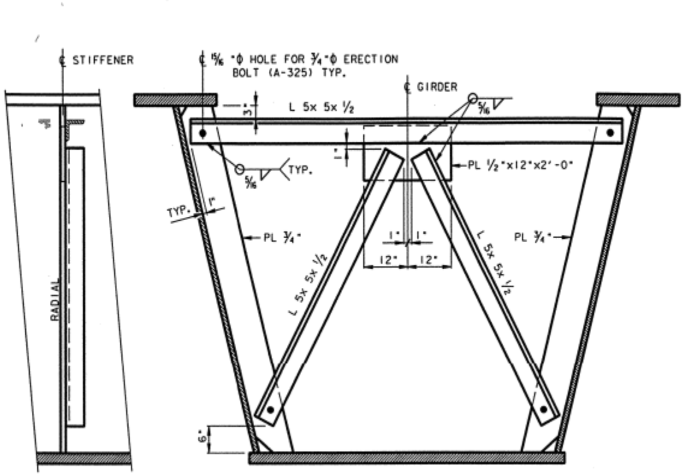

DIAFRAM ~ TYPE B

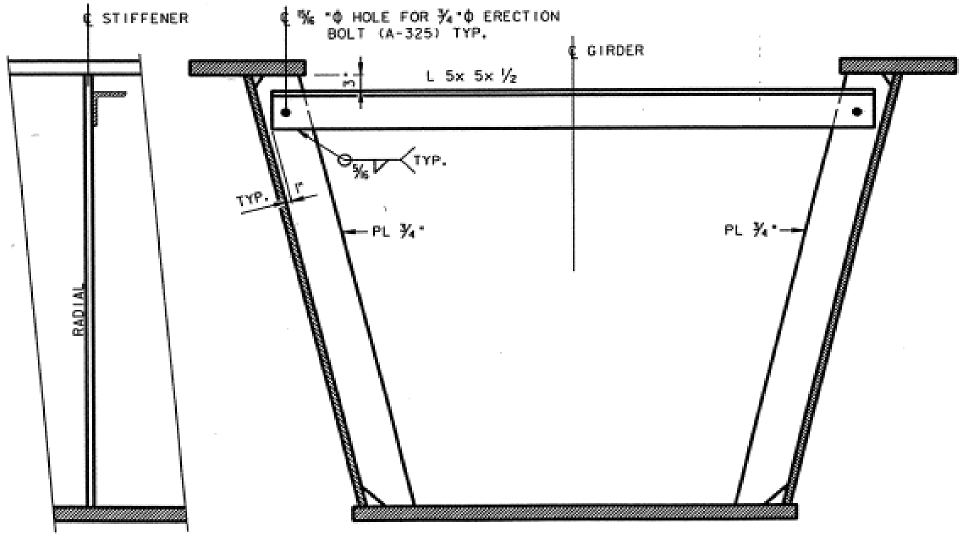

DIAFRAM ~ TYPE C

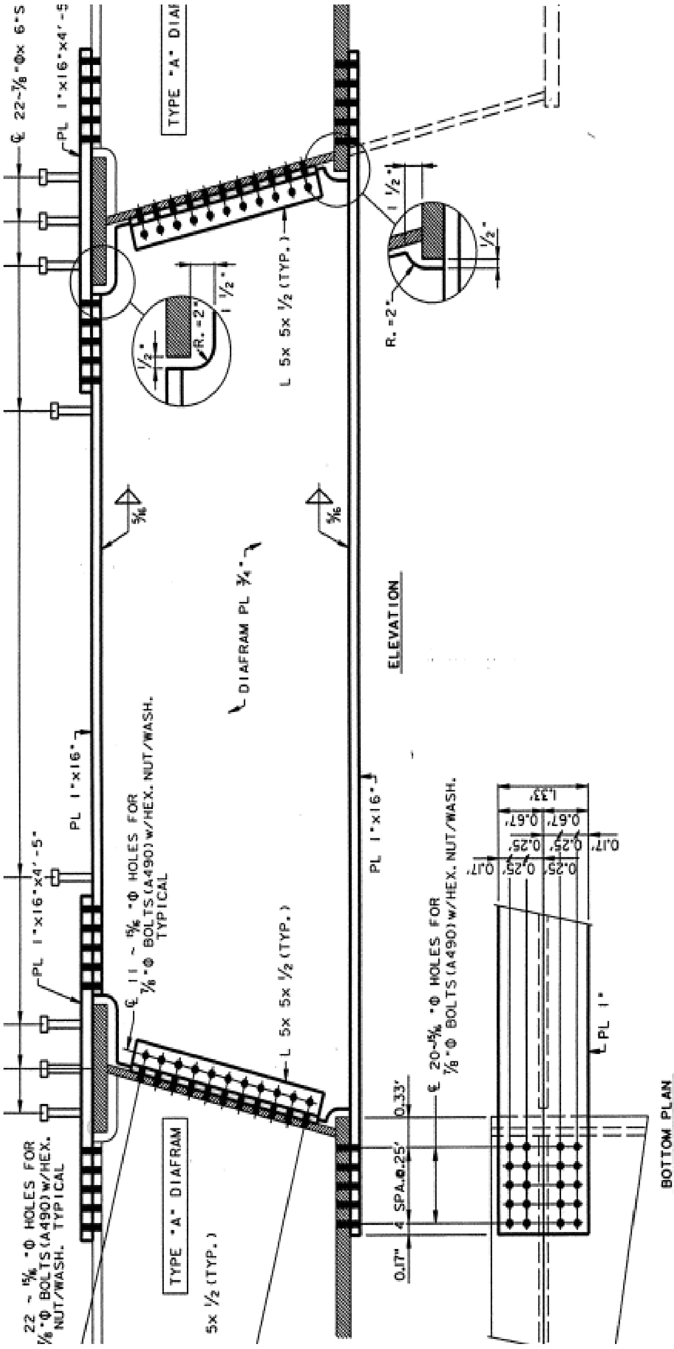

DIAFRAM ~ TYPE D

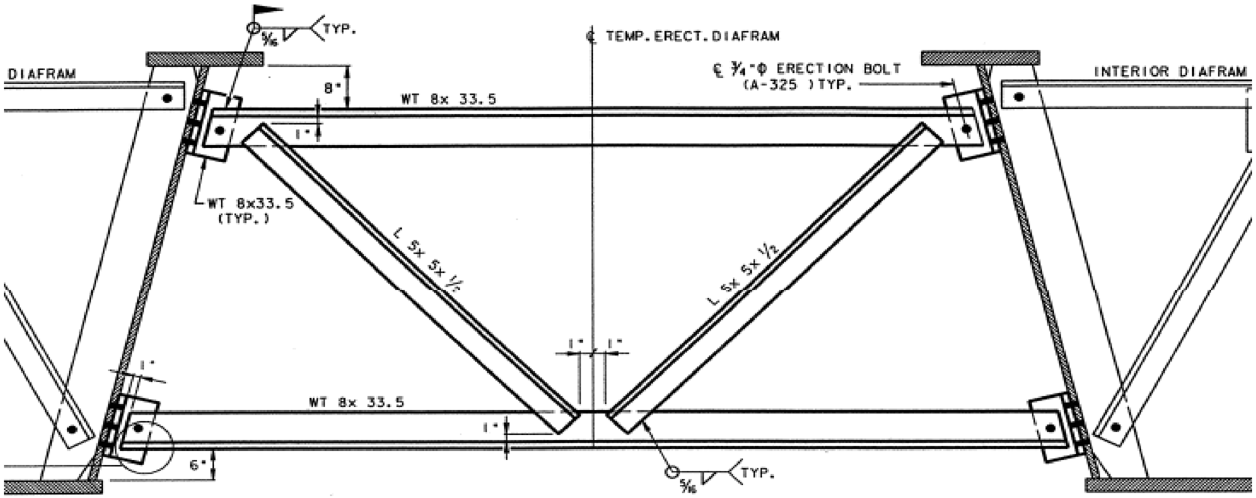

DIAFRAM ~ TYPE F (TEMPORARY)

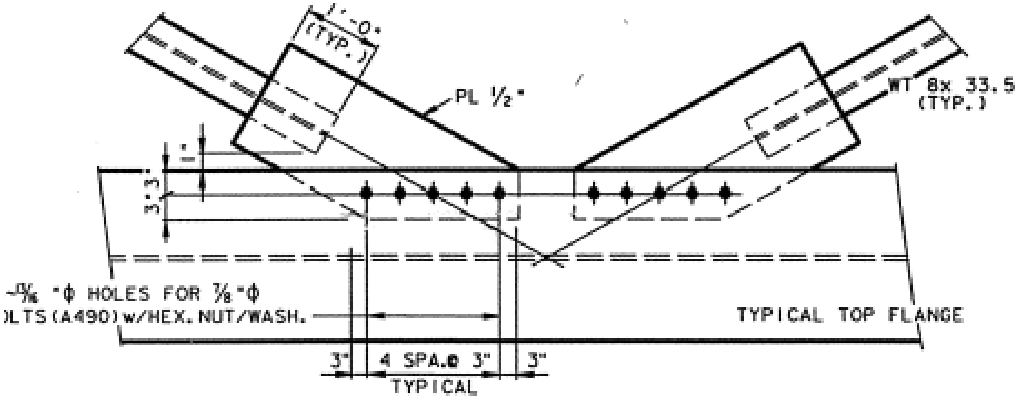

PLAN

Bridge 4: 12-102-0271-07-637

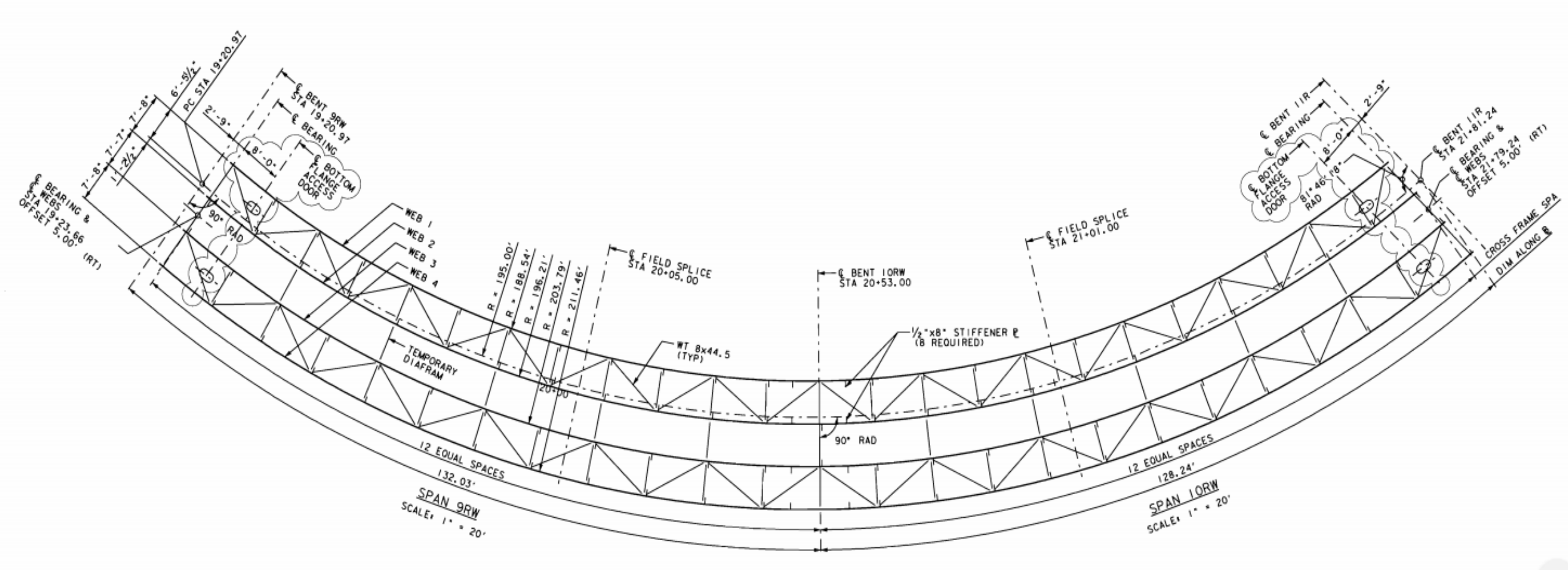

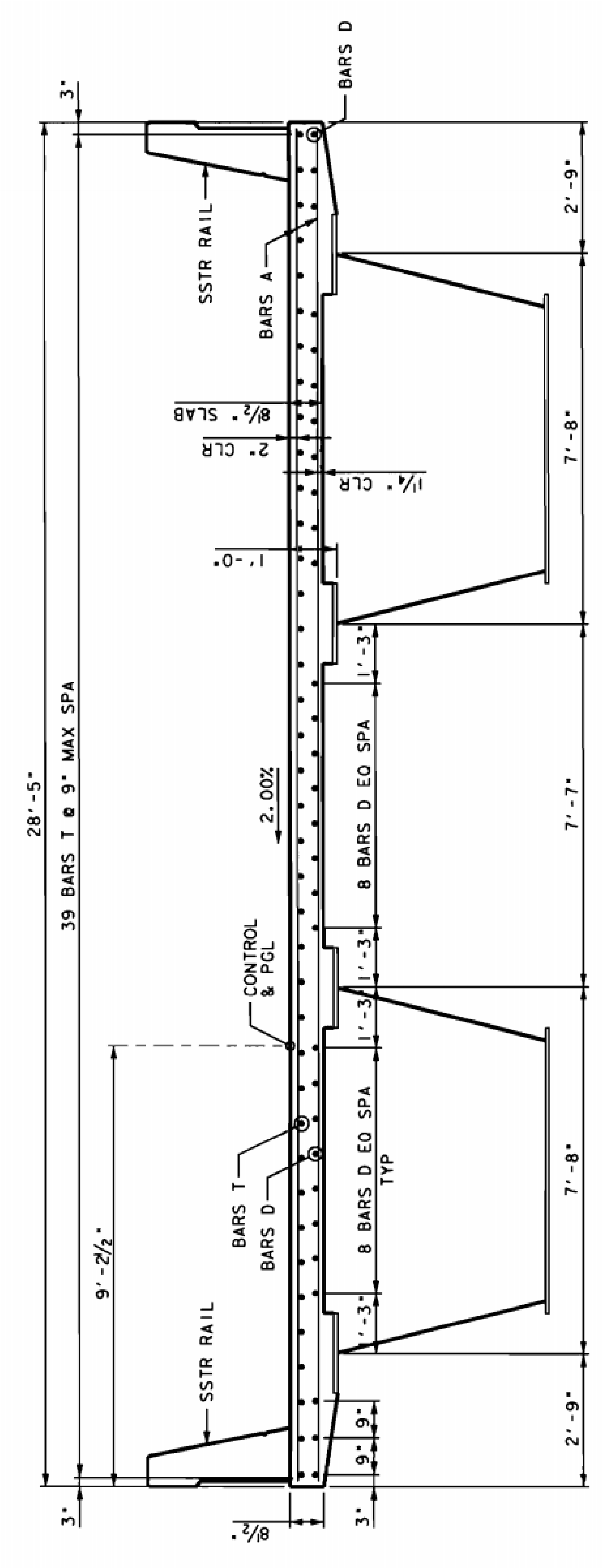
28'-5"
39 BARS T @ 9" MAX SPA
3"
3"
9'-2½"
SSTR RAIL
SSTR RAIL
BARS D
BARS A
8½" SLAB
2" CLR
1¼" CLR
1'-0"
2.00%
CONTROL & PGL
BARS T
BARS D
1'-3"
1'-3"
1'-3"
1'-3"
8 BARS D EQ SPA
8 BARS D EQ SPA TYP
9"
9"
3"
8½"
2'-9"
7'-8"
7'-7"
7'-8"
2'-9"

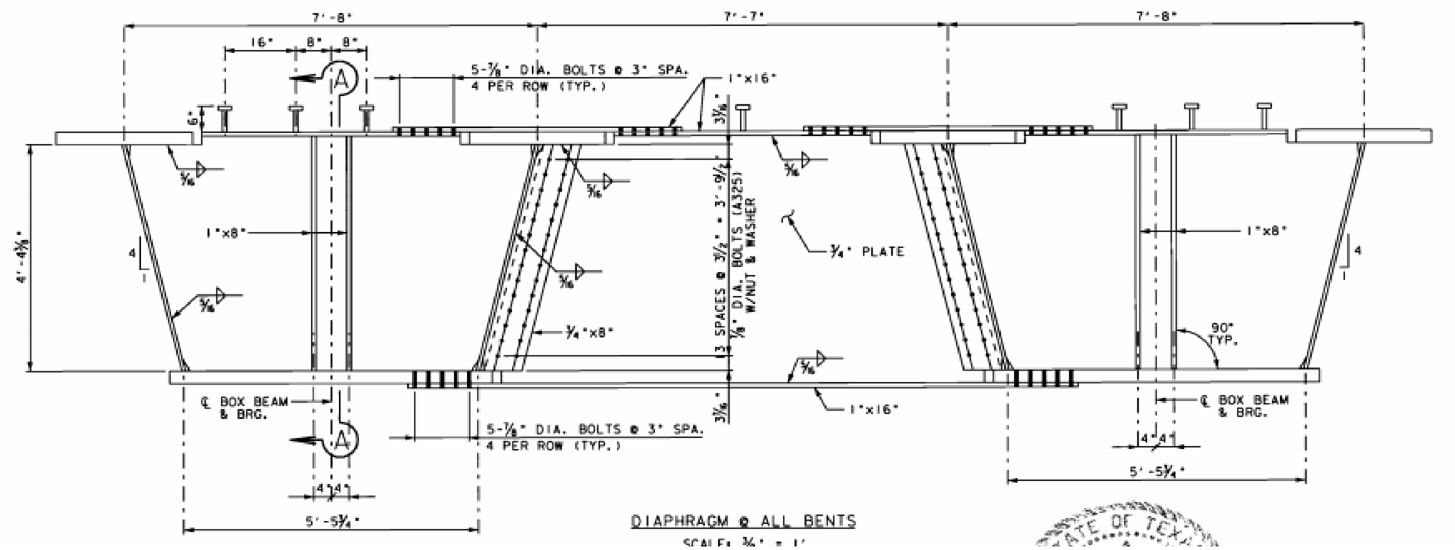

DIAPHRAGM @ ALL BENTS

SCALE: 3/8" = 1'

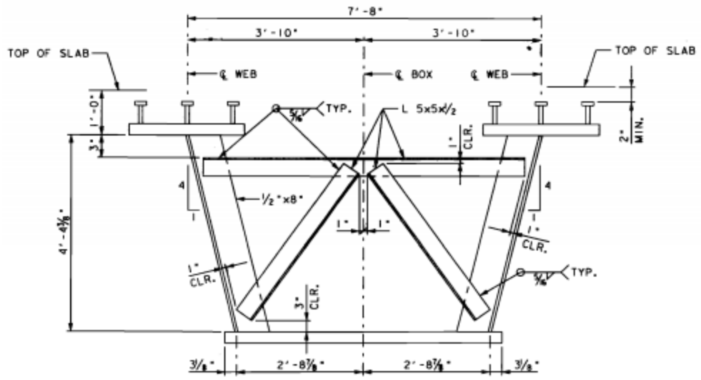

TYPE B INTERMEDIATE DIAPHRAGM

3/8" = 1'-0"

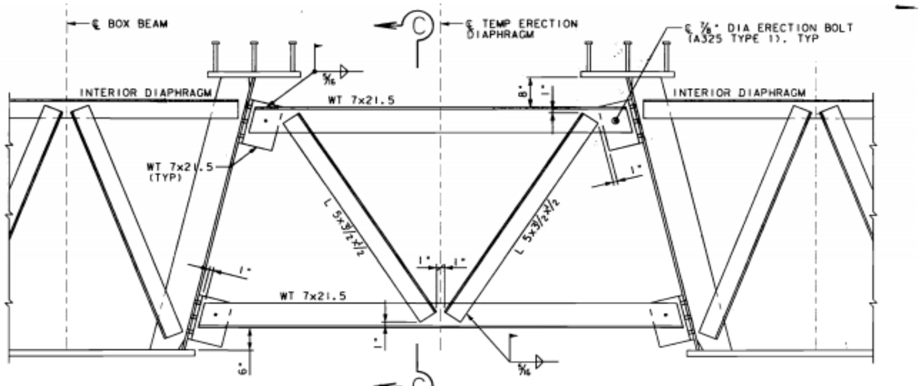

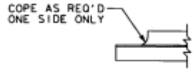

PLAN

TEMPORARY DIAPHRAGM

N. T. S.

NOTE:
ALL ANGLES PLACED WITH LONG LEG VERTICAL, TYP
TEMPORARY ERECTION DIAPHRAGMS SHALL BE IN PLACE DURING PLACEMENT AND CURING OF DECK, AFTER WHICH THESE DIAPHRAGMS SHALL BE REMOVED WITH THE EXCEPTION OF THE 7/8" DIA HS 'HEX HEAD TYPE' BOLTS THROUGH THE WEB. FOR LOCATION OF TEMPORARY DIAPHRAGMS, SEE FRAMING PLAN.

Bridge 5: 14-227-0-0015-13-452

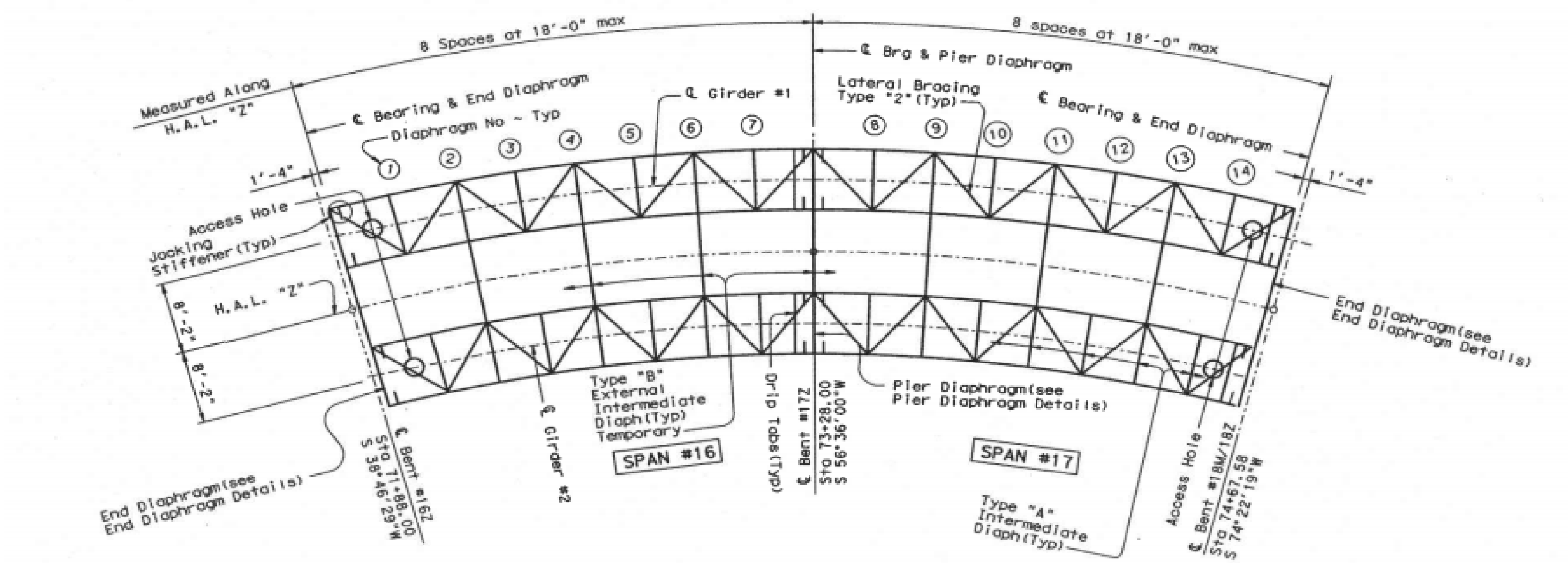

FRAMING PLAN

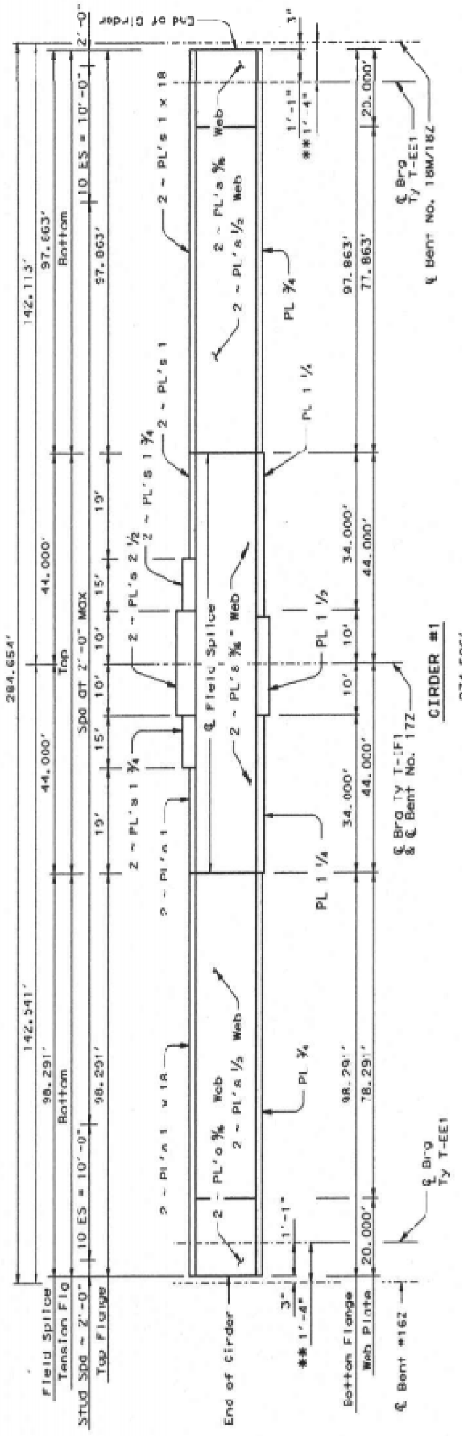
GIRDER #1

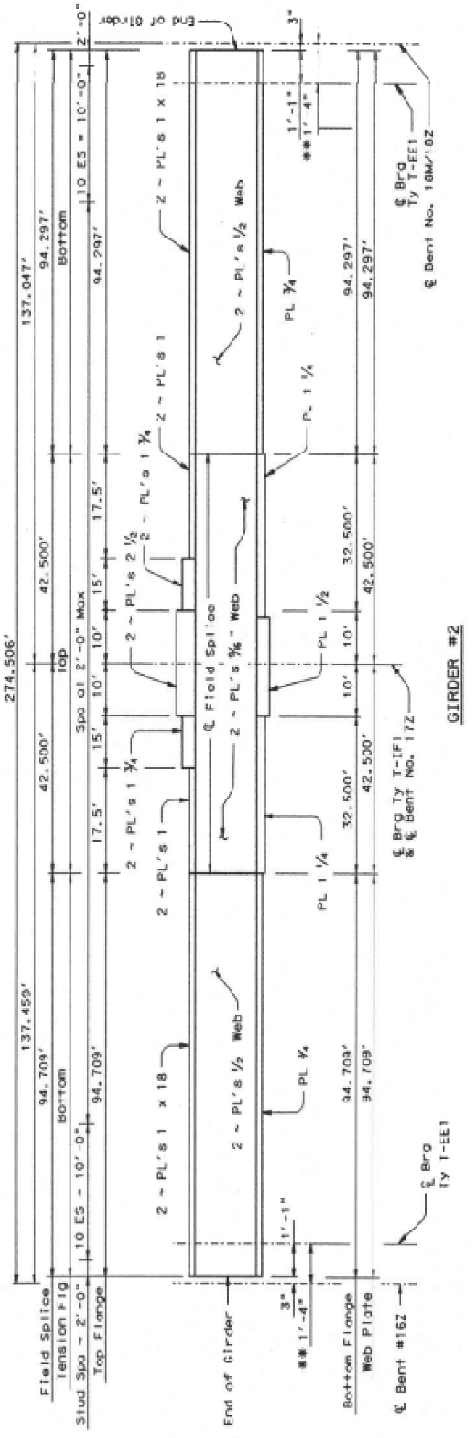
GIRDER #2

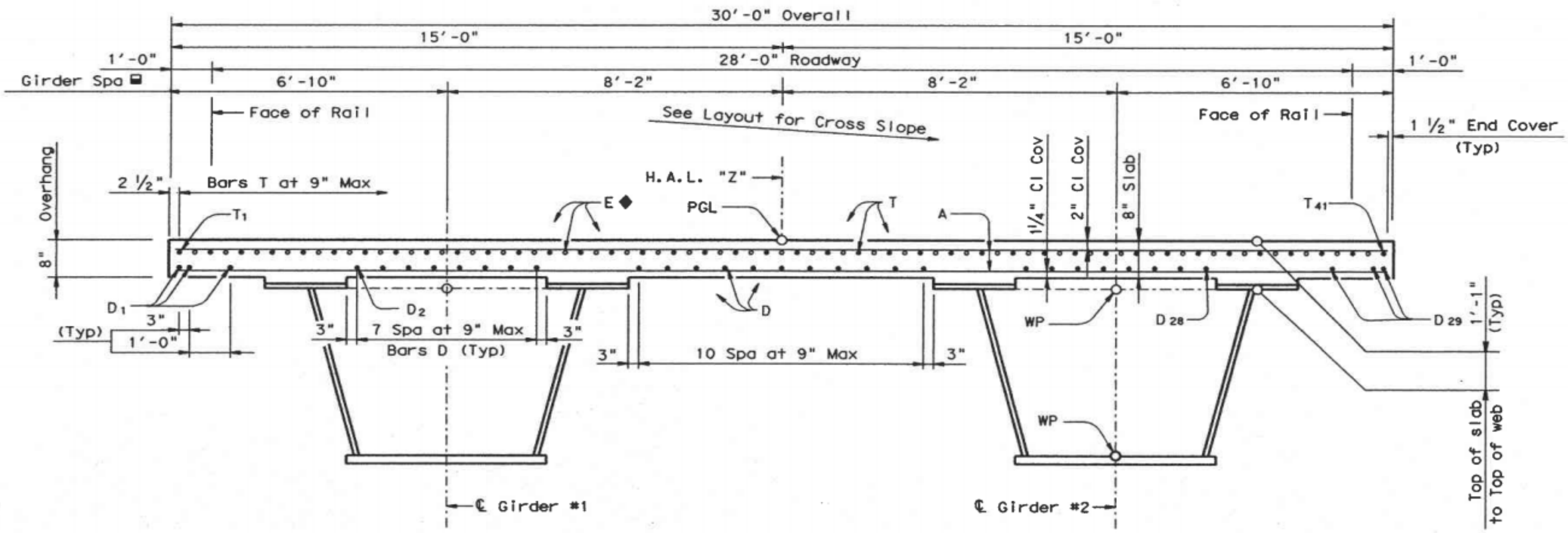

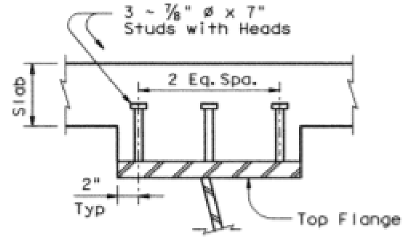

SHEAR CONNECTOR STUD DETAIL

Studs shall be Electric arc end-welded to the flanges with complete fusion. (See Span details for spacing along girder.)

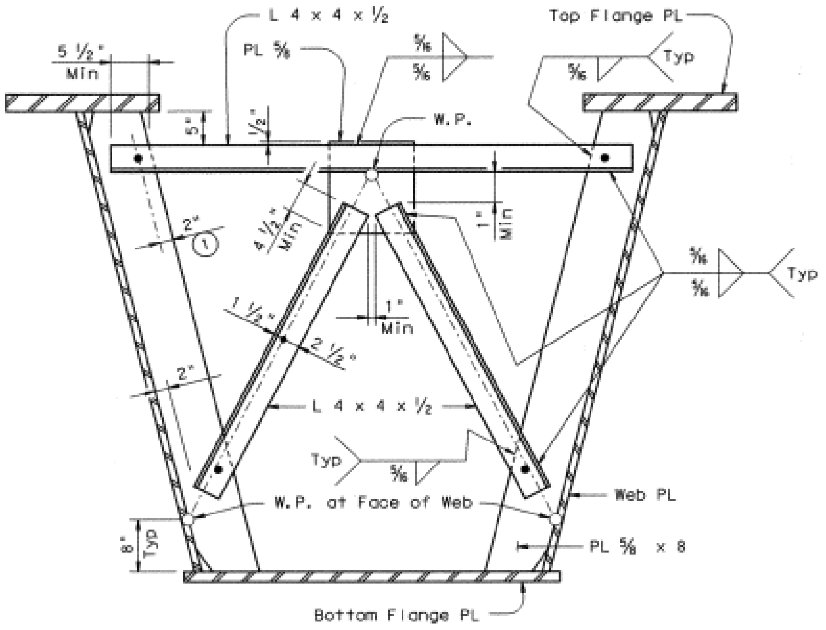

TYPICAL SECTION AT TYPE "A" INTERNAL INTERMEDIATE DIAPHRAGM

To be fully installed in the shop.

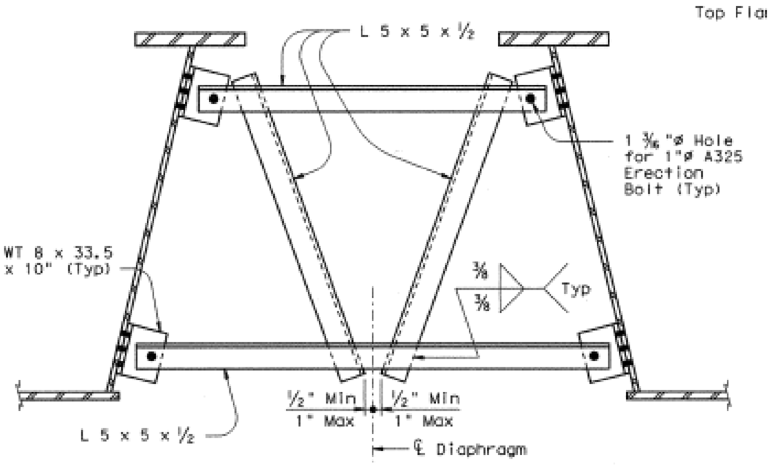

TYPICAL SECTION AT TYPE "B" EXTERNAL INTERMEDIATE DIAPHRAGM (TEMPORARY)

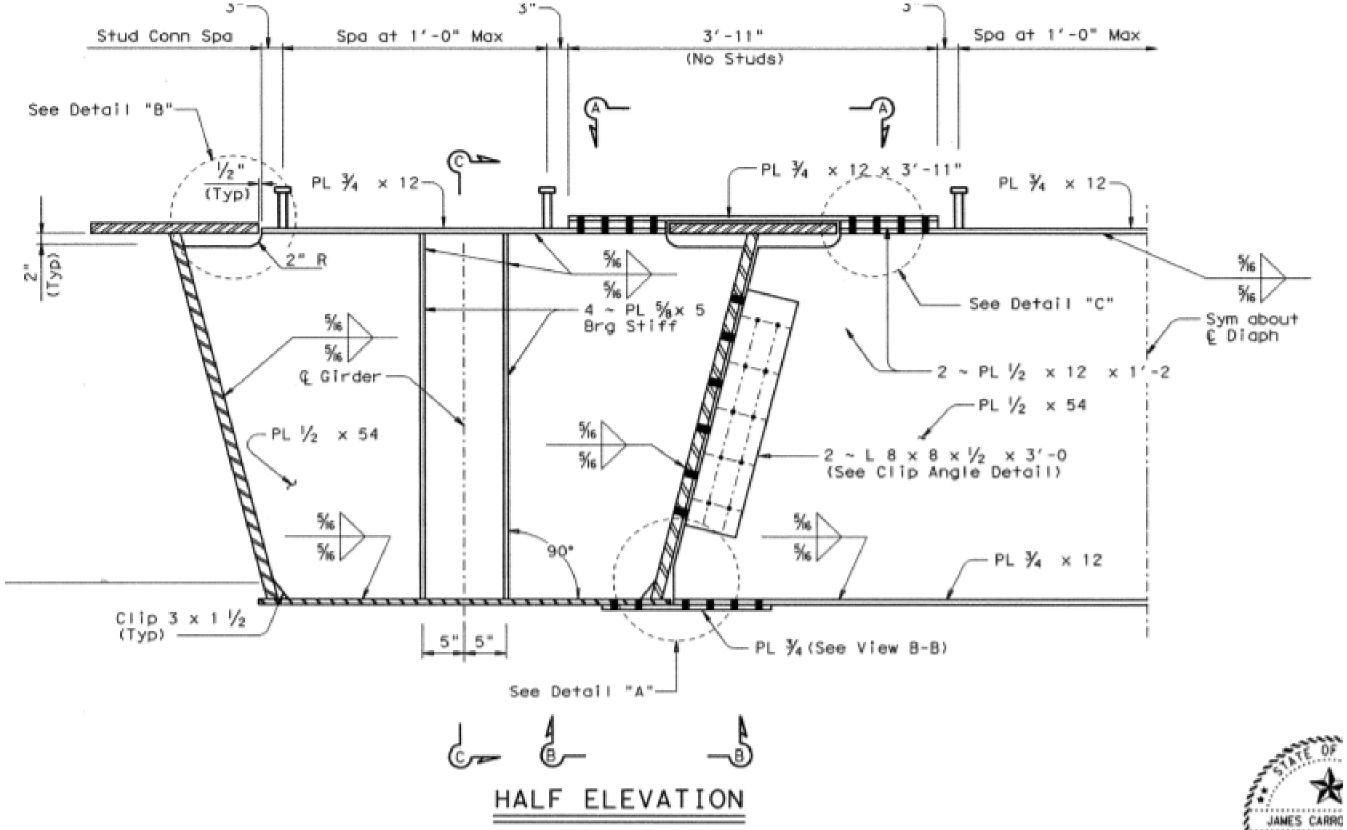

END DIAPHRAGM DETAILS

(At Bent Nos 16Z & 18M/18Z)

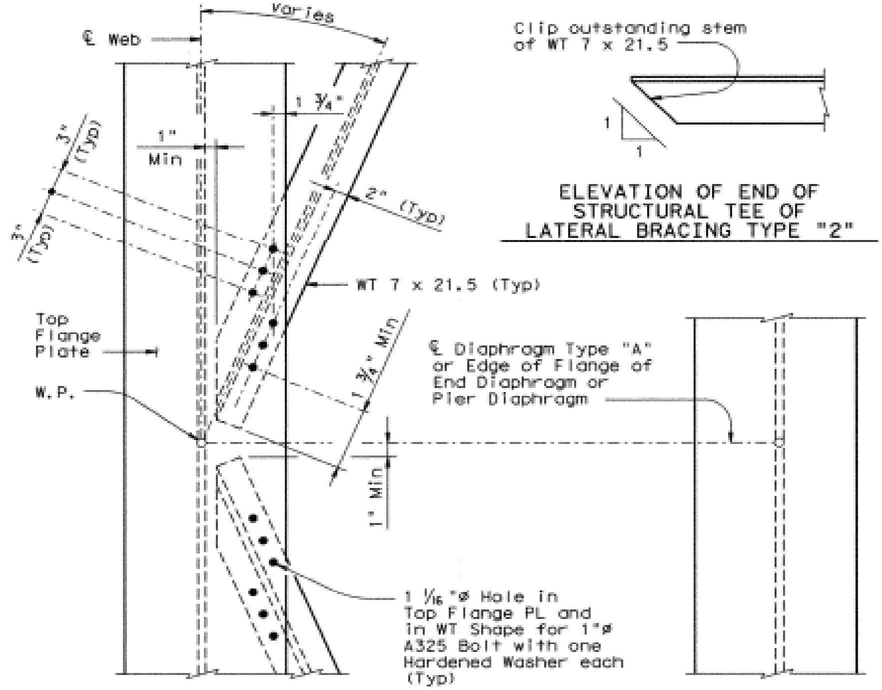

ELEVATION OF END OF
STRUCTURAL TEE OF
LATERAL BRACING TYPE "2"

TYPICAL PLAN VIEW OF
LATERAL BRACING TYPE "2"

Installed in shop except at locations spanning a field splice, which shall be installed in the field.

Bridge 6: 12-102-0271-07-575

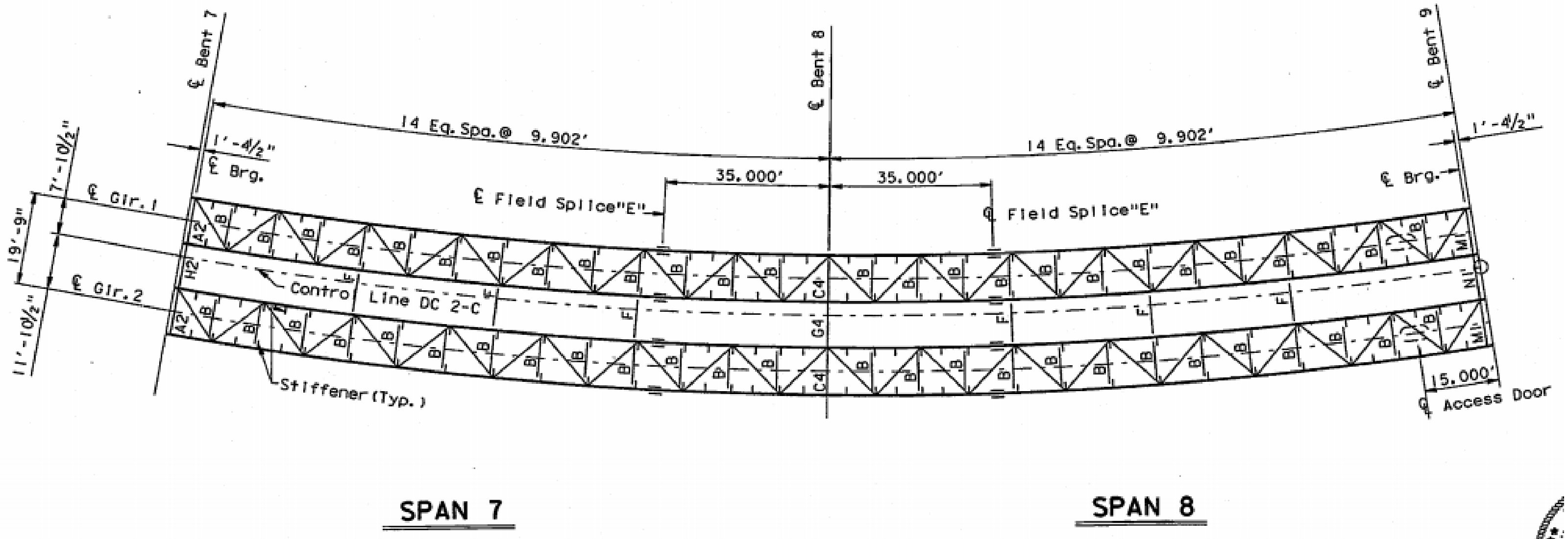

LATERAL BRACING INFORMATION

SPAN	MEMBER SIZE	CONNECTION DETAIL #
5	WT 8 × 38.5	7, 8, or 9
6	WT 8 × 38.5	7, 8, or 9
7	WT 7 × 21.5	10, 11, or 12
8	WT 7 × 21.5	10, 11, or 12

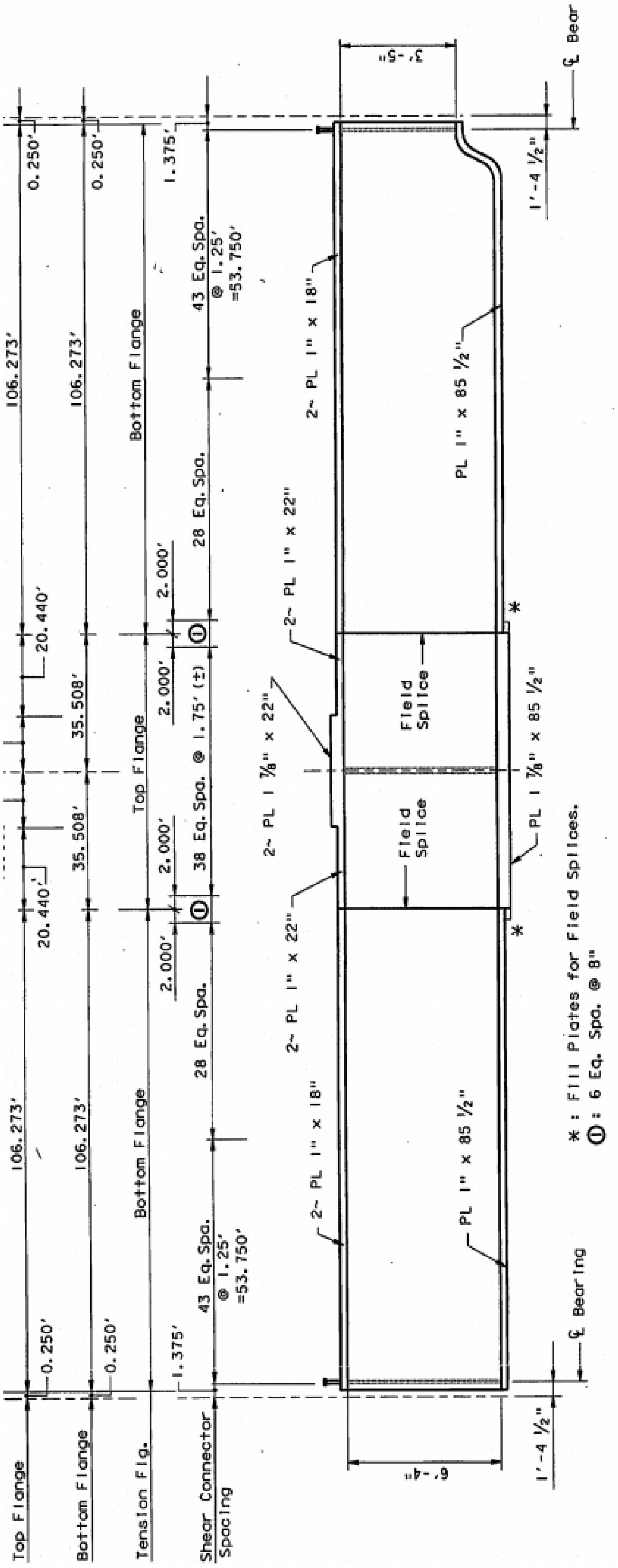

* : Fill Plates for Field Splices.

① : 6 Eq. Spa. @ 8"

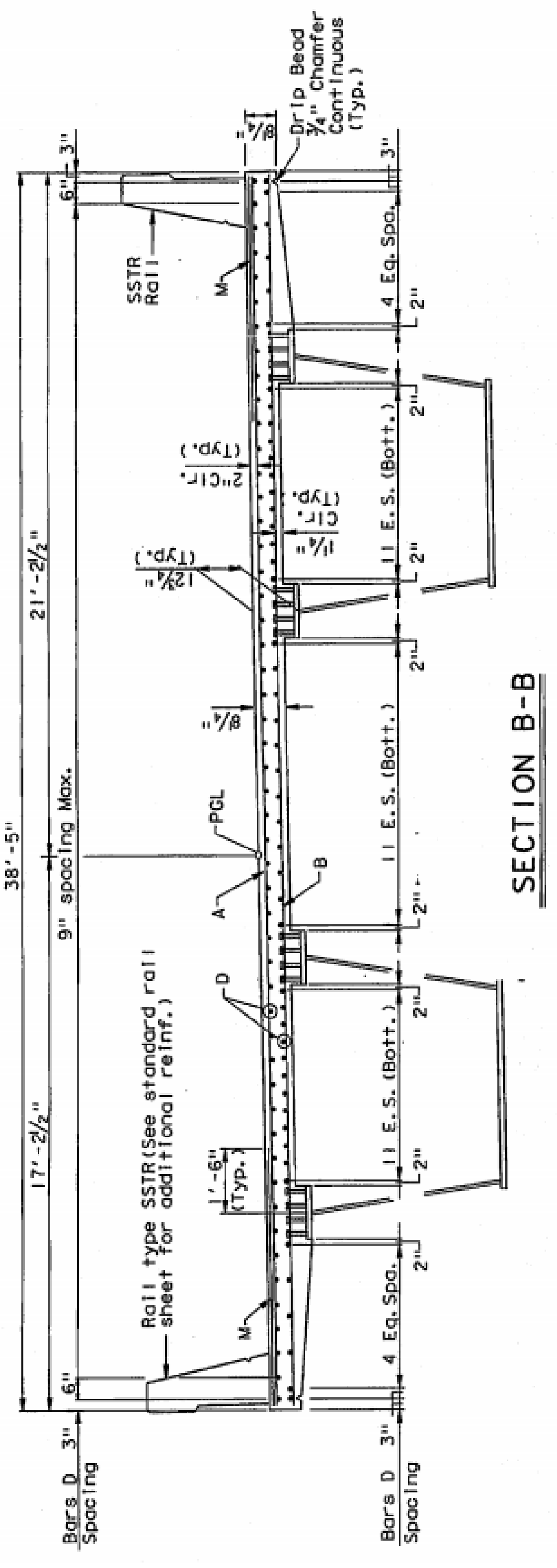
SECTION B-B

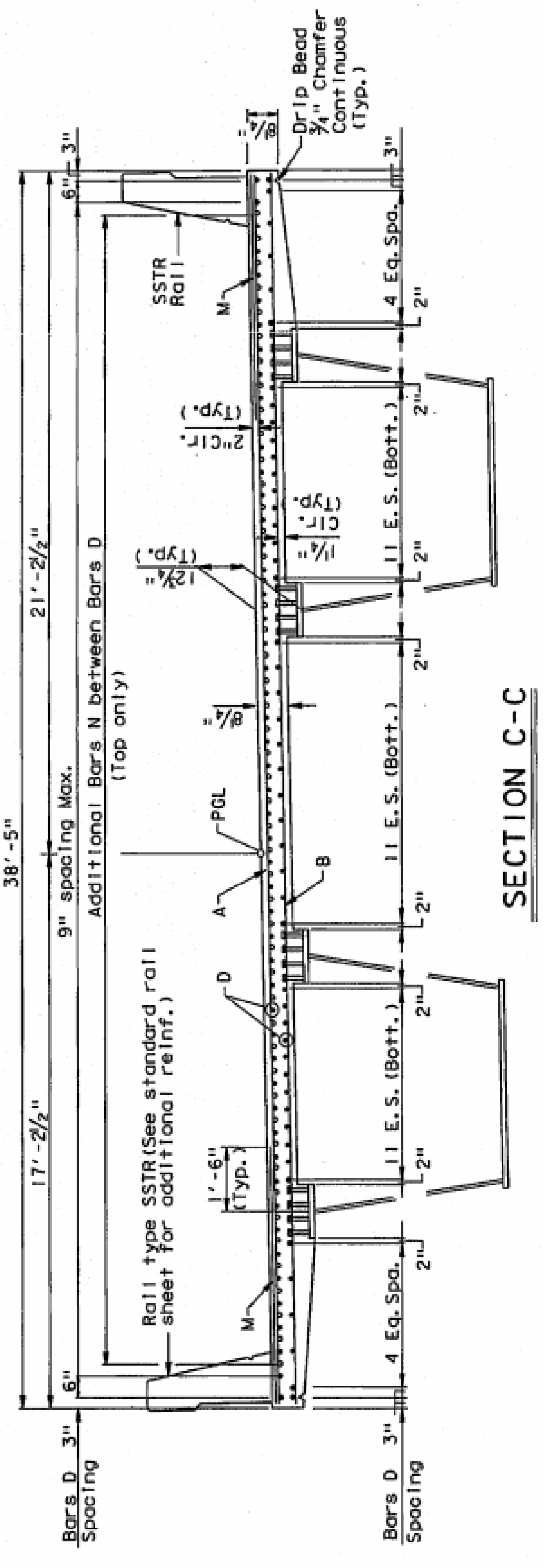
SECTION C-C

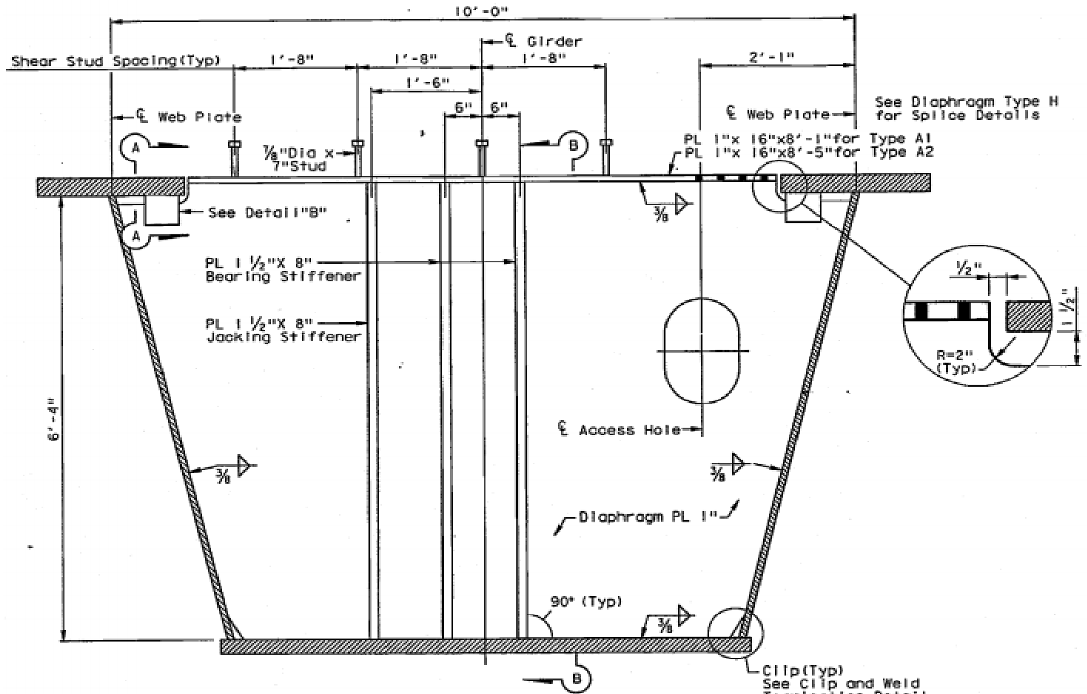

DIAPHRAGM~TYPE A1 & A2

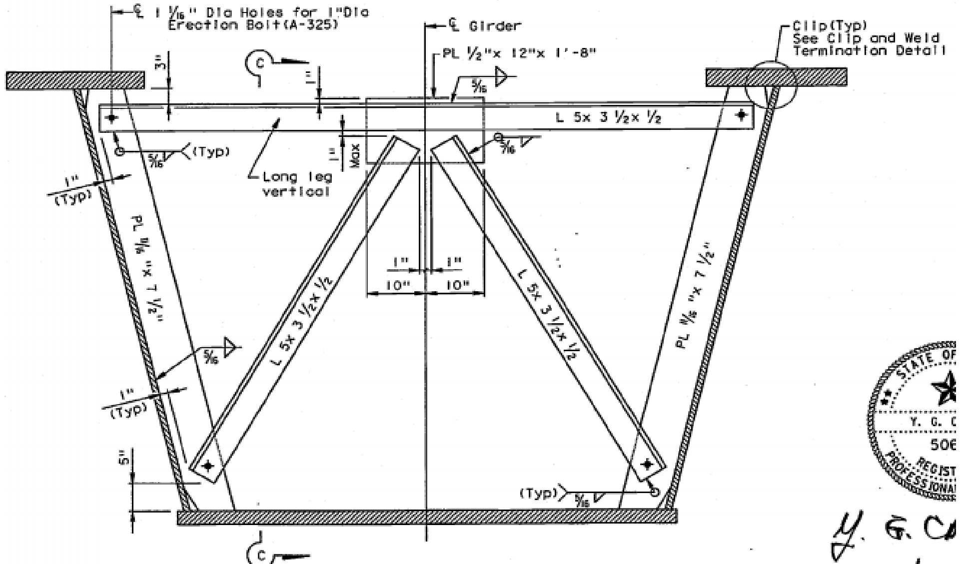

DIAPHRAGM~TYPE B

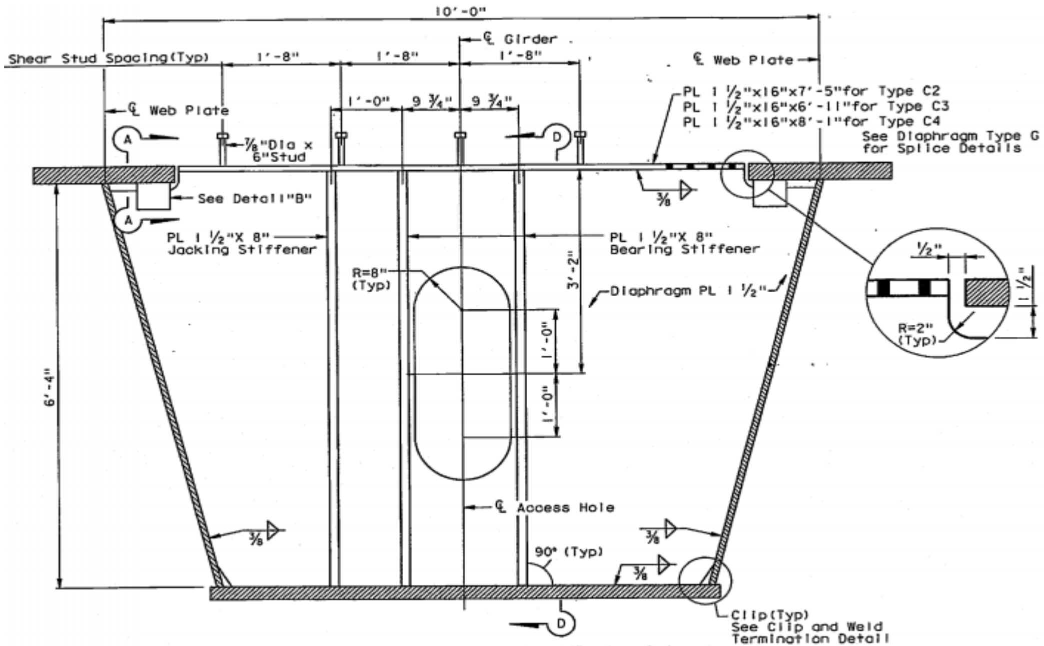

DIAPHRAGM~TYPE C2, C3 & C4

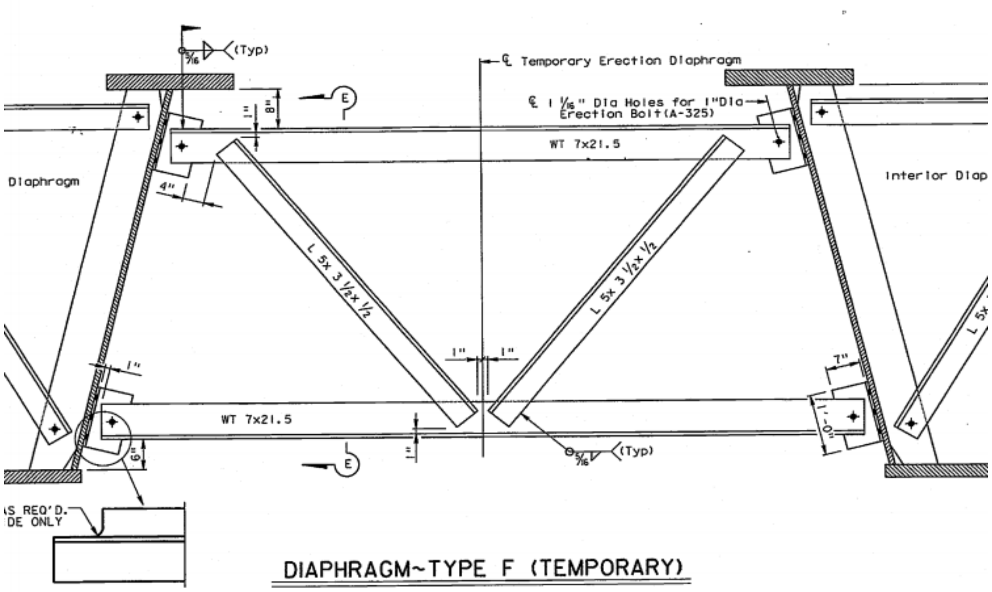

DIAPHRAGM~TYPE F (TEMPORARY)

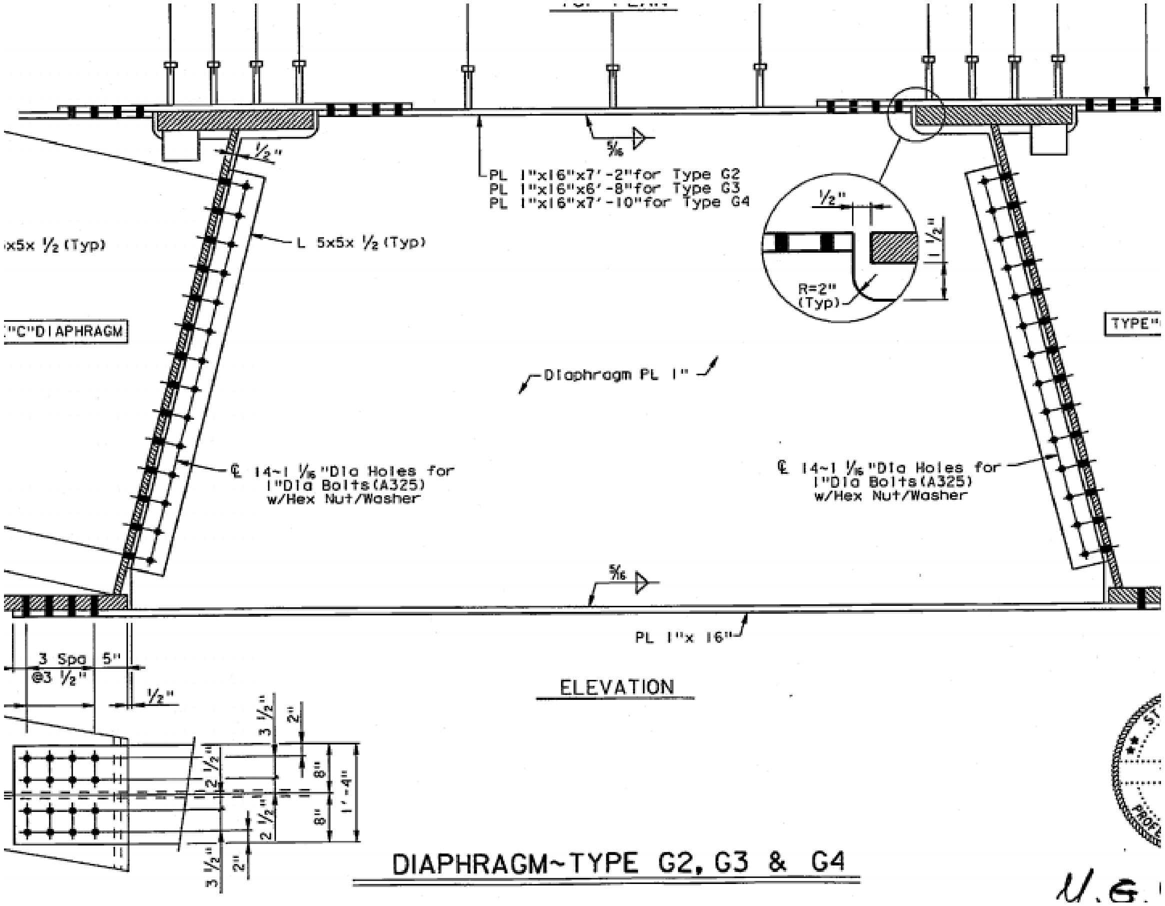

DIAPHRAGM~TYPE G2, G3 & G4

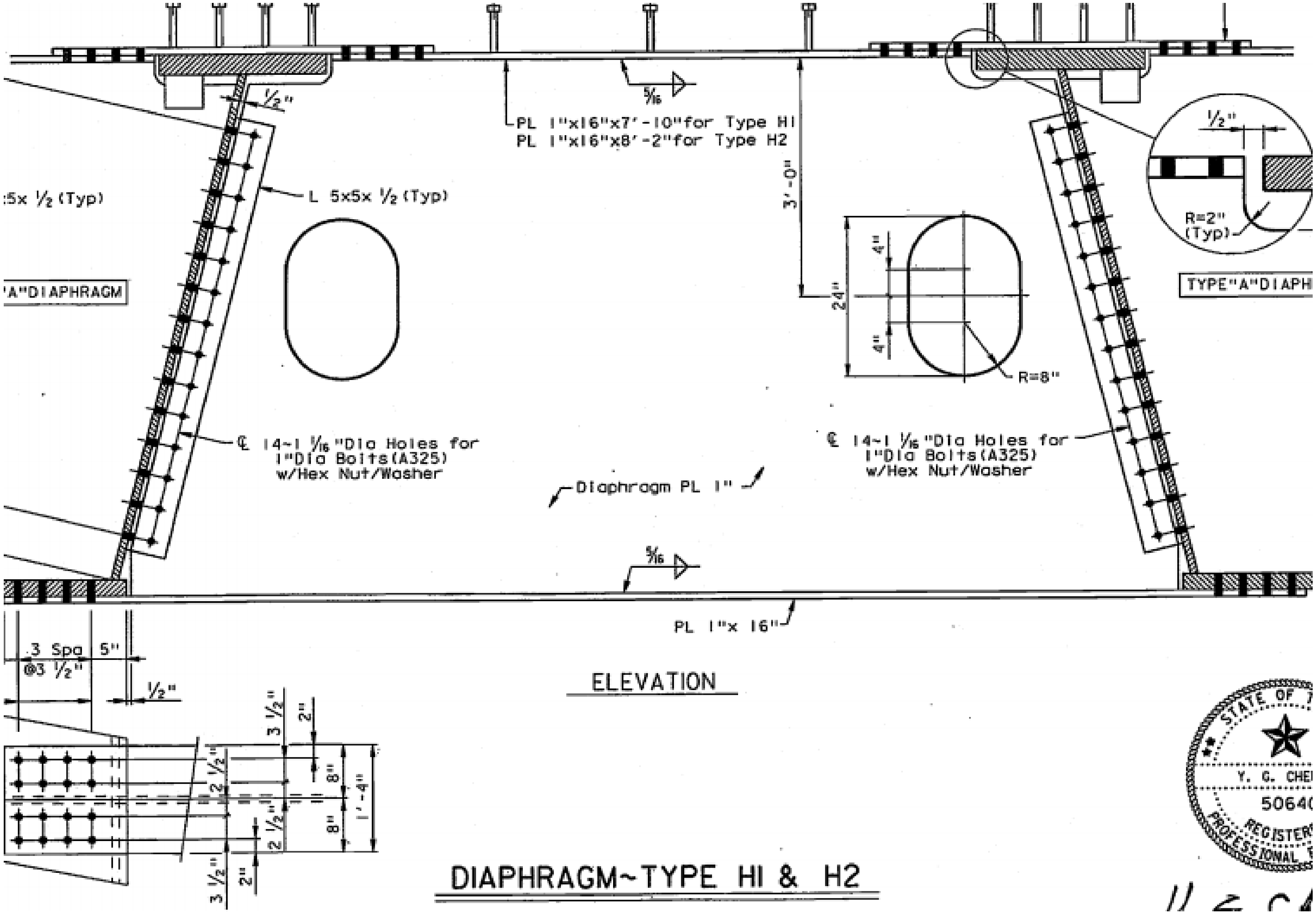

DIAPHRAGM~TYPE H1 & H2

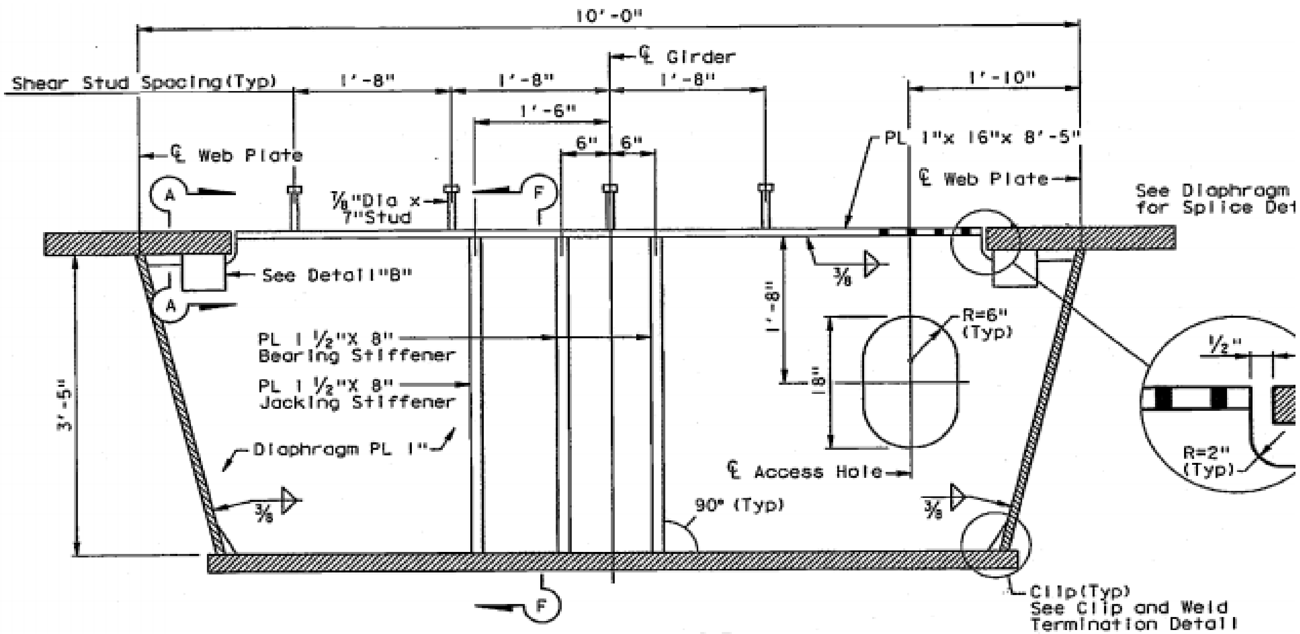

DIAPHRAGM~TYPE MI

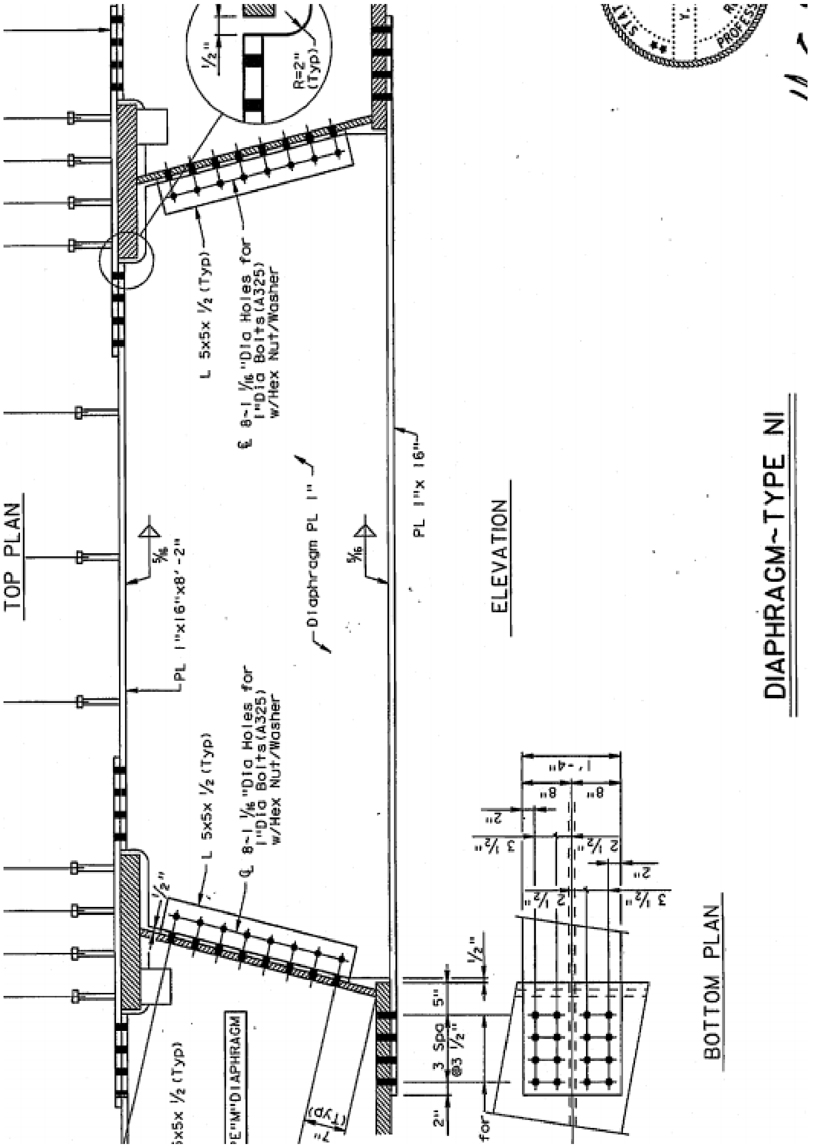
TOP PLAN
ELEVATION
BOTTOM PLAN
DIAPHRAGM~TYPE NI
PL 1"x16"x8'-2"
5/16
Diaphragm PL 1"
PL 1"x 16"
L 5x5x 1/2 (Typ)
℄ 8-1 1/16"Dia Holes for 1"Dia Bolts(A325) w/Hex Nut/Washer
R=2" (Typ)
1/2"
E"M"DIAPHRAGM
5x5x 1/2 (Typ)
3 Spa @3 1/2"
5"
2"
for
1'-4"
8"
2 1/2"
3 1/2"
2"

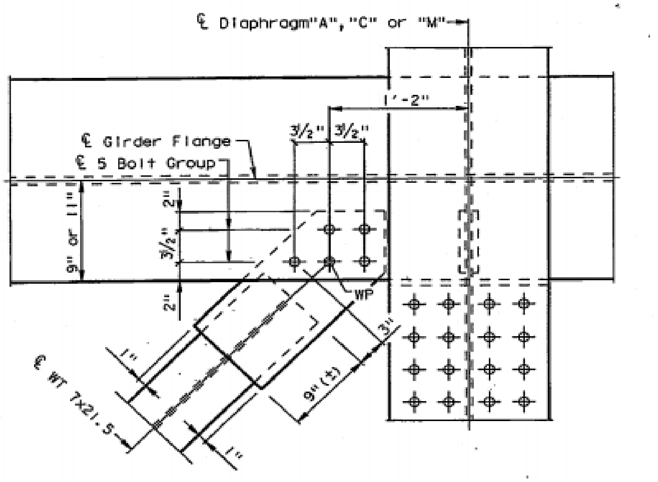

LATERAL BRACING CONNECTION DETAIL "I2"

Bridge 7: 12-102-0177-07-394

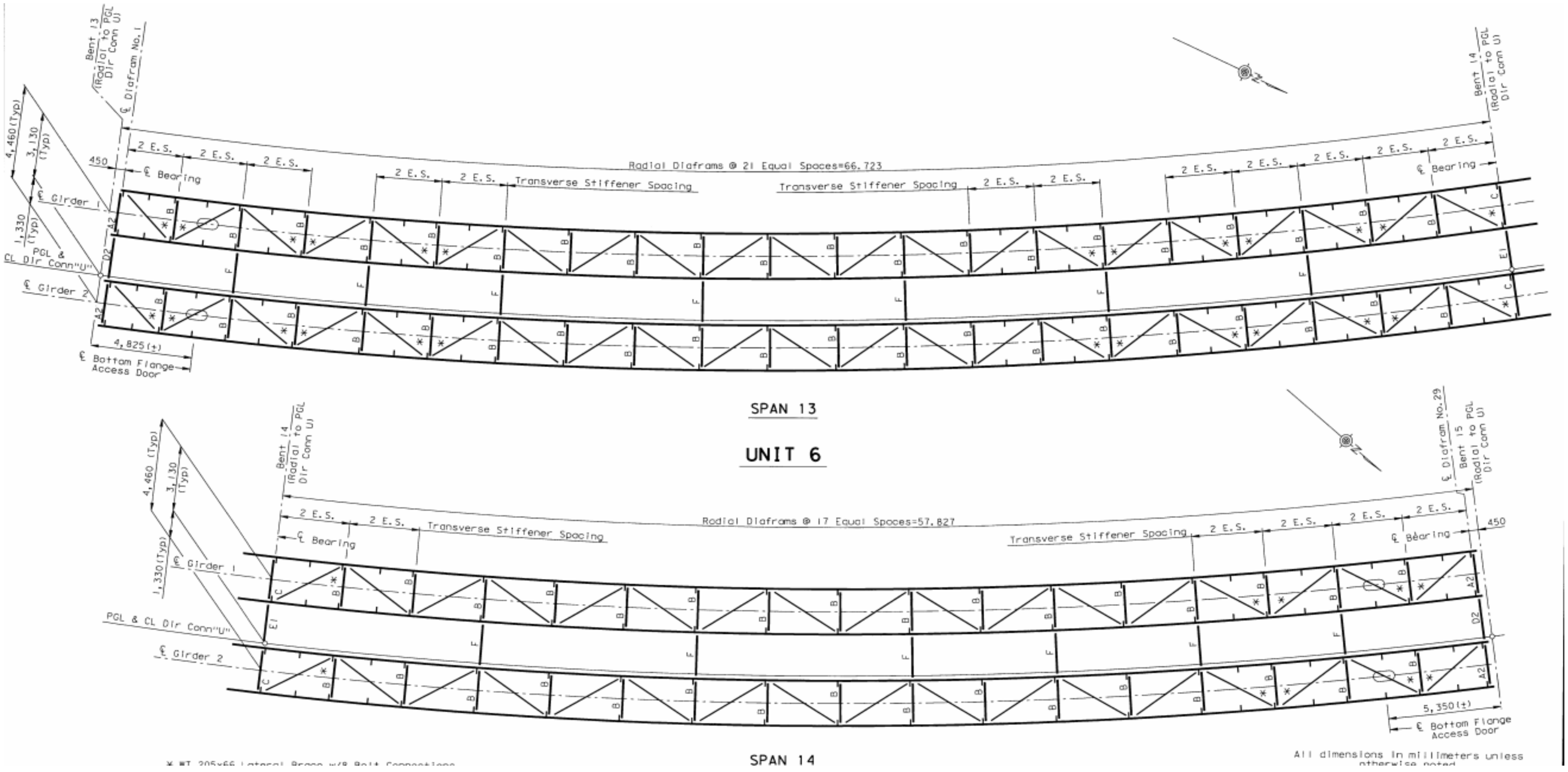

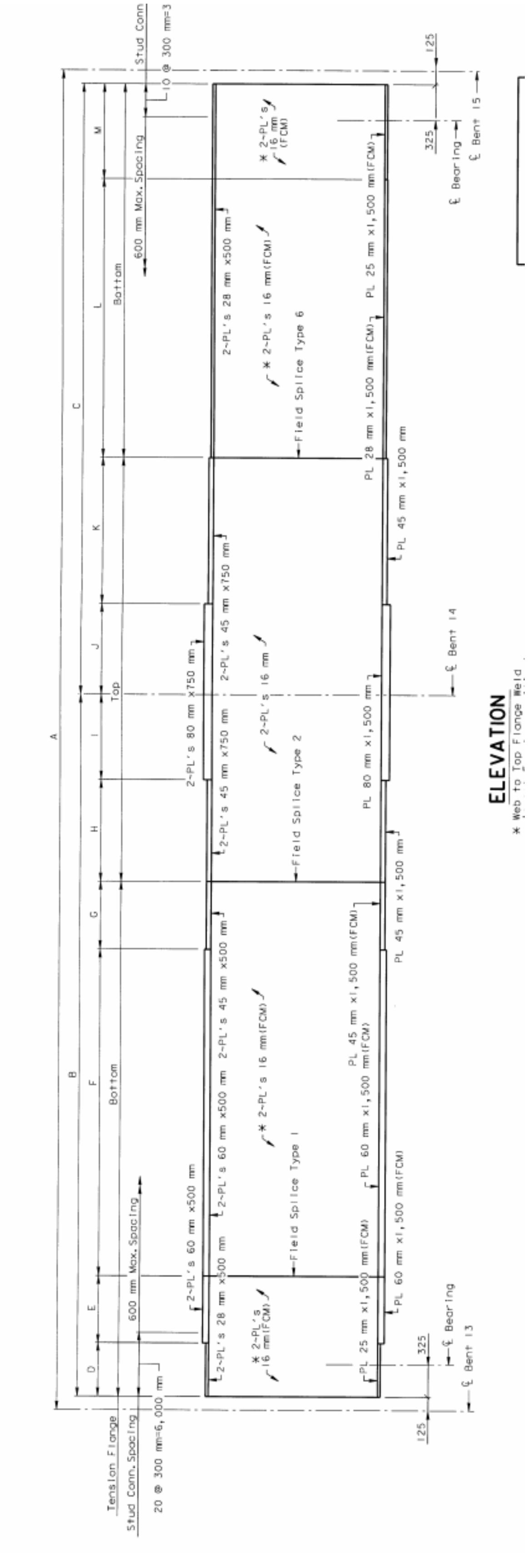

ELEVATION

* Web to Top Flange Weld

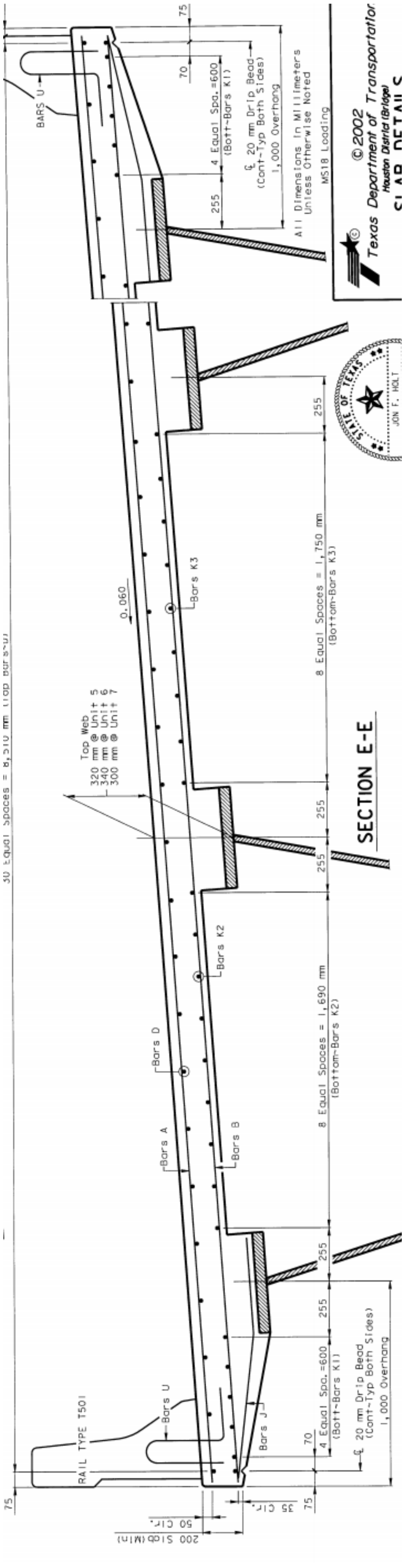
30 Equal Spaces = 8,510 mm (Top Bars-D)
BARS U
75
70
4 Equal Spa.=600 (Bott-Bars K1)
℄ 20 mm Drip Bead (Cont-Typ Both Sides)
1,000 Overhang
255
All Dimensions In Millimeters Unless Otherwise Noted
MS18 Loading
© 2002
Texas Department of Transportation
Houston District (Bridge)
SLAB DETAILS
JON F. HOLT
255
8 Equal Spaces = 1,750 mm (Bottom-Bars K3)
Bars K3
0.060
Top Web
320 mm @ Unit 5
340 mm @ Unit 6
300 mm @ Unit 7
255
255
SECTION E-E
Bars K2
8 Equal Spaces = 1,690 mm (Bottom-Bars K2)
Bars D
Bars A
Bars B
255
255
4 Equal Spa.=600 (Bott-Bars K1)
℄ 20 mm Drip Bead (Cont-Typ Both Sides)
1,000 Overhang
70
Bars J
Bars U
RAIL TYPE T501
75
75
35 Clr.
50 Clr.
200 Slab(Min)

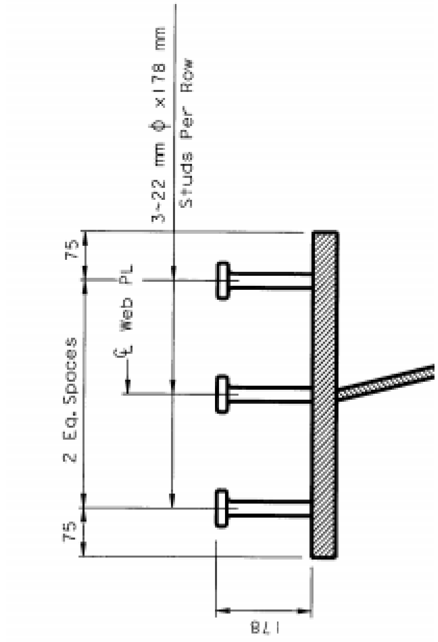
3-22 mm ⌀ x178 mm
Studs Per Row
75
℄ Web PL
2 Eq. Spaces
75
178

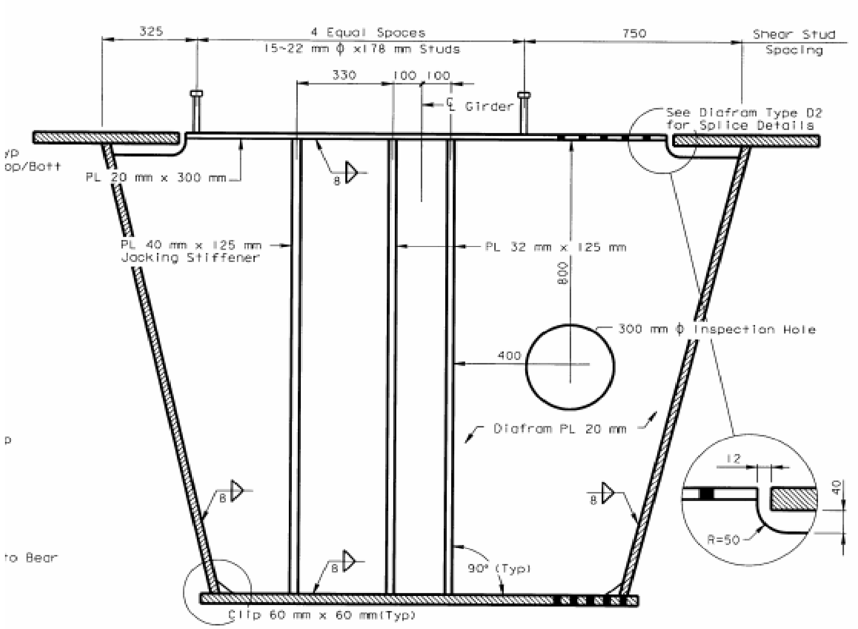

DIAFRAM ~ TYPE A2

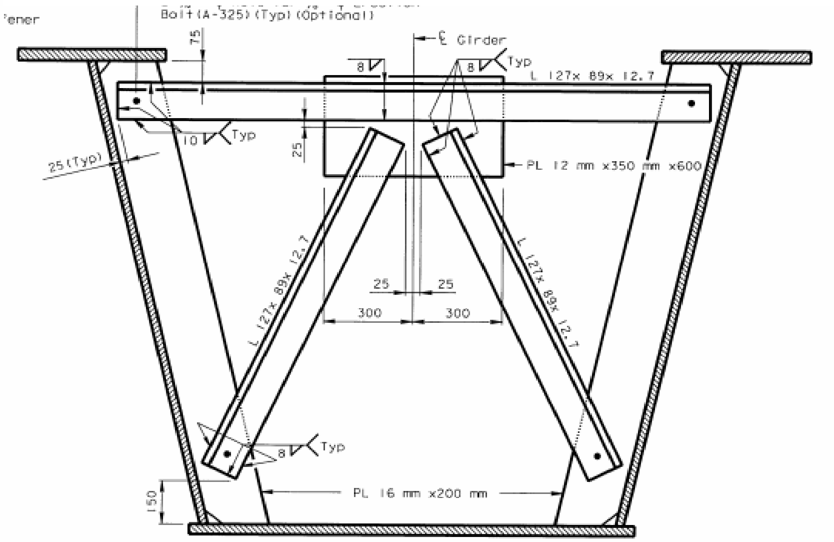

DIAFRAM ~ TYPE B

Note: All Angles Placed with Long Leg Vertical(Typ)

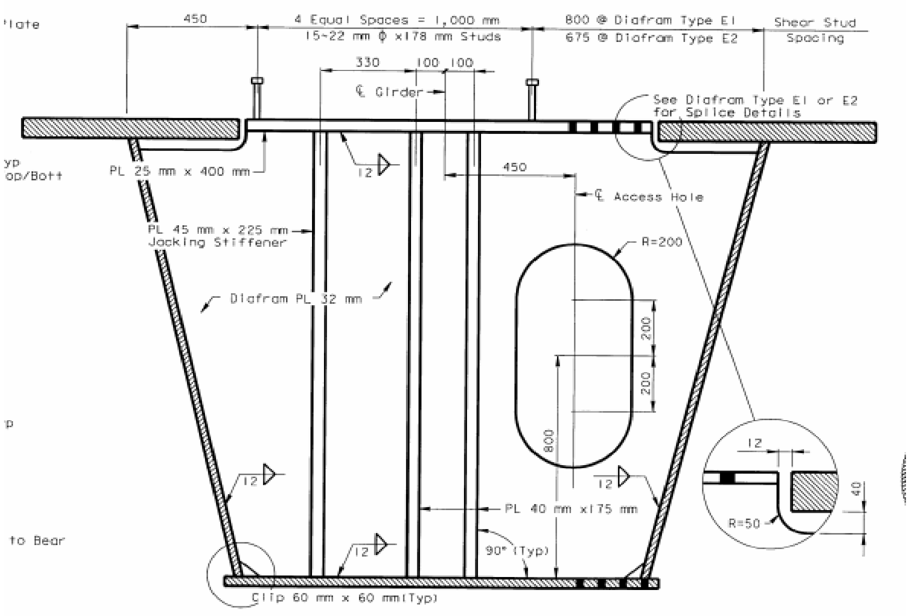

DIAFRAM ~ TYPE C

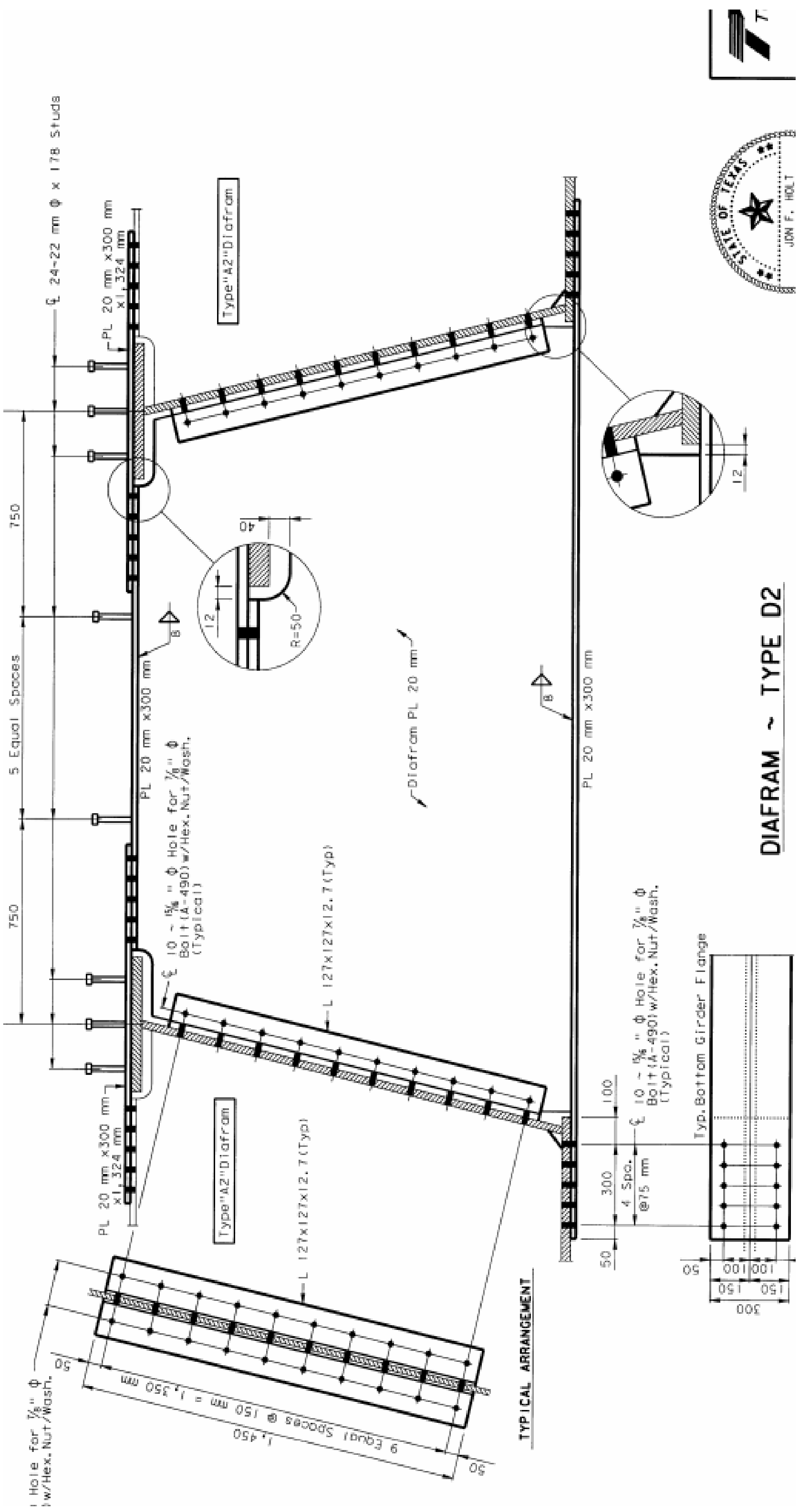

DIAFRAM ~ TYPE D2

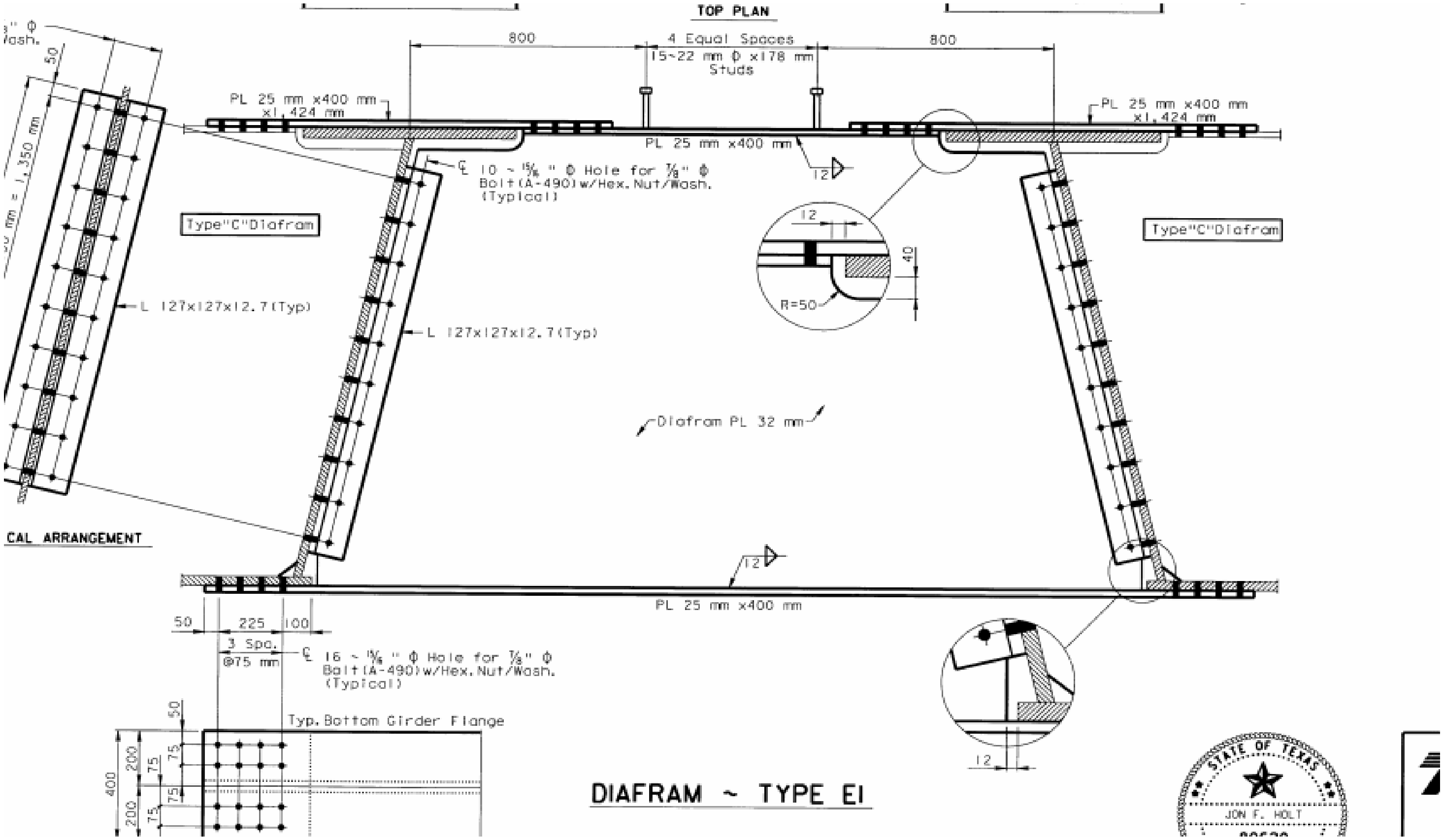

DIAFRAM ~ TYPE EI

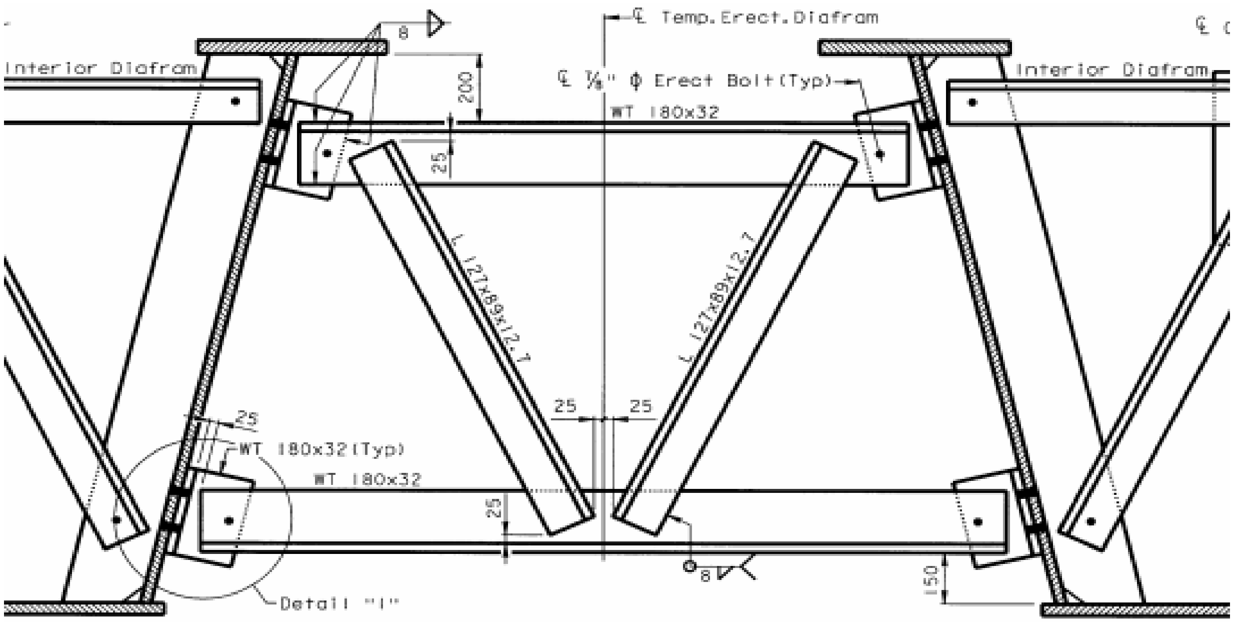

DIAFRAM ~ TYPE F (TEMPORARY)

GENERAL NOTES:

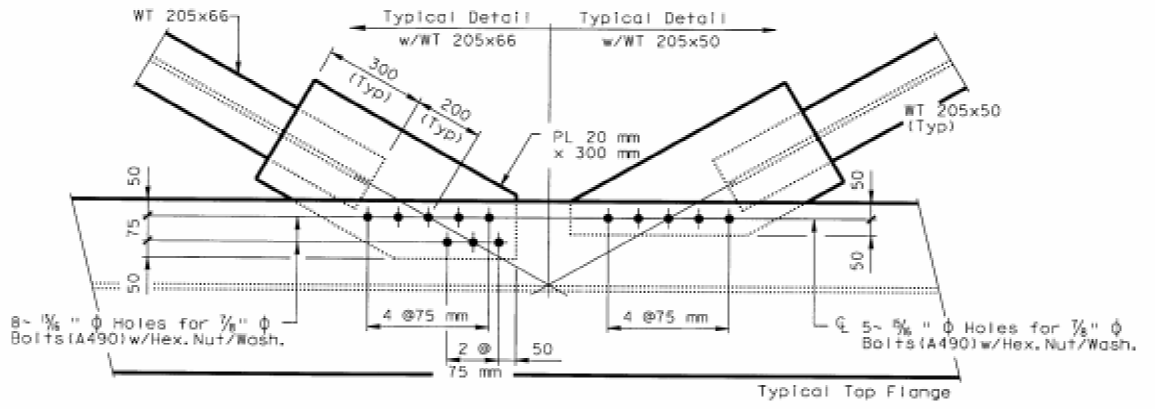

PLAN

Bridge 8: 12-102-0271-06-661

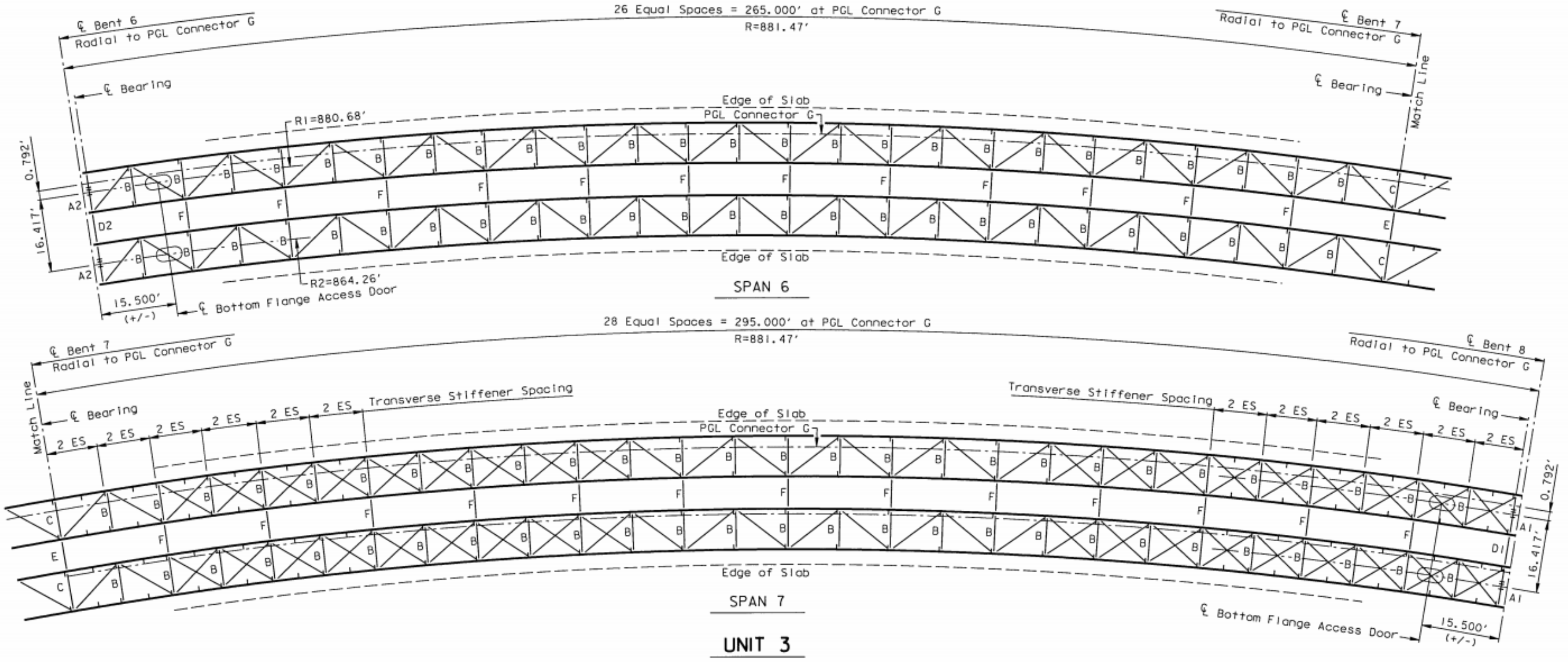

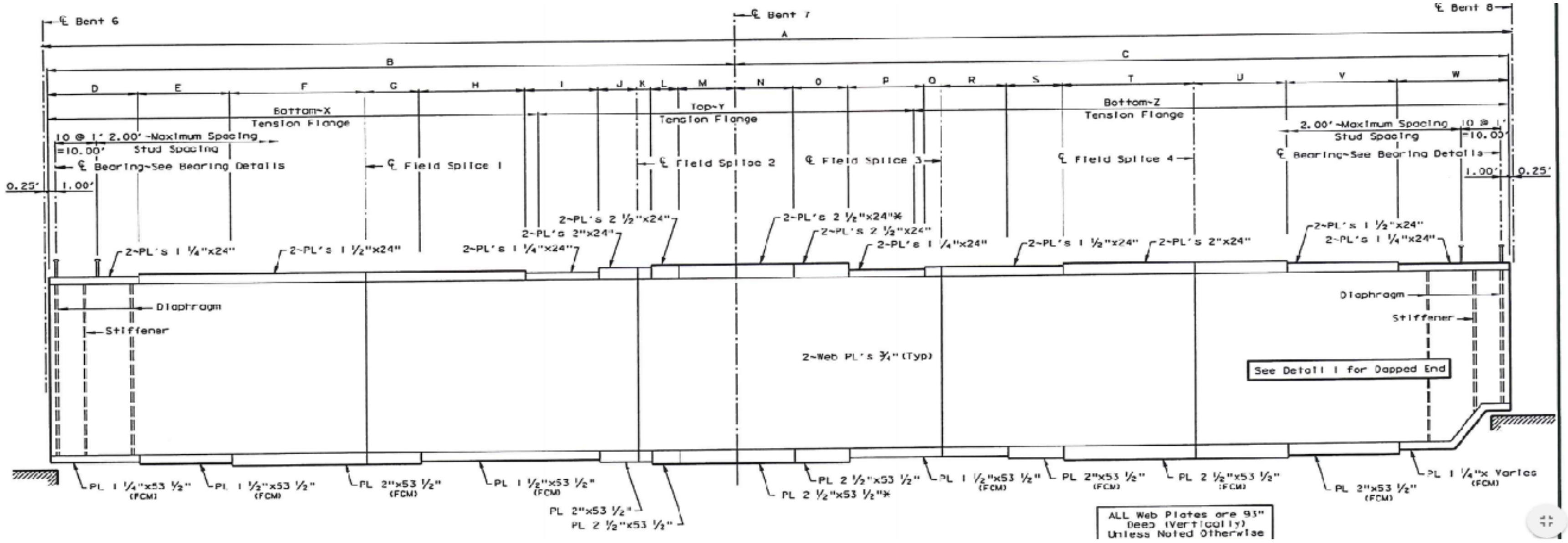
℄ Bent 6
℄ Bent 7
℄ Bent 8
A
B
C
D
E
F
G
H
I
J
K
L
M
N
O
P
Q
R
S
T
U
V
W
Bottom~X
Tension Flange
Top~Y
Tension Flange
Bottom~Z
Tension Flange
10 @ 1' 2.00'~Maximum Spacing
=10.00' Stud Spacing
℄ Bearing~See Bearing Details
0.25'
1.00'
℄ Field Splice 1
℄ Field Splice 2
℄ Field Splice 3
℄ Field Splice 4
2.00'~Maximum Spacing 10 @ 1'
Stud Spacing =10.00
℄ Bearing~See Bearing Details
1.00'
0.25'
2~PL's 1 ¼"x24"
2~PL's 1 ½"x24"
2~PL's 1 ¼"x24"
2~PL's 2"x24"
2~PL's 2 ½"x24"
2~PL's 2 ½"x24"*
2~PL's 2 ½"x24"
2~PL's 1 ¼"x24"
2~PL's 1 ½"x24"
2~PL's 2"x24"
2~PL's 1 ½"x24"
2~PL's 1 ¼"x24"
Diaphragm
Stiffener
2~Web PL's ¾" (Typ)
Diaphragm
Stiffener
See Detail 1 for Dapped End
PL 1 ¼"x53 ½" (FCM)
PL 1 ½"x53 ½" (FCM)
PL 2"x53 ½" (FCM)
PL 1 ½"x53 ½" (FCM)
PL 2"x53 ½"
PL 2 ½"x53 ½"
PL 2 ½"x53 ½"
PL 2 ½"x53 ½"*
PL 1 ½"x53 ½" (FCM)
PL 2"x53 ½" (FCM)
PL 2 ½"x53 ½" (FCM)
PL 2"x53 ½" (FCM)
PL 1 ¼"x Varies (FCM)
ALL Web Plates are 93" Deep (Vertically) Unless Noted Otherwise

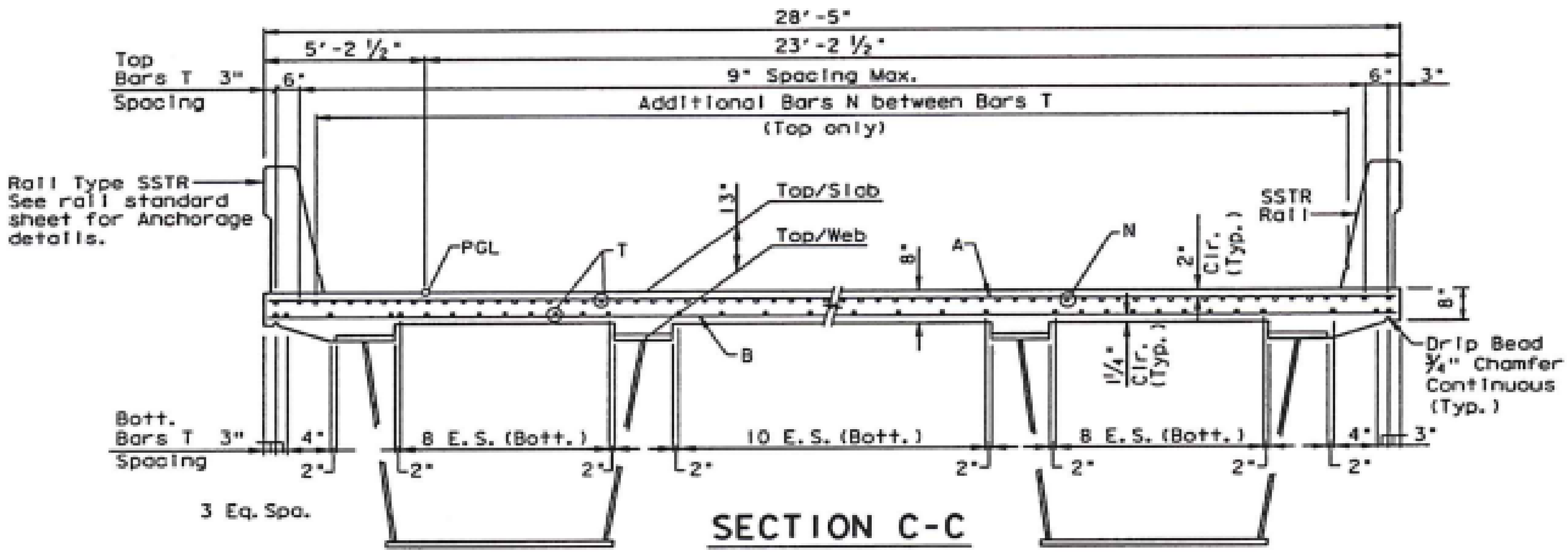

SECTION C-C

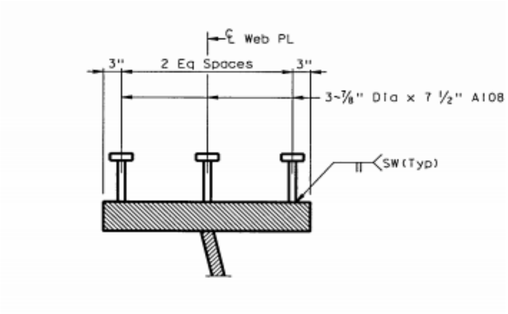

SHEAR CONNECTOR DETAIL

NOTE:

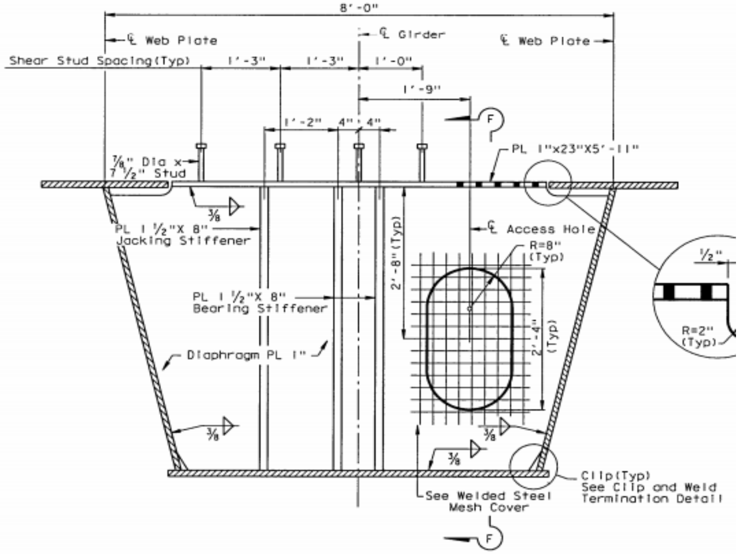

DIAPHRAGM~TYPE A1

Girder 1 Shown, Girder 2 Similar w/Opposite Hand Access Hole

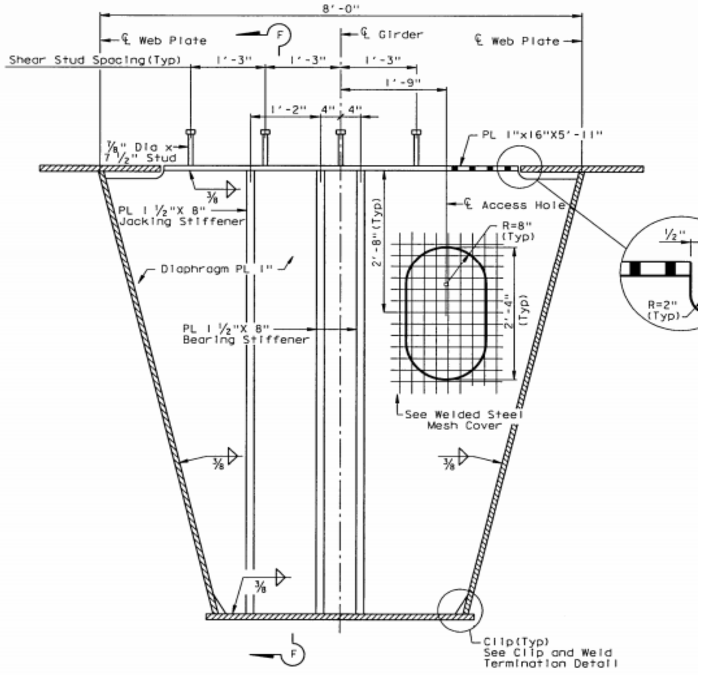

DIAPHRAGM~TYPE A2

Girder 1 Shown, Girder 2 Similar w/Opposite Hand Access Hole

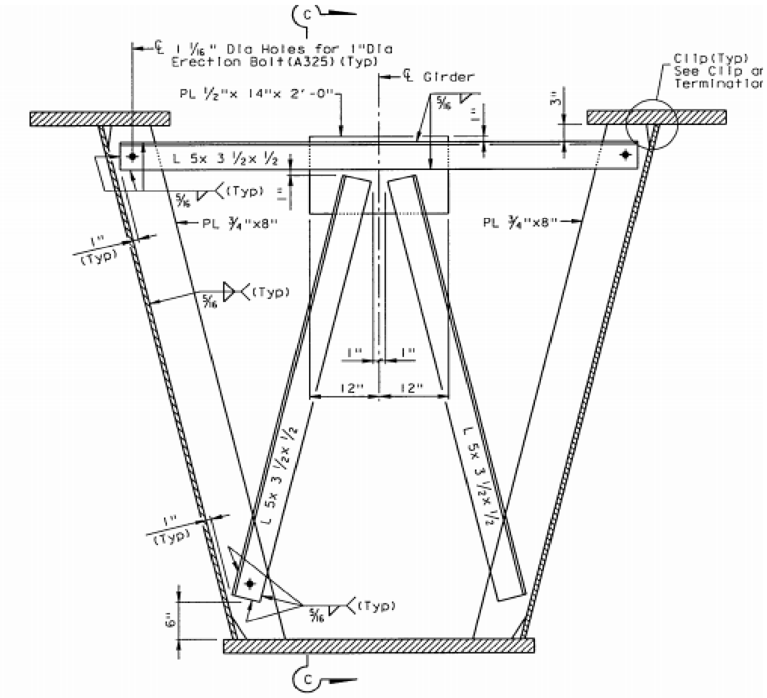

DIAPHRAGM~TYPE B

Note: All Angles Placed with Long Leg Vertical

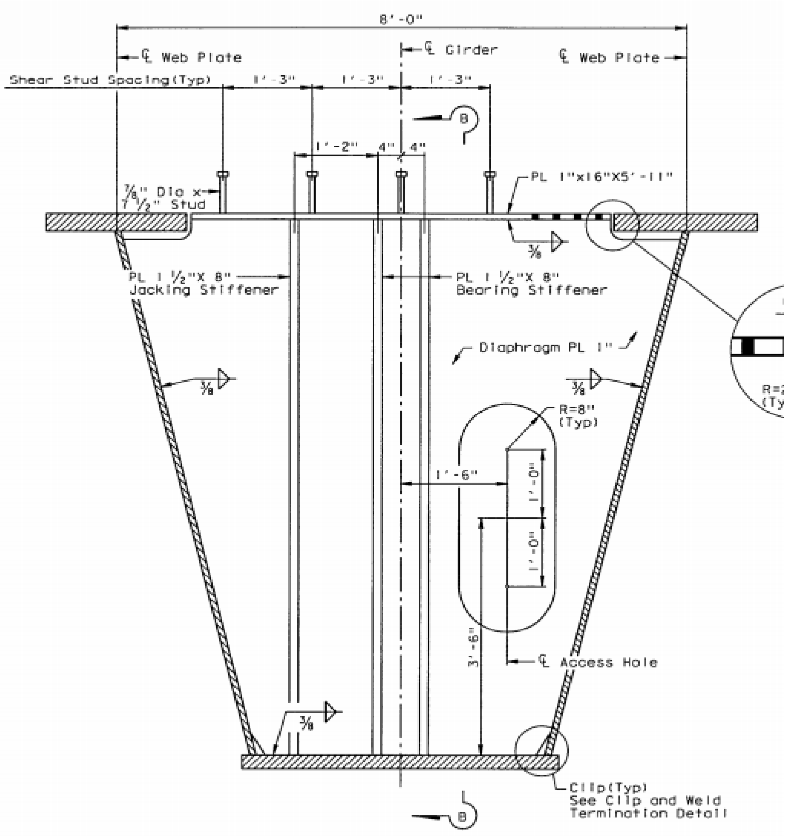

DIAPHRAGM~TYPE C

Girder 1 Shown, Girder 2 Similar w/Opposite Hand Access Hole

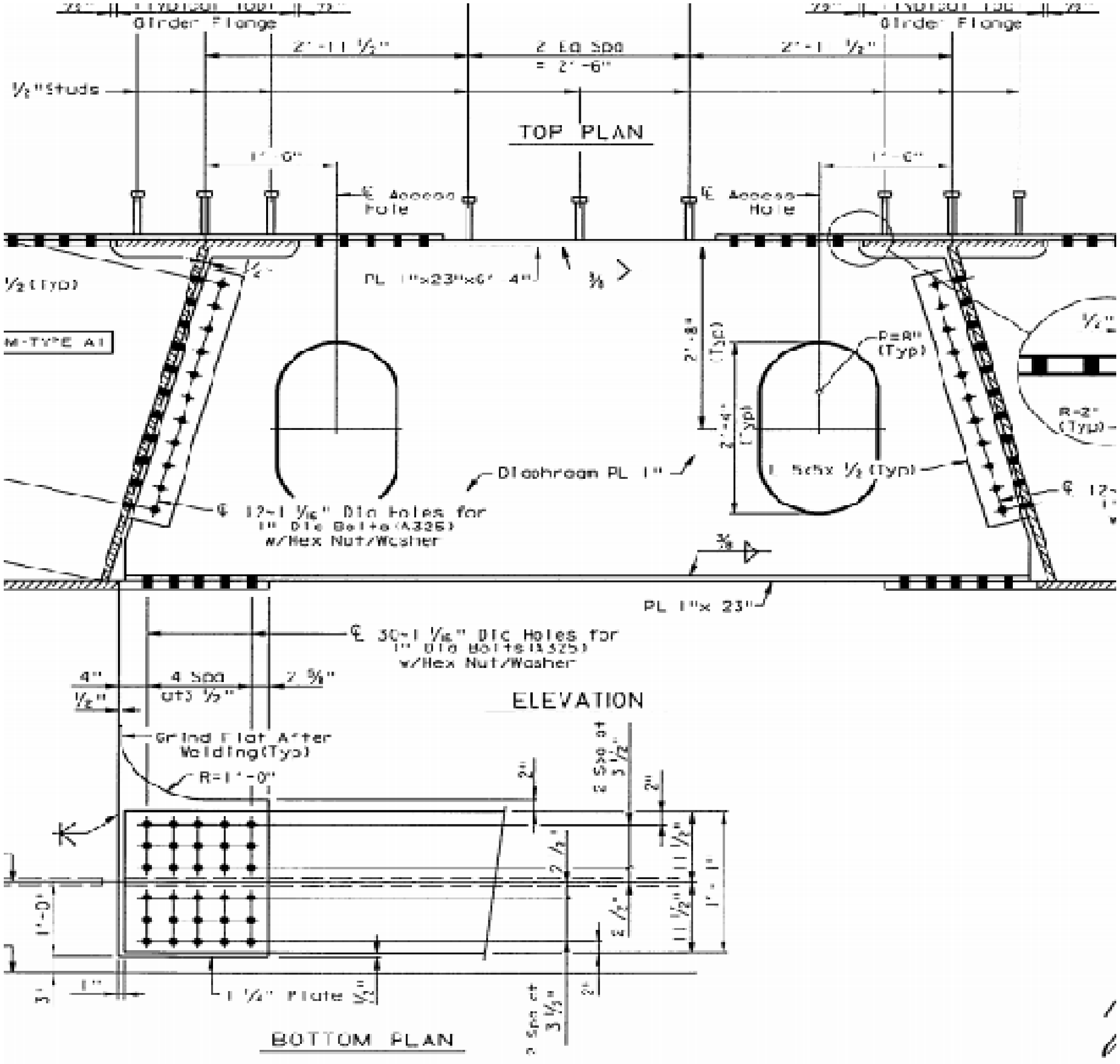

DIAPHRAGM-TYPE DI

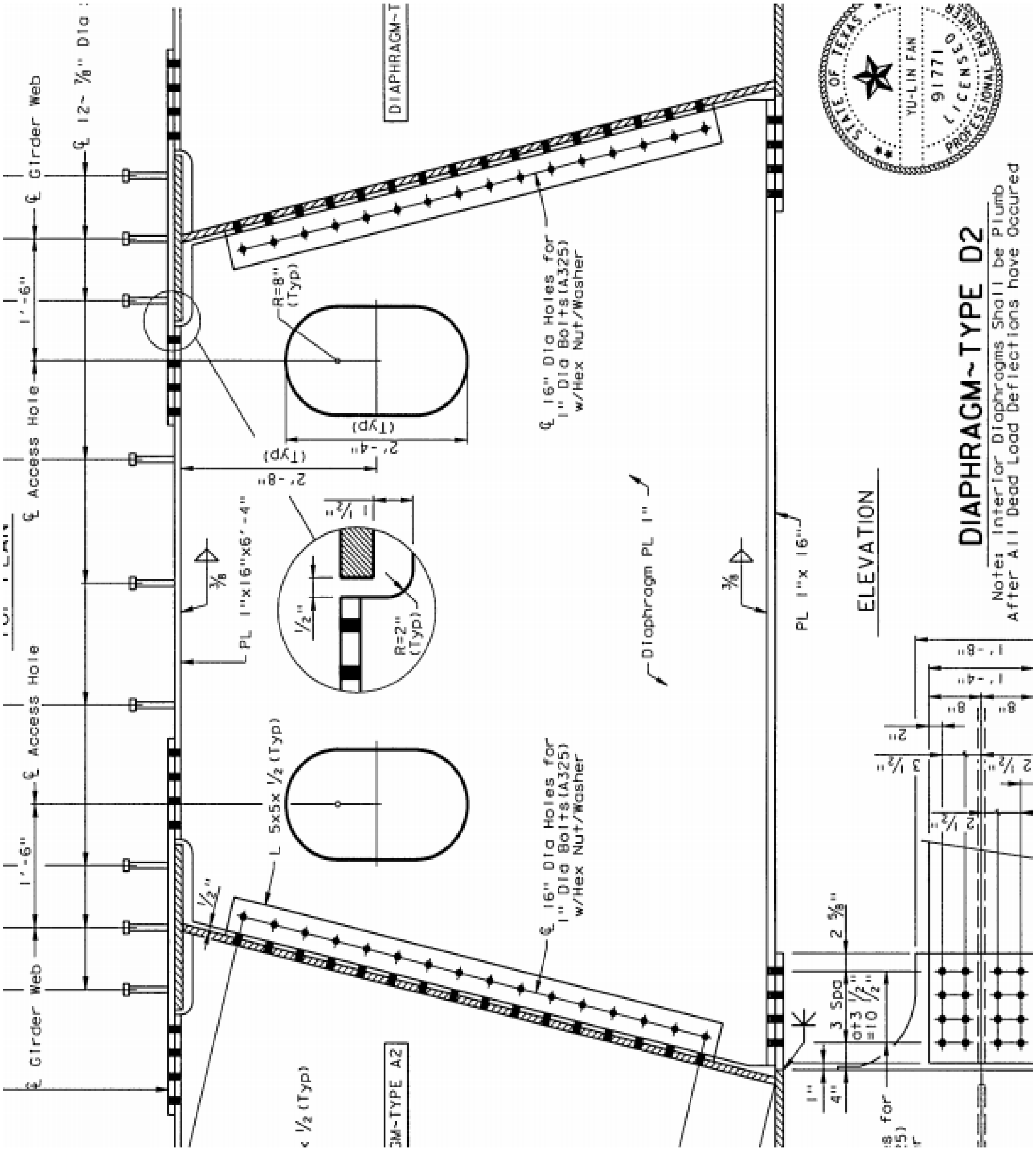DIAPHRAGM~TYPE D2
Note: Interior Diaphragms Shall be Plumb After All Dead Load Deflections have Occured
ELEVATION
℄ Girder Web
℄ Girder Web
℄ 12~ 7/8" Dia
℄ Access Hole
℄ Access Hole
1'-6"
1'-6"
2'-8" (Typ)
2'-4" (Typ)
R=8" (Typ)
R=2" (Typ)
1 1/2"
1/2"
1/2"
3/8
3/8
PL 1"x16"x6'-4"
PL 1"x 16"
Diaphragm PL 1"
L 5x5x 1/2 (Typ)
℄ 16" Dia Holes for 1" Dia Bolts (A325) w/Hex Nut/Washer
℄ 16" Dia Holes for 1" Dia Bolts (A325) w/Hex Nut/Washer
DIAPHRAGM-TYPE A2
2 5/8"
3 Spa at 3 1/2" =10 1/2"
1"
4"
1'-8"
1'-4"
8"
8"
2"
3 1/2"
2 1/2"
2 1/2"
2 1/2"
YU-LIN FAN
91771

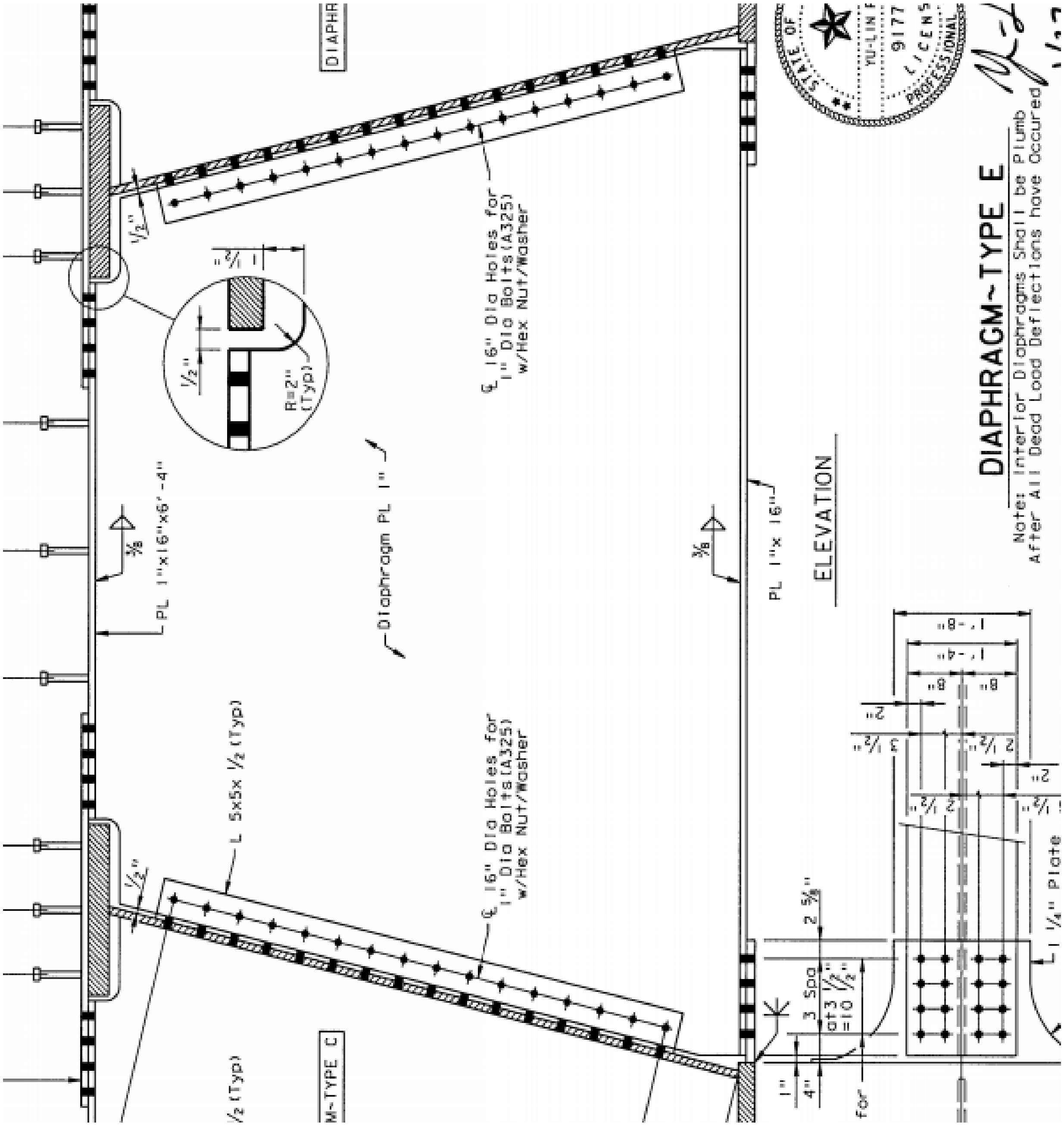
DIAPHR
M-TYPE C
DIAPHRAGM~TYPE E
Note: Interior Diaphragms Shall be Plumb After All Dead Load Deflections have Occured
ELEVATION
PL 1"x16"x6'-4"
Diaphragm PL 1"
L 5x5x 1/2 (Typ)
1/2 (Typ)
℄ 16" Dia Holes for 1" Dia Bolts(A325) w/Hex Nut/Washer
℄ 16" Dia Holes for 1" Dia Bolts(A325) w/Hex Nut/Washer
R=2" (Typ)
1/2"
1/2"
1/2"
1 1/2"
3/8
3/8
PL 1"x 16"
1 1/4" Plate
3 Spa at 3 1/2" =10 1/2"
2 5/8"
1"
4"
for
1'-8"
1'-4"
8"
8"
2"
2"
2 1/2"
2 1/2"
1 1/2"
1 1/2"
YU-LIN
9177
LICENS
PROFESSIONAL

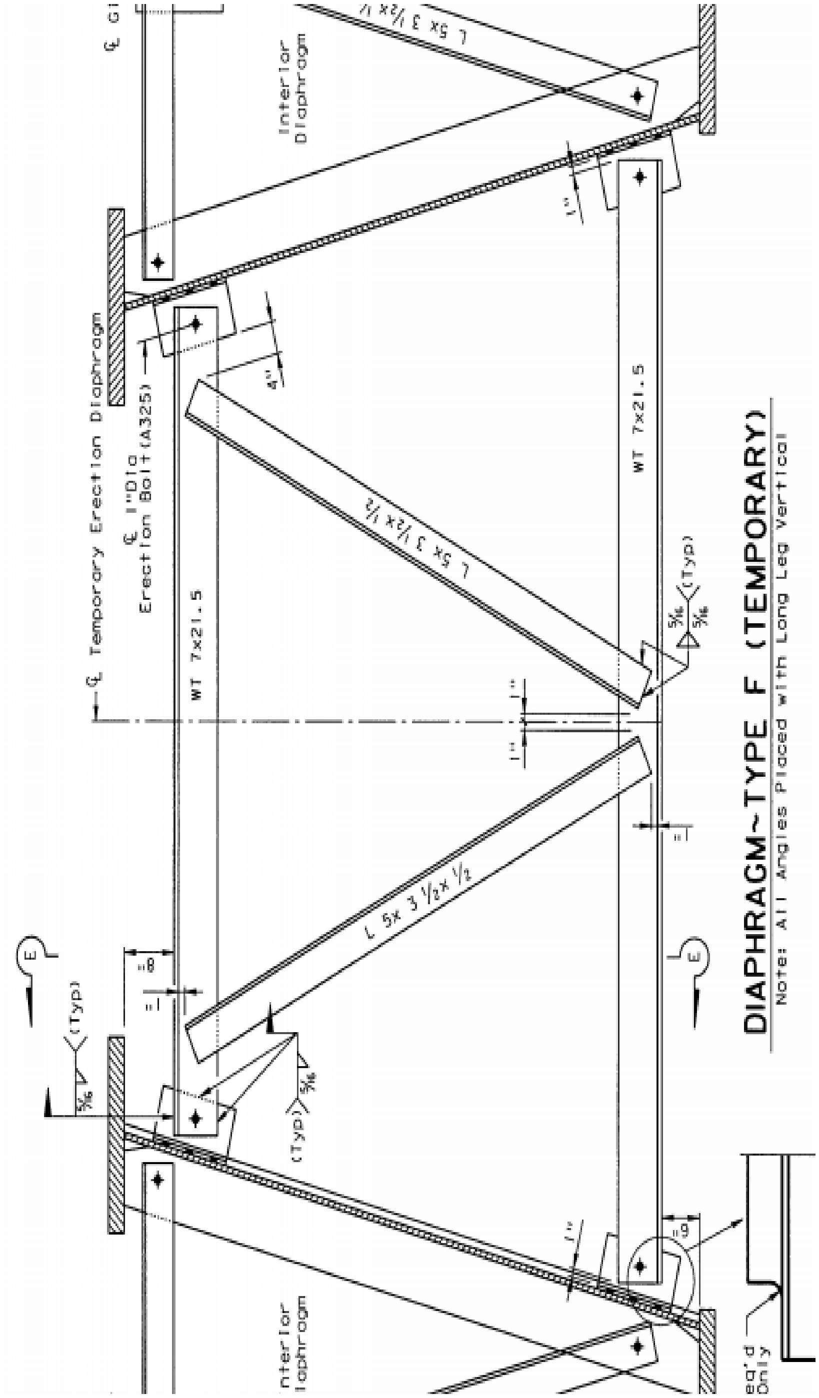

DIAPHRAGM~TYPE F (TEMPORARY)

Note: All Angles Placed with Long Leg Vertical

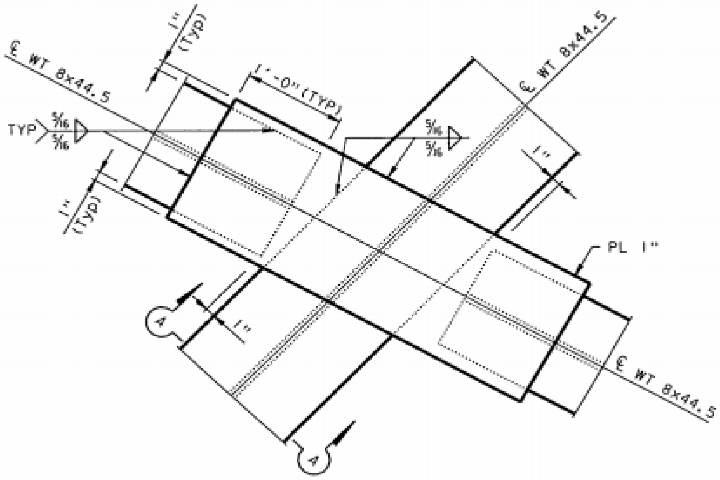

LATERAL BRACING DETAIL "3"

((FOR X-BRACING)

Bridge 9: 12-102-0177-07-394

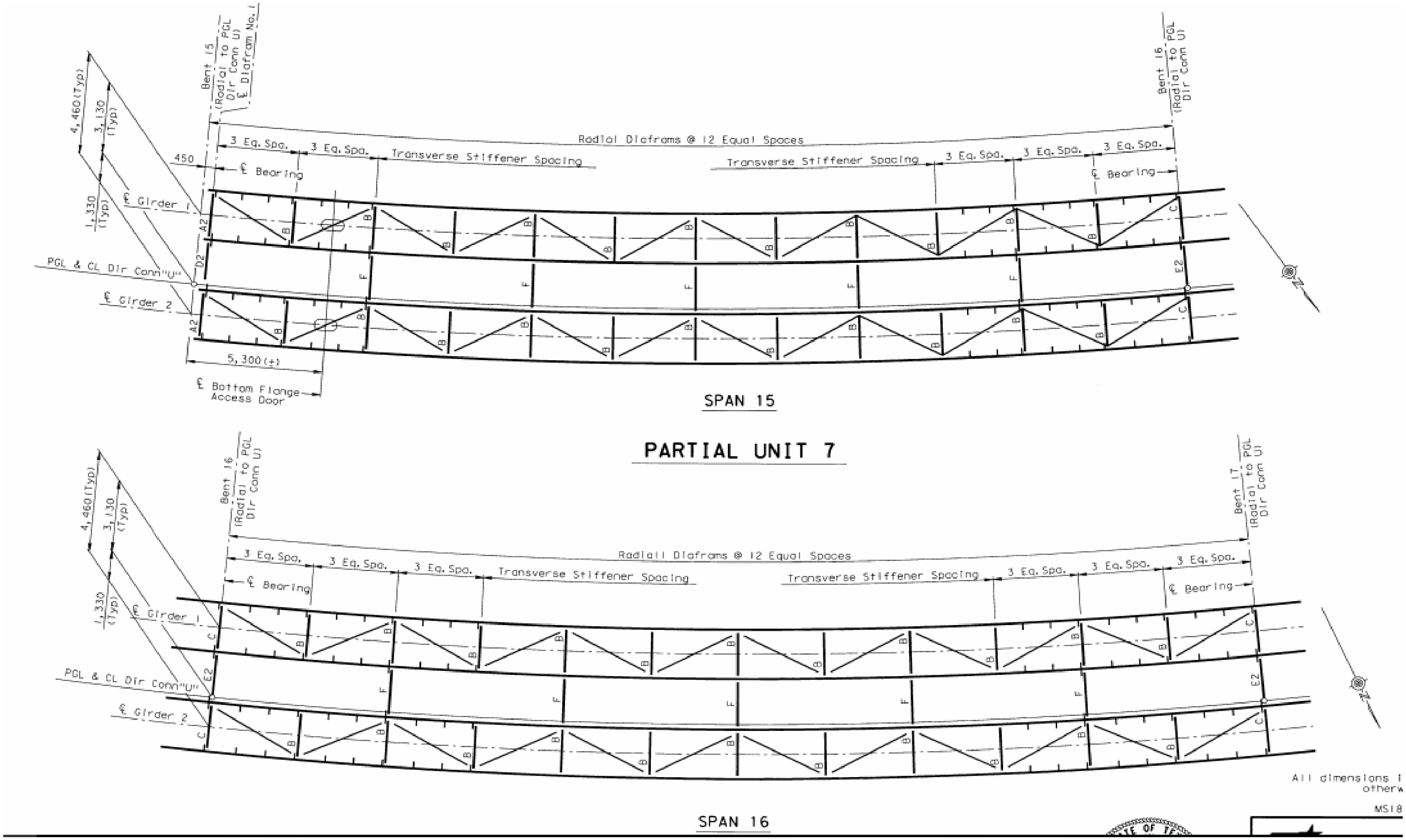

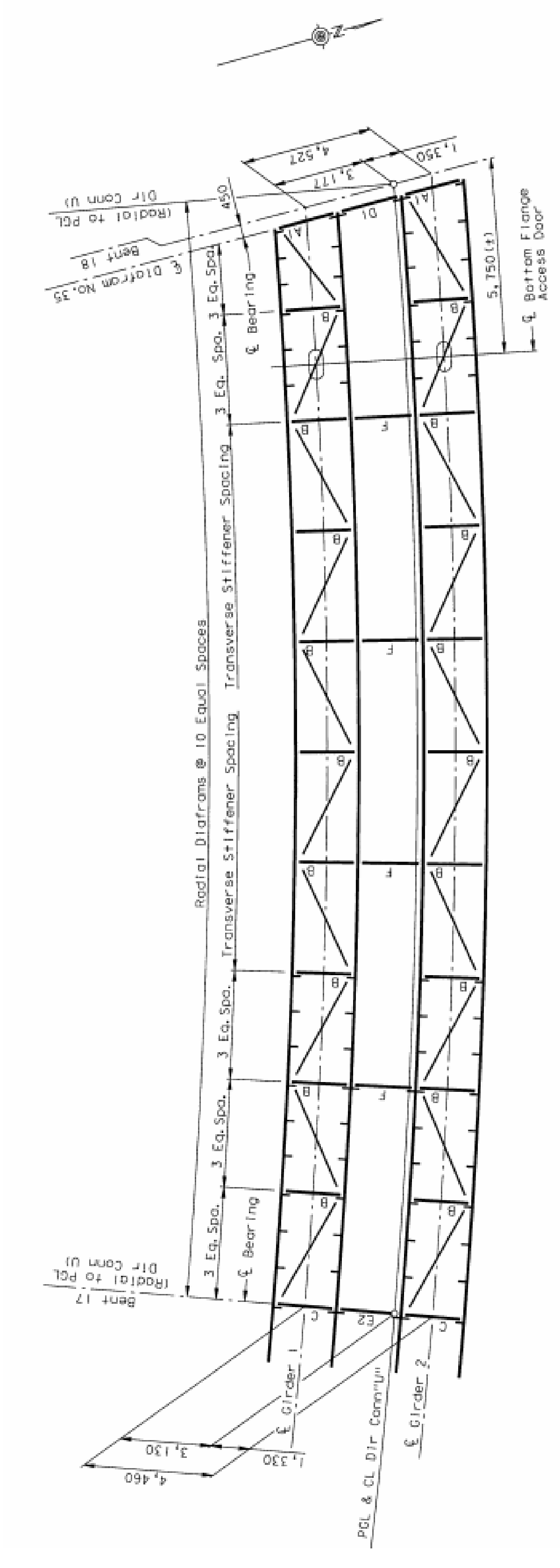
N
4,527
3,177
1,350
450
Bent 18
(Radial to PGL Dir Conn U)
℄ Diafram No. 35
3 Eq. Spa.
℄ Bearing
3 Eq. Spa.
Transverse Stiffener Spacing
Radial Diaframs @ 10 Equal Spaces
Transverse Stiffener Spacing
3 Eq. Spa.
3 Eq. Spa.
3 Eq. Spa.
℄ Bearing
Bent 17
(Radial to PGL Dir Conn U)
5,750(±)
℄ Bottom Flange Access Door
A
B
F
10
C
E2
℄ Girder 1
PGL & CL Dir Conn "U"
℄ Girder 2
3,130
1,330
4,460

SPAN 17

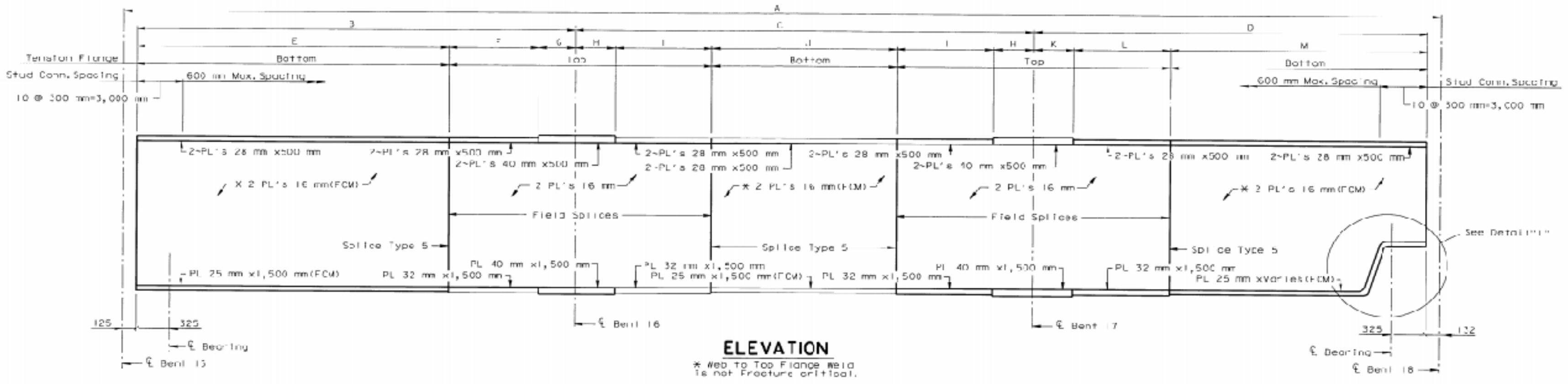

ELEVATION

* Web to Top Flange Weld
is not Fracture critical.

All Web Plates
are 1,500 mm Deep
(Vertically)

TABLE OF VARIABLE GIRDER DIMENSIONS(METERS)

GIRDER	A	B	C	D	E	F	G	H	I	J	K	L	M
1	124.752	41.833	45.549	37.113	29.819	7.917	4.097	4.396	8.516	9.725	4.379	8.481	24.253
2	127.955	42.648	46.434	38.616	30.431	8.053	4.164	4.469	8.663	20.170	4.452	8.628	25.536

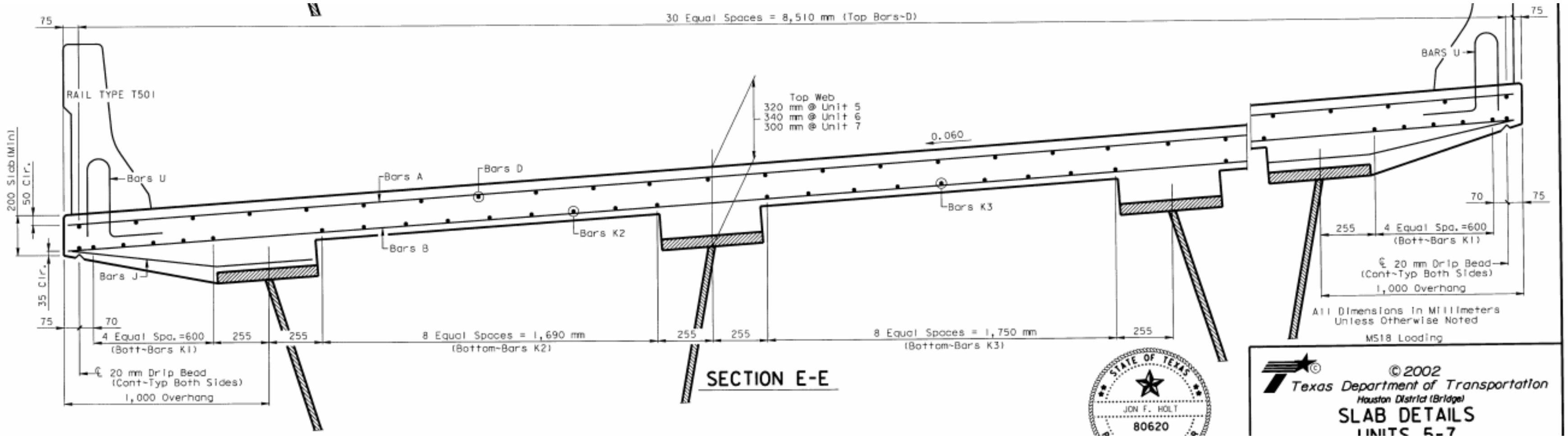
30 Equal Spaces = 8,510 mm (Top Bars-D)
75
75
RAIL TYPE T501
BARS U
Bars U
Top Web
320 mm @ Unit 5
340 mm @ Unit 6
300 mm @ Unit 7
0.060
Bars A
Bars D
Bars B
Bars K2
Bars K3
Bars J
200 Slab(Min)
50 Clr.
35 Clr.
75
70
4 Equal Spa.=600
(Bott-Bars K1)
255
255
8 Equal Spaces = 1,690 mm
(Bottom-Bars K2)
255
255
8 Equal Spaces = 1,750 mm
(Bottom-Bars K3)
255
℄ 20 mm Drip Bead
(Cont-Typ Both Sides)
1,000 Overhang
70
75
255
4 Equal Spa.=600
(Bott-Bars K1)
℄ 20 mm Drip Bead
(Cont-Typ Both Sides)
1,000 Overhang
All Dimensions In Millimeters
Unless Otherwise Noted
MS18 Loading
SECTION E-E
JON F. HOLT
80620
© 2002
Texas Department of Transportation
Houston District (Bridge)
SLAB DETAILS

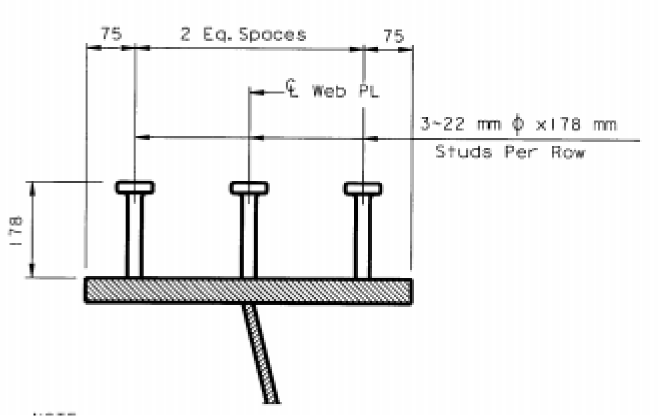
75
2 Eq. Spaces
75
℄ Web PL
3-22 mm ϕ x178 mm
Studs Per Row
178

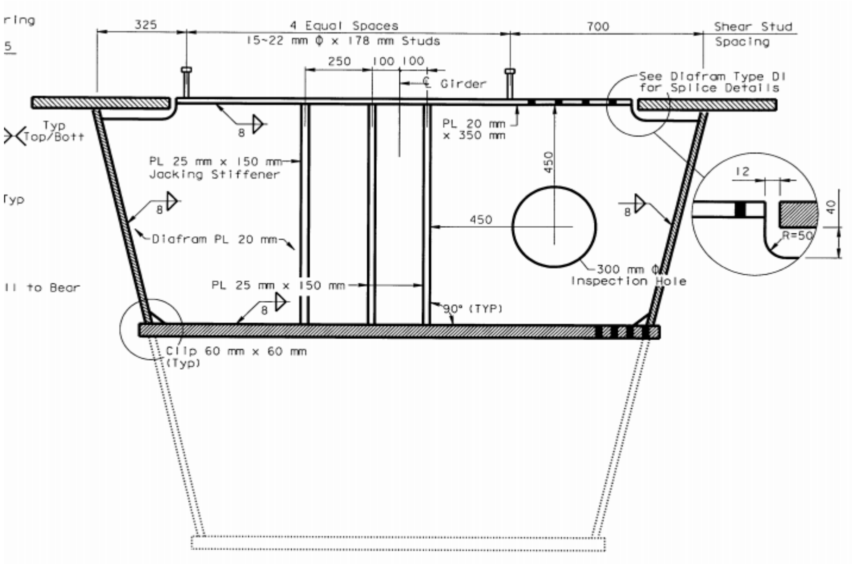

DIAFRAM ~ TYPE A1

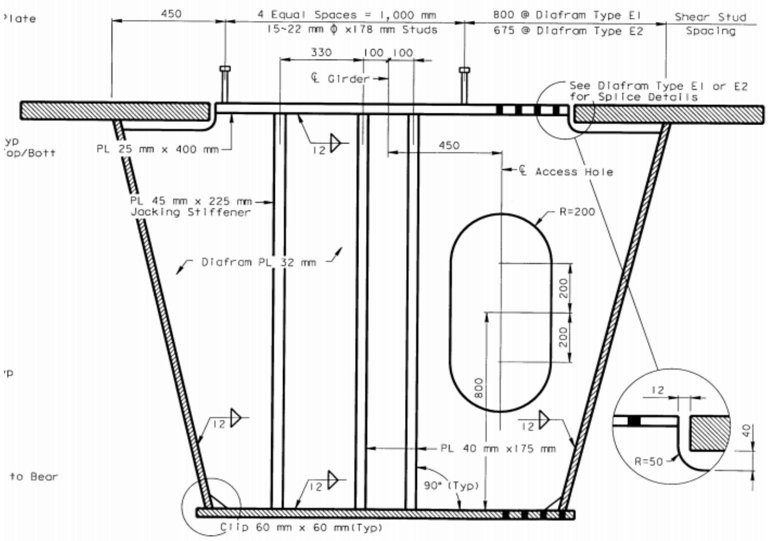

DIAFRAM ~ TYPE C

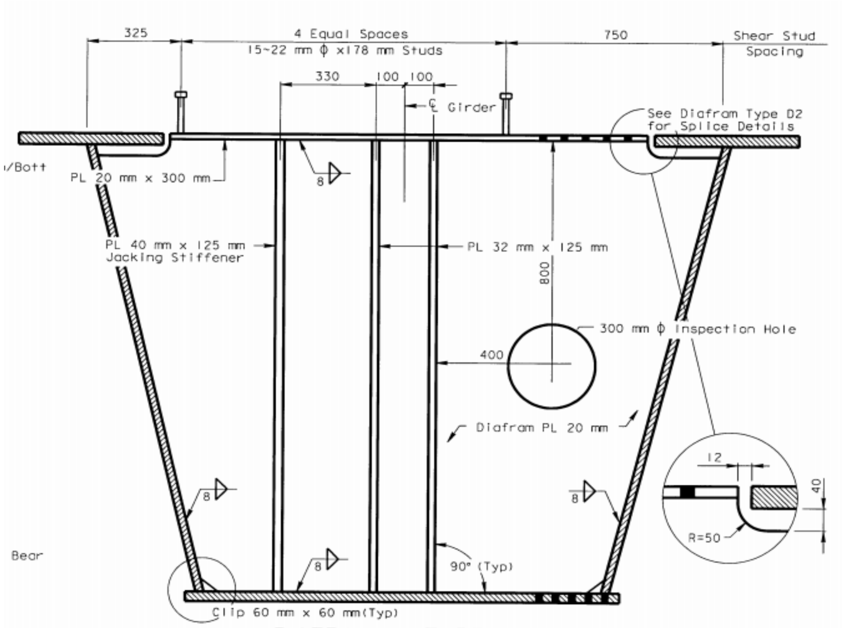

DIAFRAM ~ TYPE A2

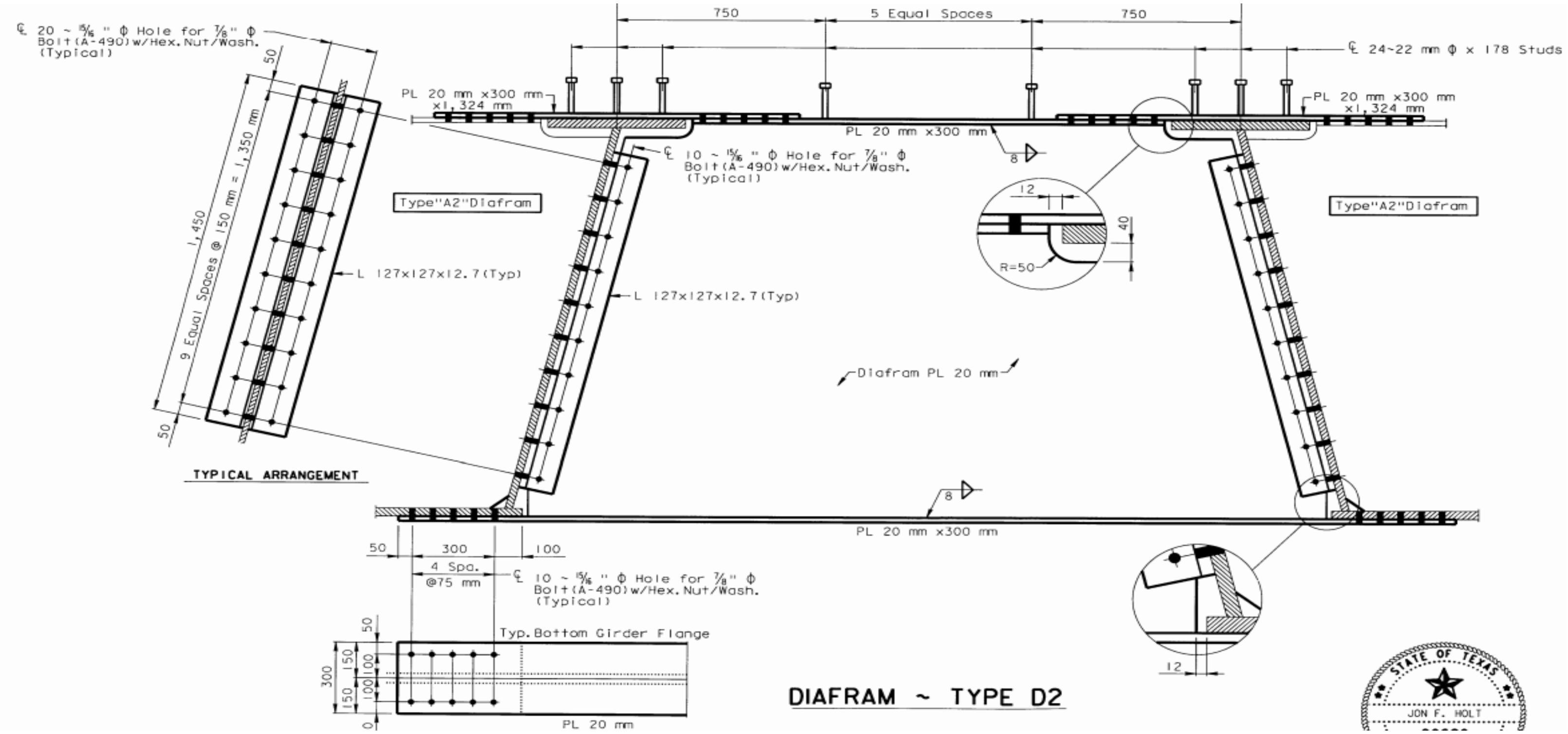

DIAFRAM ~ TYPE D2

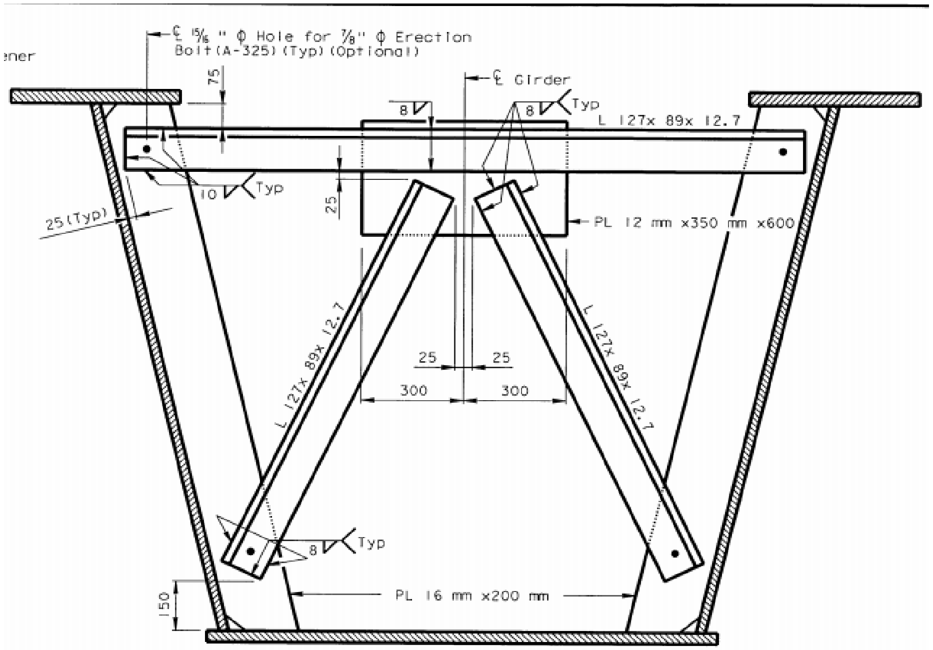

DIAFRAM ~ TYPE B

Note: All Angles Placed with
Long Leg Vertical (Typ)

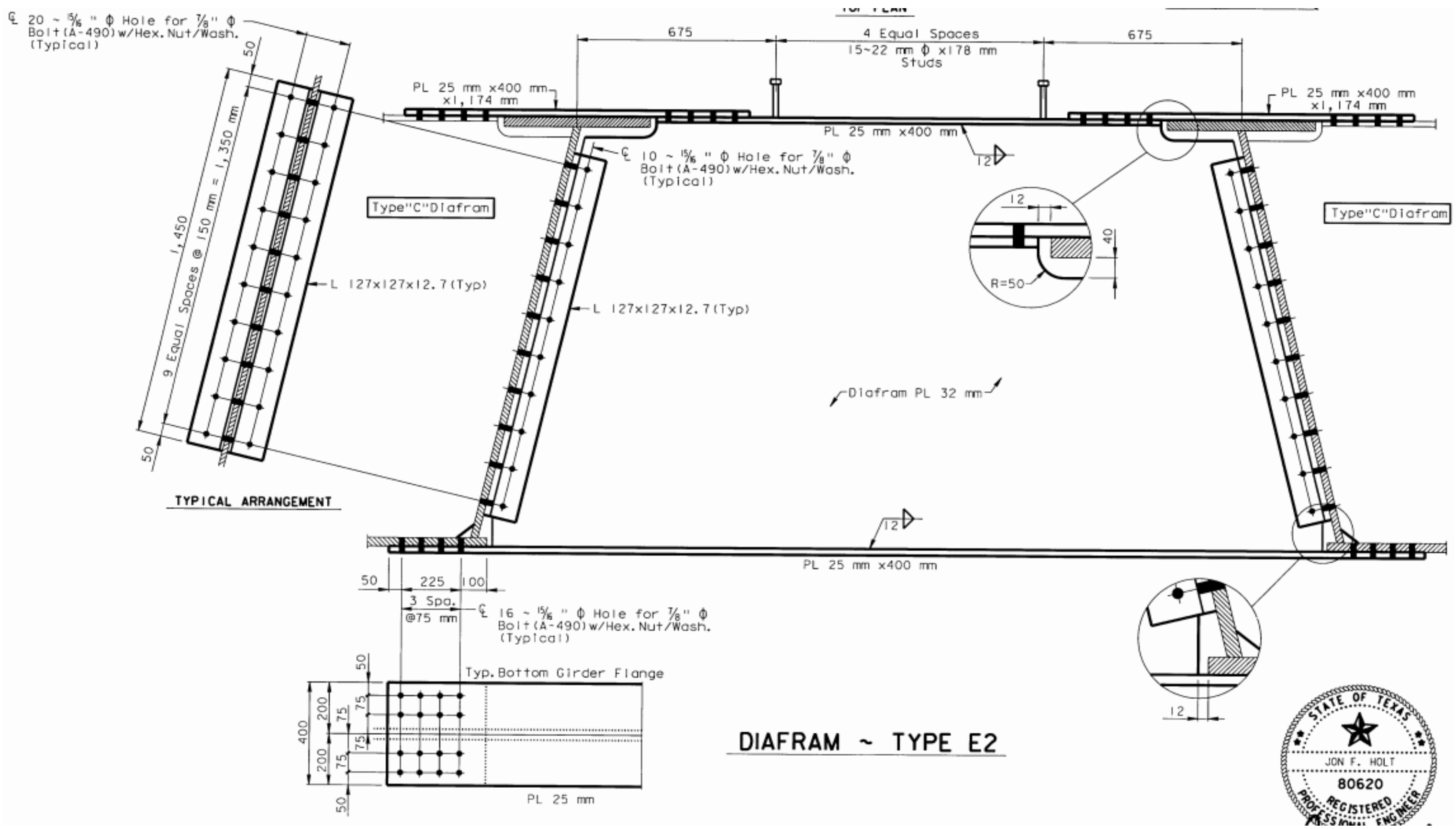

DIAFRAM ~ TYPE E2

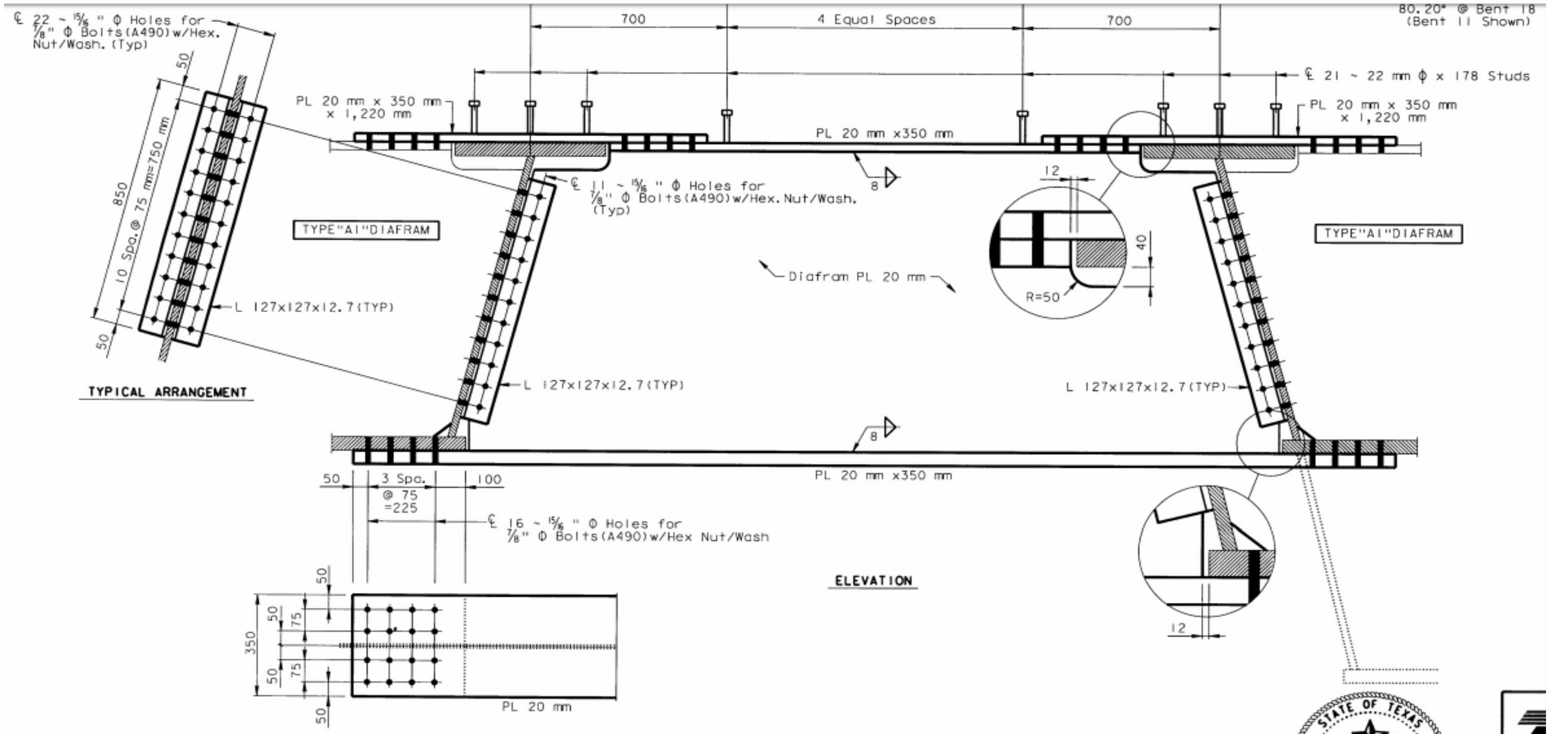

DIAFRAM ~ TYPE DI

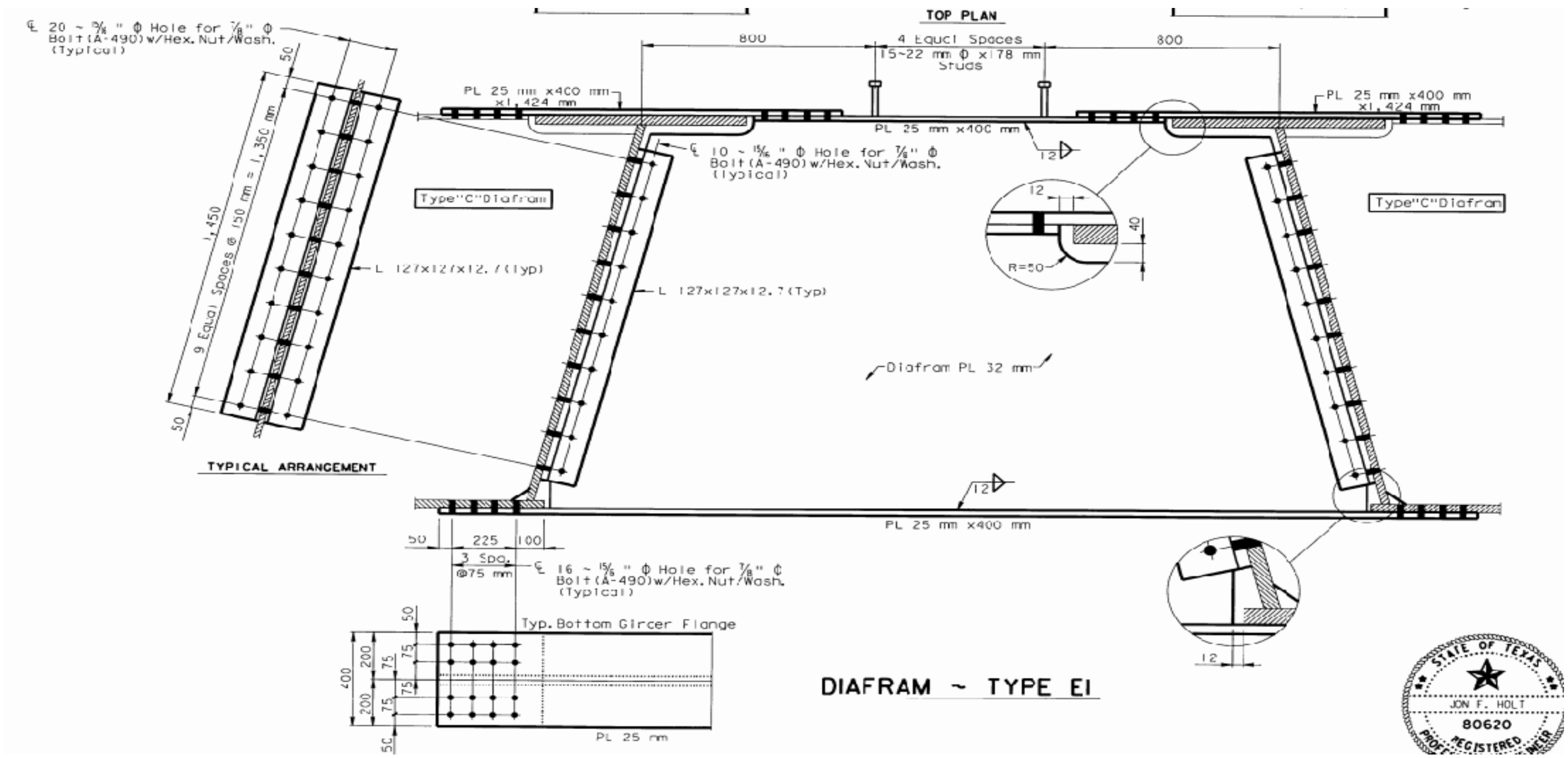
TOP PLAN
800
4 Equal Spaces
15~22 mm Φ x178 mm Studs
800
PL 25 mm x400 mm x1,424 mm
PL 25 mm x400 mm x1,424 mm
PL 25 mm x400 mm
12
℄ 20 ~ 15/16 " Φ Hole for 7/8" Φ Bolt (A-490) w/Hex. Nut/Wash. (Typical)
℄ 10 ~ 15/16 " Φ Hole for 7/8" Φ Bolt (A-490) w/Hex. Nut/Wash. (Typical)
Type"C"Diafram
Type"C"Diafram
L 127x127x12.7(Typ)
L 127x127x12.7(Typ)
1,450
9 Equal Spaces @ 150 mm = 1,350 mm
50
50
TYPICAL ARRANGEMENT
12
40
R=50
Diafram PL 32 mm
12
PL 25 mm x400 mm
50
225
100
3 Spa. @75 mm
℄ 16 ~ 15/16 " Φ Hole for 7/8" Φ Bolt (A-490) w/Hex. Nut/Wash. (Typical)
Typ. Bottom Girder Flange
PL 25 mm
400
200
200
50
75
75
75
50
12
DIAFRAM ~ TYPE EI

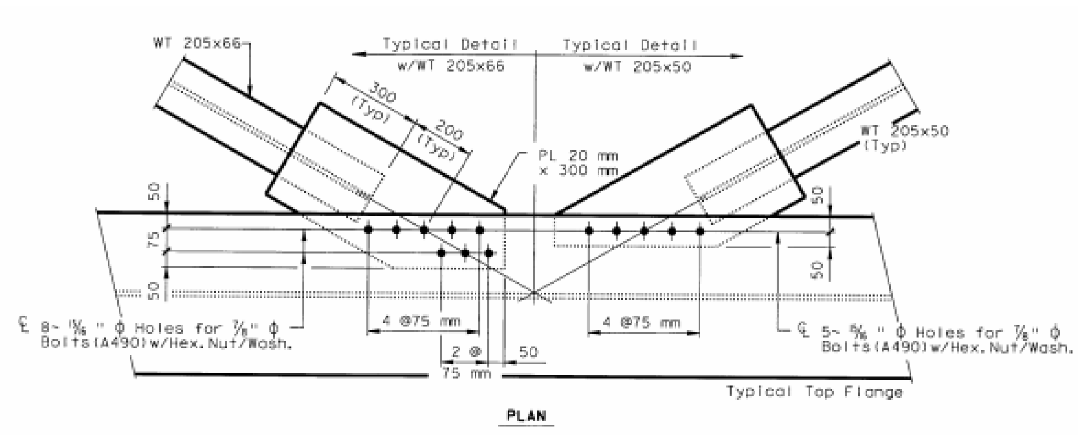
WT 205x66
Typical Detail w/WT 205x66
Typical Detail w/WT 205x50
300 (Typ)
200 (Typ)
PL 20 mm x 300 mm
WT 205x50 (Typ)
50
75
50
50
50
4 @75 mm
4 @75 mm
2 @ 75 mm
50
℄ 8~ 15/16 " Φ Holes for 7/8" Φ Bolts (A490) w/Hex. Nut/Wash.
℄ 5~ 15/16 " Φ Holes for 7/8" Φ Bolts (A490) w/Hex. Nut/Wash.
Typical Top Flange
PLAN

Bridge 10: 14-227-0-0015-13-450

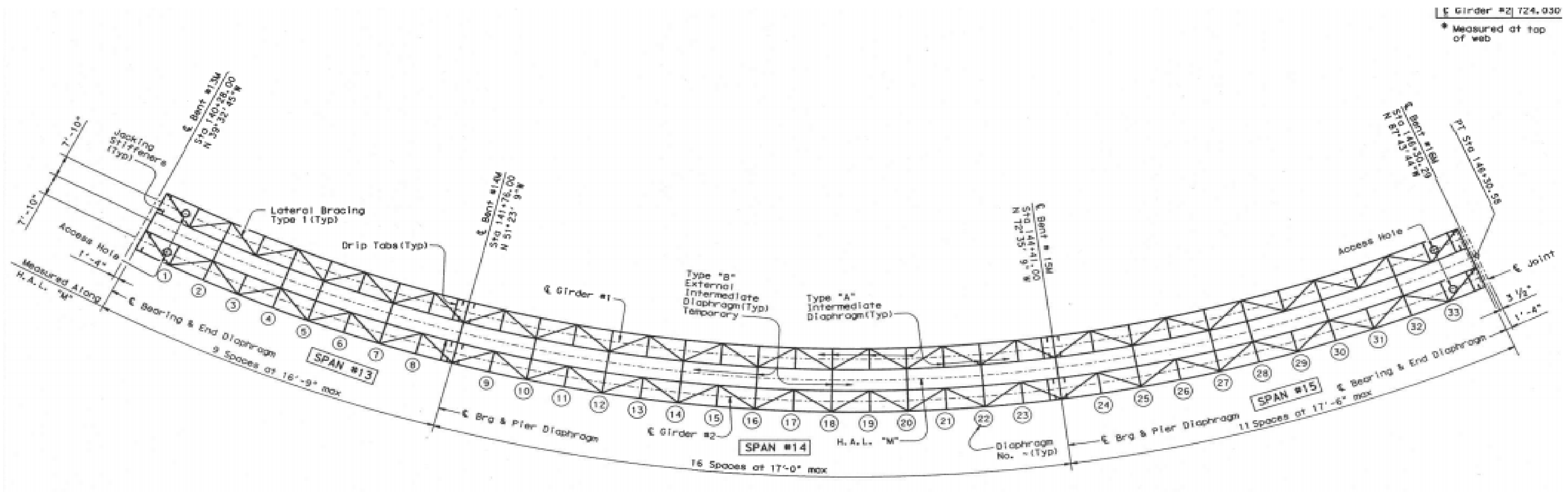

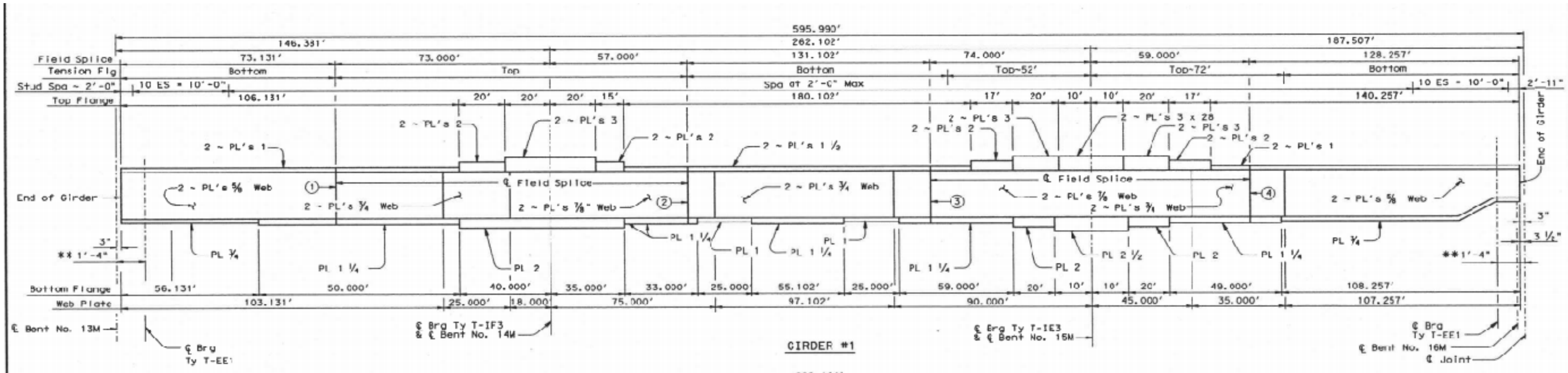

GIRDER #1

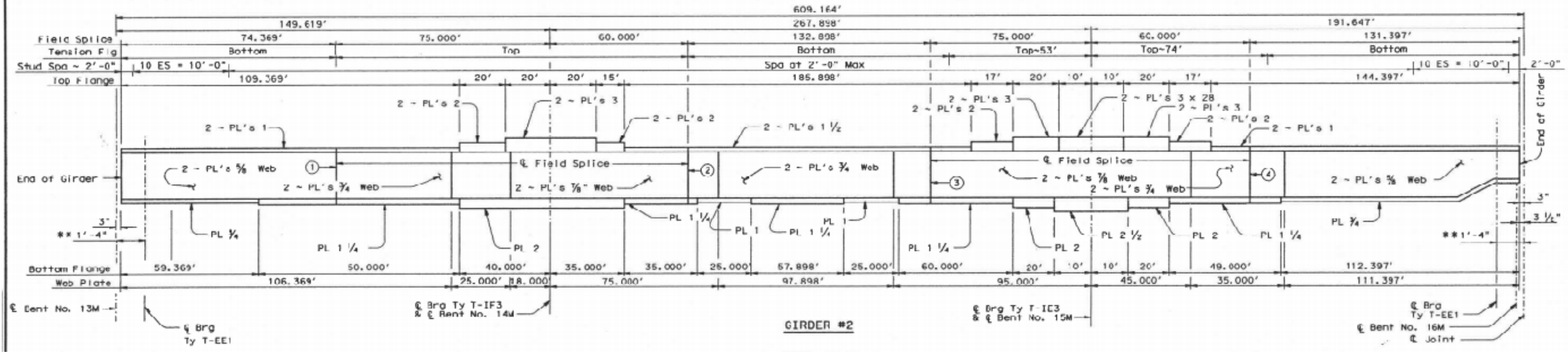

GIRDER #2

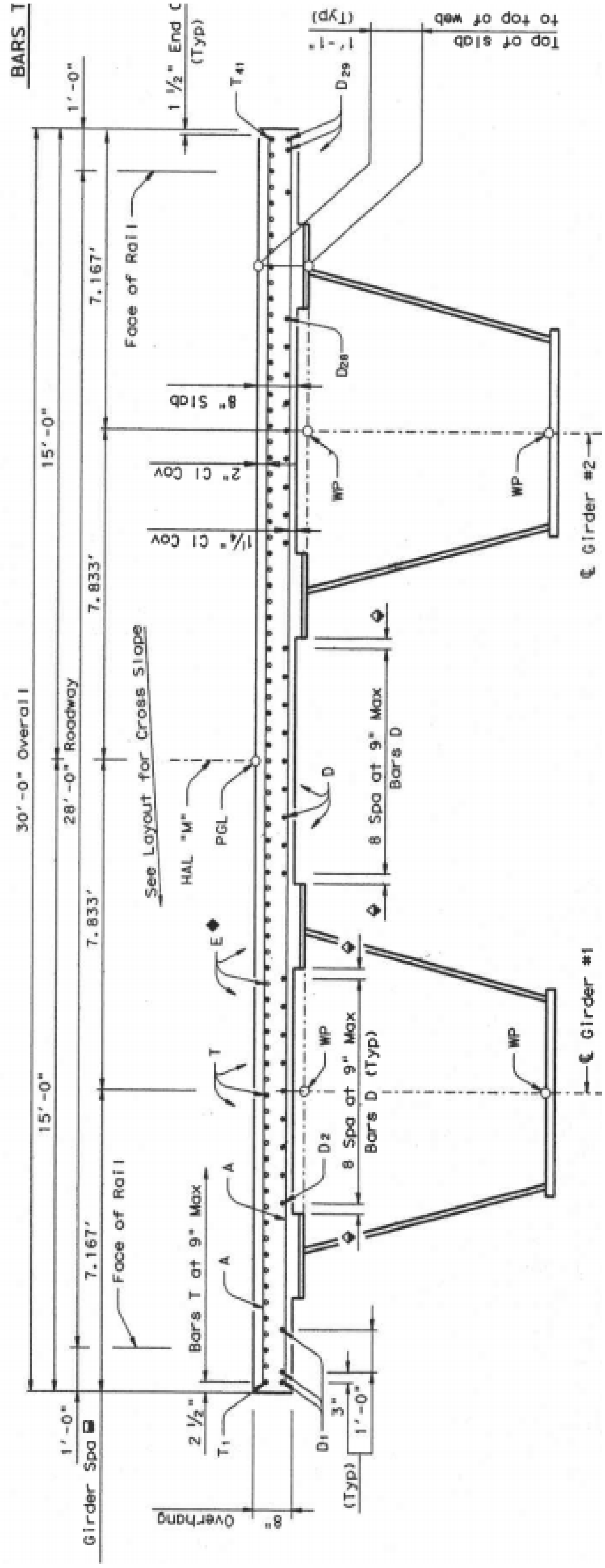

BARS T
1 1/2" End Cl (Typ)
1'-0"
T41
D29
1'-1" (Typ)
Top of slab to top of web
7.167'
Face of Rail
D28
8" Slab
15'-0"
2" Cl Cov
WP
1 1/4" Cl Cov
7.833'
℄ Girder #2
See Layout for Cross Slope
30'-0" Overall
28'-0" Roadway
HAL "M"
PGL
D
8 Spa at 9" Max
Bars D
E
T
WP
8 Spa at 9" Max
Bars D (Typ)
℄ Girder #1
D2
A
A
Bars T at 9" Max
7.167'
15'-0"
Face of Rail
1'-0"
Girder Spa
2 1/2"
T1
D1
3"
1'-0"
(Typ)
Overhang
8"

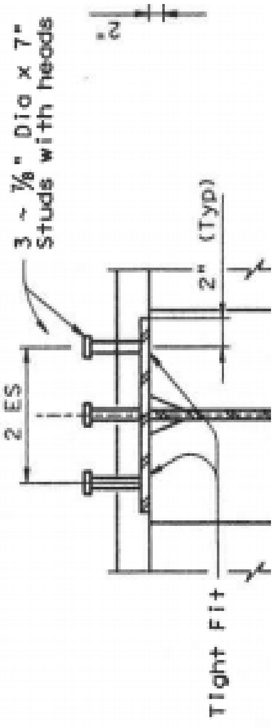

3 ~ 7/8" Dia x 7" Studs with heads
2"
2 ES
2" (Typ)
Tight Fit

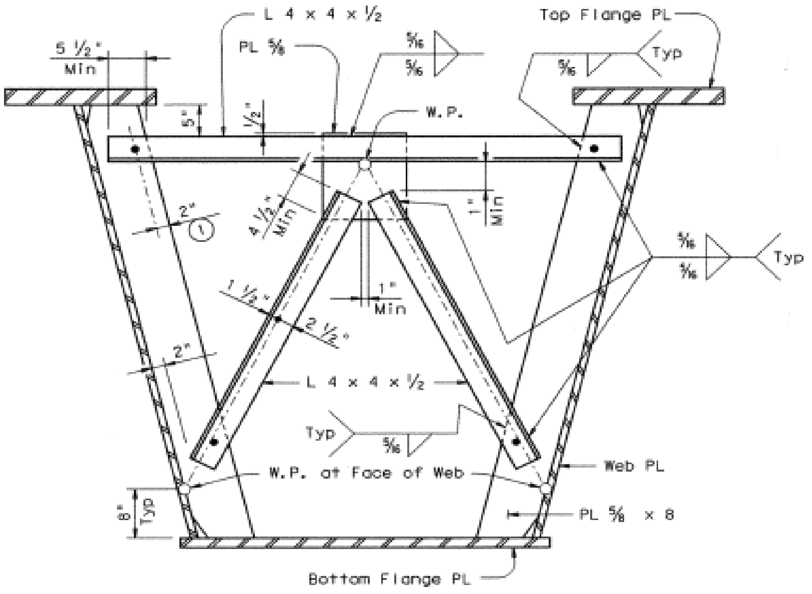

TYPICAL SECTION AT TYPE "A" INTERNAL INTERMEDIATE DIAPHRAGM

To be fully installed in the shop.

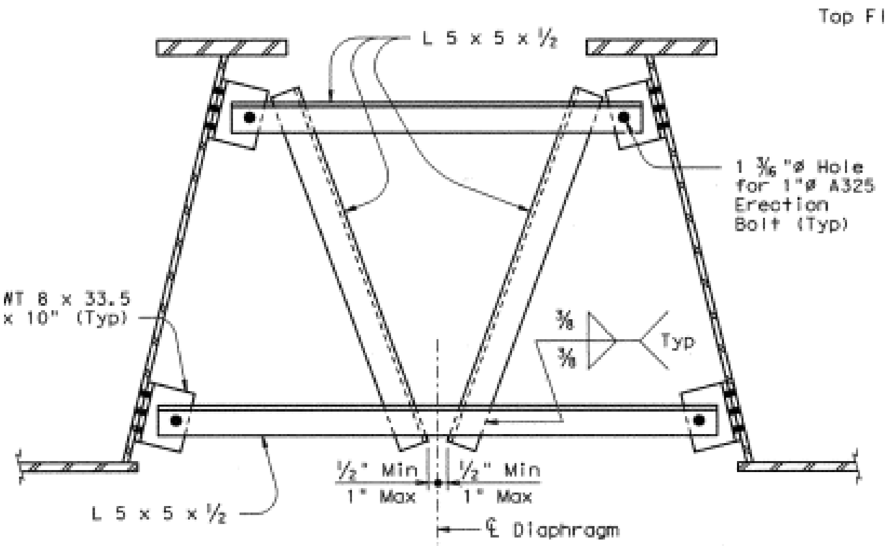

TYPICAL SECTION AT TYPE "B" EXTERNAL INTERMEDIATE DIAPHRAGM (TEMPORARY)

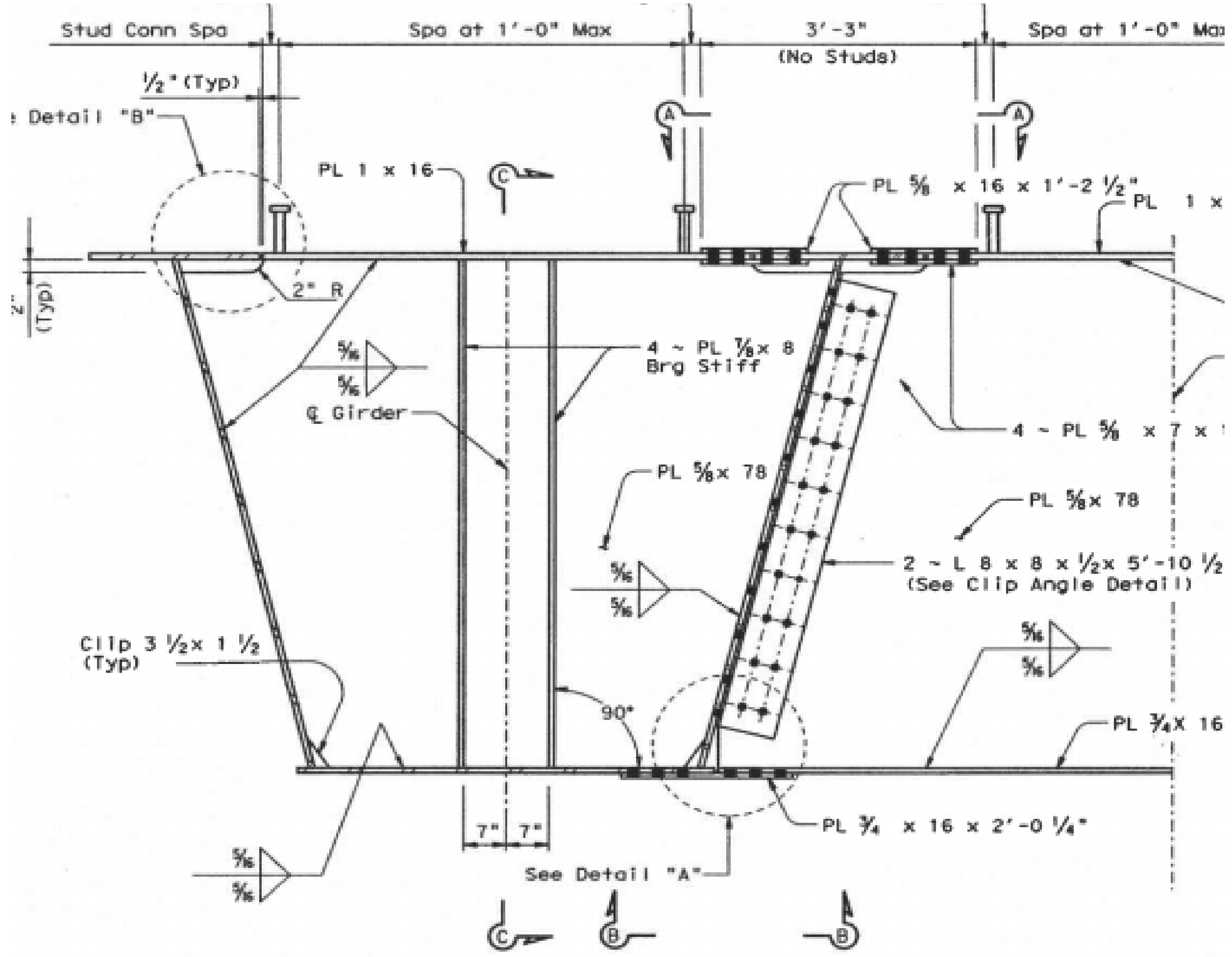

HALF ELEVATION

END DIAPHRAGM DETAILS

(At Bent No. 13M)

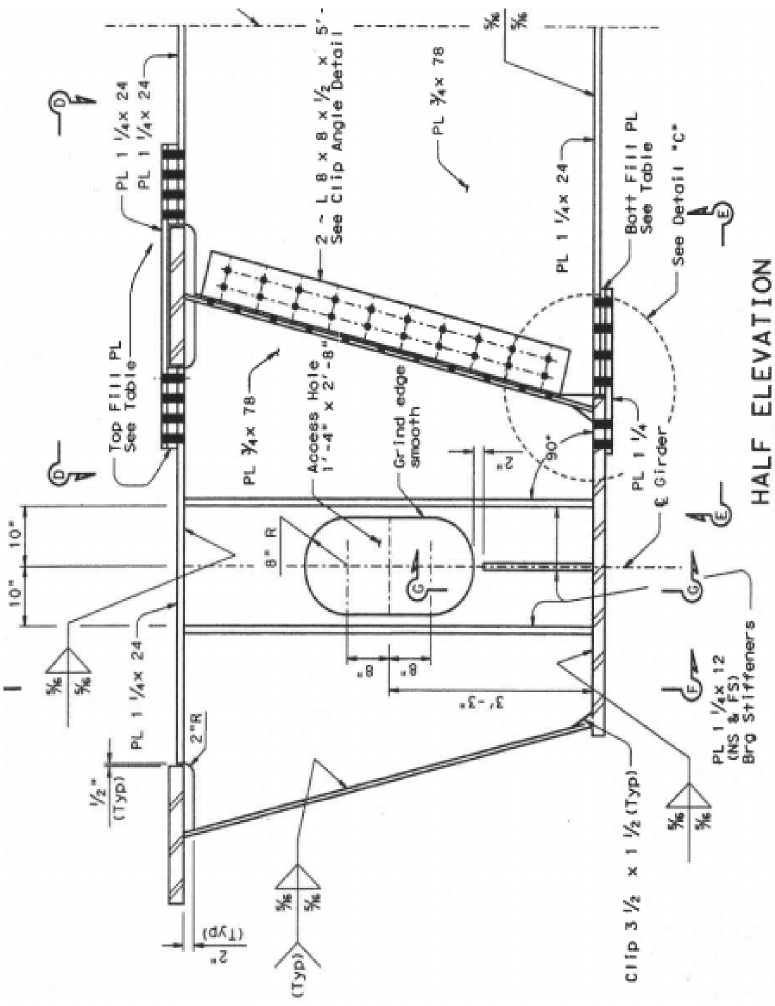

HALF ELEVATION

PIER DIAPHRAGM DETAILS

(At Bent Nos. 14M & 15M)

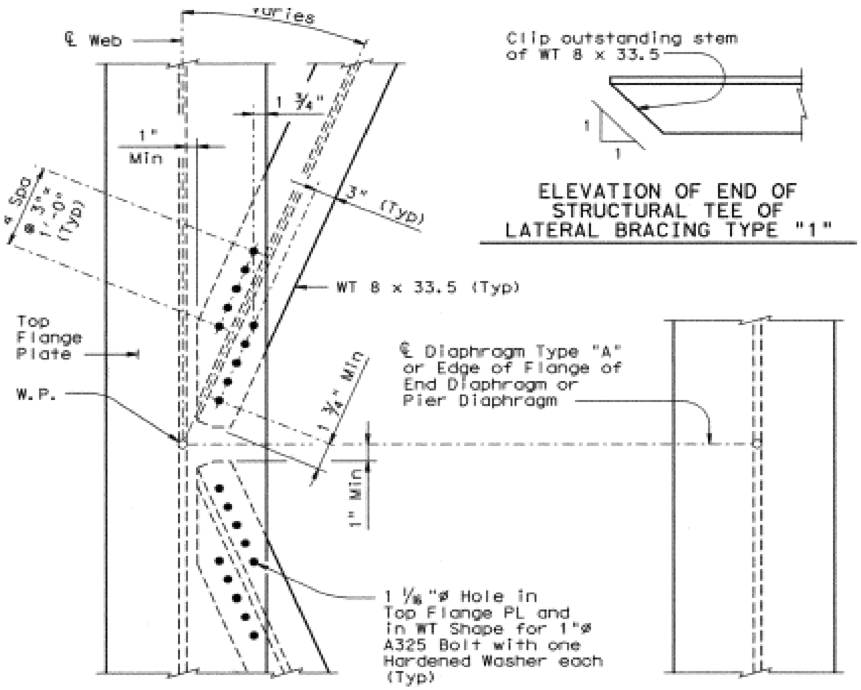

ELEVATION OF END OF
STRUCTURAL TEE OF
LATERAL BRACING TYPE "1"

TYPICAL PLAN VIEW OF
LATERAL BRACING TYPE "1"

Installed in shop except at locations spanning a
field splice, which shall be installed in the field.

Bridge 11: 12-102-0271-07-593

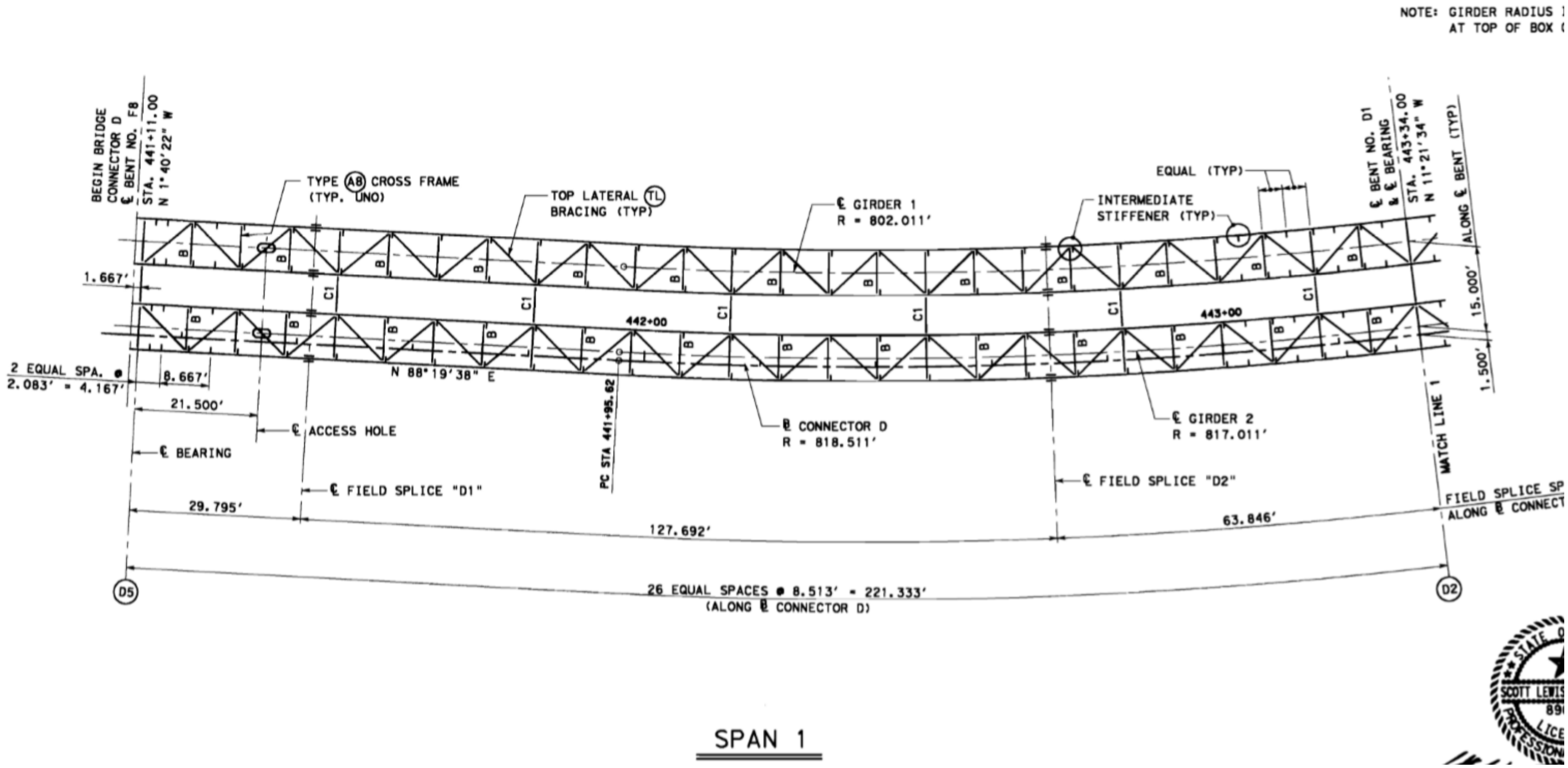

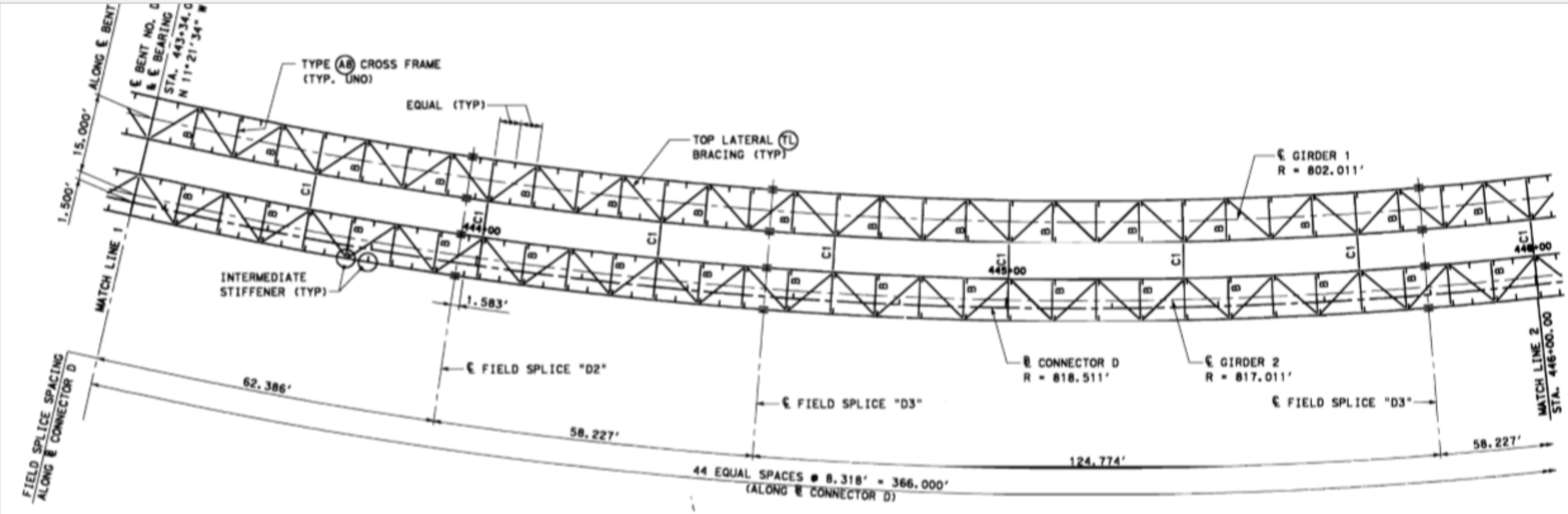

PARTIAL SPAN 2

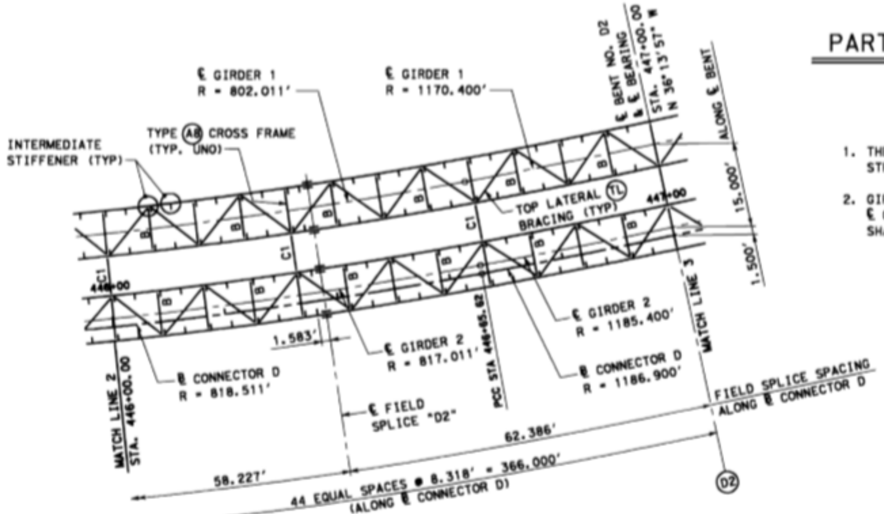

PARTIAL SPAN 2

NOTES

1. THE CONTRACTOR SHALL LOCATE PICK-UP POINTS SO ERECTION STRESSES DO NOT EXCEED ALLOWABLE STRESSES.
2. GIRDER DIMENSIONS SHOWN ARE MEASURED HORIZONTALLY ALONG ℄ GIRDERS AT TOP OF WEB UNLESS NOTED OTHERWISE. THE CONTRACTOR SHALL MAKE ADJUSTMENTS FOR GRADE AND CAMBER.

ABBREVIATIONS

(A8) = TYPE A8 CROSS FRAME
B = TOP STRUT ONLY (L6x6x⅜)
C1 = TYPE C1 TEMPORARY EXTERNAL CROSS FRAME
(D2) = TYPE D2 DIAPHRAGM
(TL) = TOP LATERAL BRACING (WT9x71.5)

SCOTT LEWIS MONTGOMER
89028

4/5/

Texas Department of Trans

© 2004 TxDOT

URS
9801 WESTHEIMER, SUITE 500
HOUSTON, TEXAS 77042
713.914.6699

KATY FREEWAY
RECONSTRUCTION PROG
DIRECT CONNECTOR
UNIT D1
FRAMING PLAN

HS25 LOADING

		DN: JTC	CK: CDR	DW: KA	
			STATE		
			TEXAS		
		12	HARRIS	0271	07

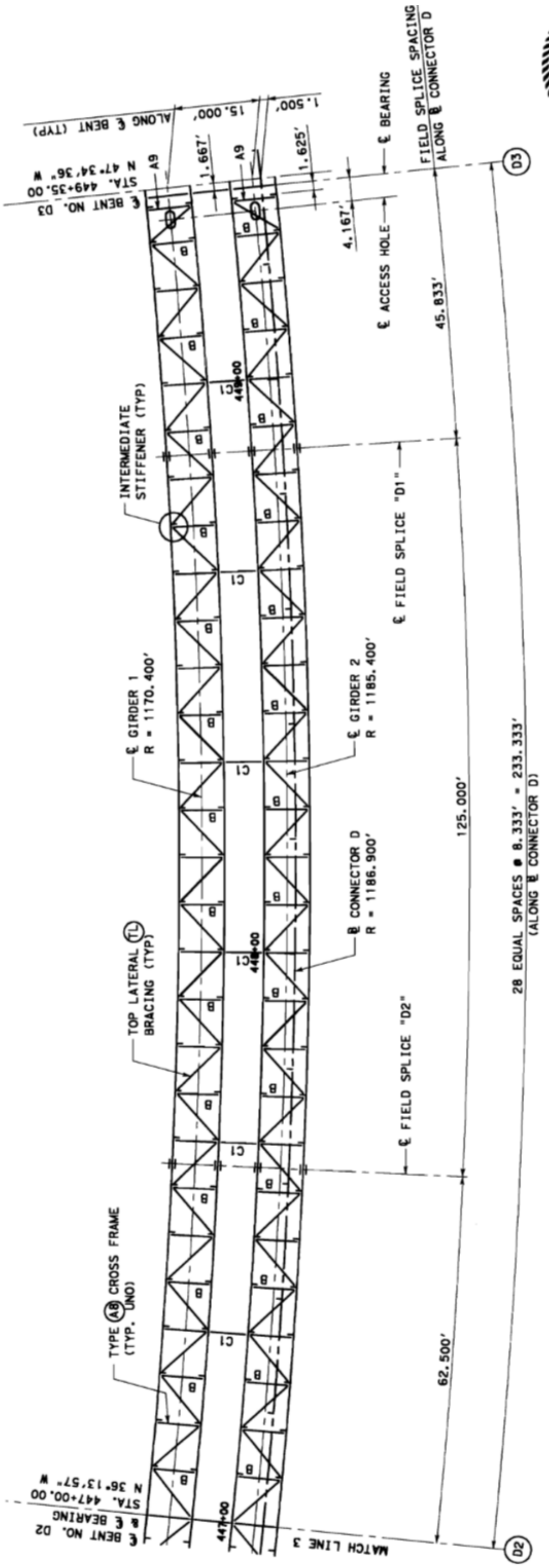

SPAN 3

SCOTT LEWIS MONTGOMERY
89028

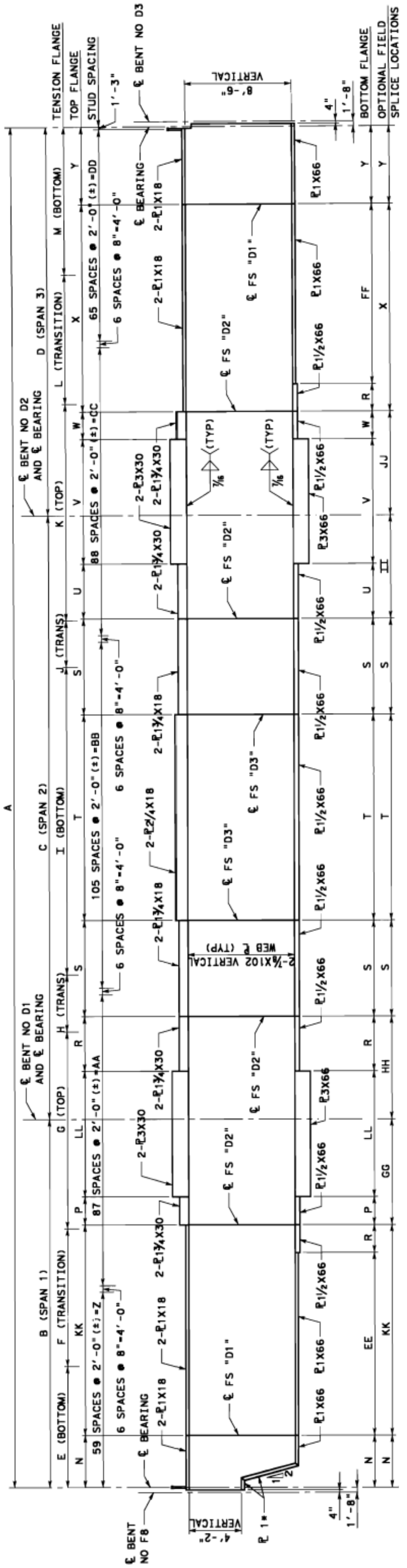A
B (SPAN 1)
C (SPAN 2)
D (SPAN 3)
TENSION FLANGE
TOP FLANGE
STUD SPACING
E (BOTTOM)
F (TRANSITION)
G (TOP)
H (TRANS)
I (BOTTOM)
J (TRANS)
K (TOP)
L (TRANSITION)
M (BOTTOM)
℄ BENT NO D1 AND ℄ BEARING
℄ BENT NO D2 AND ℄ BEARING
℄ BENT NO D3
℄ BENT NO F8
℄ BEARING
1'-3"
59 SPACES @ 2'-0" (±) = Z
6 SPACES @ 8" = 4'-0"
87 SPACES @ 2'-0" (±) = AA
105 SPACES @ 8" = 4'-0"
105 SPACES @ 2'-0" (±) = BB
88 SPACES @ 2'-0" (±) = CC
65 SPACES @ 2'-0" (±) = DD
2-♇1X18
2-♇1¾X30
2-♇3X30
2-♇1¾X18
2-♇2¼X18
℄ FS "D1"
℄ FS "D2"
℄ FS "D3"
2-⅝X102 VERTICAL WEB ℄ (TYP)
⁷⁄₁₆ (TYP)
♇1X66
♇1½X66
♇3X66
♇1*
4'-2" VERTICAL
8'-6" VERTICAL
1
2
4"
1'-8"
N
KK
R
P
LL
S
T
U
V
W
X
Y
EE
GG
HH
II
JJ
FF
BOTTOM FLANGE
OPTIONAL FIELD SPLICE LOCATIONS

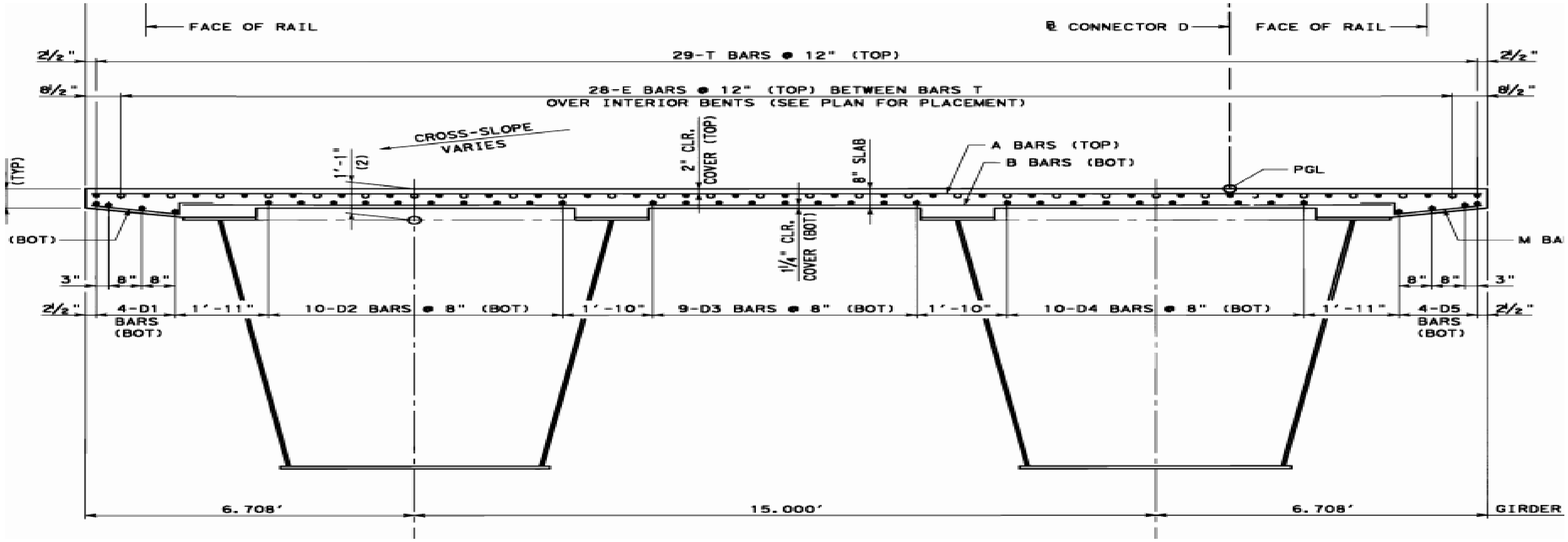

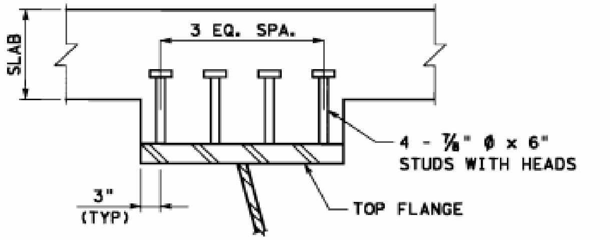

SHEAR CONNECTOR STUD DETAIL

STUDS SHALL BE ELECTRIC ARC END WELDED
TO THE FLANGES WITH COMPLETE FUSION.
(SEE GIRDER ELEVATIONS FOR SPACING ALONG GIRDER)

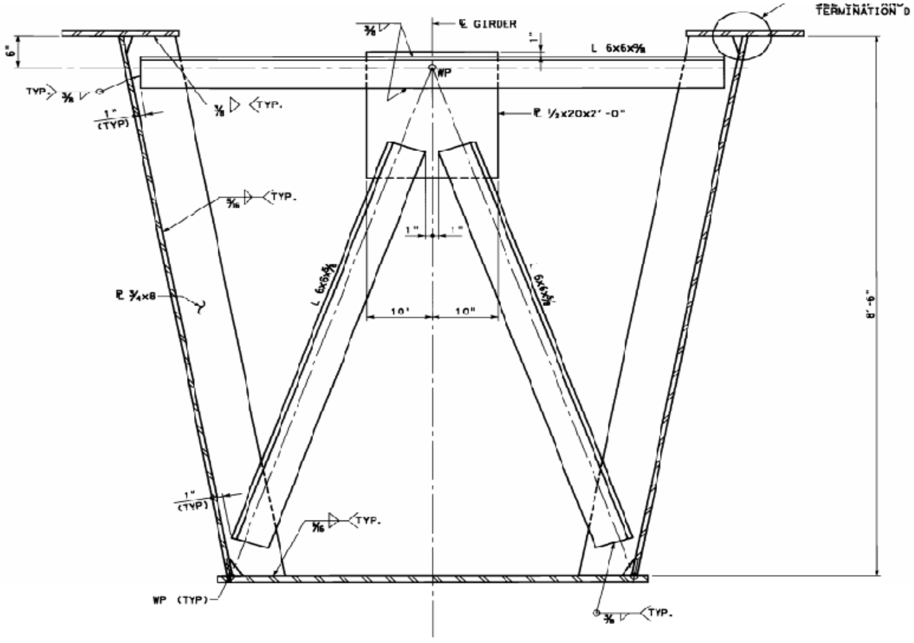

CROSS FRAME - TYPE A8

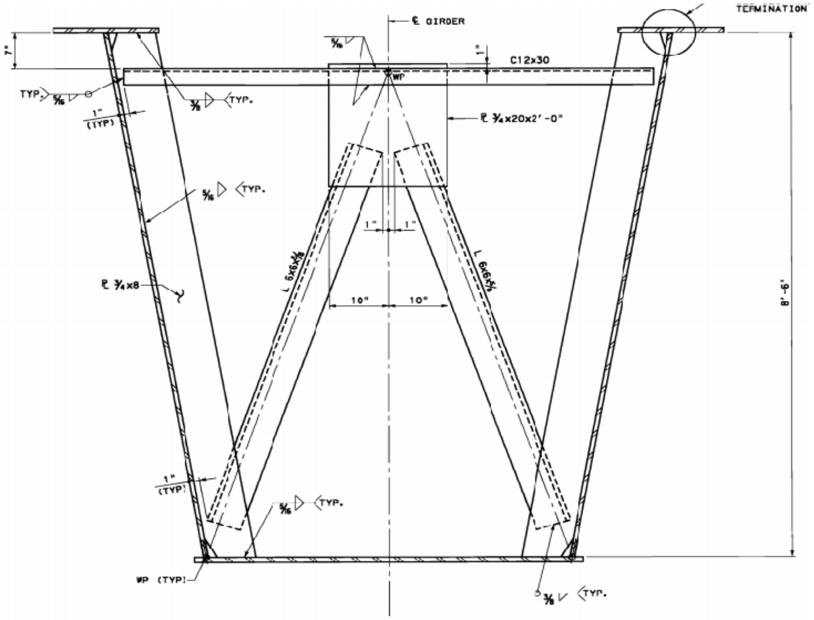

CROSS FRAME - TYPE A9

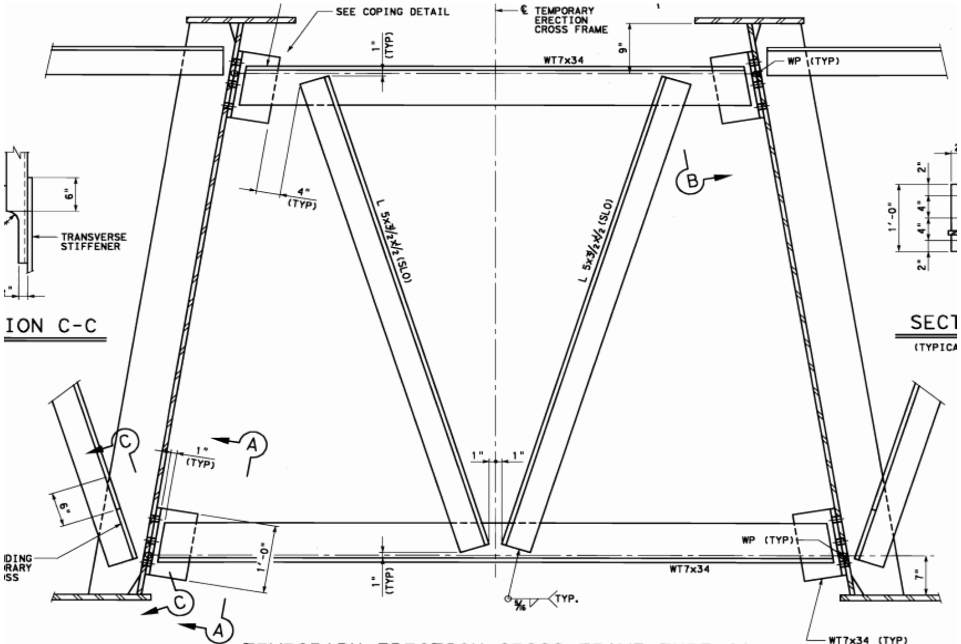

TEMPORARY ERECTION CROSS FRAME TYPE C1

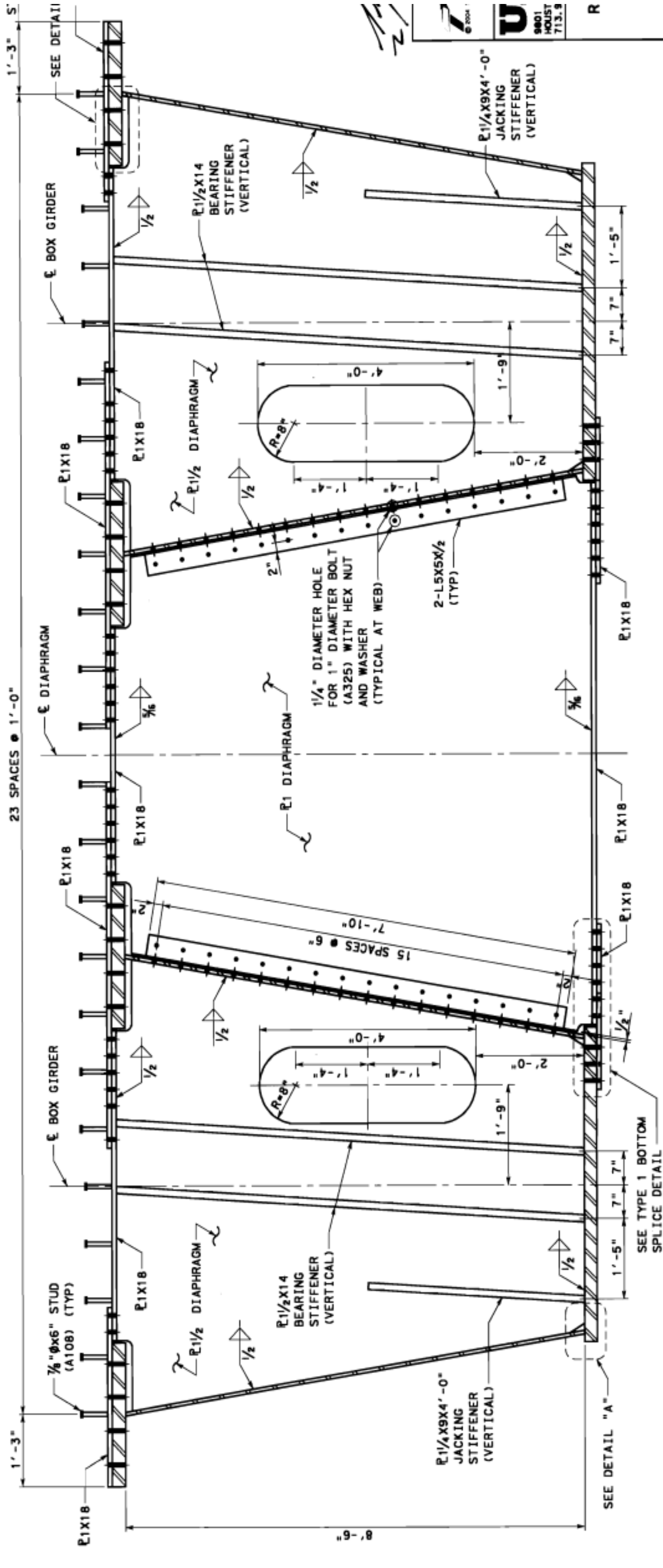

DIAPHRAGM - TYPE D2

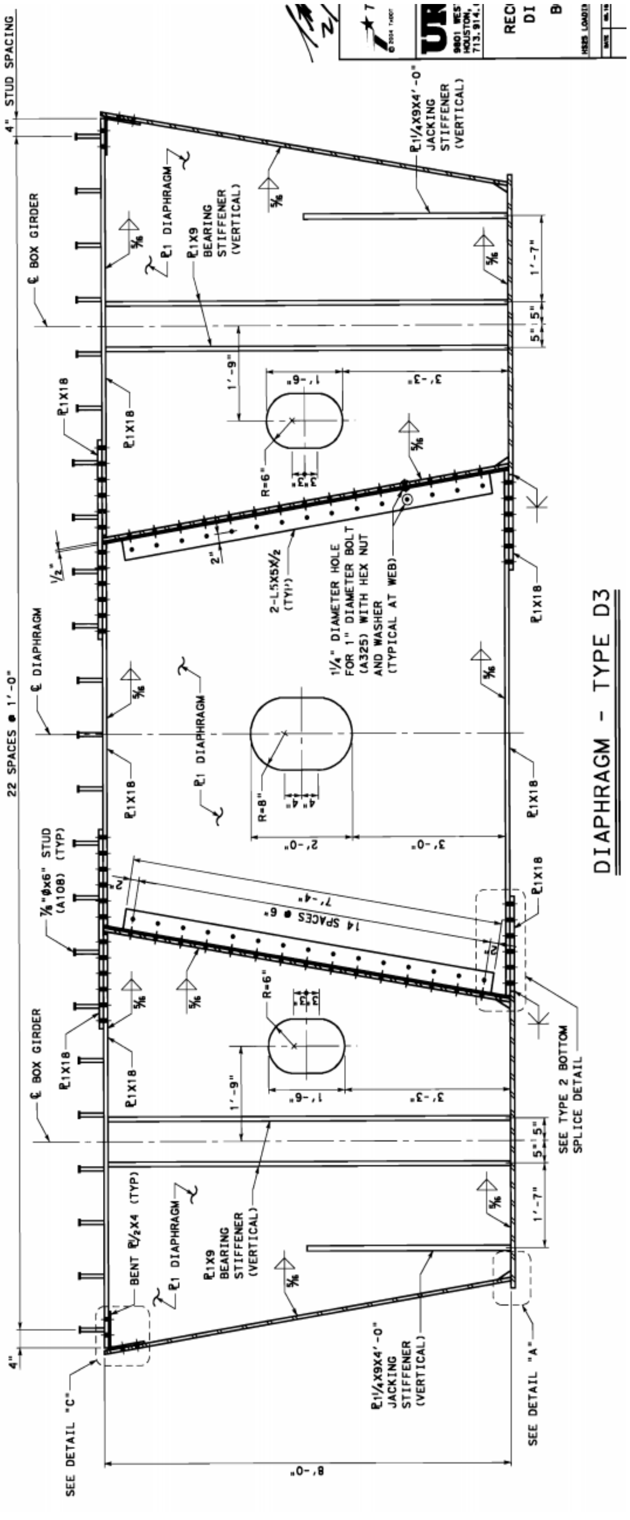

DIAPHRAGM - TYPE D3

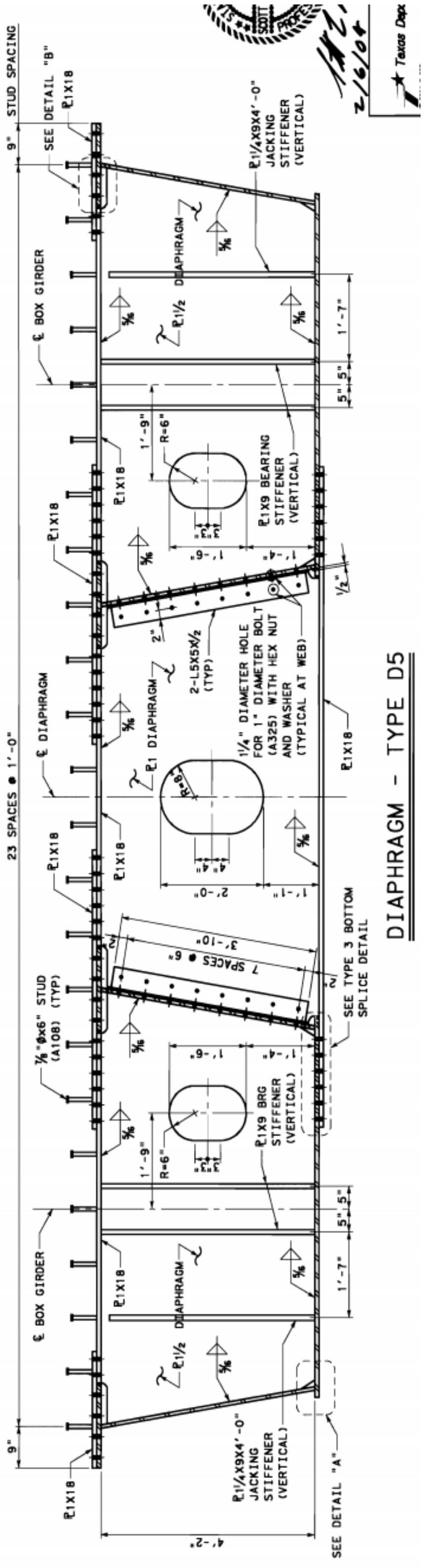

DIAPHRAGM - TYPE D5

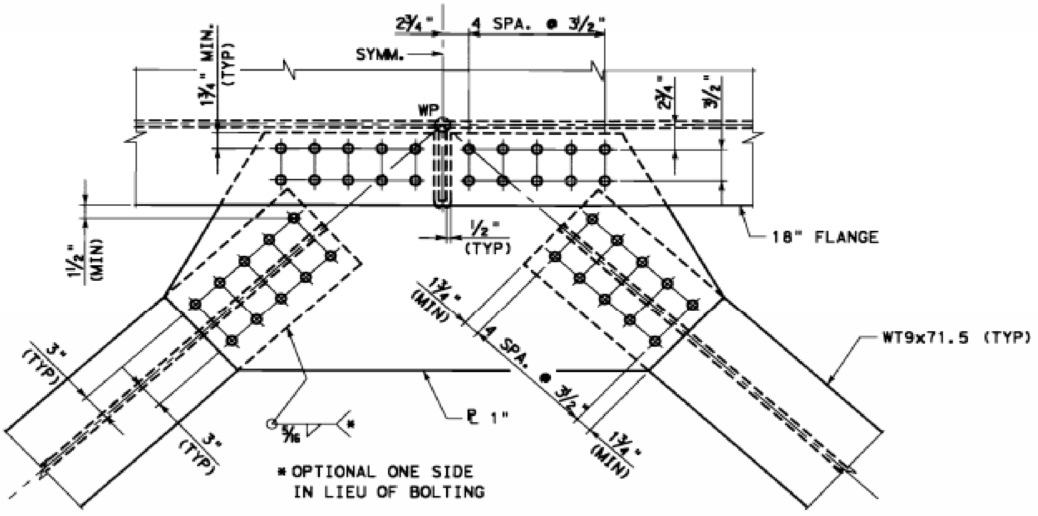

TOP LATERAL BRACING CONNECTION

DETAIL - UNIT D1

(18" TOP FLANGE)

Bridge 12: 12-102-0271-07-639

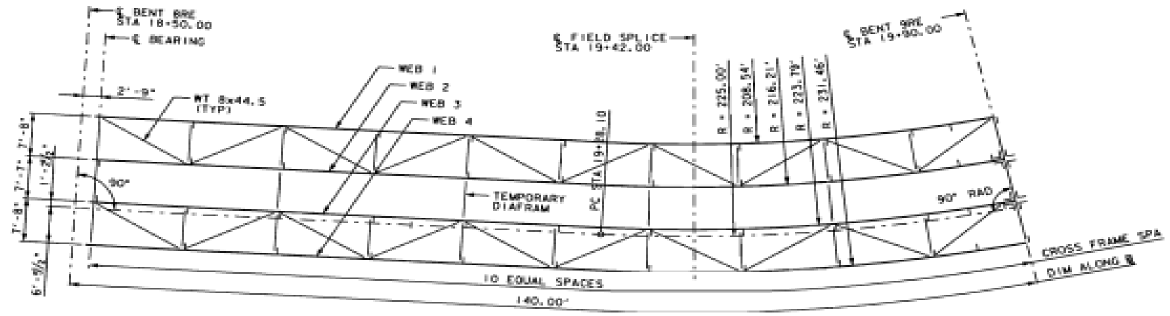

SPAN 8RE

SCALE: 1" = 20'

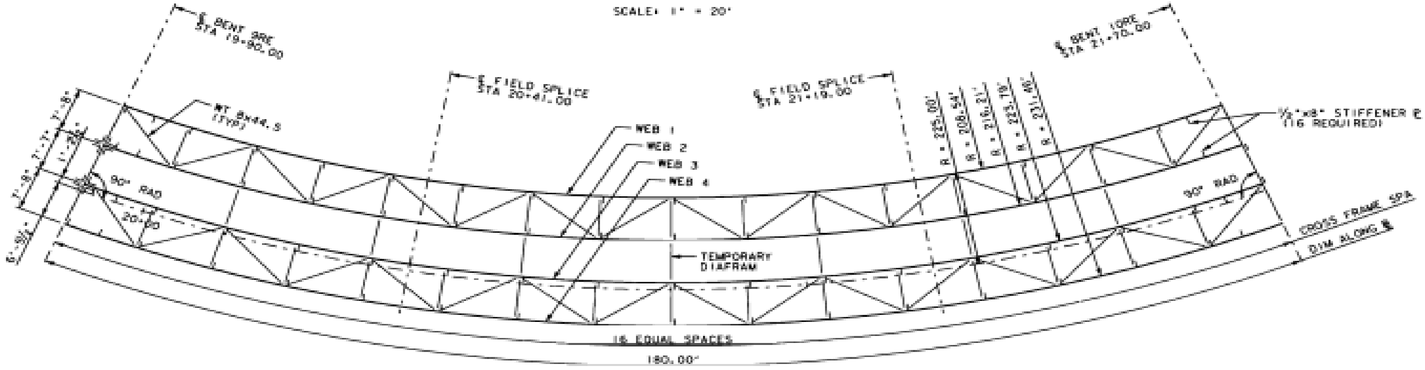

SPAN 9RE

SCALE: 1" = 20'

14
S1
C.

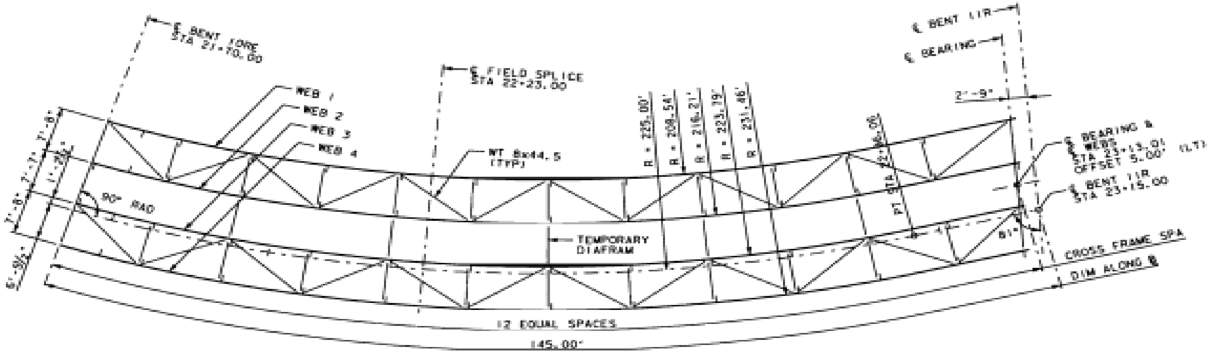

SPAN 10RE

SCALE: 1" = 20'

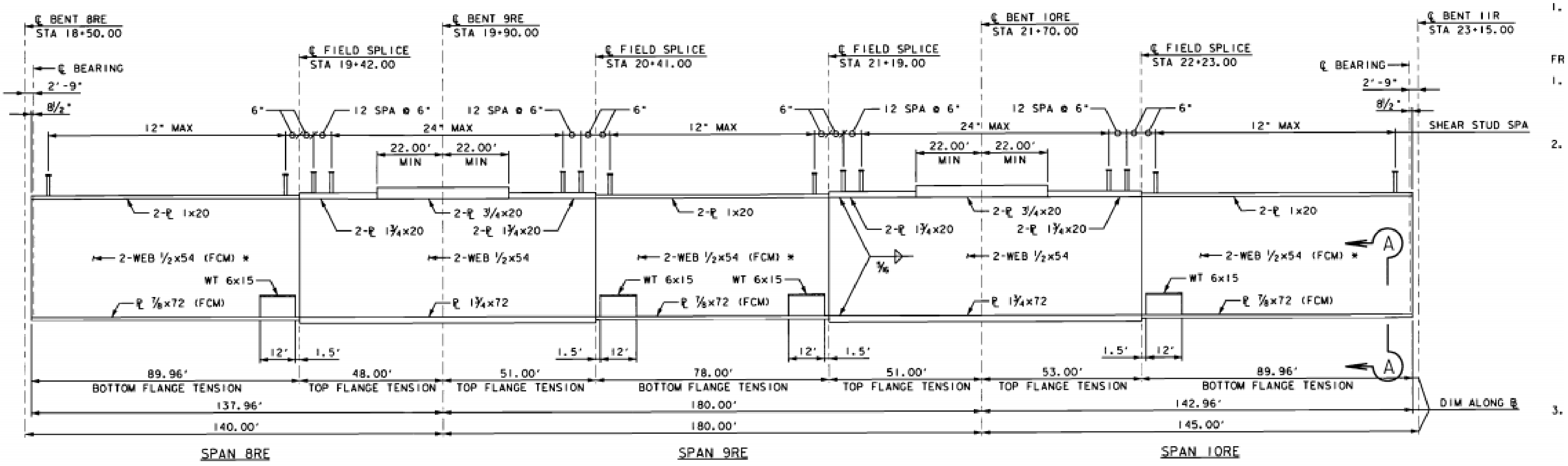

* WEB TO TOP FLANGE WELD
IS NOT FRACTURE CRITICAL

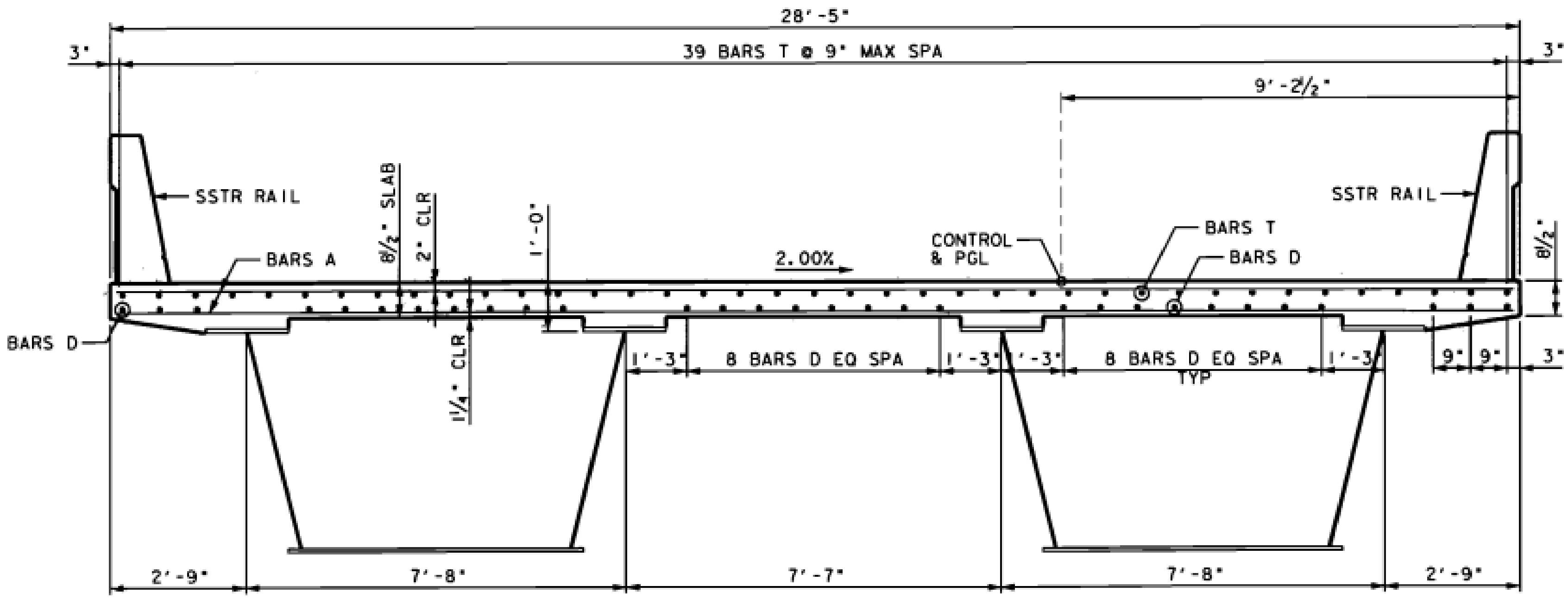

TYPICAL SECTION

SCALE: ¼" = 1'

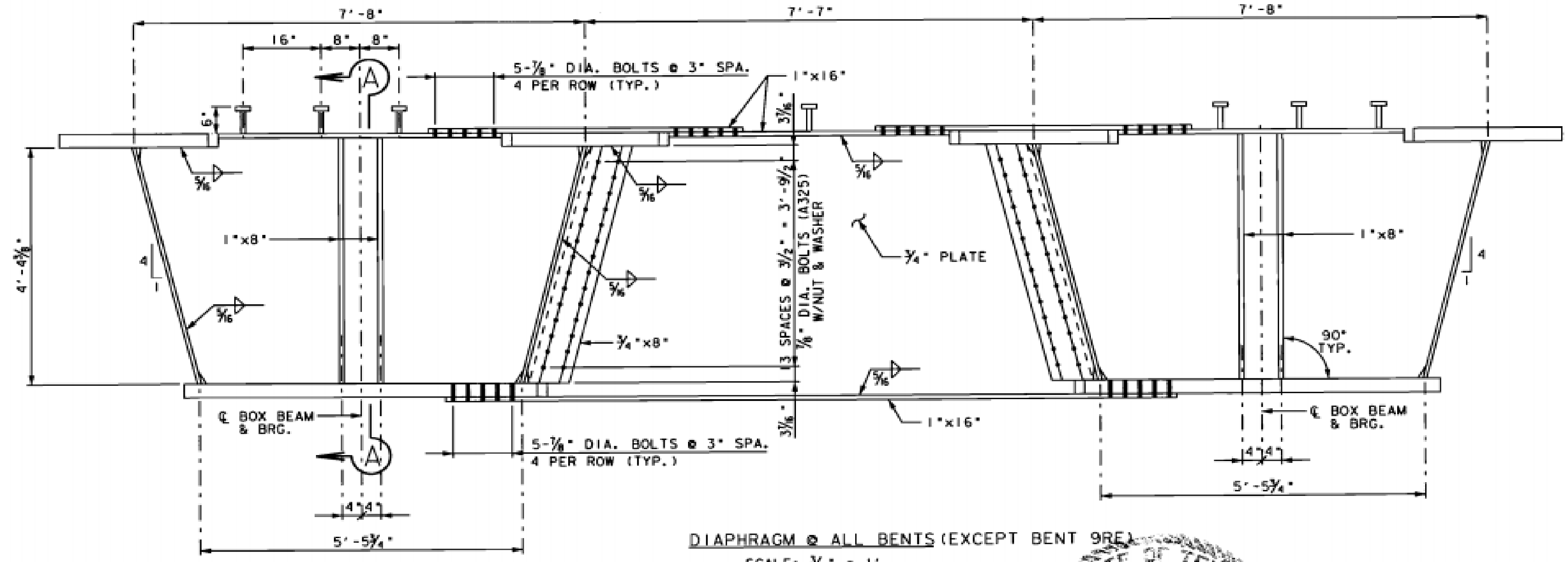

DIAPHRAGM @ ALL BENTS (EXCEPT BENT 9RE)

SCALE: 3/8" = 1'

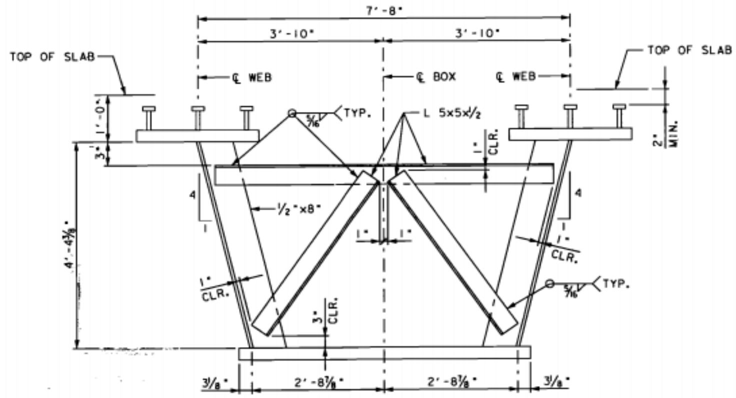

TYPE B INTERMEDIATE DIAPHRAGM

3/8" = 1'-0"

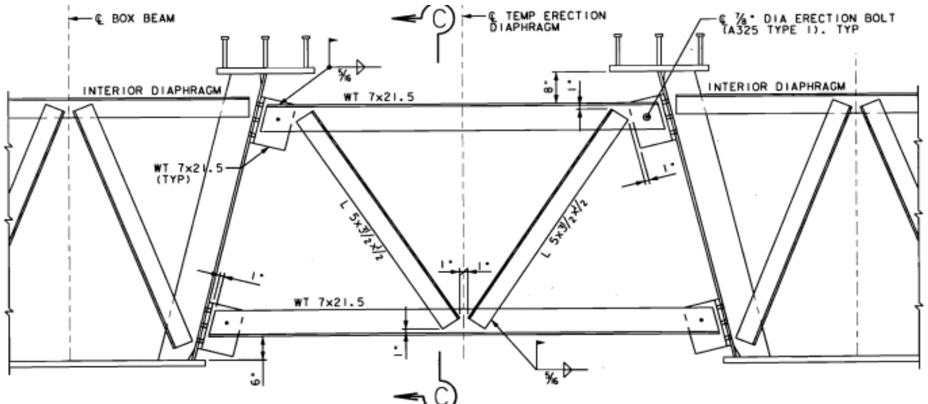

TEMPORARY DIAPHRAGM

N.T.S.

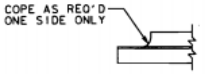

PLAN

NOTE:
ALL ANGLES PLACED WITH LONG LEG VERTICAL, TYP
TEMPORARY ERECTION DIAPHRAGMS SHALL BE IN PLACE DURING PLACEMENT AND CURING OF DECK, AFTER WHICH THESE DIAPHRAGMS SHALL BE REMOVED WITH THE EXCEPTI OF THE 7/8" DIA HS 'HEX HEAD TYPE' BOLTS THROUGH THE WEB. FOR LOCATION OF TEMPORARY DIAPHRAGMS, SEE FRAMING PLAN.

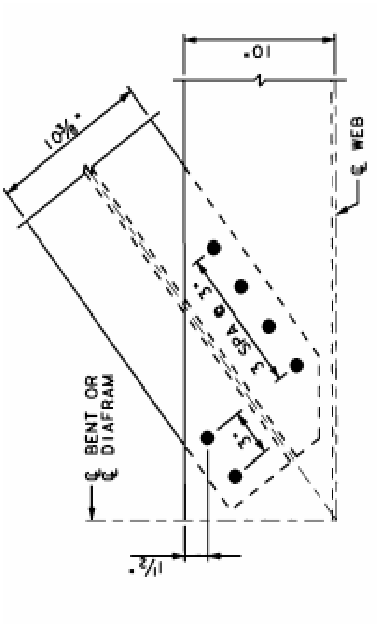

LATERAL BRACING PLAN

SCALE: 1" = 1'-0"

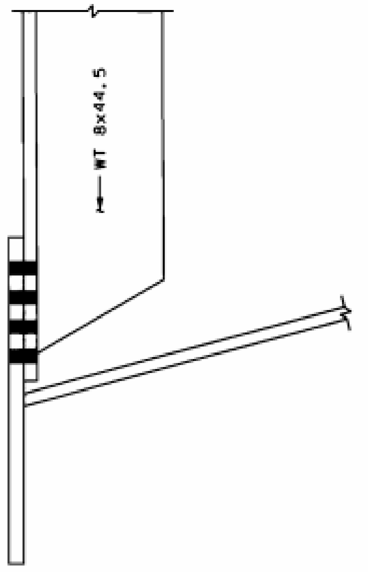

LATERAL BRACING ELEVATION

SCALE: 1" = 1'-0"

Bridge 13: 14-227-0-0015-13-452

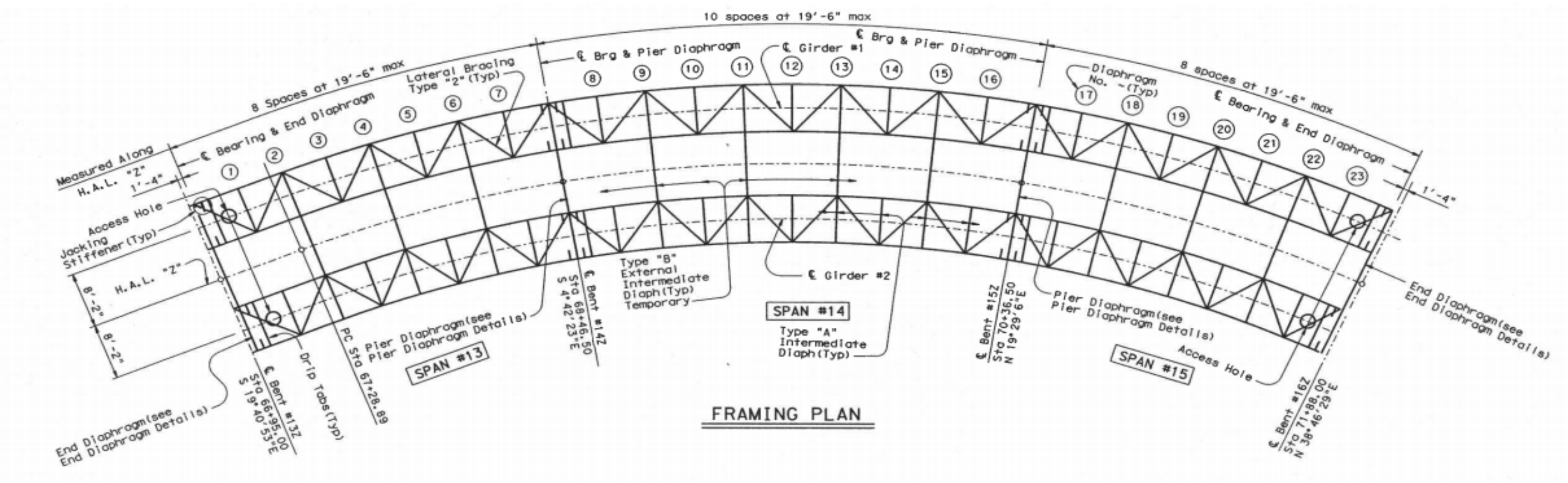

FRAMING PLAN

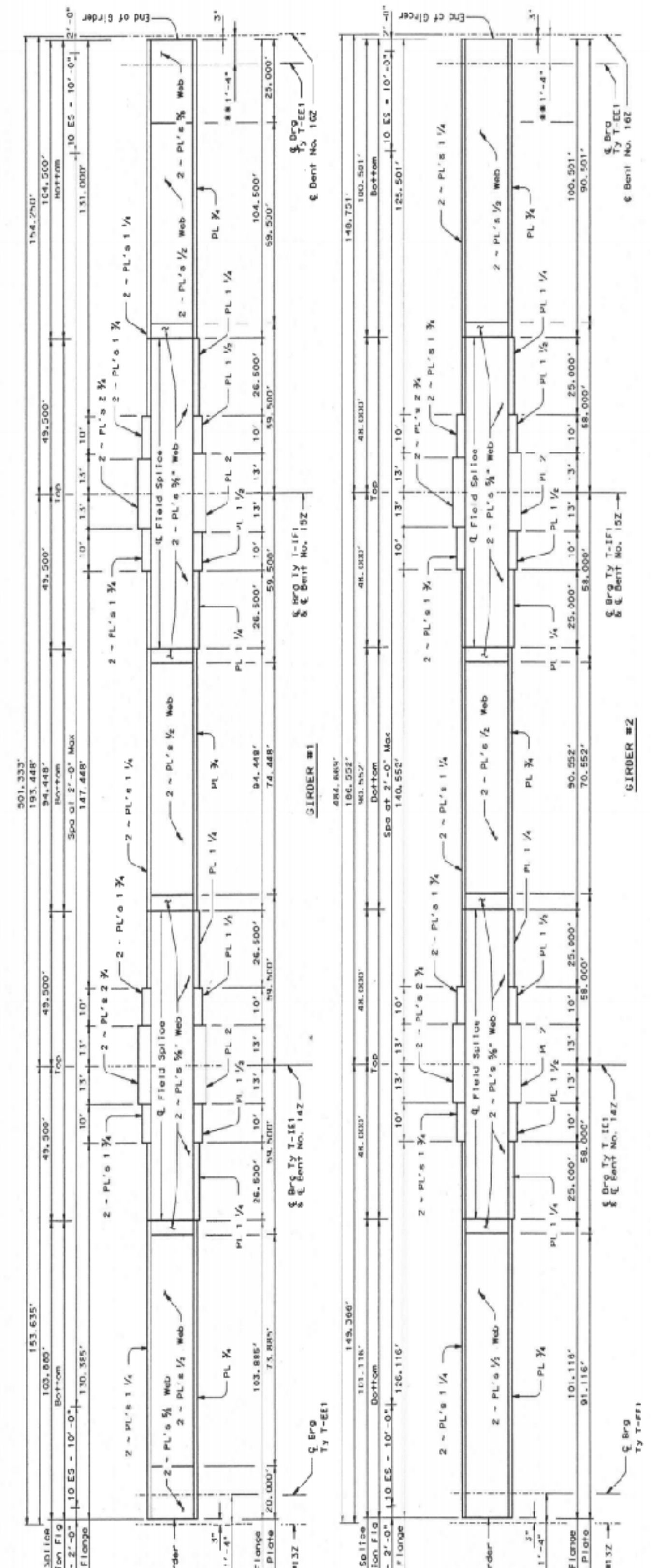
GIRDER #1
GIRDER #2
Field Splice
Tension Flg
Stud Spa - 2'-0"
Top Flange
End of Girder
Bottom Flange
Web Plate
℄ Bent #13Z
℄ Field Splice
℄ Brg Ty T-EE1
℄ Bent No. 16Z
℄ Brg Ty T-IF1 & ℄ Bent No. 15Z
℄ Brg Ty T-IE1 & ℄ Bent No. 14Z
501.333'
484.866'

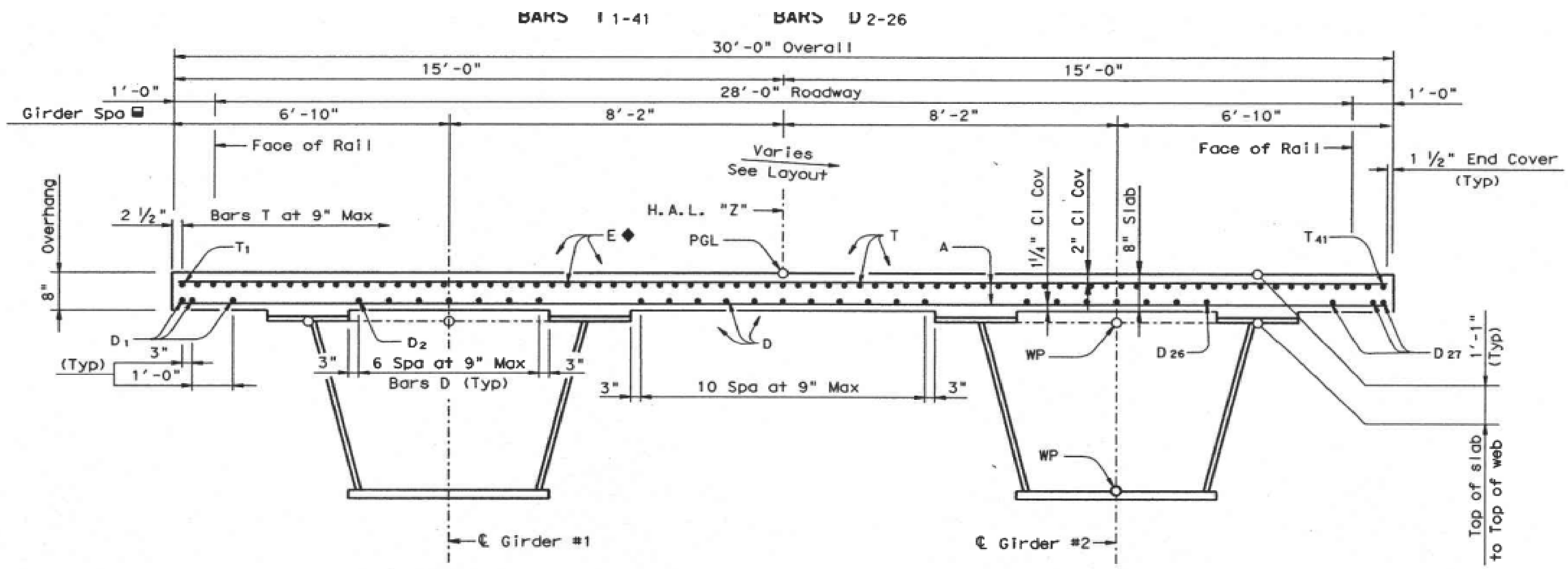

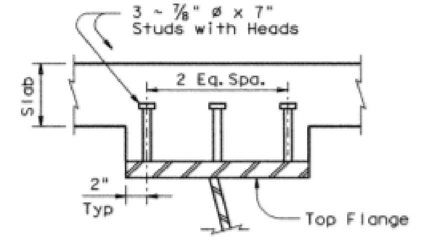

SHEAR CONNECTOR STUD DETAIL

Studs shall be Electric arc end-welded to the flanges with complete fusion. (See Span details for spacing along girder.)

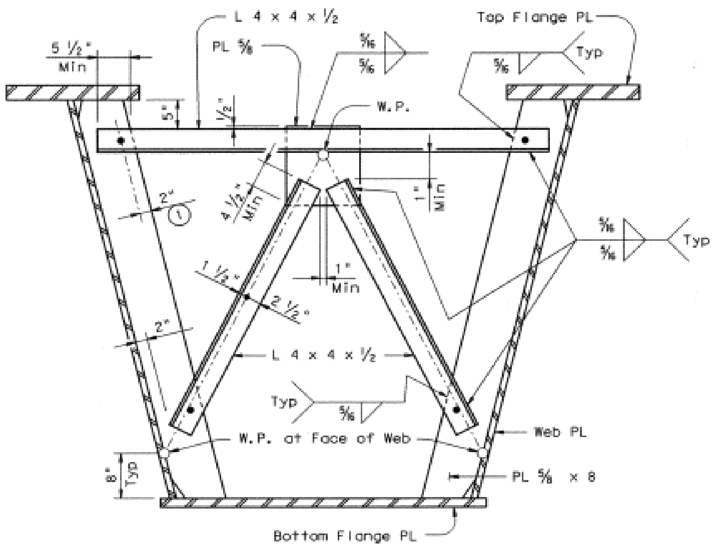

TYPICAL SECTION AT TYPE "A" INTERNAL INTERMEDIATE DIAPHRAGM

To be fully installed in the shop.

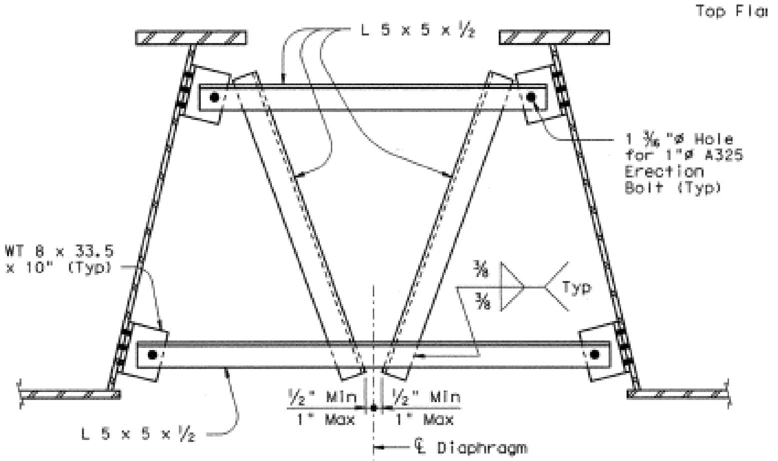

TYPICAL SECTION AT TYPE "B" EXTERNAL INTERMEDIATE DIAPHRAGM (TEMPORARY)

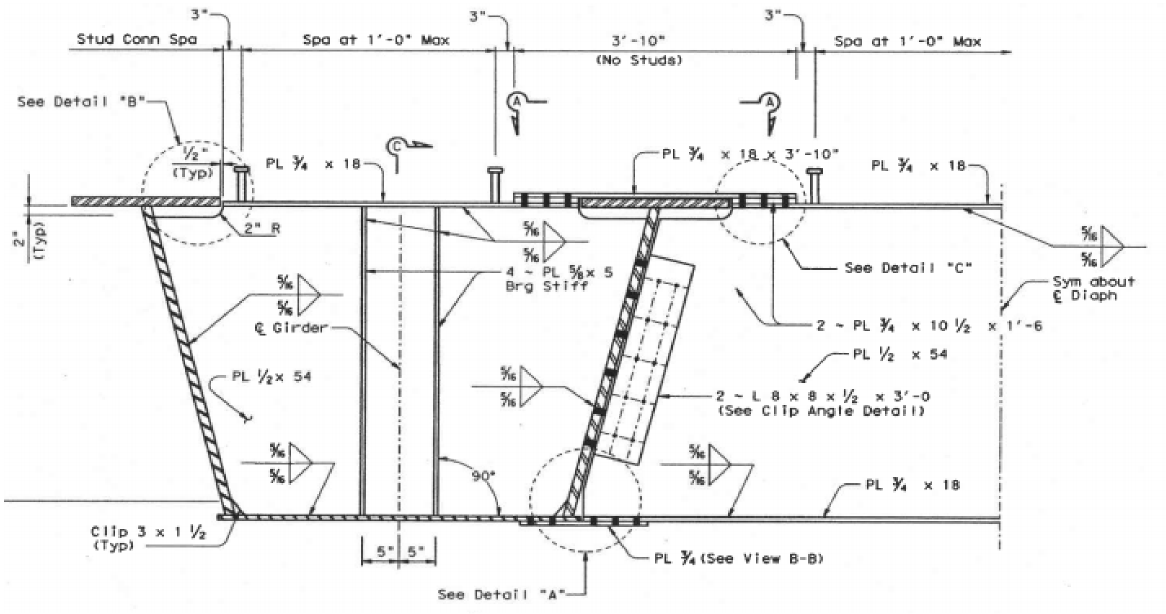
3"
3"
3"
Stud Conn Spa
Spa at 1'-0" Max
3'-10"
(No Studs)
Spa at 1'-0" Max
See Detail "B"
A
A
C
½"
(Typ)
PL ¾ x 18
PL ¾ x 18 x 3'-10"
PL ¾ x 18
2"
(Typ)
2" R
5⁄16
5⁄16
4 ~ PL ⅝ x 5
Brg Stiff
See Detail "C"
5⁄16
5⁄16
Sym about
℄ Diaph
5⁄16
5⁄16
℄ Girder
2 ~ PL ¾ x 10 ½ x 1'-6
PL ½ x 54
PL ½ x 54
5⁄16
5⁄16
2 ~ L 8 x 8 x ½ x 3'-0
(See Clip Angle Detail)
5⁄16
5⁄16
90°
5⁄16
5⁄16
PL ¾ x 18
Clip 3 x 1 ½
(Typ)
5"
5"
PL ¾ (See View B-B)
See Detail "A"

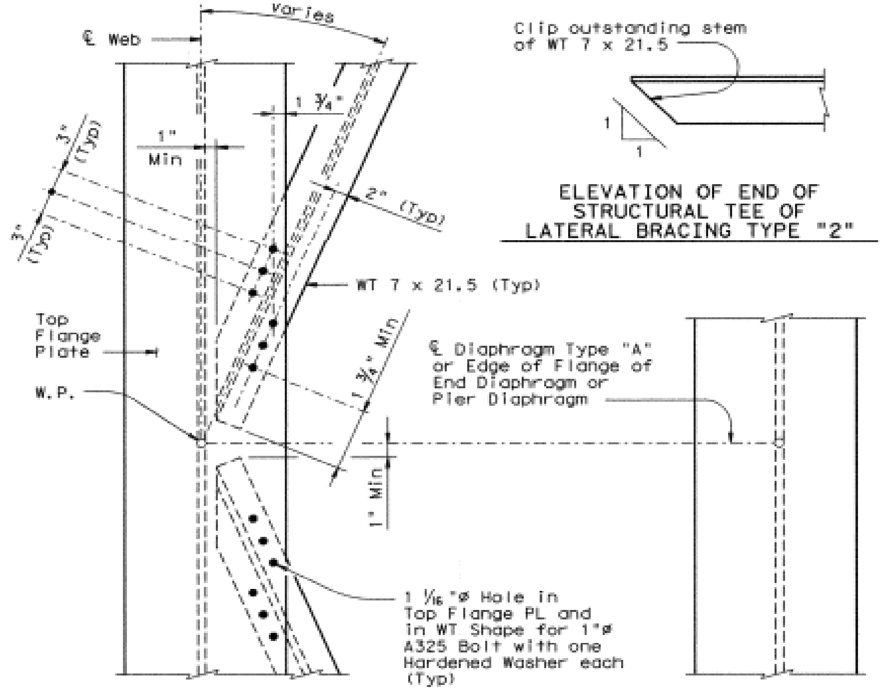

ELEVATION OF END OF
STRUCTURAL TEE OF
LATERAL BRACING TYPE "2"

TYPICAL PLAN VIEW OF
LATERAL BRACING TYPE "2"

Installed in shop except at locations spanning a field splice, which shall be installed in the field.

Bridge 14: 18-057-0-0009-11-460

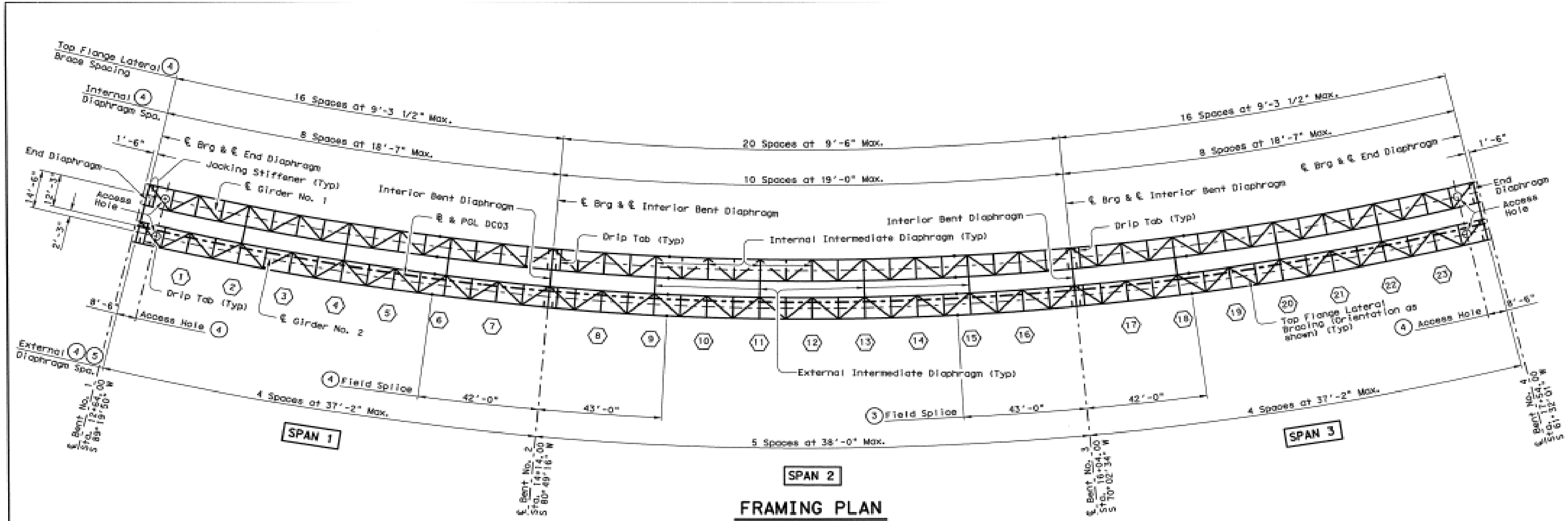

FRAMING PLAN

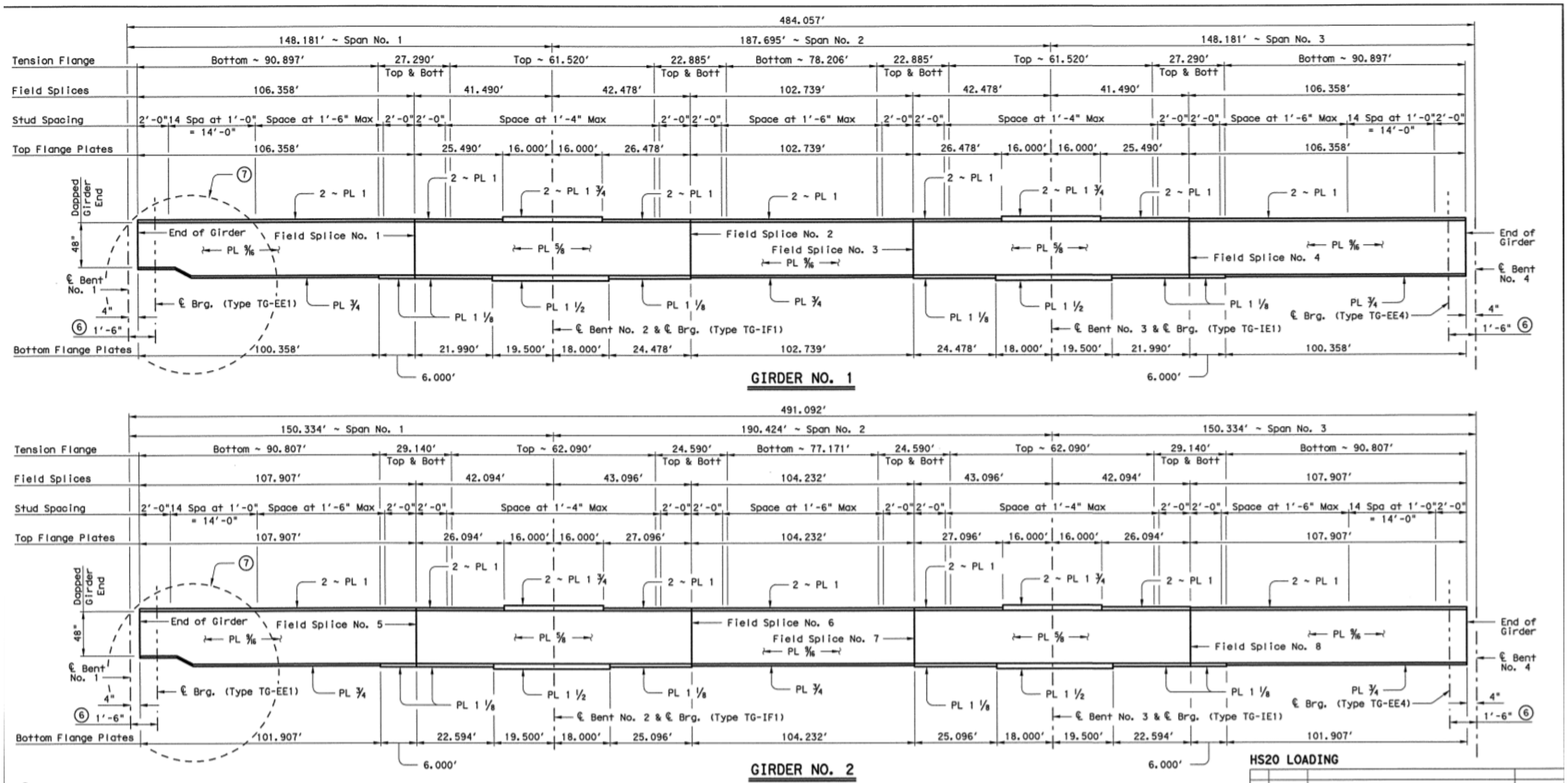

⑥ Measured horizontally at bottom of web along centerline of girder.

⑦ See TRAPEZOIDAL STEEL BOX GIRDER DETAILS, Sheet 3 of 4 for Dapped Girder End Details.

GIRDER ELEVATION

All Web Plates are 60″ deep except at dapped ends.
Web depths are measured perpendicular to flanges.
All Top Flange Plates are 22″ Wide.
All Bottom Flange Plates are 70″ Wide except at dapped ends.

HS20 LOADING

NO.	DATE	REVISION	APPROVED

HDR Engineering, Inc.
17111 Preston Road, Suite 200
Dallas, Texas 75248-1229

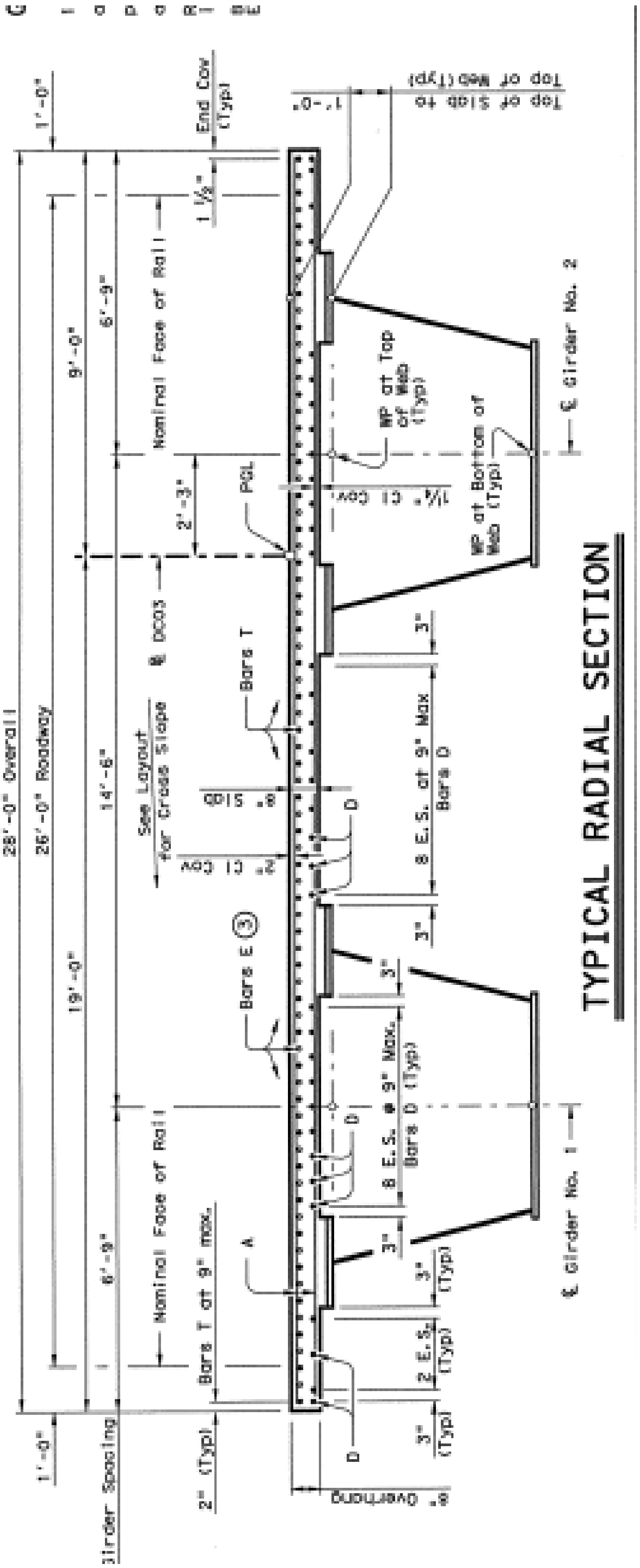

TYPICAL RADIAL SECTION

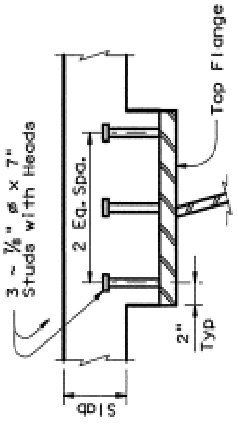

SHEAR CONNECTOR STUD DETAIL

Studs shall be Electric arc end-welded to the flanges with complete fusion. (See Span details for spacing along girder.)

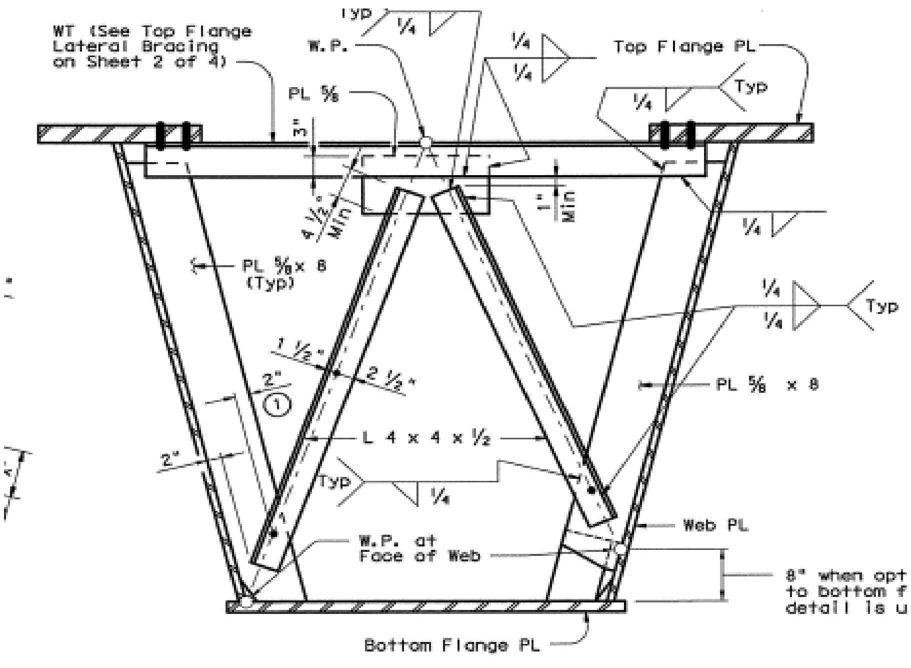

TYPICAL SECTION AT INTERNAL INTERMEDIATE DIAPHRAGM

To be fully installed in the shop.

Note: Apply silicon bead uniformly around edge of access hole cover plate before securing

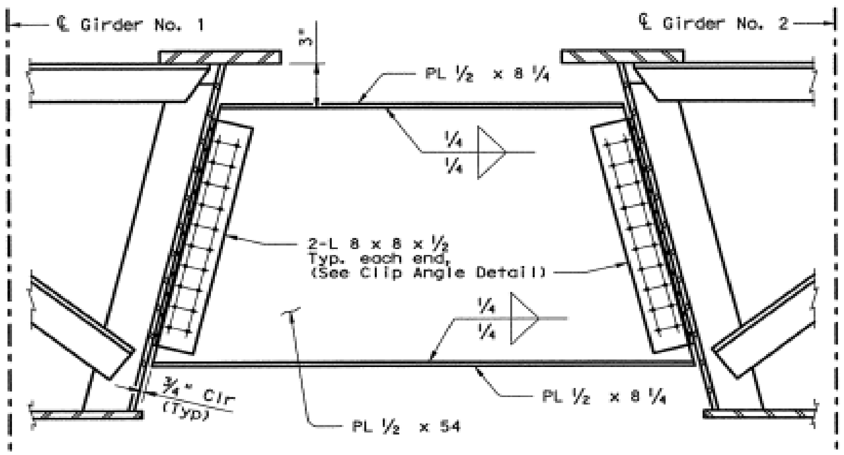

TYPICAL SECTION

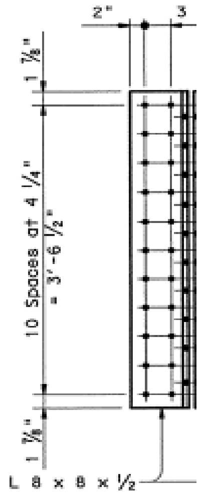

CLIP

EXTERNAL INTERMEDIATE DIAPHRAGM

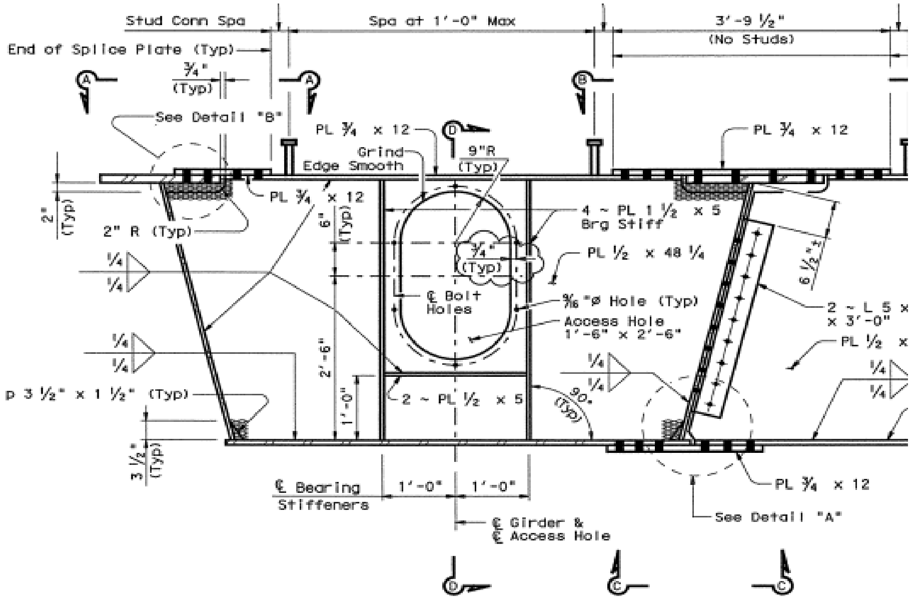

HALF ELEVATION

RAGM DETAILS - BENT NO. 1

TRAPEZOIDAL STEEL BOX GIRDER DETAILS
d Diaphragm Access Hole Cover Plate
e installed at each End Diaphragm)

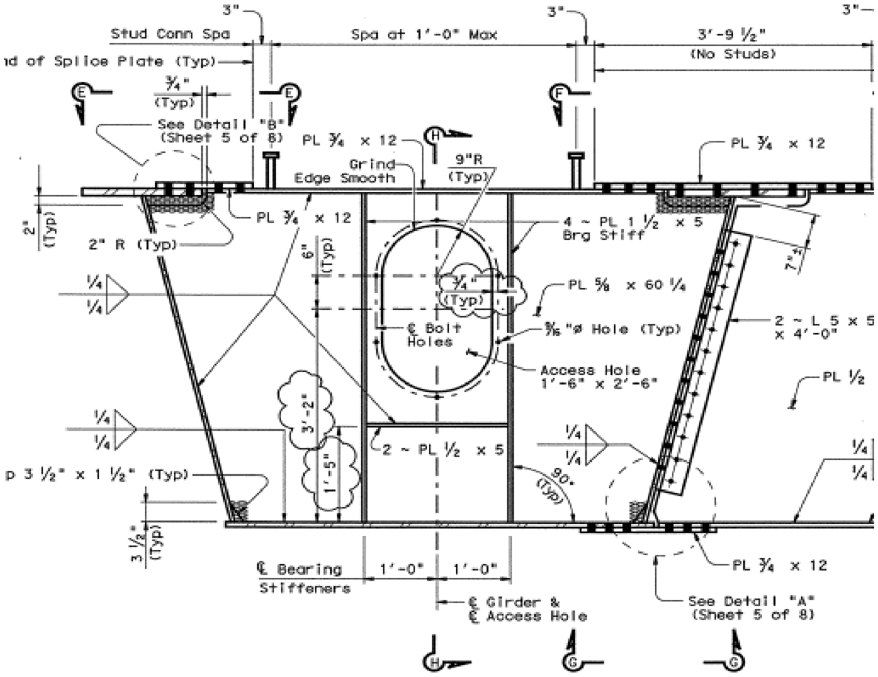

HALF ELEVATION

GM DETAILS - BENT NO. 4

PEZOIDAL STEEL BOX GIRDER DETAILS
Diaphragm Access Hole Cover Plate
installed at each End Diaphragm)

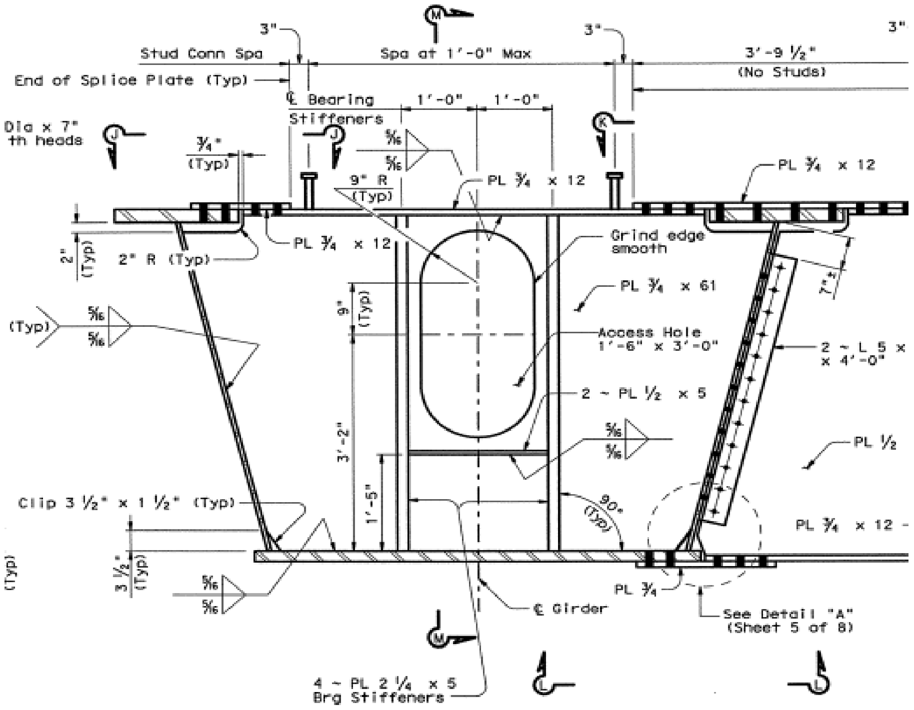

HALF ELEVATION

INTERIOR BENT DIAPHRAGM DETAILS

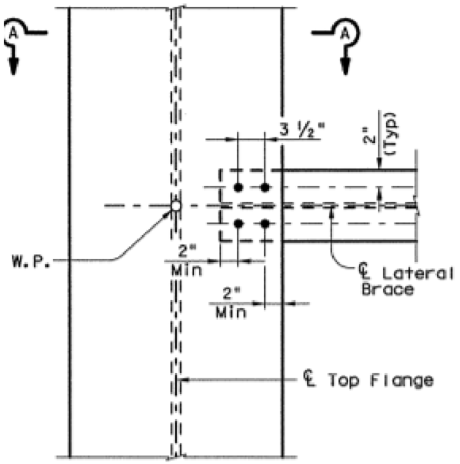

DETAIL 1

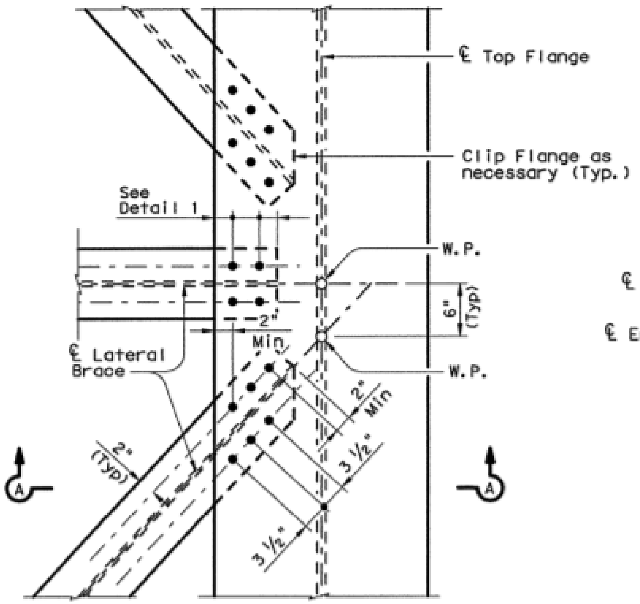

DETAIL 2

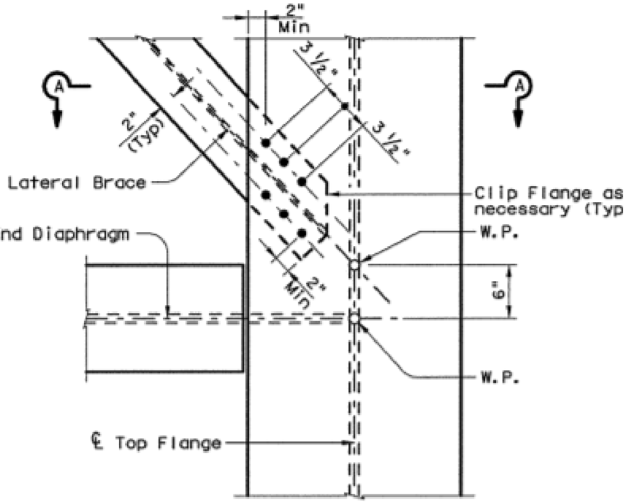

DETAIL 3

LATERAL BRACING CONNECTION DETAILS

Provide 1 $\frac{1}{16}$" Dia Hole in Top Flange PL and in WT Shape at spacing
shown for 1" Dia A325 Type 3 Bolt with one Hardened Washer each (typ.)

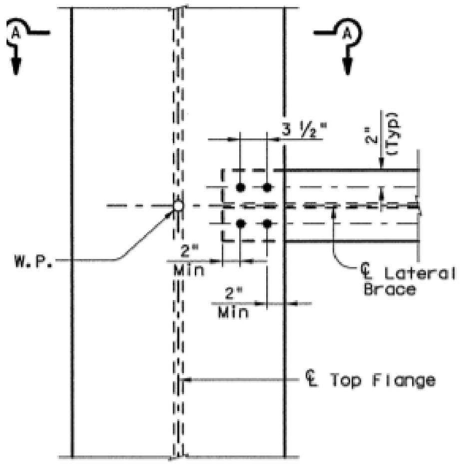

DETAIL 1

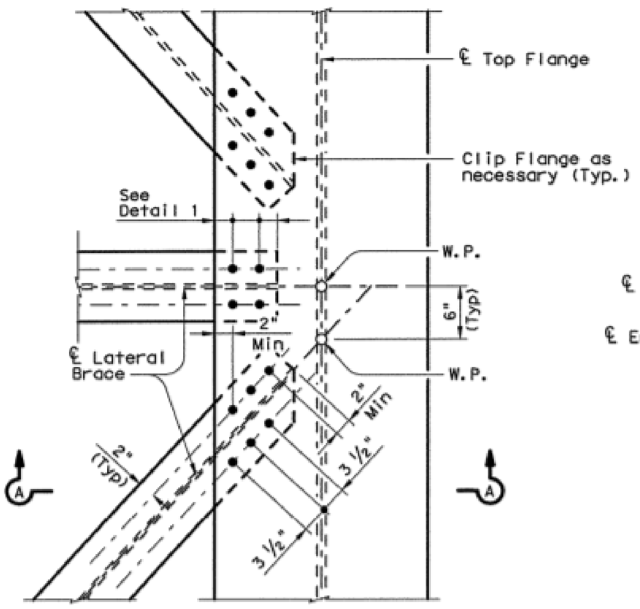

DETAIL 2

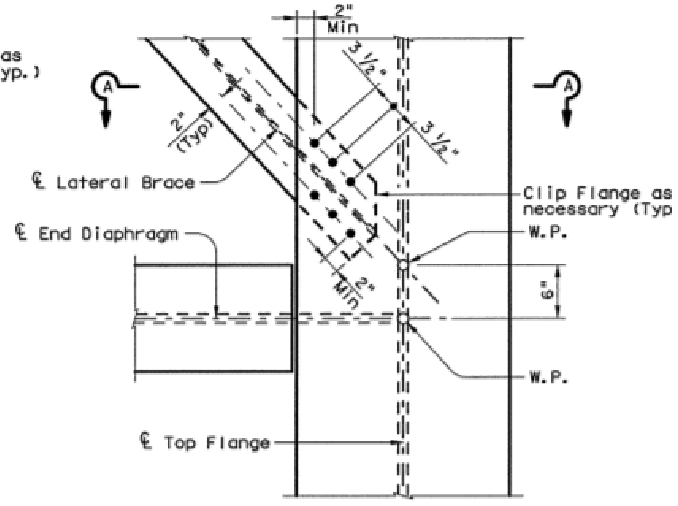

DETAIL 3

LATERAL BRACING CONNECTION DETAILS

Provide 1 ¹⁄₁₆" Dia Hole in Top Flange PL and in WT Shape at spacing shown for 1" Dia A325 Type 3 Bolt with one Hardened Washer each (typ.)

LOCATION	DIAGONAL BRACE	HORIZONTAL STRUT
DC02 - 326.00' UNIT	WT 7 X 30.5	WT 5 X 16.5
DC03 - 490.00' UNIT	WT 7 X 21.5	WT 5 X 16.5
DC03 - 360.00' UNIT	WT 7 X 34	WT 5 X 16.5
DC03 - 310.00' UNIT	WT 7 X 24	WT 5 X 16.5
DC03 - 340.00' UNIT	WT 7 X 34	WT 5 X 16.5
DC04 - 345.00' UNIT	WT 7 X 21.5	WT 5 X 16.5
DC04 - 330.00' UNIT	WT 7 X 21.5	WT 5 X 16.5
DC04 - 663.00' UNIT	WT 7 X 30.5	WT 5 X 16.5

LATERAL BRACING MEMBER SIZES

Bridge 15: 12-102-0271-06-689

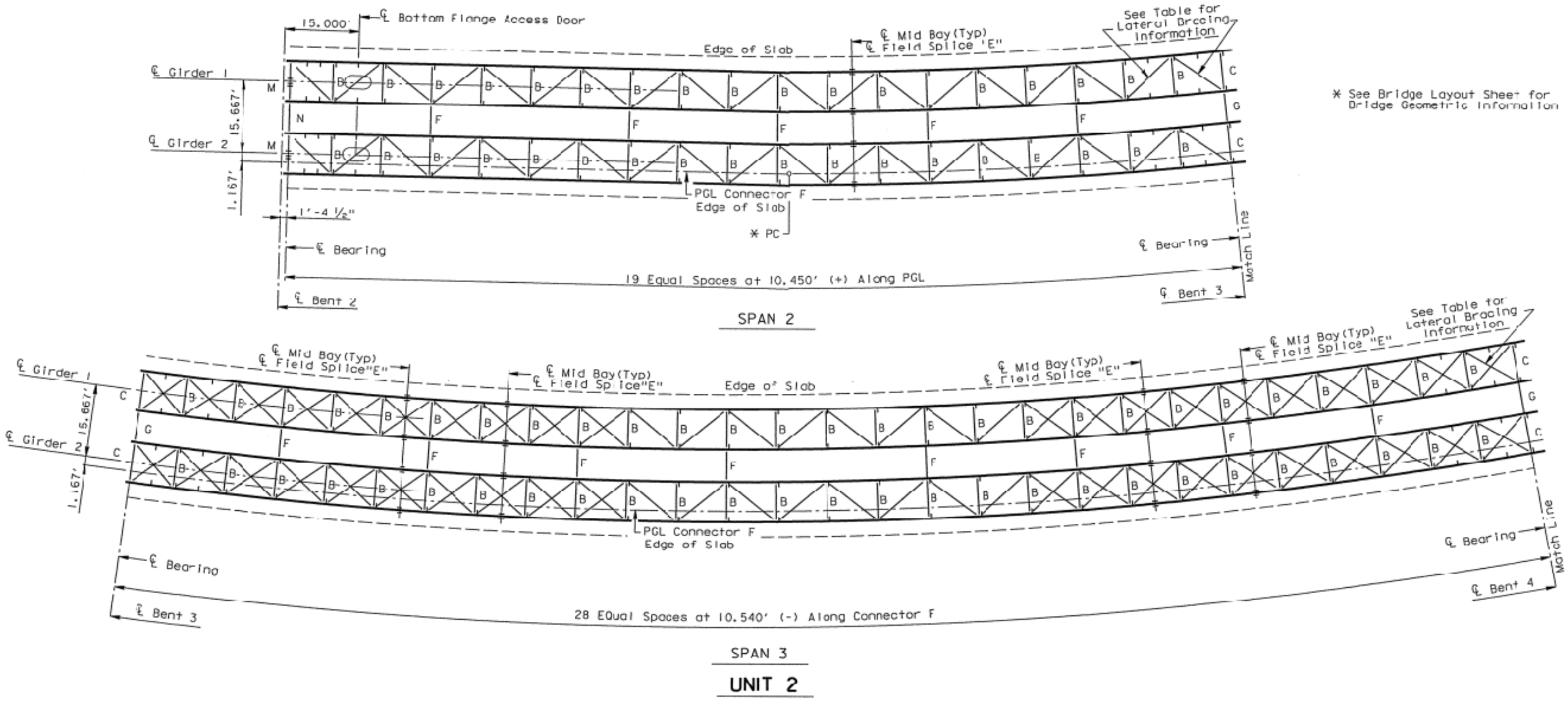

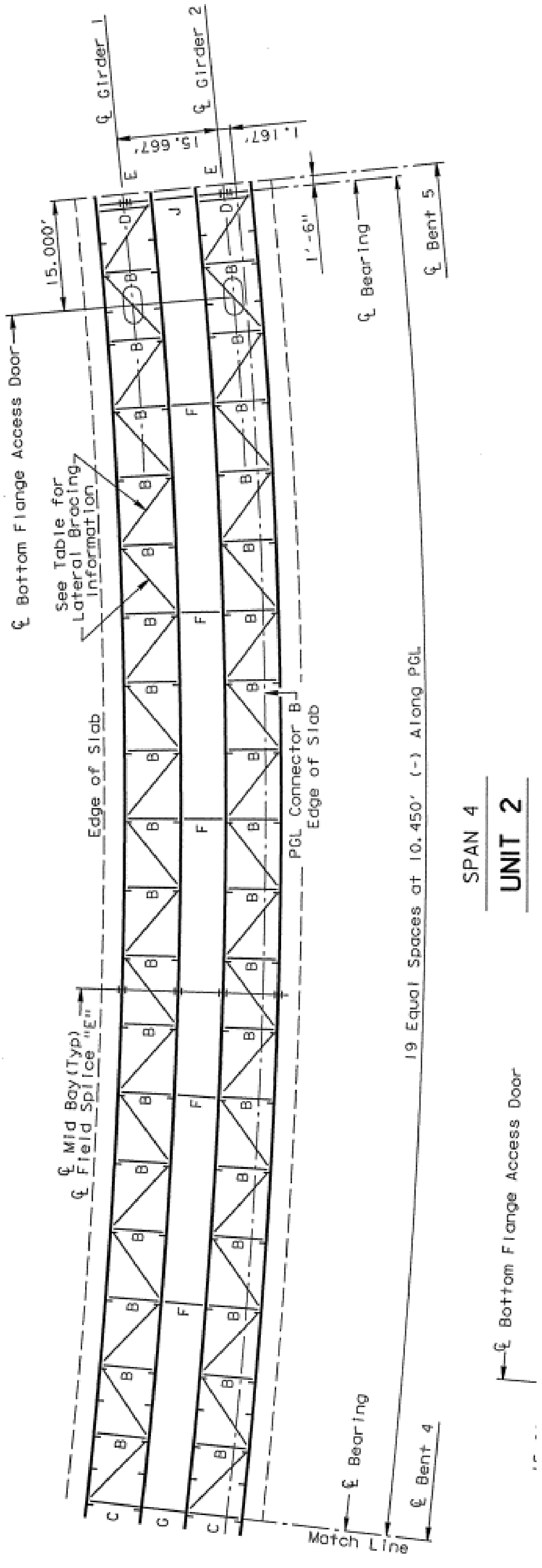
℄ Girder 1
℄ Girder 2
15.667'
1.167'
15.000'
℄ Bottom Flange Access Door
See Table for Lateral Bracing Information
Edge of Slab
PGL Connector B
Edge of Slab
1'-6"
℄ Bearing
℄ Bent 5
19 Equal Spaces at 10.450' (-) Along PGL
℄ Mid Bay (Typ)
℄ Field Splice "E"
℄ Bottom Flange Access Door
℄ Bearing
℄ Bent 4
Match Line
C
G
C
E
E
D
D
J
B
F

SPAN 4

UNIT 2

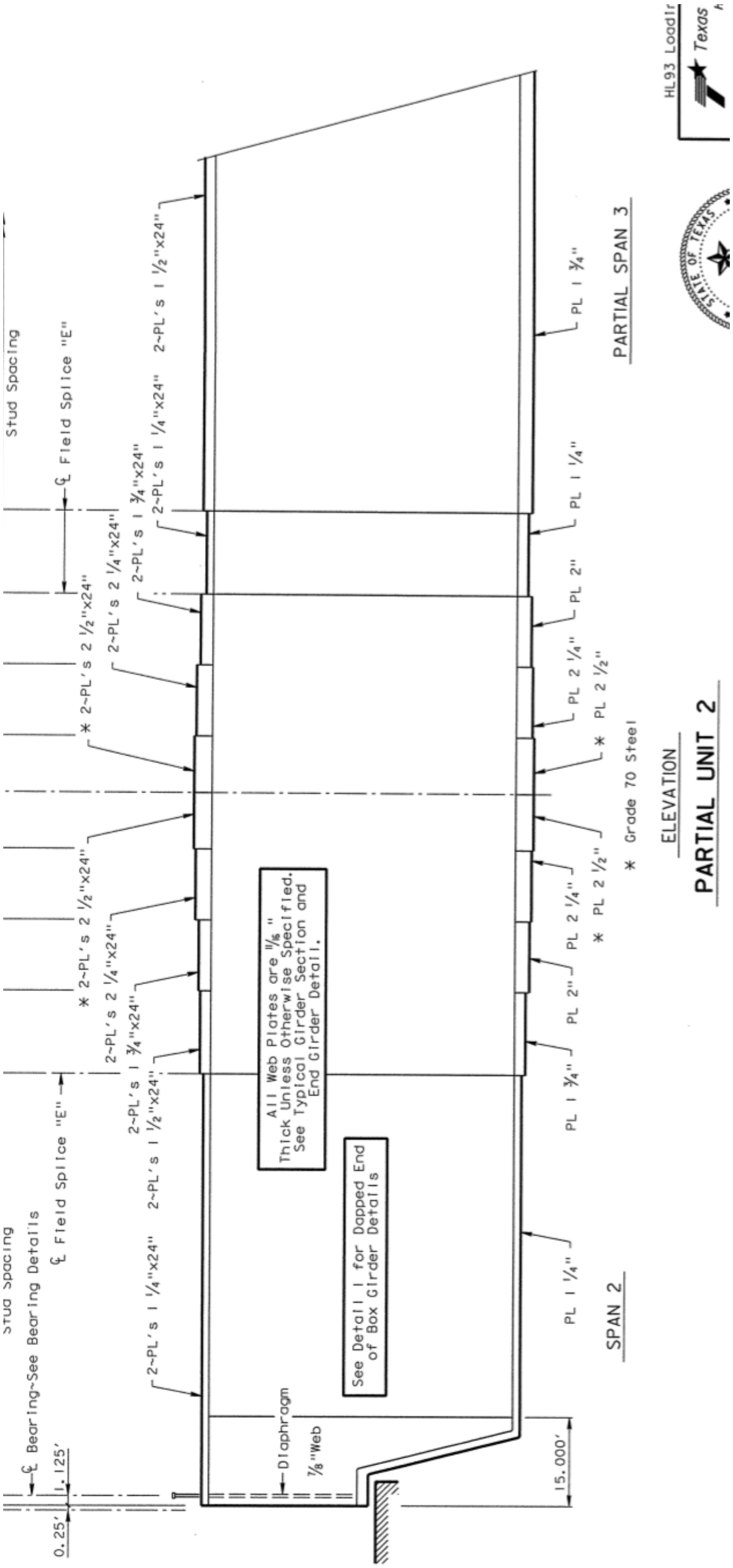

All Web Plates are 11/16" Thick Unless Otherwise Specified. See Typical Girder Section and End Girder Detail.

See Detail I for Dapped End of Box Girder Details

* Grade 70 Steel

ELEVATION

PARTIAL UNIT 2

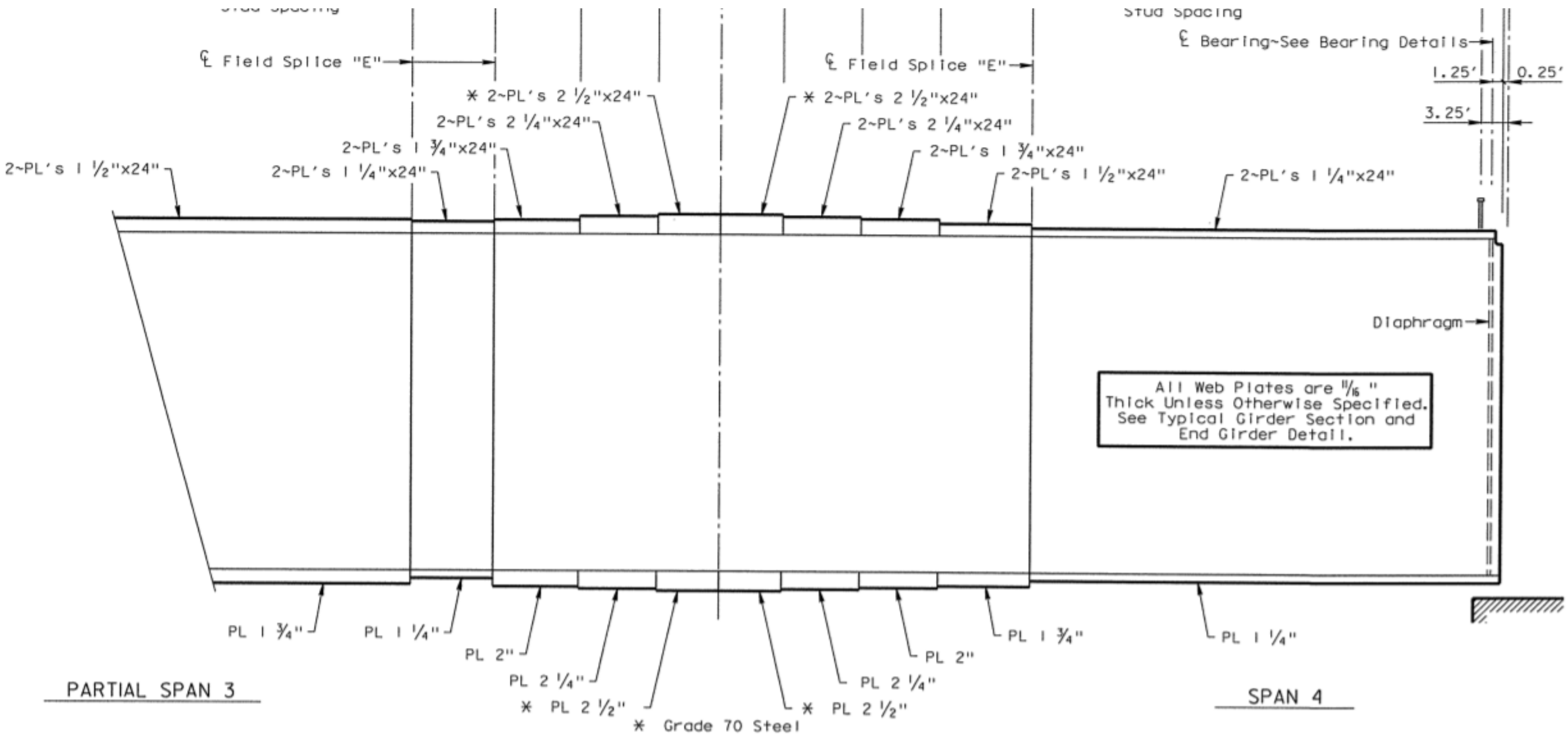

ELEVATION

PARTIAL UNIT 2

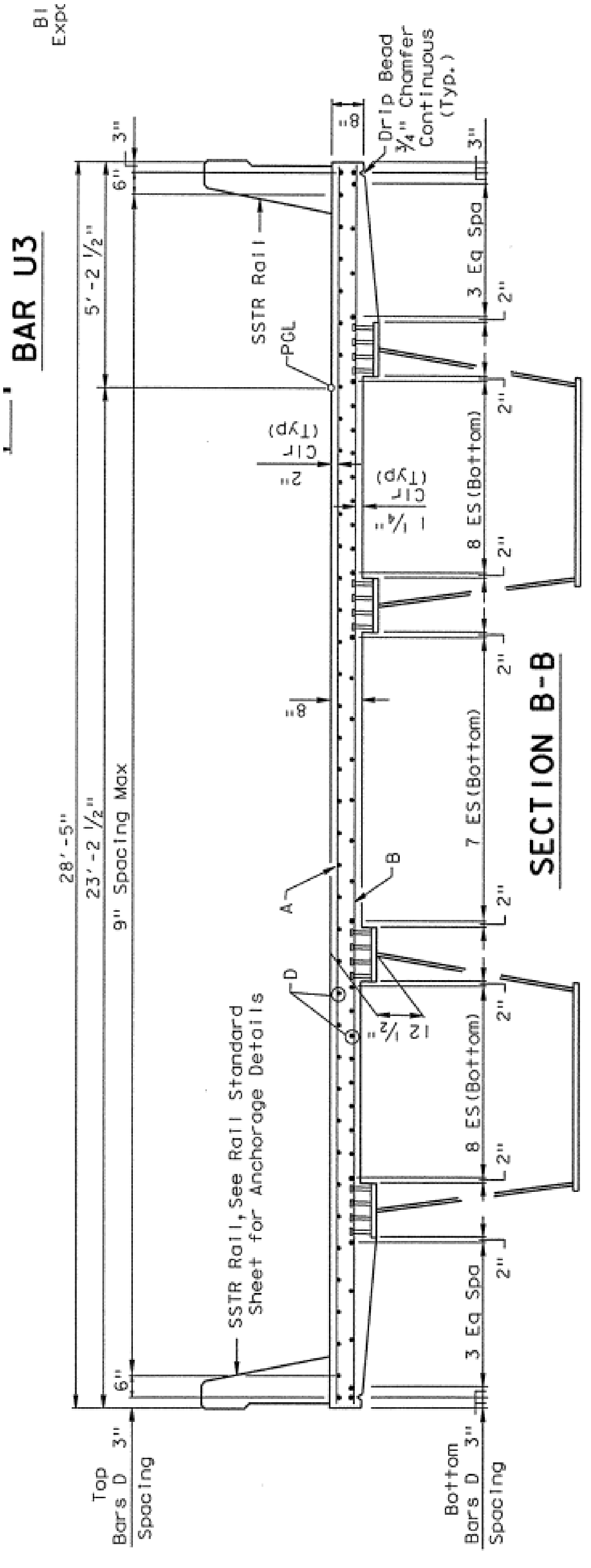

SECTION B-B

Bl
Expc
BAR U3
Drip Bead
¾" Chamfer
Continuous
(Typ.)
8"
3"
6"
5'-2 ½"
SSTR Rail
PGL
2"
Clr
(Typ)
1 ¼"
Clr
(Typ)
3 Eq Spa
2"
8 ES(Bottom)
2"
2"
7 ES(Bottom)
2"
8"
28'-5"
23'-2 ½"
9" Spacing Max
A
B
D
½"
12
8 ES(Bottom)
2"
2"
3 Eq Spa
2"
SSTR Rail, See Rail Standard
Sheet for Anchorage Details
6"
Top
Bars D 3"
Spacing
Bottom
Bars D 3"
Spacing

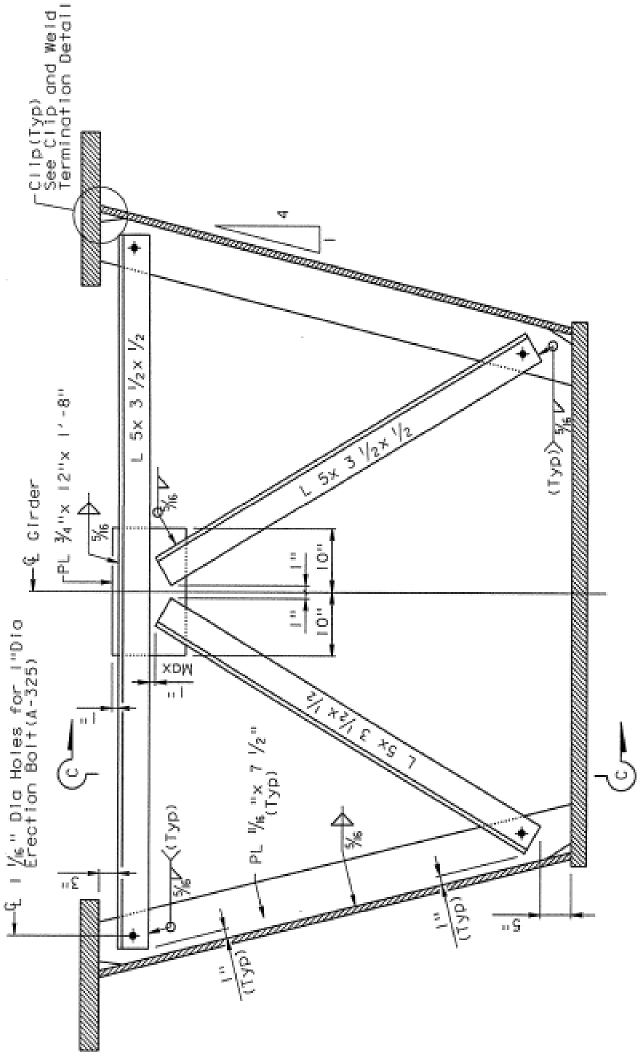

DIAPHRAGM~TYPE B

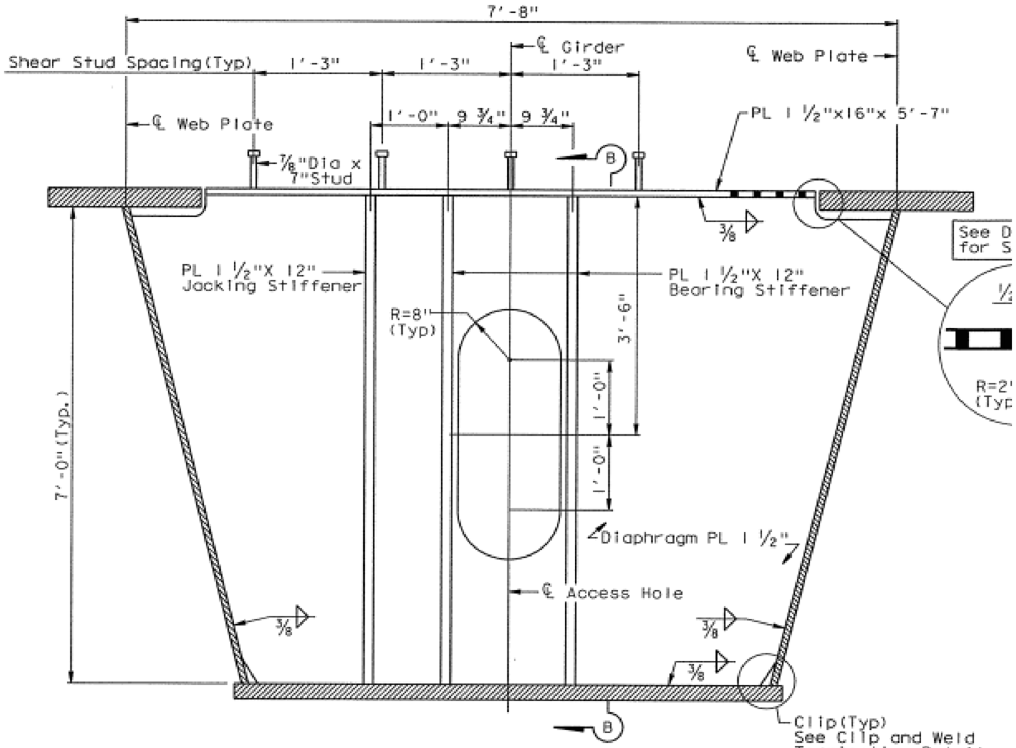

DIAPHRAGM~TYPE C

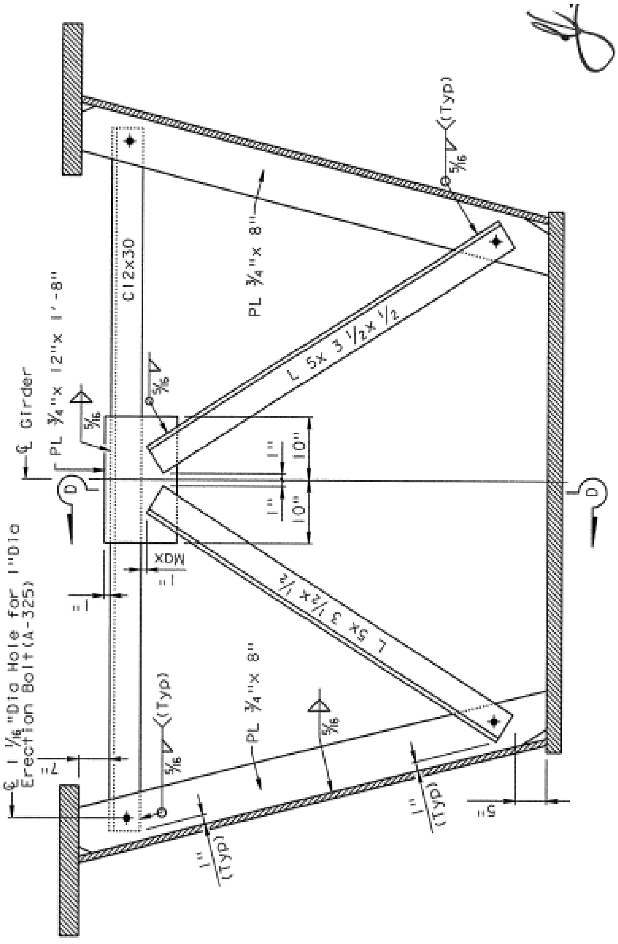

DIAPHRAGM~TYPE D

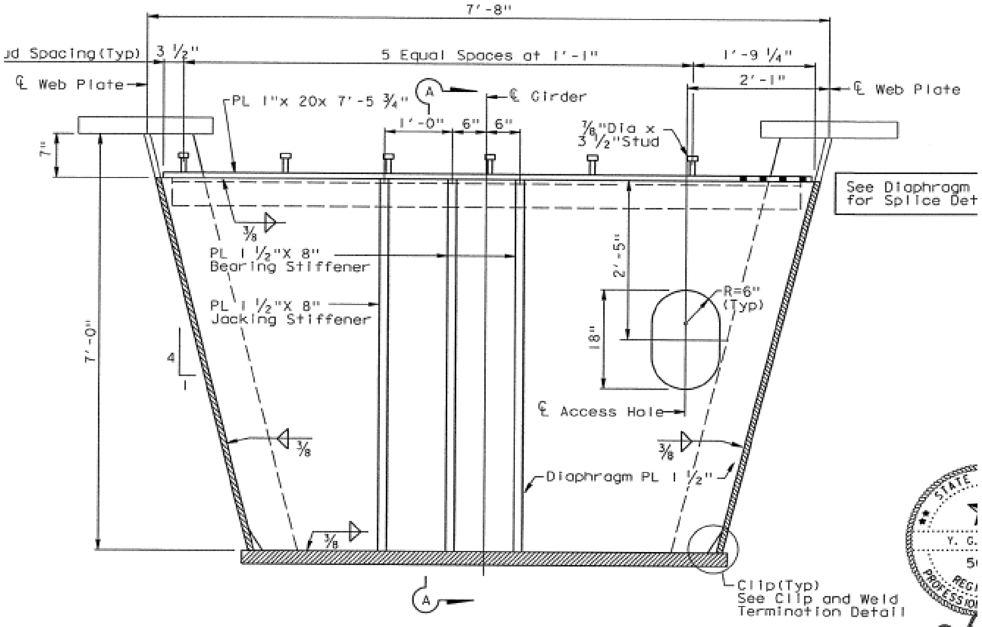

ELEVATION

DIAPHRAGM~TYPE E

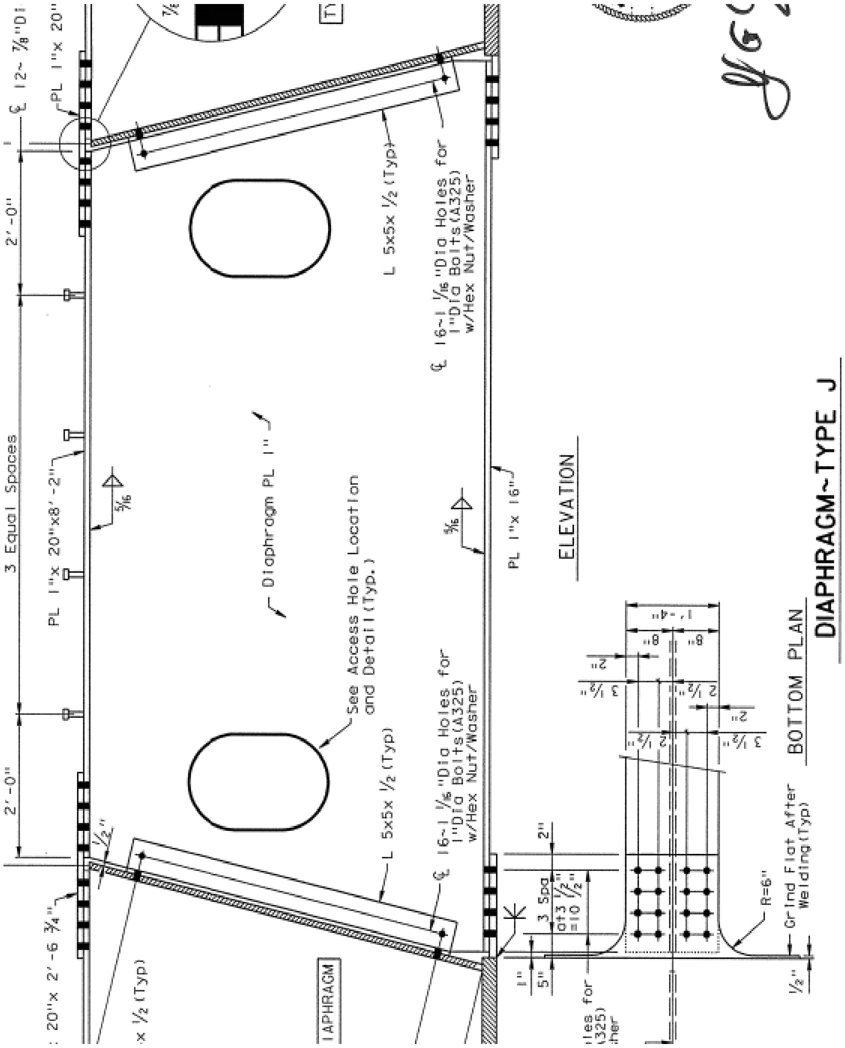
DIAPHRAGM~TYPE J
ELEVATION
BOTTOM PLAN
3 Equal Spaces
2'-0"
2'-0"
℄ 12~ 7/8"Di
PL 1"x 20"
PL 1"x 20"x8'-2"
PL 1"x 20"x 2'-6 3/4"
5/16
Diaphragm PL 1"
See Access Hole Location and Detail (Typ.)
L 5x5x 1/2 (Typ)
L 5x5x 1/2 (Typ)
x 1/2 (Typ)
℄ 16~1 1/16"Dia Holes for 1"Dia Bolts(A325) w/Hex Nut/Washer
℄ 16~1 1/16"Dia Holes for 1"Dia Bolts(A325) w/Hex Nut/Washer
les for (325) sher
PL 1"x 16"
1/2"
IAPHRAGM
TY
1'-4"
8"
8"
2"
3 1/2"
2 1/2"
2 1/2"
3 1/2"
2"
2"
3 Spa @ 3 1/2" =10 1/2"
1"
5"
R=6"
Grind Flat After Welding (Typ)
1/2"

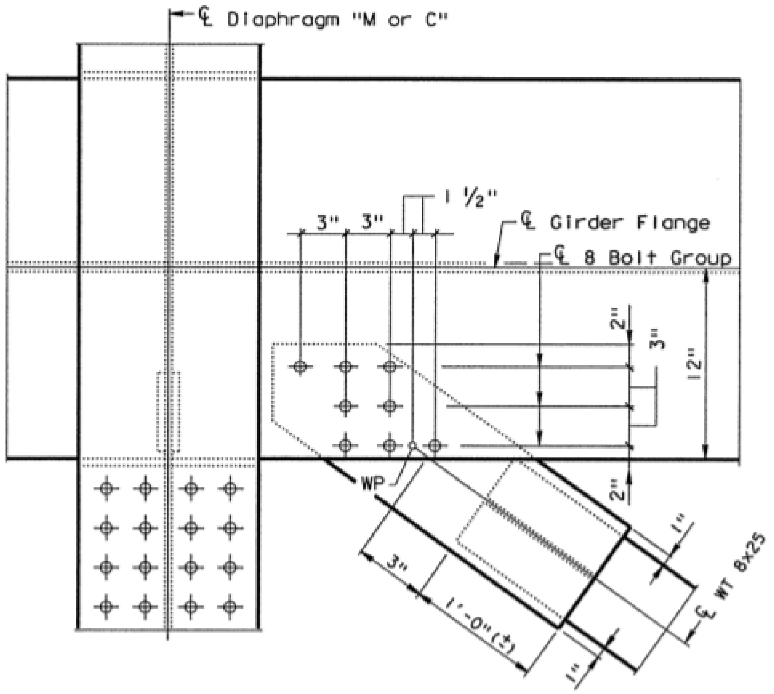

LATERAL BRACING CONNECTION DETAIL "4"

APPENDIX B. GRILLAGE

Bridge 1: Hinge and Section Data

	Long. Ext. 1.1		**Long. Int. 1.1**		**Long. Ext. 2.1**		**Long. Int. 2.1**	
	M	***C***	***M***	***C***	***M***	***C***	***M***	***C***
Positive SF	325620	5.8E-05	301909	0.00019	409992	6E-05	382836	0.0002
Negative SF	198418	5.8E-05	203118	6.4E-05	267269	6E-05	272043	6.7E-05
Normalized Moment Curvature	-1.36	-35	-1.38	-35	-1.36	-35	-1.38	-35
	-1.36	-23	-1.38	-23	-1.36	-23	-1.38	-23
	-1	-1	-1	-1	-1	-1	-1	-1
	-0.75	-0.56	-0.8	-0.56	-0.7	-0.56	-0.8	-0.56
	0	0	0	0	0	0	0	0
	0.92	0.56	0.87	0.19	0.95	0.56	0.91	0.25
	1	1	1	1	1	1	1	1
	1	3	1	3	1	3	1	3
	1	13	1	13	1	13	1	13

	Frac. Ext. 1.1		**Frac. Int. 1.1**		**Trans.**		**Trans. End**	
	M	***C***	***M***	***C***	***M***	***C***	***M***	***C***
Positive SF	12736	1.14E-04	1730	2.42E-03	1910	0.00187	371	0.00187
Negative SF	1915	5.15E-04	2066	5.37E-04	1640	0.00187	316	0.00187
Normalized Moment Curvature	-1	-35	-1	-20	-1	-30	-1	-30
	-1	-23	-1	-10	-1	-22	-1	-22
	-1	-1	-1	-5	-1	-1	-1	-1
	-0.91	-0.22	-1	-1	-0.76	-0.22	-0.76	-0.22
	0	0	0	0	0	0	0	0
	1	1	0.88	0.22	0.76	0.22	0.77	0.14
	1	3	1	1	1	1	1	1
	1	5	1	5	1	3	1	3
	1	15	1	15	1	13	1	13

Note: M = moment (kip-in.) and C = curvature (1/in.).

Section	**Start (ft)**	**End (ft)**
1.1	0	47
2.1	47	166
1.1	166	220

Bridge 2: Hinge and Section Data

	Long. Ext. 1.1		**Long. Int. 1.1**		**Frac. Ext. 1.1**		**Frac. Int. 1.1**	
	M	***C***	***M***	***C***	***M***	***C***	***M***	***C***
Positive SF	250798	5.96E-05	221238	0.000154	13209	1.05E-04	1130	2.45E-3
Negative SF	144085	5.96E-05	142720	6.91E-05	1844	7.36E-04	1611	5.44E-4
Normalized Moment Curvature	-1.35	-35	-1.38	-35	-1	-35	-1	-20
	-1.35	-25	-1.38	-25	-1	-22	-1	-10
	-1	-1	-1	-1	-1	-1	-1	-1
	-0.72	-0.56	-0.8	-0.56	-0.76	-0.36	-1	-1
	0	0	0	0	0	0	0	0
	0.91	0.56	0.955	0.45	1	1	0.98	0.56
	1	1	1	1	1	3	1	1
	1	3	1	3	1	5	1	5
	1	13	1	13	1	15	1	15

	Trans.		**8.1.1.1.1.1.1.1 Trans. End**	
	M	***C***	***M***	***C***
Positive SF	1970	0.00168	1367	0.00168
Negative SF	1598	0.00168	1104	0.00168
Normalized Moment Curvature	-1.1	-25	-1.1	-25
	-1.1	-15	-1.1	-15
	-1	-1	-1	-1
	-0.76	-0.22	-0.76	-0.22
	0	0	0	0
	0.76	0.22	0.76	0.22
	1	1	1	1
	1	3	1	3
	1	13	1	13

Note: M = moment (kip-in.) and C = curvature (1/in.).

Section	**Start (ft)**	**End (ft)**
1.1	0	115

Bridge 3: Hinge and Section Data

	Long. Ext. 1.1		**Long. Int. 1.1**		**Long. Ext. 2.1**		**Long. Int. 2.1**	
	M	***C***	***M***	***C***	***M***	***C***	***M***	***C***
Positive SF	469639	7.72E-05	454024	0.000203	556185	7.86E-05	539178	0.00016
Negative SF	303757	4.96E-05	314564	5.22E-05	407572	5.05E-05	417493	5.3E-05
Normalized Moment Curvature	-1.36	-35	-1.37	-35	-1.37	-35	-1.38	-35
	-1.36	-23	-1.37	-23	-1.37	-23	-1.38	-23
	-1	-1	-1	-1	-1	-1	-1	-1
	-0.75	-0.56	-0.8	-0.56	-0.7	-0.56	-0.8	-0.56
	0	0	0	0	0	0	0	0
	0.88	0.36	0.85	0.14	0.91	0.36	0.96	0.33
	1	1	1	1	1	1	1	1
	1	3	1	3	1	3	1	3
	1	13	1	13	1	13	1	13

	Long. Ext. 3.1		**Long. Int. 3.1**		**Frac. Ext. 3.1**		**Frac. Int. 3.1**	
	M	***C***	***M***	***C***	***M***	***C***	***M***	***C***
Positive SF	720943	5.36E-05	707906	0.000125	13389	1.30E-4	2978	1.99E-3
Negative SF	528265	5.36E-05	540368	5.62E-05	2402	5.84E-4	2835	4.43E-4
Normalized Moment Curvature	-1.37	-35	-1.38	-35	-1	-35	-1	-20
	-1.37	-23	-1.38	-23	-1	-23	-1	-10
	-1	-1	-1	-1	-1	-1	-1	-3
	-0.7	-0.56	-0.8	-0.56	-0.9	-0.22	-1	-1
	0	0	0	0	0	0	0	0
	0.91	0.36	0.91	0.25	1	1	0.86	0.22
	1	1	1	1	1	3	1	1
	1	3	1	3	1	5	1	5
	1	13	1	13	1	15	1	15

Note: M = moment (kip-in.) and C = curvature (1/in.).

	Trans		Trans End	
	M	***C***	***M***	***C***
Positive SF	2325	0.002166	2166	0.002166
Negative SF	1937	0.002166	1814	0.002166
Normalized Moment Curvature	-1.12	-30	-1.15	-30
	-1.12	-13	-1.15	-20
	-1	-1	-1	-1
	-0.76	-0.22	-0.76	-0.22
	0	0	0	0
	0.77	0.14	0.77	0.14
	1	1	1	1
	1	3	1	3
	1	13	1	13

Note: M = moment (kip-in.) and C = curvature (1/in.).

Section	**Start (ft)**	**End (ft)**
1.1	0	17
2.1	17	38
3.1	38	185
2.1	185	206
1.1	206	230

Bridge 4: Hinge and Section Data

	Long. Ext. 1.1		**Long. Int. 1.1**		**Long. Ext. 2.2**		**Long. Int. 2.2**	
	M	***C***	***M***	***C***	***M***	***C***	***M***	***C***
Positive SF	190121	8.16E-05	163477	0.000285	265333	4.94E-05	242505	0.00016
Negative SF	97566	8.16E-05	102225	9.49E-05	143129	8.89E-05	147628	0.0001
Normalized Moment Curvature	-1.35	-35	-1.35	-35	-1.4	-30	-1.4	-30
	-1.35	-25	-1.35	-25	-1.4	-20	-1.4	-20
	-1	-1	-1	-1	-1	-1	-1	-1
	-0.7	-0.56	-0.8	-0.56	-0.86	-0.56	-0.92	-0.56
	0	0	0	0	0	0	0	0
	0.95	0.56	0.89	0.19	0.54	0.4	0.94	0.36
	1	1	1	1	1	1	1	1
	1	3	1	3	1	3	1	3
	1	13	1	13	1	13	1	13

	Long. Ext. 3.2		**Long. Int. 3.2**		**Frac. Ext. 1.1**		**Frac. Int. 1.1**	
	M	***C***	***M***	***C***	***M***	***C***	***M***	***C***
Positive SF	269552	8.63E-05	248898	0.00022	11005	1.04E-4	1361	2.26E-3
Negative SF	199102	8.63E-05	201214	9.89E-05	1607	4.66E-4	1740	5.03E-4
Normalized Moment Curvature	-1.35	-35	-1.35	-35	-1	-35	-1	-20
	-1.35	-25	-1.35	-25	-1	-25	-1	-10
	-1	-1	-1	-1	-1	-1	-1	-3
	-0.7	-0.56	-0.89	-0.56	-0.92	-0.22	-1	-1
	0	0	0	0	0	0	0	0
	0.95	0.56	0.93	0.25	1	1	1	1
	1	1	1	1	1	3	1	3
	1	3	1	3	1	5	1	5
	1	13	1	13	1	15	1	15

Note: M = moment (kip-in.) and C = curvature (1/in.).

	Trans		**Trans End 1**		**Trans End 2**		**Trans Pier**	
	M	***C***	***M***	***C***	***M***	***C***	***M***	***C***
Positive SF	2107	0.00152	1971	0.00152	1325	0.00152	3400	0.00152
Negative SF	1745	0.00152	1633	0.00152	1094	0.00152	2822	0.00152
Normalized Moment Curvature	-1.2	-25	-1.2	-25	-1.2	-25	-1.2	-25
	-1.2	-15	-1.2	-15	-1.2	-15	-1.2	-15
	-1	-1	-1	-1	-1	-1	-1	-1
	-0.76	-0.22	-0.76	-0.22	-0.76	-0.22	-0.76	-0.22
	0	0	0	0	0	0	0	0
	0.76	0.22	0.76	0.22	0.76	0.22	0.76	0.22
	1	1	1	1	1	1	1	1
	1	3	1	3	1	3	1	3
	1	13	1	13	1	13	1	13

Note: M = moment (kip-in.) and C = curvature (1/in.).

Section	**Start (ft)**	**End (ft)**
1.1	0	80
2.2	80	108
3.2	108	154
2.2	154	182
1.1	182	260

Bridge 5: Hinge and Section Data

	Long. Ext. 1.1		**Long. Int. 1.1**		**Long. Ext. 2.2**		**Long. Int. 2.2**	
	M	***C***	***M***	***C***	***M***	***C***	***M***	***C***
Positive SF	130422	0.000132	126415	0.000343	177826	0.000141	175804	0.000284
Negative SF	80979	8.46E-05	84913	8.83E-05	115300	9.08E-05	120784	9.48E-05
Normalized Moment Curvature	-1.35	-35	-1.35	-35	-1.35	-35	-1.35	-35
	-1.35	-25	-1.35	-25	-1.35	-25	-1.35	-25
	-1	-1	-1	-1	-1	-1	-1	-1
	-0.7	-0.56	-0.8	-0.56	-0.7	-0.56	-0.8	-0.56
	0	0	0	0	0	0	0	0
	0.97	0.64	0.85	0.14	0.936	0.36	0.85	0.14
	1	1	1	1	1	1	1	1
	1	3	1	3	1	3	1	3
	1	13	1	13	1	13	1	13

	Long. Ext. 3.2		**Long. Int. 3.2**		**Long. Ext. 4.2**		**Long. Int. 4.2**	
	M	***C***	***M***	***C***	***M***	***C***	***M***	***C***
Positive SF	180799	0.000138	178975	0.00027	204632	0.000139	203853	0.000278
Negative SF	136766	8.88E-05	139570	9.23E-05	161921	8.93E-05	164301	9.26E-05
Normalized Moment Curvature	-1.35	-35	-1.38	-35	-1.4	-35	-1.42	-35
	-1.35	-25	-1.38	-25	-1.4	-25	-1.42	-25
	-1	-1	-1	-1	-1	-1	-1	-1
	-0.7	-0.56	-0.8	-0.56	-0.7	-0.56	-0.8	-0.56
	0	0	0	0	0	0	0	0
	0.936	0.36	0.85	0.14	0.936	0.36	0.85	0.14
	1	1	1	1	1	1	1	1
	1	3	1	3	1	3	1	3
	1	13	1	13	1	13	1	13

Note: M = moment (kip-in.) and C = curvature (1/in.).

	Frac. Ext. 1.1		**Frac. Int. 1.1**		**Trans/Trans Pier**		**Trans End 1&2**	
	M	***C***	***M***	***C***	***M***	***C***	***M***	***C***
Positive SF	5557	2.32E-4	1612	2.61E-3	1876	0.00168	890	0.00168
Negative SF	1615	5.81E-4	1868	5.80E-4	1513	0.00168	714	0.00168
Normalized Moment Curvature	-1	-35	-1	-20	-1.1	-25	-1.1	-25
	-1	-20	-1	-10	-1.1	-15	-1.1	-15
	-1	-1	-1	-1	-1	-1	-1	-1
	-0.83	-0.4	-1	-1	-0.76	-0.22	-0.76	-0.22
	0	0	0	0	0	0	0	0
	1	1	0.84	0.22	0.76	0.22	0.76	0.22
	1	3	1	1	1	1	1	1
	1	5	1	5	1	3	1	3
	1	15	1	15	1	13	1	13

Note: M = moment (kip-in.) and C = curvature (1/in.).

Section	**Start (ft)**	**End (ft)**
1.1	0	91
2.2	91	112
3.2	112	126
4.2	126	147
3.2	147	161
2.2	161	182
1.1	182	280

Bridge 6: Hinge and Section Data

	Long. Ext. 1.1		**Long. Int. 1.1**		**Long. Ext. 2.2**		**Long. Int. 2.2**	
	M	***C***	***M***	***C***	***M***	***C***	***M***	***C***
Positive SF	326511	6.38E-05	300556	0.000159	473215	7.08E-05	438043	8.05E-05
Negative SF	175770	6.38E-05	178676	7.16E-05	226048	7.08E-05	232720	8.05E-05
Normalized Moment Curvature	-1.37	-35	-1.38	-35	-1.4	-35	-1.45	-35
	-1.37	-25	-1.38	-25	-1.4	-20	-1.45	-17
	-1	-1	-1	-1	-1	-1	-1	-1
	-0.7	-0.56	-0.8	-0.56	-0.7	-0.56	-0.8	-0.56
	0	0	0	0	0	0	0	0
	0.97	0.64	0.85	0.14	0.936	0.36	0.85	0.14
	1	1	1	1	1	1	1	1
	1	3	1	3	1	3	1	3
	1	13	1	13	1	13	1	13

	Long. Ext. 3.2		**Long. Int. 3.2**		**Frac. Ext. 1.1**		**Frac. Int. 1.1**	
	M	***C***	***M***	***C***	***M***	***C***	***M***	***C***
Positive SF	481552	6.91E-05	451631	0.000121	15849	1.23E-4	1915	2.55E-3
Negative SF	294883	6.91E-05	302235	7.76E-05	2130	5.55E-4	1139	3.96E-3
Normalized Moment Curvature	-1.38	-35	-1.36	-35	-1	-35	-1	-20
	-1.38	-20	-1.36	-19	-1	-20	-1	-12
	-1	-1	-1	-1	-1	-1	-1	-2
	-0.7	-0.56	-0.8	-0.56	-0.83	-0.56	-1	-1
	0	0	0	0	0	0	0	0
	0.936	0.36	0.85	0.14	1	1	0.97	0.56
	1	1	1	1	1	1	1	1
	1	3	1	3	1	5	1	5
	1	13	1	13	1	15	1	15

Note: M = moment (kip-in.) and C = curvature (1/in.).

	Trans/Trans Pier		**Trans End 1 & 2**	
	M	***C***	***M***	***C***
Positive SF	2422	0.0016	1211	0.0016
Negative SF	2023	0.0016	1011	0.0016
Normalized Moment Curvature	-1.15	-25	-1.15	-25
	-1.15	-15	-1.15	-15
	-1	-1	-1	-1
	-0.76	-0.22	-0.76	-0.22
	0	0	0	0
	0.76	0.22	0.76	0.22
	1	1	1	1
	1	3	1	3
	1	13	1	13

Note: M = moment (kip-in.) and C = curvature (1/in.).

Section	**Start (ft)**	**End (ft)**
1.1	0	98
2.2	98	119
3.2	119	154
2.2	154	175
1.1	175	280

Bridge 7: Hinge and Section Data

	Long. Ext. 1.1		**Long. Int. 1.1**		**Long. Ext. 2.1**		**Long. Int. 2.1**	
	M	***C***	***M***	***C***	***M***	***C***	***M***	***C***
Positive SF	213076	7.09E-05	188227	0.000244	354649	7.85E-05	323880	0.000141
Negative SF	121565	7.09E-05	120700	8.12E-05	226366	7.85E-05	225805	9.03E-05
Normalized Moment Curvature	-1.35	-35	-1.37	-35	-1.35	-35	-1.35	-35
	-1.35	-25	-1.37	-25	-1.35	-25	-1.35	-20
	-1	-1	-1	-1	-1	-1	-1	-1
	-0.7	-0.56	-0.8	-0.56	-0.7	-0.56	-0.8	-0.56
	0	0	0	0	0	0	0	0
	0.97	0.64	0.87	0.19	0.936	0.36	0.93	0.36
	1	1	1	1	1	1	1	1
	1	3	1	3	1	3	1	3
	1	13	1	13	1	13	1	13

	Long. Ext. 3.1		**Long. Int. 3.1**		**Long. Ext. 3.2**		**Long. Int. 3.2**	
	M	***C***	***M***	***C***	***M***	***C***	***M***	***C***
Positive SF	297884	7.57E-05	265857	0.000194	298366	7.57E-05	266127	0.000136
Negative SF	180976	7.57E-05	179504	8.71E-05	187592	7.57E-05	187181	8.71E-05
Normalized Moment Curvature	-1.35	-35	-1.38	-35	-1.35	-35	-1.38	-35
	-1.35	-25	-1.38	-25	-1.35	-25	-1.38	-21
	-1	-1	-1	-1	-1	-1	-1	-1
	-0.7	-0.56	-0.8	-0.56	-0.7	-0.56	-0.8	-0.56
	0	0	0	0	0	0	0	0
	0.936	0.36	0.977	0.45	0.936	0.36	0.977	0.45
	1	1	1	1	1	1	1	1
	1	3	1	3	1	3	1	3
	1	13	1	13	1	13	1	13

Note: M = moment (kip-in.) and C = curvature (1/in.).

	Long. Ext. 4.1		**Long. Int. 4.1**		**Long. Ext. 4.2**		**Long. Int. 4.2**	
	M	***C***	***M***	***C***	***M***	***C***	***M***	***C***
Positive SF	297327	7.47E-05	266825	0.000187	297795	7.47E-05	268404	0.000187
Negative SF	210110	7.47E-05	209302	8.43E-05	214882	7.47E-05	214860	8.43E-05
Normalized Moment Curvature	-1.35	-35	-1.36	-35	-1.35	-35	-1.37	-35
	-1.35	-25	-1.36	-25	-1.35	-25	-1.37	-25
	-1	-1	-1	-1	-1	-1	-1	-1
	-0.7	-0.56	-0.8	-0.56	-0.7	-0.56	-0.8	-0.56
	0	0	0	0	0	0	0	0
	0.936	0.36	0.85	0.14	0.936	0.36	0.85	0.14
	1	1	1	1	1	1	1	1
	1	3	1	3	1	3	1	3
	1	13	1	13	1	13	1	13

	Long. Ext. 5.2		**Long. Int. 5.2**		**Long. Ext. 6.1**		**Long. Int. 6.1**	
	M	***C***	***M***	***C***	***M***	***C***	***M***	***C***
Positive SF	437012	7.92E-05	409104	0.000138	225491	7.18E-05	198753	0.000183
Negative SF	355101	7.92E-05	354835	8.86E-05	127166	7.18E-05	126139	8.25E-05
Normalized Moment Curvature	-1.36	-35	-1.38	-35	-1.36	-35	-1.38	-35
	-1.36	-25	-1.38	-25	-1.36	-25	-1.38	-25
	-1	-1	-1	-1	-1	-1	-1	-1
	-0.7	-0.56	-0.8	-0.56	-0.7	-0.56	-0.8	-0.56
	0	0	0	0	0	0	0	0
	0.936	0.36	0.85	0.14	0.936	0.36	0.88	0.25
	1	1	1	1	1	1	1	1
	1	3	1	3	1	3	1	3
	1	13	1	13	1	13	1	13

Note: M = moment (kip-in.) and C = curvature (1/in.).

	Frac. Ext. 2.1		**Frac. Int. 2.1**		**Frac. Ext. 6.1**		**Frac. Int. 6.1**	
	M	***C***	***M***	***C***	***M***	***C***	***M***	***C***
Positive SF	11389	1.26E-4	1288	3.22E-3	11389	1.26E-4	1288	3.22E-3
Negative SF	2220	5.66E-4	1999	4.60E-4	2220	5.66E-4	1999	4.60E-4
Normalized Moment Curvature	-1	-35	-1	-20	-1	-35	-1	-20
	-1	-20	-1	-10	-1	-20	-1	-10
	-1	-1	-1	-5	-1	-1	-1	-5
	-0.86	-0.22	-1	-1	-0.86	-0.22	-1	-1
	0	0	0	0	0	0	0	0
	1	1	0.93	0.36	1	1	0.93	0.36
	1	3	1	1	1	3	1	1
	1	5	1	5	1	5	1	5
	1	15	1	15	1	15	1	15
	Trans		**Trans End 1**		**Trans End 2**		**Trans Pier**	
	M	***C***	***M***	***C***	***M***	***C***	***M***	***C***
Positive SF	1683	0.00168	1938	0.00168	1810	0.00168	3844	0.00168
Negative SF	1341	0.00168	1546	0.00168	1443	0.00168	3076	0.00168
Normalized Moment Curvature	-1.06	-25	-1.09	-25	-1.09	-25	-1.09	-25
	-1.06	-15	-1.09	-15	-1.09	-15	-1.09	-15
	-1	-1	-1	-1	-1	-1	-1	-1
	-0.76	-0.22	-0.76	-0.22	-0.76	-0.22	-0.76	-0.22
	0	0	0	0	0	0	0	0
	0.76	0.22	0.76	0.22	0.76	0.22	0.76	0.22
	1	1	1	1	1	1	1	1
	1	3	1	3	1	3	1	3
	1	13	1	13	1	13	1	13

Note: M = moment (kip-in.) and C = curvature (1/in.).

Section	**Start (ft)**	**End (ft)**
1.1	0	18.5
2.1	18.5	137.5
3.1	137.5	144.5
3.2	144.5	165.5
4.2	165.5	186.5
5.2	186.5	244
4.2	244	272
4.1	272	286
6.1	286	377
1.1	377	409

Bridge 8: Hinge and Section Data

	Long. Ext. 1.1		**Long. Int. 1.1**		**Long. Ext. 2.1**		**Long. Int. 2.1**	
	M	***C***	***M***	***C***	***M***	***C***	***M***	***C***
Positive SF	370539	5.49E-05	349445	0.000133	403697	5.59E-05	382149	0.000135
Negative SF	233674	5.49E-05	243588	5.98E-05	257589	5.59E-05	267853	6.09E-05
Normalized Moment Curvature	-1.37	-35	-1.37	-35	-1.37	-35	-1.38	-35
	-1.37	-25	-1.37	-25	-1.37	-25	-1.38	-23
	-1	-1	-1	-1	-1	-1	-1	-1
	-0.7	-0.56	-0.8	-0.56	-0.7	-0.56	-0.8	-0.56
	0	0	0	0	0	0	0	0
	0.91	0.56	0.87	0.19	0.915	0.56	0.98	0.7
	1	1	1	1	1	1	1	1
	1	3	1	3	1	3	1	3
	1	13	1	13	1	13	1	13

	Long. Ext. 3.1		**Long. Int. 3.1**		**Long. Ext. 4.2**		**Long. Int. 4.2**	
	M	***C***	***M***	***C***	***M***	***C***	***M***	***C***
Positive SF	466905	5.82E-05	439859	0.000099	435027	5.73E-05	414385	0.000139
Negative SF	287156	5.82E-05	298668	6.36E-05	273090	5.73E-05	289604	6.27E-05
Normalized Moment Curvature	-1.38	-35	-1.39	-35	-1.35	-35	-1.39	-35
	-1.38	-25	-1.39	-25	-1.35	-25	-1.39	-25
	-1	-1	-1	-1	-1	-1	-1	-1
	-0.7	-0.56	-0.8	-0.56	-0.7	-0.56	-0.8	-0.56
	0	0	0	0	0	0	0	0
	0.924	0.56	0.97	0.64	0.936	0.36	0.96	0.45
	1	1	1	1	1	1	1	1
	1	3	1	3	1	3	1	3
	1	13	1	13	1	13	1	13

Note: M = moment (kip-in.) and C = curvature (1/in.).

	Long. Ext. 5.2		**Long. Int. 5.2**		**Long. Ext. 6.2**		**Long. Int. 6.2**	
	M	***C***	***M***	***C***	***M***	***C***	***M***	***C***
Positive SF	471122	5.72E-05	450807	0.000138	538066	5.84E-05	513367	9.83E-05
Negative SF	333928	5.72E-05	348645	6.21E-05	396561	5.84E-05	411494	6.32E-05
Normalized Moment Curvature	-1.37	-35	-1.38	-35	-1.37	-35	-1.38	-35
	-1.37	-25	-1.38	-25	-1.37	-25	-1.38	-25
	-1	-1	-1	-1	-1	-1	-1	-1
	-0.7	-0.56	-0.8	-0.56	-0.7	-0.56	-0.8	-0.56
	0	0	0	0	0	0	0	0
	0.936	0.36	0.85	0.14	0.932	0.56	0.88	0.25
	1	1	1	1	1	1	1	1
	1	3	1	3	1	3	1	3
	1	13	1	13	1	13	1	13

	Long. Ext. 7.1		**Long. Int. 7.1**		**Frac. Ext. 3.1**		**Frac. Int. 3.1**	
	M	***C***	***M***	***C***	***M***	***C***	***M***	***C***
Positive SF	531378	5.93E-05	506462	0.0001	10423	1.04E-4	1636	2.39E-3
Negative SF	356981	5.93E-05	368277	6.45E-05	1661	7.3E-4	2162	5.3E-4
Normalized Moment Curvature	-1.37	-35	-1.39	-35	-1	-35	-1	-20
	-1.37	-25	-1.39	-25	-1	-22	-1	-10
	-1	-1	-1	-1	-1	-1	-1	-5
	-0.7	-0.56	-0.8	-0.56	-0.77	-0.36	-1	-1
	0	0	0	0	0	0	0	0
	0.932	0.56	0.97	0.64	1	1	0.83	0.22
	1	1	1	1	1	3	1	1
	1	3	1	3	1	5	1	5
	1	13	1	13	1	15	1	15

Note: M = moment (kip-in.) and C = curvature (1/in.).

	Frac. Ext. 7.1		**Frac. Int. 7.1**		**Trans/Trans Pier**		**Trans End 1**	
	M	***C***	***M***	***C***	***M***	***C***	***M***	***C***
Positive SF	10423	1.04E-4	1636	2.39E-3	1970	0.00168	857	0.00163
Negative SF	1661	7.3E-4	2162	5.3E-4	1598	0.00168	697	0.00163
Normalized Moment Curvature	-1	-35	-1	-20	-1.09	-30	-1.09	-30
	-1	-22	-1	-10	-1.09	-22	-1.09	-20
	-1	-1	-1	-5	-1	-1	-1	-1
	-0.77	-0.36	-1	-1	-0.76	-0.22	-0.76	-0.22
	0	0	0	0	0	0	0	0
	1	1	0.83	0.22	0.76	0.22	0.76	0.22
	1	3	1	1	1	1	1	1
	1	5	1	5	1	3	1	3
	1	15	1	15	1	13	1	13

	Trans End 2	
	M	***C***
Positive SF	1112	0.00168
Negative SF	900	0.00168
Normalized Moment Curvature	-1.09	-25
	-1.09	-15
	-1	-1
	-0.76	-0.22
	0	0
	0.76	0.22
	1	1
	1	3
	1	13

Note: M = moment (kip-in.) and C = curvature (1/in.).

Section	**Start (ft)**	**End (ft)**
1.1	0	20.5
2.1	20.5	62.5
3.1	62.5	139.5
2.1	139.5	174.5
4.2	174.5	202.5
5.2	202.5	223.5
6.2	223.5	300.5
4.2	300.5	335.5
2.1	335.5	363.5
3.1	363.5	384.5
7.1	384.5	489.5
3.1	489.5	524.5
1.1	524.5	560

Bridge 9: Hinge and Section Data

	Long. Ext. 1.1		**Long. Int. 1.1**		**Long. Ext. 1.2**		**Long. Int. 1.2**	
	M	***C***	***M***	***C***	***M***	***C***	***M***	***C***
Positive SF	207692	7.21E-05	183132	0.000249	207889	7.21E-05	184293	0.000249
Negative SF	119209	7.21E-05	121462	8.29E-05	124631	7.21E-05	127592	8.29E-05
Normalized Moment Curvature	-1.35	-35	-1.37	-35	-1.35	-35	-1.38	-35
	-1.35	-24	-1.37	-23	-1.35	-23	-1.38	-23
	-1	-1	-1	-1	-1	-1	-1	-1
	-0.7	-0.56	-0.8	-0.56	-0.7	-0.56	-0.8	-0.56
	0	0	0	0	0	0	0	0
	0.91	0.56	0.87	0.19	0.92	0.56	0.98	0.52
	1	1	1	1	1	1	1	1
	1	3	1	3	1	3	1	3
	1	13	1	13	1	13	1	13

	Long. Ext. 2.2		**Long. Int. 2.2**		**Long. Ext. 3.2**		**Long. Int. 3.2**	
	M	***C***	***M***	***C***	***M***	***C***	***M***	***C***
Positive SF	236543	7.43E-05	210295	0.000191	270759	7.59E-05	242600	0.000195
Negative SF	137495	7.43E-05	140681	0.000086	168541	7.59E-05	171669	8.78E-05
Normalized Moment Curvature	-1.38	-35	-1.39	-35	-1.35	-35	-1.39	-35
	-1.38	-25	-1.39	-25	-1.35	-25	-1.39	-25
	-1	-1	-1	-1	-1	-1	-1	-1
	-0.7	-0.56	-0.8	-0.56	-0.7	-0.56	-0.8	-0.56
	0	0	0	0	0	0	0	0
	0.93	0.56	0.97	0.64	0.939	0.56	0.96	0.45
	1	1	1	1	1	1	1	1
	1	3	1	3	1	3	1	3
	1	13	1	13	1	13	1	13

Note: M = moment (kip-in.) and C = curvature (1/in.).

	Frac. Ext. 3.1		Frac. Int. 3.1		Trans		Trans Pier 1 & 2	
	M	***C***	***M***	***C***	***M***	***C***	***M***	***C***
Positive SF	10410	1.20E-4	1386	2.45E-3	1970	0.00168	1588	0.00163
Negative SF	1613	8.37E-4	1628	5.45E-4	1598	0.00168	1291	0.00163
Normalized Moment Curvature	-1	-35	-1	-20	-1.09	-30	-1.1	-30
	-1	-22	-1	-10	-1.09	-22	-1.1	-20
	-1	-1	-1	-5	-1	-1	-1	-1
	-0.8	-0.36	-1	-1	-0.76	-0.22	-0.76	-0.22
	0	0	0	0	0	0	0	0
	1	1	0.875	0.22	0.76	0.22	0.76	0.22
	1	3	1	1	1	1	1	1
	1	5	1	5	1	3	1	3
	1	15	1	15	1	13	1	13

	Trans End 1 & 2	
	M	***C***
Positive SF	985	0.00163
Negative SF	799	0.00163
Normalized Moment Curvature	-1.09	-30
	-1.09	-20
	-1	-1
	-0.76	-0.22
	0	0
	0.76	0.22
	1	1
	1	3
	1	13

Note: M = moment (kip-in.) and C = curvature (1/in.).

Section	**Start (ft)**	**End (ft)**
1.1	0	77
1.2	77	91
2.2	91	119
3.2	119	145.5
2.2	145.5	173.5
1.1	173.5	243.5
2.2	243.5	271.5
3.2	271.5	298
2.2	298	326
1.2	326	333
1.1	333	417

Bridge 10: Hinge and Section Data

	Long. Ext. 1.1		**Long. Int. 1.1**		**Long. Ext. 2.2**		**Long. Int. 2.2**	
	M	***C***	***M***	***C***	***M***	***C***	***M***	***C***
Positive SF	217603	9.71E-05	212466	0.000254	278214	0.000103	270328	0.000208
Negative SF	140128	6.24E-05	142863	6.53E-05	179860	0.000066	183001	6.94E-05
Normalized Moment Curvature	-1.36	-35	-1.37	-35	-1.35	-35	-1.38	-35
	-1.36	-24	-1.37	-23	-1.35	-23	-1.38	-23
	-1	-1	-1	-1	-1	-1	-1	-1
	-0.7	-0.56	-0.8	-0.56	-0.7	-0.56	-0.8	-0.56
	0	0	0	0	0	0	0	0
	0.966	0.64	0.84	0.14	0.92	0.56	0.98	0.52
	1	1	1	1	1	1	1	1
	1	3	1	3	1	3	1	3
	1	13	1	13	1	13	1	13

	Long. Ext. 3.1		**Long. Int. 3.1**		**Long. Ext. 3.2**		**Long. Int. 3.2**	
	M	***C***	***M***	***C***	***M***	***C***	***M***	***C***
Positive SF	296612	0.000104	286104	0.000157	298104	0.000104	288148	0.000157
Negative SF	178276	6.71E-05	181632	7.05E-05	188232	6.71E-05	191464	7.05E-05
Normalized Moment Curvature	-1.38	-35	-1.39	-35	-1.37	-35	-1.39	-35
	-1.38	-25	-1.39	-25	-1.37	-25	-1.39	-25
	-1	-1	-1	-1	-1	-1	-1	-1
	-0.7	-0.56	-0.8	-0.56	-0.7	-0.56	-0.8	-0.56
	0	0	0	0	0	0	0	0
	0.97	0.64	0.97	0.64	0.885	0.36	0.96	0.45
	1	1	1	1	1	1	1	1
	1	3	1	3	1	3	1	3
	1	13	1	13	1	13	1	13

Note: M = moment (kip-in.) and C = curvature (1/in.).

	Long. Ext. 4.2		Long. Int. 4.2		Long. Ext. 5.2		Long. Int. 5.2	
	M	***C***	***M***	***C***	***M***	***C***	***M***	***C***
Positive SF	384584	0.000108	375509	0.000113	392385	0.000105	383816	0.000156
Negative SF	281405	6.95E-05	284502	7.28E-05	320221	6.73E-05	322860	7.01E-05
Normalized Moment Curvature	-1.37	-35	-1.39	-35	-1.38	-35	-1.39	-35
	-1.37	-25	-1.39	-23	-1.38	-25	-1.39	-23
	-1	-1	-1	-1	-1	-1	-1	-1
	-0.7	-0.56	-0.8	-0.56	-0.7	-0.56	-0.8	-0.56
	0	0	0	0	0	0	0	0
	0.885	0.36	0.96	0.45	0.885	0.36	0.96	0.45
	1	1	1	1	1	1	1	1
	1	3	1	3	1	3	1	3
	1	13	1	13	1	13	1	13

	Long. Ext. 6.2		Long. Int. 6.2		Long. Ext. 7.2		Long. Int. 7.2	
	M	***C***	***M***	***C***	***M***	***C***	***M***	***C***
Positive SF	409398	0.000106	402775	0.000158	40078	0.000109	393203	0.00115
Negative SF	331376	6.81E-05	333892	7.09E-05	289823	7.03E-05	293010	7.36E-05
Normalized Moment Curvature	-1.38	-35	-1.38	-35	-1.38	-35	-1.38	-35
	-1.38	-25	-1.38	-23	-1.38	-23	-1.38	-23
	-1	-1	-1	-1	-1	-1	-1	-1
	-0.7	-0.56	-0.8	-0.56	-0.7	-0.56	-0.8	-0.56
	0	0	0	0	0	0	0	0
	0.885	0.36	0.96	0.45	0.919	0.36	0.96	0.45
	1	1	1	1	1	1	1	1
	1	3	1	3	1	3	1	3
	1	13	1	13	1	13	1	13

Note: M = moment (kip-in.) and C = curvature (1/in.).

	Long. Ext. 8.1		**Long. Int. 8.1**		**Long. Ext. 8.2**		**Long. Int. 8.2**	
	M	***C***	***M***	***C***	***M***	***C***	***M***	***C***
Positive SF	311592	0.000106	300765	0.000111	314537	0.000106	306241	0.000159
Negative SF	186784	6.81E-05	190210	7.15E-05	196656	6.81E-05	199977	7.15E-05
Normalized Moment Curvature	-1.38	-35	-1.38	-35	-1.38	-35	-1.38	-35
	-1.38	-23	-1.38	-23	-1.38	-23	-1.38	-23
	-1	-1	-1	-1	-1	-1	-1	-1
	-0.7	-0.56	-0.8	-0.56	-0.7	-0.56	-0.8	-0.56
	0	0	0	0	0	0	0	0
	0.88	0.36	0.96	0.45	0.88	0.36	0.977	0.64
	1	1	1	1	1	1	1	1
	1	3	1	3	1	3	1	3
	1	13	1	13	1	13	1	13

	Long. Ext. 9.1		**Long. Int. 9.1**		**Long. Ext. 10.1**		**Long. Int. 10.1**	
	M	***C***	***M***	***C***	***M***	***C***	***M***	***C***
Positive SF	286913	0.000103	276390	0.000155	267679	0.000102	257893	0.000152
Negative SF	172623	6.64E-05	175858	6.96E-05	164251	6.53E-05	167380	6.85E-05
Normalized Moment Curvature	-1.38	-35	-1.38	-35	-1.38	-35	-1.38	-35
	-1.38	-23	-1.38	-23	-1.38	-23	-1.38	-23
	-1	-1	-1	-1	-1	-1	-1	-1
	-0.7	-0.56	-0.8	-0.56	-0.7	-0.56	-0.8	-0.56
	0	0	0	0	0	0	0	0
	0.88	0.36	0.955	0.45	0.87	0.36	0.955	0.45
	1	1	1	1	1	1	1	1
	1	3	1	3	1	3	1	3
	1	13	1	13	1	13	1	13

Note: M = moment (kip-in.) and C = curvature (1/in.).

	Long. Ext. 11.2		**Long. Int. 11.2**		**Long. Ext. 12.2**		**Long. Int. 12.2**	
	M	***C***	***M***	***C***	***M***	***C***	***M***	***C***
Positive SF	321647	0.000103	312965	0.000207	462765	0.00011	460216	0.000164
Negative SF	238811	6.06E-05	241427	6.89E-05	368211	7.05E-05	371099	7.36E-05
Normalized Moment Curvature	-1.38	-35	-1.38	-35	-1.38	-35	-1.38	-35
	-1.38	-23	-1.38	-23	-1.38	-23	-1.38	-23
	-1	-1	-1	-1	-1	-1	-1	-1
	-0.7	-0.56	-0.8	-0.56	-0.7	-0.56	-0.8	-0.56
	0	0	0	0	0	0	0	0
	0.87	0.36	0.955	0.45	0.93	0.36	0.955	0.45
	1	1	1	1	1	1	1	1
	1	3	1	3	1	3	1	3
	1	13	1	13	1	13	1	13

	Frac. Ext. 1.1		**Frac. Int. 1.1**		**Frac. Ext. 2.2**		**Frac. Int. 2.2**	
	M	***C***	***M***	***C***	***M***	***C***	***M***	***C***
Positive SF	4870	2.69E-4	1288	3.14E-3	7056	2.69E-4	1597	2.02E-3
Negative SF	1882	6.73E-4	1963	4.48E-4	2966	6.73E-4	2950	4.48E-4
Normalized Moment Curvature	-1	-35	-1	-20	-1	-35	-1	-20
	-1	-20	-1	-10	-1	-20	-1	-10
	-1	-1	-1	-3	-1	-1	-1	-5
	-0.86	-0.4	-1	-1	-0.7	-0.4	-1	-1
	0	0	0	0	0	0	0	0
	1	1	0.93	0.36	1	1	0.88	0.56
	1	3	1	1	1	3	1	1
	1	5	1	5	1	5	1	5
	1	15	1	15	1	15	1	15

Note: M = moment (kip-in.) and C = curvature (1/in.).

	Frac. Ext. 3.1		**Frac. Int. 3.1**		**Trans**		**Trans End 1 & 2**	
	M	***C***	***M***	***C***	***M***	***C***	***M***	***C***
Positive SF	4870	2.69E-4	1288	3.14E-3	1683	0.00163	1810	0.00163
Negative SF	1882	6.73E-4	1963	4.48E-4	1341	0.00163	1443	0.00163
Normalized Moment Curvature	-1	-35	-1	-20	-1.09	-30	-1.09	-30
	-1	-20	-1	-10	-1.09	-22	-1.09	-20
	-1	-1	-1	-3	-1	-1	-1	-1
	-0.86	-0.4	-1	-1	-0.76	-0.22	-0.76	-0.22
	0	0	0	0	0	0	0	0
	1	1	0.93	0.36	0.76	0.22	0.76	0.22
	1	3	1	1	1	1	1	1
	1	5	1	5	1	3	1	3
	1	15	1	15	1	13	1	13

	Trans Pier 1 & 2	
	M	***C***
Positive SF	2573	0.00168
Negative SF	2056	0.00168
Normalized Moment Curvature	-1.1	-30
	-1.1	-20
	-1	-1
	-0.76	-0.22
	0	0
	0.76	0.22
	1	1
	1	3
	1	13

Note: M = moment (kip-in.) and C = curvature (1/in.).

Section	**Start (ft)**	**End (ft)**
1.1	0	53
2.2	53	95
3.2	95	102
4.2	102	116
5.2	116	123
6.2	123	161.5
7.2	161.5	175.5
8.2	175.5	210.5
9.1	210.5	217.5
10.1	217.5	238.5
3.1	238.5	294.5
10.1	294.5	315.5
9.1	315.5	322.5
8.1	322.5	343.5
8.2	343.5	364.5
11.1	364.5	378.5
6.2	378.5	399.5
12.2	399.5	424
6.2	424	438
11.2	438	459
3.2	459	494
1.1	494	603

Bridge 11: Hinge and Section Data

	Long. Ext. 1.1		**Long. Int. 1.1**		**Long. Ext. 1.2**		**Long. Int. 1.2**	
	M	***C***	***M***	***C***	***M***	***C***	***M***	***C***
Positive SF	447209	5.19E-05	408675	9.05E-05	448318	5.19E-05	411855	9.05E-05
Negative SF	247199	5.19E-05	250474	5.82E-05	255876	5.19E-05	259154	5.82E-05
Normalized Moment Curvature	-1.38	-35	-1.39	-35	-1.38	-35	-1.38	-35
	-1.38	-24	-1.39	-23	-1.38	-23	-1.38	-23
	-1	-1	-1	-1	-1	-1	-1	-1
	-0.7	-0.56	-0.8	-0.56	-0.7	-0.56	-0.8	-0.56
	0	0	0	0	0	0	0	0
	0.91	0.56	0.86	0.36	0.9	0.56	0.96	0.64
	1	1	1	1	1	1	1	1
	1	3	1	3	1	3	1	3
	1	13	1	13	1	13	1	13
	Long. Ext. 2.2		**Long. Int. 2.2**		**Long. Ext. 3.2**		**Long. Int. 3.2**	
	M	***C***	***M***	***C***	***M***	***C***	***M***	***C***
Positive SF	530622	5.46E-05	472660	6.18E-05	539602	5.22E-05	508662	8.94E-05
Negative SF	293839	5.46E-05	296990	6.18E-05	387820	5.22E-05	390551	5.75E-05
Normalized Moment Curvature	-1.38	-35	-1.37	-35	-1.37	-35	-1.39	-35
	-1.38	-23	-1.37	-21	-1.37	-23	-1.39	-25
	-1	-1	-1	-1	-1	-1	-1	-1
	-0.7	-0.56	-0.8	-0.56	-0.7	-0.56	-0.8	-0.56
	0	0	0	0	0	0	0	0
	0.92	0.56	0.91	0.56	0.92	0.56	0.96	0.45
	1	1	1	1	1	1	1	1
	1	3	1	3	1	3	1	3
	1	13	1	13	1	13	1	13

Note: M = moment (kip-in.) and C = curvature (1/in.).

	Long. Ext. 4.2		**Long. Int. 4.2**		**Long. Ext. 5.1**		**Long. Int. 5.1**	
	M	***C***	***M***	***C***	***M***	***C***	***M***	***C***
Positive SF	802228	5.61E-05	774300	9.56E-05	535682	5.36E-05	494752	9.34E-05
Negative SF	624428	5.61E-05	626681	6.14E-05	326054	5.36E-05	329068	0.00006
Normalized Moment Curvature	-1.37	-35	-1.4	-35	-1.37	-35	-1.36	-35
	-1.37	-23	-1.4	-23	-1.37	-23	-1.36	-23
	-1	-1	-1	-1	-1	-1	-1	-1
	-0.7	-0.56	-0.8	-0.56	-0.7	-0.56	-0.8	-0.56
	0	0	0	0	0	0	0	0
	0.92	0.56	0.977	0.64	0.92	0.56	0.977	0.64
	1	1	1	1	1	1	1	1
	1	3	1	3	1	3	1	3
	1	13	1	13	1	13	1	13

	Long. Ext. 5.2		**Long. Int. 5.2**		**Long. Ext. 6.1**		**Long. Int. 6.1**	
	M	***C***	***M***	***C***	***M***	***C***	***M***	***C***
Positive SF	537206	5.36E-05	498665	9.34E-05	539611	0.000053	503906	9.17E-05
Negative SF	335055	5.36E-05	338073	0.00006	351542	0.000053	354478	0.000059
Normalized Moment Curvature	-1.37	-35	-1.39	-35	-1.37	-35	-1.39	-35
	-1.37	-23	-1.39	-23	-1.37	-23	-1.39	-23
	-1	-1	-1	-1	-1	-1	-1	-1
	-0.7	-0.56	-0.8	-0.56	-0.7	-0.56	-0.8	-0.56
	0	0	0	0	0	0	0	0
	0.92	0.56	0.977	0.64	0.92	0.56	0.977	0.64
	1	1	1	1	1	1	1	1
	1	3	1	3	1	3	1	3
	1	13	1	13	1	13	1	13

Note: M = moment (kip-in.) and C = curvature (1/in.).

	Frac. Ext. 1.2		Frac. Int. 1.2		Frac. Ext. 6.1		Frac. Int. 6.1	
	M	***C***	***M***	***C***	***M***	***C***	***M***	***C***
Positive SF	15220	1.09E-4	1584	2.29E-3	11569	1.09E-4	1347	2.29E-3
Negative SF	2476	4.91E-4	2458	5.09E-4	1859	4.91E-4	1799	5.09E-4
Normalized Moment Curvature	-1	-35	-1	-20	-1	-35	-1	-20
	-1	-22	-1	-11	-1	-22	-1	-10
	-1	-1	-1	-5	-1	-1	-1	-5
	-0.7	-0.22	-1	-1	-0.88	-0.22	-1	-1
	0	0	0	0	0	0	0	0
	1	1	0.93	0.56	1	1	0.87	0.22
	1	3	1	1	1	3	1	1
	1	5	1	5	1	5	1	5
	1	15	1	15	1	15	1	15

	Trans		Trans End 1		Trans End 2		Trans Pier 1	
	M	***C***	***M***	***C***	***M***	***C***	***M***	***C***
Positive SF	1683	0.00168	663	0.00168	407	0.00168	1810	0.00168
Negative SF	1341	0.00168	524	0.00168	319	0.00168	1443	0.00168
Normalized Moment Curvature	-1.06	-30	-1.09	-30	-1.09	-30	-1.1	-30
	-1.06	-22	-1.09	-20	-1.09	-20	-1.1	-20
	-1	-1	-1	-1	-1	-1	-1	-1
	-0.76	-0.22	-0.76	-0.22	-0.76	-0.22	-0.76	-0.22
	0	0	0	0	0	0	0	0
	0.76	0.22	0.76	0.22	0.76	0.22	0.76	0.22
	1	1	1	1	1	1	1	1
	1	3	1	3	1	3	1	3
	1	13	1	13	1	13	1	13

Note: M = moment (kip-in.) and C = curvature (1/in.).

	Trans Pier 2	
	M	***C***
Positive SF	1556	0.00168
Negative SF	1239	0.00168
Normalized Moment Curvature	-1.05	-30
	-1.05	-22
	-1	-1
	-0.76	-0.22
	0	0
	0.76	0.22
	1	1
	1	3
	1	13

Note: M = moment (kip-in.) and C = curvature (1/in.).

Section	**Start (ft)**	**End (ft)**
1.1	0	62.5
1.2	62.5	118.5
2.2	118.5	153.5
3.2	153.5	167.5
4.2	167.5	245
3.2	245	280
5.2	280	315
5.1	315	336
6.1	336	462
5.1	462	490
5.2	490	518
3.2	518	553
4.2	553	629.5
3.2	629.5	650.5
2.2	650.5	678.5
1.2	678.5	734.5
1.1	734.5	824

Bridge 12: Hinge and Section Data

	Long. Ext. 1.1		**Long. Int. 1.1**		**Long. Ext. 2.2**		**Long. Int. 2.2**	
	M	***C***	***M***	***C***	***M***	***C***	***M***	***C***
Positive SF	177808	8.01E-05	150041	0.000279	265809	4.91E-05	242338	0.00016
Negative SF	91919	8.01E-05	95191	9.29E-05	148519	8.83E-05	152662	0.000103
Normalized Moment Curvature	-1.38	-35	-1.36	-35	-1.39	-35	-1.38	-35
	-1.38	-24	-1.36	-23	-1.39	-21	-1.38	-19
	-1	-1	-1	-1	-1	-1	-1	-1
	-0.7	-0.56	-0.8	-0.56	-0.7	-0.56	-0.8	-0.56
	0	0	0	0	0	0	0	0
	0.93	0.56	0.89	0.19	0.54	0.4	0.91	0.56
	1	1	1	1	1	1	1	1
	1	3	1	3	1	3	1	3
	1	13	1	13	1	13	1	13

	Long. Ext. 3.2		**Long. Int. 3.2**		**Frac. Ext. 1.1**		**Frac. Int. 1.1**	
	M	***C***	***M***	***C***	***M***	***C***	***M***	***C***
Positive SF	271522	8.54E-05	249832	0.000216	9162	1.04E-4	1291	3.40E-3
Negative SF	206366	8.54E-05	208809	9.71E-05	1456	1.04E-4	1448	4.86E-4
Normalized Moment Curvature	-1.35	-35	-1.37	-35	-1	-35	-1	-20
	-1.35	-23	-1.37	-23	-1	-22	-1	-11
	-1	-1	-1	-1	-1	-5	-1	-5
	-0.7	-0.56	-0.8	-0.56	-1	-1	-1	-1
	0	0	0	0	0	0	0	0
	0.92	0.56	0.96	0.45	1	1	0.86	0.14
	1	1	1	1	1	3	1	1
	1	3	1	3	1	5	1	5
	1	13	1	13	1	15	1	15

Note: M = moment (kip-in.) and C = curvature (1/in.).

	Trans		**Trans End 1**		**Trans End 2**		**Trans Pier 1**		**Trans Pier 2**	
	M	***C***	***M***	***C***	***M***	***C***	***M***	***C***	***M***	***C***
Positive SF	2107	0.00152	1053	0.00152	1836	0.00152	1836	0.00152	2618	0.00152
Negative SF	1745	0.00152	872	0.00152	1522	0.00152	1522	0.00152	2172	0.00152
Normalized Moment Curvature	-1.12	-30	-1.12	-30	-1.13	-30	-1.13	-30	-1.13	-30
	-1.12	-22	-1.12	-21	-1.13	-21	-1.13	-21	-1.13	-21
	-1	-1	-1	-1	-1	-1	-1	-1	-1	-1
	-0.76	-0.22	-0.76	-0.22	-0.76	-0.22	-0.76	-0.22	-0.76	-0.22
	0	0	0	0	0	0	0	0	0	0
	0.76	0.22	0.76	0.22	0.76	0.22	0.76	0.22	0.76	0.22
	1	1	1	1	1	1	1	1	1	1
	1	3	1	3	1	3	1	3	1	3
	1	13	1	13	1	13	1	13	1	13

Note: M = moment (kip-in.) and C = curvature (1/in.).

Section	**Start (ft)**	**End (ft)**
1.1	0	84
2.2	84	112
3.2	112	153
2.2	153	181
1.1	181	258
2.2	258	286
3.2	286	336.5
2.2	336.5	364.5
1.1	364.5	465

Bridge 13: Hinge and Section Data

	Long. Ext. 1.1		**Long. Int. 1.1**		**Long. Ext. 2.1**		**Long. Int. 2.1**	
	M	***C***	***M***	***C***	***M***	***C***	***M***	***C***
Positive SF	141226	0.000132	137479	0.000344	131426	0.00013	127379	0.000338
Negative SF	94747	0.000085	96545	8.84E-05	89122	8.37E-05	90702	0.000087
Normalized Moment Curvature	-1.38	-35	-1.38	-35	-1.39	-35	-1.4	-35
	-1.38	-24	-1.38	-23	-1.39	-23	-1.4	-23
	-1	-1	-1	-1	-1	-1	-1	-1
	-0.7	-0.56	-0.8	-0.56	-0.7	-0.56	-0.8	-0.56
	0	0	0	0	0	0	0	0
	0.97	0.64	0.89	0.19	0.88	0.36	0.91	0.56
	1	1	1	1	1	1	1	1
	1	3	1	3	1	3	1	3
	1	13	1	13	1	13	1	13

	Long. Ext. 3.2		**Long. Int. 3.2**		**Long. Ext. 4.2**		**Long. Int. 4.2**	
	M	***C***	***M***	***C***	***M***	***C***	***M***	***C***
Positive SF	183037	0.000141	181343	0.000282	206928	9.14E-05	204910	0.000285
Negative SF	127072	9.04E-05	130833	9.41E-05	154578	9.14E-05	158006	0.000095
Normalized Moment Curvature	-1.36	-35	-1.37	-35	-1.36	-35	-1.37	-35
	-1.36	-23	-1.37	-23	-1.36	-23	-1.37	-23
	-1	-1	-1	-1	-1	-1	-1	-1
	-0.7	-0.56	-0.8	-0.56	-0.8	-0.56	-0.83	-0.56
	0	0	0	0	0	0	0	0
	0.93	0.36	0.97	0.52	0.93	0.56	0.96	0.33
	1	1	1	1	1	1	1	1
	1	3	1	3	1	3	1	3
	1	13	1	13	1	13	1	13

Note: M = moment (kip-in.) and C = curvature (1/in.).

	Long. Ext. 5.2		**Long. Int. 5.2**		**Frac. Ext. 2.1**		**Frac. Int. 2.1**	
	M	***C***	***M***	***C***	***M***	***C***	***M***	***C***
Positive SF	255210	9.29E-05	251558	0.000214	4670	2.45E-4	1313	3.58E-3
Negative SF	206924	9.29E-05	209171	9.61E-05	1517	1.10E-4	1654	5.11E-4
Normalized Moment Curvature	-1.36	-35	-1.39	-35	-1	-35	-1	-20
	-1.36	-23	-1.39	-23	-1	-18	-1	-10
	-1	-1	-1	-1	-1	-1	-1	-5
	-0.85	-0.56	-0.83	-0.56	-0.84	-0.22	-1	-1
	0	0	0	0	0	0	0	0
	0.95	0.56	0.97	0.45	1	1	0.95	0.36
	1	1	1	1	1	3	1	1
	1	3	1	3	1	5	1	5
	1	13	1	13	1	15	1	15

	Trans		**Trans End 1 & 2**		**Trans Pier 1 & 2**	
	M	***C***	***M***	***C***	***M***	***C***
Positive SF	1683	0.00168	523	0.00168	2430	0.00168
Negative SF	1341	0.00168	415	0.00168	1946	0.00168
Normalized Moment Curvature	-1.06	-30	-1.05	-30	-1.06	-30
	-1.06	-22	-1.05	-21	-1.06	-21
	-1	-1	-1	-1	-1	-1
	-0.76	-0.22	-0.76	-0.22	-0.76	-0.22
	0	0	0	0	0	0
	0.76	0.22	0.76	0.22	0.76	0.22
	1	1	1	1	1	1
	1	3	1	3	1	3
	1	13	1	13	1	13

Note: M = moment (kip-in.) and C = curvature (1/in.).

Section	**Start (ft)**	**End (ft)**
1.1	0	12.75
2.1	12.75	89.75
1.1	89.75	96.75
3.2	96.75	124.75
4.2	124.75	131.75
5.2	131.75	162.5
4.2	162.5	169.5
3.2	169.5	197.5
1.1	197.5	204.5
2.1	204.5	281.5
1.1	281.5	288.5
3.2	295.5	316.5
4.2	316.5	323.5
5.2	323.5	354.5
4.2	354.5	361.25
3.2	361.5	389.25
1.1	389.25	396.25
2.1	396.25	473.25
1.1	473.25	439

Bridge 14: Hinge and Section Data

	Long. Ext. 1.1		**Long. Int. 1.1**		**Long. Ext. 2.1**		**Long. Int. 2.1**	
	M	***C***	***M***	***C***	***M***	***C***	***M***	***C***
Positive SF	173059	0.000077	141867	0.000273	212111	8.09E-05	179280	0.000215
Negative SF	92595	0.000077	95620	9.09E-05	105407	8.09E-05	111621	9.69E-05
Normalized Moment Curvature	-1.34	-35	-1.36	-35	-1.39	-35	-1.35	-35
	-1.34	-23	-1.36	-23	-1.39	-23	-1.35	-21
	-1	-1	-1	-1	-1	-1	-1	-1
	-0.7	-0.56	-0.8	-0.56	-0.7	-0.56	-0.8	-0.56
	0	0	0	0	0	0	0	0
	0.92	0.56	0.87	0.19	0.95	0.56	0.91	0.25
	1	1	1	1	1	1	1	1
	1	3	1	3	1	3	1	3
	1	13	1	13	1	13	1	13
	Long. Ext. 3.2		**Long. Int. 3.2**		**Long. Ext. 4.2**		**Long. Int. 4.2**	
	M	***C***	***M***	***C***	***M***	***C***	***M***	***C***
Positive SF	216831	8.15E-05	185714	0.000271	250576	8.53E-05	222027	0.000161
Negative SF	117869	8.15E-05	122621	9.75E-05	123737	8.53E-05	131276	0.000103
Normalized Moment Curvature	-1.36	-35	-1.37	-35	-1.39	-35	-1.37	-35
	-1.36	-23	-1.37	-23	-1.39	-21	-1.37	-19
	-1	-1	-1	-1	-1	-1	-1	-1
	-0.7	-0.56	-0.8	-0.56	-0.8	-0.56	-0.83	-0.56
	0	0	0	0	0	0	0	0
	0.95	0.56	0.97	0.45	0.98	0.56	0.96	0.33
	1	1	1	1	1	1	1	1
	1	3	1	3	1	3	1	3
	1	13	1	13	1	13	1	13

Note: M = moment (kip-in.) and C = curvature (1/in.).

	Long. Ext. 5.2		**Long. Int. 5.2**		**Frac. Ext. 1.1**		**Frac. Int. 1.1**	
	M	***C***	***M***	***C***	***M***	***C***	***M***	***C***
Positive SF	254768	8.39E-05	226322	0.000221	9168	1.04E-4	1220	2.28E-3
Negative SF	162599	8.39E-05	166674	9.96E-05	1539	1.04E-4	1522	5.06E-4
Normalized Moment Curvature	-1.35	-35	-1.38	-35	-1	-35	-1	-20
	-1.35	-23	-1.38	-23	-1	-23	-1	-10
	-1	-1	-1	-1	-1	-5	-1	-5
	-0.85	-0.56	-0.83	-0.56	-1	-1	-1	-1
	0	0	0	0	0	0	0	0
	0.98	0.56	0.97	0.45	1	1	0.88	0.22
	1	1	1	1	1	3	1	1
	1	3	1	3	1	5	1	5
	1	13	1	13	1	15	1	15

	Trans		**Trans End 1 & 2**		**Trans Pier 1 & 2**	
	M	***C***	***M***	***C***	***M***	***C***
Positive SF	1683	0.00168	297	0.002611	2192	0.00168
Negative SF	1341	0.00168	216	0.00168	1750	0.00168
Normalized Moment Curvature	-1.06	-30	-1	-30	-1.06	-30
	-1.06	-22	-1	-21	-1.06	-21
	-1	-1	-1	-1	-1	-1
	-0.76	-0.22	-0.76	-0.22	-0.76	-0.22
	0	0	0	0	0	0
	0.76	0.22	0.77	0.14	0.76	0.22
	1	1	1	1	1	1
	1	3	1	3	1	3
	1	13	1	13	1	13

Note: M = moment (kip-in.) and C = curvature (1/in.).

Bridge 15: Hinge and Section Data

	Long. Ext. 1.1		**Long. Int. 1.1**		**Long. Ext. 1.2**		**Long. Int. 1.2**	
	M	***C***	***M***	***C***	***M***	***C***	***M***	***C***
Positive SF	323409	5.78E-05	293107	0.000147	323958	5.78E-05	295102	0.000147
Negative SF	203763	5.78E-05	207149	6.61E-05	212854	5.78E-05	216195	6.61E-05
Normalized Moment Curvature	-1.36	-35	-1.38	-35	-1.36	-35	-1.38	-35
	-1.36	-23	-1.38	-23	-1.36	-23	-1.38	-23
	-1	-1	-1	-1	-1	-1	-1	-1
	-0.7	-0.56	-0.8	-0.56	-0.7	-0.56	-0.8	-0.56
	0	0	0	0	0	0	0	0
	0.91	0.56	0.87	0.19	0.91	0.56	0.87	0.19
	1	1	1	1	1	1	1	1
	1	3	1	3	1	3	1	3
	1	13	1	13	1	13	1	13

	Long. Ext. 2.1		**Long. Int. 2.1**		**Long. Ext. 2.2**		**Long. Int. 2.2**	
	M	***C***	***M***	***C***	***M***	***C***	***M***	***C***
Positive SF	384229	5.99E-05	350980	0.000153	385000	5.99E-05	350195	0.000107
Negative SF	246757	5.99E-05	250145	6.88E-05	256878	5.99E-05	260221	6.88E-05
Normalized Moment Curvature	-1.36	-35	-1.38	-35	-1.36	-35	-1.38	-35
	-1.36	-23	-1.38	-23	-1.36	-23	-1.38	-23
	-1	-1	-1	-1	-1	-1	-1	-1
	-0.7	-0.56	-0.8	-0.56	-0.7	-0.56	-0.8	-0.56
	0	0	0	0	0	0	0	0
	0.95	0.56	0.91	0.25	0.95	0.56	0.91	0.25
	1	1	1	1	1	1	1	1
	1	3	1	3	1	3	1	3
	1	13	1	13	1	13	1	13

Note: M = moment (kip-in.) and C = curvature (1/in.).

	Long. Ext. 3.2		**Long. Int. 3.2**		**Long. Ext. 4.2**		**Long. Int. 4.2**	
	M	***C***	***M***	***C***	***M***	***C***	***M***	***C***
Positive SF	415986	6.06E-05	383112	0.000155	448197	0.000061	411657	0.000108
Negative SF	285021	6.06E-05	288302	6.96E-05	326085	0.000061	329189	6.95E-05
Normalized Moment Curvature	-1.36	-35	-1.38	-35	-1.37	-35	-1.39	-35
	-1.36	-23	-1.38	-23	-1.37	-23	-1.39	-23
	-1	-1	-1	-1	-1	-1	-1	-1
	-0.7	-0.56	-0.8	-0.56	-0.8	-0.56	-0.83	-0.56
	0	0	0	0	0	0	0	0
	0.95	0.56	0.97	0.45	0.98	0.56	0.96	0.33
	1	1	1	1	1	1	1	1
	1	3	1	3	1	3	1	3
	1	13	1	13	1	13	1	13

	Long. Ext. 5.2		**Long. Int. 5.2**		**Frac. Ext. 1.1**		**Frac. Int. 1.1**	
	M	***C***	***M***	***C***	***M***	***C***	***M***	***C***
Positive SF	582446	4.79E-05	550752	9.82E-05	12087	1.15E-4	1347	2.12E-3
Negative SF	469228	8.62E-05	471302	9.82E-05	2126	8.06E-4	2067	4.72E-4
Normalized Moment Curvature	-1.24	-35	-1.25	-35	-1	-35	-1	-20
	-1.24	-19	-1.25	-17	-1	-23	-1	-10
	-1	-1	-1	-1	-1	-1	-1	-5
	-0.85	-0.56	-0.96	-0.56	-0.78	-0.36	-1	-1
	0	0	0	0	0	0	0	0
	0.55	0.4	0.96	0.56	1	1	0.77	0.22
	1	1	1	1	1	3	1	1
	1	3	1	3	1	5	1	5
	1	13	1	13	1	15	1	15

Note: M = moment (kip-in.) and C = curvature (1/in.).

	Frac. Ext. 2.1		**Frac. Int. 2.1**		**Trans**		**Trans End 1 & 2**	
	M	***C***	***M***	***C***	***M***	***C***	***M***	***C***
Positive SF	12087	1.15E-4	1347	2.12E-3	1970	0.00168	1588	0.00168
Negative SF	2126	8.06E-4	2067	4.72E-4	1598	0.00168	1291	0.00168
Normalized Moment Curvature	-1	-35	-1	-20	-1.06	-30	-1.11	-30
	-1	-23	-1	-10	-1.06	-22	-1.11	-22
	-1	-1	-1	-5	-1	-1	-1	-1
	-0.78	-0.36	-1	-1	-0.76	-0.22	-0.76	-0.22
	0	0	0	0	0	0	0	0
	1	1	0.77	0.22	0.76	0.22	0.77	0.14
	1	3	1	1	1	1	1	1
	1	5	1	5	1	3	1	3
	1	15	1	15	1	13	1	13

	Trans Pier 1 & 2	
	M	***C***
Positive SF	2701	0.00168
Negative SF	2193	0.00168
Normalized Moment Curvature	-1.09	-30
	-1.09	-21
	-1	-1
	-0.76	-0.22
	0	0
	0.76	0.22
	1	1
	1	3
	1	13

Note: M = moment (kip-in.) and C = curvature (1/in.).

Section	**Start (ft)**	**End (ft)**
1.1	0	100
2.1	100	114
2.2	114	135
3.2	135	156
4.2	156	177
5.2	177	207.5
4.2	207.5	228.5
3.2	228.5	249.5
1.2	249.5	256.5
1.1	256.5	277.5
2.1	277.5	410.5
1.1	410.5	424.5
1.2	424.5	431.5
3.2	431.5	452.5
4.2	452.5	473.5
5.2	473.5	504
4.2	504	525
3.2	525	546
2.2	546	567
1.1	567	695